634

ARKIV FÖR FYSIK

UTGIVET AV

K. SVENSKA VETENSKAPSAKADEMIEN

Band 4

Med 42 avhandlingar

STOCKHOLM
ALMQVIST & WIKSELLS BOKTRYCKERI AB

LONDON
H. K. LEWIS & CO., LTD
136, GOWER STREET

1952

PARIS
LIBRAIRIE C. KLINCKSIECK
11 RUE DE LILLE

Häfte	1—2	innehållande	Nr	1— 4	utkom	den	14	aug.	1952
»	3	»	Nr	5—11	»	»	15	»	1952
»	4	»	Nr	12—19	»	»	16	»	1952
»	5	»	Nr	20—31	»	»	18	»	1952
»	6	»	Nr	32—42	»	»	19	»	1952

FJÄRDE BANDETS INNEHÅLL

Sid.

1. LINDSTRÖM, G., Nuclear resonance absorption applied to precise measurements of nuclear magnetic moments and the establishment of an absolute energy scale in β-spectroscopy .... 1—80
2. KONDAIAH, E., Some nuclear disintegrations and the nuclear shell theory.... 81—158
3. REUTERSWÄRD, C., Two-directional focusing with short uniform magnetic fields 159—171
4. BORELIUS, G. and BERGLUND, S., Calorimetric study of the precipitation of carbon dissolved in α-iron .... 173—182
5. WALLER, I. and FRÖMAN, P. O., On neutron diffraction phenomena according to the kinematical theory. I .... 183—189
6. FRÖMAN, P. O., On neutron diffraction phenomena according to the kinematical theory. II .... 191—202
7. REUTERSWÄRD, C., The isotopic abundance of K^{40} .... 203—205
8. SKÖLDBORN, H., Determination of the self-absorption and relative efficiency of some important liquid scintillators .... 207—215
9. OLSSON, P. O., A differential equation for the phase shifts in scattering problems 217—221
10. SIEGBAHN, K., A β-spectro-goniometer for coincidence and angular correlation measurements .... 223—271
11. JOHANSSON, S., The disintegration of As^{73} .... 273—285
12. MILEIKOWSKY, C. and PAULI, R. T., A 1.5 MV accelerator for heavy particles with analyzing magnet for use in nuclear research .... 287—298
13. MILEIKOWSKY, C. and PAULI, R. T., Some investigations of (p, α) reactions on thin separated O^{18} and N^{15} targets. Techniques and results........ 299—322
14. HJALMAR, E. and SLÄTIS, H., Q-values for (αp)-reactions on fluorine and sodium 323—329
15. FORSLING, W. and GHOSH, A., On the non-existence of a long-lived isomer of Ti^{51} .... 331—336
16. MILEIKOWSKY, C., A nuclear spectrometer for heavy particles .... 337—346
17. NILSSON, S. G., The motion of electrons in the field of a homogeneously winded toroid .... 347—351
18. THORÆUS, R., Quantitative measurements of low dose-rate roentgen rays in terms of the international r-unit by closed ionization chambers........ 353—361
19. THULIN, S., On the decay of $Kr^{88} \rightarrow Rb^{88} \rightarrow Sr^{88}$ .... 363—381
20. MEITNER, L., Spaltung und Schalenmodell der Atomkerne .... 383—386
21. OHLIN, P., A spectrometer for an investigation of angular dependence of the structure in the continuous X-ray spectrum .... 387—390
22. LUNDIN, L., An improved recording microphotometer .... 391—398
23. HULTHÉN, E., Spectroscopic intensity modulation........ 399—406
24. ALFVÉN, H., On the Zeeman effect measurements of the sun's general magnetic field .... 407—410
25. MALMFORS, K. G., A simple cosmic-ray-meter, plotting hourly values, corrected for pressure .... 411—413

Sid.

26. de **Haas**, E., Tests on dust separators with the Siegbahn-Schönander electron microscope .... 415—421
27. **Ingelstam**, E. and **Djurle**, E., Phase contrast measurements of the ruling structure of optical gratings. I .... 423—439
28. **Edlén**, B., Observations on the He I isoelectronic sequence .... 441—453
29. **Bohr**, A., **Koch**, J. and **Rasmussen**, E., Hyperfine structure and nuclear moments of Xe^{129} and Xe^{131} .... 455—468
30. **Orring**, J., Energy determination of the Se^{77m} γ-ray .... 469—470
31. **Fernández-Morán**, H., Application of the ultrathin freezing-sectioning technique to the study of cell structures with the electron microscope .... 471—483
32. **Slätis**, H. and **Siegbahn**, K., Determination of multipole orders from internal pair formation .... 485—494
33. **Brogren**, G. and **Rylander**, C.-G., Scintillation counters for X-rays .... 495—499
34. **Andersson**, B., On the stress-tensor of viscous isotropic fluids .... 501—503
35. von **Friesen**, S. and **Kristiansson**, K., Photo-electric determination of the density of tracks in nuclear emulsions .... 505—515
36. **Sandström**, A. E., A large bent crystal vacuum spectrograph .... 517—534
37. **Hast**, N., Observations regarding resistant surface films of crystals .... 535—539
38. **Linde**, J. O., An investigation of the validity of the Wiedemann-Franz-Lorenz law .... 541—554
39. **Lundborg**, N. and **Johansson** C. H., Experimental determination of the speed of propagation of cracks in glass as a function of the stress .... 555—558
40. **Atterling**, H. and **Lindström**, G., Notes on the 225-cm cyclotron at the Nobel Institute for Physics, Stockholm .... 559—563
41. **Berggren**, H. and **Cederberg**, I., The translucent zone of reaction in the dentin. A radioautographic study .... 565—571
42. **Fogel**, K.-G., On the determination of eigenvalues and eigenphase for the Yukawa potential .... 573—579

ARKIV FÖR FYSIK Band 4 nr 1

Communicated 12 September 1951 by MANNE SIEGBAHN and ERIK HULTHÉN

Nuclear resonance absorption applied to precise measurements of nuclear magnetic moments and the establishment of an absolute energy scale in β-spectroscopy

By GUNNAR LINDSTRÖM

With 37 figures in the text

Contents

Acknowledgements 2
Introduction 3
Chapter I. Theoretic Introduction 3
§ 1. The nuclear magnetic moment 3
§ 2. The resonance principle 5
§ 3. The relaxation times 6
§ 4. Bloch's phenomenologic theory 8
§ 5. The line-width 10
§ 6. The field at the nucleus 12
Chapter II. Experimental arrangement 12
§ 1. The magnet 12
§ 2. The high-frequency system 13
§ 3. The high-frequency bridge 19
§ 4. The magnetic nuclear resonance signal 21
§ 5. The magnetic field stabilizer 23
§ 6. The method of comparing two signals on the oscillograph 26
Chapter III. Some precision measurements of nuclear magnetic moments 30
§ 1. The μ_D/μ_H ratio 30
§ 2. The susceptibility correction 33
§ 3. The μ_{Li^7}/μ_H ratio 36
§ 4. The $\mu_{B^{11}}/\mu_H$ ratio 39
§ 5. The $\mu_{F^{19}}/\mu_H$ ratio 41
§ 6. The $\mu_{Na^{23}}/\mu_H$ ratio 44
§ 7. The $\mu_{Al^{27}}/\mu_H$ ratio 46
§ 8. Some control ratios 47
§ 9. Error discussion 47
§ 10. The results 50
Chapter IV. Some absolute measurements 52
§ 1. The problem 52
§ 2. The β-spectrograph 54
§ 3. The theoretic line-shape 57
§ 4. The field determinations 62
§ 5. The *F*- and *I*-lines of ThB 64
§ 6. The ratio between the *I*- and *F*-line 68
§ 7. The *ThC″–L*-line 72
§ 8. The results 73
§ 9. Error discussion 76
Summary 78

Acknowledgements

The present investigation has been carried out at the Nobel Institute of Physics, Stockholm. I wish to express my most sincere thanks to the Director of the Institute, Professor MANNE SIEGBAHN, for his never failing interest during the course of this work and for his valuable advice.

Some preliminary measurements on nuclear magnetic moments were carried out in collaboration with Professor KAI SIEGBAHN during 1948. I wish to take this opportunity to thank him for suggesting that I develop the technique and continue the work as well as for all interesting discussions and suggestions.

Ing. NILS MARK has given me highly skilled technical assistance in the experimental work.

I wish to thank Docent LARS MELANDER and Fil. mag. WILHELM FORSLING for kind assistance with chemical problems in connection with the measurements.

I am also indebted to many other members of the staff of the Institute. My thanks are particularly due to Fil. lic. ARNE HEDGRAN and Fil. mag. STIG JOHANSSON for many helpful discussions and suggestions regarding the β-spectroscopic part of this work.

The present investigation has been supported by grants from the Swedish National Science Research Council and the Swedish Atomic Committee for which I should like to express my gratitude.

Mrs VIRGINIA UHLEMANN has been kind enough to assist me in the English text.

Stockholm, September, 1951.

Gunnar Lindström.

Introduction

Nuclear magnetic moments have been determined by several different methods.

1. Hyperfine splitting in spectra.
2. Intensity variations in band spectra.
3. Molecular beam methods.
4. Nuclear induction.
5. Nuclear resonance absorption.

Only the last three methods are suitable for precision work. The molecular beam method was first used by STERN and RABI. RABI and his co-workers (1, 2) have applied the magnetic resonance principle to molecular beam methods and developed it into a method of high precision. This method has given many valuable results. Some of them are reported in a survey by KELLOGG and MILLMAN (3) and in a recent article by KUSCH (4).

"The nuclear resonance absorption" and "Nuclear induction" methods have been introduced simultaneously and independently by PURCELL, TORREY and POUND (5) and by BLOCK, HANSEN and PACKARD respectively (6, 7). These two methods are rather similar in principle, the difference being indicated by the names.

Both of them give extremely narrow line-widths and are therefore suitable for precision work.

The nuclear resonance absorption method has been used in the present investigation. The purpose has been:

1. To construct an apparatus for the precision measurement of nuclear magnetic moments.
2. To measure some of the nuclear magnetic moments of light nuclei with high accuracy in order that these may be used as secondary standards in measuring other moments or chemical shifts.
3. To measure the magnetogyric ratio γ_p for the proton in absolute units.
4. To measure some internal conversion lines of thorium in absolute units so that these values may be used as standards in β-spectroscopy.
5. To show whether or not the positron and electron masses are equal.

CHAPTER I

Theoretic introduction

The purpose of this chapter is to give an idea of the principles and to introduce some important quantities rather than to give a rigorous theory for nuclear induction or resonance absorption. A more detailed theory has been given by BLOCH (8) and by BLOEMBERGEN, PURCELL and POUND (9). A survey has also been given by PAKE (10).

§ 1. The nuclear magnetic moment

If the nuclear magnetic moment of a proton is calculated with the simple assumption that the nuclear charge is equally distributed on a sphere one obtains:

$$\bar{\mu}^* = \frac{e}{2\,M c} \cdot \bar{p} \tag{1}$$

where $\bar{\mu}^*$ is the nuclear moment vector, M the proton mass, e the charge, c the velocity of light and $\bar{p}$ the angular momentum vector. This expression is not in agreement with experiments, but we can multiply it by a dimensionless factor g of the order of unity to place it in agreement.

$$\bar{\mu}^* = g \cdot \frac{e}{2\,M c} \cdot \bar{p} \tag{2}$$

g is the gyromagnetic ratio.

The quantum theory gives $(\bar{p})^2 = \bar{I}\,(\bar{I} + 1)\,\hbar^2$ where $\bar{I}$ is the nuclear spin. Let us also introduce the nuclear magneton $\beta_{\text{nuc.}} = \frac{e\hbar}{2\,M c}$. This gives

$$\bar{\mu}^* = g\,\beta_{\text{nuc}} \sqrt{\bar{I}\,(I + 1)}. \tag{3}$$

The component p along the magnetic field is equal to $m\hbar$, where

$$I, (I - 1),\ (I - 2) \ldots 1 \geq m \geq -1,\ \ldots - I.$$

The vector $\bar{\mu}^*$ coincides with $\bar{p}$ and can be divided into two components, μ_H along the field and $\mu_\perp$ perpendicular to the field

$$\mu_H = g\,\beta_{\text{nuc}}\,m$$

$$\mu_H = g\,\beta_{\text{nuc}} \sqrt{I\,(I + 1) - m^2}.$$

The angle φ between the maximum value $\bar{\mu}^*$ and the component along the field is given by

$$\varphi = \cos^{-1} \frac{m}{\sqrt{I\,(I + 1)}}.$$

In the following the component μ_H along the field will be called *the magnetic moment* of the nucleus μ and the maximum value will always be denoted by μ^*.

If the nucleus is in a magnetic field H, the potential energies u are represented by

$$u_m = -\mu_H \cdot H = g\,\beta_{\text{nuc}}\,m\,H + \text{const.}$$

This gives $2\,I + 1$ different energy levels, corresponding to the Zeeman-splitting in a magnetic field.

The difference $\Delta\,u$ between two adjacent energy levels is

$$\Delta\,u = h\nu = -g\,\beta_{\text{nuc}} \cdot H$$

or

$$\omega = 2\,\pi\nu = -g \frac{e}{2\,M c} \cdot H$$

where ω is the Larmor-frequency.

Using protons and $H = 7000$ Gauss the numerical value for ν is about 30 Mc. This indicates that it will be possible to introduce transitions between the energy levels with an ordinary radio-frequency field. Let us also introduce the magnetogyric ratio $\gamma = \frac{\text{magnetic moment}}{\text{impulse moment}}$ in the expressions for the Larmor-frequency

$$\omega = \gamma \cdot H. \tag{4}$$

§ 2. The resonance principle

Let us suppose that we have a constant magnetic field H along the z-axis and a small rotating field H_1 in the x, y-plane

$$H_x = H_1 \cos \omega t$$

$$H_y = H_1 \sin \omega \mathrm{t} \qquad H_1 \ll H$$

$$H_z = H_0 .$$

The nucleus will precess around H_0 with the Larmor-frequency $\omega_0 = \gamma H_0$. The field H_1 will exert a torque

$$\vec{T} = [\bar{\mu}^* \cdot \bar{H}_1].$$

If the rotating field frequency ω is the same as the Larmor-frequency ω_0, the angle φ between H_0 and $\bar{\mu}^*$ will change and a reorientation take place, but the average effect will be zero if $\omega \neq \omega_0$.

Rabi (11) has given an exact solution for the time dependent probability for a transition of the type $m = \frac{1}{2} \rightarrow m = -\frac{1}{2}$ and his result is

$$C_{\frac{1}{2} \rightarrow -\frac{1}{2}} = \frac{\sin^2 \Theta}{1 + \left(\frac{\omega_0}{\omega}\right)^2 - 2\left(\frac{\omega_0}{\omega}\right) \cdot \cos \Theta} \cdot \sin^2 \left[\frac{\omega t}{2} \sqrt{1 + \left(\frac{\omega_0}{\omega}\right)^2 - 2\left(\frac{\omega_0}{\omega}\right) \cdot \cos \Theta}\right]$$

where

$$\tan \Theta = \frac{H_1}{H_0} = \frac{\omega_1}{\omega_0}, \quad \omega_1 = \gamma H_1 \text{ and } \omega_0 = \gamma H_0$$

H_1 is always much smaller than H_0 in investigations of the type discussed in the following sections, and by introducing this assumption in the previous equation one obtains

$$C_{+\frac{1}{2} \rightarrow -\frac{1}{2}} \simeq \frac{\Theta^2}{\left(1 - \frac{\omega_0}{\omega}\right)^2 + \left(\frac{\omega_0}{\omega}\right) \cdot \Theta} \cdot \sin^2 \frac{\omega t}{2} \sqrt{\left(1 - \frac{\omega_0}{\omega}\right)^2 + \frac{\omega_0}{\omega} \cdot \Theta^2}. \tag{5}$$

The probability will oscillate between 0 and 1 at resonance ($\omega = \omega_0$) which gives

$$C_{+\frac{1}{2} \rightarrow -\frac{1}{2}} = C_{-\frac{1}{2} \rightarrow +\frac{1}{2}}.$$

Majorana (12) has given an approximative expression for the probability for different I values based on a perturbation theory. It is interesting to see that the probability is $\frac{1}{2}$ for $|\omega - \omega_0| = \omega_1$. This means that the natural half-width is equal to twice the amplitude of the high-frequency field. Of course this is true only if the magnetic field is so homogeneous that the line width depends on this probability alone.

The unhomogeneity of the magnetic field in most cases is much larger than the high frequency amplitude and determines the half-width of the signals. Let us assume that the resonance frequencies of the spins are distributed over a small frequency interval and that the distribution is given by the following normalized function

$$\int_0^\infty \varphi(\nu)\, d\nu = 1 \text{ and near the resonance is } \varphi(\nu) \simeq \varphi(\nu_0).$$

The energy absorbed by the system is then given by

$$E(t) = \int_0^\infty C_{-\frac{1}{2}\to+\frac{1}{2}}(\nu)\, \gamma \hbar H_0\, n\, \varphi(\nu)\, d\nu$$

where n is the difference in population between two adjacent energy levels.

The power absorbed is represented by

$$P(t) = \frac{d\,E(t)}{d\,t} = \frac{1}{4} \cdot \omega_1^2 \gamma \hbar H_0 \varphi(\nu_0)\, n J_0(\gamma H_1 t)$$

and for small t we find $J_0(0) = 1$ which gives

$$P = \tfrac{1}{4} \gamma^2 H_1^2 \varphi(\nu_0)\, n \gamma \hbar H_0. \tag{6}$$

This yields no net absorption because the Bessel function vanishes as $(\gamma H_1 t)^{-\frac{1}{2}}$ for large t-values. This indicates that the free spins, initially oriented in one direction, start oscillating under the influence of the applied signal, getting out of phase. Hence for large t-values there are always as many in the field direction as opposite. Some kind of interaction with the environment field is necessary in order to obtain stationary absorption. This interaction can be described by two relaxation times T_1 and T_2.

§ 3. The relaxation times

The magnetic field tends to arrange the nuclei in the direction of the magnetic field, but the energy difference between two Zeeman levels $\Delta u = \hbar \omega$ is much less than the thermal energy kT, meaning that the distribution will be given by a Boltzmann factor.

Let N_{m_1} and N_{m_2} be the number of nuclei in state m_1 and m_2.

$$\frac{N_{m_1}}{N_{m_2}} = \frac{e^{-\frac{m_1 \gamma \hbar H}{kT}}}{e^{-\frac{m_2 \gamma \hbar H}{kT}}} = e^{-\frac{(m_1 - m_2)\gamma \hbar H}{kT}} \tag{7}$$

and approximately

$$\frac{N_{m_1}}{N_{m_2}} \simeq 1 + \frac{\gamma \hbar H}{k T} \tag{7 a}$$

for two adjacent levels.

For protons ($m = \pm \frac{1}{2}$) in 10 000 Gauss and at room temperature this gives

$$\frac{N_{+\frac{1}{2}}}{N_{-\frac{1}{2}}} \simeq 1 + 7 \cdot 10^{-6}.$$

The surplus in the lower energy state is thus only about seven nuclei in a million. It is this small surplus that makes the absorption of power possible.

Let us now look at equation (7 a) in another way. Suppose that we have a sample outside the magnet. The earth field is so small that the nuclei are almost equally distributed in all energy-levels. If the sample is placed in a magnetic field, this means that the spin temperature T_s at the first moment must be much higher than the room temperature T but after a certain time all spins are oriented in agreement with (7) and the spin system is cooled to T.

$$\frac{N_{m_1}}{N_{m_2}} \simeq 1 + \frac{\gamma \hbar H}{k T_s}; \quad T_s \to T. \tag{7 b}$$

This mechanism can be characterized by a time constant called *the spin-lattice relaxation time* T_1.

Purcell and Pound (13) have shown that distributions corresponding even to negative spin temperatures can be realized. It is also possible to measure in a low field with a distribution corresponding to a high field if T_1 is sufficiently large. This may be accomplished by simply lowering the field faster than T_1, as has been shown by Ramsey and Pound (14).

Assume that we have two energy levels m_1 and m_2 and that the probability for a transition from m_1 to m_2 is $C_{m_1 \to m_2}$; that the probability for a transition $m_2 \to m_1$ is $C_{m_2 \to m_1}$; and for simplicity that

$$C_{m_1 \to m_2} = C_{m_2 \to m_1} = C.$$

This is the probability for one particle and the total probability is, for example

$$W_{m_1 \to m_2} = C_{m_1 - m_2} \cdot N e^{-\frac{u_m}{kT}} = N_{m_1} C.$$

The surplus $n = N_{m_2} - N_{m_1}$ will change by 2 for each transition which means that

$$\frac{dn}{dt} = 2 N_{m_2} C - 2 N_{m_1} C$$

and with the equilibrium value $n_0 = \frac{g \beta_{\text{nuc}} H_0}{kT}$

$$\frac{dn}{dt} = 2C(n_0 - n)$$

and

$$n = n_0(1 - e^{-2Ct}).$$

From this expression one can define the *spin-lattice relaxation time* $T_1 = \frac{1}{2C}$. The measured T_1 values lie between $10^{-4}\,s$ and several hours. For instance for protons in water $T_1 = 2.53 \pm 0.07\,s$ (15). A survey of relaxation-time measurements in crystals is given by PURCELL (16).

The life time for a spin can change by a spin-spin collision. The field from one nucleus acting on another can give a resonance field, which gives a transition to another energy level. The frequency for such a transition can be estimated in the following way.

$$\delta\omega \sim \gamma H^1$$

where the local field H^1 is of the order of 5 Gauss for protons 1 Å apart. With this numerical value

$$\delta\omega = 10^4\,s^{-1}.$$

This indicates that the phase memory for the spins is of the order of $10^{-4}\,s$. The uncertainty principle gives the following level broadening.

$$\delta u\left(\frac{1}{\delta\omega}\right) \sim \hbar.$$

The spin-spin relaxation time T_2 can now be defined as

$$T_2 = \frac{1}{\delta\omega}.$$

§ 4. Block's phenomenologic theory

The magnetic field tends to arrange the nuclei in different energy levels giving a resultant macroscopic magnetization $\bar{M}$. BLOCH (8) points out that the spreading of energy levels causes the nuclei to precess with slightly different Larmor frequencies. This means that they will go out of phase in a time of the order of T_2, destroying the magnetization in the x and y directions.

It is easy to calculate the magnetization M_0 along the field

$$M_0 = \sum_{m=-I}^{m=+I} N_m\,\mu_H$$

and with

$$\frac{g\,\beta_{\text{nuc}}\,H}{k\,T} \ll 1$$

one obtains

$$M_0 = \frac{N}{3kT}\,g^2\,\beta_{\text{nuc}}^2\,I(I+1)\,H.$$

The volume susceptibility χ_0 depending on the surplus nuclei along the field is then

$$\chi_0 = \frac{N}{3\,k\,T} g^2 \beta_{\text{nuc}}^2 I\,(I+1). \tag{8}$$

Bloch has given the following differential equations for the different components of the magnetization vectors,

$$\frac{d\,M_x}{d\,t} = -\frac{M_x}{T_2}$$

$$\frac{d\,M_y}{d\,t} = -\frac{M_y}{T_2}$$

$$\frac{d\,M_z}{d\,t} = -\frac{M_z - M_0}{T_1}$$

where M_z is the component along the field; M_x and M_y are the components perpendicular to the field and M_0 is the equilibrium value given earlier.

These equations will be modified if a rotating high frequency field is applied perpendicular to the static field.

$$\left.\begin{aligned} \frac{d\,M_{x,y}}{d\,t} &= \gamma\,[\overline{H}\cdot\overline{M}]_{x,y} - \frac{M_{x,y}}{T_2} \\ \frac{d\,M_z}{d\,t} &= \gamma\,[\overline{H}\cdot\overline{M}]_z - \frac{M_0 - M_z}{T_1} \\ H_x &= H_1 \cos\omega t \\ H_y &= H_1 \sin\omega\,\mathrm{t} \\ H_z &= H_0 \end{aligned}\right\} \tag{8 a}$$

This can be transformed to a rotating coordinate system with

$$M_x = u\cos\omega t - v\sin\omega\,\mathrm{t}$$

$$M_y = \pm\,(u\sin\omega t + v\cos\omega t).$$

The sign depends on the sign of γ. Bloch has given the following time independent solution.

$$\left.\begin{aligned} M_z &= \frac{1+(T_2\,\Delta\,\omega)^2}{1+(T_2\,\Delta\,\omega)^2+(\gamma\,H_1)^2\,T_1\,T_2}\cdot M_0 \\ u &= \frac{|\gamma|\,H_1\,T_2\,(\Delta\,\omega\,T_2)}{1+(T_2\,\Delta\,\omega)^2+(\gamma\,H_1)^2\,T_1\,T_2}\cdot M_0 \\ v &= \frac{-|\gamma|\,H_1\,T_2}{1+(T_2\,\Delta\,\omega)^2+(\gamma\,H_1)^2\,T_1\,T_2}\cdot M_0 \end{aligned}\right\} \tag{9}$$

where $\Delta\,\omega = \omega_0 - \omega$.

Let us introduce the complex susceptibility $\chi = \chi' - i\chi''$ and write $\bar{M} = \chi \bar{H}$. The susceptibilities can then be given by:

$$\chi' = \frac{|\gamma|\, T_2 (\varDelta\omega T_2)\, \chi_0 H_0}{1 + (\varDelta\omega T_2)^2 + (\gamma H_1)^2 T_1 T_2}$$

$$\chi'' = \frac{|\gamma|\, T_2 \chi_0 H_0}{1 + (\varDelta\omega T_2)^2 + (\gamma H_1)^2 T_1 T_2} \tag{9 a}$$

where $\frac{M_0}{H_0} = \chi_0$.

The out-of-phase component χ'', which is responsible for the absorption has a maximum for $\varDelta\omega = 0$ and the optimum value is

$$\chi'' = \frac{|\gamma|\, T_2 \chi_0 H_0}{1 + (\gamma H_1)^2 T_2 T_2}. \tag{9 b}$$

The component χ' which is in phase with the rotating field gives the dispersion and will asymptotically approach the same maximum value as χ'' for $\varDelta\omega = \sqrt{1 + (\gamma H_1)^2 T_1 T_2}$ if $(\gamma H_1)^2 T_1 T_2 \gg 1$.

The energy of the system is

$$-\int \bar{M}\, d\bar{H} = -\int \bar{M} \frac{d\bar{H}}{dt}\, dt$$

and the absorbed power is

$$P = \frac{d}{dt} \int \bar{M} \frac{d\bar{H}}{dt}\, dt = -\bar{M}\dot{\bar{H}}.$$

The contribution from χ'' gives the average absorbed power

$$P = \omega H_1^2 \chi''$$

and by introducing the expression for χ'' and χ_0 given above one obtains

$$P = \frac{\omega H_1^2 |\gamma| H_0 T_2}{1 + (\gamma H_1)^2 T_1 T_2} \frac{N}{3kT} g^2 \beta_{\text{nuc}}^2 I(I+1). \tag{10}$$

The calculation indicated above is made with classic assumptions, but a quantum mechanical analysis will give the same expression, which has been shown by BLOEMBERGEN, PURCELL and POUND (9).

The expression for the absorbed power (equation 10) shows that the power will increase with the amplitude of the rotating field H_1 if $\gamma^2 H_1^2 T_1 T_2 \ll 1$ but it also shows that there will be saturation if $\gamma^2 H_1^2 T_1 T_2 > 1$.

§ 5. The line width

Let us assume that the amplitude H_1 is chosen so that $\gamma^2 H_1^2 T_1 T_2 \ll 1$. This means that the susceptibilities given by (9 a) are reduced to

$$\chi' = \frac{|\gamma| T_2^2 (\omega - \omega_0) \chi_0 H_0}{1 + [T_2 (\omega - \omega_0)]^2}$$

$$\chi'' = \frac{|\gamma| T_2 H_0 \chi_0}{1 + [T_2 (\omega - \omega_0)]^2}. \tag{11}$$

Fig. 1 shows how χ' and χ'' vary with $(\omega - \omega_0)$.

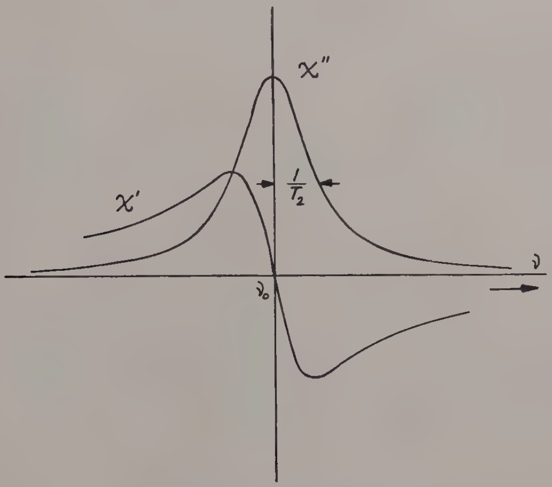

Fig. 1. Curves showing the behavior of the real and imaginary part of the magnetic susceptibility are drawn near the resonance value here.

The half maximum will take place at

$$T_2^2 (\omega - \omega_0)^2 = 1$$

which gives $(\omega - \omega_0) = \frac{1}{T_2}$ at half maximum.

The line-width at half maximum is then given by $\frac{2}{T_2}$.

Of course, this is only true in a perfectly homogeneous magnetic field.

We have also seen that the natural line-width is given by the half-value of the probability for a transition from one energy level to another and for protons this gives $2 \gamma H_1$. A high H_1 value will therefore both cause saturation and increase the line-width.

The line-width is almost always limited by unhomogeneities in the magnetic field. It is therefore extremely important to have a high degree of homogeneity in the field as will be discussed later. It may be mentioned here that the relative half-width for protons has been as low as 1/170000 in the present investigation.

§ 6. The field at the nucleus

The field at the nucleus is not the same, of course, as the applied field $H_0 = H_0^1 + H_m \sin(\omega_m t)$, where H_0^1 is the static field, H_m the amplitude and ω_m the frequency of the modulation field. It comprises also the field from the atomic electrons H_1, the contribution from the bulk susceptibility H_2, and let us assume that there can be a contribution H_3, which represents all other fields.

The field at the nucleus H^* is then given by

$$H^* = H_0 + H_1 + H_2 + H_3. \tag{12}$$

It has been shown (8, 9) that paramagnetic ions will lower the relaxation time T_1, wherefore the chosen h.f. field can be higher before saturation takes place (see also equation 10). Hence, many workers have used paramagnetic ions in their solutions. It was supposed that the contributions from these ions were the same for all nuclei in a mixture, but DICKINSON (17) has shown that this is not the case. Therefore it is difficult to compare values given for a sample containing paramagnetic ions with those taken without such ions. For this reason no paramagnetic ions have been used in this investigation. However, if they are used the contribution from them can be included in H_2.

Many workers have found that the measured μ values may depend on the chemical composition (18, 19, 20, 21, 22). This contribution can be included in H_3.

The ratio between the magnetic moments for two nuclei A and B is now easily obtained from the foregoing equations

$$\frac{\mu_A}{\mu_B} = \frac{I_A}{I_B} \cdot \frac{\omega_A}{\omega_B} \cdot \frac{H_A^*}{H_B^*}. \tag{13}$$

The spins are determined by other methods in many cases. The Larmor frequencies ω_A and ω_B can be measured with a high degree of accuracy by the method used in this investigation. But unfortunately it is not always possible to calculate all the field factors in (12) with the same accuracy. These factors will be discussed in more detail in connection with the experimental results in chapter III.

Many workers have given the ratio ν_A/ν_B and the data for the solution instead of μ_A/μ_B. In this investigation both quantities will be given.

CHAPTER II

Experimental arrangement

§ 1. The magnet

The magnet has been described in detail in an earlier paper (18). Therefore, it will be only briefly discussed here. The outline and dimensions are seen in figure 2.

The pole-pieces were made optically flat. The distance between them is 42.000 ± 0.001 mm. This should give an unhomogeneity of the order of one

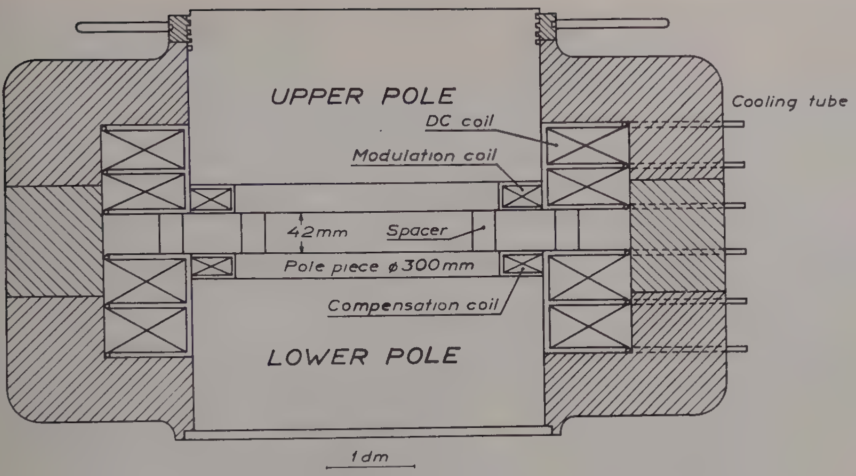

Fig. 2. Cross section of the magnet.

part in 40 000. The first part of this investigation comprised a search through the magnetic field using a proton sample, thus locating the most homogeneous spots. This is a rather lengthy operation necessitating photographs of the resonance curves with subsequent measurement of the line-width and comparison of the widths from different positions. The sample used was 12 mm in diameter and 30 mm long. The half-widths of the lines in the central parts were of the order one part in 50 000 but at two positions the widths were about one part in 100 000 or even smaller. Different types of shims were tried in order to obtain still narrower lines and the narrowest line measured was about one part in 170 000. Unfortunately, it was found that the homogeneity changed a little from time to time, necessitating changes in the shimming. This is laborious and does not seem worth the trouble because the line-width without shims is always between 1 : 100 000 and 1 : 150 000.

It is not only the homogeneity which changes a little from time to time. Even the location of the aforementioned positions are changed, but they are rather easily localized by moving the sample a little and looking at the oscillograph screen at the same time. No changes of this kind are found after thermal equilibrium has been established in the magnet (see also chapter III § 1).

§ 2. The high-frequency system

Nuclear magnetic resonance signals can be obtained with a rather simple arrangement but when high accuracy is desired a more complicated apparatus is required. The high-frequency system used in the measurements mentioned before, has been completely changed. The main difficulties with the earlier arrangements were:

1) The frequency stability of the generators was insufficient.
2) The mechanical stability of the bridges was insufficient.

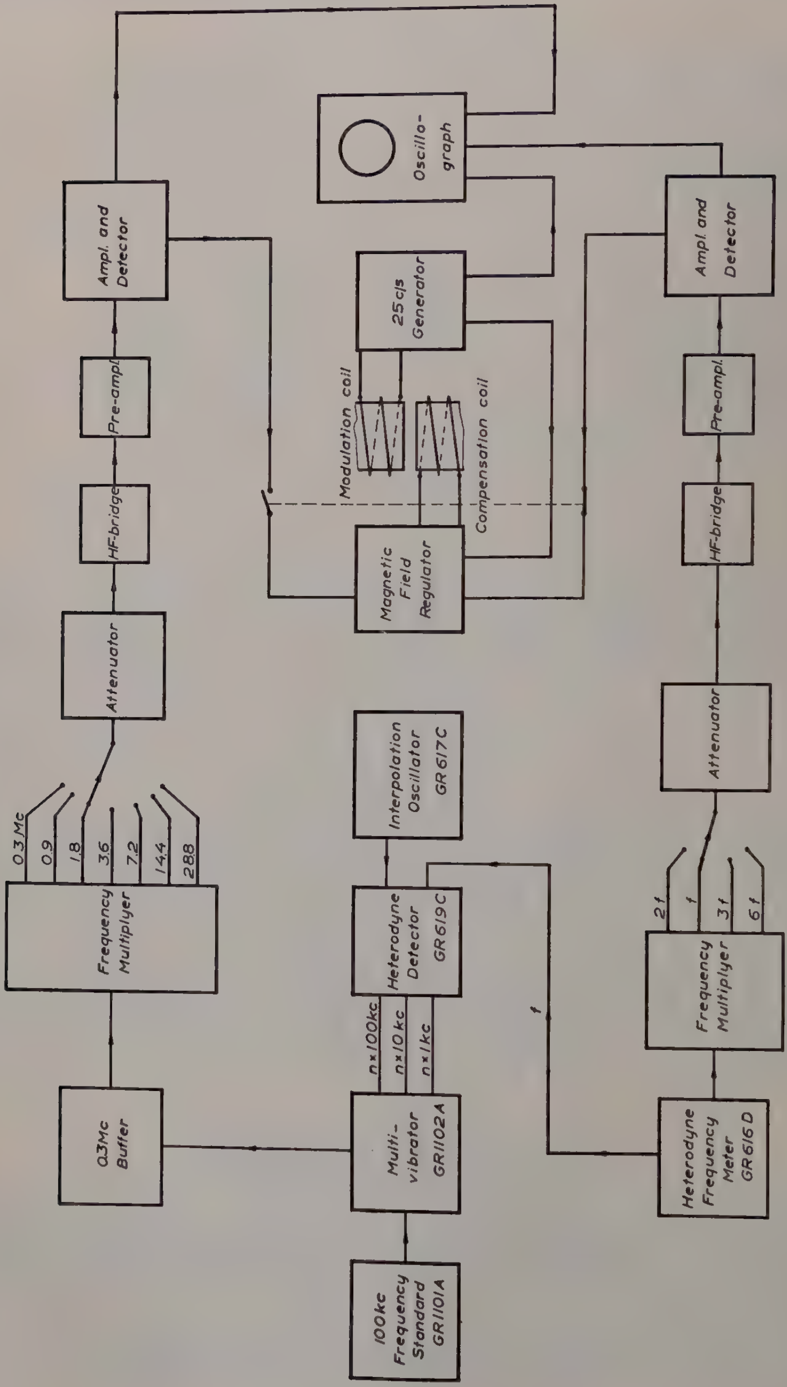

Fig. 3. Block diagram of the experimental arrangement.

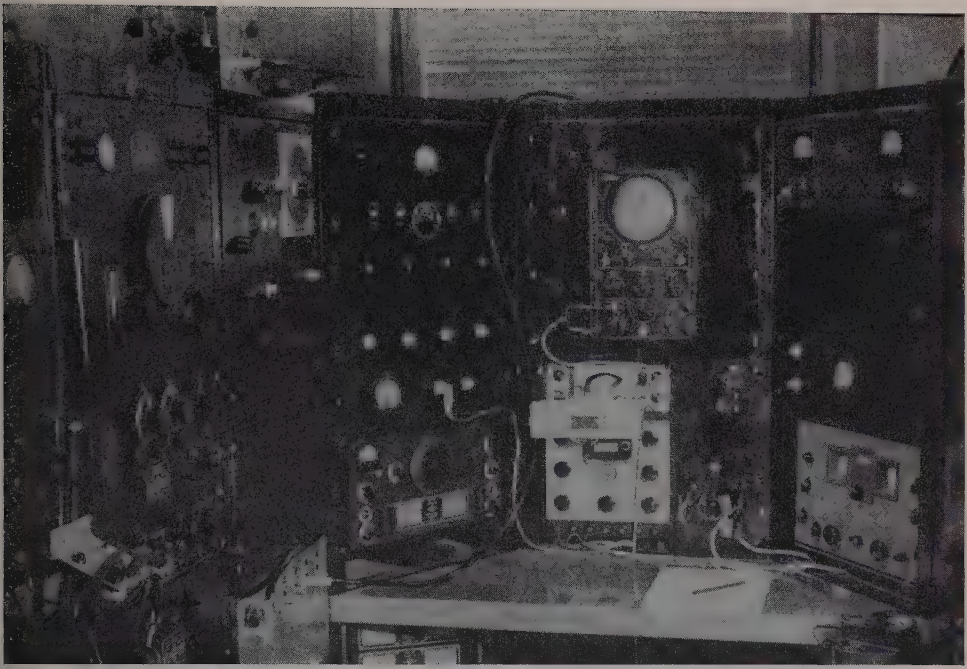

Fig. 4 a. View of the experimental set up around the control desk.

3) The signal-to-noise ratio in many cases was too low.
4) The adjustment of the frequencies of the generators to the right value by only looking at the screen was rather uncertain.

In the arrangement used in this investigation, many of these difficulties have been removed. Fig. 3 shows a block diagram and fig. 4 a and b photographs of the complete apparatus.

As seen from this diagram there are two different frequency channels. One is fed directly from the multivibrator unit driven by a crystal frequency standard (G. R. 1101 A); the other is fed from a heterodyne frequency meter. (G. R. 616 D).

The signal (300 kilocycles) from the multivibrator unit is amplified and multiplied in the frequency multiplier unit from which the frequencies 0.9, 1.8, 3.6, 7.2, 14.4 and 28.8 megacycles can be obtained (see fig. 5). One of these signals can then be amplified or attenuated in an ordinary output amplifier matched to the different high frequency bridges described later.

The signals from the bridges are first amplified in a pre-amplifier. This type of amplifier with an excellent signal-to-noise ratio was first described by Wallman (23). Fig. 6 shows a diagram of one of the pre-amplifiers used in this investigation. The signals from these amplifiers are further amplified in ordinary communication receivers. (National HRO 50, HRO and Hammarlund 129 X have been used in this investigation.)

As the rectifiers in these high-frequency amplifiers are not satisfactory in

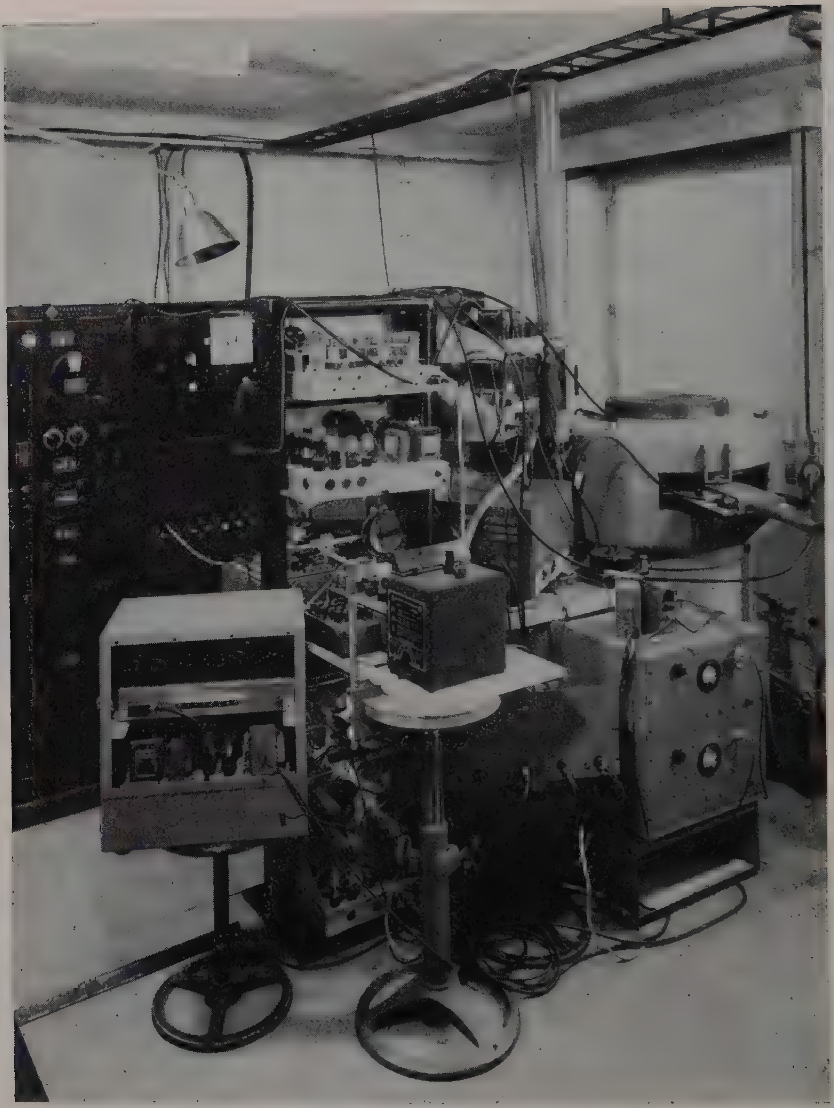

Fig. 4 b. View of the experimental set up seen behind the control desk. The magnet is seen in the background.

measurements of this type they have been changed to well-stabilized rectifiers of the type shown in figure 7.

A micro-ammeter is connected in series with the second detector tube in these receivers to indicate the signal level. The low frequency part of the amplifiers has also been changed slightly to make it suitable for a 25-cycle signal. This signal is then visualized on the double beam oscillograph (Cossor Mod. 1035).

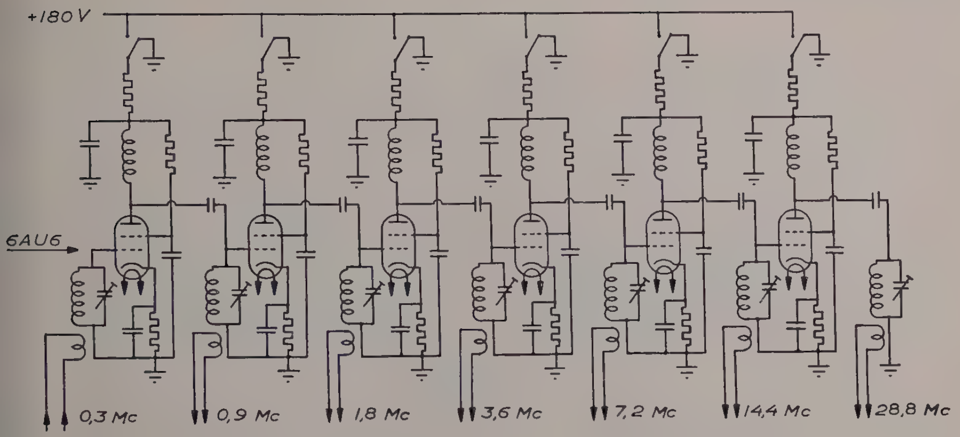

Fig. 5. Diagram of the frequency multiplier.

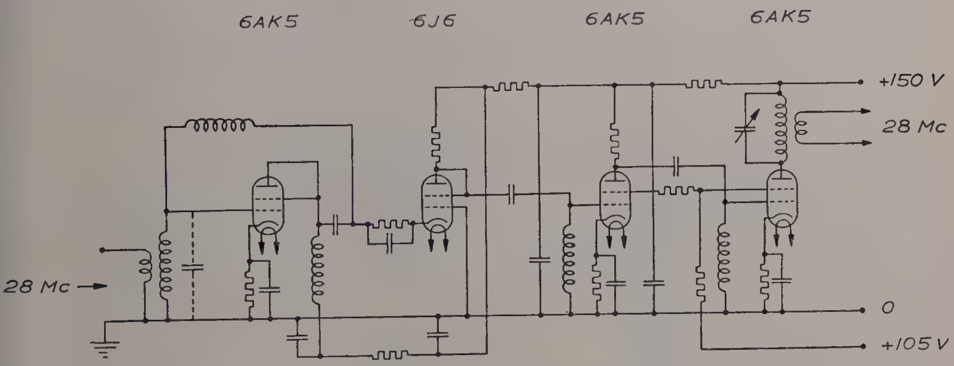

Fig. 6. Diagram of one of the pre-amplifiers used.

The frequency f from the heterodyne frequency meter, which can be varied between 200 kilocycles and five megacycles, is amplified and multiplied in a unit of the type shown in figure 8.

From the different channels in this unit f, $2f$, $3f$ and $6f$ megacycles may be obtained; i.e., 200 kilocycles to about 30 megacycles. This signal can then be attenuated or amplified in the manner described earlier.

The advantage with this arrangement is that the frequency can be measured continuously by the interpolation oscillator (G. R. 617 C). The frequency f (or sometimes $2f$, $3f$, or $6f$) beats against $n \cdot 10$ kilocycles from the frequency standard. The beat frequency is always less than five kilocycles, the range of the interpolation oscillator. The correct frequency is then $n \cdot 10$ kilocycles $\pm$ the frequency found on the interpolation oscillator. This oscillator is calibrated with $n \cdot 1$ kilocycles or $n \cdot 100$ cycles from the standard. The manufacturer claims the accuracy of the scale to be better than ± 1 cycle per second, making it

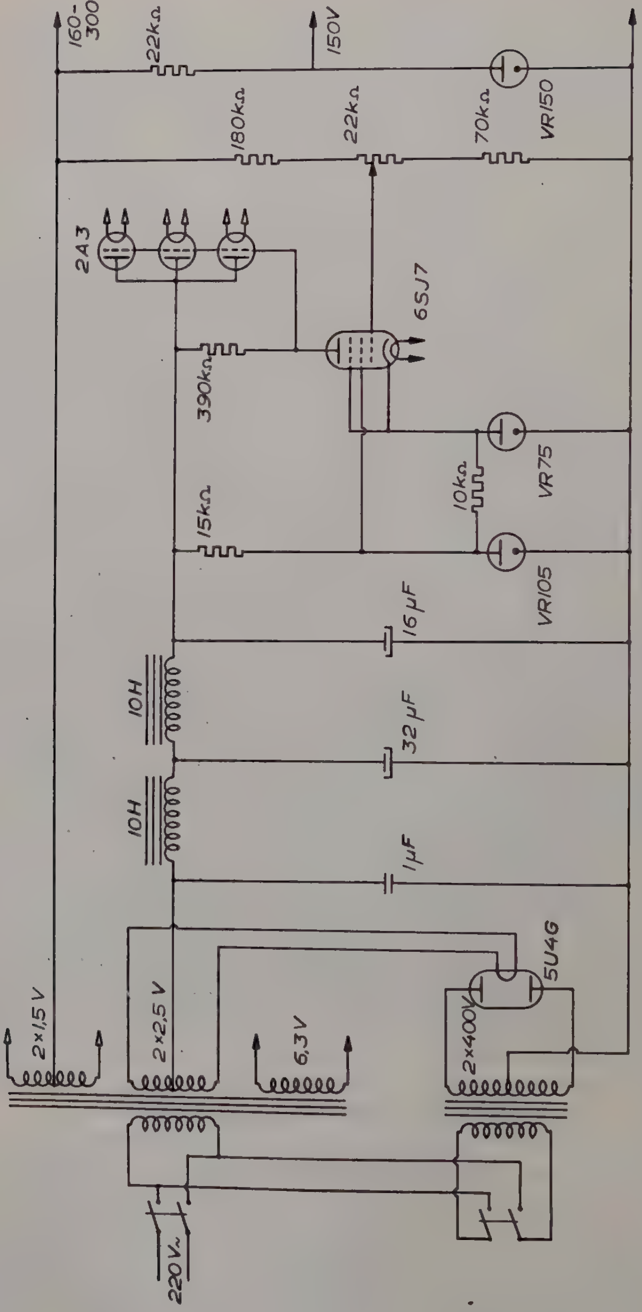

Fig. 7. Diagram showing a typical stabilized rectifier.

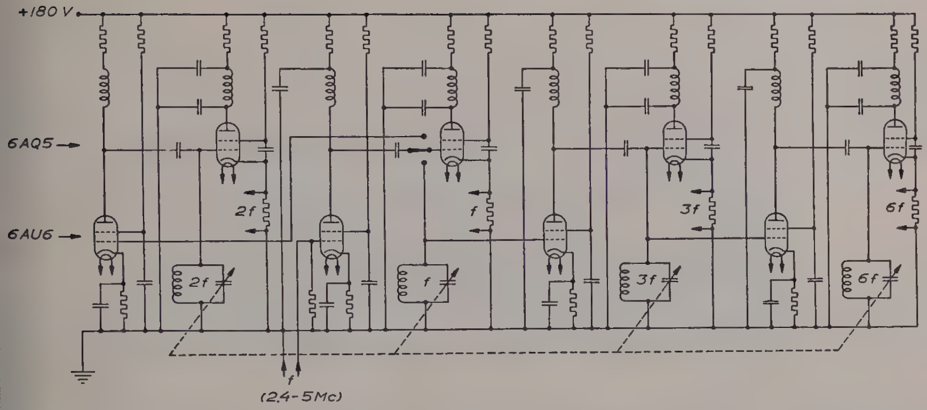

Fig. 8. Diagram showing the amplifier and frequency multiplier used for frequencies from 200 kc to 30 Mc.

possible to measure the frequency with an accuracy of ± 1 cycle. The frequency stability of the temperature-controlled heterodyne frequency-meter permits this accuracy if the measurements are carried out in the manner described later.

§ 3. The high-frequency bridge

The high-frequency bridges used in this investigation are the same in principle as those proposed by PURCELL et al, the main difference being the use of a transformer to obtain the 180° phase shift between the two arms, rather than a difference in the length of $\frac{\lambda}{2}$ between the connections in the two parts of the bridge.

One of the bridges used is shown in figure 9. The center-tapped secondary

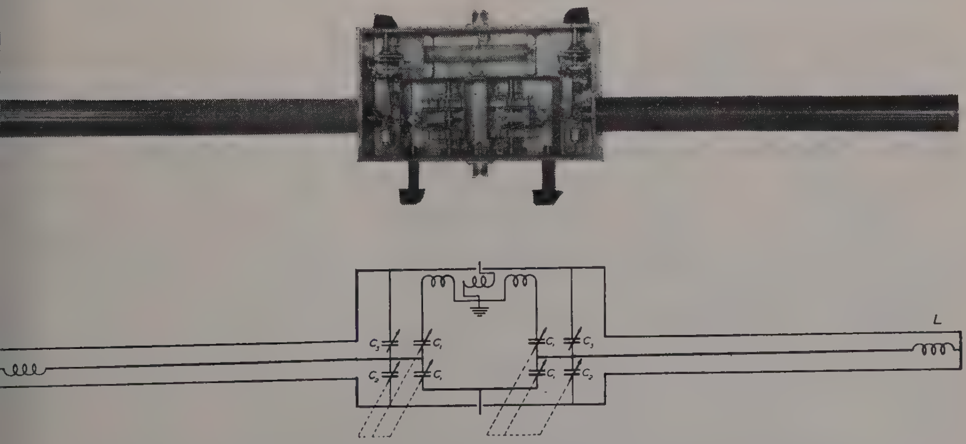

Fig. 9. One of the high frequency bridges together with its wiring diagram.

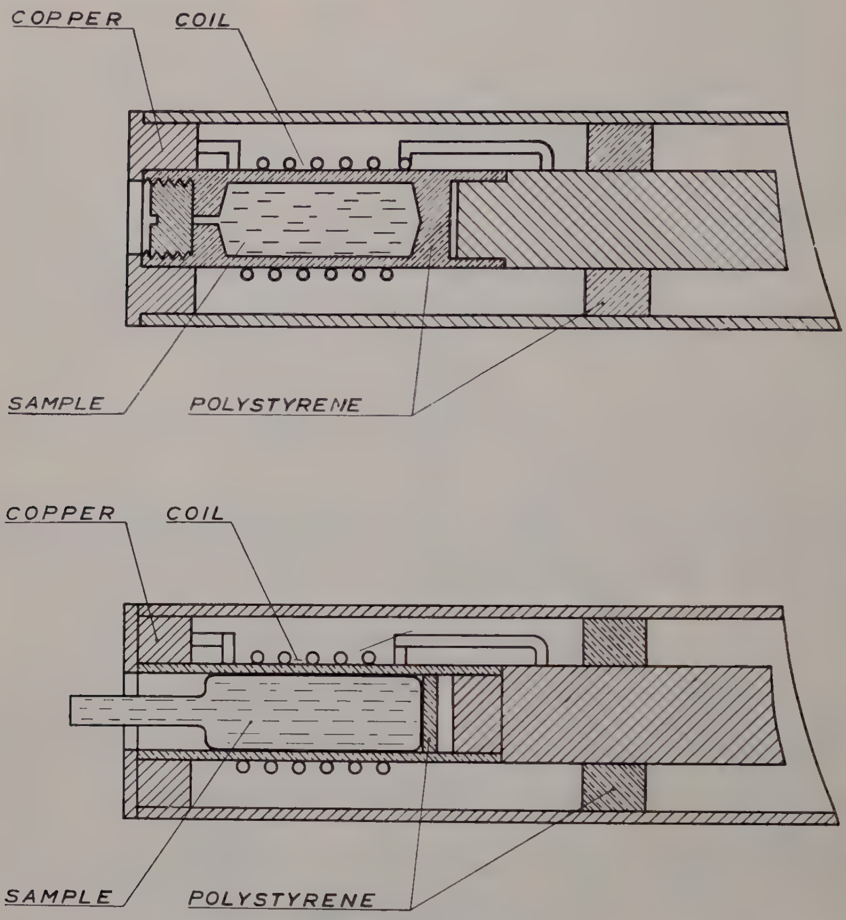

Fig. 10. Two of the coils and sample holders used in connection with the high-frequency bridges.

winding of the transformer gives signals with a phase difference of 180° to the two T-sections. The condensers C_1 in the arms and the shunting condenser C_2 are ganged so that C_2 increases when the two other condensers decrease. The condensers are matched so that an adjustment of these condensers provides a phase-independent adjustment of the amplitude for the balance of the bridge. An adjustment of C_3 gives an almost amplitude-independent adjustment of the phase.

In these measurements, balance in amplitude to one part in 50 000 has sometimes been obtained. This requires a very rigid type of bridge. A small unbalance in amplitude is desirable for the sensitivity, as will be shown later. Moreover with the method used here it is also desirable to have the unbalance in phase as small as possible, wherefore the adjustment of C_2 is critical. Hence, the final adjustment is made with an ordinary screw at the bridge-cover.

Fig. 10 shows some of the sample-coils (L in the drawing in fig. 9) used n this investigation. These are made mechanically rigid in order that the ridges may be moved without disturbing the coil position. In one type, the amples can be changed without moving the bridge, insuring the placement of he samples at the same spots in the field. The Q of the resonance circuit is f the order of 100.

§ 4. The magnetic nuclear resonance signal

It has been shown in the foregoing chapter that the susceptibility can be xpressed as a function of some characteristic constants. We shall now see how this affects the signal amplitude from the bridge described in the preceding paragraph.

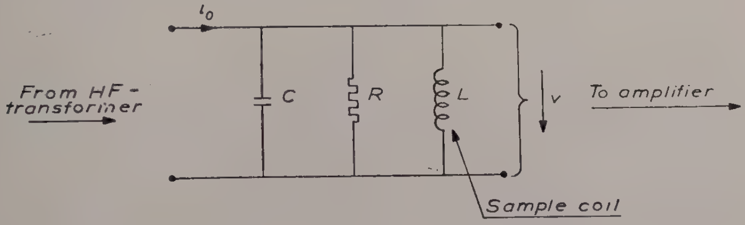

Fig. 11. Simplified diagram of the bridge-circuit.

Let us assume that the amplitude and frequency of the modulation sweep is so small that the time-independent field solution is valid. The coupling condensors C_1, in the bridge-circuit are so small, that we may consider the resonance circuit with the sample as being driven by a constant current generator with $i_0 = i\,\omega\,C_1\,v_1$ where v_1 is the voltage from the high-frequency transformer. The corresponding diagram is shown in fig. 11. The inductance L can be written $L = L_0\,(1 + 4\,\pi\,\chi\,q)$. At resonance $1/\omega\,C = \omega\,L$. The admittance Y is then given by

$$Y = \frac{1}{R} + i\,\omega\,C\left[1 - \frac{1}{\omega^2\,L_0\,C\,(1 + 4\,\pi\,\chi\,q)}\right]$$

where q is a filling factor and with $4\pi\chi q \ll 1$

$$Y \simeq \frac{1}{R} + \frac{i\,4\,\pi\,\chi\,q}{\omega\,L_0}.$$

The complex susceptibility χ is equal to $\chi' - i\,\chi''$ which means that the real part of Y, $\{Y\}_{\mathrm{re}}$ is a function of the absorption χ'' and the imaginary part, $\{Y\}_{\mathrm{im}}$ is a function of the dispersion.

The voltage v across the sample coil is given by

$$v = \frac{i_0}{Y} = R\,i_0\left(1 + \frac{i\,4\,\pi\,\chi\,q\,R}{\omega\,L_0}\right)^{-1}.$$

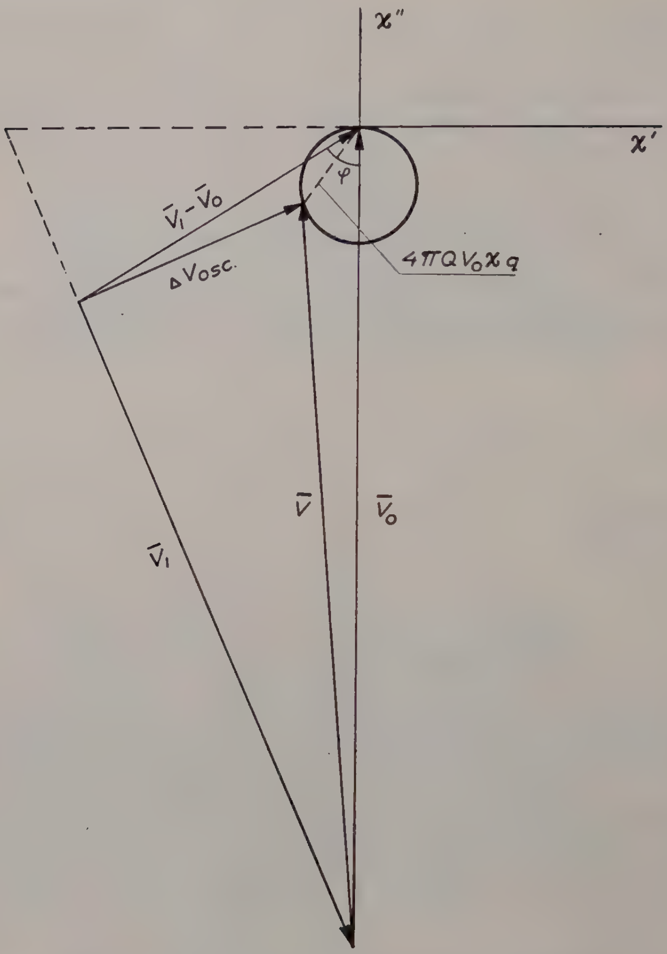

Fig. 12. Vector diagram of the voltages of the two parts of the bridges and of the voltage generated by nuclear resonance.

By introducing the voltage without nuclear resonance in the sample $v_0 = i_0 R$ and $Q = R/\omega L_0$ we obtain

$$v = v_0 (1 - i\, 4\pi \chi q Q).$$

The signal to the amplifier (v_{amp}) is then the difference between the signals coming from the two arms.

$$v_{\mathrm{amp}} = v - v_1 = (v_0 - v_1) - i\, 4\pi Q v_0 q \chi.$$

These voltages are all complex and there is both amplitude and phase difference between them. Assuming that the difference in phase between the vectors $v_0 - v_1$ and v_0 is φ (see Fig. 12), the signal to the amplifier is

$$v_{\text{amp}} = (v_0 - v_1) - 4\pi Q q |v_0| e^{i\varphi} (\chi'' - i\chi').$$

The susceptibilities are always small, which means that the first term in this expression is much larger than the second one, and depends only on the degree of balance of the bridge. The signal on the oscillograph, $(\Delta v)_{\text{osc}}$, will therefore be proportional to the real value of the foregoing expression.

$$(\Delta v)_{\text{osc}} \simeq 4\pi Q q |v_0| [-\chi'' \cos\varphi + \chi' \sin\varphi]. \tag{14}$$

It is obvious from this expression that the signal depends on the absorption χ'', only if the bridge is balanced in-or out-of-phase ($\varphi = 0$ or π) and that it is a function of the dispersion, only if the bridge is balanced in amplitude $\left(\varphi = \pm \frac{\pi}{2}\right)$.

The susceptibility lies between 10^{-5} and 10^{-7} CGS-units or even less, which means that with a Q-value of 100, the signal amplitude will range from the order of magnitude of millivolts down to microvolts or less.

The values for χ' and χ'' from (11) can be substituted in (14) and it is easy to see that the locus of $(\Delta V)_{\text{osc}}$ is a circle if $\gamma_2 H_1^2 T_1 T_2 \ll 1$. This case is represented in Fig. 12. The locus of $(\Delta V)_{\text{osc}}$ will be an ellipse if the saturation term is taken into account.

The signal is proportional to v_0 but it must be remembered also that H_1 is proportional to v_0 which means that saturation and line broadening will take place when $\gamma^2 H_1^2 T_1 T_2$ is of the order of one, as has been discussed earlier.

Bloembergen, Purcell and Pound (9, 24) have given the following expression for the maximum signal-to-noise ratio

$$\frac{\text{Signal}}{\text{Noise}} \sim q N Q^{1/2} V_c^{1/2} \gamma^{5/2} H_0^{3/2} T_2^{1/2} T_1^{-1/2} \tau^{1/2} \hbar^2 I (I+1) (kT)^{-3/2} F^{-1/2}$$

where N is the number of resonating nuclei, F the noise figure of the amplifier and V_c the volume of the coil. This signal-to-noise ratio increases as $\nu_0^{7/4}$ since H_0 is proportional to ν_0 and Q to $\nu_0^{1/2}$. It is therefore much easier to obtain nuclear magnetic resonance signals at higher fields than at lower because $\nu^{7/4} \sim H_0^{7/4}$.

The importance of having a high density of nuclei N and a good filling factor is evident as well. The effect is also proportional to the coil size, but this is limited by unhomogeneity in the field.

It should also be pointed out here that the sensitivity of the amplifier is best when the bridge remains slightly unbalanced.

§ 5. The magnetic field stabilizer

A new type of magnetic field stabilizer has been constructed and built during this investigation.

The principle of this stabilizer is shown in figures 13 and 14. The nuclear resonance signal from the amplifier is rectified in the double bridge and the

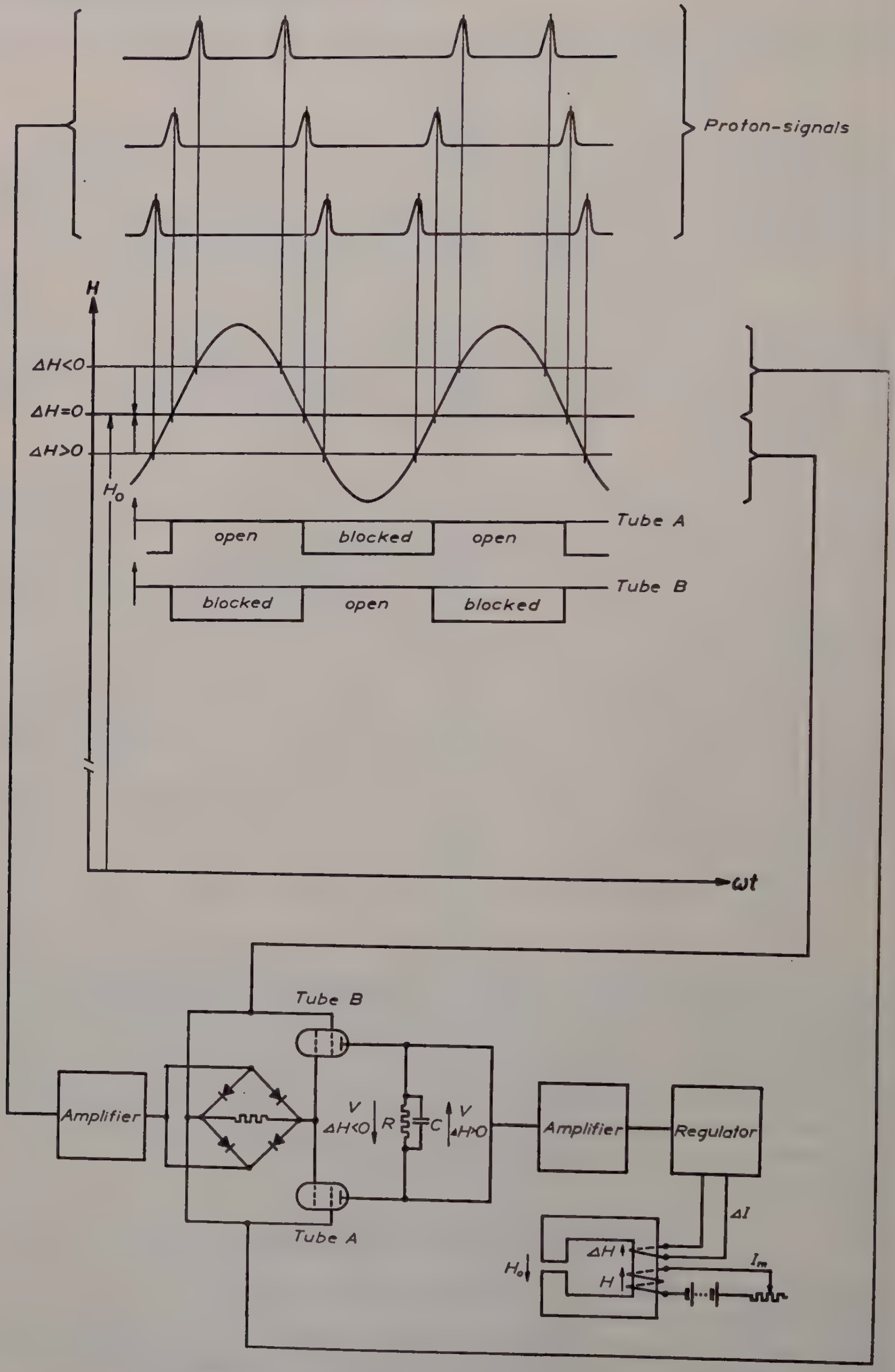

Fig. 13. Block diagram illustrating the principle of the magnetic field stabilizer.

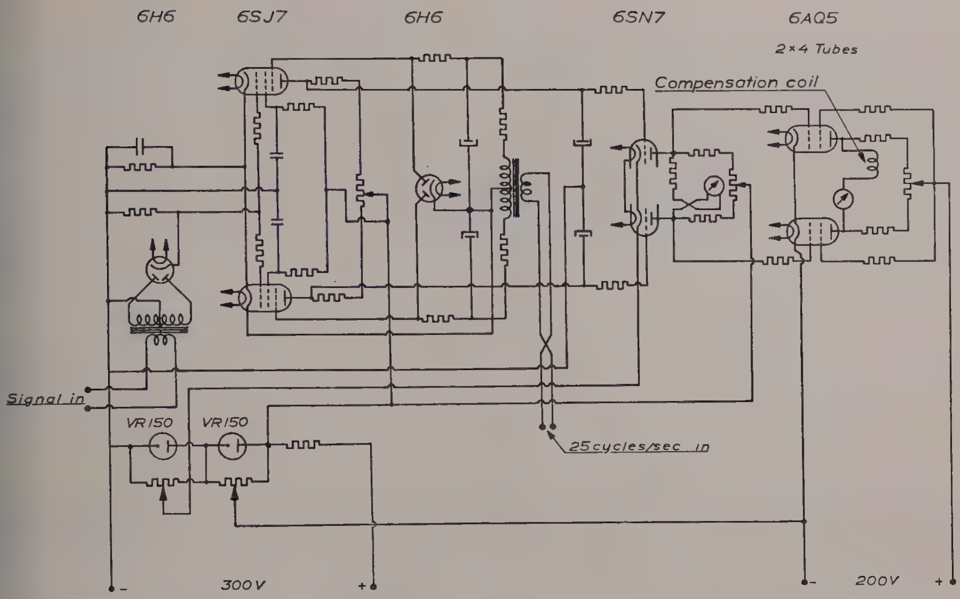

Fig. 14. Wiring diagram of the stabilizer.

rectified signal is fed to the grids of the two tubes. The screen grids of these tubes are controlled by the 25 cycle modulation signal so that the tubes are open during alternate half cycles of the modulation field.

Let us suppose that resonance takes place at the upper half cycle. This means that tube *A* charges the resistance *R* more than tube *B*, giving a voltage drop from *A* to *B*. If, on the other hand, resonance occurs at the lower half-cycle, there will be a voltage drop from *B* to *A*. Accordingly the sign of the voltage across *R* indicates whether the main field *H* is too high or too low.

The integrated voltage across *R* will be zero of course, if resonance takes place at zero passage of the modulation field. The time constant CR must be chosen so that there is no 25 cycle component across *R*. In the circuit used (fig. 14) this time constant is of the order of one second.

It is evident from the diagram of the circuit how the unbalance in voltage across *R* is amplified in a balanced direct current amplifier and then regulates the power tubes connected in parallel. These tubes change the magnetic field so resonance will take place very near the zero passage.

The regulating function is very steep and depends on the degree of amplification in the equipment. Fig. 15 shows the regulating function for the amplifier used. A change of about three percent in the main current to the magnet will change the field less than one part in a million.

The instrument shown between the two halves of the 6SN7 tube indicates the unbalance. It is an extremely sensitive detector of the instant on the modulation curve at which resonance occurs. By using two such sets of equipment one can compare two signals and adjust the frequencies so that resonance takes place at the same instant on the modulation curve.

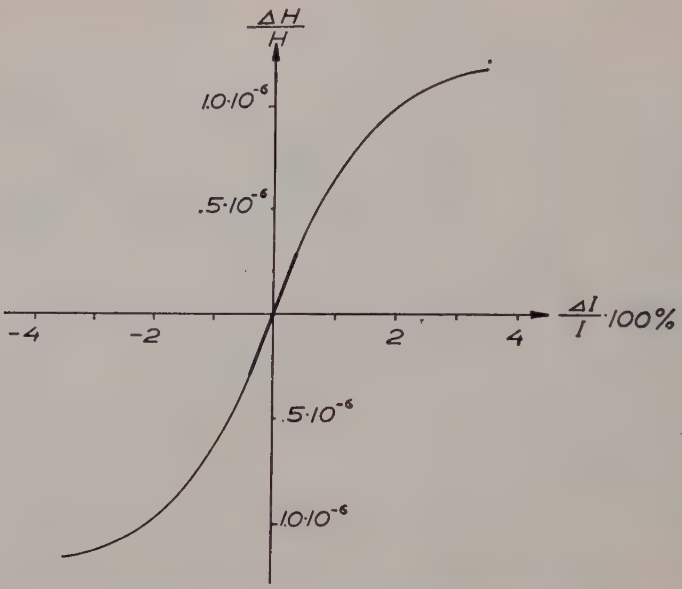

Fig. 15. The regulating function of the magnetic field stabilizer. The fractional change in the magnetic field is plotted versus the change in direct current to the magnet.

This method has been used several times in the present investigation, but the signals have also been photographed and measured as described in the next paragraph.

Another possibility exists; i.e., the use of two such stabilizers, one for controlling the magnetic field and one for controlling the variable frequency. In this manner it is possible to stabilize even this frequency to very high degree, thus permitting extremely accurate frequency measurements. This method will probably be used in a later investigation of chemical effects.

§ 6. The method of comparing two signals on the oscillograph

It has been shown earlier that absorption or dispersion curves respectively may be obtained, depending on whether the high-frequency bridge is balanced in phase or in amplitude. JACOBSOHN and WANGSNESS (25) have discussed the following equations given by BLOCH (8) in his first paper:

$$\frac{du}{dt} + \frac{u}{T_2} + (\Delta\omega)v = 0$$

$$\frac{dv}{dt} + \frac{v}{T_2} - (\Delta\omega)u = -|\gamma| H_1 M_z$$

$$\frac{dM_z}{dt} + \frac{M_z}{T_1} - |\gamma| H_1 v = \frac{M_0}{T_1}$$

where u and v are the components of the magnetic moment in- and out-of-phase. They have shown that the dispersion curves will be asymmetric and the absorption curves symmetric. The shape of the curves depends also on the gradient in the magnetic field and on harmonics from the 25 cycle modulation. Thus, it is a rather complicated problem to know where the correct resonance value is within the line-width. SMALLER (26) has discussed the equations of motion of the magnetic moment in a homogeneous magnetic field $H_{(t)}$ and a superimposed rotating magnetic field of amplitude H_1 and angular frequency ω. This solution to (8 a) can be written in terms of a complex function $F = v + iu$.

$$\frac{dF}{dt} = [\omega_r + i\,\Delta\omega(t)]\,F = -|\gamma|\,H_1 M$$

$$\Delta\omega(t) = |\gamma|\,H_0(t) - \omega$$

$$\omega_r = \frac{1}{T_2}$$

$M = \chi_0 H_0(t)$ is the magnetic moment at equilibrium. With a sinus wave modulation of the magnetic field one gets

$$\Delta\omega(t) = \bar{\omega} + \omega_m \cos(\omega_s t).$$

The time-independent solution is then

$$F = |\gamma|\,H_1 H_0 \int_0^\infty dT \exp\left[-iT\bar{\omega} - T\omega_r - i\,\omega_m \int_{t-T}^{t} \cos\omega_s t'\,dt'\right].$$

He has expanded this integral in a Fourier series in terms of the ordinary Bessel's function $J_K(x)$. If a lock-in amplifier is used, these equations become much simpler because there are no harmonics of the modulation frequency.

These equations have been used by SMALLER, YASAITIS and ANDERSON (27) in their determination of the μ_D/μ_H value. They have discussed the equations and shown that it is apparently safe to measure the resonance frequency at the center of gravity of the lines.

The lock-in amplifier has not been used in the present investigation. Therefore the line shape depends on the 25 cycle modulation harmonics. The foregoing equations will consequently be very complicated and it is hard to say at which instant on the curves the resonance takes place. However, it is not necessary that this be known if the method described hereafter is used.

Fig. 16 shows the principle of this method. The modulation amplitude H_m is chosen so that the resonance splits into two curves depending on the two resonance values in one modulation cycle. The distances a_H, a'_H, a_D and a'_D do not depend on the line shape if the bridges are balanced so that the slopes are identical at equivalent points. It is always possible to balance the bridges so that this is the case.

In the present investigation, two bridges of this kind are used simultaneously. One of the bridges contains a proton sample and the other a sample with the nuclei under investigation. The signals from the bridges are fed into a double beam oscillograph. The variable frequency is adjusted so that the

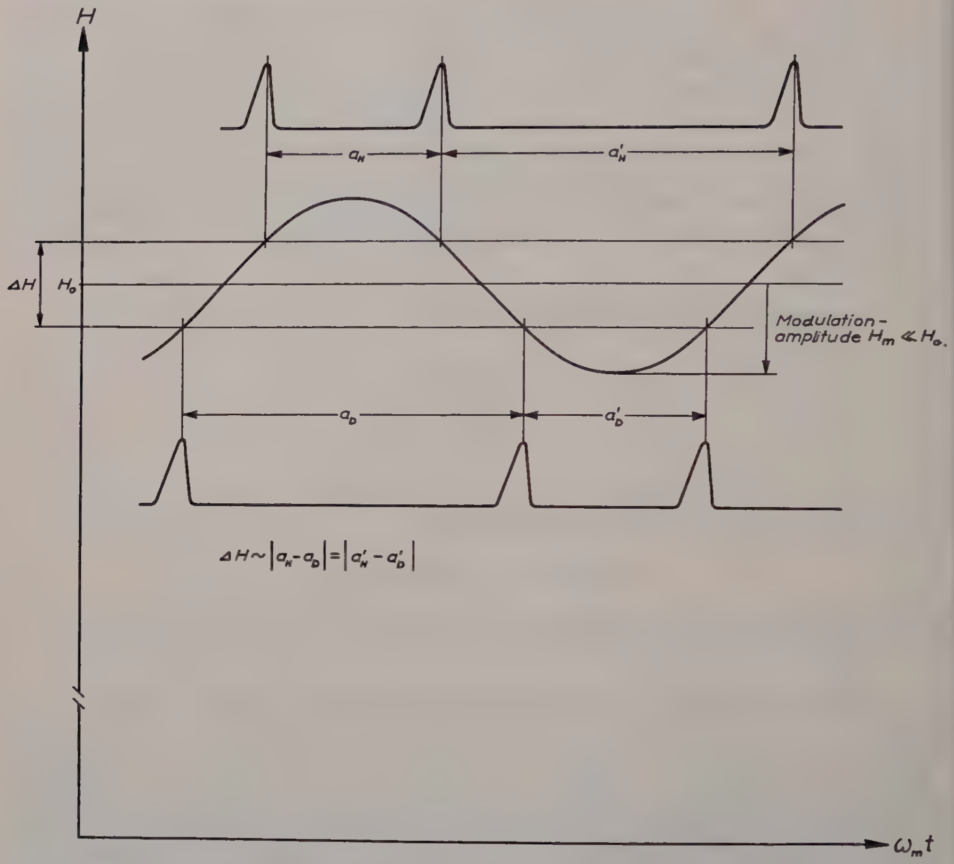
H
ΔH
H_0
a_H
a'_H
Modulation-amplitude $H_m \ll H_0$.
a_D
a'_D
$\Delta H \sim |a_H - a_D| = |a'_H - a'_D|$
$\omega_m t$

Fig. 16. This figure illustrates the method of comparing the signals on a double-beam oscillograph. The distances a_{H}, a_{D}, a'_{H} and a'_{D} will be independent of where they are measured if the method described in the text is used.

resonances occur at about the same time on the oscillograph. The screen is then photographed at the time when the frequency is measured. Fig. 17 shows a typical picture of this kind belonging to the μ_D/μ_H investigation described in chapter III § 1. Two pictures are taken with about the same frequency corresponding to the two parts of the modulation cycle indicated in fig. 16. The distances $a_H - a_D$ and $a'_H - a'_D$ are proportional to the field difference ΔH. The frequency is then changed and new photographs are taken. This is repeated between 15 and 20 times at each frequency determination. The bridges are then changed and the measurements repeated.

The distances a_H and a_D are then measured on the film and plotted against the frequencies as shown in figure 18.

The points are on a straight line if resonance takes place near the zero-passage of the modulation field, but are on a sine-curve if ΔH is of the order of half the modulation amplitude.

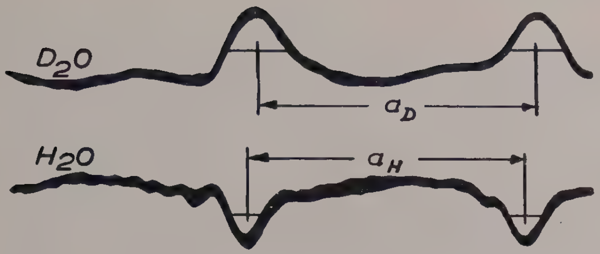

Fig. 17. A typical picture of the kind indicated in figure 16.

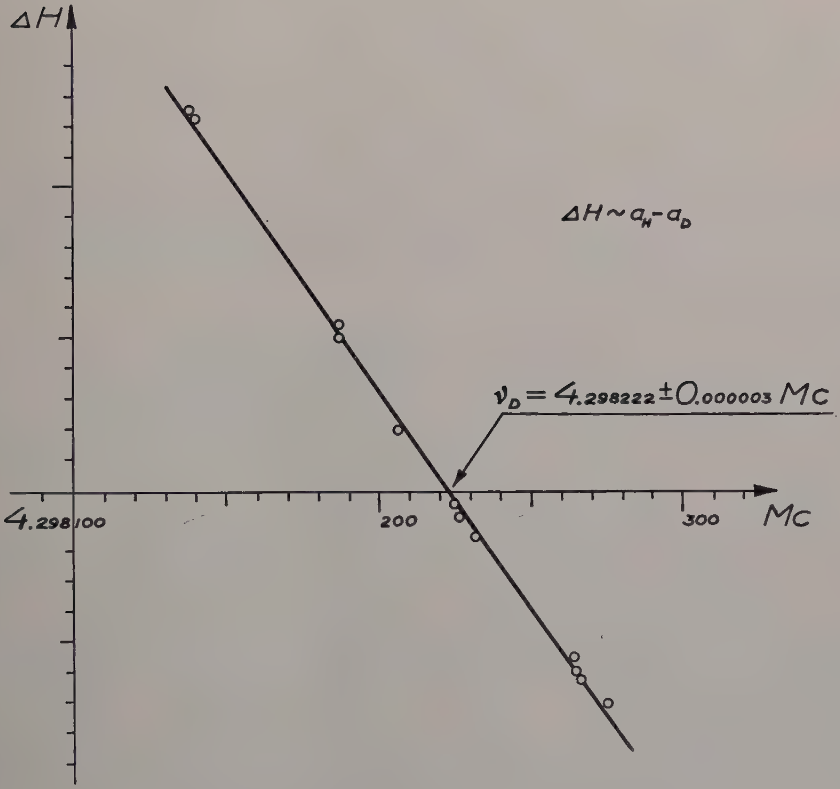

Fig. 18. Signal differences $\Delta H = a_H - a_D$ versus frequency.

The bridges are rebalanced many times during a run and the pictures are selected so that the deviation in a_H or a_D values measured at the peaks and at the bottom of the curves is within a given limit: i.e., in some cases, less than one tenth of the line-width. The values used are taken at the half-value, as indicated in fig. 17. The deviation in this figure is just within the given limits. There is no deviation at all in the best pictures, and even the "a" values measured at equivalent points on the wiggles are in agreement with the values measured at the half-maximum.

This method is very sensitive and gives the same value with widely different modulation amplitudes. The modulation amplitude has been varied 0.06 to 0.6 Gauss at about 7000 Gauss with a proton and a deuteron sample at fixed places. The deviation in the resonance values was less than one part in 5 000 000 and corresponds to the accuracy in the frequency determination.

It is important to work with weak high-frequency signals because the line-width will increase if the signals are nearly saturated. The high-frequency power used in this investigation is therefore much less than that which gives saturation. (It was at least 10 times less. See chapter I § 5.)

CHAPTER III

Some precision measurements of nuclear magnetic moments

§ 1. The ratio μ_D/μ_H

This is an extremely important relation. Many workers have measured it both by the induction (27, 28, 29) and by the nuclear resonance absorption method (18, 22, 30, 31). The first precision measurement was made by KELLOG, RABI and RAMSEY (32) with the molecular beam method. The different results are listed in table 3.

In an early measurement (18) this ratio was determined by a double bridge method with the proton sample in one position and a deuteron sample in the other. The bridges were fed by two ordinary high-frequency generators and the signals compared on a double beam oscillograph. The difference in magnetic field between the two places was then measured by two proton samples. This calibration of the field was made only twice. The results were in such a good agreement that it was assumed the field difference was constant.

In the present investigation the technique described in chapter II, § 6 has been used. The first preliminary values (33) were measured almost immediately after the magnet had been turned on, with only one change of the bridges. This was repeated at three different times and the values appeared to be in good agreement. However, subsequently, when the measurements had been repeated about 20 times, it was found that the values were distributed in three different groups, and the differences between the groups were larger than the estimated errors.

The explanation of this grouping is that the field difference was constant during one measurement but could have changed when the bridges were changed, inasmuch as the magnet current was not controlled during this time. To prove this, consecutive measurements were made with the results which may be seen in figure 19. It is apparent from this figure that the results are in agreement after about two hours. A thermometer shows that there is thermal equilibrium in the magnet after this period.

Another set of measurements demonstrated that it was also necessary to hold the field constant within half the amplitude of the modulation field to obtain good agreement between successive measurements.

Therefore, the measurements listed in tables 1 and 2 were taken after thermal equilibrium had been established in the field. The drift in the field

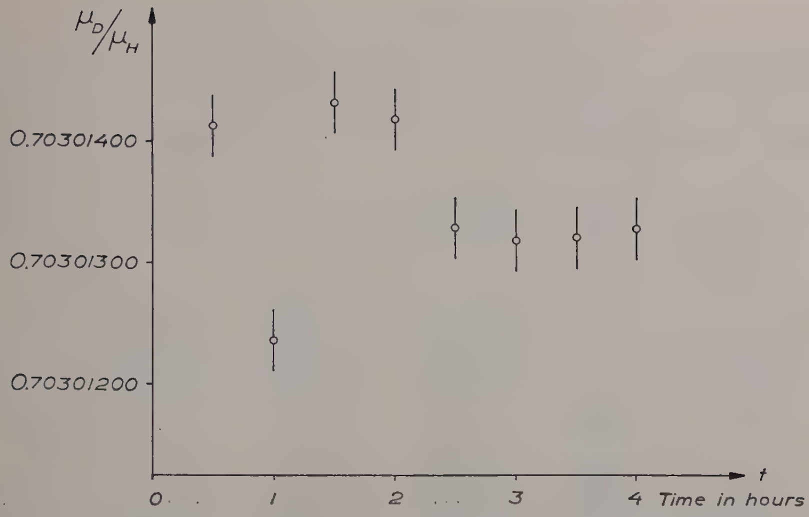

ig. 19. Consecutive measurements versus time. This figure indicates that the values will be in agreement about two hours after the magnet has been turned on.

Table 1

μ_D/μ_H for D_2O and Paraffin oil

agnetic field about 6580 Gauss and modulation amplitude about 0.3 Gauss

No.	ν_D in Mc ν_{D_I} (Position I)	 $\nu_{D_{II}}$ (Position II)	ν_H in Mc Position I and II	$2\nu_D=\nu_{D_I}+\nu_{D_{II}}$	$\frac{2\nu_D}{\nu_H}$	Deviation from mean value
1	4.298225	4.298185	28.000000	8.596410	0.30701464	−0.00000001
2	4.298225	4.298189	28.000000	8.596414	0.30701479	+0.00000014
3	»	4.298187	28.000000	8.596412	0.30701471	+0.00000006
4	4.298224	»	28.000000	8.596411	0.30701468	+0.00000003
5	4.298219	4.298190	28.000000	8.596409	0.30701461	−0.00000004
6	4.298222	»	28.000000	8.596412	0.30701471	+0.00000006
7	»	4.298186	28.000000	8.596408	0.30701457	−0.00000008
8	4.298223	4.298182	28.000000	8.596405	0.30701446	−0.00000019
9	»	4.298188	28.000000	8.596411	0.30701468	+0.00000003
10	4.298221	4.298190	28.000000	8.596411	0.30701468	+0.00000003
11	»	4.298188	28.000000	8.596409	0.30701461	−0.00000004
12	4.298226	»	28.000000	8.596414	0.30701479	+0.00000014
13	»	4.298191	28.000000	8.596407	0.30701454	−0.00000011
				Mean value	0.30701465	
				Max. deviation		±0.00000019
				Estimated error		±0.00000015
				Probable error		±0.00000002

Table 2

μ_D/μ_H for D_2O and H_2O

Magnetic field about 6580 Gauss and modulation amplitude about 0.3 Gauss

No.	ν_D in Mc		ν_H in Mc Position I and II	$2\nu_D = \nu_{D_I} + \nu_{D_{II}}$	$\frac{2\nu_D}{\nu_H}$	Deviation from mean value
	ν_{D_I} (Position I)	$\nu_{D_{II}}$ (Position II)				
1	4.298216	4.298162	28.000000	8.596378	0.30701350	+ 0.00000013
2	4.298218	»	28.000000	8.596380	0.30701357	+ 0.00000020
3	»	4.298156	28.000000	8.596374	0.30701336	− 0.00000001
4	4.298223	»	28.000000	8.596379	0.30701354	+ 0.00000017
5	4.298236	4.298146	28.000000	8.596382	0.30701364	+ 0.00000027
6	»	4.298147	28.000000	8.596383	0.30701368	+ 0.00000031
7	4.298190	4.298185	28.000000	8.596375	0.30701339	+ 0.00000002
8	4.298206	4.298161	28.000000	8.596367	0.30701311	− 0.00000026
9	4.298215	4.298157	28.000000	8.596372	0.30701329	− 0.00000008
10	»	4.298160	28.000000	8.596375	0.30701339	+ 0.00000002
11	4.298205	»	28.000000	8.596365	0.30701304	− 0.00000033
12	»	4.298165	28.000000	8.596370	0.30701321	− 0.00000016
13	4.298205	»	28.000000	8.596370	0.30701321	− 0.00000016
14	»	4.298165	28.000000	8.596370	0.30701321	− 0.00000016
15	4.298210	»	28.000000	8.596375	0.30701339	+ 0.00000002
				Mean value	0.30701337	
				Max. deviation		± 0.00000033
				Estimated error		± 0.00000025
				Probable error		± 0.00000004

was not more than about one part in 50 000, which corresponds to about half the amplitude of the modulation field.

This drift in the magnetic field satisfactorily explains the deviation of the value given in this paper from the earlier values.

This value is of such importance that the curves used in determining the resonance frequencies by the method described in chapter II, § 6 have been selected so that the permitted difference between the a-values measured at the peaks and at the bottom of the curves is less than one tenth of the line-width. The a-values used in determining the resonance frequencies were measured at half-amplitude as indicated in fig. 17. Between 15 and 20 pictures of this kind have been used for each value in the tables.

The values between horizontal lines in the tables are successive and the quotation marks indicate how the values from the two places are combined.

The probable error $\left(0.6745 \sqrt{\frac{\Sigma \Delta^2}{n(n-1)}}\right)$ in the tables is of the order of some parts in 10^7, but the different values do not appear to be quite statistically distributed. It is supposed that this difference depends in part on the line shape and in part on the method of changing the bridges. This effect will be discussed further at the end of this chapter. The estimated probable errors

± 0.00000015 and ± 0.00000025 are therefore chosen so that the major part of the values are within the given limits. The maximum errors given in the first communication of these results correspond to the maximum permitted deviation in the a_D and a_H values, but a new examination of these curves shows that these differences are statistically distributed within the limits of the estimated probable error.

The results clearly show there is a difference in the measured magnetic moment for the proton in H_2O and in paraffin oil. However, correction for the bulk susceptibility must be made before comparison is possible.

§ 2. The susceptibility correction

It has been pointed out earlier in this paper (chapter I) that the field seen by the nucleus H^* consists of several components,

$$H^* = H_0 + H_1 + H_2 + H_3$$

where H_1 represents the contribution of the field from the shielding effect of the atomic electrons. At least in the first approximation this contribution is the same for an isotopic pair and cannot explain the difference between H_2O and paraffin oil. H_2 represents the contribution from the bulk-susceptibilities. It also represents the field caused by paramagnetic ions.

The last component H_3 represents all other small fields that might be a function of the chemical composition.

No paramagnetic ions have been added to the samples in this investigation. The only contribution to H_2 is therefore from the bulk-susceptibility, which has been measured for the samples used (34). The values for the volume-susceptibilities are $(-0.7056 \pm 0.0006)\ 10^{-6}$ for paraffin oil, $(-0.7170 \pm 0.0006)\ 10^{-6}$ for D_2O if the volume-susceptibility for H_2O is arbitrarily set at $-0.7200 \cdot 10^{-6}$ CGS-units.

DEBYE (35) has calculated these effects for electric dipoles. Following his method we can divide H_2 into two different components

$$H_2 = H' + H''.$$

Let us assume that the magnetization has a constant value over the volume of a small sphere enclosing the nucleus in question. The radius of this sphere must be large in comparison with molecular dimensions but small as compared with ordinary macroscopic magnitudes. The component H' is then the additional field due to the presence of the sample, excluding the part contained in the small sphere. The field H' consists of two parts, the field due to the magnetic poles on the surface of the small spherical cavity and the "demagnetization field" due to the magnetic poles on the outer surface of the sample.

The first part is easily calculated from the integral

$$\int_S \frac{M\, d\omega}{r^3} \cos \Theta = \frac{4\pi M}{3}$$

where M is the magnetization and S is taken over the surface of the sphere. The other part of H' can also be calculated by the same type of integral, but the integration must be along the surface of the sample. It is easy to see that the results will be $-\frac{4\pi}{3}M$ for a spherical sample and $-2\pi M$ for an infinite cylinder. The value for the sample used will be between these limits. The numerical value for the sample used (see fig. 10) is approximately $-1.84\pi M$. This gives

$$H' = \left(\frac{4\pi}{3} - 1.84\pi\right) M \simeq 1.6\, M$$

and the corrections for the values in tables 1 and 2 can now easily be calculated in the following way

$$\frac{\mu_D}{\mu_H} = \frac{2\nu_D}{\nu_H}\frac{H_H}{H_D} = \frac{2\nu_D}{\nu_H}[1 + 1.6\,\Delta]$$

where

$$\Delta = [\chi'_H - \chi'_D]$$

and with the numerical factors given earlier

$$\Delta = -0.3 \cdot 10^{-8} \text{ for } D_2O \text{ and } H_2O$$

$$\Delta = 0.114 \cdot 10^{-7} \text{ for } D_2O \text{ and paraffin oil.}$$

The values corrected for different bulk-susceptibilities are

$$\mu_D/\mu_H = 0.30701466 \pm 0.00000015 \text{ for } D_2O \text{ and paraffin oil}$$

$$\mu_D/\mu_H = 0.30701337 \pm 0.00000025 \text{ for } D_2O \text{ and } H_2O \text{ (Destilled).}$$

The ratio of the magnetic moments for protons in H_2O and in paraffin oil is then 1.0000042 ± 0.0000015 where the given error corresponds to the estimated error above.

The second part H'' does not depend on the susceptibility. It has been shown that this part, in the electrical case, is zero for cubic crystals and liquids where the molecules are moving independently of each other. We need not suppose that it is zero in this case, but it seems reasonable to assume that it is independent of the bulk-susceptibility as stated earlier in this section. If it is not zero, we can always include it in H_3.

The result shows the difference in average magnetic field for the proton nuclei in paraffin oil and H_2O to be $(4.2 \pm 1.5) \cdot 10^{-6} H_0$. This has subsequently been confirmed by GUTOWSKY and MCCLURE (36); their value being $(3.4 \pm 0.5)\, 10^{-6}$. Inasmuch as they have measured the difference directly, the good agreement indicates that the errors given are conservative. THOMAS (37) has also measured this quantity and his value is $(2.2 \pm 0.5)\, 10^{-6}$. The small difference between his result and the two first mentioned may depend on different types of oil because the molecular structure is not known.

DICKINSON (17) has made a very interesting investigation of the influence of paramagnetic ions in different types of samples. Some of his results are shown in figure 20.

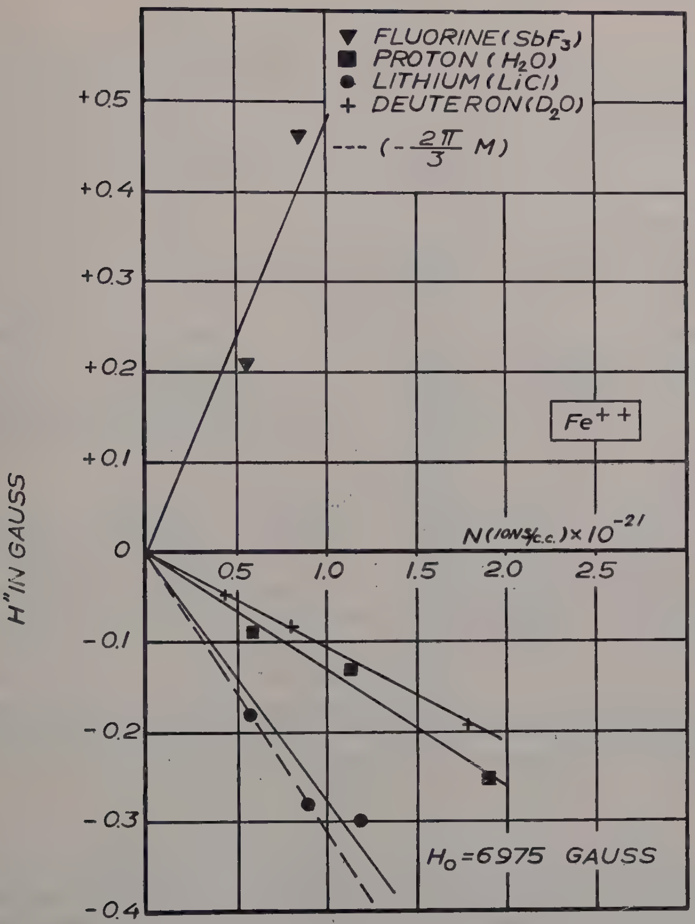

Fig. 20. Illustration of the dependence of H_2 on a resonating nucleus. (W. C. Dickinson, Phys. Rev. *81*, 727, (1951).

Fig. 20 shows that the influence of paramagnetic ions is quite different for different types of samples and that it also depends on the sample shape.

Many workers in this field have assumed that the field H_2 is the same if the two nuclei under investigation are in the same sample but Dickinson's investigation shows that this is not always true.

Newell (38) has shown that a difference exists between D^2 and H^1 in magnetic shielding depending on changes in amplitude of molecular vibration. He has calculated the numerical value $(1.1 \pm 0.2)\,10^{-7}$ by using the first term in a formula given by Ramsey (39). He also points out that this effect could be cancelled by molecular vibrations in the second term in Ramsey's formula. The total effect is so small, however, that it can be omitted in this case.

Table 3 shows some of the latest results for the ratio. The values given by Smaller, Yasaitis and Anderson (27) is not in complete agreement with the

Table 3

Comparison with other value of μ_D/μ_H

Author	Sample	μ_D/μ_H	Stated error
Bloch, Levinthal and Packard (28)	$H_2O + D_2D + MnSO_4$	0.3070126	±0.0000020
Bitter, Alpert, Nagle and Poss (30)	Liquid H_2 / Liquid D_2	0.307021	±0.000005
Wimett (31)	$H_2O + D_2O$	0.3070117	±0.0000017
Levinthal (29)	$H_2O + D_2O$	0.3070117	±0.0000015
Smaller, Yasaitis and Anderson (27)	$H_2O + D_2O$ $H_2 + D_2$	0.30701217 0.30701222	±0.00000012 ±0.00000010
Lindström	H_2O / D_2O Paraffin oil / D_2O	0.30701337 0.30701466	±0.00000025 ±0.00000015

value obtained in this investigation. They used a mixed sample, with two different coils around it and compared the signals from the coils in the manner described in chapter II, § 6. It is difficult to see why the mixture should change the ratio, but Dickinson (17) has shown that the F^{19} resonance frequency, for example, depends on both the chemical compound and the mixture of the chemical compounds. It is therefore possible that the discrepancy may be explained by the mixture. Other small effects may also be considdered such as the method of comparing the lines. This discrepancy will later be further investigated.

Hipple, Sommer and Thomas (40) have measured the magnetic moment for the proton in nuclear magnetons and obtained the value

$$\mu_p = 2.79268 \pm 0.00006 \ \ (42).$$

This result is not corrected for the shielding effect of the atomic electrons. They have calculated the diamagnetic correction from Ramsey's formula (39) using the relative measurements between H_2 and mineral oil, reported by Thomas (37).

The corrected result is

$$\mu_p = 2.79276 \pm 0.00006 \text{ nuclear magnetons } (41).$$

The corrections for the difference between hydrogen gas and H_2O is so small that it may be omitted $(0.3 \pm 0.3)\,10^{-6}$ (36).

With these corrections one obtains

$$\mu_D = 0.857415 \pm 0.000020 \text{ nuclear magnetons}$$

where the error is dependent only on the accuracy in the μ_p value.

§ 3. The ratio μ_{Li^7}/μ_{H^1}

This ratio has been measured in the same way as the μ_D/μ_H ratio, but the pictures for determining the frequency ratios have not been selected with the

Table 4

$\nu_{\mathrm{Li}^7} / \nu_{H^1}$

No.	Sample	ν_{Li^7}		ν_{H^1} Position I and II	$\frac{\nu_{\mathrm{I}} + \nu_{\mathrm{II}}}{2}$	$\nu_{\mathrm{Li}^7} / \nu_{H^1}$	Mean values
		Position I	Position II				
1	$LiNO_3$	5.597452	5.595234	14.400000	5.596343	0.3886349	
2	H_2O	»	5.595186	14.400000	5.596319	0.3886333	
3		5.597462	»	14.400000	5.596324	0.3886336	0.3886339
4	$LiNO_3$	11.192889	11.192454	28.800000	11.192673	0.3886345	
5	H_2O	11.192976	»	28.800000	11.192715	0.3886359	
6		»	11.192400	28.800000	11.192688	0.3886350	0.3886351
7	$LiNO_3 + H_2O$	11.193102	11.192220	28.800000	11.192661	0.3886341	
8	$LiNO_3 + H_2O$	»	11.192256	28.800000	11.192679	0.3886347	
9		11.193006	»	28.800000	11.192631	0.3886330	
10		»	11.192301	28.800000	11.192653	0.3886338	
11		11.192925	»	28.800000	11.192613	0.3886324	0.3886335
				Mean value		0.3886341	
				Max. deviation		±0.0000018	
				Estimated error		±0.0000010	
				Probable error		±0.0000002	

same care as in the μ_D / μ_H ratio. The permitted deviation in the a_H and a_{Li^7} values measured at the peak and at the bottom of the curves in this case is about one fifth of the line-width. Therefore, larger deviations may be expected in these ratios than in the previous case.

The results are seen in table 4. Values one to three are taken at 3382 Gauss ($\nu_H = 14.4$ Mc) and values four to six at 6764 Gauss (28.8 Mc), with a distilled water sample and a saturated water solution of $LiNO_3$. The mean value at the lower field is 0.3886339 and at the higher field is 0.3886351. The values seven to eleven are taken with two identical saturated water solutions at the higher field. The mean value in this case is 0.3886335. The spread in these values is so large that it is impossible to state with the degree of accuracy used herein, whether there is a real difference or not. The probable error has no significance in this case, but is noted for inclusion in a discussion of errors at the end of this chapter. The estimated probable error is chosen so that the three mean values are within the limits. Accordingly, with this degree of accuracy there seems to be no field effect and no effect of the bulk susceptibility.

The result is then $\nu_{\mathrm{Li}^7} / \nu_{\mathrm{H}^1} = 0.3886341 \pm 0.0000010$, without any correction for the diamagnetic shielding.

Lamb (43) has shown that the component H_1 in the expression for H^* (equation 12) is

$$H_1 (O)_z = \frac{e H_0}{3 m c^2} \cdot v(o)$$

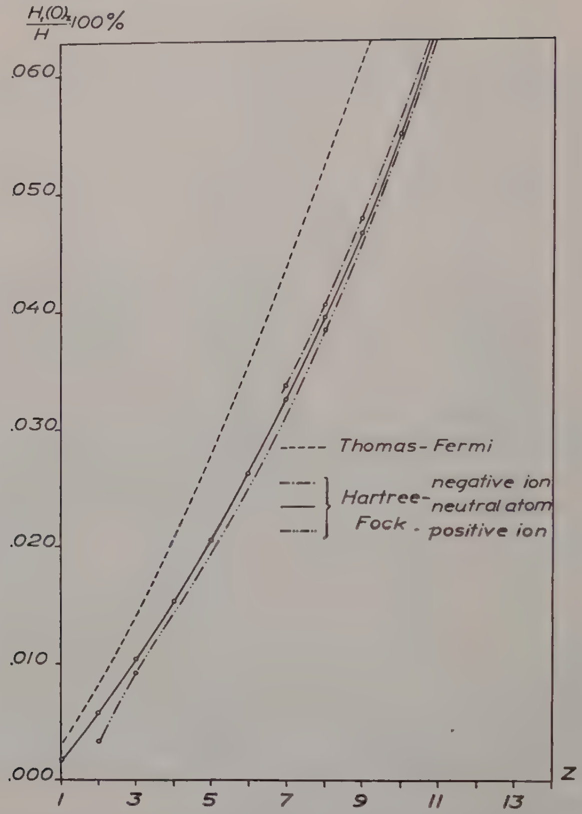

Fig. 21. A comparison between the diamagnetic corrections calculated by Lamb and by Dickinson. (W. C. Dickinson, Phys. Rev. 77, 736, (1950).

where $v(o)$ is the electrostatic potential at the nucleus produced by electrons. He has also calculated the values by placing $v(o) = -\frac{ze}{r_{av}}$ and using $r_{av} = \frac{a_0}{z^{1/2}}$ for the effective screening radius. This gives

$$H_1(O)_z = \gamma \alpha^2 z^{4/3} H_0$$

where γ is a number of the order of unity, a_0 the Bohr radius, and α the fine-structure constant. He has calculated a value for γ estimating a Fermi-Thomas model of the atom. This gives the following numerical value:

$$H_1(O)_z = -0.319 \cdot 10^{-4} \cdot z^{4/3} \cdot H_0.$$

This expression has been used by many workers in calculating the diamagnetic corrections, but increased accuracy necessitates a better value. DICKINSON (20) has tried to calculate the $v(o)$ functions for many different elements and considers his errors to be less than five percent. His values seem to be those best known at present, wherefore they are used in all determinations in this paper.

In the case of lithium he obtained 0.000101 H_0 and RAMSEY (39) has given 0.0000268 H_0 for H_2. The difference between H_2 and H_2O is negligible in this case (36).

It was shown in the first chapter that the ratio between the magnetic moments for two nuclei is:

$$\frac{\mu_A}{\mu_B} = \frac{I_A}{I_B} \cdot \frac{\omega_A}{\omega_B} \cdot \frac{H_B^*}{H_A^*}$$

with $I = \frac{1}{2}$ for H^1, $I = \frac{3}{2}$ for Li^7 and if the difference in bulk-susceptibility can be omitted one obtains

$$\frac{\mu_{\mathrm{Li}^7}}{\mu_{\mathrm{H}'}} = 3 \frac{\nu_{\mathrm{Li}^7}}{\nu_{\mathrm{H}^1}} \cdot \frac{\left[1 - 0.000027 + \left(\frac{H_3}{H_0}\right)_{\mathrm{H}^1}\right]}{\left[1 - 0.000101 + \left(\frac{H_3}{H_0}\right)_{\mathrm{Li}^7}\right]}$$

where $\left(\frac{H_3}{H_0}\right)_{\mathrm{H}^1}$ and $\left(\frac{H_3}{H_0}\right)_{\mathrm{Li}^7}$ includes any small effects of the chemical compounds. The investigation of μ_D/μ_H showed $\left(\frac{H_3}{H_0}\right)_{\mathrm{H}^1}$ to be small as compared with the estimated error in the ratio. Thus, it may safely be omitted in this case giving

$$\frac{\mu_{\mathrm{Li}^7}}{\mu_{\mathrm{H}^1}} = 1.165989 \pm 0.000007 \text{ for } \mathrm{LiNO_3}.$$

In this expression $\left(\frac{H_3}{H_0}\right)_{\mathrm{Li}^7}$ is included in the value. This is indicated by noting that it is valid for $LiNO_3$. In this case five percent uncertainty of the diamagnetic corrections is added to the uncertainty in the frequency ratio.

By using the absolute value for μ_p one obtains

$$\mu_{\mathrm{Li}^7} = 3.25633 \pm 0.00009 \text{ nuclear magnetons.}$$

The error here depends principally on the uncertainty in the μ_P value.

§ 4. The ratio $\mu_{\mathrm{B}^{11}}/\mu_{\mathrm{H}^1}$

This ratio is measured in the same way as the $\mu_{\mathrm{Li}^7}/\mu_{\mathrm{H}^1}$ ratio. The results appear in table 5.

The values 1 to 4 are measured with a saturated water solution of $K_2B_2O_4$ and distilled water. The mean value is 0.3208387. The values 9 to 13 are measured with the same samples but at the double field ($\nu_H = 28.7$ Mc). The mean value is 0.3208384. At approximately this field (28.8 Mc) the ratio is also measured with a saturated solution of $Na_2B_2O_4$ (14 to 17). The mean value is 0.3208379. This ratio is also measured with two identical samples containing saturated $Na_2B_2O_4$ (5 to 8), giving 0.3208375.

Table 5

$\nu_{B^{11}}/\nu_{H^1}$

No.	Sample	$\nu_{B^{11}}$ in Mc		ν_{H^1} in Mc Position I and II	$\frac{\nu_I + \nu_{II}}{2}$	$\nu_{B^{11}}/\nu_{H^1}$	Mean values
		Position I	Position II				
1	$\frac{K_2B_2O_4}{H_2O}$	4.620984	4.619182	14.400000	4.620083	0.3208391	
2		4.620970	»	14.400000	4.620076	0.3208386	
3		»	4.619172	14.400000	4.620071	0.3208383	
4		4.620989	»	14.400000	4.620080	0.3208389	0.3208387
5	$\frac{Na_2B_2O_4}{H_2O}$	4.621017	4.619092	14.400000	4.620055	0.3208372	
6		4.621025	»	14.400000	4.620064	0.3208378	
7		4.621044	4.619068	14.400000	4.620056	0.3208372	
8		4.621065	»	14.400000	4.620066	0.3208379	0.3208375
9	$\frac{K_2B_2O_4}{H_2O}$	9.208958	9.207172	28.700000	9.208385	0.3208385	
10		»	9.207196	28.700000	9.208389	0.3208389	
11		9.208906	»	28.700000	9.208380	0.3208380	
12		»	9.207202	28.700000	9.208381	0.3208381	
13		9.208928	»	28.700000	9.208385	0.3208385	0.3208384
14	$\frac{Na_2B_2O_4}{H_2O}$	9.241076	9.239150	28.800000	9.240113	0.3208373	
15		9.241150	»	28.800000	9.240150	0.3208385	
16		»	9.239178	28.800000	9.240164	0.3208390	
17		9.241016	»	28.800000	9.240097	0.3208367	0.3208379
				Mean value		0.3208381	
				Max. deviation		±0.0000014	
				Estimated error		±0.0000008	
				Probable error		±0.0000001	

The deviation of different measurements is larger than the difference between the mean values, wherefore there seems to be no chemical effect between $K_2B_2O_4$ and $Na_2B_2O_4$ and no field effect with the degree of accuracy used herein. The mean value for all measurements in this case is $0.3208381 \pm \pm 0.0000008$, where the estimated error is chosen in the same way as in the previous case.

DICKINSON has given $H_1(o) = 0.000199\,H_0$. With this shielding correction one obtains

$$\frac{\mu_{B^{11}}}{\mu_{H^1}} = 3\,\frac{\nu_{B^{11}}}{\nu_{H^1}}\left[1 + 0.000172 + \left(\frac{H_3}{H_0}\right)_{B^{11}}\right]$$

and with $\left(\frac{H_3}{H_0}\right)_{B^{11}}$ included in the ratio

$$\frac{\mu_{B^{11}}}{\mu_{H^1}} = 0.962680 \pm 0.000010 \quad \text{for} \quad \left\{\begin{matrix} K_2B_2O_4 \\ Na_2B_2O_4 \end{matrix}\right\} \quad \text{and} \quad H_2O$$

and in nuclear magnetons $\mu_{B^{11}} = 2.68853 \pm 0.00007$.

This ratio has also been measured by DONALD A. ANDERSON (44) with an uncorrected frequency ratio of 0.320827 ± 0.000004. This value does not agree within the stated limits with the value given above. He has reported 3.2 Gauss for the value of the line-width for the B^{11} signal, while the line-width is less than 0.1 Gauss in this investigation. His line-width seems therefore to depend principally on unhomogeneities in the field. ANDERSON also reports fluctuations in the magnetic field of the order of 10^{-4}. As has been shown earlier, this can change the value (fig. 19). The fluctuation of the field and the broad resonance curve (his error corresponds to 1/50 of the line-width) can easily explain the difference. He can have a much greater systematic error than the given probable error.

§ 5. The ratio $\mu_{F^{19}}/\mu_{H^1}$

This ratio is of special interest because there is a remarkably large dependence upon the chemical compound used in the case of F^{19}. The chemical shift was first suggested by SIEGBAHN and LINDSTRÖM (18) in order to explain the difference in resonance values obtained from different chemical compounds. This dependence has later been confirmed for F^{19} (20, 45) as well as for other nuclei (46).

The $\mu_{F^{19}}/\mu_{H^1}$ ratio has been measured in the same way as described earlier in this paper with two different samples, $CFCl_3$ and $CHFCl_2$. The results are given in tables 6 and 7.

The ratio between the resonance-frequencies from some other fluorine samples and one of the standard samples ($CFCl_3$ or $CHFCl_2$) has also been measured.

This comparison has been performed by measuring alternatively the resonance frequencies for the standard-sample and the other sample against a fixed water-sample. In this case the two bridges are mechanically fixed in the magnetic field and the fluorine samples can therefore be changed without changing the position in the field.

The individual results are seen in table 8. The different results are shown graphically in fig. 22.

The samples used have been prepared in the following way:

1. $CFCl_3$ Liquid.
2. $CHFCl_2$ Liquid.
3. HF 21.5 M.
4. SbF_3; Sb_2O_3 was dissolved in 21.5 M HF to a saturated solution. This solution was then filtered before it was used.
5. HBF_4. 1.1 g of H_3BO_3 was dissolved in 3 ml 21.5 M HF. A test portion of this solution did not precipitate a lead nitrate solution, which proves that a small excess of H_3BO_3 exists.

The liquids 1 and 2 were kept in ordinary glass containers, but the other reagents were kept in paraffined glass containers.

The greatest difference $171.8 \cdot 10^{-6}$ is found between HF and $CFCl_3$ and the value for $CHFCl_2$ is almost half-way between these two. This suggests that the difference in this case depends mainly on the H–F bond. The most marked difference between $CFCl_3$ and $CHFCl_2$ is the existence of an H–F bond between the molecules in the latter compound. In the HF solution there are bonds of the type H–F–H. The present measurement indicates therefore that the F^{19} nucleus in $CFCl_3$ is almost undisturbed by the chemical bond.

Table 6

$\nu_{F^{19}}/\nu_{H^1}$ for $CHFCl_2$

No.	$\nu_{F^{19}}$ in Mc		ν_{H^1} in Mc Position I and II	$\frac{\nu_I + \nu_{II}}{2}$	$\nu_{F^{19}}/\nu_{H^1}$	Mean values
	Position I	Position II				
1	13.547555	13.549010	14.400000	13.548282	0.9408529	
2	13.547585	»	14.400000	13.548297	0.9408540	
3	»	13.549090	14.400000	13.548337	0.9408567	
4	13.547480	»	14.400000	13.548285	0.9408531	
5	»	13.549095	14.400000	13.548287	0.9408533	0.9408540
6	20.229156	20.228481	21.500000	20.228412	0.9408564	
7	»	20.228500	21.500000	20.228328	0.9408525	
8	20.229282	»	21.500000	20.228391	0.9408554	
9	»	20.228560	21.500000	20.228421	0.9408568	
10	20.229174	»	21.500000	20.228367	0.9408543	0.9408550
				Mean value	0.9408545	
				Max. deviation	±0.0000023	
				Estimated error	±0.0000030	
				Probable error	±0.0000004	

Table 7

$\nu_{F^{19}}/\nu_{H^1}$ for $CFCl_3$

No.	$\nu_{F^{19}}$ in Mc		ν_{H^1} in Mc Position I and II	$\frac{\nu_I + \nu_{II}}{2}$	$\nu_{F^{19}}/\nu_{H^1}$	Mean values
	Position I	Position II				
1	13.547865	13.551005	14.400000	13.549435	0.9409330	
2	»	13.551045	14.400000	13.549455	0.9409344	
3	13.547860	»	14.400000	13.549453	0.9409342	
4	»	13.551010	14.400000	13.549435	0.9409330	
5	13.547980	»	14.400000	13.549495	0.9409371	
6	»	13.550970	14.400000	13.549475	0.9409358	0.9409346
7	20.230842	20.229084	21.500000	20.229963	0.9409285	
8	20.230890	»	21.500000	20.229987	0.9409296	
9	»	20.229210	21.500000	20.230050	0.9409326	
10	20.230848	»	21.500000	20.230029	0.9409316	
11	»	20.229270	21.500000	20.230059	0.9409330	0.9409311
				Mean value	0.9409330	
				Max. deviation	±0.0000045	
				Estimated error	±0.0000030	
				Probable error	±0.0000006	

Table 8

Ratios for different fluorine compounds

No.	Samples		ν_A in Mc	ν_B in Mc	ν_H in Mc	$\frac{\nu_{F^{19}}(A)}{\nu_{F^{19}}(B)}$	Mean values
	A	B					
1	$CFCl_3$	$CHFCl_2$	13.551005	13.549875	14.400000	1.0000834	
2			13.550970	13.549860	14.400000	1.0000819	$\frac{\nu_{F^{19}}(CFCl_3)}{\nu_{F^{19}}(CHFCl_2)} = 1.0000826$
3			20.238042	20.230174	21.500000	1.0000825	
4	$CHFCl_2$	SbF_3	13.551005	13.550975	14.400000	1.0000022	
5			13.550875	»	14.400000	0.9999926	
6			»	13.550895	14.400000	0.9999985	
7			13.550980	»	14.400000	1.0000063	$\frac{\nu_{F^{19}}(CHFCl_2)}{\nu_{F^{19}}(SbF_3)} = 1.0000006$
8			»	13.550935	14.400000	1.0000033	
9	$CFCl_3$	HF	13.551955	13.549645	14.400000	1.0001705	
10			13.551995	»	14.400000	1.0001734	
11			»	13.549635	14.400000	1.0001742	
12			13.551955	»	14.400000	1.0001712	$\frac{\nu_{F^{19}}(CFCl_3)}{\nu_{F^{19}}(HF)} = 1.0001718$
13			»	13.549655	14.400000	1.0001697	
14	$CHFCl_2$	HF	13.550845	13.549655	14.400000	1.0000878	$\frac{\nu_{F^{19}}(CHFCl_2)}{\nu_{F^{19}}(HF)} = 1.0000878$
15	$CHFCl_2$	HBF_4	13.550845	13.549945	14.400000	1.0000664	
16			13.550800	»	14.400000	1.0000631	
17			»	13.549875	14.400000	1.0000683	
18			13.550895	»	14.400000	1.0000753	$\frac{\nu_{F^{19}}(CHFCl_2)}{\nu_{F^{19}}(HBF_4)} = 1.0000686$
19			»	13.549945	14.400000	1.0000701	
20	$CFCl_3$	HBF_4	13.552050	13.549945	14.400000	1.0001554	$\frac{\nu_{F^{19}}(CFCl_3)}{\nu_{F^{19}}(HBF_4)} = 1.0001554$

It also seems reasonable that the values for SbF_3 and HBF_4 are between those of $CHFCl_3$ and HF. There are measurements made by other workers, however, which are difficult to explain in this simple manner. DICKINSON (17) and GUTOWSKY and HOFFMAN (45) have measured the difference between HF and $C_2F_3Cl_3$ with resultant values rather near the value for $CHFCl_2$ (see also fig. 22). This may be explained as a disturbance by the C–C bond or by the surrounding F^{19} nuclei.

There is a possibility that measurements on other sets of well defined molecules like the first three could give valuable information of the mechanism of the chemical shifts.

RAMSEY (47) has suggested that the chemical splitting depends on a paramagnetic disturbance and DICKINSON has attempted to explain some deviations by a combined paramagnetic and diamagnetic disturbance.

However, it seems reasonable to assume that the $\nu_{F^{19}}/\nu_{H^1}$ value for $CFCl_3$ gives the best value for $\mu_{F^{19}}/\mu_{H^1}$ because $CFCl_3$, $CHFCl_2$ and HF indicate that this gives the smallest disturbance.

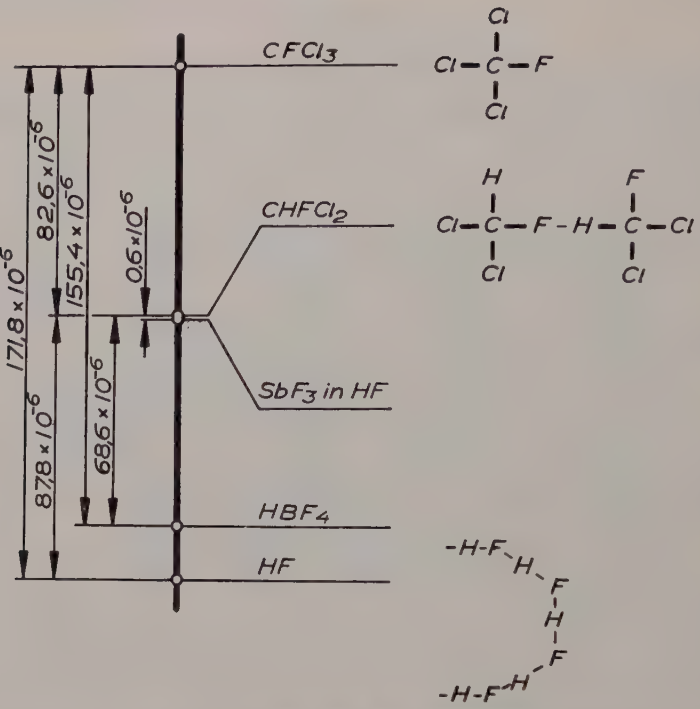

Fig. 22. The results for some flourine compounds are here shown graphically. The fractional values given are tabulated in table 8.

Dickinson gives 0.000437 H_0 as the diamagnetic correction for F^{19} and H^1. By using this correction one gets

$$\frac{\mu_{F^{19}}}{\mu_{H^1}} = (1 + 0.000437)\frac{\nu_{F^{19}}}{\nu_{H^1}} = 0.941344 \pm 0.000020$$

for $CFCl_3$ and probably for the F^{19} nucleus.

$$\mu_{F^{19}} = 2.62895 \pm 0.00010 \text{ nuclear magnetons.}$$

§ 6. The ratio $\mu_{Na^{23}}/\mu_{H^1}$

This ratio has been measured with two different chemical compounds, NaB and $Na_2B_2O_4$, in saturated water solutions, at two different fields ($\nu_H = 14.4$ and $\nu_H = 28.8$ megacycles). It has also been measured with two identical saturated NaBr solutions. The individual results are listed in table 9.

It is obvious from this table that there is no chemical effect and no field effects within the limits

$$\frac{\nu_{Na^{23}}}{\nu_{H^1}} = 0.2645182 \pm 0.0000007.$$

Table 9

$\nu_{\mathrm{Na}^{23}}/\nu_{H^1}$

No.	Sample	$\nu_{\mathrm{Na}^{23}}$ in Mc		ν_{H^1} in Mc	$\frac{\nu_{\mathrm{I}}+\nu_{\mathrm{II}}}{2}$	$\nu_{\mathrm{Na}^{23}}/\nu_{H^1}$	Mean values
		Position I	Position II	Position I and II			
1	$\frac{\mathrm{NaBr}}{\mathrm{H_2O}}$	3.809822	3.808278	14.400000	3.809050	0.2645174	
2		3.809852	»	14.400000	3.809065	0.2645184	0.2645188
3	$\frac{\mathrm{Na_2B_2O_4}}{\mathrm{H_2O}}$	3.809884	3.808251	14.400000	3.809067	0.2645186	
4		3.909852	»	14.400000	3.809051	0.2645176	
5		3.809842	3.808278	14.400000	3.809060	0.2645181	
6		3.809846	»	14.400000	3.809062	0.2645181	0.2645181
7	$\frac{\mathrm{NaBr}}{\mathrm{H_2O}}$	7.618538	7.617716	28.800000	7.618127	0.2645183	
8		7.618559	»	28.800000	7.618137	0.2645186	
9		»	7.617711	28.800000	7.618135	0.2645186	
10		7.618582	»	28.800000	7.618141	0.2645188	
11		7.618314	7.617912	28.800000	7.618113	0.2645180	
12		7.618290	»	28.800000	7.618101	0.2645175	
13		»	7.617924	28.800000	7.618107	0.2645178	
14		7.618296	»	28.800000	7.618110	0.2645179	
15		»	7.617939	28.800000	7.618118	0.2645181	0.2645182
16	$\frac{\mathrm{NaBr+H_2O}}{\mathrm{NaBr+H_2O}}$	7.618266	7.618011	28.800000	7.618137	0.2645186	
17		»	7.618050	28.800000	7.618158	0.2645193	
18		7.618200	»	28.800000	7.618125	0.2645182	
19		»	7.618074	28.800000	7.618137	0.2645186	
20		7.618221	»	28.800000	7.618147	0.2645189	0.2645187
				Mean value		0.2645182	
				Max. deviation		±0.0000011	
				Estimated error		±0.0000007	
				Probable error		±0.0000001	

The diamagnetic shielding correction is $(0.000629 - 0.000027)\,H_0 = 0.000602\,H_0$ and with $I_{\mathrm{Na}^{23}} = {}^3/_2$ one obtains

$$\frac{\mu_{\mathrm{Na}^{23}}}{\mu_{\mathrm{H}^1}} = \frac{3\,\nu_{\mathrm{Na}^{23}}}{\nu_{\mathrm{H}^1}}\left[1 + 0.000602 + \left(\frac{H_3}{H_0}\right)_{\mathrm{Na}^{23}}\right]$$

and with $\left(\frac{H_3}{H_0}\right)_{\mathrm{Na}^{23}}$ included in the value.

$$\frac{\mu_{\mathrm{Na}^{23}}}{\mu_{\mathrm{H}^1}} = 0.794032 \pm 0.000025 \quad \text{for} \quad \begin{Bmatrix}\mathrm{NaBr} \\ \mathrm{Na_2B_2O_4}\end{Bmatrix} \text{ and } \mathrm{H_2O}$$

which gives:

$$\mu_{\mathrm{Na}^{23}} = 2.21754 \pm 0.00010 \text{ nuclear magnetons.}$$

Table 10

$\nu_{\mathrm{Al}^{27}} / \nu_{H^1}$

No.	Sample	$\nu_{\mathrm{Al}^{27}}$ in Mc		ν_{H^1} in Mc Position I and II	$\frac{\nu_{\mathrm{I}} + \nu_{\mathrm{II}}}{2}$	$\nu_{\mathrm{Al}^{27}} / \nu_{H^1}$	Mean values
		Position I	Position II				
1	$\frac{\mathrm{AlCl_3}}{\mathrm{H_2O}}$	3.752993	3.751404	14.400000	3.752199	0.2605693	
2		3.752967	»	14.400000	3.752186	0.2605684	
3		»	3.751390	14.400000	3.752179	0.2605680	
4		3.752998	»	14.400000	3.752194	0.2605690	
5		»	3.751373	14.400000	3.752186	0.2605684	
6		3.753013	»	14.400000	3.752193	0.2605689	0.2605687
7	$\frac{\mathrm{AlCl_3}}{\mathrm{H_2O}}$	7.504072	7.504720	28.800000	7.504396	0.2605693	
8		7.504100	»	28.800000	7.504410	0.2605697	
9		»	7.504731	28.800000	7.504415	0.2605700	
10		7.504053	»	28.800000	7.504392	0.2605692	
11		»	7.504738	28.800000	7.504396	0.2605693	0.2605695
12	$\frac{\mathrm{AlCl_3 + H_2O}}{\mathrm{AlCl_3 + H_2O}}$	7.507286	7.506726	28.810000	7.507006	0.2605695	
13		7.507263	»	28.810000	7.506995	0.2605691	
14		»	7.506810	28.810000	7.507036	0.2605705	
15		7.507302	»	28.810000	7.507056	0.2605712	
16		»	7.506783	28.810000	7.507042	0.2605707	0.2605702
				Mean value		0.2605694	
				Max. deviation		±0.0000014	
				Estimated error		±0.0000010	
				Probable error		±0.0000002	

§ 7. The ratio $\mu_{\mathrm{Al}^{27}} / \mu_{\mathrm{H}^1}$

This ratio has been measured in the same way as the previous one. The only chemical compound used in this case is a saturated water solution of $\mathrm{AlCl_3}$. It has been measured at two different fields ($\nu_{\mathrm{H}} = 14.4$ and $\nu_{\mathrm{H}} = 28.8$ Mc), both with protons in distilled water and with protons in an equal water solution of $\mathrm{AlCl_3}$. The individual results are seen in table 10.

The result is

$$\frac{\nu_{\mathrm{Al}^{27}}}{\nu_{\mathrm{H}^1}} = 0.2605694 \pm 0.0000010.$$

The diamagnetic shielding correction is $(0.000768)\, H_0$. With $I_{\mathrm{Al}^{27}} = {}^5/_2$ one obtains

$$\frac{\mu_{\mathrm{Al}^{27}}}{\mu_{\mathrm{H}^1}} = 5 \frac{\nu_{\mathrm{Al}^{27}}}{\nu_{\mathrm{H}^1}} \left[1 + 0.000768 + \left(\frac{H_3}{H_0} \right)_{\mathrm{Al}^{27}} \right]$$

and with $\left(\frac{H_3}{H_0} \right)_{\mathrm{Al}^{27}}$ included in the value

$$\frac{\mu_{\mathrm{Al}^{27}}}{\mu_{\mathrm{H}^1}} = 1.303848 \pm 0.000050 \text{ for } \mathrm{AlCl_3} \text{ and } \mathrm{H_2O}$$

which gives

$$\mu_{\mathrm{Al}^{27}} = 3.64133 \pm 0.00015 \text{ nuclear magnetons.}$$

§ 8. Some control ratios

Some control measurements have been made in order to check the accuracy with which the bridges could be changed.

These measurements have been made with two fixed bridges as described in § 5. The ratios have in some cases been determined without changing the samples, by changing only the frequency to the bridge. This is possible, of course, only when the same sample contains the nuclei under investigation. The individual results are seen in table 11.

The results are in good agreement with the results calculated from the proton ratios in the previous sections. This indicates that the bridges can be changed and replaced with sufficient accuracy.

Table 11

Some control measurements

$\nu_{H^1} = 14.400000$ Mc

No.	Ratio and sample	Result	Calculated from tables 4, 5 and 9
1	$\dfrac{\nu_{Na^{23}}(Na_2B_2O_4)}{\nu_{Li^7}(LiNO_3)}$	0.6806341	
2		0.6806326	
	Mean value	0.6806333	0.6806356 ± 0.0000035
3	$\dfrac{\nu_{Na^{23}}(Na_2B_2O_4)}{\nu_{B^{11}}(Na_2B_2O_4)}$	0.8244570	
4		0.8244622	
5		0.8244582	
	Mean value	0.8244591	0.8244600 ± 0.0000040

§ 9. Error discussion

Let us examine the frequency ratios for two different nuclei. The sources of error are:

a) The frequency meter.
b) The determination of the resonance frequency by the method described in chapter II.
c) Systematic errors in the resonance curves.
d) Uncertainties in changing the bridges.
e) Uncertainties in the resonance coils and sample containers.
f) Unhomogeneities in the magnetic field.
g) The susceptibility correction.
h) The diamagnetic correction.
i) The chemical compound.

a) All frequencies are measured against the same crystal frequency, which has been compared with the standard frequencies from Bureau of Standards,

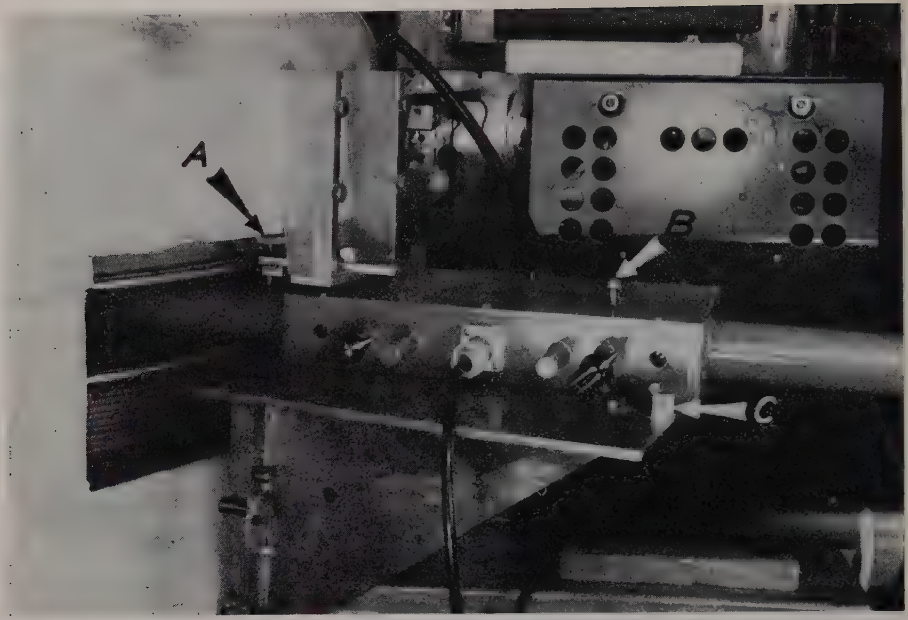

Fig. 23. This picture shows how the bridges are fixed in the magnetic field. A is a screw around which the bridge can be moved. B is a screw for the final balancing of the bridge and C is an adjustable edge.

Washington D. C., USA. The frequency ratios are not changed by an error in the absolute value of the crystal frequency, but the absolute field value used in chapter IV is dependent on it.

The only uncertainty lies in the linearity of the interpolation oscillator. General Radio claims that the accuracy is better than ± 1 c/s. The error caused by the frequency determination is therefore of the order of 1/5000000.

b) Figure 18 shows how the resonance frequency is determined. Fifteen to twenty points are used in this determination and the bridges are rebalanced several times. The values seem to be so well defined that the only error lies in the permitted deviation in the "*a*" values.

c) The bridges are balanced so that the "*a*" values will be independent of where they are measured, but it is not easy to see the deviation on the screen. Therefore, many pictures have been taken, but only those for which the deviations in "*a*" values are within a given limit have been used in the frequency determination. In the μ_D/μ_H determination, for instance, this means only approximately 50 per cent have been used. The deviations in the selected pictures appear to be statistically distributed.

d) The bridges are placed in the magnetic field using the arrangement indicated in fig. 23. One set of measurements was made with a deuteron and a proton sample; one was fixed and the other taken out and replaced several times. No discrepancies in the ratio between the fields at the two positions was found, demonstrating that the bridges may be replaced with good accuracy.

e) The uncertainty in localizing the bridges depends also on asymmetry in the coils and sample containers (see fig. 11). The dimensions of the containers are made equal within about 0.1 millimeter. The amount of copper per square centimeter is nearly the same but the wire diameter and number of turns depends on the frequency. The specific susceptibility of copper is only $0.086 \cdot 10^{-6}$ cgs units, wherefore the error caused by the difference in coil shape is negligible. However, some experiments have been performed with a deuteron and a proton sample and different types of coils. In the present experiment the amount of copper was changed by a factor of approximately two but no deviations were found.

f) The shape of the lines depends, of course, on the unhomogeneity in the magnetic field. Although this is not the same at the two positions used, it seems reasonable to assume that the deviations, at least in a first approximation, should be the same for different samples. This is equivalent to the assumption that the $\varphi(\nu)$ function introduced in chapter I depends only on unhomogeneities in the field.

g) The susceptibility correction made in § 1 is not absolutely correct, of course, but the whole correction is so small that even an error of ± 100 per cent is negligible in comparison with the given limits of error.

h) In many cases the diamagnetic correction is large as compared with the experimental errors and it is difficult to state the accuracy of the corrections. Fig. 25 is taken from Dickinson's paper. It shows the difference between his values and those calculated by Lamb. The values are calculated with different assumptions and the deviations are rather small. Dickinson's values, discussed in § 2 seem to be the best values known. He considers them to be correct within ± 5 per cent. This error is used in the foregoing numerical calculations.

i) The values given in this investigation have not been corrected for the chemical compounds used in the samples. This investigation shows that there is a chemical difference of about four parts in a million for H^1 samples, two parts in 10 000 for F^{19} samples. Other workers have shown deviations as large as one part in 1000 for N^{14} and N^{15} (45). Therefore all values have been given with an indication of the samples used in order that they may be corrected when the mechanism is found. It may also be pointed out here that all measurements have been carried out at room temperature.

The deviations Δ from the mean values are statistically distributed only within a set of consecutive measurements. This indicates that there is a systematic error from time to time, which is larger than the probable error. The deviations from time to time are small, seeming to depend in part on the mechanical construction and in part on the balancing of the bridges. The sample-coils have been taken out from the bridges and replaced from time to time to avoid a systematic mechanical error. The estimated error has therefore been chosen so that the mean values from successive measurements fall within the given limits. The maximum error includes all individual errors.

Table 12

Comparison with some previous values

Nucleus	Sample	Proton ratio	Reference
Li^7	$LiNO_3$	0.3886341 ± 0.0000010	Present study
		0.388625 ± 0.000040	(48)
		0.38862 ± 0.00002	(49)
B^{11}	$Na_2B_2O_4$ $K_2B_2O_4$	0.3208381 ± 0.0000008	Present study
	$Na_2B_2O_4$	0.320848 ± 0.000021	(50)
	$K_2B_2O_4$	0.320827 ± 0.000004	(44)
		0.32076 ± 0.00009	(48)
F^{19}	$CFCl_3$	0.9409330 ± 0.0000030	Present study
	$CHFCl_2$	0.9408545 ± 0.0000030	
	SbF_3	0.9408539 ± 0.0000045	
	HF	0.9407719 ± 0.0000030	
	HF	0.94077 ± 0.00010	(51)
	HF	0.94086 ± 0.00005	(50)
	HF	0.94075 ± 0.00017	(49)
	SbF_3	0.94086 ± 0.00017	(49)
Na^{23}	$Na_2B_2O_4$ NaBr	0.2645182 ± 0.0000007	Present study
	NaJ or NaCl	0.26450 ± 0.00003	(48)
	$NaAsO_2$	0.26454 ± 0.00007	(49)
	$Na_2B_2O_4$	0.264518 ± 0.000014	(50)
	NaBr	0.264492 ± 0.000015	(50)
Al^{27}	$AlCl_3$	0.2605694 ± 0.0000010	Present study
	$AlCl_3$	0.26056 ± 0.00003	(48)
	$AlCl_3$	0.26062 ± 0.00011	(49)
	$AlCl_3$	0.260579 ± 0.000013	(50)

§ 10. Results

The results from the present investigation are listed in table 12 together with corresponding values reported by other workers in this field.

The values in this investigation have been given with much smaller errors than the previous ones. Some deviations have been discussed in connection with the individual measurements and will not be further discussed here.

The values given in this paper can be combined with other values. Some of these relations will be discussed in this paragraph.

The accuracy in the μ_D/μ_H ratio is of theoretic importance.

BREIT and MEYEROTT (52) have given the following relation between the hyperfine structure splitting and the nuclear magnetic moments

$$\frac{\Delta \nu_H}{\Delta \nu_D} = \frac{4}{3}\left(\frac{m_H}{m_D}\right)^3 \cdot \frac{\mu_H}{\mu_D}$$

where m_H and m_D are the reduced masses for an electron in H^1 and respectively D^2.

If the present value for μ_D/μ_H is used in calculating the $\frac{\Delta\nu_H}{\Delta\nu_D}$ ratio, this gives:

$$4.339372 \pm 0.000005.$$

This value is not in agreement with the value 4.3386484 ± 0.0000030 measured by PRODELL and KUSCH (53) by the molecular beam method. The discrepancy is only (0.0167 ± 0.0002)%[1] but exceeds the given error by a factor of approximately 40.

BOHR (54) has explained the major part of this difference by taking into account the compound structure of the deuteron. He points out that there will be an asymmetry between the magnetic interaction of the electron with the proton and the neutron which comprise the deuteron.

It may therefore be possible to get information on the nuclear structure from precision measurements of the hyperfine splitting frequencies and nuclear magnetic moments for two isotopes of the same element.

LOW (55) has investigated the effects of internal nuclear motion on the hyperfine structure of deuterium, obtaining a result in good agreement with the present measurements, but he points out that the experimental and theoretic uncertainties are too large to permit any statements on the nuclear structure.

LOGAN and KUSCH (56) have measured the ratios

$$\frac{g_J\,(\mathrm{Na}^{23}\,2\,S_{\frac{1}{2}})}{g_I\,(\mathrm{Na}^{23}\,2\,S_{\frac{1}{2}})} = -\,2488.39 \pm 0.15$$

and TAUB and KUSCH (57)

$$\frac{g_I\,(H^1)}{g_J\,(\mathrm{Na}^{23}\,2\,S_{\frac{1}{2}})} = -\,15.1927\cdot 10^{-4} \pm 0.005\ \%.$$

This gives

$$\frac{g_I\,(\mathrm{Na}^{23},\,2\,S_{\frac{1}{2}})}{g_I\,(H^1)} = 0.26451 \pm 0.00002.$$

This is to be compared with the present value

$$\frac{\nu_{\mathrm{Na}^{23}}}{\nu_{\mathrm{H}^1}} = 0.2645182 \pm 0.0000007$$

and indicates that the nuclear g-value measured in an atom in the $2\,S_{\frac{1}{2}}$ state is equal to the true nuclear g-value within the limits of the diamagnetic corrections.

The $\frac{\nu_{\mathrm{Na}^{23}}}{\nu_{\mathrm{H}^1}}$ ratio can be combined with the result above and that of GARDNER and PURCELL (58) for $\frac{2\,g_L}{g_I}$ giving the ratio between the g-values for the electron and the path

$$\frac{g_s}{g_L} = 2\,(1 + 0.00114 \pm 0.00006)$$

---

[1] The μ_D/μ_H value given by SMALLER YASAITIS and ANDERSON (27) gives: (0.01702 ± 0.00007)%.

with the assumption that

$$g_J(\mathrm{Na}^{23}\,2\,S_{\frac{1}{2}}) = g_s.$$

The intrinsic magnetic moment of the electron has been calculated by SCHWINGER (59) as a consequence of the quantum electrodynamic theory and he gives

$$\frac{g_s}{g_L} = 2\left(1 + \frac{\alpha}{2\pi}\right) = 2\,(1 + 0.00116).$$

The present value is in good agreement with the theoretic value and with earlier values.[1] The given accuracy is limited only by the $\frac{g_I}{g_J}$ value given by LOGAN and KUSCH.

It is difficult to explain the differences between the nuclear moments for different chemical compounds with the present theories. It is therefore impossible to give the ratios for the true nuclear magnetic moments with higher accuracy than the splitting between different compounds. For this reason, the chemical compounds for which the ratios are valid have been indicated in the present investigation.

DICKINSON (20) points out that molecular perturbations of the electrons in the outer electronic shells would be expected to have only a small effect on the $\left(\frac{H_3}{H_0}\right)$-value. He has calculated the entire contribution of the $(2\,s)^2\,(2\,p)^6$ shell in the case of F^{19}. This total effect is only of the order of 30 per cent of the splitting found in § 5 between $\left(\frac{\nu_{\mathrm{F}^{19}}}{\nu_{\mathrm{H}}}\right)$ in $\mathrm{CHFCl_2}$ and $\mathrm{CFCl_3}$.

CHAPTER IV

Some absolute measurements

§ 1. The problem

HEDGRAN and LIND (60, 61) have recently made some precision measurements of the ratio between β- and γ-lines, through which they found an interesting discrepancy between the calculated values and various absolute values.

For example, HEDGRAN has given the $H\varrho$-ratio between the secondary electrons from the annihilation radiation and those from the ThC″-L-line[2].

$$\frac{(H\,\varrho)\text{-annihilation}}{(H\,\varrho)\text{-ThC}''\text{-L}} = 1.0002 \pm 0.0002.$$

---

[1] The value $\frac{g_s}{g_L} = 2\,(1+0.001145 \pm 0.000013)$ has recently been given by S. KOENIG, A. G. PRODELL and P. KUSCH Phys. Rev. *83*, 678, (1951).

[2] This notation has been introduced by C. D. ELLIS, Nature, Lond., *129*. 276 (1932).

If the annihilation energy is calculated from the constants given by DU MOND and COHEN (62) ($m \cdot c^2 = 510.969 \pm 0.010$ keV) this gives

$$(H\varrho)_{\mathrm{L}} = 2607.20 \pm 0.5 \text{ Gauss} \cdot \text{cm}.$$

HEDGRAN has also given the ratio between the ThC″-L and Au^{198} K-conversion lines.

$$\frac{(H\varrho)_{\mathrm{L}}}{(H\varrho)_{\mathrm{Au}^{198}}} = 1.17315 \pm 0.0002.$$

This gold line has been measured by DUMOND et al. (63) with a crystal spectrograph. HEDGRAN and LIND have made some control experiments with a double focusing β-spectrograph and their weighted mean value for the Au^{198} γ-line is 411.22 keV.

This gives

$$(H\varrho)_{\mathrm{L}} = 2604.5 \pm 05 \text{ Gauss} \cdot \text{cm}.$$

These two values for the ThC″-L-line are not in agreement within the combined limits of error. This indicates that there must be some systematic error or that a difference in mass exists between the electron and the positron.

From an experimental point of view a difference in mass could exist, of course, because the direct measurements of $\frac{e}{m}$ for the positron are not made with this accuracy. There is also a possibility that the Einstein law of equivalence between mass and energy is incorrect, inasmuch as this law has been used in calculating the energies. This law has not been proved with higher accuracy than about 0.1 per cent, but in no case have the predictions of this special theory failed when used in connection with atomic systems.

The existence of a mass difference would of course be of great importance to the theory and the purpose of the investigation described below has been to prove experimentally whether or not such a difference exists.

The most direct method of accomplishing this would be measurements of the $\frac{e}{m}$ values for the electron and positron. However, it would also be possible to check it by measuring the $(H\varrho)_{\mathrm{L}}$ value in absolute units. If this value is in agreement with 2607.2 ± 0.5 it proves that the masses are equal within the limits of error, but if it corresponds to 2604.5 ± 0.5, it shows that the masses are unequal.

The ThB-F-line is the calibration-line used most at low energies and the spread between the absolute values given by different workers is greater than the accuracy obtained in relative measurements in β-spectroscopy. The measurements described in this chapter are therefore made partly to check the aforementioned mass difference and partly to determine reference lines to be used for calibrating purposes in β-spectroscopy.

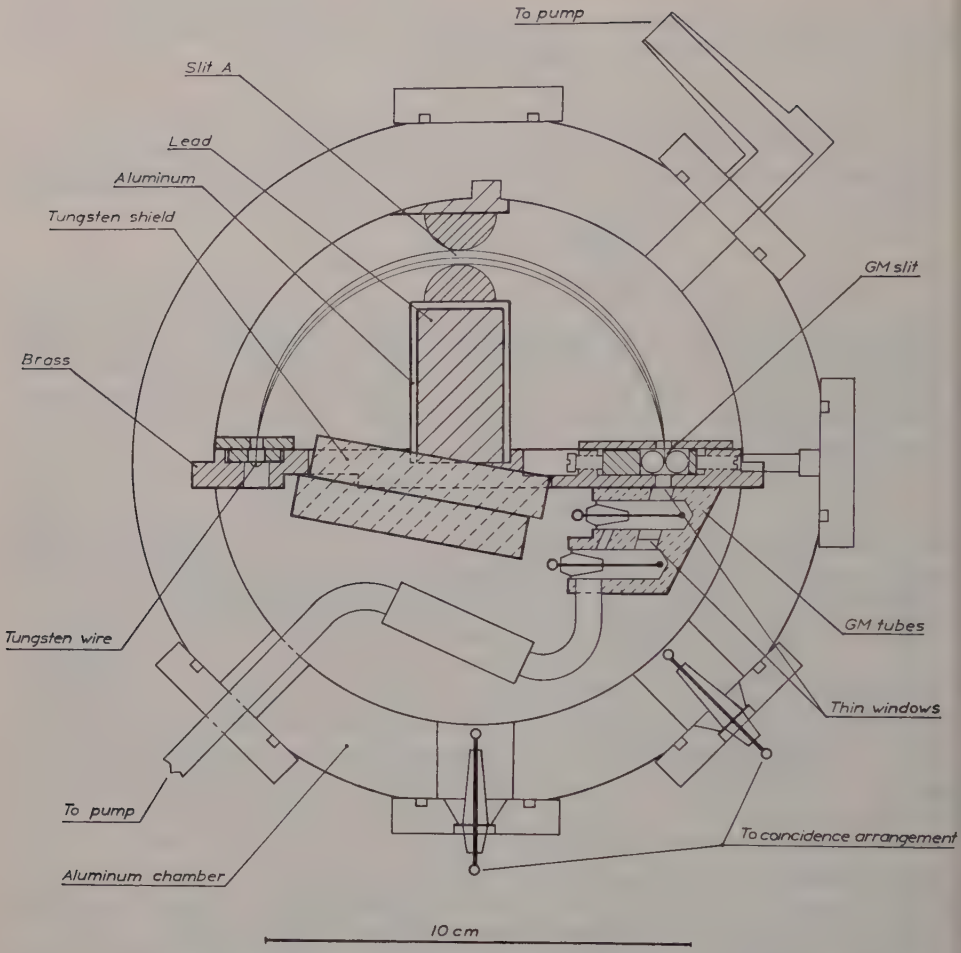

Fig. 24. Semicircular β-spectrograph for Geiger-Müller registration.

§ 2. The β-spectrograph

The β-spectrograph used in this investigation is of the semicircular type. Fig. 24 shows the general dimensions of the spectrograph and fig. 25 is a photograph of it.

The vacuum chamber is made of aluminum; all connections are of brass. The lead shields are covered with aluminum.

The slits are made by brass cylinders. This type of slit has been chosen, because even at a small distance from the edge there will be a great deal of material for the electrons to penetrate. These types of slits seem therefore to be more suitable for β-rays than those with sharp edges.

The two cylinders forming the G. M.-slit are held pressed together by three screws. The distance between them can be varied by placing different copper

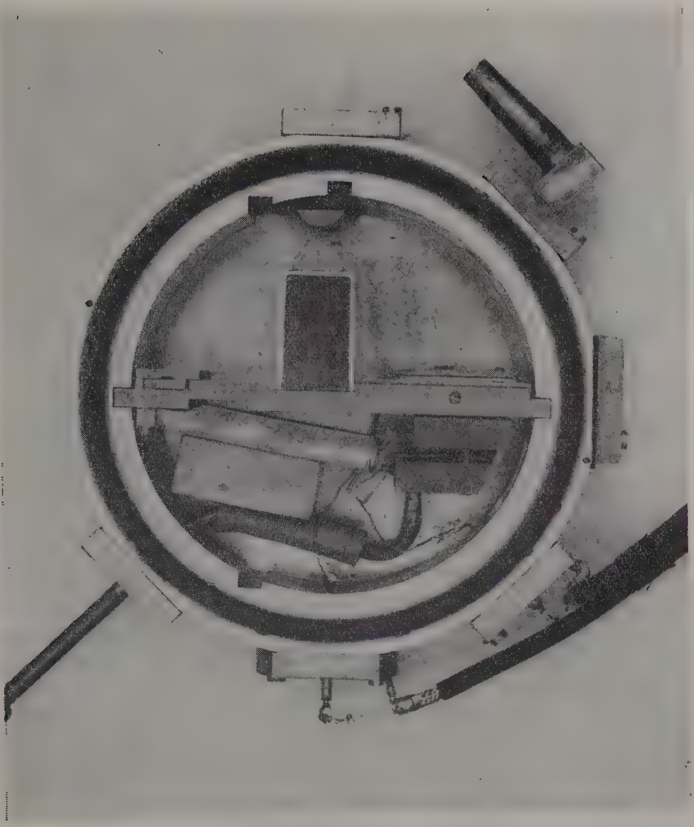

Fig. 25. Photograph of the semicircular β-spectrograph.

sheets between them. The slit can he adjusted by two of the screws so that it is perpendicular to the holder.

Both the G. M.-slit and the activated wire are fixed on the same holder; this can be taken out of the spectrograph. Fig. 26 shows a drawing of the holder. Fig. 27 indicates the manner in which the distance between the wire and the slit is measured.

The part with the G. M.-slit can be moved in the holder by a rod which goes through a Wilson-seal in the chamber. This possibility has been used in only a few cases, which will be discussed in connection with the measurements. In most cases, the holder with the G. M.-slit has been fixed to the main holder by the screw shown in the figure. The other slit shown in fig. 24 can be changed by moving the lead pieces on which the slit is fixed. The distance from the center of this slit and a line through the wire and the G. M.-slit has always been adjusted so that it is equal (± 0.2 per cent) to half the distance between the slit and the wire (i.e., 2ϱ).

The distance between the G. M.-tube and the wire is about 95 millimeters, which means that there will be a high background from the 2.6 MeV γ-ray at the tube. A single tube was first tried but the background was so high that

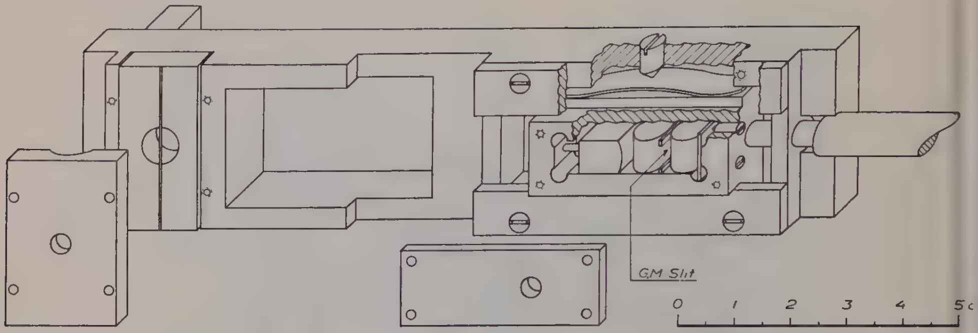

Fig. 26. Mounting for filament, slit and G. M. tube.

it was possible to measure only the F-line. Therefore a double tube of the kind shown in fig. 24 was constructed. It is important to have a very thin window at the G. M.-slit because the scattering angle must be so small that the beam can find the second tube.

The mean scattering angle may be calculated from a formula given by WILLIAMS (64). The mean deviation calculated by this formula is of the order of 35° for the F-line with a one mg/cm^2 mica window. It is therefore necessary to use much thinner windows. The windows used in this investigation are prepared from a nylon solution[1] and are about 10 μg/cm^2. The mean deviation is then negligible.

It is also important to have a window between the two parts of the tubes to prevent the passage of photons from one tube to the other. This window consists of 0.2 mg/cm^2 aluminum foil. The background with this double-tube arrangement is only about 1/20 of that with a single tube.

The background is also reduced by a factor of 2.5 by using tungsten shields instead of lead between the wire and the tube.

The same diffusion pump is used for both the chamber and the G. M.-tube. The vacuum obtained is about 10^{-5} mm Hg. The tube is filled with a mixture of propane gas (12 per cent), butane gas (28 per cent) and argon (60 per cent) to a pressure of about 6 cm Hg. The plateau lies at about 1000 volts and is about 100 volts.

The method of measuring the magnetic field will be discussed in § 4, but it may be mentioned here that a proton sample can be placed inside the chamber through one of the holes, to see if the field is influenced by the material in the chamber. No difference in field could be found when the field was measured first inside the chamber and subsequently with another proton sample at the same position but with the chamber removed from the field. This measurement was made with a relative accuracy better than one part in 200 000.

The rectifiers for the high voltages to the two tubes are electronically stabilized in the manner indicated in figure 7. The resolution of the coincidence arrangement was about 10^{-6} seconds and the pulses were counted with a scale of 64.

---

[1] This technic has been described by J. BROWN, F. FELBER, J. RICHARDS and D. SAXON, Rev. Sci. Inst. *19*, 818, (1948).

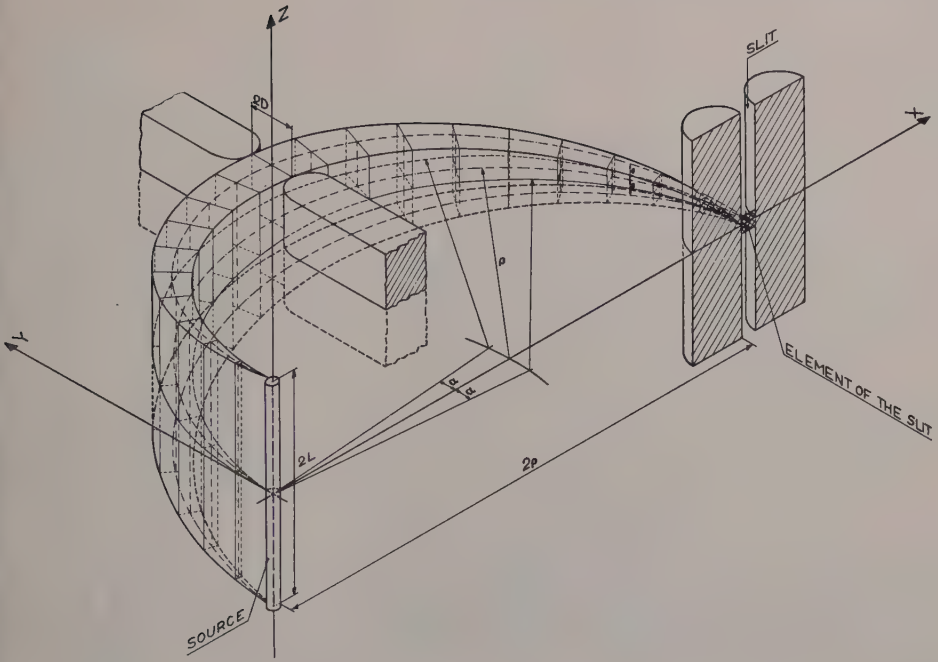

Fig. 27. Focusing principle of semicircular method.

§ 3. The theoretic line-shape

Many workers (65, 66, 67, 68) have given more or less complicated algebraic expressions for the line-shape from different kinds of sources; but in this case, with a very thin wire source, a combined algebraic and graphic method seems easiest and most surveyable.

Let us first calculate the contribution from a source of infinitesimal width. The quantities are defined in fig. 27.

The equation for the different paths in the x, y-plane is

$$(x - \varrho \cdot \cos \alpha)^2 + (y - \varrho \cdot \sin \alpha)^2 = \varrho^2$$

and for $y = 0$

$$x_1 = 0$$

$$x_2 = 2\varrho \cdot \cos \alpha$$

and with

$$\varepsilon_\alpha = 2\varrho - x_2$$

$$\varepsilon_\alpha = 2\varrho(1 - \cos \alpha) \simeq \varrho\, \alpha^2 \qquad (1)$$

The error introduced by neglecting the higher terms in the expansion of cos α will be negligible because $(\sin \alpha)_{\max} = \frac{3}{50}$.

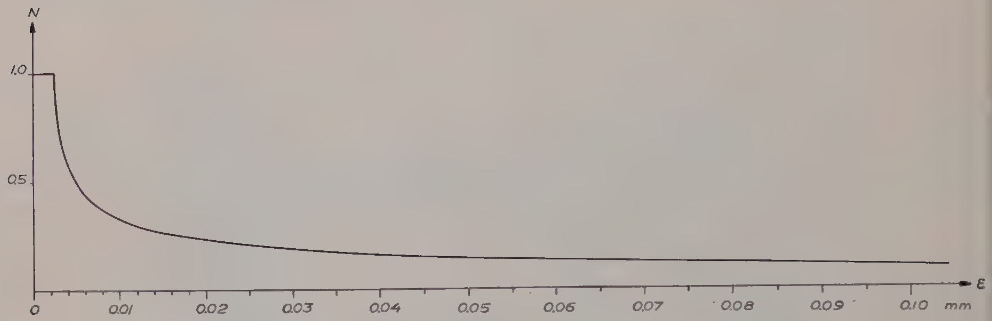

Fig. 28. Intensity curve for an infinitely narrow line-source.

The equation for the different possibilities in the Z direction is

$$\frac{Z}{\pi \varrho} = \sin \theta \simeq \theta \qquad -L \leq Z \leq +L \tag{2}$$

The maximum value of $\sin \theta$ is only about $\frac{3}{300}$ which shows that (2) is given with sufficient accuracy.

The solid angle of these two contributions entering the element of the detecting slit is thus given by

$$\frac{d\alpha \cdot d\theta}{2\pi} = \frac{1}{4\pi^2} \cdot \frac{1}{\sqrt{\varrho^3}} \cdot \frac{1}{\sqrt{\varepsilon_a}} \cdot dl \cdot d\varepsilon$$

and the intensity is

$$I = \frac{1}{4\pi^2} \cdot \frac{1}{\sqrt{\varrho^3}} \cdot \frac{1}{\sqrt{\varepsilon_a}}. \tag{3}$$

This gives the number of particles at unit area at any point along the detector slit coming from a point source at $x = 0$, $y = 0$ and $z = 0$.

Let us now assume a point on a line source at a distance z from the x, y plane. The particles from this point will arrive at the detector at a distance ε_θ if $a = 0$ where ε_θ is given by

$$\left(\frac{2\varrho}{\cos\theta} - 2\varrho\right) \cdot \cos\theta \simeq \varrho\,\theta^2$$

and they will arrive at

$$\varepsilon = \varepsilon_\theta + \varepsilon_a \text{ if } a \neq 0.$$

This means that $\varepsilon_a = \varepsilon - \varepsilon_\theta$ has to be introduced in equation (3) which gives

$$I = \frac{1}{4\pi^2} \cdot \frac{1}{\sqrt{\varrho^3}} \cdot \frac{1}{\sqrt{\varepsilon - \varepsilon_\theta}}.$$

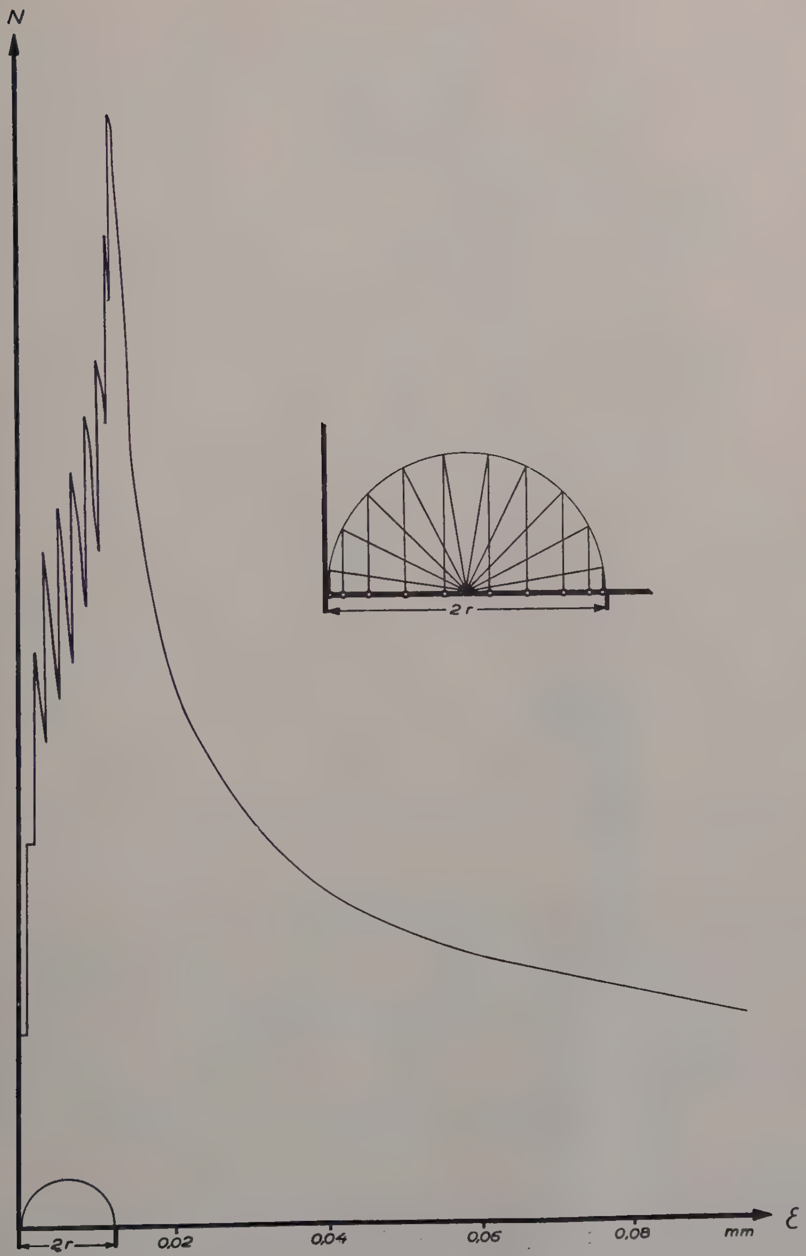

Fig. 29. Numerically integrated intensity curve for a thin line-source.

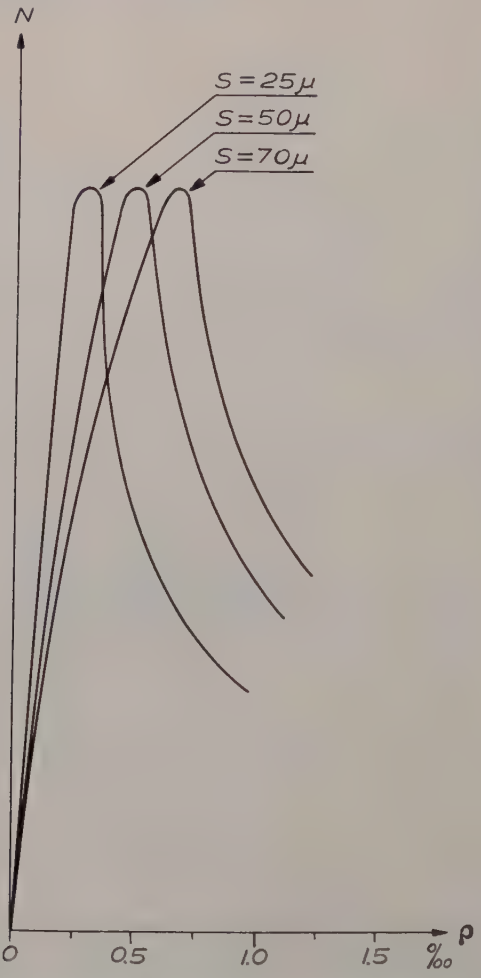

Fig. 30. Expected intensity distribution for three different G. M. slits.

The total intensity due to a wire of infinitesimally small breadth is now equal to

$$I_{\text{tot}} = 2\int_0^L I\,dl \quad \text{and with} \quad \varepsilon_\theta = \varrho \cdot \theta^2 = \varrho\left(\frac{Z}{\varrho\,\pi}\right)^2.$$

This gives

$$I_{\text{tot}} = \frac{1}{2\,\pi\,\varrho} \cdot \sin^{-1}\sqrt{\frac{L^2}{\pi^2\,\varrho\,\varepsilon}}. \tag{4}$$

This equation is only true, of course, as long as $\varepsilon \geq \frac{L^2}{\pi^2\,\varrho}$. WOOSTER points out that if ε decreases to less than this value, it means that less and less of

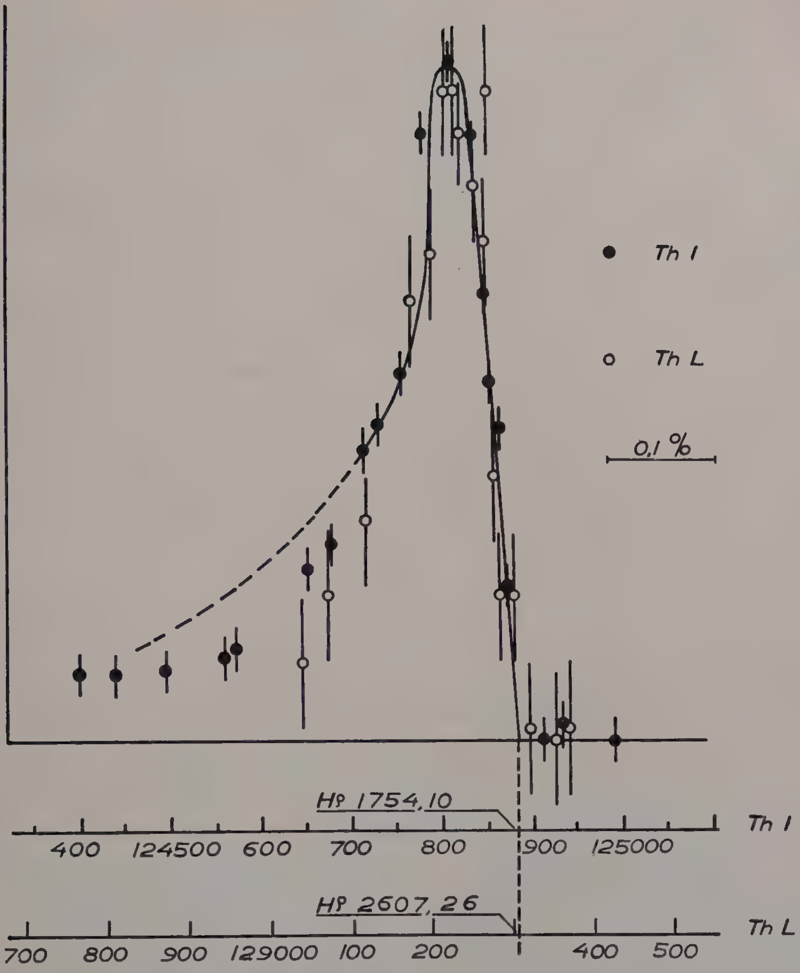

Fig. 31. The curve is that expected from the calculations. The points are normalized experimental values from the I- and L-lines.

the source length will contribute to the intensity. The active source length (Z) is therefore given by

$$Z^2 = \pi^2 \varepsilon \varrho \qquad Z \leq L$$

The contribution from a wire can now be estimated by adding contributions of the kind given by equation (4). Fig. 28 shows the intensity distribution from an infinitely thin wire and fig. 29 indicates how 10 infinitely narrow wire samples are arranged to give approximately the same intensity at the detector as a wire with a diameter of 12 μ.

Fig. 30 shows the expected distribution curve with three different G. M.-slits. ε_s corresponding to the total high energy slope is in excellent agreement

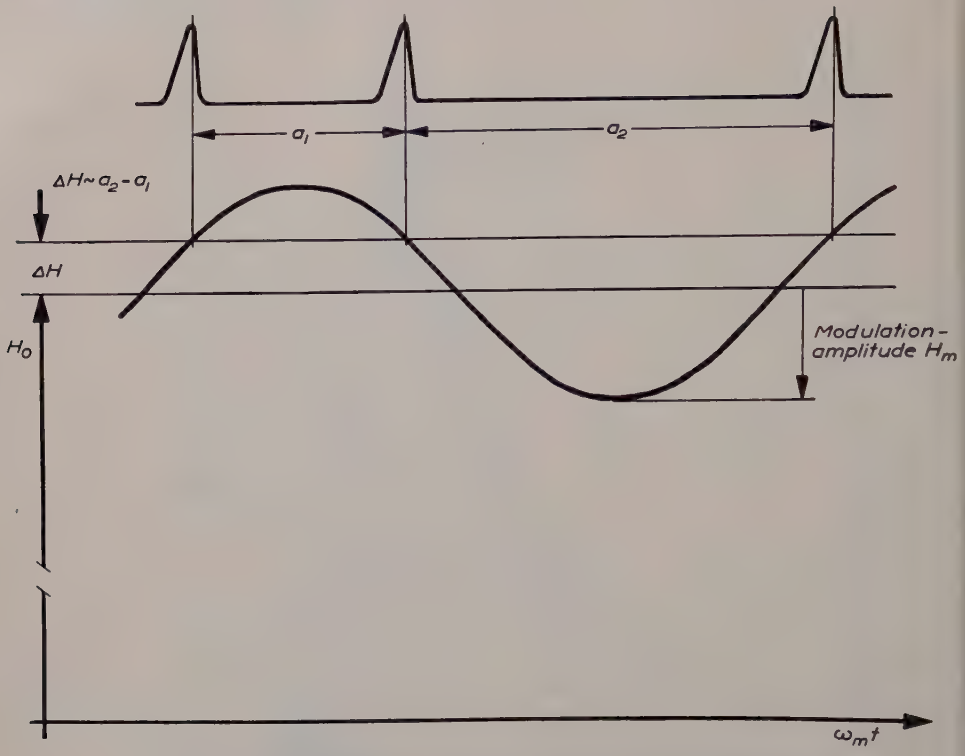

Fig. 32. The principle used in measuring the magnetic field.

with that measured from the experimental curves as can be seen from fig. 31. The total experimental line-width, however, is a little larger than that calculated, but it seems reasonable that this deviation should be explained by the following factors:

1. The wire may not be aligned exactly parallel to the magnetic field.
2. The G. M.-slit and the wire may not be exactly parallel.
3. There may be some small scattering effects at the slit edge.
4. Effects depending on the structure of the wire and on impurities on the source.

§ 4. The field determination

The magnetic field along the path in the β-spectrograph has been measured with a proton-sample by a method similar to the one described in chapter II § 6. Therefore, it will only be briefly discussed here.

Fig. 32 shows graphically how the field is measured. The high-frequency bridges are adjusted so the corresponding slopes are equal, as described earlier. Fig. 33 gives the experimental curves for $a_1 - a_2 = \Delta H$ as a function of the

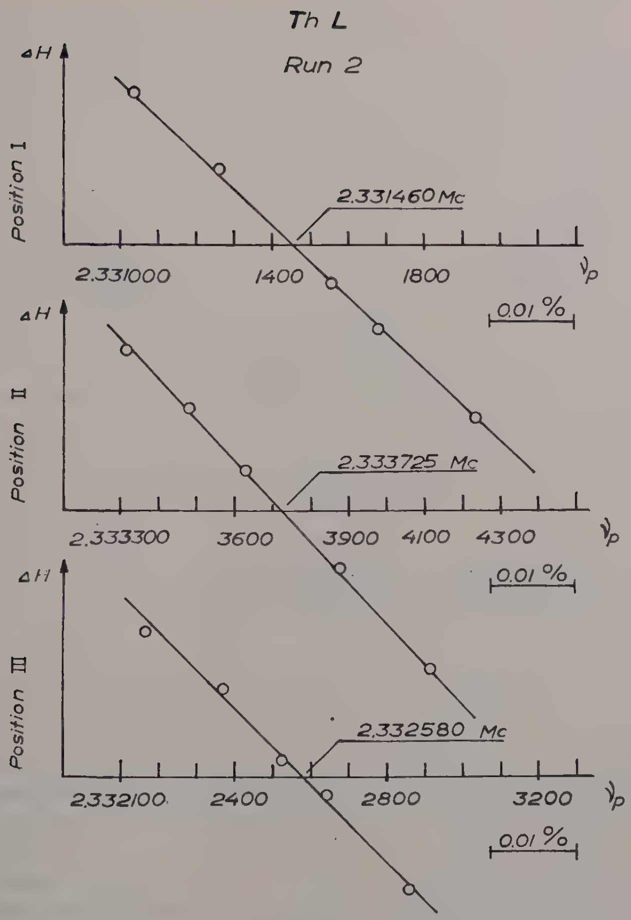

Fig. 33. The ΔH values defined in figure 32 plotted versus proton frequency for three different positions along the path.

proton frequency ν_p. The correct frequency value ($\Delta H \sim a_1 - a_2 = 0$) can be determined easily with greater accuracy than one part in 100 000.

The modulation amplitude used in the field determination has been between one part in 3000 (at the field corresponding to the *ThB–F*-line) and one part in 12 000 (at the field corresponding to the *ThC″–L*-line). The modulation amplitude was varied by a factor of five from these values in order to check whether the ν_p value depended on this amplitude. No amplitude dependence was found.

The three ν_p values in fig. 33 correspond to the sample positions indicated in fig. 34. In some cases the field has been measured at five different places along the path, but the correction will be about the same with only three values as in the example shown in fig. 33, because the field changes very slowly along the path.

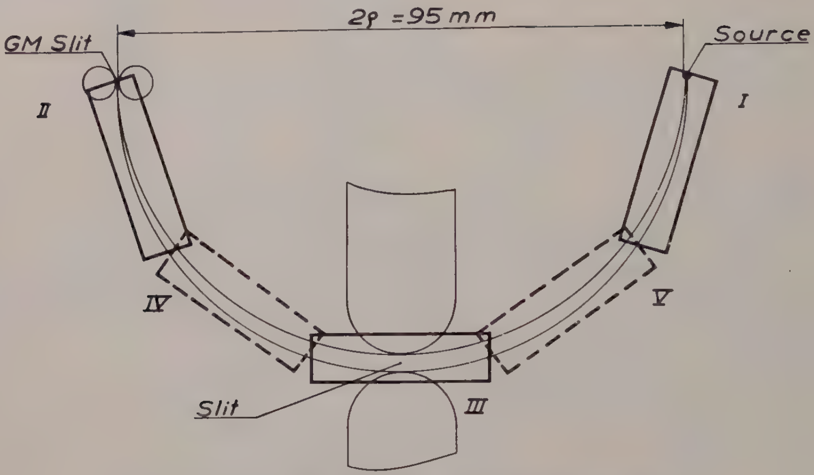

Fig. 34. The different sample positions along the path.

The mean field strength H_{Mean} along the path has been calculated by means of a HARTREE correction (69) in the following manner.

$$H_{\text{Mean}} = H_1 + \frac{1}{2}\int_0^{\pi} \sin\theta\,(\Delta H)_\theta \cdot d\theta \tag{5}$$

where H_1 is the field strength at the filament, θ the angle between radius vector through the filament and a radius from a point on the path and $(\Delta H)_\theta$ the difference in field strength at this point from that of the field at the filament.

The water sample was placed in a high-frequency bridge of the kind discussed in Chapter II § 3, but the sample coil was located so the sample could be placed in the positions shown in fig. 34. The effective sample dimensions were: length 30 millimeters and diameter 6 millimeters.

A proton sample can be placed inside the vacuum chamber (fig. 24) through one of the holes, in order to check whether the field strength is changed by the chamber. No difference could be found between the field measured inside the chamber and that measured at the same position with the chamber removed. The field has therefore been measured along the path just before the chamber was placed in the field at a fixed magnet-current and just after the chamber was removed at the current corresponding to the high energy part of the β-lines.

§ 5. The *F*- and *I*-lines of ThB

In most cases the activity has been deposited on tungsten wires with a diameter of 12 μ. The wires have been activated by a Thorium sample of about three mC. A voltage of about 800 volts has been applied between the wire and the sample container. In this way it was possible to get about 0.5 mC on the wire. This figure was measured by comparing the activity on the sample with the γ-radiation from a *Ra*-standard using a gold γ-tube.

The *F*- and *I*-lines of *ThB* are internal conversion lines belonging to the same γ-radiation. They have been measured in the following way.

The activated wire was placed in the spectrograph parallel to the magnetic field. The G. M.-slit was also adjusted so it was parallel to the field and the wire. A comparator was used in making these adjustments and also in measuring the distance 2ϱ. The radius of curvature was measured from the nearest slit edge to the nearest edge of the wire.

The field corresponding to a certain line was calculated and the magnetic field adjusted to approach this value. The field was then measured along the path as described earlier.

Following this measurement, the chamber was placed in the field so that the path shown in the drawing (fig. 34) coincided with the measured path.

The number of counts per minute from the coincidence apparatus was then measured as a function of the direct current to the magnet. No modulation field was used during these measurements. The current to the magnet was measured in arbitrary units, comparing the voltage over a temperature-controlled manganin resistance with a normal element. This comparison was made with a Wolff compensator (Otto Wolff, Berlin 8584).

Fig. 31 shows a typical curve of this type. The line drawn in this figure is a theoretic curve calculated as indicated in § 3. The high-energy part of this line was then located as shown in the figure.

The current to the magnet was changed to this value. This change is always less than 0.05 percent. The chamber was then removed and the field measured again along the path. These ν_p values were used in calculating the $(\nu_p \varrho)$-values given in the tables.

The procedure described here was subsequently repeated for all the measured lines. The temperature in the magnetic field was also noted, so the measured radius of curvature could be corrected. This correction is always smaller than two to four parts in 10^5.

These measurements have been made with different slits and sources as indicated in table 13. The entire spectrograph was also rotated 180° in the magnet once so that a different part of the magnet was used (table 13 run 5).

Most of the measurements have been made with a fixed distance between slit and source but two measurements of the *F*-line (runs 1 and 2) were carried out with a fixed magnetic field. In these cases the G. M.-tube and the slit were mounted on a movable slide on the holder. The slide was connected to a rod, which was connected through a Wilson-seal with a micro-indicator. The number of counts per minute was plotted as a function of the scale readings on the micro-indicator. The radius of curvature was subsequently measured at the point corresponding to the highest energy of the line.

The G. M.-slit was defined by copper foils pressed between the slit-edges. The slit-height was three millimeters.

The results for the *F*- and *I*-lines are tabulated in tables 13 and 14.

The errors and the results will be discussed in greater detail in § 8 and § 9.

The *F*- and *I*-lines are in rather good agreement with the theoretic line-shape if the experimental line-width is of the order of 0.14 percent or more. The *I*- and *L*-lines are in agreement with the theoretic one even for G. M.-slits corre-

Table 13

ThB–F-line

Run	$\nu_p \cdot \varrho$ Mc · cm	Deviation from mean value Mc · cm	Tungsten wire diameter mm	G.M. slit width mm
1	5.91212	− 0.00005	0.012	0.120
2	5.91280	+ 0.00068	0.012	0.160
3	5.91204	− 0.00013	0.012	0.146
4	5.91212	− 0.00004	0.012	0.100
5	5.91213	+ 0.00004	0.012	0.065
6	5.91231	+ 0.00014	0.012	0.065
7	5.91082	− 0.00135	0.012	0.075
8	5.91164	− 0.00053	0.012	0.092
9	5.91301	+ 0.00085	0.012	0.090
10	5.91219	+ 0.00002	0.012	0.072
11	5.91245	+ 0.00028	0.012	0.046
12	5.91237	+ 0.00021	0.036	0.047

Mean value 5.91217 Mc · cm
Probable error ± 0.00015 Mc · cm
Estimated error ± 0.00050 Mc · cm
$(H\varrho)_F = 1388.56 \pm 0.15$ Gauss · cm (see also § 6 and § 9).

Table 14

ThB–I-line

Half-width ~ 0.08 per cent

Run	$\nu_p \cdot \varrho$ Mc · cm	Deviation from mean value Mc · cm	Tungsten wire diameter mm
1	7.46863	+ 0.00045	0.012
2	7.46780	− 0.00038	0.012
3	7.46747	− 0.00071	0.012
4	7.46843	+ 0.00025	0.012
5	7.46856	+ 0.00038	0.012

Mean value 7.46818 Mc · cm
Probable error ± 0.00020 Mc · cm
Estimated error ± 0.00070 Mc · cm
$(H\varrho)_I = 1754.01 \pm 0.20$ Gauss · cm (see also § 6 and § 9)

sponding to much narrower line-widths (Fig. 31), but this is not the case with the *F*-line. Fig. 35 shows a normalized *F*- and *I*-line plotted in the same diagram. It is interesting to see that the *F*-line can be divided in three different lines of the same shape as the *I*-line as shown by dotted lines in the figure.

All measurements made by G. M.-slits of the order of 0.060 millimeter or less indicate that this *K*-conversion line is complex and may consist of three

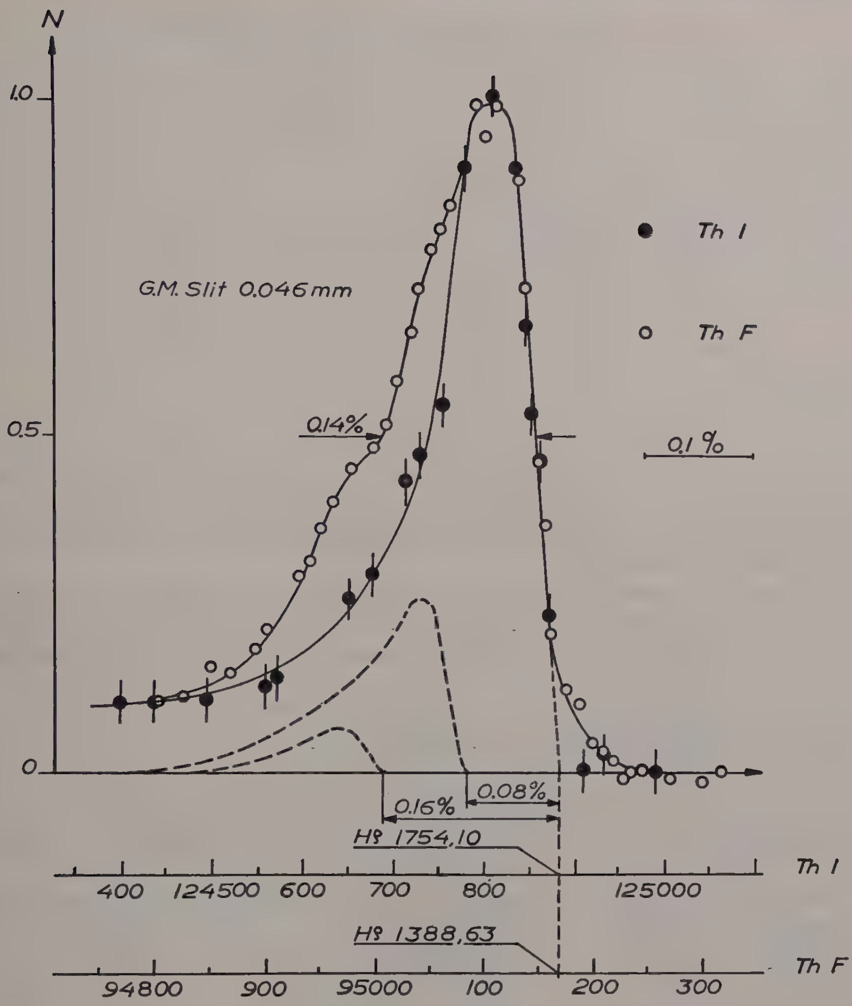

Fig. 35. The F- and I-lines are normalized here and plotted on the same diagram. The dotted lines indicate that the discrepancy can be explained by assuming three lines of the same shape as the I-line.

lines. The relative distances between the main F-line and the other lines are about 0.08 percent and 0.16 percent respectively. The uncertainties in these values are rather large because of the big statistic errors.

The main F-line, however, is much stronger than the other lines and its high energy slope is undisturbed. The measured energy is therefore independent of a line-broadening.

These measurements will be repeated with stronger sources and under different conditions to prove whether this line-broadening is real, which all investigations heretofore indicate, or only an energy-dependent broadening of the line of instrumental origin.

§ 6. The ratio between the *I*- and *F*-lines

The *F*- and *I*-lines are internal conversion lines from the *K*- and *L*-shell. K. SIEGBAHN (68) has shown that this affords a possibility of determining the $H\varrho$-value in Gauss centimeters without knowing the field in absolute units and without measuring the radius of curvature.

Let us assume a γ-radiation of energy $E\gamma$ from the nucleus. This radiation is largely converted to β-radiation through an internal conversion process, by expelling *K*, *L* and *M* electrons.

The energy of a K electron is $E_K = E_\gamma - E_{K\,\mathrm{abs}}$

The energy of a L_{I} electron is $E_{L_{\mathrm{I}}} = E_\gamma - E_{L_{\mathrm{I}}\,\mathrm{abs}}$

and this gives

$$E_{L_{\mathrm{I}}} - E_K = E_{K\,\mathrm{abs}} - E_{L_{\mathrm{I}}\,\mathrm{abs}} = h\nu_{L_{\mathrm{I}} \to K}\,. \tag{6}$$

This difference can be calculated from *X*-ray data; but it should be pointed out here that the γ-radiation belonging to the *F*- and *I*-lines is that of the excited *RaC* atom ($RaB \to RaC + \beta$) with the atomic number 83. *RaC* is therefore an isotope of bismuth.

The energy difference $K - L_{\mathrm{I}}$ can not be measured directly, because no direct *X*-ray transitions of this type exist. However, it can be calculated from the following transitions used by K. SIEGBAHN in a previous determination.

$$K - L_{\mathrm{I}} = \begin{cases} (K - M_{\mathrm{II}}) - (L_{\mathrm{I}} - M_{\mathrm{II}}) = K_{\beta_3} - L_{\beta_4} \\ (K - M_{\mathrm{III}}) - (L_{\mathrm{I}} - M_{\mathrm{III}}) = K_{\beta_1} - L_{\beta_3} \\ (K - L_{\mathrm{III}}) + (L_{\mathrm{III}} - M_{\mathrm{V}}) - (L_{\mathrm{I}} - M_{\mathrm{V}}) = K_{\alpha_1} + L_{\alpha_1} - L_{\beta_9} \end{cases}$$

These differences have been calculated by using the following *X*-ray data.

$K_{\alpha_1} = 160.453$ *X* units E. INGELSTAM, Nova Acta Reg. Soc., Uppsala No. 5
$K_{\beta_1} = 141.655$ *X* units
$K_{\beta_3} = 142.484$ *X* units

$L_{\alpha_1} = 1141.54$ *X* units Y. CAUCHOIS, Cah. Phys. 7, 1, 1942
$L_{\beta_3} = 936.64$ *X* units
$L_{\beta_4} = 974.91$ *X* units
$L_{\beta_9} = 896.06$ *X* units

The atomic constants given by DUMOND and COHEN (62) have also been used in calculating the following energies

$$h\nu_{L_{\mathrm{I}} \to K} = \begin{cases} \text{from } K_{\beta_3} - L_{\beta_4} = 74.137 \text{ eV} \\ \text{from } K_{\beta_1} - L_{\beta_3} = 74.127 \text{ eV} \\ \text{from } K_{\alpha_1} + L_{\alpha_2} - L_{\beta_9} = 74.134 \text{ eV} \end{cases}$$

Mean value 74.133 eV

The value 74.133 eV has been used in the following calculations.

The equilibrium condition for a moving electron with the mass m, velocity v and charge e in a magnetic field H is given by

$$H\varrho = \frac{m v}{e}$$

where ϱ is the radius of curvature. This expression can be combined with the mass relation according to the relativity theory. It is

$$m = \frac{m_0}{\sqrt{1 - \left(\frac{v}{c}\right)^2}}$$

and gives

$$m = m_0 \sqrt{1 + \left(\frac{H\varrho}{c}\right)^2 \left(\frac{e}{m_0}\right)^2}. \tag{7}$$

From the energy difference between two shells we obtain

$$(m_2 - m_1)\, c^2 = h \nu c \tag{8}$$

where ν is the wave-number corresponding to the transition.

By combining these two equations with $\varrho_1 = \varrho_2 = \varrho$ we obtain

$$\sqrt{\left(\frac{e}{m_0 c}\right)^2 (H_2\varrho)^2 + 1} - \sqrt{\left(\frac{e}{m_0 c}\right)^2 (H_1\varrho)^2 + 1} = \frac{h}{m_0} \cdot \frac{\nu}{c}.$$

Solving with respect to $(H_2\varrho)$

$$\left.\begin{aligned}
(H_2\varrho)^2 &= A + \sqrt{A^2 + B} \\
A &= \frac{a^2 + 1}{(a^2 - 1)^2} \left(\frac{s\, m_0 c}{e}\right)^2 \\
B &= \frac{4 - s^2}{(a^2 - 1)^2} \left(\frac{s\, m_0 c}{e}\right)^4 \cdot \frac{1}{s^2} \\
s &= \frac{E_{L_\mathrm{I}} - E_K}{m_0 c^2} \quad \text{and} \quad a = \frac{H_1}{H_2}.
\end{aligned}\right\} \tag{9}$$

Equation (9) shows that the $H\varrho$ value may be calculated by using the X-ray measurements mentioned above, atomic constants and the field ratio between the F and I lines.

Table 15 shows the individual results. The ratio between two lines can be measured with higher accuracy than the individual lines. The lines have been normalized in both height and $H\varrho$ scale and plotted on the same diagram.

Table 15

The ratio $\left(\frac{\nu_{p_I}}{\nu_{p_F}}\right)_{\varrho=\text{const}}$

Half-width for the I-line ~ 0.08 per cent

Run	$a = \left(\frac{\nu_{p_I}}{\nu_{p_F}}\right)_{\varrho=\text{const}}$	Deviation from mean value	Tungsten wire mm
1	1.26322	+ 0.00005	0.012
2	1.26312	− 0.00005	0.012
3	1.26310	− 0.00007	0.012
4	1.26318	+ 0.00001	0.012
5	1.26323	+ 0.00006	0.012
6	1.26319	+ 0.00002	0.012
Mean value $a = 1.26317$			
Probable error		± 0.00002	
Max. deviation		± 0.00007	

The magnetic field has been measured in ν_p units both before and after a measurement, as mentioned in § 5, affording an opportunity for small corrections in the values after the curves have been normalized and plotted on the same diagram. The linear relation between these two field determinations ($\Delta H \leq 0.05\,\%$) has been checked by further measurements between these two values, and is sufficient for this purpose.

Fig. 36 shows graphically how the calculated $(H\varrho)_\text{I}$ value depends on the different parameters.

The result is $(H\varrho)_\text{I} = 1754.03$ Gauss · cm with a probable error of ± 0.11. This error has been calculated by taking the mean square error of the following quantities.

$\Delta = \pm 0.06$ eV	which corresponds to the difference between the three transitions discussed earlier in this paragraph.
$\Delta\left(\frac{m_0 c}{e}\right) = \pm 0.000035 \cdot 10^{-7}$ e. m. u.	which corresponds to the mean square error given by DuMond and Cohen (62).
$\Delta \frac{1}{a} = 0.00002$	which corresponds to the probable error in table 15.

It is interesting to combine this $(H\varrho)$ value with the corresponding $\nu_p \cdot \varrho$ value from table 14.

The relation between the magnetic field H and the proton frequency ν_p can easily be derived from the equations given in chapter I.

$$\omega_p = \gamma_p \cdot H$$

$$H = \frac{2\pi}{\gamma_p} \cdot \nu_p$$

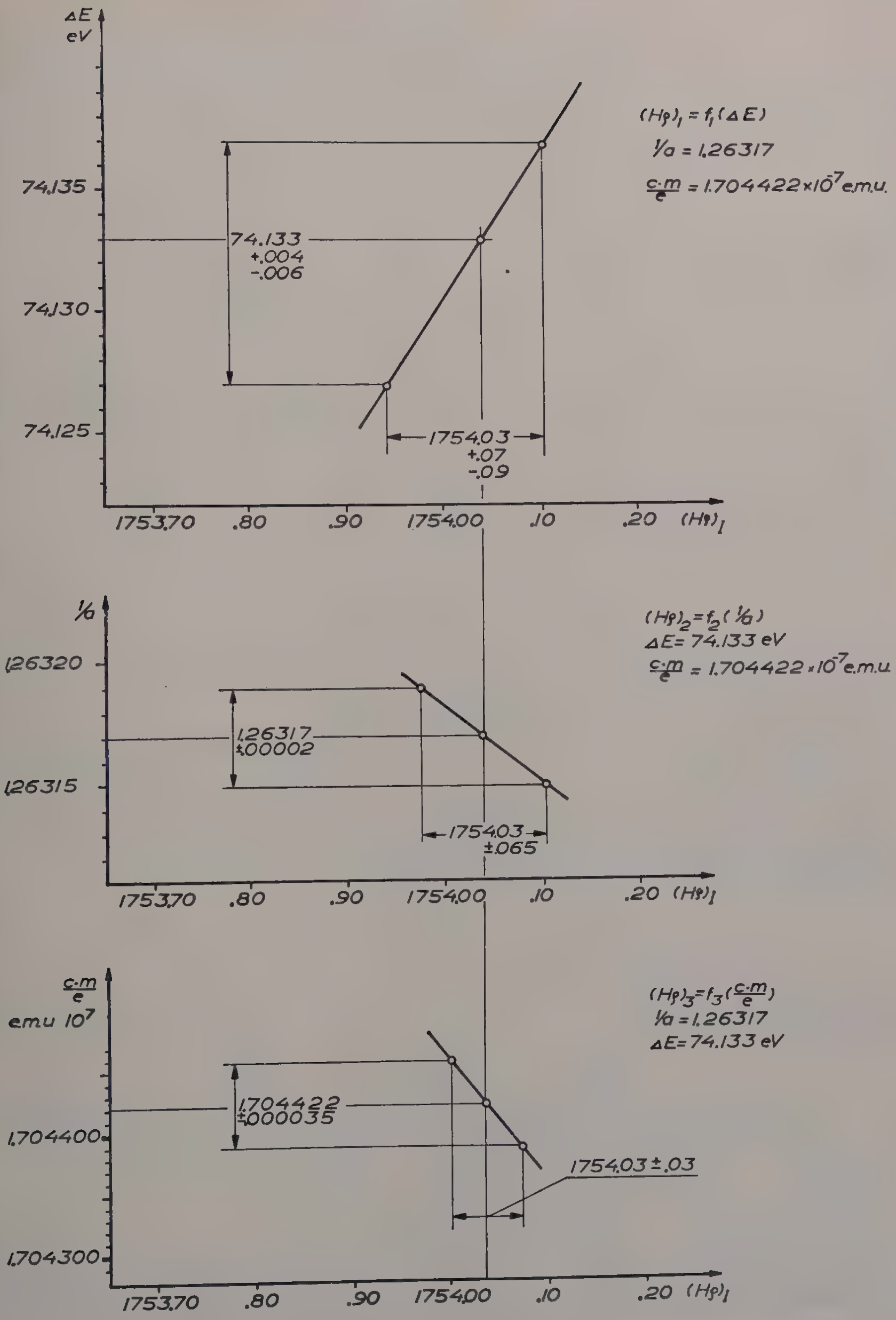

Fig. 36. The influence of the different uncertainties on the calculation of $(H\varrho)_{\mathrm{I}}$.

and this gives

$$\gamma_p = 2\pi \left(\frac{\nu_p \varrho}{H \varrho}\right)$$

and with the numerical values given above

$$\gamma_p = (2.67525 \pm 0.00020) \cdot 10^4 \ \mathrm{sec}^{-1} \ \mathrm{Gauss}^{-1}.$$

This value is in extremely good agreement with the following value given by THOMAS, DRISCOLL and HIPPLE (70).

$$\gamma_p = (2.67523 \pm 0.00006) \cdot 10^4 \ \mathrm{sec}^{-1} \ \mathrm{Gauss}^{-1}.$$

It seems possible that the method described in the foregoing paragraph could be used to check this value with still greater accuracy, if the $E_{L_{\mathrm{I}}} - E_K$ value could be determined with smaller errors and if a stronger thorium sample were available.

This determination may also be used to check other relations between the atomic constants as is apparent from § 8.

§ 7. The *ThC″–L*-line

The ThC″–L-line is an internal conversion line ejected from the K shell of $_{82}$Pb. It has been shown in § 1 that this line is of special interest in the discussion of a possible difference in mass between β^- and β^+.

The $(H\varrho)$ value of this line has been measured in the manner described in the preceding sections.

The individual results are seen in table 16 and the mean value is $(H\varrho)_L = 2607.17 \pm 0.30$. This error corresponds to a maximum estimated error (see also § 9). The result will be discussed in § 8.

The kinetic energy of the conversion electrons is given by

$$E_{\mathrm{kin}} = \left[\sqrt{\left(\frac{H\varrho c}{10}\right)^2 + \left(\frac{m_0 c^2}{e}\right)^2} - \frac{m_0 c^2}{e}\right] \cdot 10^{-10} \ \mathrm{keV} \qquad (10)$$

where $H\varrho$ is in Gauss · cm

$$c = (2.997902 \pm 0.0000086) \cdot 10^{10} \ \mathrm{cm/sec}$$

and

$$\frac{m_0 c^2}{e} = 510.9689 \pm 0.0102 \ \mathrm{keV}.$$

This gives

$$E_{\mathrm{kin}} = 422.838 \pm 0.085 \ \mathrm{keV}.$$

The real γ-energy can now be calculated by adding the edge energy of the corresponding X-ray level.

In finding this energy it is advisable to start with the L_{III} edge and subsequently calculate the others with the aid of data from emission spectra.

Table 16

ThC″–L-Line

Run	$\nu_p \cdot \varrho$ Mc · cm	Deviation from mean value Mc · cm	Tungsten wire diameter mm	G.M. slit width mm	Half-width per cent
1	11.09996	−0.00059	0.012	0.090	0.16
2	11.10057	+0.00002	0.012	0.072	0.13
3	11.10112	+0.00057	0.012	0.046	0.08
4	11.10054	−0.00001	0.036	0.047	0.08
Mean value	11.10055 Mc · cm				
Probable error		±0.00020			
Estimated error		±0.00080			
$(H\varrho)_L = 2607.17 \pm 0.30$ se also § 6 and § 9					

$$\text{i.e.}\quad {}_{82}\text{Pb}\ L_{\text{III}}\ \text{edge} = 948.37\ (71)\ X\ \text{units}\qquad \text{gives}\ 13.045\ \text{keV}$$

$$K_a = 165.031\ (72)\ X\ \text{units}\qquad \text{gives}\ 74.964\ \text{keV}$$

$$\lambda_g / \lambda_s = 1.0020204 \pm 0.0000114$$

$$E_\lambda = (12396.44 \pm 1.74)\ \text{mÅ} \cdot \text{keV} = 12371.44\ X u \cdot \text{keV}$$

$$\therefore\ (E)_{{}_{82}\text{Pb}_\text{K}} = 88.009\ \text{keV}$$

This gives the γ-energy corresponding to *ThC″–L*-line

$$\therefore\ (E_\gamma) = 510.85 \pm 0.08\ \text{keV}.$$

This result will be discussed in greater detail in the following paragraphs.

§ 8. The results

We have seen in the preceding sections how the different values have been measured and calculated. The experimental results are summarized in table 17.

Table 17

Line	$\nu_p \cdot \varrho$ Mc · cm	Probable error	Estimated error	$(H\varrho)^1$ Gauss · cm with estimated error	γ-energy in keV
Th B–F	5.91217	0.00015	0.00050	1388.56 ± 0.15	238.63 ± 0.04²
Th B–I	7.46818	0.00020	0.00070	1754.01 ± 0.20	238.62 ± 0.04²
Th C″–L	11.10055	0.00020	0.00080	2607.17 ± 0.30	510.85 ± 0.08²

---

[1] See also foot-note page 74.

[2] Calculated by using $\gamma_p = (2.67523 \pm 0.00006) \cdot 10^4\ \text{sec}^{-1}\ \text{Gauss}^{-1}$.

The γ-values corresponding to the $(H\varrho)$-values are calculated as shown in § 7 with the following X-ray values.

$_{83}$Bi L_{III} edge	921.50 (73) X units	gives K edge = 90.528 eV
$_{83}$Bi K_{α}	160.453 (72) X units	
$_{83}$Bi L_{I} edge	755.26 (73) X units	gives L_{I} edge = 16.380 eV
$_{82}$Pb L_{III} edge	948.37 (71) X units	gives K edge = 88.009 eV
$_{82}$Pb K_{α}	165.031 (72) X units	

HEDGRAN (61) has given the following $(H\varrho)$-ratio between the secondary electrons from the annihilation radiation and those from the ThC''–L-line. (U-radiator.)

$$\frac{(H\varrho)_A}{(H\varrho)_L} = 1.0002 \pm 0002.$$

The $(H\varrho)_L$ value calculated from this ratio is 2607.2 ± 0.5 (based on an annihilation energy of 510.96 keV). This value is in excellent agreement with the absolute value 2607.17 ± 0.30 Gauss · cm given in the present paper and it shows that the β^- and β^+ masses are equal within the given limits of error.

It also shows that the Au^{198} γ-value given by DUMOND et al. (63) (411.2 ± ± 0.1 keV) is too low, inasmuch as the value for the ThC''–L-line calculated by HEDGRAN from his relative measurement and this γ-value gives 2604 ± 0.5 Gauss · cm. This suggests that there is a systematic error in the gold value of the order of 0.1 percent.[1]

It may be mentioned here that PRIMAKOFF and VILLARS (74) have tried to investigate the difference in wavelength between the electron positron annihilation and the compton-wavelength suggested by DUMOND (75) in the following way.

The annihilation energy 2 mc^2 is equal to the sum of the energy of the two hard photons and all accompanying soft photons. They have discussed the intensity of the energy spectrum belonging to these soft photons and given the following average energy $\bar{E}_{\text{soft}}$ carried by this spectrum per individual pair recombination.

$$E_{\text{soft}} = \frac{3}{2\pi} \cdot \frac{1}{137} \left(\frac{v}{c}\right)^2 2\, m c^2 \simeq 10^{-7}\, m c^2.$$

They have also shown that "any measurement of the emitted hard photon or ejected photo-electron energy, by extrapolation of the corresponding line-shape on the high energy side, will be independent of the actual presence of the soft photon emission, to about one part per million". The effect of the soft photon emission is therefore so small that it is impossible to find it with the present accuracy.

---

[1] Professor Jesse W. M. DUMOND has told me in a private communication that his group has recently found an unsuspected systematic error in the crystal spectrograph of the correct sign and order of magnitude to explain this difference. He has also given me information about recent measurements of the γ-energies corresponding to the F-, I- and L-lines. These values seem to be in very good agreement with my values if a tentative correction curve is used. I wish to thank Professor DUMOND for this information.

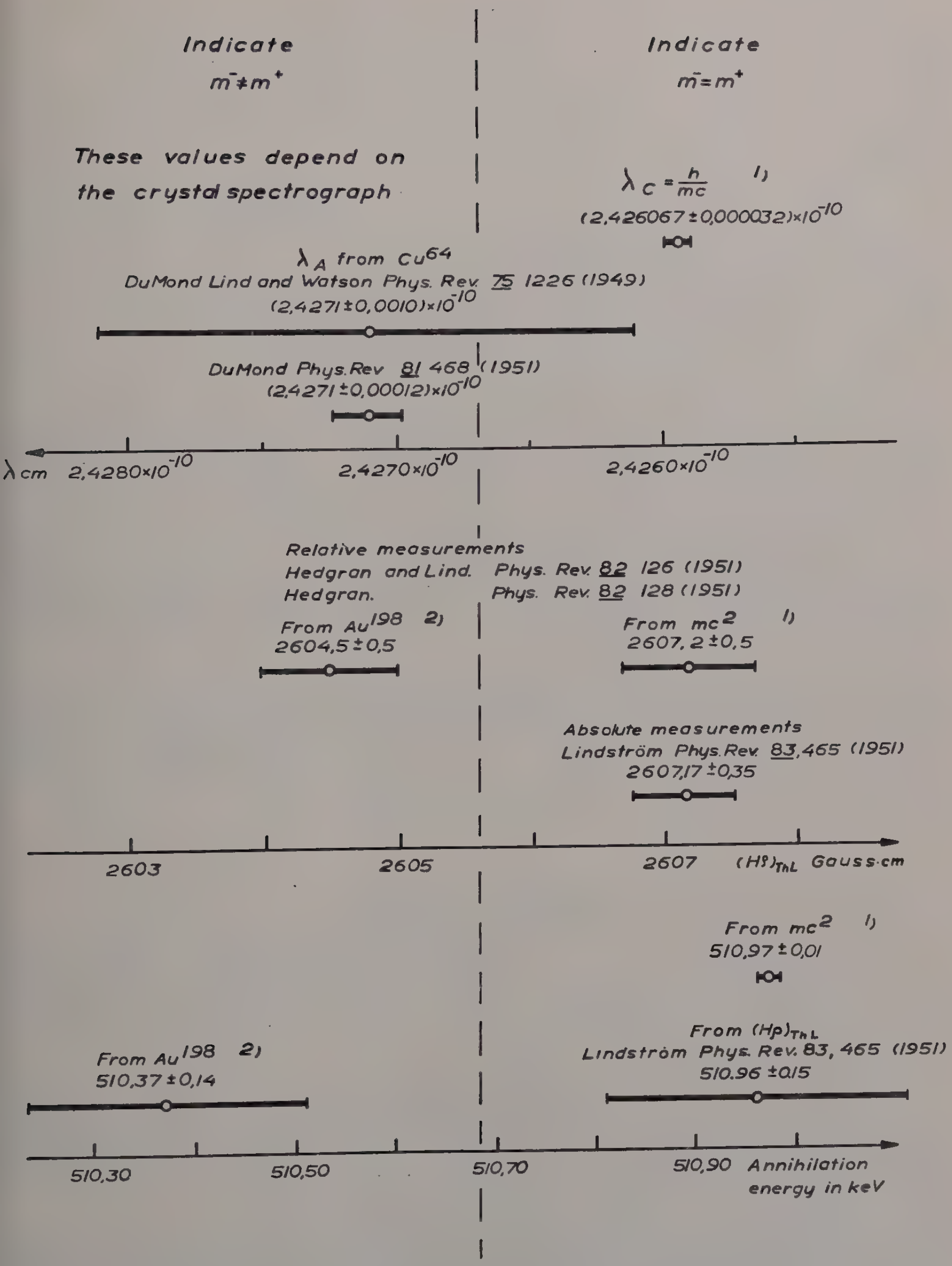

1) DuMond and Cohen Phys Rev. 82 555 (1951)
2) DuMond et al. Phys. Rev. 73 1392 (1948) 75 1226 (1949) 76 1838 (1949)

Fig. 37. Comparison between values given by different workers.

It is of course possible to combine the present values in equations of the form (9) and (10) and then to calculate $\frac{e}{m}$ and $\frac{h}{m_0}$ by using the $(H\gamma)$-values, the γ_p value and X-ray data. It is obvious that this will give values in agreement with the values given by DuMond and Cohen (62), but with larger errors.

It would be possible to check these values, by this method, if these and the corresponding X-ray measurements could be made with higher accuracy, but the present accuracy is not sufficient.

Fig. 37 shows graphically the different values for the annihilation wavelength and the $(H\varrho)$-value for the ThC''–L-line. All values indicating $\beta^- \neq \beta^+$ are due to the crystal-spectrograph used by DuMond et al.[1]

The ThB–F-line has been determined by many workers (68, 76, 77, 78, 79, 80) and the values range from 1381 to 1398 Gauss · cm.

All these values, except that given by Siegbahn are determined by using coils for measuring the magnetic field. This is a very difficult technique for precision measurement and it is difficult to obtain a closer accuracy in an absolute determination than to 0.2 percent. Some workers have also supposed the gradient of the field along the path to be independent of the field value and have therefore measured this gradient at a rather high field. The present investigation shows, however, that this is not the case and that it is necessary to measure the field along the path at each run. It seems possible to explain most of the variations between the old values and the present ones by this assumption.

It may be pointed out here that the technique of measuring the magnetic field used in the present investigation would be fairly easy to duplicate at other laboratories. The relative accuracy is very high and depends only on the homogeneity of the magnetic field. It is therefore suggested that all precision measurements of magnetic fields should be given in ν_P-units as in tables 13, 14 and 16. The value in Gauss can then be calculated by using the γ_p value.

§ 9. Error discussion

We have already seen in § 3 and fig. 33 that the high energy part of the line-shape is in excellent agreement with the calculated one, and as some reasons for a deviation on the low energy side have also been discussed, we shall not go into this in greater detail.

The intersection between the slope and the background has always been used in determining the $(H\varrho)$ values in the present investigation. The ratio between the line-peak and the background has been about 1.5 for the L-line, about 3.5 for the I-line and about 9.5 for the F-line. The background has been measured with smaller statistic errors than the individual points on the lines, but a little uncertainty in localizing the intersection still exists.

An estimate of this uncertainty gives the relative errors respectively $\pm 3 \cdot 10^{-5}$, $\pm 4 \cdot 10^{-5}$ and $\pm 6 \cdot 10^{-5}$ for the F-, I- and L-lines. These values also include a small deviation of the calculated from the measured line-shape.

---

[1] See also note on page 74.

The uncertainty in the relative field measurements is negligible at the L- and I-lines, but the shape of the proton-resonance signals at the field corresponding to the F-line (292 Gauss) is not so well defined as at the higher fields. This gives an uncertainty of not more than $2 \cdot 10^{-5}$.

The absolute value of the field has been calculated by the γ_p value given by THOMAS, DRISCOLL and HIPPLE. This value has been checked in the present investigation and it seems safe to use the error given by them. This gives a constant error of $\pm 2.5 \cdot 10^{-5}$.

The distance 2ϱ has been measured by a comparator, and the measured value has been corrected for the difference in temperature within the magnetic field during a run and the temperature at which the distance was measured. A conservative estimate gives the relative maximum error $\pm 3 \cdot 10^{-5}$, which also includes both edge effects on the wire and at the slit and deviations depending on unparallelism between the wire and the slit.

The source and the slit have been adjusted so as to be as parallel as possible to the magnetic field. This has been accomplished, using the microscope belonging to the comparator, by adjusting them to be perpendicular to the edge of the holder. The holder has then been placed parallel to the pole pieces in the magnet. This parallelism is not especially good, however, inasmuch as the vacuum chamber rests on the lower pole and there are rubber gaskets between the head point of the chamber and the aluminum cover (see also fig. 26). The total measured unparallelism is less than 0.2 millimeters on the entire holder-length (100 millimeters). This gives a maximum relative deviation of the measured values from the ϱ-values perpendicular to the field of $4 \cdot 10^{-6}$. However, as a conservative estimate let us take 10^{-5}.

All these errors, except the one depending on the γ_p value, should be statistically distributed. It is therefore probable that a mean square error gives the correct error magnitude.

$$\Delta = 10^{-5}\sqrt{36 + 4 + 9 + 1} = 7 \cdot 10^{-5}.$$

Thus the total relative error is of the order of $(7 + 2.5) \cdot 10^{-5} \simeq 10^{-4}$.

The "estimated error" given in the tables refers to this error discussion, but has somewhat arbitrarily been chosen a little higher, depending on the degree of consistency among the individual values.

The probable errors given are calculated in the usual way from

$$0.7\sqrt{\frac{\sum_{1}^{N} \delta_i^2}{N(N-1)}}.$$

SUMMARY

1. An apparatus for precision measurement of nuclear magnetic moments has been constructed.

2. A new method of comparing two magnetic resonance signals on an oscillograph is discussed.

3. A magnetic field stabilizer using a proton sample has been constructed.

4. The following frequency ratios have been determined.

$$
\begin{array}{llll}
\nu_D/\nu_H & = 0.15350668 \pm 0.00000012 & \text{for } H_2O \text{ and} & D_2O \\
\nu_{Li^7}/\nu_H & = 0.3886341 \pm 0.0000010 & \text{for } H_2O \text{ and} & LiNO_3 \\
\nu_{B^{11}}/\nu_H & = 0.3208381 \pm 0.0000008 & \text{for } H_2O \text{ and} & \left\{\begin{array}{l} Na_2B_2O_4 \\ K_2B_2O_4 \end{array}\right. \\
\nu_{F^{19}}/\nu_H & = 0.9409330 \pm 0.0000030 & \text{for } H_2O \text{ and} & CFCl_3 \\
\nu_{Na^{23}}/\nu_H & = 0.2645182 \pm 0.0000007 & \text{for } H_2O \text{ and} & \left\{\begin{array}{l} Na_2B_2O_4 \\ NB_2 \end{array}\right. \\
\nu_{Al^{27}}/\nu_H & = 0.2605694 \pm 0.0000010 & \text{for } H_2O \text{ and} & AlCl_3
\end{array}
$$

The diamagnetic correction and the values in nuclear magnetons are discussed.

5. A chemical dependance of the order of $(4.2 \pm 1.5)\, 10^{-6}$ for the proton resonance frequencies in H_2O and paraffin oil has been found. Some fluorine compounds have also been investigated giving a chemical dependance of up to $(171.8 \pm 2.0)\, 10^{-6}$.

6. The $\nu_{Na^{23}}/\nu_H$ ratio has been combined with some values given by other workers, giving the ratio between the g-values for the electron and the path $g_s/g_L = 2\,(1 + 0.00114 \pm 0.00006)$.

7. A small β-spectrograph for absolute determinations has been constructed. The line-shape has been discussed.

8. The $(H\varrho)$-values for the F-, I- and L-lines of $Th\,(B + C + C'')$ has been determined, giving the following numerical values. 1388.56 ± 0.15; 1754.01 ± 0.20 and 2607.17 ± 0.30 Gauss · cm respectively.

9. It has been shown that the β^- and β^+ masses are equal within an accuracy of 0.01 %.

10. The magnetogyric ratio γ_p has been determined to $(2.67525 \pm 0.00020)\, 10^4$ $\sec^{-1}$ Gauss^{-1}.

Nobel Institute for Physics, Stockholm 50, Sweden.

References

1. J. J. Rabi, J. R. Zacharias, S. Millman and P. Kusch, Phys. Rev. *53*, 318, (1938).
2. J. J. Rabi, S. Millman P. Kusch and J. R. Zacharias, Phys. Rev. *55*, 526, (1939).
3. J. B. M. Kellog and S. Millman, Rev. Mod. Phys., *18*, 323, (1946).
4. P. Kusch, Physica, Amsterdam, *17*, 339, (1951).
5. E. M. Purcell, H. C. Torrey and R. V. Pound, Phys. Rev. *69*, 37, (1946).
6. F. Bloch, W. W. Hansen and M. Packard, Phys. Rev. *69*, 127, (1946).
7. F. Bloch, W. W. Hansen and M. Packard, Phys. Rev. *70*, 474, (1946).
8. F. Bloch, Phys. Rev. *70*, 460, 1946.
9. N. Bloembergen, E. M. Purcell and R. V. Pound, Phys. Rev. *73*, 679, (1948).
10. G. E. Pake, Am. Jour. of Phys. *18*, 438, (1950).
11. I. I. Rabi, Phys. Rev. *51*, 652, (1937).
12. E. Majorana, Nouvo Cimento *9*, 43 (1932).
13. E. M. Purcell and R. V. Pound, Phys. Rev. *81*, 279, (1951).
14. N. F. Ramsey and R. V. Pound, Phys. Rev. *81*, 278, (1951)
15. E. L. Hahn, Phys. Rev. *80*, 580, (1950).
16. E. M. Purcell, Physica, Amsterdam *17*, 282, (1951).

17. W. C. Dickinson, Phys. Rev. *81*, 717, (1951).
18. K. Siegbahn and G. Lindström, Ark. för Fysik, *1*, 193, (1949).
19. W. D. Knight, Phys. Rev. *76*, 1259, (1949).
20. W. C. Dickinson, Phys. Rev. *77*, 736, (1950).
21. W. G. Proctor and F. C. Yu, Phys. Rev. *77*, 717, (1950).
22. G. Lindström, Phys. Rev. *78*, 817, (1950).
23. H. Wallman and G. E. Walley: Vacuum type Amplifiers, McGraw-Hill Book Co., New York 1948.
H. Wallman, A. B. Macnee and C. P. Gadsden, Proc I. R. E. *36* ,700, (1948).
24. N. Bloembergen, Nuclear Magnetic Relaxation, Drukkereij Fa Schotanus et Jens, Utrecht (1948).
25. B. A. Jacobsohn and R. K. Wangsness, Phys. Rev. *73*, 942, (1948).
26. B. Smaller, Phys. Rev. *83*, 812, (1951).
27. B. Smaller, E. Yasaitis and H. L. Anderson, Phys. Rev. *81*, 896, (1951).
28. F. Bloch, E. C. Levintahl and M. Packard, Phys. Rev. *72*, 1125 (1947).
29. E. C. Levinthal, Phys. Rev. *78*, 204, (1950).
30. F. Bitter, N. L. Alpert, D. E. Nøgle, H. L. Poss, Phys. Rev. *72*. 1271, (1947).
31. T. F. Wimett, M. I. T. Research Laboratory of Electronics Report. (July 1949).
32. J. B. M. Kellog, I. I. Rabi and N. F. Ramsey, Phys. Rev. *56*, 728, (1939).
33. These values were reported in the survey by J. E. Mack, Rev. Mod. Phys. *22*, 64, (1950).
34. These measurements were kindly made by A. Ehrenberg at the Medical Nobel Institute in Stockholm.
35. P. Debye, Polar Molecules, Dover Publications, New York 1945.
36. H. S. Gutowsky and McClure, Phys. Rev. *81*, 276, (1951).
37. H. A. Thomas, Phys. Rev, *80*, 901, (1950).
38. G. F. Newell, Phys. Rev. *80*, 476, (1950) and private communication.
39. N. F. Ramsey, Phys. Rev. *77*, 567, (1950); *79*, 117, (1950).
40. J. A. Hipple, H. Sommer and H. A. Thomas, Phys. Rev. *76*, 1877, (1949) Phys. Rev. *80*, 487, (1950).
41. H. Sommer, H. A. Thomas and J. A. Hipple, Phys. Rev. *82*, 697, (1951).
42. This result is in agreement with the value $\mu_p = 2.79245 \pm 0.00020$ reported by F. Bloch and C. D. Jeffries, Phys. Rev. *80*, 305, (1950).
43. W. E. Lamb, Phys. Rev. *60*, 817, (1941).
44. D. A. Anderson, Phys. Rev. *76*, 434, (1949).
45. H. S. Gutowsky and C. J. Hoffman, Phys. Rev. *80*, 110, (1950).
46. W. G. Proctor and F. C. Yu, Phys. Rev. *78*, 471, (1950).
47. N. F. Ramsey, Physica Amsterdam, *XVII*, 303, (1951).
48. F. Bitter, Phys. Rev. *75*, 1326, (1949).
49. J. R. Zimmerman and D. Williams, Phys. Rev. *76*, 350, (1949).
50. R. E. Shiff and D. Williams, Phys. Rev. *82*. 651, (1951).
51. H. L. Poss, Phys. Rev. *75*, 600, (1949).
52. G. Breit and E. R. Meyerott, Phys. Rev. *72*, 1023, (1947).
53. A. G. Prodell and P. Kusch, Phys. Rev. *79*, 1009, (1950).
54. A. Bohr, Phys. Rev. *73*, 1109, (1948).
55. F. Low, Phys. Rev. *77*, 361, (1950).
56. R. A. Logan and P. Kusch, Phys. Rev. *81*, 280, (1951).
57. H. Taub and P. Kusch, Phys. Rev. *75*, 1481, (1949).
58. J. H. Gardner and E. M. Purcell, Phys. Rev. *76*, 1262, (1949).
59. J. Schwinger, Phys. Rev. *73*, 416, (1948); *74*, 1212, (1948).
60. A. Hedgran and D. Lind, Phys. Rev. *82*, 126, (1951).
61. A. Hedgran, Phys. Rev. *82*, 128, (1951).
62. J. W. M. DuMond and E. R. Cohen, Phys. Rev. *82*, 555, (1951).
63. J. W. M. DuMond et al. Phys. Rev. *73*, 1392, (1948). Phys. Rev. *75*, 1226, (1949). Phys. Rev. *76*, 1838, (1949).
64. E. J. Williams, Proc. Roy. Soc. *169*, 531, (1939).
65. W. A. Wooster, Proc. Roy. Soc. *A 114*, 729, (1927).
66. K. T. Li, Proc. Camb. Phil. Soc. *33*, 164, (1937).
67. J. L. Lawson and A. W. Tyler, Rev. Sci. Inst. *11*, 6, (1940).
68. K. Siegbahn, Arkiv f. mat., astr. o. fysik *30 A*, No. 20, (1944).
69. D. R. Hartree, Proc. Camb. Phil. Soc. 21, 746, (1923).
70. H. A. Thomas, D. L. Driscoll and J. A. Hipple Phys. Rev. *78*, 787, (1950).

71. Y. CAUCHOIS, C. R. Paris *215*, 135, (1942).
72. E. INGELSTAM, Nova Acta Reg. Soc. Sci. Upsala No. 5 (1936).
73. Y. CAUCHOIS, Cah. Phys. *8*, 25.
74. H. PRIMAKOFF and F. VILLARS. To be published in Phys. Rev. I wish to thank Dr. PRIMAKOFF for sending me a copy of this paper.
75. J. W. M. DUMOND, Phys. Rev. *81*, 468, (1951).
76. R. ARNOULT, Ann. de Phys. *12*, 241, (1939).
77. C. D. ELLIS, Proc. Roy. Soc. London (A), *139*, 336, (1933); *143*, 350, (1934).
78. J. SURUGUE, Ann. de Phys. *8*, 484, (1937).
79. Sze SHIH-YUAN, Ann. de Phys. *19*, 59, (1 33).
80. G. LINDSTRÖM, Phys. Rev. *83*, 465, (1951). (Preliminary values).

Tryckt den 8 november 1951

Uppsala 1951. Almqvist & Wiksells Boktryckeri AB

ARKIV FÖR FYSIK Band 4 nr 2

Communicated 12 September 1951 by Manne Siegbahn and Erik Hulthén

Some nuclear disintegrations and the nuclear shell theory

By Evani Kondaiah

With 33 figures in the text

Contents

Page

Chapter 1. Introduction . . . . 84—92

A. Methods employed in studying the disintegrations of radio-active elements 85

1.1. The cloud chamber 85
1.2. Absorption 86
1.3. β-spectrometers 87
1.4. Scintillation spectrometer 88
1.5. Coincidence technique 89
1.6. Directional correlation measurement technique 89

B. Methods used in the present investigations 90

1.7. Absorption 90
1.8. The β-spectrometers 90
1.9. The scintillation spectrometer 90
1.10. The coincidence technique 90

C. Procedure for setting up the disintegration schemes 91

1.11. On the basis of energy relations 91
1.12. On the basis of intensity relations 91
1.13. On the basis of coincidence results 91
1.14. Isomeric transitions 92

D. Procedure for assigning quantum numbers to the nuclear levels 92

1.15. On the basis of comparative half-lives 92
1.16. On the basis of multipole order nature of γ rays 92
1.17. The nuclear shell theory 92

Chapter 2. Apparatus and methods . . . . 93—100

A. Irradiations and preparation of the samples 93

2.1. The Harwell pile 93
2.2. The cyclotron 93
2.3. Chemical separations 94
2.4. Preparation of β-samples 94
2.5. Preparation of γ-samples 94

B. Calibration of the apparatus 95

2.6. Calibration of the β-spectrometers 95
2.7. Calibration of the γ-tubes 95
2.8. Calibration of the scintillation spectrometer 96

C. Energy determination of β- and γ-rays 96

2.9. β-rays 96
2.10. γ-rays 97

Page

D. Intensity estimations 98

2.11. Intensity estimations of the internal conversion lines 98
2.12. β-ray intensities 99
2.13. γ-ray intensities 100

Chapter 3. Theoretical part . . . . 100—112

A. β-decay 100

3.1. Fermi's formulation 100
3.2. Fermi function 102
3.3. The β-ray selection rules 102
3.4. Forbidden β-transitions 103
3.5. Correction factors for the Fermi plot of first forbidden β-spectra . . . 104

B. γ-emission 105

3.6. Methods of determining multipole order nature of the γ-rays 105
3.7. Multipole order from the internal conversion 106
3.8. Multipole order from the ratio of K to L conversion 106
3.9. Multipole order from the transition probabilities 106
3.10. Methods used to determine the multipole order in the present cases . . 107
3.11. γ-ray selection rules 107
3.12. The electric dipole case 108

C. The nuclear shell theory 108

3.13. Magic numbers and shells in nuclei 108
3.14. One particle model of the nucleus 108
3.15. *F-H* level scheme 109
3.16. The spin-orbit coupling scheme 110

D. Errors 111

3.17. Errors in the intensity estimations 111
3.18. Statistical errors 111
3.19. Errors in the energy measurements due to source thickness 111
3.20. Finite resolution error 112

Chapter 4. Measurements . . . . 112—145

A. Radio-activity of Ru^{103} 112

4.1. History 112
4.2. Half-life 113
4.3. β-spectrum 113
4.4. Photo-spectrum 113
4.5. Coincidence measurements 115
4.6. Fermi plot 116
4.7. Correction factors for the Fermi plot 117
4.8. Possible causes of deviation 118
4.9. Internal conversion 120
4.10. Multipole order 120
4.11. Results 121

B. Radio-activity of Rh^{103m} 121

4.12. History 121
4.13. Internal conversion 121
4.14. Multipole order 121
4.15. Results 122

C. Radio-activity of Pd^{109} 122

4.16. History 122
4.17. Results 122

D. Radio-activity of Ag^{109m} 122

4.18. Results 122

Page
E. Radio-activity of Ce^{141} . . . 122
4.19. History . . . 122
4.20. Chemical purification . . . 124
4.21. β-spectrum . . . 124
4.22. Fermi analysis . . . 124
4.23. Intensity estimations . . . 124
4.24. Internal conversion . . . 126
4.25. Multipole order . . . 126
4.26. Results . . . 126

F. Radio-activity of Ce^{143} . . . 126
4.27. History . . . 126
4.28. Half-life . . . 127
4.29. β-spectrum . . . 127
4.30. Fermi analysis . . . 127
4.31. Photo-spectrum . . . 130
4.32. Scintillation spectrum . . . 130
4.33. Coincidence measurements . . . 134
4.34. Intensity estimations . . . 134
4.35. Internal conversion . . . 134
4.36. Multipole order . . . 134
4.37. Results . . . 134

G. Radio-activity of Pr^{143} . . . 136
4.38. Result . . . 136

H. Radio-activity of Nd^{147} . . . 136
4.39. History . . . 136
4.40. Half-life . . . 136
4.41. β-spectrum . . . 136
4.42. Fermi analysis . . . 136
4.43. Photo-spectrum . . . 137
4.44. Intensity estimations . . . 137
4.45. Internal conversion . . . 141
4.46. Multipole order . . . 141
4.47. Results . . . 143

I. Radio-activity of Pm^{149} . . . 143
4.48. History . . . 143
4.49. Half-life . . . 143
4.50. β-spectrum . . . 143
4.51. Fermi plot . . . 144
4.52. Results . . . 144

J. Radio-activity of Os^{193} . . . 144
4.53. History . . . 144
4.54. Multipole order . . . 144
4.55. Results . . . 145

Chapter 5. Disintegration schemes . . . 145—148
5.1. Disintegration scheme for Ru^{103} and $Rh^{103\,m}$ . . . 145
5.2. Disintegration scheme for Pd^{109} and $Ag^{109\,m}$ . . . 145
5.3. Disintegration scheme for Ce^{141} . . . 145
5.4. Disintegration scheme for Ce^{143} and Pr^{143} . . . 146
5.5. Disintegration scheme for Nd^{147} and Pm^{147} . . . 147
5.6. Disintegration of Pm^{149} . . . 148
5.7. Disintegration scheme for Os^{193} . . . 148

Chapter 6. Discussion . . . 148—154
6.1. Ru^{103} and $Rh^{103\,m}$ . . . 149
6.2. Pd^{109} and $Ag^{109\,m}$ . . . 152

Page
6.3. Ce^{141} 152
6.4. Ce^{143} and Pr^{143} 153
6.5. Nd^{147} 153
6.6. Os^{193} 154
References 155

Preface

10 radio-active isotopes have been studied using mainly β-spectrometer and coincidence techniques. Preliminary reports regarding these isotopes have previously appeared mainly in the form of letters elsewhere. In this paper we describe the experiments in detail and discuss the assignments of spins and parities on the basis of the nuclear shell theory. Since the preliminary reports have appeared, experimental determination of the spins of some isotopes have been reported and isomeric transitions have been reclassified. In view of these new developments, it has become necessary to revise the spin and parity assignments in some cases.

CHAPTER 1

Introduction

In this paper we are going to report on the study of the radiations emitted by some artificial radio-active substances and their mode of decay. A normally non-radio-active element can be made radio-active by bombarding it with high energy particles (α, β, proton, neutron, deutron etc.) or radiation (γ or X). When a substance is subjected to such a bombardment, there can arise instantaneous γ-rays with which we are not concerned at present. We are concerned here only with γ-radiation connected with β-decay and meta-stable states.

β-radiation:

The electrons ejected by radio-active substances during the process of radioactive decay may be divided into three different groups, namely, negatrons (β^-), positrons (β^+) and conversion electrons (e^-). While these types of radiations are all electrons, they differ as regards their origin and mode of formation. The β^- and β^+ differ in the sign of their charge. In general, β^- particles are emitted by nuclei in which the ratio of neutrons to protons is greater than that corresponding to stability, while β^+ particles are emitted by nuclei which have an excess of protons. In the latter case, a nucleus may neutralize its excess positive charge by capturing an orbital electron also. The most probable case of orbital electron capture is K-capture in which case an electron in the K-shell of the atom happens to penetrate the nucleus. As a result an electron in the neighbouring L shell falls into the vacancy created in the K shell and the energy released by this transition from a higher to a lower electron orbit appears as X-ray. Some times an electron known as Auger electron is observed instead of a X-ray. Auger electrons are electrons originating in the electron orbits of the atom. Further, a nucleus in an excited state can transfer its excess energy to one of the orbital electrons instead of emitting a γ-ray. Thus, conversion electrons are electrons originating in the electron orbits of the atom where as β^- or β^+-particles are electrons originating from the nucleus at the time of emission. The three processes β^-, β^+ and orbital electron capture can be represented as:

$$\begin{aligned} N &\rightarrow P + \beta^- + \nu \\ P &\rightarrow N + \beta^+ + \nu \qquad \text{(1.1)} \\ P + e^- &\rightarrow N + \nu \end{aligned}$$

where ν is the neutrino, postulated by PAULI to account for the continuous nature of β-radiation and laws of conservation. It is a hypothetical particle of zero rest mass and zero charge.

A radio-active substance may decay by one or more of the three (β^-, β^+, K-capture) processes depending upon its position in the isotope chart. The process of orbital electron capture (or K-capture as it is often called) is alternative to positron emission and often competes with positron decay. If an unstable nucleus with an excess of protons does not possess at least 1.02 Mev of decay energy (the annihilation energy required for the formation of a positron), K-capture is the only process available and no positron emission occurs.

γ-radiation:

A γ-ray is a quantized electro-magnetic radiation of high energy and short wavelength and is emitted by a nucleus which is in an excited state. Often a nucleus is left in an excited state after undergoing β-decay. By the emission of one or more γ-rays, the nucleus is able to get rid of its excess energy and thereby reach the ground state. A γ-ray has a single and well defined energy unlike nuclear β-radiation which has a continuous energy spectrum. A γ-ray originates from the nucleus where as a X-ray which is also a quantized electro-magnetic radiation has its origin in the electronic shells of the atom. A γ-ray or an internal conversion electron due to it, is also emitted in a radioactive decay known as isomeric transition in which the nucleus happens to remain in an excited state for an easily measurable time. Otherwise the γ-ray transition probabilities are much higher than those of the β-rays. The meta-stable levels of a nucleus differ from the other excited levels in their half-lives, the former being much greater.

In the following pages we describe in detail the study of these radiations emitted by some radio-active nuclei and propose disintegration schemes showing the probable modes of decay of the nuclei concerned. Some information regarding the spins and parities of the nuclear levels is also obtained and is compared with the predictions made by the nuclear shell theory.

A. Methods employed in studying the disintegrations of radio-active elements

1.1. The cloud chamber

The cloud chamber, a versatile instrument for detecting radiations, is used for studying the disintegrations of the radio-active elements also. The β-radiation is studied by using a magnetic field to deflect a well collimated beam of β-particles from a radio-active source. The energy of the β-particles is obtained from the radius of curvature of the paths of β-particles traced on a photographic film. The sign of curvature determines the positive or negative charge of the β-particles under investigation. The γ-radiation can be studied in a similar way by studying the photo electrons ejected from a radiator of high Z value.

The cloud chamber studies are, however, very tedious as quite a large number of photographs have to be studied to obtain good statistics.

1.2. Absorption

β-radiation:

The β-particles emitted by radio-active atoms are gradually slowed down and finally stopped by collisions with electrons of the absorbing material. The range of a given radiation depends upon its maximum energy and on the density of electrons in the absorber. It is found that the range is nearly independent of the nature of absorber when the absorber thickness is expressed in mass per cm^2. Usually aluminum is used as absorber for β-particles. The absorption curve of β-particles is usually plotted on a semi-logarithmic graph paper with the activity as the ordinate (log. scale) and the thickness of Al (in mg/cm^2) as the abscissa (linear scale). The shape of the curve thus obtained depends on the experimental arrangement of the source, absorbers and counter as well as on the shape of the β-spectrum. The simplest way of determining the maximum range of the β-particles from such a curve is by visual method i.e. to see where the curve cuts the absorber thickness axis after duly taking into account the back-ground. This method, however, is not useful when γ-radiation is present and FEATHER (F5) developed a comparison method in which the range of the β-particles emitted by any substance is measured in terms of the range of a standard β-emitter. Different authors have proposed different expressions for the range-energy relation. We do not consider here these in detail. Glendenin (G2) has given an empirical range-energy curve in his review on absorption methods.

Photons:

The photons emitted by radio-active substances are absorbed in matter by three different types of processes — (i) photo-electric effect, (ii) compton effect, (iii) pair-production. In the photo-electric effect, the photon imparts all its energy to an electron in an atom of the absorbing material, giving the photo-electron a kinetic energy equal to the original energy minus the binding energy of the electron. For photons of high energy and absorbers of low atomic number such as Al, the Compton effect predominates over the photo-electric effect. In this process (Compton effect) only a part of the energy of the photon is imparted to the Compton electron, depending on the angle between the initial and final directions of the photon. The maximum energy of the Compton electrons is a measure of the energy of the incident photons. The third process viz. pair-production occurs when the photon disappears and gives rise to a pair of electrons of opposite charge. These two electrons of opposite charge proceed in opposite directions to conserve momentum and each has a kinetic energy equal to one half of the energy of the photon minus the energy equivalent to the rest mass of an electron (0.51 Mev). Pair-production can occur only in cases where the photon has energy greater than two electron masses (1.02 Mev). It is found that the absorption of photons by matter is exponential and is given by,

$$N_t = N_0 e^{-\mu t} \quad \ldots\ldots\ldots\ldots\ldots\ldots\ldots \quad (1.2.)$$

where μ is the mass absorption coefficient (taking into account the above three effects), t is the thickness in gm/cm^2 and N_0 and N_t are the number of counts observed when absorbers of zero and t gm/cm^2 thickness are used; N_0 and N_t are thus measures of activities in the two cases respectively. In practice, the count is plotted along the log. scale against the thickness of absorber interposed between the source and the detector along the linear scale when a straight line is obtained on the semi logarithmic graph paper. From it the thickness of the absorber necessary to reduce the activity to a half its value is obtained and this thickness is called the half-thickness. Curves giving the relation between half-thickness and energy of the γ-ray are given in literature (G2), from which the energy of the γ-ray can be obtained. If the mass absorption coefficient μ, is known for the different photon energies, then from equn. (1.2),

$$t_{1/2} = \frac{\ln 2}{\mu} = \frac{0.693}{\mu} \quad \ldots\ldots\ldots\ldots\ldots\ldots \quad (1.2').$$

In cases where two or more γ or X-rays are present, the various components can be separated from the observed curve on the semi-logarithmic graph paper, by extrapolation and subtraction in the order of decreasing half-thickness. However, this becomes useless when two γ- or X-rays of similar energy are present. Generally lead is used for the absorption of γ rays while aluminum or copper is used for X-rays.

In general, the results obtainable by absorption methods are rather qualitative and only in favourable cases is it possible to obtain rough values of the energies of the β and γ rays. We have used absorption method only in the case of γ-rays to see whether there exist any γ-rays of high energies and low intensities which may escape our attention in the spectrometric studies of the photo-spectra.

1.3. β-spectrometers

There are several types of β-spectrometers described in literature. Most of these employ magnetic field to focus the electrons emitted by the radio-active sources. In general, a β-spectrometer mainly consists of a source holder, magnetic coils, shutters and a detector. If the β-spectrometer is made of non-ferromagnetic materials, the magnetic field obtained by the current in the coils is proportional to the current. In cases where some ferromagnetic material like iron is used, the pole pieces are shaped in such a way that this linearity is preserved. Electrons of different energies are focused at the detector by changing the current. The constant connecting the current and the magnetic field is different for different spectrometers but is independent of the value of the magnetic field or current for the same spectrometer. The constant of a spectrometer is usually determined by determining the current necessary to focus some internal conversion line whose energy or $H\varrho$ value is accurately known. In the cases where the current-$H\varrho$ relationship is not linear, the magnetic field has to be determined accurately for every value of current set up by some other means. The relationship between the magnetic field and the energy of the electrons focussed by this magnetic field is given by,

$$W = (1 + \eta^2)^{1/2}, \text{ where } \eta = H\varrho \cdot (\mathrm{e/mc}) = H\varrho/1704.2$$

η being the momentum of the electrons.

The energy distribution of the β-rays emitted by a radio-active source is then studied using a β-ray spectrometer by observing the number of β-rays recorded in the different energy intervals.

The different types of β-spectrometers use different types of focusing. For example, there are spectrometers using (i) semi-circular focusing, (ii) lens focusing, (iii) double focusing etc. In the semi-circular focusing type, the electrons emitted by the radioactive source pass through a transverse homogeneous magnetic field and are deflected into circular paths. The electrons then come to a focus after making half a circle, due to geometrical relationships. The lens focusing type, unlike the semi-circular focusing type, focuses electrons in all planes achieving space focusing. It employs the focusing action of a coil, when a β-ray is admitted along the axis of the coil. SIEGBAHN (S6) and independently DEUTSCH et al. (D1) have constructed such type of β-spectrometers and showed that this type of focusing is superior to the semi-circular focusing, giving increased light intensity in relation to the resolving power. It is, however, possible to combine these two types of focusing achieving high resolution together with good light intensity. The double focusing spectrometer (H6) of this Institute utilises both axial and radial focusing in an inhomogeneous magnetic field which is continuously measured with good precision.

A GEIGER MÜLLER tube or photographic plate or a crystal dectector may be used to record the focused electrons. The shutter system between the source and the detector serves the purpose of limiting the pencil of rays and eliminating the scattered radiations from the source.

1.4. Scintillation spectrometer

The γ-radiation emitted by a radio-active source can be studied (i) by making observations on internal conversion electrons or electrons obtained by using an external foil, or (ii) directly by using a phosphor detector. In case (i) the β-ray spectrometer is used to study the electrons connected with the γ-radiation and thereby information regarding the γ-ray is obtained. In case (ii) a scintillation spectrometer which consists of mainly a phosphor, a photomultiplier tube, amplifiers, a pulse discriminator and a pulse recorder, is used. Different phosphors having different characteristics are described in literature (G1) suitable for detecting γ-rays, X-rays or electrons. The incident γ-radiation causes scintillations inside the phosphor. The light rays from these flashes are collected by the light gathering mirror and focused upon the sensitive area of the photo-cathode of the multiplier tube. An appreciable number of photo-electrons are ejected from the photo-cathode for each quantum of the γ-radiation incident on the phosphor, forming a single pulse of photo-electrons. This pulse is amplified by the secondary emission amplification of the several dynodes in the multiplier tube. The output signal pulse then passes through amplifiers and the discriminator and is finally recorded by the recorder. The purpose of the pulse discriminator is to allow pulses of only a particular size to be recorded by the recorder. By studying the energy of two or more known γ-rays, one can calibrate the pulse size (in volts as shown by the discriminator) in terms of the γ-ray energy. The energy of any other unknown γ-ray can then be determined using this scale and observing the number of pulses recorded as a function of the pulse size. The scintillation spectrometer gives very high intensity as the γ-source can be placed directly on the phosphor. However, the relation between the pulse size and the γ-ray energy is not fully known theoretically. Further, the resolution in the case of scintillation spectrometer is much inferior to that of a β-spectrometer. The energy values obtained by scintillation spectrometer are rather approximate compared to the values obtainable by a β-spectrometer.

1.5. Coincidence technique

Coincidence technique is very useful in the study of the nuclear disintegration schemes. If a β-ray is followed by a γ-ray, $\beta\gamma$-coincidences can be observed. If a γ-ray is followed by one or more γ-rays, one can study the $\gamma\gamma$-coincidences. Further, if one or more of these γ-rays, are internally converted, one can also make an investigation of the βe^--coincidences where e^- stands for the converted electron. A study of such coincidence measurements confirms a disintegration scheme proposed on energy relationships.

$\beta\gamma$-coincidences are investigated using a β-tube and a γ-tube between which the sample is mounted. A β-tube is a G. M. tube having a thin window such that low energy β-particles can also enter it while a γ-tube is generally covered with a cathode of high Z material such as lead, brass or gold, because the efficiency of the γ-tube for γ-rays depends upon the quantum efficiency of the cathode material which is known to be higher for high Z materials. Similarly $\gamma\gamma$-coincidences are investigated using two γ-tubes or two crystal detectors for γ-rays, while two β-tubes are used in the investigation of βe^-- or e^-e^--coincidences.

$\beta\gamma$- or βe^--coincidences can also be investigated using a spectrometer. In the first case, to investigate the coincidences in the spectrometer, the γ-tube has to be placed in the immediate neighbourhood of the sample while the β-rays are focused into the β-tube at the far off end of the spectrometer by means of the current in the magnetic coils of the spectrometer. In studying βe^--coindicences in the spectrometer the γ-tube in the above arrangement has to be replaced by a β-tube.

βe^--coincidences or e^-e^--coincidences can be investigated using a special conctruction of two spectrometers such as the Goniometer constructed by SIEGBAHN (S7). In this case a portion of the β-spectrum or one of the internal conversion lines is focused into one spectrometer while the other internal conversion line is focused into the other spectrometer.

A coincidence arrangement essentially consists of two detecting apparatus and the pulses coming out of these apparatus are lead into a coincidence circuit which allows through it pulses which come together within a particular time interval called the resolving time ($\sim$ microsecond).

1.6. Directional correlation measurement technique

When a nucleus emits two γ-rays in succession, there can be some correlation between the directions of emission of these two γ-rays. This correlation denoted by a function $W(\Theta)$ which gives the relative probability that the second quantum will be emitted at an angle Θ with the first, is determined by the angular momenta of the three levels involved in the two transitions and by the multipole order of the radiation emitted in these transitions. This has been theoretically investigated by HAMILTON (H7) and later by others. The first experimental evidence was obtained by DEUTSCH et al. There can also be directional correlation between either the internal conversion electrons of two successive γ-rays emitted by a nucleus or between a forbidden continuous β-spectrum and the internal conversion electrons of a γ-ray following it. Directional correlation measurements between electrons were reported by ZUNTI and recently SIEGBAHN (S7) made a number of such measurements with his β-spectrogoniometer. The directional correlation measurements are, however, laborious and in general the directional correlation theory by itself does not lead to any unique assignment of spins and parities to the nuclear levels concerned. We have not undertaken any such investigations.

B. Methods used in the present investigations

1.7. Absorption

The absorption method described in Art. 1.2 has been used to study hard γ-rays. A β-tube of usual bell type G. M. counter together with a decade scale was used. The distance between the source and the counter was 9 cm. The thickness of the counter window was 3.7 mg/cm^2. Lead absorbers of uniform thickness were prepared by rolling. In some cases copper absorbers have been used to study the X-rays.

1.8. The β-spectrometers

All the investigations presented here, have been carried out mainly using two β-spectrometers (S3, S4) of this Institute. Both are lens type magnetic spectrometers. With the shutter arrangement used, the intermediate image spectrometer (S4) has a light intensity about five times that of the older type (S3). Both the spectrometers consist of iron. But, the linear relationship between the current in the coils and the magnetic field obtained, is maintained even at very low fields by demagnetising the spectrometer after each run. Very thin nylon windows which allow electrons above 5 kev have been used. The G. M. counter was filled with a mixture of methane and argon, giving a long constant plateau of about 100 volts so that observations extending over long periods could be made with ease and certainty. A decade scale of 100 of the type described by ÅSTRÖM (Å1), was used in conjunction with the G. M. tube. In the latter investigations we have used only the intermediate image spectrometer (S4) because it has high transmission compared to any other spectrometer of this Institute.

1.9. The scintillation spectrometer

A scintillation spectrometer for rapid detection and measurement of X- and γ-ray energies, has been constructed by ÅSTRÖM (Å2) in this Institute. A thallium-activated sodium iodide crystal has been used as phosphor. This scintillation spectrometer has been used in the investigations on Ce, together with the β-spectrometer.

1.10. The coincidence technique

The $\beta\gamma$- and $\gamma\gamma$-coincidence measurements have been investigated in some cases to establish and check the disintegration schemes suggested in this work. The β-tube was a usual bell shaped G. M. counter with 3 mg/cm^2 mica window. The γ-tubes were of the cylindrical type of length 11 cm and diameter 11.5 cm. They were provided with 0.1 mm thick gold catodes and were filled with 90 mm argon and 10 mm ethyl alcohol. The γ-tubes have got a plateau of about 500 volts and the β-tube, about 300 volts. Coincidences have been measured in a standard set up. A lead wall of 1.5 cm thick separated the two γ-tubes placed side by side in the $\gamma\gamma$-coincidence set up. The 5 mm thick aluminum wall, in the case of $\beta\gamma$-coincidence set up, is sufficient to stop β-particles of energy up to 2.5 Mev without affecting much the intensity of γ-rays while the 1.5 cm thick lead shield in the case of $\gamma\gamma$-coincidence set up practically eliminates the possibility that a γ-ray may eject secondary electrons in both the γ-tubes at the same time giving rise to false coincidences.

Calculation of the efficiency of the γ-tubes is dealt with in Chapter 2.

For the measurement of the βe^--coincidences inside the spectrometer, the sample holder chamber of the intermediate image spectrometer (S4) has been demounted and a chamber holding a β-tube has been substituted in its place. The sample was supported just in front of this β-tube and aluminum foils of different thicknesses were interposed in between the sample and the β-tube. It has been possible to manipulate these aluminum foils from outside the spectrometer in such a way that a foil of any required thickness could be introduced with ease without disturbing the vacuum in the spectrometer. This method was used by us first in the investigations of Ba^{131} (K4) and later on in the investigation of OS^{193} (K7).

C. Procedure for setting up the disintegration schemes

1.11. On the basis of energy relations

After establishing the energies of the β- and γ-rays emitted by a particular radioactive substance, one can make a suggestion from these energies as to the mode of decay. In many cases the energy of a γ-ray would be equal to the difference in the energies of two β-rays. In such a case, it is quite probable that this particular γ-ray is emitted in a transition between the two nuclear levels to which the two β-rays lead to. In some cases the energies of two γ-rays add up to equal the energy of a third γ-ray. In such a case, it may be proposed that there is a branching in the decay of a particular nuclear level to another level, where one of the modes of decay involves the highest of the three γ-ray energies while the other mode of decay involves the other two γ-rays in succession. In cases where a third β-ray leading to the intermediate level proposed in the above manner is observed, such a proposal gets more confirmation.

1.12. On the basis of intensity relations

It is possible to check the above disintegration schemes proposed on the energy relations, if the intensities of the β- and γ-rays are known. For instance, an intense β-ray shall not be followed by a relatively less intense γ-ray unless there is a branching in the mode of decay to compensate the intensity and the branching γ-rays are observed. Similarly an intense γ-ray shall not follow a weak β-ray unless there are other γ-transitions terminating on that level explaining the intensity of the particular γ-ray in question. In general, two or more γ-rays of unequal intensity should not be placed in succession unless there is observed a β- or a γ-ray to take into account the difference in intensity.

1.13. On the basis of the coincidence results

The $\beta\gamma$-coincidence rate versus thickness of absorber before the β-tube curve for a simple β-spectrum followed by one or more γ-rays will be a straight line parallel to the thickness of absorber axis. For a complex β-spectrum consisting of only two β-components, one leading to the ground level of the daughter nucleus and the other to an excited level wherefrom it decays to the ground level emitting γ-rays, the $\beta\gamma$-coincidence curve plotted as a function of thickness of absorber before the β-tube, generally falls down along a straight line cutting the absorber thickness axis at a value equal to the range of the softer β-component. For other modes of decay, such a $\beta\gamma$-coincidence curve will be of different shapes which should be explainable on the basis of the disintegration scheme presented.

Similarly when several γ-rays are present, the $\gamma\gamma$-coincidence rate per recorded γ

can be calculated on the basis of a proposed disintegration scheme taking into account the intensities of the radiations and the efficiency of the γ-tubes for different energies of the γ-rays. The value calculated in this way, should agree with the observed $\gamma\gamma$-coincidence rate if the disintegration scheme proposed is correct.

In cases where the γ-rays are internally converted, the βe^-- or e^-e^--coincidence measurements made in a spectrometer using two β-tubes together with absorbers should agree with the conclusions that can be drawn from the disintegration scheme.

We have used the coincidence technique in a few cases to confirm the disintegration schemes. Some disintegration schemes are discussed in Chapter 5.

1.14. Isomeric transitions

In the case of isomeric transitions unlike the usual γ-ray transitions the γ-ray has a measurable half-life (from a second to several days) and no coincidences of this γ-ray with other radiations will be observable. Further, the γ-ray emitted in an isomeric transition generally involves a spin change of 3 units or more and may be known from internal conversion coefficient as well as the K to L internal conversion ratio.

D. Procedure for assigning quantum numbers to the nuclear levels

1.15. On the basis of the comparative half-lives

The β-transitions are characterised by their order of forbiddenness. If the observed half-life t of a β-transition is corrected by a theoretical factor f, the comparative half-life, ft is obtained. It is found that β-transitions of different orders of forbiddenness fall into different groups of ft values. The different order forbidden β-spectra have different selection rules regarding spins and parities involved in the β-transitions (K1). It is therefore possible to obtain some idea about the spins and parities of the nuclear levels involved in a β-transition from the comparative half-lives. This has been treated in some detail in Chapter 3.

1.16. On the basis of multipole order nature of γ-rays

There are selection rules regarding spins and parities which explain the occurence of different multipole order γ-rays (D2). The nature (electric or magnetic radiation) as well as the multipolarity of a γ-ray are exhibited in the total internal conversion coefficient of the γ-ray, the K to L internal conversion ratio of the γ-ray and its half-life. The last one is particularly useful in the case of isomeric transitions where such measurements are comparatively easy. From the measurements of internal conversion coefficients, K to L internal conversion ratios, and half-lives of γ-rays, one can obtain an idea of the multipole order nature of the γ-rays and from this the spins and parities of the levels involved can be obtained. This has also been treated in Chapter 3.

1.17. The nuclear shell theory

The values of spins and parities of the levels, obtained experimentally in the above manner, are finally compared with the theoretical predictions made on the basis of a single particle model of the nucleus. The nuclear shell theory is described in some detail in Chapter 3 and a discussion of the experimental results, in the light of the nuclear shell theory, is given in Chapter 6.

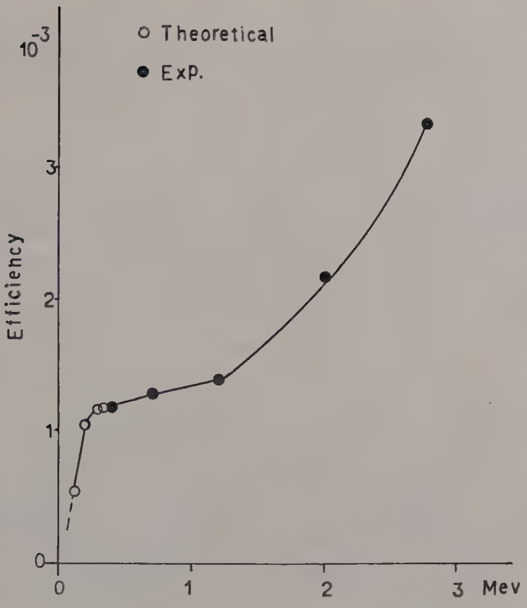

Fig. 2.1.

CHAPTER 2

Apparatus and methods

In this Chapter we shall consider in detail the methods employed in the present investigations, the apparatus used and calibration of the apparatus.

A. Irradiations and preparation of the samples

2.1. The Harwell pile

All the irradiations exept Pd^{109}, were made at the Harwell pile in England. The neutron flux used was stated to be ~ 10^{11} neutrons/cm^2/sec. All the isotopes considered in this work were produced by (n,γ)-process. The isotopes obtained were, in general, of good specific activity. My sincere appreciation is due to the Harwell pile authorities for the close co-operation in undertaking these irradiations.

2.2. The cyclotron

Pd^{109} was, however, irradiated in the Cyclotron of this Institute which produces deutrons of about 7 Mev energy with a flux of about ~ 10^8 neutrons/cm^2/sec. The flux in this case is estimated by irradiating a known weight of potassium permanganate by slow neutrons for a known length of time and estimating the specific activity obtained thereby, using a previously calibrated β-tube.

2.3. Chemical separations

All the chemical separations in the present investigations were performed in the radio-chemical laboratory of this Institute. Details of chemical separations are mentioned under the isotopes concerned.

2.4. Preparation of β-samples

In β-spectroscopy preparation of samples is a crucial point. Various ways of mounting the samples have been mentioned in literature from time to time. The main precautions, to be taken, are the following. (i) The sample should be made as thin as compatible with the specific activity available. It should be well grinded in the case of powders. If it is a solution it should be carefully evaporated so that big crystals are not formed. The layer of adhesive over the sample, if any, should be thin.

(ii) The backing material on which the sample is spread should be as thin as possible to minimise back-scattering.

(iii) Recently it has been pointed out by Braden et al. (B2) that samples mounted on non-conducting media give rise to distortions in β-spectra as they get charged.

The best way of preparing β-samples is to separate the required isotope on a thin metallic foil using an isotope separator on the lines reported by Broström et al. (B3). Bergström et al. (B1) have utilized this method. This method is unique in producing infinitely thin samples free from any impurities. But it is not always possible to utilise this method. It is yet extremely difficult to separate requisite quantities of the rare-earth elements and elements like Ru which have low vapour pressure and high boiling point. One requires good specific activities, if the samples prepared in this way are to be used in a β-spectrometer.

Another way of preparing thin samples is by evaporating the concerned element over a thin conducting film. But this is also limited by the boiling point of the element concerned.

Consequently a comparatively simpler way of preparing the β-samples has been adopted. Finely grinded sample has been spread on a thin aluminum foil. Very thin aluminum foils (0.15 mg/cm^2) have been used and the sample powder was spread on them evenly. Some times the powder has been covered with a thin film of zapon lack. Very thin zapon lack solution can be obtained by dissolving zapon lack in alcohol in the proportion of 1: 5 or so. A drop or two of such a solution has been used to fix the sample. In some cases where low energy part of the β-spectrum has been studied, a water suspension of the powder was used without any zapon-lack covering. In all these cases care was taken not to allow the sample to cluster at the edges.

Very thin backing-foils for the β-samples can be prepared using zapon lack or nylon or cellophane; but these should be made conducting by covering their back side with a conducting medium like beryllium.

2.5. Preparation of γ-samples

The active sample was pressed into a copper cylinder. Copper cylinders of different sizes with different wall thicknesses have been used according to the necessities of the different isotopes. Big copper cylinders 9 mm. in diameter and 9 mm. in height were used when a large quantity of the sample had to be taken due to low specific activity. The thickness of the walls is dictated by the maximum energy of the electrons emitted by the isotope. The higher the maximum energy of the electrons emitted, the thicker should be the wall thickness. Thin lead foils of varying thicknesses 0.01 to 0.03 mm. were fixed to these copper cylinders for the photo-effect to take place. The intensity of the photo-lines is a function of the thickness of the radiator and the energy of the γ-ray. For high energy γ-rays, it is necessary to use thick lead foils where as for low energy γ-rays, saturation takes place and thick lead foils absorb the photo-electrons and thereby diminish the intensity of the photo-lines. The lead foils used in the present investigations were prepared by rolling lead sheets under pressure. Very thin lead foils can be prepared by evaporation; but there is not a great certainty of uniformity.

B. Calibration of the apparatus

2.6. Calibration of the β-spectrometers

The β-spectrometers (S3, S4) used in the present investigations were calibrated with the F line of ThB as well as the annihilation γ-radiation. The $H\varrho$-value of the F line has been given very accurately by LINDSTRÖM (L1) as 1388.55 ± 0.2 gauss cm. If we define the resolving power as the ratio of the full width at half maximum to the $H\varrho$-value, then both the spectrometers were used at a resolution of about 4 % depending upon the size of the sample.

2.7. Calibration of the γ-tubes

If we consider a simple β-spectrum followed by a γ-ray, then by observing the $\beta\gamma$-coincidences in a standard set up, it is possible to calculate the efficiency of the γ-tube as well as that of the β-tube. If N_β is the count recorded by the β-tube, N_γ, the count recorded by the γ-tube and $N_{\beta\gamma}$, the number of $\beta\gamma$-coincidences, then one can write the following relations:

$$\begin{aligned} e_\gamma &= N_{\beta\gamma}/N_\beta \\ e_\beta &= N_{\beta\gamma}/N_\gamma \end{aligned} \quad \ldots\ldots\ldots\ldots\ldots\ldots \quad (2.1)$$

where e_β and e_γ are the efficiencies of the β- and γ-tubes respectively.

Similarly if we have two γ-rays in cascade following a single β-ray, and if we measure the $\gamma\gamma$-coincidences also with two γ-tubes using the same geometry the following relations can be written:

$$\begin{aligned} N_{\beta\gamma}/N_\beta &= e_{\gamma_1} + e_{\gamma_2} \\ N_{\gamma\gamma}/N_\gamma &= \frac{2\, e_{\gamma_1} \cdot e_{\gamma_2}}{e_{\gamma_1} + e_{\gamma_2}} \end{aligned} \quad \ldots\ldots\ldots\ldots\ldots\ldots \quad (2.2)$$

where e_{γ_1} and e_{γ_2} are the efficiencies of the two γ-tubes.

By means of equations (2.1) or (2.2) it is possible to determine the efficiency of the γ-tubes. Using the above relations, the gold cathode γ-tubes used in the present investigations were previously calibrated at this Institute for γ-radiation from Au^{198}, Cs^{134}, Co^{60} etc. However, the efficiency of these γ-tubes below 400 Kev was not known. As in the present investigations, we often come across γ-ray energies less than 400 Kev, it is deemed necessary to have an idea of the efficiency of these γ-tubes in the low energy region. We have estimated the efficiency of these γ-tubes in the following way.

BRADT et al. (B4) have given theoretical curves for the efficiency of γ-rays. The efficiency for gold can be obtained using these theoretical values from the following relation, viz.

$$E_{\mathrm{real}} = E_{\mathrm{theo.}} \cdot e^{-t\mu}, \quad \ldots \ldots \ldots \ldots \ldots \quad (2.3)$$

where μ is the mass absorption coefficient, and t, the thickness of the absorber. The γ-tubes in our case consist of 1 mm thick glass walls and 0.1 mm thick gold cathode. Consequently, the thickness of the glass walls is also to be taken into account when $t\mu$ in equation (2.3) becomes,

$$t\mu = (t_{\mathrm{g}}\,\mu_{\mathrm{g}} + t_{\mathrm{Au}}\,\mu_{\mathrm{Au}})$$

where g stands for glass and Au for gold. Evans (E2) has given the linear absorption coefficient of γ-rays in lead and aluminum. Using the relations given in their paper viz.

$$\left.\begin{aligned} T &= T_{\mathrm{Pb}}\,(\varrho/11.35)\,(207.2/W)\,(Z/82)^4 \\ \sigma &= \sigma_{\mathrm{Pb}}\,(\varrho/11.35)\,(207.2/W)\,(Z/82) \end{aligned}\right\} \quad \ldots \ldots \ldots \ldots \quad (2.4)$$

where T and σ are the linear photo-electric and Compton absorption coefficients, ϱ, the density, W, the atomic weight and Z, the atomic number of the absorber in question viz. gold or glass. From (2.4) the required values for μ can be calculated. We ignore pair production in calculating the absorption coefficient because we are concerned at present with the low energy region where pair-production does not occur. Using the above relations, absolute efficiency for the γ-tubes is calculated and the calculated values of efficiency are normalised to fit the previously investigated curve (experimental) at the value for Au^{198}. The efficiency curve is given in Fig. 2.1 where the full points represent the values previously obtained from coincidence measurements and circles represent the values now calculated by the method mentioned above.

2.8. Calibration of the scintillation spectrometer

The scintillation spectrometer used in the investigations was calibrated using the Na^{22} annihilation γ-radiation. The scale is considered to be approximately linear in the region used. The calibration has been further checked by the energy of X or γ-rays emitted by the sample under investigation whose energies were reliably determined by some other means.

C. Energy determination of β- and γ-rays

2.9. β-rays

FERMI (F2) put the theory of β-decay into mathematical form. His theory gives an energy dependence for the β-spectrum and in the case of an allowed β-spectrum it can be put in the form,

$$P\,dW = (G^2/2\pi^3)\,C \cdot \theta\,(Z, W) \cdot \eta\,W\,(W_0 - W)^2\,dW \quad \ldots \ldots \quad (2.5)$$

where $P\,dW$ is the probability per unit time of the ejection of a β-particle with energy between W and $(W + dW)$, G is the Fermi constant, C consists of nuclear matrix elements which are expected to be comparatively independent of energy and charge, θ (z, w) is the Fermifunction which is considered in some detail later on, η is the momentum of the β-particle, W is the energy of the β-particle and W_0 is the maximun energy of the β-particles emitted.

The β-spectrum curve runs tangent to the momentum axis; so it is difficult to make an accurate determination of W_0 direct from the β-spectrum. However, equation (2.5) can be put in a form convenient for an accurate determination of W_0, namely,

$$\left[\frac{P\,dW}{\theta\cdot\eta\cdot W}\right]^{1/2} = k\,(W_0-W) \quad \ldots\ldots\ldots\ldots\ldots \quad (2.6)$$

where k is a constant.

Now, $P\ dW$ is the same as N, the number of observed electrons per unit energy range in unit time. If we plot $(N/\theta.W.\eta)^{1/2}$ as a function of the energy W, we should obtain a straight line with an intercept at $W = W_0$, if Fermi's theory is correct. KURIE et al. (K2) first suggested such a plot.

However, such a plot will not yield a straight line throughout the energy region if the β-spectrum consists of more than one component. The lower energy components will make the FERMI plot deviate upwards from the straight line. In such a case, one has to take into account the highest energy component and make once more Fermi analysis of the β-spectrum to obtain the next highest energy component. If this Fermi plot still shows some lower energy component, the process has to be repeated until all the points in the Fermi plot are accounted for. In the present investigations it has been possible to resolve as many as six components in the case of Cerium. Though such a procedure enables one to determine the energies of the β-components in principle, the accuracy goes down rapidly as the number of β-components increases. It is always safe to check such a determination of β-energies by measuring the energy of the γ-rays connected with them. This is considered in the next article.

For a thick sample and sample-backing, there can often occur an upward deviation in the Fermi plot from straight line at the low energy end. Such a deviation could be mistaken as a low energy β-component. In cases where the γ-ray energy measurements match the β-ray maxima obtained from the Fermi analysis, there is no reason for such suspicion. Further, when a β-ray is of low intensity or has a β-maximum near to that of the next higher β-maximum, it is not always possible to resolve it from the Fermi plot. Such a β-ray has to be postulated only from γ-ray measurements. Cases like this have been encountered in Neodymium and Cerium in the present investigations.

2.10. γ-rays

The γ-ray energies can be studied using a β-spectrometer by means of magnetic analysis of secondary electrons. There are three effects occuring when a γ-ray passes through a radiator; (i) the photo-electric effect, (ii) the compton effect, (iii) the pair-production, the third one being useful for γ-rays of energy greater than 2 mc^2. The photo-electric effect is the best for determination of γ-ray energies up to about 800 kev.

If a γ-ray of energy E_γ ejects an electron from the K shell of the radiator, then we observe the photo-electron having energy, $E_K = E_\gamma - K$, where K is the binding energy of the electron in the K shell of the radiator. Similarly, if the γ-ray ejects an electron from the L shell of the radiator, then a photo-electron of energy $E_L =$

$E_\gamma - L$, where L is the binding energy of the electron in the L shell, is obtained and so on. The probability of emission of a K-electron is highest and the probability decreases as we consider the L, M and N-shells. It is comparatively easy to observe the K and L-shell photo peaks of a γ-ray and in favourable cases M shell peak may also be observed if a strong source and high resolving power are employed. However, it is sufficient if one observes K and L photo-lines of a γ-ray, to make an unambiguous determination of the γ-ray energy.

In some photo-spectra the L photo-line of a γ-ray may occur at the same energy as the K photo-line of another γ-ray. In such cases, the determination of γ-ray energy becomes ambiguous. But, if the γ-ray energy can be determined in some other way, for instance, from the internal conversion lines in the β-spectrum, it can be reliably stated. Otherwise one has to choose some other radiator whose difference in K and L binding energies do not coincide with the difference in energy of the γ-rays in question. Such cases of ambiguity in photo-spectra have occured in some of the investigations presented in this work. But all such cases were independently checked either from the internal conversion line measurements in β-spectra or from the γ-ray measurements using the scintillation spectrometer.

In many cases absorption in lead has been used to know whether there are any high energy γ-rays.

In cases where the internal conversion is high or the γ-ray is of low energy such that no K or L photo-line is observable, the only way of determining the γ-ray energy is by measuring the energy of the corresponding internal conversion lines in the β-spectrum. The energy of the γ-ray is given by the sum of the energy of the peak and the binding energy of the electron. As the γ-ray is emitted by the daughter nucleus, the binding energy of the daughter nucleus has to be added. The γ-ray energies deduced from the K and L internal conversion electron peaks, are quite reliable.

D. Intensity estimations

2.11. Intensity estimations of the internal conversion lines

From the β-spectrum, it is possible to estimate the ratio of the intensity of a conversion line to that of the β-continuum or to that of another conversion line. Such estimations are useful for obtaining a knowledge of the multipole order nature of the γ-rays. There are, great uncertainties in estimating these intensity ratios. The least uncertainty occurs in estimating the intensity ratio of the K and L lines of the same γ-ray, when they are well resolved. The main source of error is the thickness of source and the error increases as the energy of the γ-ray decreases. At low energies, below 100 kev, there are several uncertainties. They are:

(i) Back-scattering due to the source-backing. This is a function of the thickness of the source-backing.

(ii) Due to the thickness of the sample, the electrons originating in the inner layers come out with less energy and are counted as belonging to a lower energy than they actually belong to. This depends upon the thickness of the sample. For thick samples, low energy electrons originating in the bottom layers of the sample may be completely absorbed in the sample itself while high energy electrons come out with lower energy. Due to this cause, the whole shape of β-spectrum as well as that of conversion

electron lines can appear different with different samples depending upon their thickness. For instance, one can compare the two β-spectra (Figs. 4.21, 4.22) given in the case of Nd^{147} taken with samples of different thickness.
(iii) Due to the thickness of the window of the β-tube, very low energy electron lines will be either partially or completely cut off. In our case, the β-tube has a very thin window giving rise to no distortions above about 20 kev. This window of the β-tube has cut off electrons of energy less than 5 kev only.
(iv) When two electron lines are so close together that they are not well resolved by the spectrometer, the electrons from the higher energy line are scattered into the lower energy line. This gives rise to a serious discrepancy when the lower energy line is of low intensity as well. In this connection the reader is referred to the β-spectrum of Ru^{103} Fig.(4.2).

One has to keep in mind these factors while considering the intensities of the internal conversion lines. In the case where the internal conversion lines are well resolved and situated in the high energy region, so that absorption and scattering do not play a great role, the intensities are rather reliable. In the case of two well resolved but closely situated conversion lines, their intensity ratio is also reliable even at low energies since the uncertainties due to thickness of source etc. are of the same order of magnitude for both the lines.

The intensity ratios have been obtained by comparing the areas under the conversion lines in a divided form β-spectrum after subtracting the β-continuum.

2.12. β-ray intensities

When a β-spectrum is complex, it is of great use to have a knowledge of the intensities of the different β and γ-components. It helps in checking a disintegration scheme and it is essential to estimate the transition probabilities (ft-values) for the different components and thereby obtain information regarding spins and parities of the different levels.

If all the β-components have straight line plots, it is easy to estimate the relative intensities of these components to a fair degree of accuracy. In such a case one has only to back calculate N, the number of β-particles emitted per unit interval of $H\varrho$ after extrapolating the straight line Fermi plot. After that, one has to plot these values of N against $H\varrho$ and compare the areas enclosed by each of the component curves. Such a procedure assumes that the Fermi plot is straight through out the energy region which is found to be true for all allowed and most of the first forbidden transitions as well.

In cases where one or more of the β-components are expected to give rise to a known definite shape other than straight line Fermi plot, the calculation of N is somewhat complicated as one has to construct such a shaped Fermi plot and make the back-calculation for N. If such a procedure is not followed, the relative intensities obtained from extrapolation of straight line plots will not be quite accurate especially when the nonlinear component is of high intensity.

When one or other of the β-components is of much lower energy than the other, the soft component is much more absorbed in the source than the hard one depending upon thickness of the source. An opposite effect to this, is that the hard component is scattered into the soft component region. This is the major uncertainty in the determination of the β-ray intensities.

2.13. γ-ray intensities

For very thin radiators, the height of the photo-line in the photo-spectrum should be proportional to $(\tau \cdot t_r)$ where τ is the photo-electric mass absorption coefficient and t_r, the thickness of the radiator in gm/cm². For thick radiators, the problem of estimation is complicated and has been treated by Deutsch et al. (D1).

The relative intensities of the γ-rays in the present investigations have been estimated in the following manner. The height of the photo-lines over the compton back-ground for each γ-ray has been measured and divided by the product $(\tau \cdot t_r)$. The values for τ have been calculated from the linear absorption coefficients for the γ-rays given by EVANS (E1). The ratio of the resulting quantities gives a measure of the relative intensities of the γ-rays concerned.

CHAPTER 3

Theoretical part

In this Chapter we shall consider the theory of β-decay and γ-emission. We shall also give a sketch of the nuclear shell theory.

A. β-decay

3.1. Fermi's formulation

In 1934, FERMI (F2) gave the theory of β-disintegration. He introduced a new type of interaction between the nucleons and the two emitted particles electron and neutrino (based on PAULI's neutrino hypothesis), in analogy with the interaction between charges and electromagnetic field in quantum electrodynamics. The neutrino has not yet been observed directly like the β-particle. To explain this, it is postulated that the neutrino is electrically neutral and of vanishingly small mass. However, the success of FERMI's theory of β-decay gives strong support to the neutrino hypothesis.

FERMI added a perturbing energy term for each constituent nucleon to the Hamiltonian for the nuclear system and further imposed the requirement of relativistic invariance. There are five different interactions which satisfy the invariance requirement (K1). They are

(i) Scalar

$$S = (V^* \beta Q_k U)\,(\varkappa^* \beta \varphi)$$

(ii) Polar four vector

$$V = (V^* Q_k U)\,(\varkappa^* \varphi) - (V^* \alpha Q_k U)\,(\varkappa^* \alpha \varphi)$$

(iii) Tensor

$$T = (V^* \beta \sigma Q_k U)\,(\varkappa^* \beta \sigma \varphi) + (V^* \beta \alpha Q_k U)\,(\varkappa^* \beta \alpha \varphi)$$

(iv) Axial vector (3.1)

$$A = (V^* \sigma Q_k U)\,(\varkappa^* \sigma \varphi) - (V^* \gamma_5 Q_k U)\,(\varkappa^* \gamma_5 \varphi)$$

(v) Pseudoscalar

$$P = (V^* \beta \gamma_5 Q_k U)\,(\varkappa^* \beta \gamma_5 \varphi)$$

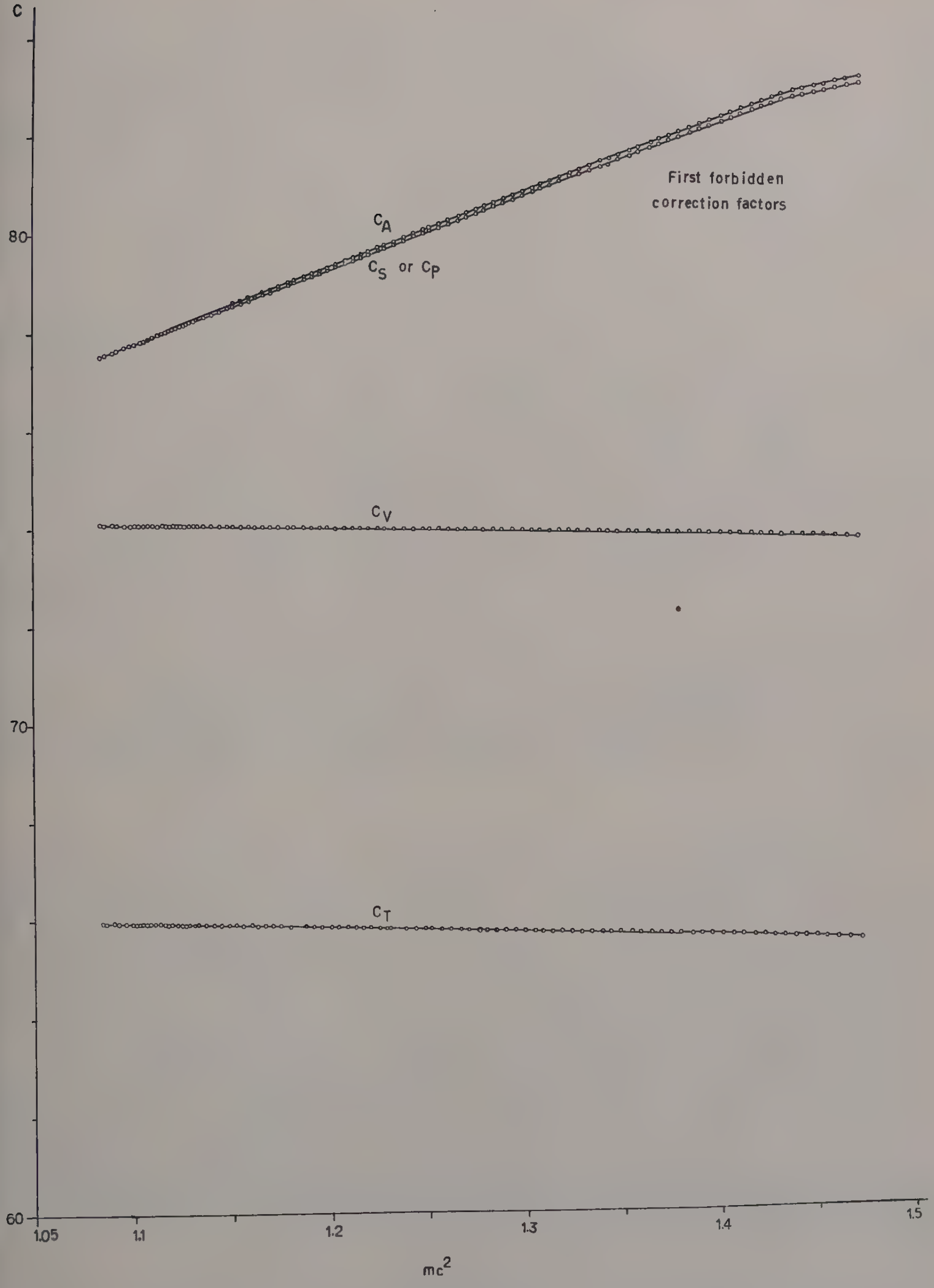
C
80
70
60
C_A
C_S or C_P
First forbidden
correction factors
C_V
C_T
1.05
1.1
1.2
1.3
1.4
1.5
mc^2

Fig. 3.1.

where U, V, $\varkappa$ and φ are the wave functions of the initial nucleon, final nucleon, electron and neutrino, Q_k is an operator which causes the nucleon to make the transition. β, a and γ_5 are the Dirac matrix operators and σ is the spin operator.

Once, one of the forms in the above five interactions is chosen, the problem becomes unique. PdW, the probability of ejection of a β-particle per unit time with energy between W and $(W + dW)$, can be calculated from equation 2.5 in which, C is calculated on the basis of one of the above interactions, and $\theta\,(Z, W)$, the "Fermi function" representing the influence of the nuclear charge Z upon the emitted β-distribution is given by

$$\theta\,(Z, W) = \frac{4}{\Gamma^2\,(1 + 2\,s)}\,(2\,\eta\,\varrho)^{2s-2}\,e^{\pi a Z W/\eta}\,|\,\Gamma\,(s + iaZW/\eta)\,|^2 \qquad (3.2)$$

In the above expression ϱ is the nuclear radius and $s = (1 - a^2 Z^2)^{1/2}$, η and W are the momentum and energy of the emitted β-particle, W is the energy of the β-particle, a is the fine structure constant.

For an allowed β-transition all the different interaction forms (3.1) give an identical energy dependence. Fermi, originally, chose the polar four vector form. It is not yet quite definite which of the forms has to be preferred. It may be that no single one of the interaction forms (3.1) is the correct one taken by itself but a combination of some of these may be correct. Allowed β-spectra do not depend upon the different types of interaction where as forbidden β-spectra are, in general, dependent on the type chosen as in the latter case the different interactions present different energy dependence. Investigations of the forbidden spectra involving a spin change of one unit greater than the degree of forbiddenness, give evidence upto date that part of the true interaction must be either tensor or axial vector (W1).

In the present investigations we come across a Fermi plot in the case of Ru^{103} which seems to be deviating from the straight line plot. An explanation of this deviation may throw new light on the true nature of interaction involved in the β-decay.

3.2. Fermi function

In making the Fermi analysis of a β-spectrum one should know the value of $\theta\,(Z, W)$ defined by equation (3.2). There are, however, no well known tables available for the complex Γ function. Several approximations have been made in the past to calculate the Fermi function. Bethe and Bacher (B5) gave a good approximation for the Fermi function. Feister (F3) has reported a comparison of the results from this approximation as well as those from other approximations with those computed without any approximations by the computation laboratory of the National Bureau of Standards of U.S.A. He concluded that Bethe's approximation is accurate within 1 % error where as other computations are not so accurate. Bleuler et al. (B9) have calculated the Fermi function and have given the results in the form of curves for different values of Z, the nuclear charge. A comparison of the rigorous values reported by Feister (F3) with these curves show that these curves are also accurate to 1 %. In these investigations, the curves of Bleuler et al. (B9) have been used in evaluating the Fermi function.

3.3. The β-ray selection rules

The various interaction forms mentioned previously give rise to different selection rules with respect to spin and parity. Spin is denoted by I. Parity refers to the property that the wave function either changes sign or does not change sign if the space co-ordinates are transformed by inversion: $(X, Y, Z) \rightarrow (-X, -Y, -Z)$. If the wave function changes sign, its parity is odd; if not it is even.

The polar interaction originally adopted by Fermi lead to the nuclear matrix element $|\int V^* 1\, U d\tau|^2$ for allowed transitions. The identity operator 1 does not alter the symmetry properties of the wave functions U and V of the initial and final nucleons; hence no difference of total angular momentum or parity between U and V can be allowed. Thus Fermi's selection rule for allowed transitions comes out to be $I = 0$, no, where "no" means no parity change is involved in the transition. Since the operator β is a scalar just as 1, it yields the same selection rules as above. The pseudoscalar operator γ_5 changes sign in mirroring transformations (i.e. in a transformation of $(Z)^{2Z+1}$ nucleus to $(Z+1)^{2Z+1}$ nucleus or vice versa); so this type of interaction, if chosen, demands a change of parity (Yes) for the allowed β-transitions.

Selection rules different from the original Fermi rules result from tensor and axial vector interactions. The Pauli spin operator σ causes the initial states U to overlap on the final states V in accordance with the selection rules:

$I = 0, \pm 1$ (no) with $0 \rightarrow 0$ forbidden in the case of allowed transitions. These are known as the Gamow — Teller or G. T. selection rules. The G. T. selection rules, seem to be favored by the experimental evidence accumulated so far. Table 3.1 gives the β-ray selection rules used in the present investigations.

Table 3.1

Forbiddenness of β transition	Change in orbital momentum	Change in spin	Change in parity	Log ft
Normal allowed	0	0,1 (No $0 \rightarrow 0$)	No	4.8 to 5.5
Allowed	2	1	No	~6.5
First forbidden	1	0,1 (No $0 \rightarrow 0$)	Yes	6.5 to 7.5
»	1	2	Yes	8 to 9[1]

[1] For these transitions $\{(W_0^2 - 1)\, ft\} \sim 10^{10}$ according to SHULL and FEENBERG (S16).

3.4. Forbidden β-transitions

Transitions which violate the allowed selection rules are described as forbidden. If 't' is the half-life of a β-transitions, then from Fermi's theory one can obtain,

$$1/t = (\text{constant})\, |M|^2\, F(Z, W_0) \quad \ldots\ldots\ldots\ldots \quad (3.3)$$

where $|M|$ is the nuclear matrix element, $F(Z, W_0)$ is a function of the nuclear charge

Z and the maximum energy of the β-particles, W_0. The important fact about the matrix element $|M|$ is that it is cut down in value by a factor $\sim 1/100$, as the degree of forbiddenness increases. So, by measuring the half-life t of a β-active element and correcting its half-life by a factor $F(Z, W_0)$ for the effects of the nuclear charge and the maximum energy of the β-transition, it will be possible to distinguish between the different orders of forbiddenness. FEENBERG et al. (F4) have given curves for the f values based on detailed calculations taking into account the dependence on Z and W_0. If one corrects the experimentally observed half-life, t by multiplying it with the f value, one obtains the comparative half-life (ft value), and by comparing this with the ft values of other elements one can obtain an idea of the forbiddenness. The distinction between allowed and forbidden transitions is not, however, so sharp because of the uncertainty in the value of the matrix element $|M|$ (equation 3.3). Decessions about spins and parities arrived at from the ft values alone become uncertain particularly in the boundary cases. NORDHEIM (N2) reconsidered the ft values in the light of the recent nuclear shell model and has found that at least in the case of odd atomic number nuclei, the straggling of ft values is reduced to a great extent when the transitions are sorted out according to type. In the present investigations the f values given by FEENBERG (F4) have been used and NORDHEIM's considerations (N2) have been applied in deciding about the forbiddenness of the β-transitions concerned. The last column in Table 3.1 gives NORDHEIM's classification of log ft values (N2).

3.5. Correction factors for the Fermi plot of first forbidden β spectra

Careful investigations of the Fermi plots of forbidden β-spectra are very useful in deciding about the correct interaction form to be used in the Fermi theory. In the following investigations, Fermi plot of Ru^{103} appears to differ from the straight line plot. An attempt has been made to apply the first forbidden correction factors to see what happens. As the ft value in this particular case indicates that it is either allowed or at the most first forbidden, no attempt to apply higher forbidden correction factors, has been made. A short outline of the procedure adopted in calculating these first forbidden correction factors and the results are given below.

Greuling (Gl) has extended Fermi's theory of β-decay to the nth forbidden approximation. He has given the correction factors in a generalised nth forbidden form. For detailed formulas for the various interactions, the reader is referred to pages 572 and 573 of reference (G1).

From equation (15) of reference (G1) we get,

$$\frac{F_1(W, Z)}{F_0(W, Z)} = k\, p^{2(S_1 - S_0 - 1)} \cdot \frac{|\Gamma(S_1 + iY)|^2}{|\Gamma(S_0 + iY)|^2}$$

where k is a constant, $S_1 = [4 - (\alpha Z)^2]^{1/2}$; $S_0 = [1 - (\alpha Z)^2]^{1/2}$, $y = \alpha\, Z\, W/p$.

Using the asymptotic expansion,

$$\ln \Gamma(Z) = \tfrac{1}{2} \ln 2\pi + (Z - \tfrac{1}{2}) \ln Z - Z + 1/12\, Z + J_1(Z), \quad \ldots \quad (3.4)$$

for the complex Γ function, as suggested by HALL (H3),

$$\frac{F_1(W,Z)}{F_0(W,Z)} = k\,p^{2\,S_1-S_0-1)}\cdot\frac{(S_1^2+Y^2)^{S_1-{}^1\!/_2}}{(S_0^2+Y^2)^{S_0-{}^1\!/_2}}$$

$$\times\ \text{exp.}\left\{2\,Y\ \text{arc tan}\ \frac{Y(S_1-S_0)}{Y^2+S_1S_0}-2\,(S_1-S_0)+\frac{1}{6}\left(\frac{S_1}{S_1^2+Y^2}-\frac{S_0}{S_0^2+Y^2}\right)\right\}^1 \qquad (3.5)$$

This has been evaluated for nuclear charge 45 for all the values of momentum for which the observations are made. Using these values of F_1/F_0, the L, M and N in equation (14) of reference (G1) were evaluated and these in turn were substituted in the expressions for the correction factors C_{1S}, C_{1V}, C_{1T} and C_{1A}. The results are

$$\begin{aligned}
C_{1S} &\sim \varrho^2\left[M_0+\frac{2}{3}q\,N_0+\frac{1}{3}q^2L_0+2\,L_1\right]\\
C_{1V} &\sim \varrho^2\left[M_0-\frac{2}{3}q\,N_0+\frac{1}{3}q^2L_0+2\,L_1+L_0\left(3\,W_0^2-\frac{0.3}{2}\right)\right]\\
C_{1T} &\sim 2\varrho^2\left[M_0-\frac{2}{3}q\,N_0+\frac{4}{9}q^2L_0+3\,L_1+\frac{L_0}{2}\left(3\,W_0^2-\frac{0.3}{2}\right)\right] \qquad (3.6)\\
C_{1A} &\sim 2\varrho^2\left[M_0+\frac{2}{3}q\,N_0+\frac{4}{9}q^2L_0+3\,L_1\right]\\
C_{1P} &\sim \varrho^2\left[M_0+\frac{2}{3}q\,N_0+\frac{1}{3}q^2L_0+2\,L_1\right]\ \{(W_0\varrho)^2-0.1\}
\end{aligned}$$

where $\varrho = 0.004\,A^{1/3}$ and $q = (W_0 - W)$ = the energy taken by the neutrino, W_0 = maximum energy of the β-articles, W = energy of the β-particle and

$$L_0 = 0.9723$$

$$M_0 = (78.89 - 5.727\,\frac{p^2}{W} - 0.3365\,W + 0.0643\,p^2)$$

$$N_0 = -(8.76 + 0.3269\,\frac{p^2}{W} - 0.0747\,W)$$

and

$$L_1 = 0.11\,p^2\,(F_1/F_0).$$

The pseudoscalar correction factor C_{1P} is the same as the scalar correction factor C_{1S} but for a factor $\{(W_0\varrho)^2 - 0.1\}$ which does not depend upon the energy distribution of the β-particles. C_{1P} therefore need not be considered separately. Other correction factors are given in Fig. 3.1, for the energy region concerned. The influence of these correction factors on the form of the Fermi plot appears to be very small.

B. γ-emission

3.6. Methods of determining multipole order nature of the γ-rays

When a γ-ray is emitted by a nucleus, it carries away certain angular momentum from the nucleus. It is useful to classify the emitted γ-radiation according to the angular momentum which it carries away from the nucleus, and according to its

---

[1] I am grateful to Dr. N. SVARTHOLM for putting this equation in this form.

properties under reflection of the coordinates (i.e. parity considerations). For each value of the angular momentum, there can be either electric or magnetic radiation. There are three different ways of experimentally obtaining information regarding the multipolarity and the nature of the γ-ray emitted. They are:

(i) Measurement of the internal conversion coefficient,
(ii) Measurement of the intensity ratio of the K and L internal conversion lines of a particular γ-ray,
(iii) Measurement of the half-life of the γ-ray.

We consider these here in some detail.

3.7. Multipole order from the internal conversion

A nucleus in an excited state can undergo a transition to a lower state not only by emitting a γ-quantum, but also by transmitting energy directly to the electrons surrounding it. This process is called internal conversion. We define the internal conversion coefficient as the ratio of the number of internal conversion electrons to the number of photons emitted. The theory of internal conversion, unlike the β-decay theory, is independent of the elusive nuclear matrix elements because they cancel out of the calculation of the ratio of the number of electrons to the number of emitted γ-rays. The internal conversion coefficient calculations depend only on the known electronic wave functions. These computations are, however, very laborious and until recently only approximate theoretical values were known. Experimentally also, only very rough estimates of internal conversion coefficients could be made especially in the case of low energy γ-rays. Exact calculations of internal conversion coefficients are at present available only for the K shell and for energies above 150 kev (R1). Possibility of using thin sources is making it possible to determine experimentally the internal conversion coefficients with better accuracy than before.

3.8. Multipole order from the ratio of K to L conversion

In most cases, the experimental determination of K to L internal conversion ratio is much more reliable than the internal conversion coefficient itself. Such a determination is also specially useful to distinguish between the electric and magnetic radiations, since the dependence on l, the multipole order, of the K to L ratio for electric and magnetic multipoles is different (H4). HEBB and NELSON (H4) gave curves for the K/L ratio as a function of the γ-ray energy for different electric multipoles; they also gave a formula for the magnetic multipole case, namely,

$$(L/K) = \frac{1}{8}\left\{1 + \frac{(Z\alpha)^2}{4}\left(\frac{W+2}{W}\right)\left[\frac{l+1}{2l+1} + \frac{l(2l+1)}{4}\left(\frac{2l-1}{2l+1} - \frac{W}{W+2}\right)^2\right]\right\} \qquad (3.7)$$

where α is the fine structure constant, W is the energy of the γ-ray in mc^2 units, and l, the multipole order of the γ-ray.

3.9. Multipole order from the transition probabilities

When the difference in angular momentum of two states of a nucleus is large enough, the transition between these two states is sufficiently forbidden and the transition proceeds with an easily measurable life time. This phenomenon, known as nuclear isomerism, was first explained by WEIZSÄCKER (W2). SEGRÉ and HELMHOLZ (S5) gave a simple expression to estimate $\lambda\gamma$ the number of quanta emitted per unit time per nucleus.

$$\log_{10}\lambda_\gamma = 20.30 - 2\log_{10}[1.3.5.\ldots(2\Lambda-1)] \\ -(2\Lambda+1)(1.30-\log_{10}E) - 2\Lambda(0.84-\tfrac{1}{3}\log_{10}A) \quad (3.8)$$

where E is the energy of the γ-ray in Mev, $\lambda\gamma$ is in $\sec^{-1}$ and $\Lambda = l$, the multipole order for electric radiation. If we assume that magnetic 2^l pole radiation has the same probability as electric 2^{l+1} pole radiation, the decay constant of magnetic 2^l pole radiation is obtained from (3.8) by inserting $\Lambda = l+1$. The above expression ignores transition by internal conversion. Taking into account the internal conversion coefficient also, the decay constant λ is given by

$$\lambda = \lambda_\gamma + \lambda_e = \lambda_\gamma(1+\alpha) \quad \ldots\ldots\ldots\ldots \quad (3.9)$$

where α is the total internal conversion coefficient. Since α may have values very large compared to 1, the value of λ is essentially dependent on the internal conversion coefficient. The half-life of an excited state is then given by,

$$\tau = 0.69/\lambda \text{ where } \lambda \text{ is defined by (3.8) and (3.9).} \quad \ldots\ldots \quad (3.10)$$

SEGRÉ and HELMHOLZ (S5) have pointed that the expression (3.8) is a very rough approximation.

3.10. Methods used to determine the multipole order in the present cases

We have tried to estimate the multipole order nature of the γ-rays from a comparison of the experimentally determined conversion coefficients and K/L ratios with those predicted by theory (R1, H4, A1). In the case of isomeric transitions, when such an estimate of the multipole order disagrees with the one estimated from the half-life of the γ-ray, it has been mentioned.

3.11. γ-ray selection rules

From the laws of conservation of total angular momenta and parities, the selection rules for the γ-ray emission are obtained. If I and I′ are the total angular momenta (or spins) of the initial and final levels of a nucleus, then the γ-ray will be predominantly multipole radiation of the lower order l, in the range $|I - I'| \leq l \leq |I + I'|$ permitted by parity and not reduced by special arguments of symmetry. For the low energy γ-rays such as we are concerned in the present work, only the lowest multipole order is of importance.

We quote below the table of selection rules used in the present work. This is taken from DANCOFF and MORRISON's paper (D2). In this Table, Δi represents the difference in the spins of the two nuclear states between which the γ-transition takes place and Λ is the order of forbiddenness. In the case of electric radiations $\Lambda = l$, the multipole order.

According to WEISSKOPF (W3), in the parity favoured (i.e. no change in parity) cases the emission of electric radiation is much more probable than the emission of magnetic radiation for the same value of angular momentum change, Δi. This

Table 3.2

Change of parity (—) Λ	Even Δi		Odd Δi	
	Radiation	Λ value	Radiation	Λ value
No	Elec. $2^{\Delta i}$	Δi	Elec. $2^{\Delta i+1}$ Mag. $2^{\Delta i}$	$(\Delta i+1)$
Yes	Elec. $2^{\Delta i+1}$ Mag. $2^{\Delta i}$	$(\Delta i+1)$	Elec. $2^{\Delta i}$	Δi

means that the electric quadrupole radiation must be more probable than the magnetic dipole radiation. On the other hand, in the parity unfavoured (i.e. involving change of parity) cases, with a few exceptions, the magnetic radiation predominates over the electric one.

Further, as there is no order of multipole radiation for which the photons carry off zero angular momentum, γ-transitions between two nuclear levels of zero total angular momentum are forbidden.

3.12. The electric dipole case

On the assumption of a single particle model, for the nucleus, MAYER (M2) has arrived at the conclusion that the low lying nuclear levels in the odd atomic number nuclei, should not decay by electric dipole emission, as these low lying levels should belong to the same nuclear shell and hence have the same parity where as an electric dipole transition demands change of parity together with a spin change of one unit according to the selection rules given in Table 3.2.

Experimentally, there is relatively little evidence for electric dipole transitions between low lying nuclear levels.

C. The nuclear shell theory

3.13. Magic numbers and shells in nuclei

Nuclei containing 2, 8, 10, 20, 28, 50, 82 neutrons or protons and 126 neutrons are known to be particularly stable (E1, M1). Several attempts have been made to explain the stability of the above numbers known as the "magic numbers" on the basis of a one particle model, namely, to a first approximation, each particle inside a nucleus may be assumed to be moving in an average potential caused by the others.

3.14. One particle model of the nucleus

SCHMIDT (S1) pointed out that the magnetic moments of nuclei, if plotted as functions of total angular momentum, j, lie between two limits $j = l + \frac{1}{2}$ and $j = l - \frac{1}{2}$ known as the "Schmidt lines". This may be explained by the assumption that the spin is due solely to the extra odd nucleon and that for one limit, $j = l + \frac{1}{2}$, its intrinsic spin and orbital momentum, l, being parallel and for the other limit $j = l - \frac{1}{2}$, they being oriented antiparallel. This gives some justification for the assumption of the one particle picture. However, the experimentally observed moments do not lie on these two boundary lines at $j = l + \frac{1}{2}$ and $j = l - \frac{1}{2}$, but in between them. Even the magnetic moments of nuclei with one particle more or less than a closed shell do not seem to fit the Schmidt lines. NORDHEIM (N1) tried to correlate the information on nuclear states from spins and magnetic moments with other nuclear properties and as a result of this he obtained a level scheme.

3.15. F-H level scheme

FEENBERG and HAMMACK (F1) worked on the idea of Elsasser that there is a correspondence between the magic numbers and the degeneracy of energy levels in the model of free particles in a simple rectangular well. The level order for a rectangular potential well is found to be:

Table 3.3

Level	1s	1p	1d	2s	1f	2p	1g	2d	3s	1h	2f	3p	1i	2g	3d	4s
Possible number of particles that can occupy the level	2	6	10	2	14	6	18	10	2	22	14	6	26	18	10	2
Total number of particles in a possible shell	2	8	20		40		70			112			168			

The letter in the level gives the orbital momentum, l, i.e. s means $l = 0$, p means $l = 1$ and so on. The number gives the number of radial nodes. 1 means no node, 2 means one node etc. The Pauli exclusion principle sets a limit to the maximum number of one kind of particles that can occupy a particular space state. There cannot be more than $2(2l + 1)$ identical particles in the level having orbital momentum l, the factor 2 representing the two possible spin orientations with respect to the orbital momentum l.

From the above Table, it appears that the level scheme obtained from a simple rectangular potential well does not explain the whole series of the magic numbers. Certain modifications in the rectangular potential well have been suggested to produce the magic numbers. A central depression in the rectangular well for the light nuclei pulls down the 2s level relative to the 1d level, thus giving rise to a closed shell at 10 corresponding to the magic number 10 and the closing of the d shell at N or $Z = 20$. Similarly, for heavier nuclei if the rectangular potential well is replaced by a wine bottle shaped potential with a central elevation, then the magic numbers, spins, parities and magnetic moments of nuclei can be more or less predicted. Feenberg explains the wine bottle potential shape for the heavier nuclei on the assumption of the Coulomb repulsion between protons. Due to the Coulomb force, the proton density within a heavy nucleus varies from a minimum value at the centre to a maximum near the boundary. However, SWIATECKI (S2) has calculated the proton and neutron densities inside nuclei and has concluded that the central elevation in the potential well is too small by a factor of 5 to 10 to account for the shell at N or $Z = 50$. Further more, he contends that the density reduction required to produce the observed shells corresponds to an almost hollow nucleus, a configuration unstable against fission.

3.16. The spin-orbit coupling scheme

Meanwhile MAYER (M1) in America and HAXEL, JENSEN and SUESS (H1) in Europe tried to explain the magic numbers from a square well and a three dimensional isotropic oscillator potential assuming strong spin-orbit coupling. The spin and the orbital momentum (l) of a nucleus couple together vectorially, and give rise to the total angular momentum (j) of the nucleus. Thus j can have two values namely $j = l + \frac{1}{2}$ and $j = l - \frac{1}{2}$ depending upon whether the spin and orbital momentum are parallel or antiparallel. The orbits with higher total angular momentum i.e. $j = l + \frac{1}{2}$ have a higher binding energy compared to the orbit with $j = l - \frac{1}{2}$. Thus all the levels with orbital momentum $l > 0$, are split into two giving rise to inverted doublets, a lower level with $j = l + \frac{1}{2}$ and an upper one with $\mathrm{j} = l - \frac{1}{2}$, so that a gap occurs at this point. MAYER assumes that (i) the spin-orbit coupling is higher for large l values; (ii) pairs of spin levels within one shell, which arise from adjacent orbital levels in the square well in such a way that the spin-orbit coupling tends to bring the energy closer together can, and very often will cross; (iii) an even number of identical nucleons in any orbit with total angular quantum number j, will always couple to give a spin zero and no contribution to the magnetic moment; (iv) an odd number of identical nucleons in a state j will couple to give a total angular momentum j and a magnetic moment equal to that of a single particle in that state; (v) for a given nucleus the "pairing energy" of the nucleons in the same orbit is greater for orbits with larger j.

Assumptions (i) and (ii) are based on the spin-orbit coupling, assumption (iii) on the statistics of nuclei and (iv) on the single particle model of the nucleus. Assumption (v) was found necessary to explain the occurence of spin values lower than the j values in the case of odd nuclei, predicted by the energy level order obtained without this assumption. For example, for nuclei in the region of the $h_{11/2}$ level (Table 3.4) the spin value 1/2 has been found more common than 11/2 in practice.

HUGHES et al. (H2) have calculated the magnitude of the doublet splitting due to spin-orbit coupling postulated by this scheme. They have found that it is consistent with that observed in He^5. Their calculated value 3.1 Mev for $_{83}Bi^{209}$ compares well with the 2 Mev splitting postulated by this scheme at $l = 5$ for the extra stability of the closed shell of 82 neutrons. It seems therefore that there is some justification for the spin-orbit coupling assumption and consequently for the assumptions (i) and (ii). Assumption (iii) is justified by the fact that all even–even nuclei have spin zero. Assumption (iv) has some justification because the single particle model is based on the finding that the magnetic moments of nuclei lie in between the "Schmidt limits". MAYER (M2) justifies the fifth assumption on theoretical grounds.

Apart from these justifications of the above assumptions, this level scheme predicts unique values of spins and parities for energy levels of most of the nuclei. We have therefore tried to compare our conclusions as regards to spins and parities with the predictions of the spin-orbit coupling scheme.

Table 3.4 gives the level order postulated by the spin-orbit coupling scheme.

Table 3.4

Osc. no.	Square well	Spin term	No of states	Total no.
0	1s	$1s_{1/2}$	2	2
1	1p	$1p_{3/2}$	4	8
		$1p_{1/2}$	2	
2	1d	$1d_{5/2}$	6	20
		$1d_{3/2}$	4	
	2s	$2s_{1/2}$	2	
3	1f	$1f_{7/2}$	8	28
		$1f_{5/2}$	6	50
	2p	$2p_{3/2}$	4	
		$2p_{1/2}$	2	
4	1g	$1g_{9/2}$	10	
		$1g_{7/2}$	8	82
	2d	$2d_{5/2}$	6	
		$2d_{3/2}$	4	
	3s	$3s_{1/2}$	2	
5	1h	$1h_{11/2}$	12	
		$1h_{9/2}$	10	126
	2f	$2f_{7/2}$	8	
		$2f_{5/2}$	6	
	3p	$3p_{3/2}$	4	
		$3p_{1/2}$	2	
	1i	$1i_{13/2}$	14	

D. Errors

3.17. Errors in the intensity estimations

During the course of previous articles we have suggested explicitly the probable sources of error. It is not always easy to estimate the errors involved in a quantitative manner. Especially in the case of intensity estimations either from β-spectrum or photo-spectrum, the results obtained may be differing from the actual values by a factor as much as 2 depending upon the energy of the electron lines and the thickness of the β-source or lead foil as the case may be.

3.18. Statistical errors

If we count a number of particles n, during a particular measurement, then the statistical error involved in the measurement is, $\sqrt{n}$ and the actual number of particles will be $(n \pm \sqrt{n})$. In most of the measurements reported in this thesis, the statistical error is $\sim 1\,\%$.

3.19. Errors in the energy measurements due to source thickness

The thickness of source in β-spectra in the region used by us, seems to affect only the intensity of the electron lines but not the energy at which they occur. For instance, in the case of Nd^{147} β-spectrum (Fig. 4.20, 4.22) the electron peak at the low energy, 44.9 kev, is not affected in position when we have used β-samples of two different thicknesses. But the K/L ratio of the electron lines (Fig. 4.20, 4.22) derived using these two different β-samples is entirely different showing that in the thick source case, the K line is very much absorbed.

HORNYAK et al. (H5) have considered in detail the effect of thickness of the radiator in the case of photo-spectra and their conclusions show that the energy of the photo line determined from its high energy edge is quite independent of the radiator thickness and the maximum shift in the photo peak due to the radiator thickness in the energy region 0.2 to 1.0 Mev is of the order of 1.5 % for resolution widths less than 5 %. The photo lines reported in the present work are symmetrical and there has been no difficulty in determining the position of the peak.

3.20. Finite resolution error

Due to the resolution (~ 4 %) of the spectrometer, electrons of all energies in this interval are simultaneously focused in the spectrometer. Consequently, at the end of the β-spectrum, the spectrometer counts some electrons even after the current is set at a value corresponding to energy greater than the real maximum energy. This gives some superfluous electrons which appear as a tail at the maximum energy end in the Fermi plot. This effect becomes specially important when we are interested in the shape of the Fermi plot at the maximum energy end or when we are obliged due to some reason or other to draw conclusions on the $\beta_{\max}$ energy from the last few points alone at the end of the β-spectrum. In all other cases when the Fermi plot is linear, this effect is not of much importance.

CHAPTER 4

Measurements

In this Chapter, we shall report, in detail, the measurements made by us on the different radio-active isotopes.

A. Radio-activity of Ru^{103}

4.1. History

The 42 day activity in Ruthenium was assigned to Ru^{103} by LIVINGOOD (L3) and SULLIVAN et al. (S12). Absorption measurements were made by BOHR et al. (B8). HOLE (H8) investigated this isotope using a β-spectrometer also. Recently MANDEVILLE and SHAPIRO (M7) have given a disintegration scheme after studying this isotope using absorption and coincidence techniques. According to these authors 92 % of disintegrations of Ru^{103} proceed by way of an inner β-ray group at 0.15 Mev coincident with a γ-ray of energy 0.52 Mev which is (4 ± 1) percent converted; a harder β-ray group having a maximum energy of 0.68 Mev leads to the ground level of Rh^{103}; about 8 % of the disintegrations are said to proceed this way.

Our first report on this isotope appeared in the form of a letter elsewhere (K3). At the same time MEI et al. (M3) reported essentially similar results on this isotope.

4.2. Half-life

In the present investigation metallic Ruthenium was bombarded in the Harwell pile and chemically purified in the radio-chemical laboratory of this institute. The resulting metallic powder was spread over a 0.15 mg/cm² aluminum foil. The thickness of a sample thus prepared was estimated as about 0.4 mg/cm². Three different samples were followed for three half-life periods each giving an average half-life of 39.8 + 0.4 days. Fig. 4.1 gives one of these half-life graphs.

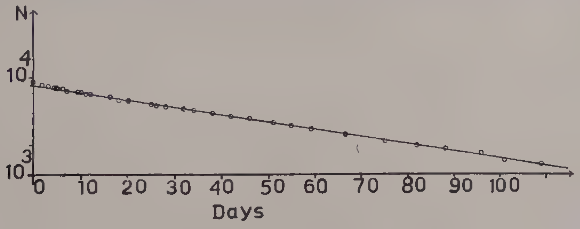

Fig. 4.1.

4.3. β-spectrum

The β-spectrum of Ru^{103} was studied several times. One of these runs is produced in Fig. 4.3. It shows three electron peaks at 17, 36 and 474 kev. The first two are identified as the *K* and *L* internal conversion lines of a 40 kev γ-ray, where as the third one is found to be the *K* line of a 497 kev γ-ray. The thin window of the G. M. tube and the high specific activity of the sample, made it possible to observe the faint *K* line for the first time, which was hitherto missing.

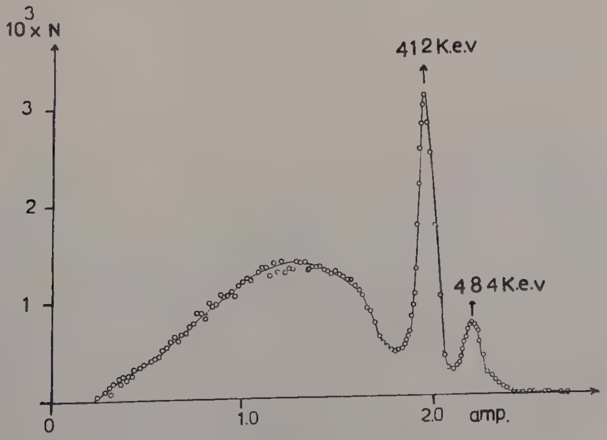

Fig. 4.2.

4.4. Photo spectrum

The metallic Ruthenium powder was filled into a thick copper capsule over which a 0.01 mm thick lead foil was placed and the photo-spectrum has been studied.

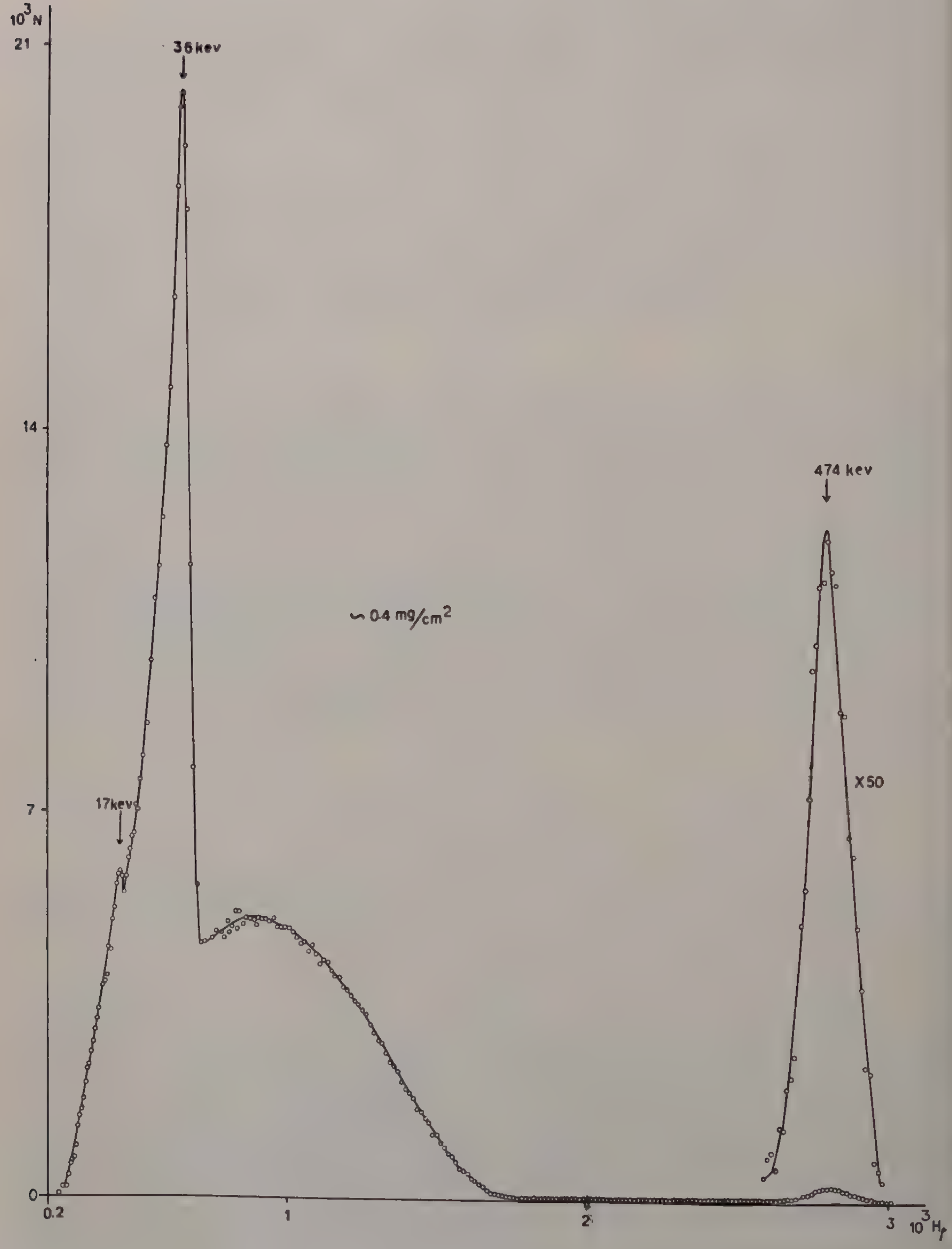

Fig. 4.3.

Fig. 4.2 gives one of these runs. There are two photo-lines; one at 412 and another at 484 kev. Taking them as the K and L lines respectively the energy of the γ-ray comes out to be either 499.6 or 499.8 kev. Thus the photo-spectrum and the K internal conversion line in the β-spectrum give the energy of this γ-ray as 498 ± 2 kev. No photo-line corresponding to the 40 kev ray has been found. This is probably due to the high internal conversion of this γ-ray.

Absorption of Ru^{103} radiations in lead showed that it emits only one unconverted γ-ray.

4.5. Coincidence measurements

a) $\gamma\gamma$-coincidences.

The $\gamma\gamma$-coincidences, using the standard set up of two γ-tubes, were investigated. The resolving time of the circuit was 0.4 micro-second. A very negligible $\gamma\gamma$-coincidence effect $(5 \pm 2)10^{-5}$ per recorded γ has been observed. Probably this small effect is spurious just as in the case of Au^{198} (S13).

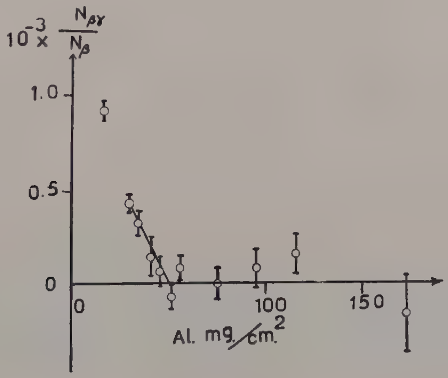

Fig. 4.4.

b) $\beta\gamma$-coincidences.

$\beta\gamma$-coincidences, using a β-tube and a γ-tube having gold cathode, were investigated. The resolving time of the circuit was again 0.4 micro-second. Aluminum absorbers of different thickness were inserted between the β-tube and the sample and the $\beta\gamma$-coincidence rate as a function of the absorber thickness has been investigated. Fig. 4.4 gives the results of this investigation. The count in the β-tube has been corrected for the γ-rays. Scattering, accidental and background coincidences have been taken into account. Fig. 4.4 shows that the soft β-spectrum is in coincidence with the 498 kev γ-ray. The $\beta\gamma$-coincidence effect falls to zero at about 50 mg/cm^2 thickness of aluminum which is in accordance with the upper limit of the soft β-spectrum found from Fermi plot, namely, 217 kev.

c) βe^--coincidences.

βe^- coincidences were investigated in the spectrograph. The 36 kev electron line of the 40 kev γ-ray has been focused into the far off β-tube and coincidences were

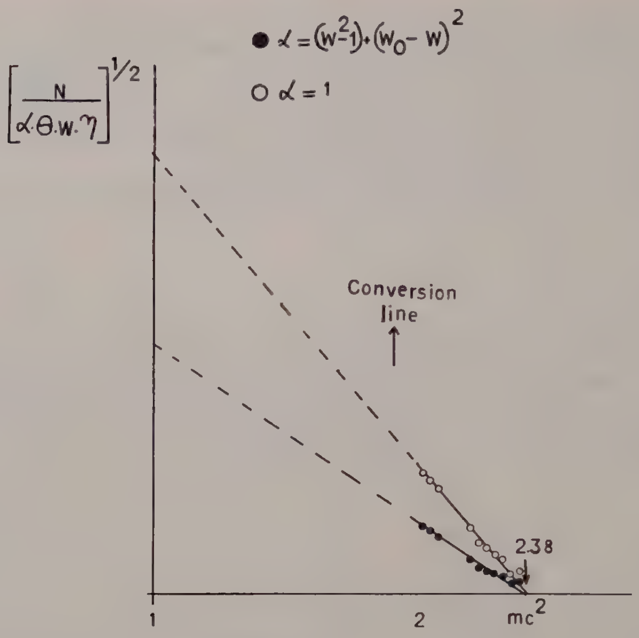

Fig. 4.5.

investigated between this and the continuous β-spectrum. No coincidences above the background coincidences, could be observed. This shows that the 40 kev γ-ray is not coincident with either of the β-components; i.e. it is emitted by a metastable level. Further, this served as a check on the arrangement used for the βe^--coincidences in the spectrograph.

4.6. Fermi plot

Fermi plot of the β-spectrum showed that it consists of two components. These are given in Figs. 4.5 and 4.6. Fig. 4.5 gives the usual Fermi plot as well as the one corrected by the α factor. Due to the low intensity of this component and the presence of the internal conversion line at 474 kev, the form of this could not be decided. Both the Fermi plots are converging to the same point. Six different β-spectra, thus investigated, gave an average of 700 ± 10 kev as the maximum energy of this hard β-component.

Fermi plot of the soft component, after taking into account the hard component, is given in Fig. 4.6. This is slightly curved towards the energy axis. Scattering in the sample cannot explain this as the deviation in that case should be upwards. The β-spectrum of Co^{60}, which is known to have a straight line Fermi plot, has been studied using a sample of similar thickness under identical conditions. This Fermi plot is given in Fig. 4.7. It shows an upward deviation from the straight line below 1.12 mc^2 and absorption overtakes this at 1.03 mc^2. The upward deviation is known to be due to scattering in the sample. In the case of Ru^{103} (Fig. 4.6) the deviation (which is downwards) starts at about 1.15 mc^2. Due to the presence of

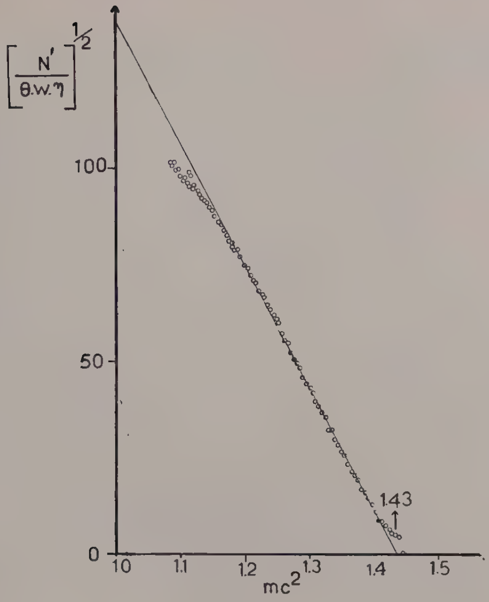

Fig. 4.6.

the L conversion peak of the 40 kev γ-ray, it has not been possible to see how the Fermi plot behaves below 1.08 mc².

Fermi function for $Z = 50$ has been used in the graph presented in Fig. 4.6. The same β-spectrum using θ for $Z = 40$ yielded a graph similar to Fig. 4.6 Fermi analysis of a β-spectrum taken after one half-life decay and in another spectrograph, has also given a shape similar tc Fig. 4.6. Thus the deviation from straight line, though small, is, rather, persistently appearing. This shape of Ru^{103} Fermi plot seems to be different from that of Y^{91} or Sr^{89} (L4) which are said to undergo first forbidden transitions involving a spin change of two units together with change in parity. However, for the present, the upper limit of the soft β-component is taken to be 217 ± 4 kev as shown in Fig. 4.6.

4.7. Correction factors for the Fermi plot

The ft value (0.45×10^6) of the soft β-component shows that it should belong either to the allowed or at the most first forbidden group on an empirical basis. We have tried to correct the Fermi plot applying the correction factors given in Art. 3.5. The results are shown in Fig. 4.8. All the points seem to lie on a ~ type curve, the low energy part being seen as convex when observed from the energy axis side. It shows that application of the correction factors does not affect the Fermi plot in any appreciable manner.

The harder β-component has been estimated ~ 1 % intensity on the basis that its Fermi plot is a straight line. The ft value for this β-component, on this basis, is 2×10^9 and $\{(W_0^2 - 1)\, ft\} \simeq 10^{10}$. Such a low intensity β-component should not effect the shape of the intense soft β-component in any observable manner. But, we have, however, corrected the hard component with the α factor (K1) namely, $\alpha = \{(W^2 - 1)$

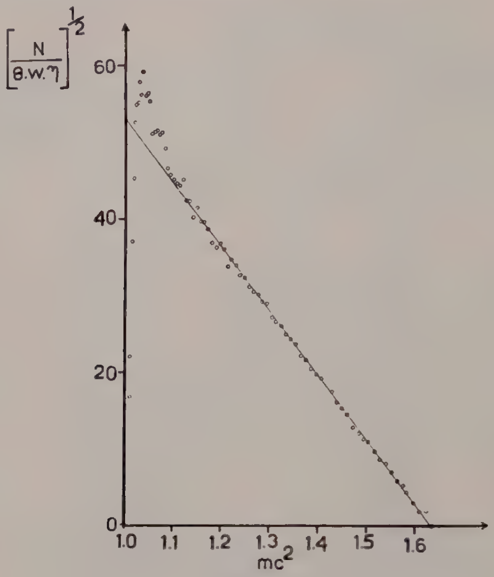

Fig. 4.7.

$+ (W_0 - W)^2\}$ using $W_0 = 2.4$ mc² and then taken it into account. The resulting Fermi plot is found to be exactly similar in shape to the one shown in Fig. 4.6.

Almost a year latter we have repeated our measurements with the same Ru metal newly bombarded in the Harwell pile with a pile factor 2. The results obtained are precisely similar to the ones obtained previously. In all, we have used samples of different thickness ranging from about 0.4 to 4 mg/cm², yielding essentially similar results including the shape of the low energy β-component. The observations have been made to a statistical accuracy better than 1 %. At about 50 kev the observed β-spectrum of Ru^{103} gives ~ 20 % less number of β-particles than is expected if it is a normal allowed β-spectrum.

4.8. Possible causes of deviation

In the past deviation from straight line Fermi plots have been explained on a variety of causes. Most of them are explained on the basis of thickness of the sample, sample backing or G. M. counter window thickness. In our case these do not seem to explain the present deviation. The G. M. counter has a thin window allowing electrons of energy greater than 5 kev and not affecting electrons above about 20 kev. The sample backing is very thin (0.15 mg/cm²). Further the β-spectrum of Co^{60} which has a similar upper energy maximum (about 1.63 mc²) when studied using a similar thickness of sample and sample backing, yields a straight line plot until 1.12 mc² and then deviates upwards below this energy due to scattering where as in the present case the deviation downwards starts at about 1.18 mc².

The presence of the intense L conversion line at 36 kev should in no way affect the shape of the β-spectrum above this energy. The hard β-component (1 % intense)

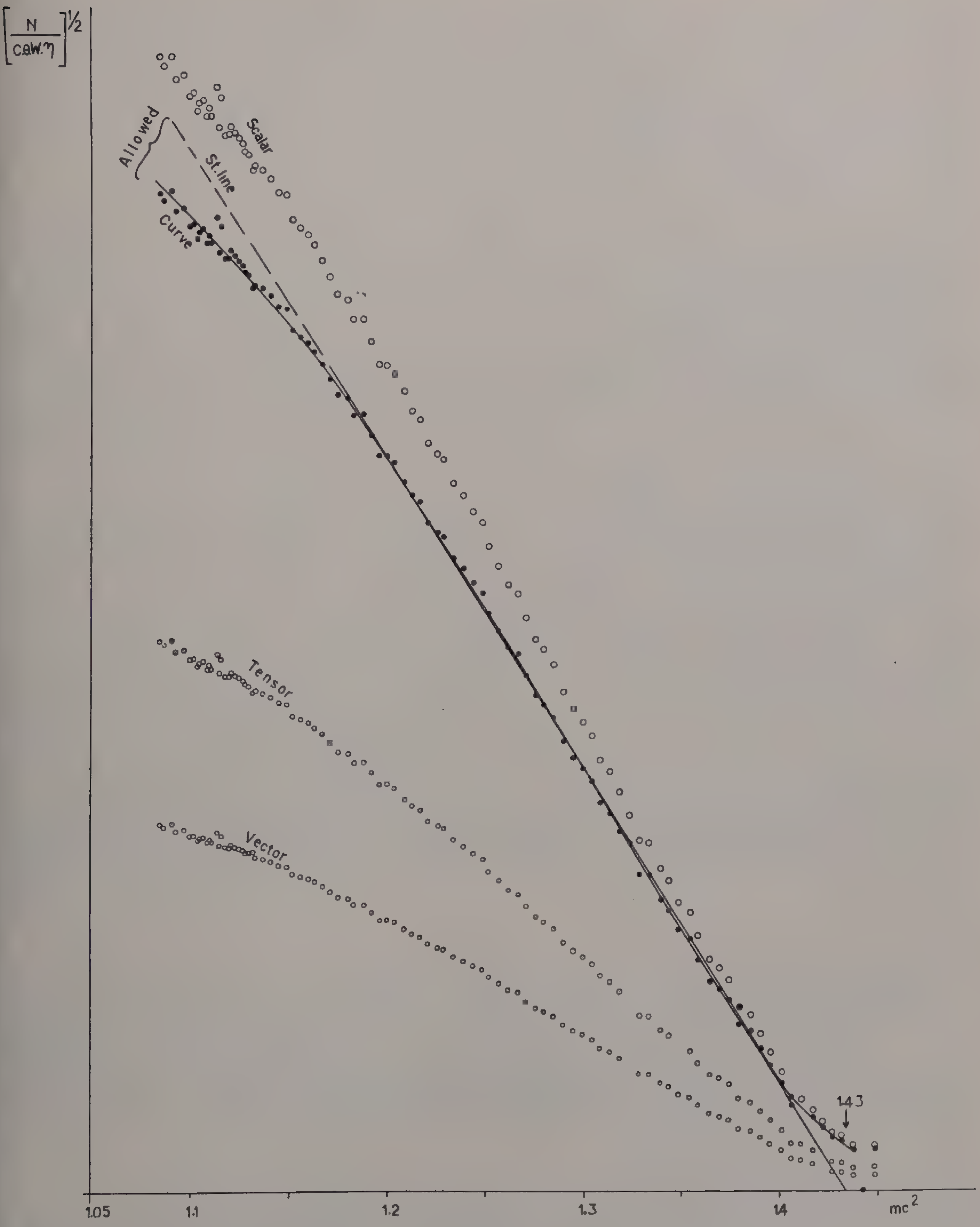
[N / cΔW.η]½
Allowed
St.line
Curve
Scalar
Tensor
Vector
1.43
1.05
1.1
1.2
1.3
1.4
mc²

Fig. 4.8.

whatever its shape may be, should not give rise to any such major effect in the soft β-component.

If the observed effect in the present case is real, then it aught to be explained by theory. According to the Fermi selection rules, allowed β-transitions involve no change in spin or parity, where as according to the G. T. rules, a spin change of one unit may also occur in some allowed transitions. According to the theory of forbidden spectra, worked out by KONOPINSKI, UHLENBECK and GREULING (G1), when the disintegration involves a spin change of one unit higher than the degree of forbiddenness, it has the special property that only one type of nuclear matrix element fails to vanish for it. However, this does not seem to affect the shape of the allowed β-spectrum even though the β-transition involves a spin change of one unit higher than the degree of forbiddenness (the degree of forbiddenness for an allowed β-transition being taken as 0). On the other hand, if we take the soft β-component as a first forbidden transition, one or the other of the correction factors calculated from theory should have explained the deviation. The numerical values of these correction factors are, however, dependent upon the maximum energy of the β-transition and as it is very low (only about 217 kev) in our case, these correction factors are not affecting the Fermi plot of the present β-spectrum in any pronounced manner.

The correction factors calculated from theory, however, need not be taken too seriously because the evaluation of the nuclear matrix elements involved in the expressions for the correction factors, is quite arbitrary. We followed the approximations mentioned by GREULING (G1) in our calculations.

Finally, it may be mentioned that such a downward deviation in Fermi plot has been reported by BUNKER et al. (B6) in the case of Th^{233} having ft value $\sim 10^6$, thus probably belonging to the first forbidden group with a spin change of 0 or 1 unit, as it may be in the present case. Th^{233} has been reported to have a half-life of 23.3 minutes and a β-ray of maximum energy 1.23 Mev. The downward deviation in the case of Th^{233} seems to occur below about 500 kev and the report states that it could bot be explained on the basis of the thickness of source or counter window cut off. These authors seem to doubt whether it is due to a low energy defocusing effect in their spectrometer. In the present case we have studied both Ru^{103} and Co^{60} samples under similar conditions and obtained deviations in Fermi plots opposite in sign; the result in the case of Ru^{103} Fermi plot may be, therefore, noted as significant.

4.9. Internal conversion

Comparison of the areas under the conversion line at 474 kev in the β-spectrum and the continuous β-spectrum gives $N_e/N_\beta \sim 1\,\%$. This can be taken as a measure of the total internal conversion coefficient for the 498 kev γ-ray since the harder β-component is only about 1 % intense and practically all the β-transitions are followed by the 498 kev γ-ray.

4.10. Multipole order

The internal conversion coefficients for the 498 kev γ-ray have been found from Rose's tables (R1) for both electric and magnetic radiations assuming different values for l. On comparing these with the experimental estimation, namely, 1 %, it seems this γ-ray may be either electric 2^3 or probably 2^2 pole radiation or a combination of this with the corresponding magnetic 2^2 or 2^1 pole radiation.

4.11. Results

a) Ru^{103} decays with a half-life of 39.8 ± 0.4 days.

b) Ru^{103} emits two β-rays having maximum energies 0.217 ± 0.004 Mev and 0.7 ± 0.01 Mev and a γ-ray of energy 0.498 ± 0.002 Mev.

c) The 0.498 Mev γ-ray is in cascade with the 0.217 Mev β-ray.

d) The 0.498 Mev γ-ray is about 1 % internally converted. It is either electric 2^3 or 2^2 pole radiation or a combination of this with the corresponding magnetic 2^2 or 2^1 pole radiation.

B. Radio-activity of Rh^{103m}

4.12. History

Rh^{103m} was studied by several investigators in the past. It was produced by bombarding stable Rhodium with fast neutrons (F6) as well as with X rays and electrons (W4). Pd^{103} was known to decay to the metastable state in Rhodium by K capture (M4). Ru^{103} after β decay was also known to lead to the metastable level in Rhodium (S8). Among others WIEDENBECK (W5) gave the half-life of this meta stable level as 45 ± 1 minutes.

4.13. Internal conversion

The two internal conversion lines, one at 17 and the other at 36 kev in the β-spectrum of Ru^{103}, shown in Fig. 4.2, are identified as the K and L lines of a 40 kev γ-ray. Before this investigation, only the line at about 36 kev was reported (H8). It was not precisely known whether it is the K or L line of a γ-ray. The thin window of the G. M. tube and the high specific activity of the sample together with the high transmission of the spectrometer made it possible to observe the faint K line at 17 kev for the first time. This solved the uncertainty about the energy of this γ-ray. The energy of this γ-ray computed from the K and L internal conversion lines comes out to be 40 ± 0.5 kev.

Due to the difficulties mentioned in Chapter 2, in determining the intensities of the lines in this low energy region, only a rough estimate of K/L ratio could be obtained. Comparison of the areas under the K and L lines after subtracting the β-continuum, gives the value, $K/(L+M) \sim 0.2$ for the 40 kev γ-ray. The main uncertainty in this estimate lies in the estimation of the area under the K line.

4.14. Multipole order

A comparison of the above estimate with theory is not strictly possible as no reliable internal conversion coefficients are yet known for such a low energy γ-ray. However, we used Hebb and Nelson's formulae (H4) to calculate N_K/N_L for different values of l for this γ-ray. These are given in the following Table.

Table 4.1

Nature of radiation	N_K/N_L
Elec. 2^5 pole	0.006
Elec. 2^4 pole	0.01
Mag. 2^4 pole	1.62
Mag. 2^3 pole	2.56
Elec. 2^3 pole	0.08

The experimental estimate $N_K/N_L \sim 0.2$ suggests that the 40 kev γ-ray is either electric 2^3 pole radiation or a mixture of both electric and magnetic radiations.

4.15. Results

a) Rh^{103m} decays to the ground level emitting an internally converted γ-ray of energy 0.04 ± 0.0005 Mev.

b) The 40 kev γ-ray consists of either electric 2^3 pole or both electric and magnetic radiations and $N_K/N_L \sim 0.2$

C. Radio-activity of Pd^{109}

4.16. History

This as well as the investigation on Ag^{109m} were reported previously (S9). We quote, here, the results and add only such details and discussions which were not reported.

4.17. Results

Fig. 4.9 gives the half-life graph for this isotope after taking into account the long living component due to other activities in Pd. It shows that Pd^{109} decays with a half-life of 13 hours which is in agreement with the previous reports (S8).

Fig. 4.10 gives the Fermi plot. The Fermi plot shows that the β-spectrum consists of a single component having maximum energy 0.95 ± 0.01 Mev. The β-spectrum has been reported previously (S9).

D. Radio-activity of Ag^{109m}

4.18. Results

a) Ag^{109m} decays to its ground level emitting an internally converted γ-ray of energy 87 kev.

b) N_K/N_{L+M} for this 87 kev γ-ray is about 1.3. The internal conversion coefficient is 92 %.

c) A comparison of the above experimental value of N_K/N_L with the graphs compiled by AXEL and GOODRICH (A1) gives $l = 3$ for the 87 kev γ-ray. The theoretical N_K/N_L for electric radiations for $l = 2$, 3 and 4 are 4.7, 1.25 and 0.5 respectively.

E. Radio-activity of Ce^{141}

4.19. History

Cerium has four stable isotopes, namely, Ce^{136} (0.193), Ce^{138} (0.250), Ce^{140} (88.48) and Ce^{142} (11.07). Slow neutron bombardment of normal Cerium would yield Ce^{139} decaying by K capture with a half-life of 140 days, Ce^{141} decaying with a half-life of about 30 days, Ce^{143} decaying with a half life of about 33 hours and Ce^{137} decaying by K capture with a half-life of about 36 hours. Ce^{137} is not, however, reported, until recently, to have been formed by slow neutron bombardment of Cerium. HILL (H9) produced this Ce^{137} activity by slow neutron bombardment of enriched Ce (with Ce^{136} 8.94 % abundance). According to his report, normal Ce (with Ce^{136} 0.193 %) did not yield Ce^{137} isotope by slow neutron bombardment. In all the cases, Ce^{141} is most readily formed by slow neutron bombardment of Ce and is a source of interference in studying radiations from other isotopes of Ce. Our main purpose is

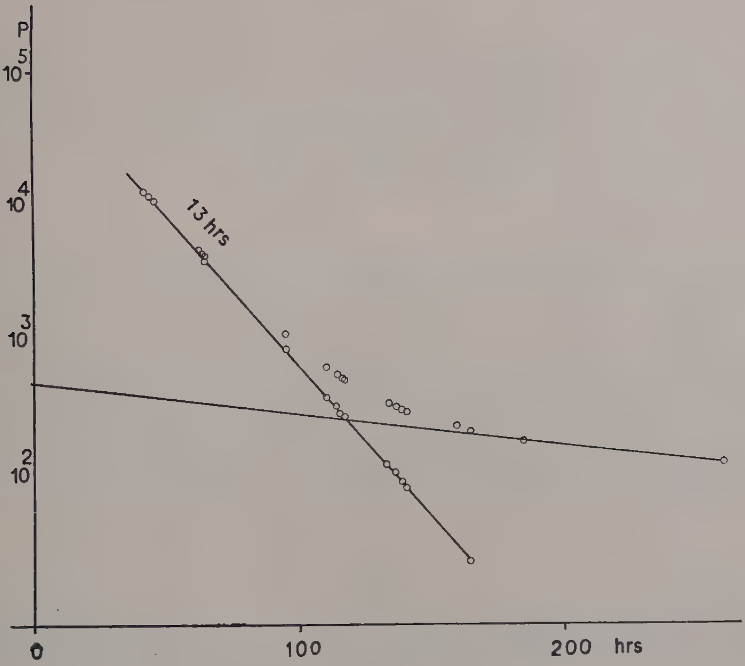

Fig. 4.9.

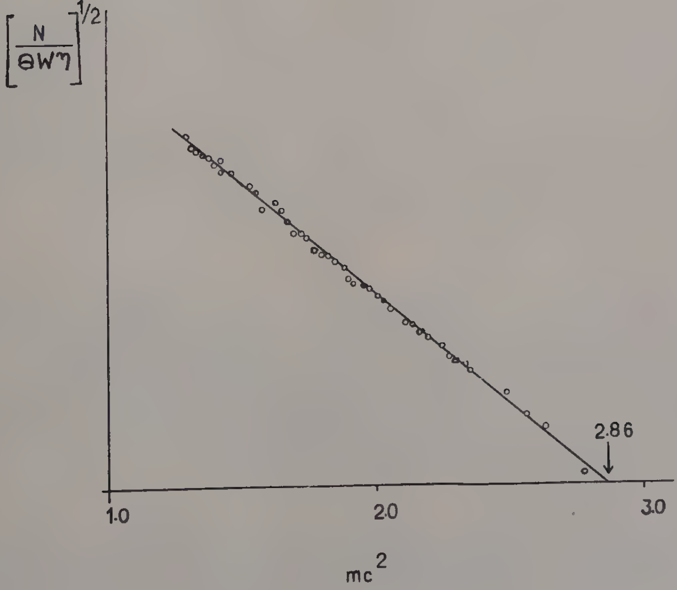

Fig. 4.10.

to study the radiations from Ce^{143} isotope as Ce^{141} was previously well studied using spectrograph and coincidence techniques (F7, S15, T1). But, by the way, we studied the radiations from Ce^{141} also using the spectrometer technique and we describe them below. As there has been disagreement in the observations made by the different investigators in the past (F7, S15. T1), we hope our measurements will help in deciding the disintegration scheme of this isotope.

4.20. Chemical purification

"Spec pure" Cerium oxide was irradiated in the Harwell pile for one week and has been chemically purified in the radio-chemical laboratory of this Institute in the following way.

The Cerium oxide sponze was boiled with concentrated sulphuric acid. Ce, Zr, Hf and Pr were precipitated as hydroxides by ammonia. The precipitate was boiled with hydrochloric acid. A small quantity of hydrofloric acid was added to it. The precipitate was filtered. Ce in the precipitate was then oxidised after adding potassium chlorate and concentrated nitric acid. Lactinium was added as carrier for Zr, Hf and Pr. Ce was finally precipitated as cerium iodate.

4.21. β-spectrum

Uniformly spread spectrometer sample of ~ 0.5 mg/cm² thickness has been prepared with an aluminum backing of 0.15 mg/cm². A spiral baffle to discriminate the positrons has been used in the spectrometer. No measurable number of positrons could be observed. Fig. 4.14, gives the β-spectrum taken within 24 hours after the sample was taken out of the pile. It consists of several electron peaks some of which are seen to decay with a short half-life (about 34 hours) where as the two electron peaks at 102 and 137 kev do not decay with this period. The inner drawing of Fig. 4.11 gives the β-spectrum of a sample taken after 18 days decay. This figure shows that there are only two electron lines one at 102 and the other at 137 kev besides the small hump in the lower energy region which is due to the Auger electrons arising from the X rays due to K internal conversion. Taking these two electron lines as the K and L lines, the energy of the γ-ray comes out to be 143.5 kev which is in agreement with the previous investigators reports. Besides this γ-ray no other internally converted γ-rays of long half-life are observed.

4.22. Fermi-analysis

The Fermi plot of this long half-life β-spectrum is given in Fig. 4.12. This reveals three components, namely, 0.915 ± 0.015 Mev, 0.582 ± 0.02 Mev and 0.444 ± 0.02 Mev. The first component at 0.915 Mev is due to Pr^{143} (13.8 day half-life) the daughter of the 33 hour Ce^{143} isotope and is in agreement with the previous reports (F8) on this isotope. The latter two components belong to Ce^{141} isotope.

4.23. Intensity estimations

In Fig. 4.11, the inner noncontinuous drawings show the two β-components of Ce^{141}. A comparison of the areas under these two components gives a ratio of their intensities as about 2.5, the 444 kev β being more intense than the 582 kev β.

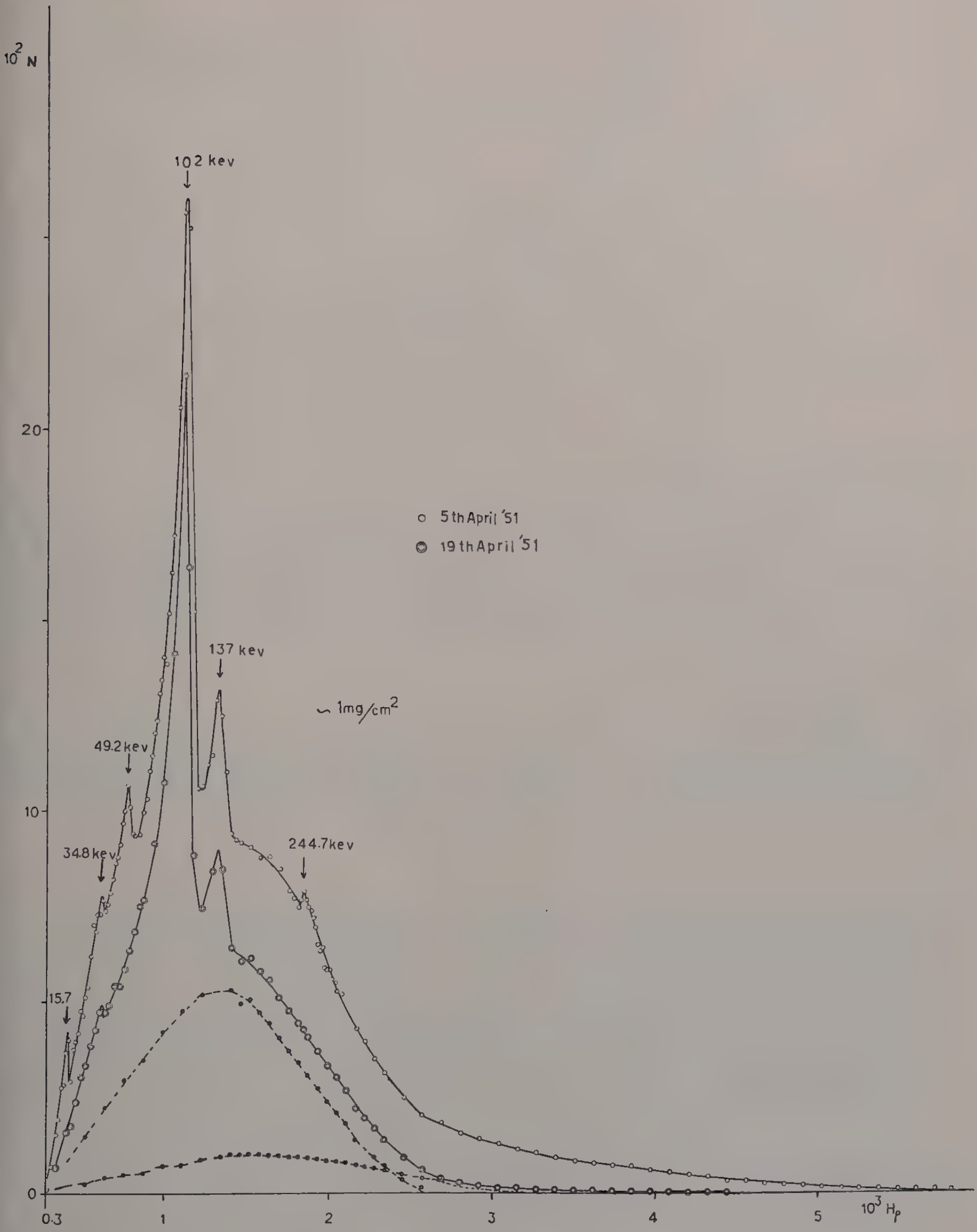
10^2 N
20
10
0
0.3
1
2
3
4
5
10^3 $H\rho$
102 kev
137 kev
49.2 kev
34.8 kev
244.7 kev
15.7
∼ 1mg/cm²
○ 5th April '51
◎ 19th April '51

Fig. 4.11.

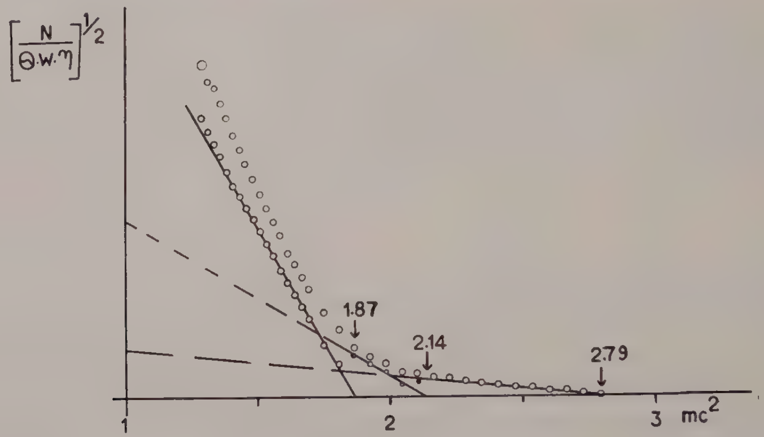

Fig. 4.12.

4.24. Internal conversion

The ratio of the areas under the internal conversion lines and the soft β-component in Fig. 4.11 gives a measure of the internal conversion coefficient for the 143 kev γ-ray since this single γ-ray seems to follow the soft β. The internal conversion coefficient, thus estimated, comes out to be 0.33. The ratio of the K to L conversion obtained by comparing the areas under the K and L lines after subtracting the β-continuum, is about 6.5.

4.25. Multipole order

The experimental values of N_K/N_L and the internal conversion coeficient are compared with theoretical values in Table 4.3. It shows that the 143 kev γ-ray is either electric quadrupole or probably magnetic dipole radiation.

4.26. Results

a) Ce^{141} emits two β-rays and a single γ-ray.
b) The energies of the β-rays are 0.582 and 0.444 Mev. The energy of the γ-ray is 0.143 ± 0.002 Mev.
c) The ratio of intensities of the two β-components is 2.5.
d) The K to L ratio for the 143 kev γ-ray is about 6.5. This γ-ray is about 33 % internally converted. This γ-ray is either electric quadrupole or probably magnetic dipole radiation.

F. Radio-activity of Ce^{143}

4.27. History

This isotope was not previously investigated systematically as is done now. It was, however, studied using absorption and coincidence techniques. The results thereby obtained were at variance (S8, S10). We have previously published a preliminary report on this isotope (K5).

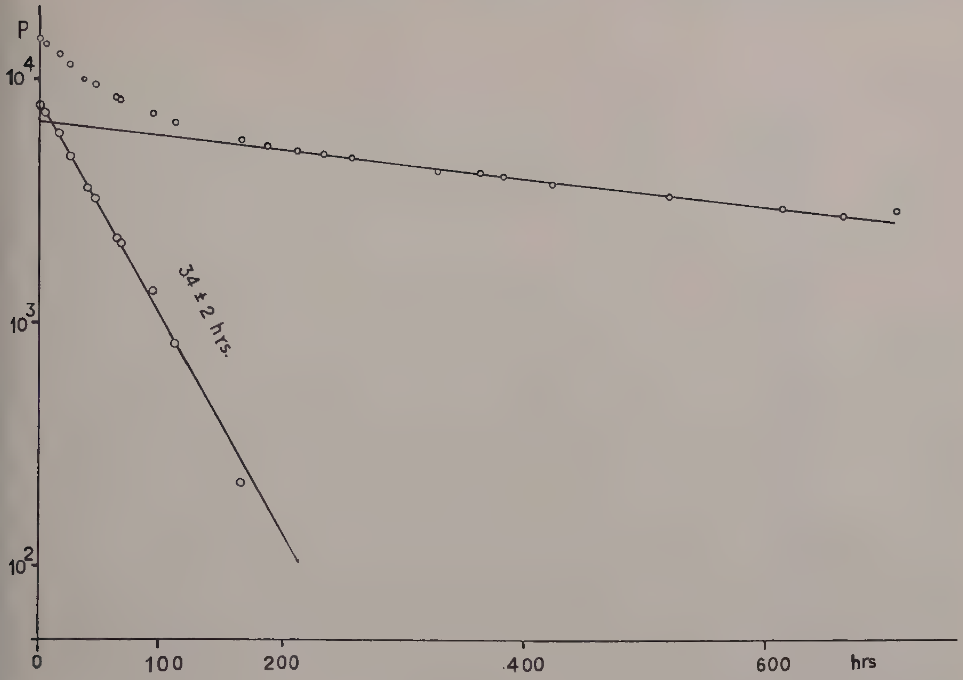

Fig. 4.13.

4.28. Half-life

The irradiation and chemical purification are described in Art. 4.20. The half-life graph after taking into account the long components due to Ce^{141} and Pr^{143}, is given in Fig. 4.13. It shows that Ce^{143} decays with a half-life of 34 ± 2 hours.

4.29. β-spectrum

The β-spectrum of the pile irradiated Ce, obtained within 24 hours after the sample was taken out of the pile, is given in Fig. 4.14. As previously mentioned, all the electron lines except the two lines at 102 and 137 kev are seen to decay with the 34 hours half-life within the statistical errors. Besides the Auger electron lines at 27.7 and 34.8 kev, there are five electron peaks belonging to Ce^{143} isotope, namely, at 15.7, 49.2, 244.7, 278.5 and 608.6 kev. The two lines at 15.7 and 49.2 kev are identified as the K and L lines of a 57 kev γ-ray; the two lines at 244.7 and 278.5 kev are identified as the K and L lines of a 283 kev γ-ray; the small hump at 608.6 kev is taken as the K line of a 649 kev γ-ray. Fig. 4.14 shows that all these lines are decaying with the same half-life. The dotted arrow in Fig. 4.14 shows the place where the K internal conversion line of a possible 348 kev γ-ray (K8) should occur.

4.30. Fermi-analysis

Fermi analysis of the β-spectrum presented in Fig. 4.14 gives as many as five components and an indication of a sixth component. They are

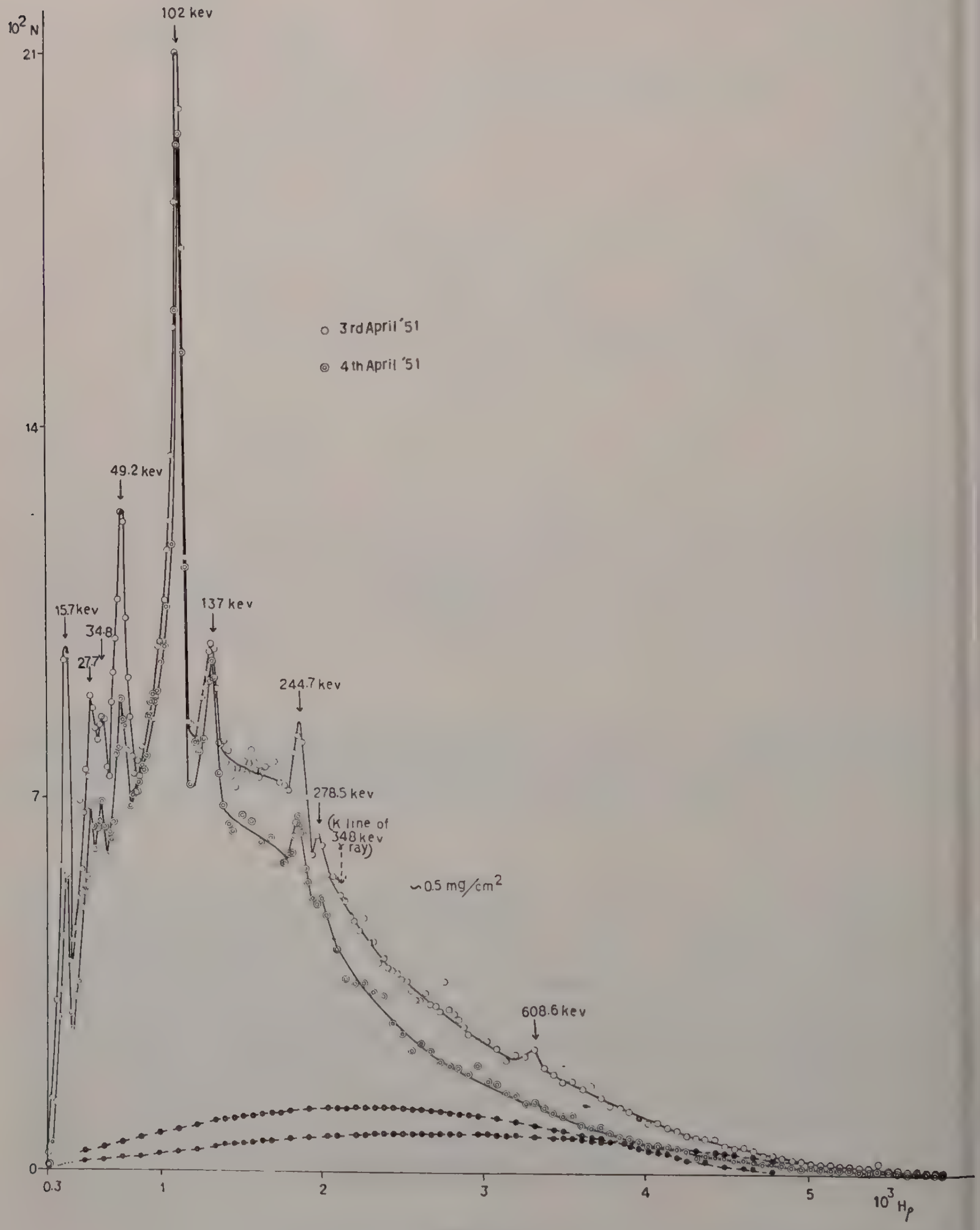
10^2 N
21
14
7
0
0.3
1
2
3
4
5
10^3 Hρ
102 kev
49.2 kev
15.7 kev
34.8
27.7
137 kev
244.7 kev
278.5 kev
(K line of 348 kev γ ray)
608.6 kev
○ 3rd April '51
◎ 4th April '51
~0.5 mg/cm²

Fig. 4.14.

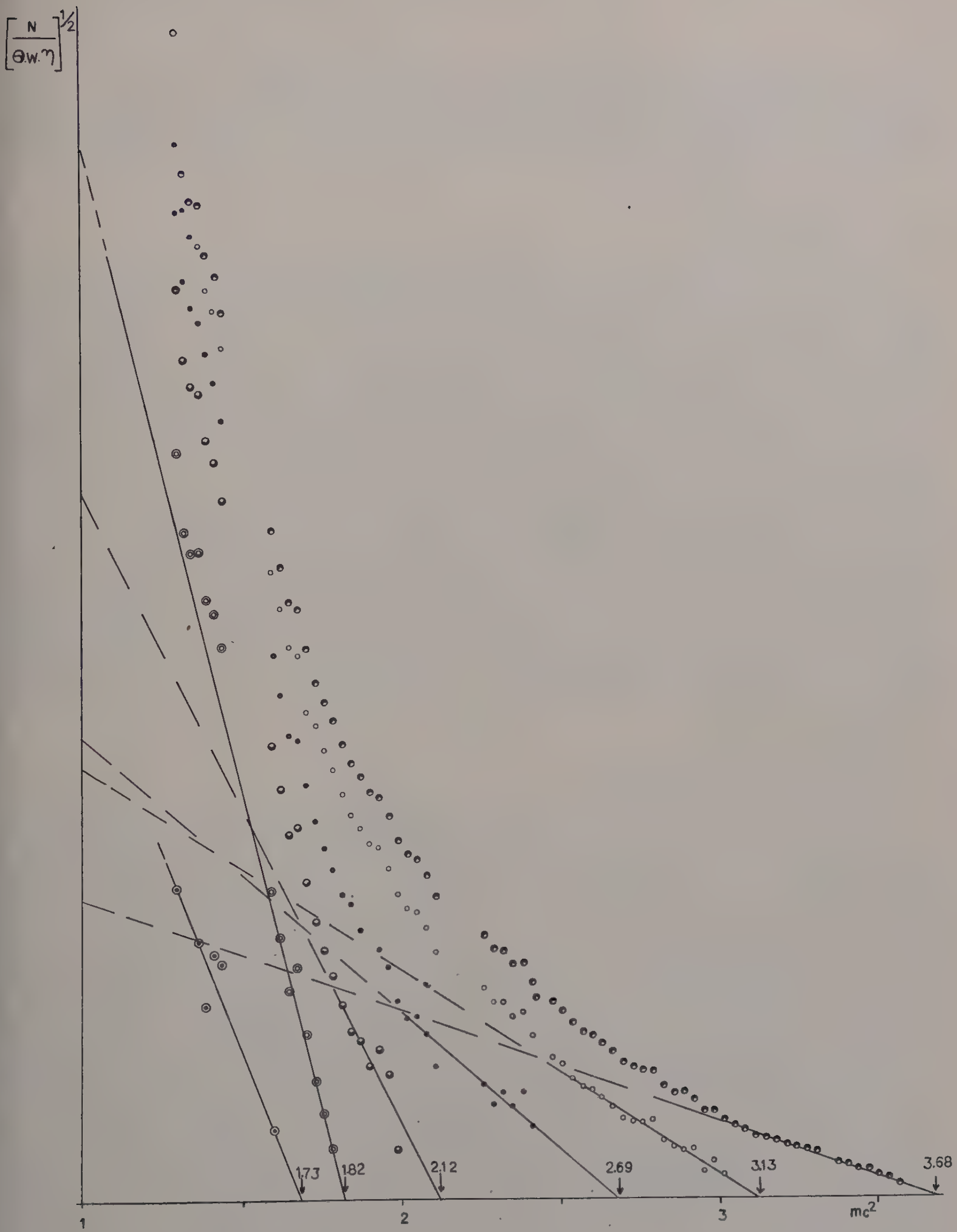

Fig. 4.15.

1.37 ± 0.01 Mev (Ce^{143}), 1.09 ± 0.02 Mev (Ce^{143}), 0.86 Mev (Pr^{143}), 0.57 Mev (Ce^{141}), 0.42 Mev (Ce^{141}) and 0.37 Mev? (Ce^{143}).

The Fermi plot is given in Fig. 4.15.

The β-components belonging to Ce^{141} and Pr^{143} have been determined more accurately by analysing the β-spectra obtained after Ce^{143} has disappeared. The β-components marked as due to Ce^{143} are found to decay with the electron lines identified as belonging to Ce^{143}.

4.31. Photo-spectrum

The photo-spectrum was taken with the sample filled in a copper capsule of 3.2 mm thick to which a thin, 0.02 mm, lead foil is fixed for the photo-effect to take place. The thick copper capsule cuts off all the β-rays emitted by this isotope. The photo-spectrum is presented in Fig. 4.16. There are six photo peaks at 55.7, 125, 197.2, 263.2, 559.2 and 617.4 kev. The first two lines at 55.7 and 125 kev are identified as the K and L photo lines due to the 143 kev γ-ray of Ce^{141} and it can be seen from the inner drawing, after taking off the compton continuum, that these two lines do not decay with the rest of the photo lines. The two lines at 197.2 and 263.2 kev are taken to be the K and L photo lines of the 283 kev γ-ray. If the line at 263.2 kev were the K photo line of another γ-ray, the corresponding L line of this γ-ray should occur at a place shown by the dotted arrow in Fig. 4.16. The two weak photo lines at 559 and 617 kev are the K lines of 649 and 705 kev γ-rays respectively. All these lines seem to decay with the 33 hour period. No photo peak corresponding to the 57 kev γ-ray could be seen. As the K binding energy of lead (87.6 Kev) is higher than the energy of this γ-ray, only the L line should occur which will of course be weak; or it may also mean that this soft γ-ray is highly internally converted.

4.32. Scintillation spectrum

In the β-spectrum (Fig. 4.14) the two internal conversion lines at 15.7 and 49.2 kev are of nearly equal intensity. It may be that these two lines are K lines of two γ-rays instead of being the K and L lines of the same γ-ray (57 kev). Further, if the line at 49 kev is a K line the corresponding γ-ray energy would be about 90 kev and the concerned L line falls at such a place in the β-spectrum that the intense K line at 102 kev of the 143 kev γ-ray may mask it. It has not been possible to decide this from the photo spectrum since the γ-ray energy (90 kev) is nearly equal to the K binding energy (87.6 kev) of lead and no K photo line would be observed. We have used the scintillation spectrometer to decide this and to see whether there exists a γ-ray of energy about 348 kev. We have placed the β-sample directly above the crystal after interposing an aluminum sheet (700 mg/cm^2) to absorb the β-rays emitted by it. Figs. 4.17, 4.18 give the scintillation spectra. Fig. 4.17 shows the presence of four γ-rays, namely, 143, 284, 649 and 705 kev. The dotted curve represents the annihilation γ-emitted by Na^{22} which is used for calibration. Fig. 4.18 shows the X rays together with the 143 kev γ-ray when another amplification factor is used. The dotted curve in this figure shows only X rays when still another amplification is used. The dotted arrow in Fig. 4.17 shows the position where a 348 kev γ-ray should occur. The scintillation spectra confirm the results obtained from the photo spectrum . As there is no indication of the 57 kev γ-ray in the scintil-

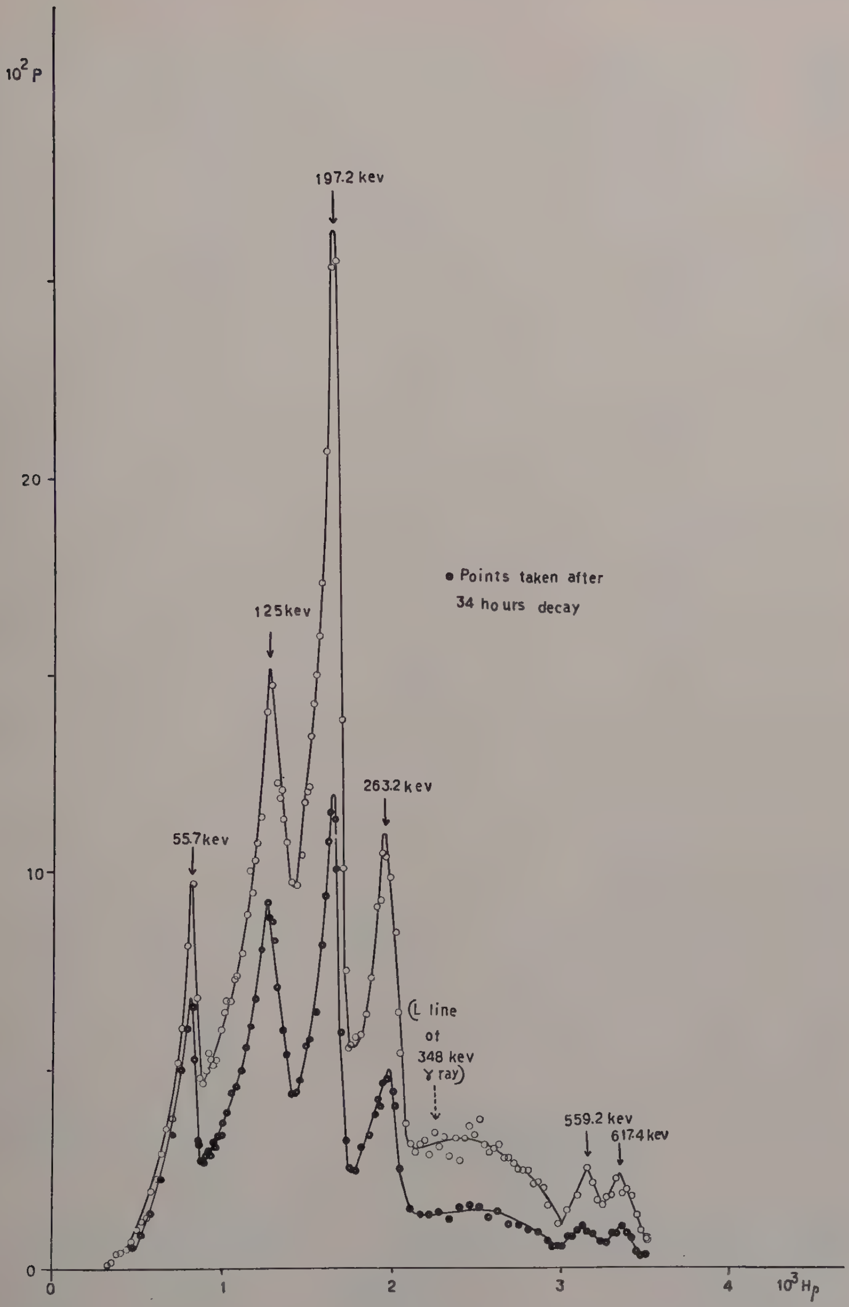
$10^2 P$
20
10
0
0
1
2
3
4
$10^3 H\rho$
197.2 kev
125 kev
263.2 kev
55.7 kev
● Points taken after 34 hours decay
(L line of 348 kev γ ray)
559.2 kev
617.4 kev

Fig. 4.16.

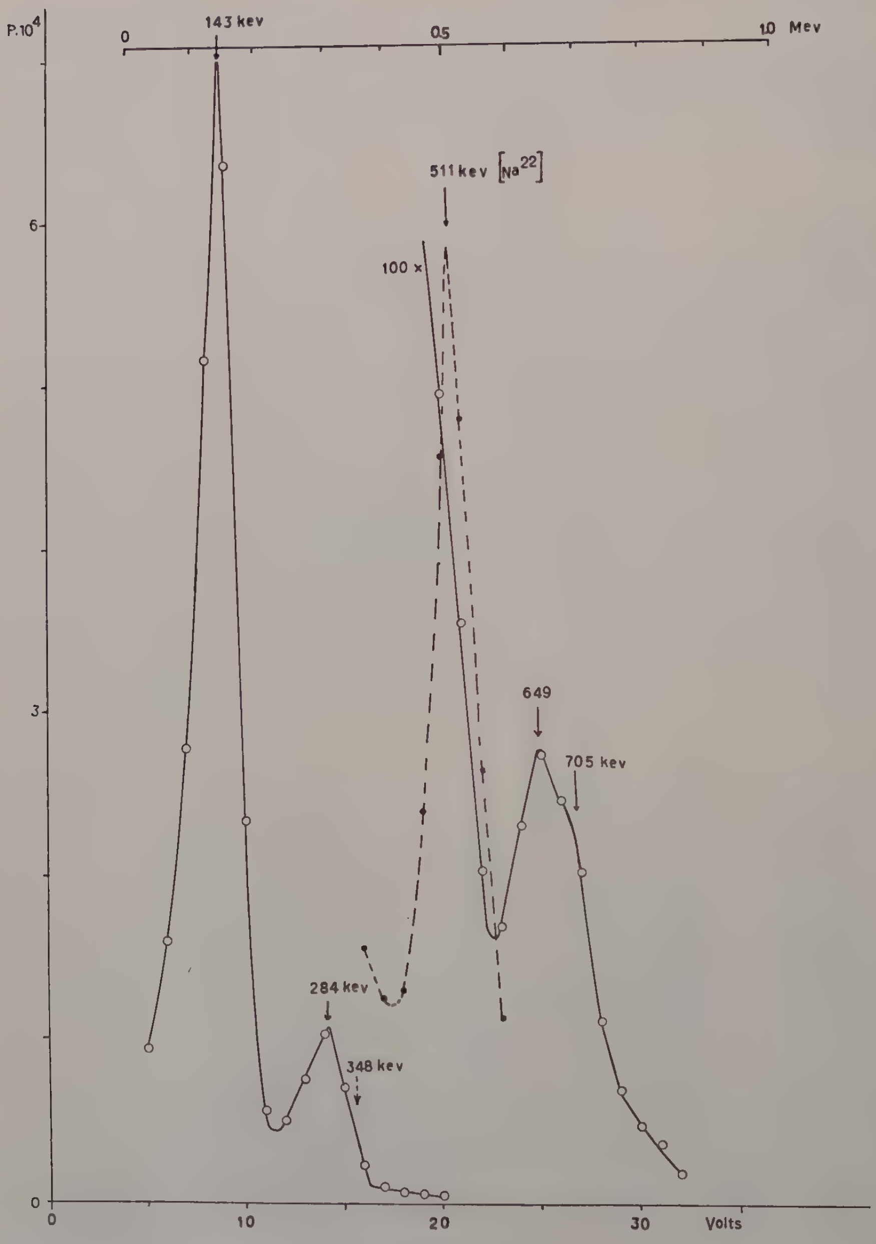
P.10⁴
0
143 kev
0.5
1.0 Mev
511 kev [Na²²]
100 ×
6
649
705 kev
3
284 kev
348 kev
0
0
10
20
30
Volts

Fig. 4.17.

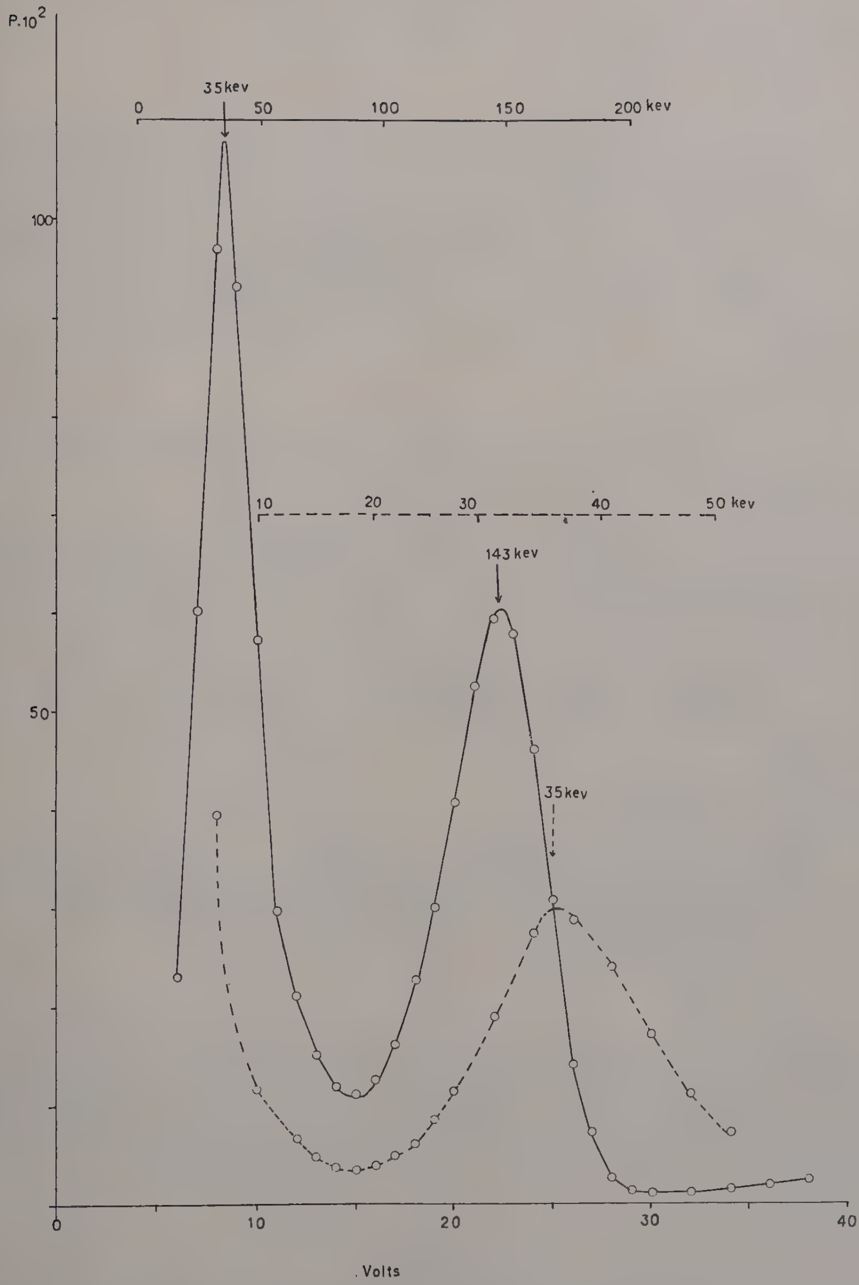
P.10^2
100
50
0
10
20
30
40
Volts
0
50
100
150
200 kev
35kev
10
20
30
40
50 kev
143 kev
35kev

Fig. 4.18.

lation spectra, we suspect that this γ-ray is highly internally converted. The Table 4.2 at the end of this section gives the energies of all the observed γ-rays emitted by the Ce sample.

4.33. Coincidence measurements

The $\beta\gamma$-coincidences were investigated in a standard set up. The resolving time of the coincidence circuit was set to be 0.4 microsecond. Aluminum absorbers of 150 and 410 mg/cm^2 were interposed before the β-tube, when $(0.64 \pm 0.15)10^{-3}$ and $(0.48 \pm 0.05)10^{-3}$ coincidences per recorded β have been observed respectively. The ranges of 440 kev (Ce^{141}) and 930 kev (Pr^{143}) β-rays in aluminum are respectively 140 and 410 mg/cm^2. So, the $\beta\gamma$-coincidence results show that (i) there is a γ-ray coincident with a β-ray of maximum energy greater than 930 kev and (ii) probably no γ-ray is coincident with a β-ray having maximum energy between 440 and 930 kev.

4.34. Intensity estimations

On the assumption that the Fermi plots are linear, the 1.09 Mev β-ray is found to be 1.4 times more intense than the 1.37 Mev γ-ray. The two β-components are shown in Fig. 4.14.

An estimate of the intensities of the γ-rays from the photo spectrum on the lines described in Art. 2.13, showed that the 705 and the 649 kev γ-rays are almost of equal intensity while the 283 kev γ-ray is about 4.5 times more intense.

Comparison of the intensities of the Auger lines with that of the K internal conversion lines in the β-spectrum showed that the Auger electrons are $\sim 12\,\%$ of the K lines. This is precisely what is to be expected for this element of high Z value and it is not necessary to assume the presence of the K capture Ce^{137} (36 hours half-life) in our samples. Probably the slow neutron capture cross section for Ce^{136} is very small.

4.35. Internal conversion

From the β-spectrum it is found that N_K/N_L is about 6 for the 283 kev γ-ray and 1 for the 57 kev γ-ray without making any corrections for absorption or scattering in the sample. On the basis of the intensities given in the disintegration scheme (Fig. 5.4) the K internal conversion coefficients for the 283 and 649 kev γ-rays are about 3 % and 1 % respectively.

4.36. Multipole order

For the 57 kev γ-ray exact theoretical internal conversion values are not yet known. The internal conversion data on the 283 and 649 kev γ-rays, on comparison with the theoretical values, show that the 283 kev γ-ray, probably, consists of electric quadrupole radiations where as the 649 kev γ-ray may be either magnetic dipole or electric quadrupole or a mixture of these two types of radiations.

4.37. Results

a) The Ce^{143} isotope emits β^- and γ-radiations and decays with a half-life of 34 ± 2 hours.

b) It emits three β-rays of energies, 1.37 ± 0.01 Mev, 1.09 ± 0.02 Mev and probably 0.37 Mev (?). The energies of the γ-rays obtained both from β and γ spectra are given in Table 4.2.

Table 4.2

Energy of the peak	Nature of the peak	Energy of the photons	Parent isotope
15.7 ± 0.5 kev 49.2 ± 1 kev	K internal conversion L » »	56.8 ± 1 kev	Ce^{143}
27.7 ± 1 kev 34.8 ± 1 kev	(K—2 L) Auger line (K—L—M) Auger line	35.4 ± 1 kev	
102 ± 1.5 kev 137 ± 1 kev 55.7 ± 1 kev 125 ± 2 kev	K internal conversion L » » K photo line L » »	143 ± 2 kev	Ce^{141}
244.7 ± 2 kev 278.5 ± 1.5 kev 197.2 ± 1 kev 263.2 ± 3 kev	K internal conversion L » » K photo line L » »	283 ± 4 kev	Ce^{143}
608.6 ± 4 kev 559.2 ± 4 kev	K internal conversion K photo line	649 ± 4 kev	Ce^{143}
617.4 ± 5 kev	K photo line	705 ± 5 kev	Ce^{143}

Table 4.3

Isotope	Energy of the γ-ray	K shell internal conversion coeff.				K/L ratio				Multipole order nature of the γ-ray
		Experimental	Theoretical			Experimental	Theoretical			
			Elec. dipole	Elec. quadrupole	Mag. dipole		Elec. dipole	Elec. quadrupole	Mag. dipole	
Ce^{141}	143 kev	0.3	0.08	0.42	0.43	6.5	9.5	4.6	6.3	Elec. quadrupole or Mag. dipole.
Ce^{143}	57 »					1	6.2	0.4	4.7	Elec. quadrupole[1]
»	283 »	0.03	0.013	0.047	0.10	6	10.2	7.3	7	Elec. quadrupole or Mag. dipole.
»	649 »	0.01	0.002	0.005	0.009	—	—	—	—	Elec. quadrupole or Mag. dipole
»	705 »	—	—	—	—	—	—	—	-	

---

[1] The theoretical K/L values for electric 2^3 pole and magnetic 2^2 pole for the 57 kev γ-ray are 0.01 and 3.4 respectively.

c) There is a γ-ray coincident with a β-ray of energy greater than 930 kev.

d) 1.09 Mev β-ray is 1.4 times more intense than the 1.37 Mev β-ray. The 283 kev γ-ray is 4.5 times more intense than 649 and 705 kev γ-rays which are of nearly equal intensity. The Auger electrons are about 12 % of the K internal conversion lines in intensity.

e) The internal conversion and multipolarity of the γ-rays are given in Table 4.3. In this Table the theoretical internal conversion coefficients are calculated using Rose's values and K/L ratios using Hebb and Nelson's formulae.

G. Radio-activity of Pr^{143}

4.38. Result

Pr^{143} is found to emit a single β-ray of energy 0.915 ± 0.015 Mev as is stated in the previous articles. This is in confirmity with the previous reports (F8) on this isotope.

H. Radio-activity of Nd^{147}

4.39. History

Slow neutron bombardment of Neodymium yields, among other short half-lives, an activity known to have a half-life of about 11 days (S8). This has been assigned to Nd^{147}. Previous to this investigation absorption and coincidence measurements (S8, M6) were reported. Cork et al. (C1) reported that no conversion electrons due to γ-radiation could be observed in the spectrometer. Our first preliminary report on this isotope appeared in the Physical Review as a letter (K6). In the same issue, EMMERICH et al. (E3) reported on the β-spectrum of Nd^{147}. The last authors results agree in part with our results although the energies reported by them for β- and γ-rays are some what higher than our results.

4.40. Half-life

"Spec pure" Nd_2O_3 was irradiated in the Harwell pile for 4 weeks. The half-life of the resulting activities has been followed for a period of two months and Fig. 4.19 gives the half-life graph. It can be seen that there are two components, one having a value 50 ± 3 hours and the other 11.6 ± 0.3 days. The first one is due to Pm^{149} and the second one gives the half-life of Nd^{147} in agreement with the previous reports (S8).

4.41. β-spectrum

The β-spectrum is shown in Fig. 4.21. Fig. 4.22 gives the β-spectrum taken with a thick (10 mg/cm^2) source. The β-spectrum has been followed over several periods of decay. Fig. 4.20 gives the β-spectrum taken at three different times. Two electron lines, one at 44.9 and the other at 82.6 kev, have been observed. If we take them as the K and L internal conversion lines of a γ-ray in Pm, the energy of the γ-ray comes out to be 90 kev. As is seen from Fig. 4.20, these lines are found to decay with the 11 day period.

4.42. Fermi-analysis

Fig. 4.23 gives the Fermi plot of the 11 day β-spectrum, taken with a sample of thickness 2 mg/cm^2, after the 2 day (Pm^{149}) β-spectrum has disappeared. It shows two components one 780 ± 10 kev and the other at 350 ± 15 kev.

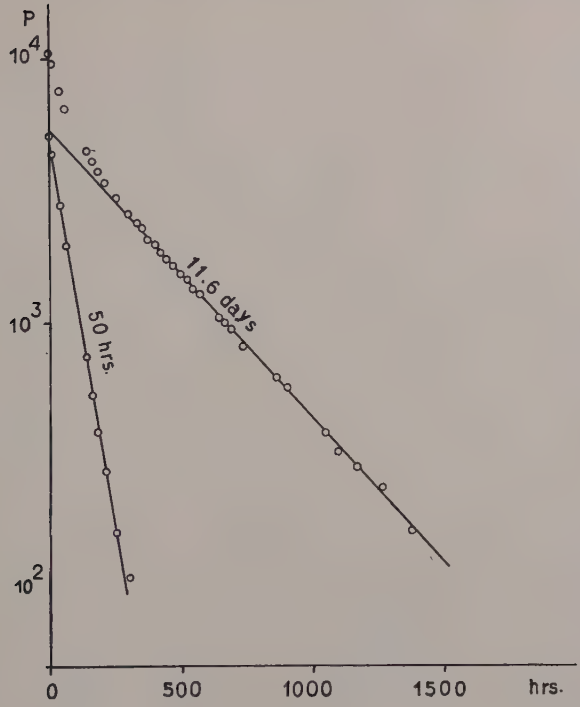

Fig. 4.19.

4.43. Photo-spectrum

The photo-spectrum is given in Fig. 4.24. There are as many as five photo-electron peaks of different intensities. The first one, at 76 kev, is identified as the *L* photo-line of a 91.8 kev γ-ray. The next two peaks, at 222 and 304 kev, are the *K* photo lines of 310 and 392 kev γ-rays respectively. The last two lines at 438 and 502 kev are the *K* and *L* photo lines of a 522 kev γ-ray. The inner drawing of Fig. 4.24 shows that all these photolines are decaying with the same half-life of 11 days. The first photo-spectrum is taken after about three days decay of the sample and no γ-ray of two days half-life has been observed.

From Fig. 4.24, it can be seen that there may exist another photo-peak at about 1577 Hρ. It has not been possible to estabish this due to low specific activity of the sample.

4.44. Intensity estimations

Using the β-spectrum taken with the thin sample the 780 kev β-ray is found to be double in intensity to the 350 kev β-ray on the assumption that both the Fermi plots are linear.[1] Using this estimate and the photo spectrum, the intensities of the γ-rays are estimated as,

91 kev (66 %), 310 kev (1 %), 392 kev (2 %) and 522 kev (32 %).

---

[1] If the β-spectrum taken with the thick sample (10 mg/cm^2) is used the hard β-component is found to be six times stronger than the soft β. This clearly stresses the importance of using thin samples in estimating the intensity ratios.

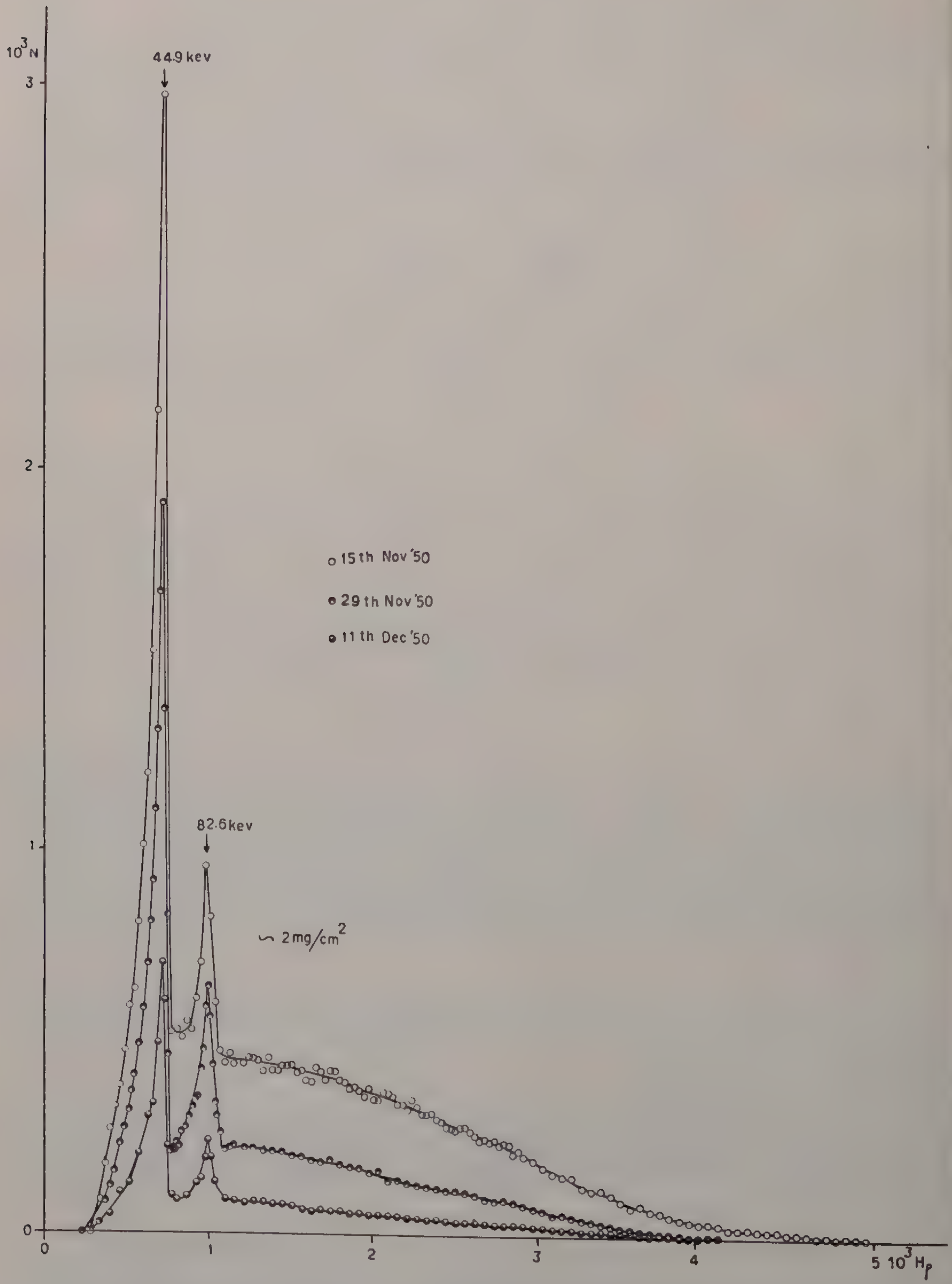
10^3N
3
2
1
0
44.9 kev
82.6 kev
○ 15th Nov '50
● 29th Nov '50
● 11th Dec '50
∽ 2mg/cm^2
0
1
2
3
4
5 10^3 Hρ

Fig. 4.20.

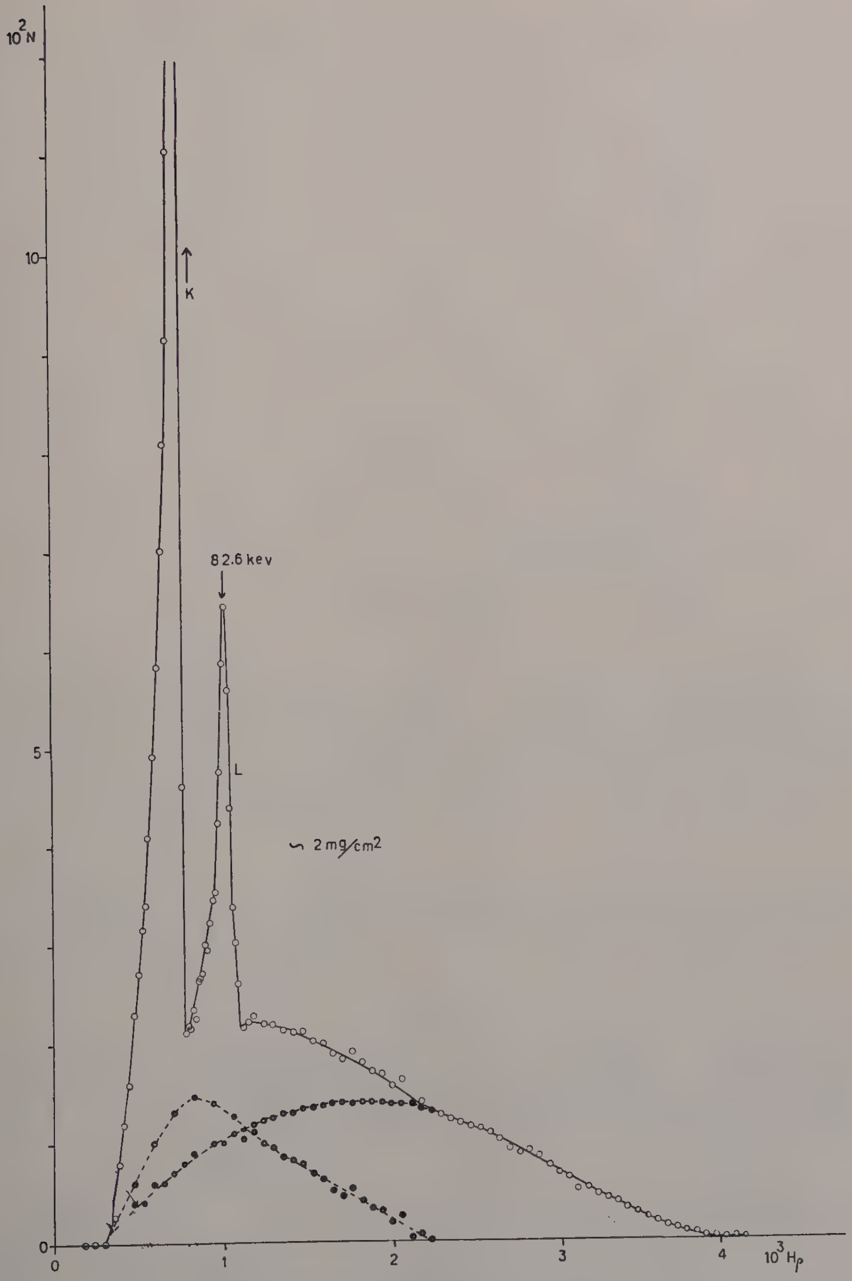

Fig. 4.21.

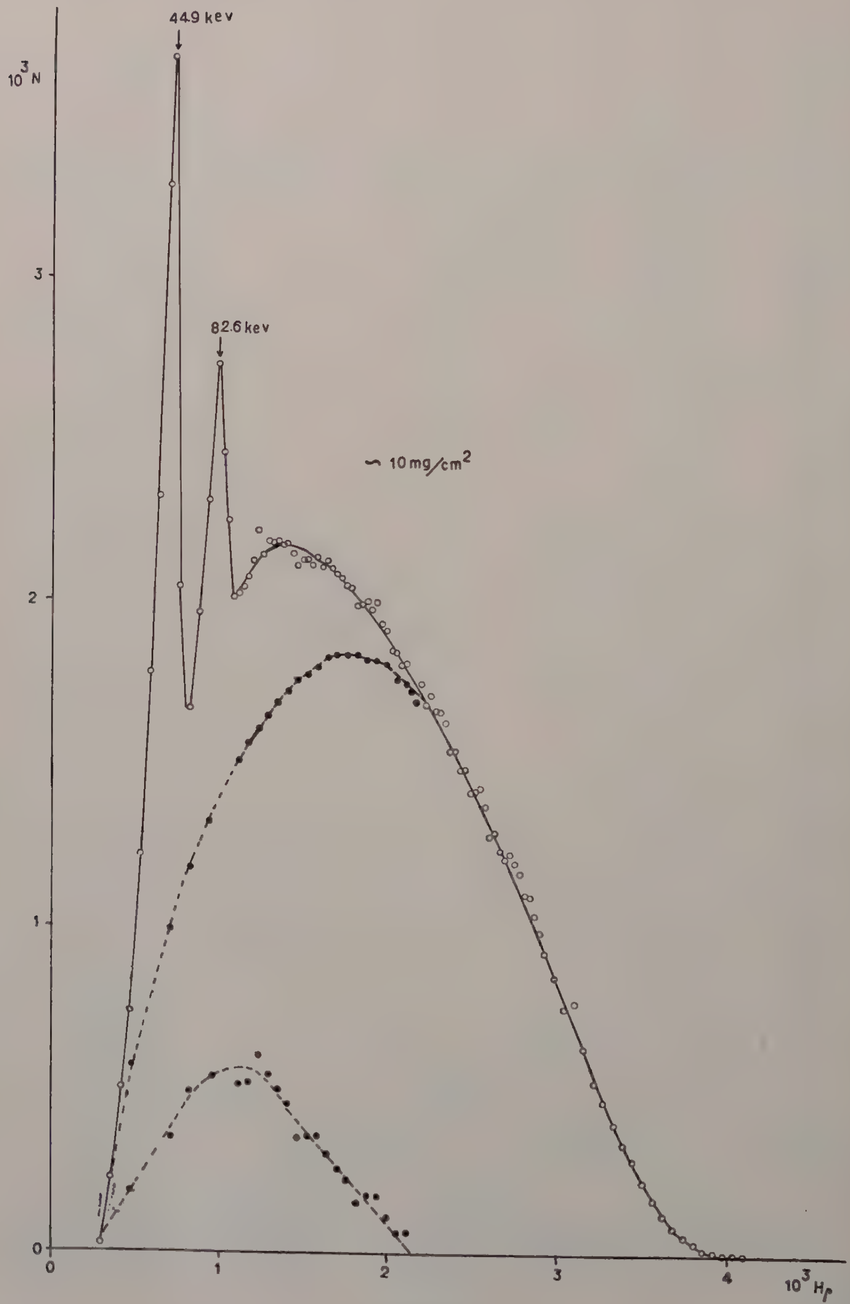

Fig. 4.22.

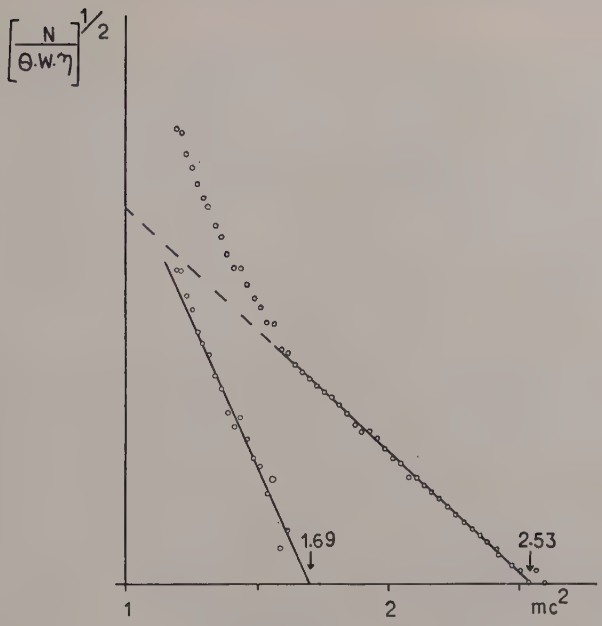

Fig. 4.23.

4.45. Internal conversion

The internal conversion coefficient for the 91 kev γ-ray, estimated from the thin sample β-spectrum, comes out as 0.9. The K to L internal conversion ratio, also estimated from the thin sample β-spectrum, comes out to be 6.5. This ratio when the thick sample β-spectrum is considered, appears to be 2, which is comparable to the value, 2.5, given by EMMERICH et al. (E4).

4.46. Multipole order

Precise theoretical internal conversion values for this soft, 91 kev, γ-ray are not yet known. However, the following Table 4.4 shows that the 91 kev γ-ray, probably, consists of magnetic dipole radiation.

Table 4.4

Nature of radiation	Theoretical K internal conversion coefficient	Experimental K internal conversion coefficient	Theoretical K/L ratio	Experimental K/L ratio	Multipole order of the γ-ray
Elec. dipole	0.29	0.8	7.1	6.5	Mag. dipole
Elec. quadrupole	1.7		2.2		
Magnetic dipole	1.8		5.6		

In the above Table the theoretical K internal conversion coefficients are calculated by extrapolating Rose's values, and the theoretical K/L ratios are calculated using Hebb and Nelson's formulae.

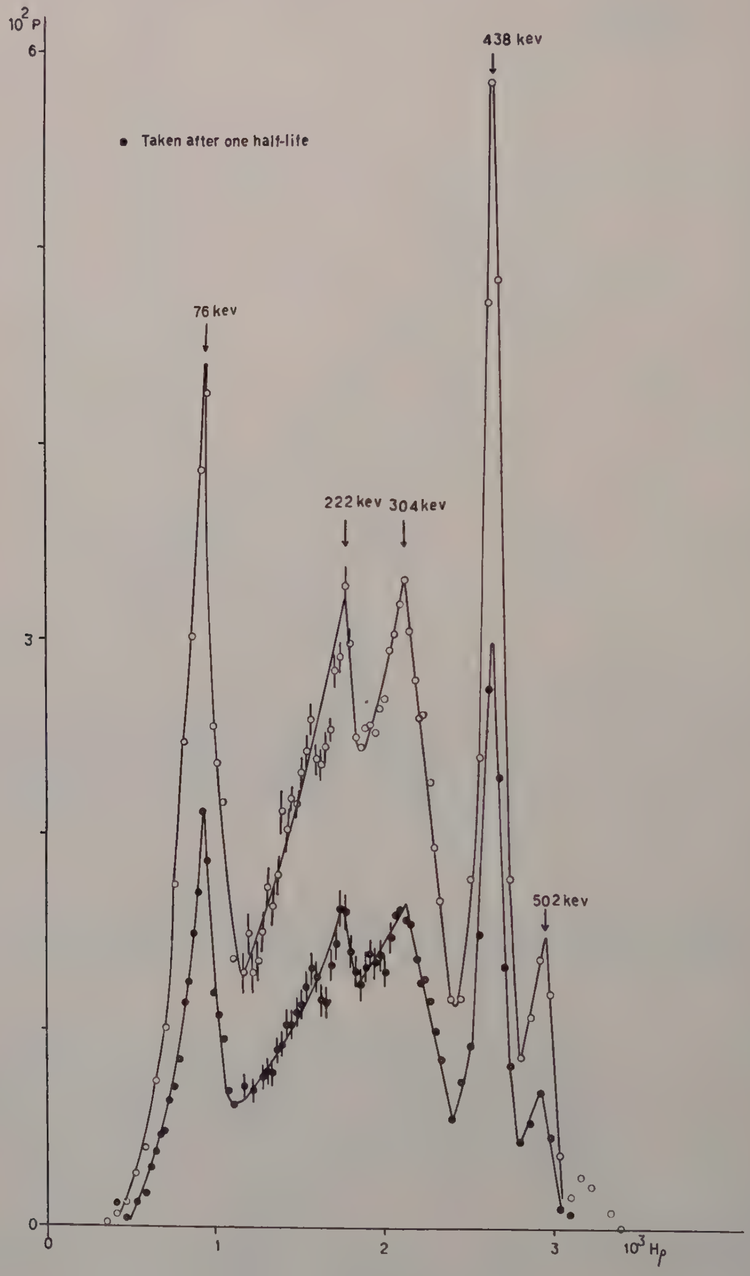
10^2 P
6
3
0
● Taken after one half-life
76 kev
222 kev
304 kev
438 kev
502 kev
0
1
2
3
10^3 Hρ

Fig. 4.24.

4.47. Results

a) Nd^{149} decays with a half-life of 11.6 ± 0.3 days.
b) It emits two β-rays of energies 0.78 ± 0.01 Mev and 0.35 ± 0.015 Mev, and γ-rays whose energies are given in Table 4.5.
c) The hard β-component has double the intensity of the soft one. The intensities of the γ-rays are also given in Table 4.5.
d) The 91 kev γ-ray has an internal conversion coefficient 0.9 and K to L internal conversion ratio 6.5.
e) The 91 kev γ-ray, probably, consists of magnetic dipole radiation.

Table 4.5

Energy of the peak	Nature of the peak	Energy of the photons	Percentage intensity
44.9 ± 0.5 kev	K internal conversion	91 ± 1 kev	66 %
82.6 ± 2 »	L » »		
76 ± 1 »	L photo line		
222 ± 5 kev	K photo line	310 ± 5 kev	1 %
304 ± 6 kev	K photo line	392 ± 6 kev	2 %
438 ± 6 kev	K photo line	522 ± 8 kev	32 %
502 ± 3 »	L » »		

I. Radio-activity of Pm^{149}

4.48. History

Pm^{149} was previously reported to have been studied using absorption methods only. It has been reported to have a half-life of 47 to 55 hours and emit a β-ray of 1.1 Mev and a wak γ-ray of 0.25 Mev energy (S8). We have previously reported on this isotope (K6).

4.49. Half-life

The half-life curve (Fig. 4.19) shows a second component of half-life 50 ± 3 hours besides the 11 day Nd^{147} component. This is due to Pm^{149}, the daughter of Nd^{149} (2 hours half-life) (S8). As the measurements started after two days decay of the sample, no trace of the 2 hour Nd^{149} is observed in the half-life curve. Instead, the daughter Pm^{149} has shown its presence.

4.50. β-spectrum

Fig. 4.20 shows the β-spectrum of Pm^{149} together with that of Nd^{147}. The inner drawings show that the hardest β-component in this β-spectrum is decaying much faster than the rest of the spectrum. No internal conversion lines are attached with this period.

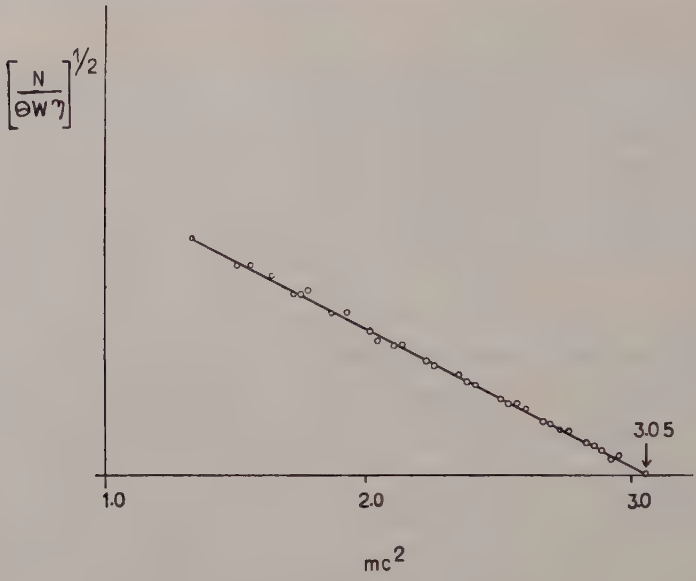

Fig. 4.25.

4.51. Fermi plot

The Fermi plot of the β-spectrum of Pm^{149} alone after taking into account the Nd^{147} β-spectrum is given in Fig. 4.25. This shows a single β-component of maximum energy 1.05 ± 0.01 Mev.

4.52. Results

a) Pm^{149} decays with a half-life of 50 ± 3 hours.
b) It emits a single β-ray of maximum energy 1.05 ± 0.01 Mev.

J. Radio-activity of Os^{193}

4.53. History

We have already published a detailed paper (K7) on this isotope. In the following, we quote the results from that paper together with a Table in connection with the determination of the multipole order nature of the 128 kev γ-ray.

4.54. Multipole order

The theoretical internal conversion coefficients for the 42 kev γ-ray are not known. A comparison of the theoretical and experimental values for the 128 kev γ-ray is given in Table 4.6. The theoretical K internal conversion coefficients are calculated by extrapolating Rose's values where as the K/L ratios, except that marked §, are calculated from Hebb and Nelson's formulae. § is obtained from Axel et al. graphs (A1).

Table 4.6

Nature of radiation	Theoretical K internal conversion coefficient	Experimental K internal conversion coefficient	Theoretical K/L ratio	Exp. K/L ratio	Multipole order of the γ-ray
Electric dipole	0.18		7.9 §		
Electric quadrupole . .	0.5	0.5	3.7	2.1	Electric quadrupole
Magnetic dipole	3.4		5.3		

4.55. Results

a) The 15 day Os^{193} emits a single β-ray of energy 0.143 ± 0.002 Mev and two γ-rays of energies 0.042 ± 0.001 Mev and 0.128 ± 0.001 Mev.

b) The 128 kev γ-ray consists of electric quadrupole radiation. The K internal conversion coefficient for this γ-ray is ~ 0.5 and $N_K/N_L = 2.1$. The N_L/N_M ratio for the 42 kev γ-ray is 1.8.

CHAPTER 5

Disintegration schemes

In this chapter we shall discuss the disintegration schemes proposed on the basis of the results given in Chapter 4.

5.1. Disintegration scheme for Ru^{103} and Rh^{103m}

The difference in energy between the two β-rays emitted by Ru^{103}, is $(0.7 - 0.217) = 0.483 \pm 0.014$ Mev, where as the energy of the γ-ray is given as 0.498 ± 0.002 Mev. These two energies agree within the limits of error mentioned. Further, the $\beta\gamma$-coincidences show that the 498 kev γ-ray follows the 217 kev β-ray. Rh^{103m} is found to decay to its ground level emitting a γ-ray of energy 40 kev. If β_2 in Fig. 5.1 were to lead to the ground level in Rh^{103} as proposed by Mandeville et al. (M7), the energy of the hard β-ray should have energy, $0.217 + 0.498 + 0.04 = 0.755$ Mev instead of 0.7 ± 0.01 Mev, as observed. The disintegration scheme proposed in Fig. 5.1 is precisely the same as the one proposed by Mei et al. (M3) independently.

5.2. Disintegration scheme for Pd^{109} and Ag^{109m}

Fig. 5.2 gives the disintegration scheme of Pd^{109} and Ag^{109m} together. As there are only one β and one γ-ray observed, the disintegration scheme is self evident.

5.3. Disintegration scheme for Ce^{141}

The difference in energy between the two β-rays emitted by this isotope is equal to the energy of the single γ-ray observed in this case. So it is fairly certain that the soft β is followed by the γ-ray while the hard β leads to the ground level in Pr. The intensities of the two β-rays are given in the decay scheme as percentages. The decay scheme is given in Fig. 5.3. This scheme is the same as the one proposed by SHEPHERD (S15) and FREEDMAN et al. (F7) and disagrees with the one proposed by TER-POGOSSIAN et al. (T1).

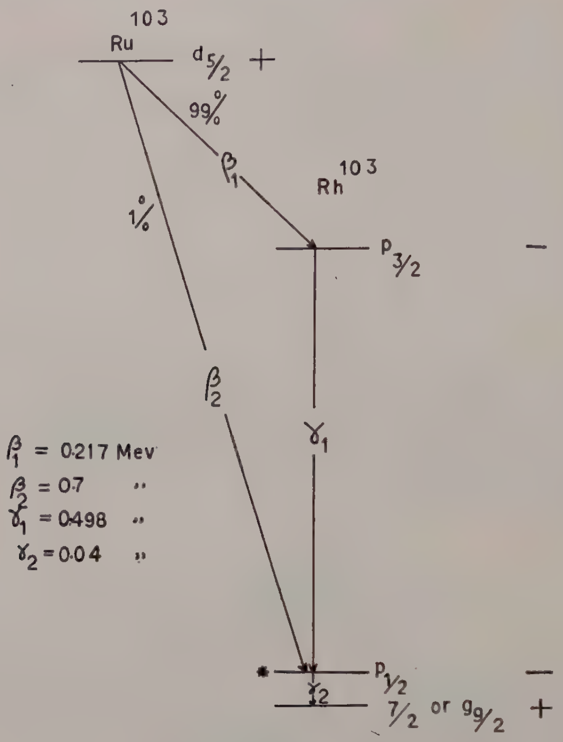

Fig. 5.1.

5.4. Disintegration scheme for Ce^{143} and Pr^{143}

The energy difference between the two β-rays at 1.37 and 1.09 Mev equals the energy of the 283 kev γ-ray within the experimental errors. Further, the energy of the 705 kev γ-ray is equal to the sum of the energies of the 649 and 57 kev γ-rays. This suggests that the 705 kev γ-ray should be placed in parallel to the 649 and 57 kev γ-rays which may be placed in cascade. It is unfortunate that the β-ray at 0.37 Mev could not be established definitely. If this β-ray is present, as is suspected, then the sum of the energies of this β-ray and the 705 kev γ-ray equals the energy of the 1.09 Mev β-ray within the experimental errors. The $\beta\gamma$-coincidence results support the idea that the 283 kev γ-ray is coincident with the 1.09 Mev β-ray (which is in energy greater than 930 kev). The γ-ray intensity relations are also such, that the 283 kev γ-ray is to be placed at the lower levels in the disintegration scheme.

The percentages in the decay scheme represent the relative intensities and are obtained from the β-and γ-ray spectra. The β_1 transition is shown by a dotted line as it is not definitely established even though strongly suspected. Pr^{143} is found to decay emitting a single β-ray of maximum energy 0.915 ± 0.015 Mev and is represented as such in the decay scheme. This is in complete agreement with the previous reports on Pr^{143} (F8, T1). The decay scheme is given in Fig. 5.4.

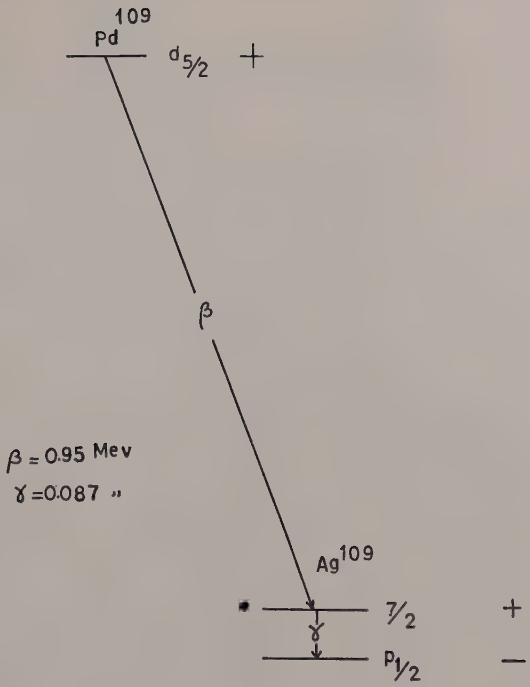

Fig. 5.2.

5.5. Disintegration scheme for Nd^{147} and Pm^{147}

The two β-rays 780 and 350 kev have a difference in energy of 430 kev. To this energy if we add the energy of the 91 kev γ-ray we obtain the energy of the 522 kev γ-ray. So it is quite probable that the soft β (350 kev) is followed by the hard γ (522 kev) where as the hard β (780 kev) is followed by the soft γ (91 kev). Further, the sum of the energies of the two γ-rays rays 91 and 310 kev is equal to the energy of the 392 kev γ-ray within the experimental errors. The coincidence studies made by Emmerich et al. (E3) agree well with the decay scheme proposed here, even though the energies reported in their paper are somewhat different. Further, they report only three γ-rays. However, their report concerns only the β-spectrum and no γ-spectrum has been reported.

The proposed decay scheme with the intensities is given in Fig.5.5. The β_3 component (3 % intensity) is proposed on the basis of the γ-rays. It has not been possible to resolve this β from the Fermi plot as this β-ray is of very low intensity and has a maximum energy in between the maximum energies of the other two intense β-rays. As no chemical purification of Nd has been undertaken, the decay scheme must be considered as tentative.

Langer et al. (L2) have reported on the Pm^{147} isotope. According to their report, it decays emitting a β-ray of maximum energy 223.2 ± 0.5 kev. We have included this also in the disintegration scheme presented in Fig. 5.5. Pm^{147} is reported not to emit any γ-rays (S8).

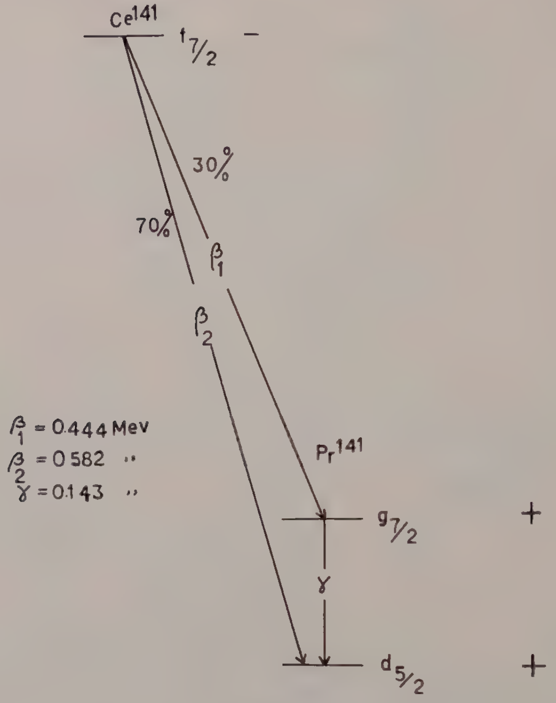

Fig. 5.3.

5.6. Disintegration of Pm^{149}

As Pm^{149} is found to decay emitting a single β-ray of maximum energy 1.05 ± 0.01 Mev, it poses no problem.

5.7. Disintegration scheme for Os^{193}

The disintegration scheme is presented in Fig. 5.6. The βe^- coincidence experiments support this scheme.

CHAPTER 6

Discussion

It is well known that nuclei with even number of protons and even number of neutrons ("even, even" nuclei) have O spin where as nuclei consisting of odd number of protons or neutrons should have a spin of an odd multiple of 1/2. While the spins of some isotopes can be measured directly, it is impossible to make this measurement for most nuclei in excited states. In the case of artificial radioactive nuclei, it is possible to obtain the characteristics of the excited states from the β-decay selection rules and from the multipole order nature of the γ-rays. We have collected some information in this way from our measurements described in Chapter 4. In this Chapter we shall discuss the assignments of spins and parities to the nuclear

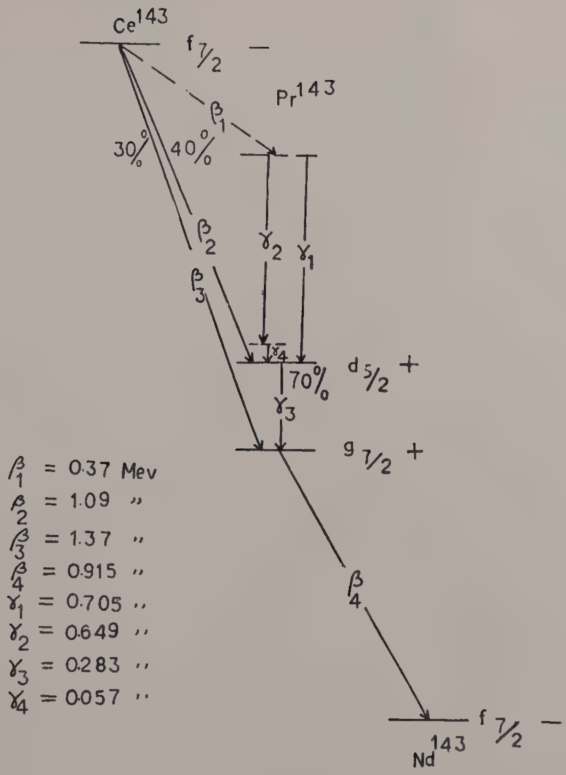

Fig. 5.4.

levels in the disintegration schemes proposed in Chapter 5 and compare the resulting conclusions with the predictions made by the nuclear shell theory described in Chapter 3. The spin and parity assignments are shown in the decay schemes; + means even parity and — means odd parity.

6.1. Ru^{103} and Rh^{103m}

The parent nucleus Ru^{103} contains 44 protons and 59 neutrons where as the daughter nucleus Rh^{103} has 45 protons and 58 neutrons. According to the spin-orbit coupling scheme, the 59 th neutron should be in a $d_{5/2}$ state with even parity. For N (neutron number) or P (proton number) between 38 and 50, only the levels $p_{1/2}$ and $g_{9/2}$ remain to be filled and only spins of 1/2 and 9/2 are known to exist in this region. Feenberg's scheme (F1) gives a preferred spin value 9/2 and even parity to the ground level in Rh^{103}. So if we assign $g_{9/2}$ state with even parity to the ground level of Rh, the meta-stable level should belong to a $p_{1/2}$ state with odd parity according to the spin-orbit coupling scheme. According to Feenberg, however, the meta stable level in Rh belongs to $s_{1/2}$ state with even parity. In both these cases the spin change is 4 units. According to the γ-ray selection rules (Table 3.2) if there is a change of parity in this transition, the γ-ray should be either magnetic 2^4 or electric 2^5 pole radiation and if there is no change of parity, it should be electric 2^4

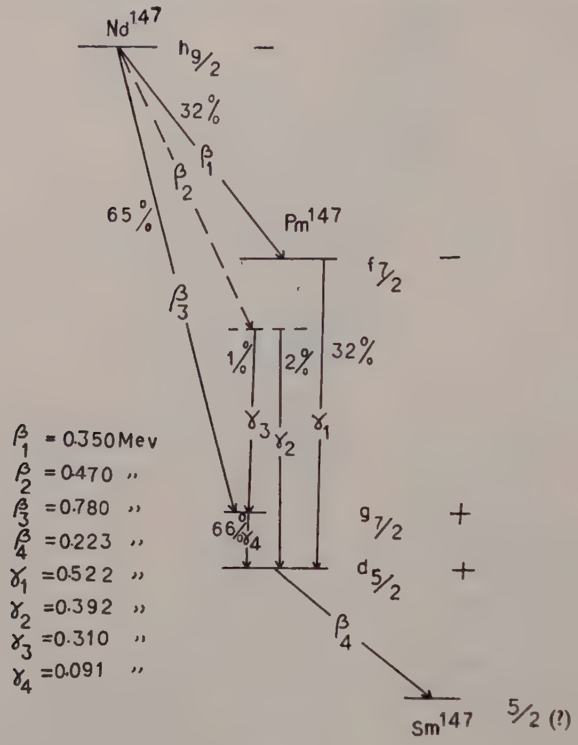

Fig. 5.5.

pole radiation. In the first case the multipole order, l of the γ-ray is 5 where as in the second case it is only 4. From Table 4.1 it seems that the experimental N_K/N_L value for the 40 kev γ-ray cannot be accounted by electric 2^4 pole radiation alone. AXEL and DANCOFF (A2) assign $l=4$ for Rh^{103m} (45 minutes halflife) on a semi empirical classification based on half-life considerations. Apart from the crudeness of the formula used to estimate the theoretical half-life, there is a major uncertainty in the theoretical estimate of the internal conversion coefficient which has to be used to correct this half-life for internal conversion.

Further, the value of $\{(W^2-1)/t\}$ for the higher energy β-transition is $\sim 10^{10}$; according to SHULL and FEENBERG (S14), it means that this β-transition involves a spin change of 2 units together with a change in parity. We have already assigned the Ru^{103} level $d_{5/2}$ state even parity which is in accordance with the spin-orbit coupling scheme and Feenberg's scheme as well. The metastable level in Rh to which the β_2 transition leads, should, therefore, be assigned to $p_{1/2}$ state with odd parity which agrees with the spin-orbit coupling scheme.

GOLDHABER and SUNYAR (G3) classify Rh^{103m} as an E3 isomer i.e. the 40 kev γ-ray is electric 2^3 pole radiation. In the chart given by MOSZKOWSKI (M9) Rh^{103} is situated close to the line for M3 with no spin correction. Our estimation of K/L ratio for the 40 kev γ-ray fits with either electric 2^3 pole or a mixture of electric 2^5 or 2^4 pole together with magnetic radiation.

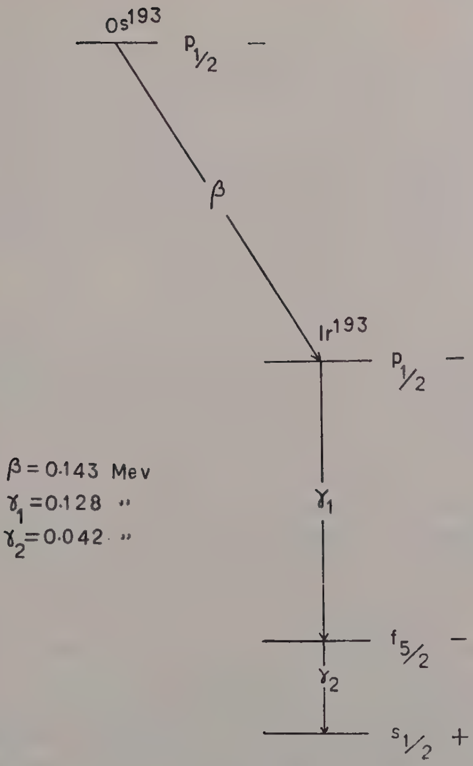

Fig. 5.6.

GOLDHABER et al. (G3) assign "7/2 even" to the metastable level and "$p_{1/2}$ odd" to the ground level. But the ft value of β_2 transition makes us assign "$p_{1/2}$ odd" to the metastable level when once the Ru^{103} level is assigned "$d_{5/2}$ even".

The *ft* value for the β_1 (217 kev) transition is 0.45×10^6 or log $ft = 5.64$. Nordheim's considerations (N2) make this β-transition probably allowed or at the most first forbidden. If it is a normal allowed transition there should not be any change in parity; there can be a spin change of 0 or 1 unit according to G. T. rules. This makes the ground level of β_1-transition belong to a $d_{5/2}$ or $d_{3/2}$ state with even parity. On the other hand, if the β_1-transition is really a first forbidden transition (which may be supported from the fact that the Fermi plot of this β-transition differs from a straight line plot) then the ground level of β_1 transition should be assigned to $p_{3/2}$ state with odd parity. Now, if this level belong to $d_{3/2}$ or $d_{5/2}$ state then the γ_1-ray (498 kev) should involve a change of parity together with a spin change of 1 or 2 units respectively i.e. it should be electric dipole or electric 2^3 pole together with magnetic 2^2 pole radiation. On the other hand, if the level in question belongs to $p_{3/2}$ state with odd parity, then the 498 kev γ-ray involves no parity change and the spin change is 1 unit, in which case it should consist of either magnetic dipole or electric quadrupole radiations. MEI et al. (M3) have resolved the *K* and *L* lines of the 498 kev γ-ray and they have found that this γ-ray is either electric quadrupole or magnetic dipole radiation. So $p_{3/2}$ state with odd parity seems to be the probable assignment for this level.

6.2. Pd^{109} and Ag^{109m}

Pd^{109} contains 46 protons and 63 neutrons whereas Ag^{109} contains 47 protons and 62 neutrons. The ground level of Ag^{109} is known to have a spin 1/2 (M8). The ft value for the single β-transition is 1.05×10^6 or log $ft = 6.0$.

The odd neutron number 63 in Pd^{109} suggests that the level in Pd^{109} should belong to a $d_{5/2}$ state with even parity. The ft value for the β-transition shows that it can be classified as an allowed transition. If it is an allowed transition, there should not be any change in parity and the metastable level in Ag^{109} should have even parity and spin 5/2, 3/2 or 7/2 according as the spin change involved in the β-transition is either O or 1 (G. T. rules).

The ground level in Ag^{109} should belong to a $p_{1/2}$ state with odd parity since its spin is known to be 1/2. The 87 kev γ-transition seems to have l value 3 or 4; the first one is preferred by our measurements on K/L ratio where as the second one is given by AXEL and DANCOFF (A2) based on the half-life of the γ-ray (40 seconds). The new classification made by GOLDHABER et al. (G3) and MOSZKOWSKI (M12) agrees with our value $l = 3$.

If the metastable level has spin 5/2, 3/2 or 7/2 and even parity and the ground level belongs to $p_{1/2}$ state with odd parity, then the 87 kev γ-ray should be either electric 2^3 pole or magnetic 2^2 pole radiation ($\Delta i = 2$) or simply electric dipole radiation ($\Delta i = 1$) or electric 2^3 pole radiation ($\Delta i = 3$) respectively. In the first and the last cases, l value is 3 where as in the electric dipole case it is only 1. On the experimental basis $l = 1$ can be ignored.

The above discussion shows that the following assignment of term scheme fits in this case with the observations: Pd^{109} level $d_{5/2}$ or $g_{7/2}$ even parity, Ag^{109} metastable level 7/2 or 5/2 even parity, and Ag^{109} ground level $p_{1/2}$ odd parity. This assignment agrees with (i) the β-transition belongs to the allowed group involving 0 or 1 unit spin change and no parity change; (ii) the γ-transition has an l value equal to 3, (iii) the new classification of isomers.

Both FEENBERG and MAYER agree that the ground level in Ag^{109} is a $p_{1/2}$ state with odd parity. Direct application of the spin-orbit coupling scheme requires that the metastable level in Ag^{109} should belong to a $g_{9/2}$ state with even parity, and $l = 5$. According to the F-H level scheme Ag^{109} metastable level should have odd parity and a preferred spin of 7/2, giving $l = 4$.

The present assignment agrees with neither of the two schemes but is in accordance with the meager experimental evidence. MOSZKOWSKI (M9) has suggested that one of the states involved in some isomeric transitions may have a spin determined by the coupling of several odd nucleons rather than by one odd nucleon.

6.3. Ce^{141}

According to spin-orbit coupling scheme the 59th proton should be in a $d_{5/2}$ state with even parity. The log ft values for the two β-rays emitted by Ce^{141} are 7.0 (444 kev γ-ray) and 7.75 (582 kev β-ray). According to NORDHEIM, these two can be classified as first forbidden transitions with $\Delta i = 0,1$ and change in parity. The log ft value of the 582 kev β-ray is slightly high for this gruop but it is too short to be classified as either first forbidden with $\Delta i = 2$ and change in parity or as a second forbidden transition.

Taking the ground level of Pr^{141} as a $d_{5/2}$ state with even parity, we arrive at the conclusion that Ce^{141} level should have odd parity and spin either 3/2, 5/2 or 7/2. Spin-orbit coupling scheme predicts $h_{9/2}$ state with odd parity for the 83rd neutron; however $f_{7/2}$ level belongs to the same shell as and is quite close to $h_{9/2}$ level. It may be that $h_{9/2}$ and $f_{7/2}$ cross just as $g_{7/2}$ and $d_{5/2}$ cross. So $f_{7/2}$ with odd parity fits well for Ce^{141} level; spins 3/2 and 5/2 are improbable according to the above considerations.

Taking $f_{7/2}$ and odd parity valid for Ce^{141} level, the ground level of 444 kev belongs to $g_{7/2}$ state with even parity. Then the 143 kev γ-ray involves a spin change of 1 unit and no parity change i.e. it is either magnetic dipole or electric quadrupole radiation. This conclusion regarding the 143 kev γ-ray agrees well with the experimental result (Table 4.3).

6.4. Ce^{143} and Pr^{143}

Ce^{143} has 58 protons and 85 neutrons, Pr^{143} 59 protons and 84 neutrons and Nd^{143} 60 protons and 83 neutrons. The log *ft* values for the 1.37 and 1.09 Mev β-rays with the intensity ratios mentioned in Fig. 5.4 are about 7.77 and 7.29 respectively. According to Nordheim's considerations these two can be classified as first forbidden transitions with spin change 0 or 1 together with a change in parity.

The log *ft* value 7.77 for the 1.37 Mev β-transition is slightly higher for the first forbidden group, but falls too short to be classified as second forbidden or even as first forbidden transition with a spin change of 2 units together with a change in parity.

According to spin-orbit coupling scheme, if we consider the neutron number 83 in Nd^{143}, it should belong to $h_{9/2}$ state with odd parity. In our previous report (K5), we have chosen $h_{9/2}$ giving weightage to the odd 83rd neutron as spin-orbit coupling scheme is expected to predict reliable spins and parities for one proton or neutron greater than for a closed configuration (magic number 82). However, since then MURAKAWA et al. (M10) measured the spin of Nd^{143} from the hyper fine structure and they report the spin of Nd^{143} as 7/2. This shows that the ground level of Nd^{143} has $f_{7/2}$ state and odd parity.

Log *ft* value for the single β-emitted by Pr^{143} is 7.58 which makes it a first forbidden transition with a spin change of 0 or 1 unit together with parity change. If we take $f_{7/2}(-)$ for the ground level in Nd^{143}, then the top level of the 915 kev β should belong to either $g_{7/2}$ or $d_{5/2}$ with even parity.

If we take the top level of the 915 kev β-ray as belonging to $g_{7/2}$ or $d_{5/2}$ with even parity, the level in Ce^{143} should belong to a $f_{7/2}$ state with odd parity and the ground level of the 1.09 Mev β should be a $d_{5/2}$ or $g_{7/2}$ with even parity. These agree well with the *ft* values of the β-rays observed.

Now let us see how this term scheme fits with the measurements on the 283 kev γ-ray. According to this picture the 283 kev γ-ray involves a spin change of 1 unit and no change in parity. It means this γ-ray should be either electric quadrupole or magnetic dipole radiation, giving $l=2$. This is in agreement with the conclusion reached from measurements on the internal conversion of this γ-ray.

6.5. Nd^{147}

Nd^{147} has 60 protons, 87 neutrons, Pm^{147} 61 protons, 86 neutrons and Sm^{147} 62 protons, 85 neutrons. MURAKAWA et al. (M10) measured the spin of Sm^{147} as 5/2 from hyper fine structure. The β-transition from Pm^{147} has log $ft \sim 7$ depending on its half-life t (2 to 4 years) (S8).

The 61 protons in Pm^{147} indicate a $d_{5/2}$ state with even parity for the lowest level in Pm^{147} (Fig. 5.5). The 91 kev γ-ray appears to be magnetic dipole radiation involving a spin change of 1 unit and no parity change. This means the top level of 91 kev γ-ray may belong to $g_{7/2}$ state with even parity. The 780 kev β-transition has log $ft = 7.4$ and can be classified as a first forbidden transition involving a spin change of 0 or 1 unit together with a change in parity. 87 neutrons suggest $h_{9/2}$ state to the level in Nd^{147}. The 350 kev β-transition has log $ft = 6.6$ which may belong to either allowed or first forbidden group. This means the top most level in Pm^{147} (Fig. 5.5) belongs to either $f_{7/2}(-)$ or $g_{7/2}(-)$ state. Then the 522 kev γ-transition would be either electric dipole or magnetic dipole or electric quadrupole radiation.

According to this assignment β-transition from Nd^{147} to the bottom level in Pm^{147} will be $h_{9/2} \rightarrow d_{5/2}$ and is higher forbidden than the other two β-transitions observed.

6.6. Os^{193}

Os^{193} consists of 76 protons and 117 neutrons; Ir^{193} has 77 protons and 116 neutrons. The 143 kev β has log $ft = 5.3$ placing it in the normal allowed group, involving 0 or 1 unit spin change and no parity change.

The 117 neutrons indicate a $p_{1/2}$ state with odd parity or $i_{13/2}$ with even parity. We may neglect the spin 13/2 as improbable as it is too high to be observed in the ground level and no isomeric transition is observed in the present case. So Os^{193} probably belongs to a $p_{1/2}$ state with odd parity.

Consequently, the top level in Ir^{193} (Fig. 5.6) should also be either $p_{1/2}$ or $p_{3/2}$ and have the same parity as the Os^{193} level.

The 128 kev γ-ray is probably electric quadrupole radiation involving a spin change of 2 units and no parity change. This means the bottom level of the 128 kev γ-ray should be either a $f_{5/2}$ or $f_{7/2}$ state with odd parity.

As it has not yet been possible, mainly due to the lack of theoretical internal conversion coefficients for L and M shells for the low energy γ-ray (42 kev), to decide the multipole order nature of the 42 kev γ-ray, nothing can be said about the ground level in Ir^{193}. According to spin-orbit coupling scheme, probably it belongs to $s_{1/2}$ state with even parity when the 42 kev γ-ray would be either electric 2^3 or magnetic 2^2 pole radiation. If we take it as $s_{1/2}$, then the β-transition from Os^{193} to the ground level in Ir^{193} would be $p_{1/2} \rightarrow s_{1/2}$ which is higher forbidden than the single β-ray observed.

Acknowledgements

My sincere thanks are due to Professor MANNE SIEGBAHN for providing me with all the facilities to work at this Institute and Professor ERIK HULTHÉN for his kind interest in my work. I am extremely grateful to Professor KAI SIEGBAHN for constant encouragement and valuable suggestions. I am very much indebted to the staff of the radiochemical laboratory of this Institute for helping me with the chemical separations. My sincere appreciations are due to Civ.-Ing. B. ÅSTRÖM for helping me with the electronic equipment. I am also thankful to all my colleagues at this Institute for interesting discussions and hearty cooperation.

Nobel Institute of Physics, Stockholm 50, Sweden.

References

A

A1. P. Axel and R. F. Goodrich, "Internal conversion data", private communication.
A2. P. Axel and S. M. Dancoff, Phy. Rev. *76*, 892 (1949).

B

B1. I. Bergström, S. Thulin and G. Andersson, Phy. Rev. *77*, 851 (1950).
B2. C. H. Braden, G. E. Owen, J. Townsend, C. S. Cook, F. B. Shull, Phy. Rev. *74*, 1539 (1948).
B3. K. J. Broström, T. Huus and J. Koch, Nature *160*, 498 (1947).
B4. H. Bradt, P. C. Gugelot, O. Huber, H. Medicus, P. Preiswerk and P. Scherrer Helvetica Physica Acta, *19*, 77 (1946).
B5. H. A. Bethe and R. F. Bacher, Rev. Mod. Phys. *8*, 194 (1936).
B6. M. E. Bunker, L. M. Langer and R. J. D. Moffat, Phy. Rev. *80*, 468 (1950).
B7. M. E. Bunker, R. Canada and A. C. G. Mitchell, Phy. Rev. *79*, 610 (1950).
B8. E. Bohr and N. Hole, Arkiv f. Mat. Astr. o. Fysik, Bd 32 A, No. 15 (1945).
B9. E. Bleuler and W. Zünti, Helvetica Physica Acta, *19*, 375 (1946).

C

C1. J. M. Cork, R. G. Shreffler and C. M. Fowler, Phy. Rev. *74*, 240 (1948).

D

D1. M. Deutsch, L. G. Elliot and R. D. Evans, Rev. Sci. instruments *15*, 178 (1944).
D2. S. M. Dancoff and P. Morrison, Phy. Rev. *55*, 122 (1939).

E

E1. W. Elsasser, J. de Phys. et. rad. *5*, 625 (1934).
E2. R. D. Evans and R. O. Evans, Rev. Mod. Phy. 20, 305 (1948).
E3. W. S. Emmerich and J. D. Kurbatov, Phy. Rev. *81*, 1062 (1951).
E4. W. S. Emmerich and J. D. Kurbatov, Phy. Rev. *83*, 40 (1951).

F

F1. E. Feenberg and K. C. Hammack, Phy. Rev. *75*, 1877 (1949).
F2. E. Fermi, Zeits. f. Physik *88*, 161 (134).
F3. I. Feister, Phy. Rev. *78*, 375 (1950).
F4. E. Feenberg and G. Trigg, Rev. Mod. Phy. *22*, 399 (1950).
F5. N. Feather, Proc. Cambridge Phy. Soc. *34*, 599 (1938).
F6. A. Flammersfeld, Naturwiss. *32*, 36 (1944).
F7. M. S. Freedman and D. W. Engelkemeir, Phy. Rev. *79*, 897 (1950).
F8. L. Feldman, L. Lidofsky, P. Macklin and C. S. Wu, Phy. Rev. *76*, 1888 (1949).

G

G1. E. Greuling, Phy. Rev. *61*, 568 (1942).
G2. L. E. Glendenin, Nucleonics, *2*, (Jan. 1948).
G3. M. Goldhaber and A. W. Sunyar, Phy. Rev. 83, 906 (1951).

H

H1. Haxel, Jensen and Suess, Phy. Rev. *75*, 1766 (1949).
H2. J. Hughes and K. J. Le Couteur, Proc. Phy. Soc. *63 A*, 1219 (1950).
H3. H. Hall, Phy. Rev. *79*, 745 (1950).
H4. M. H. Hebb and E. Nelson, Phy. Rev. *58*, 486 (1940).
H5. W. F. Hornyak, T. Lauritsen and V. K. Rasmussen, Phy. Rev. *76*, 731 (1949).
H6. A. Hedgran, K. Siegbahn and N. Svartholm, Proc. Phy. Soc. (Lond.), *63*, 960 (1950).
H7. D. R. Hamilton, Phy. Rev. *58*, 122 (1940).
H8. N. Hole, Arkiv f. Math. Astr. o. Fysik, Bd 36 A, No. 2 (1948).
H9. R. D. Hill, Phy. Rev. *82*, 449 (1951).

J

J1. W. H. Jordan and P. R. Bell, Nucleonics 5, 10, 30 (Oct. 1949).

K

K1. E. J. Konopinski, Rev. Mod. Phy. *15*, 209 (1943).
K2. Kurie, Richardson and Paxton, Phy. Rev. *49*, 368 (1936).
K3. E. Kondaiah, Phy. Rev. *79*, 891 (1950).
K4. E. Kondaiah, Arkiv för Fysik, Bd 2, Nr 28 (1950).
K5. E. Kondaiah, Phy. Rev. *83*, 471 (1951).
K6. E. Kondaiah, Phy. Rev. *81*, 1056 (1951).
K7. E. Kondaiah, Arkiv för Fysik, Bd 3, Nr 4 (1951).
K8. H. B. Keller and J. M. Cork, Phy. Rev. *83*, 216 (1951).

L

L1. G. Lindström, Phy. Rev. *83*, 465 (1951).
L2. L. M. Langer, J. W. Motz and H. C. Price, Jr., Phy. Rev. *77*, 798 (1950).
L3. J. J. Livingood, Phy. Rev. *50*, 425 (1936).
L4. L. M. Langer and H. C. Price, Jr., Phy. Rev. *76*, 641 (1949).

M

M1. M. G. Mayer, Phy. Rev. *74*, 1235 (1948).
M2. M. G. Mayer, Phy. Rev. *78*, 22 (1950).
M3. J. Y. Mei, C. M. Huddleston and A. C. G. Mitchell, Phy. Rev. *79*, 429 (1950).
M4. D. E. Matthews and M. L. Pool, Phy. Rev. *72*, 163 (1947).
M5. A. J. Moses and D. S. Martin Jr., Phy. Rev. *79*, 467 (1950).
M6. C. E. Mandeville and E. Shapiro, Phy. Rev. *79*, 391 (1950).
M7. C. E. Mandeville and E. Shapiro, Phy. Rev. *77*, 439 (1950).
M8. Mattauch-Flemmersfeld's "Isotopic report" (1949).
M9. S. A. Moszkowski, Phy. Rev. *83*, 1071 (1951).
M10. K. Murakawa and J. S. Ross, Phy Rev. *82*, 967 (1951).
M11. M. G. Mayer, Phy. Rev. *78*, 16 (1950).

N

N1. L. W. Nordheim, Phy. Rev. *75*, 1894 (1949).
N2. L. W. Nordheim, Phy. Rev. *78*, 294 (1950).

R

R1. Rose, Goertzel, Harr, Spinrad and Strong, Phy. Rev. *76*, 184 (1949).

S

S1. J. Schmidt, Zeits. f. Physik *106*, 358 (1937).
S2. W. J. Swiatecki, Proc. Phy. Soc. *63 A*, 1208 (1950).
S3. K. Siegbahn, Phil. Mag. *37*, 162 (1946).
S4. H. Slätis and K. Siegbahn. Arkiv f. Fysik, Bd 1, Nr 17 (1949).
S5. E. Segré and A. C. Helmholz, Rev. Mod. Phy. *21*, 271 (1949).
S6. K. Siegbahn, Arkiv f. Mat. Astr. o. Fysik, *30 A*, No. 1 (1943).
S7. K. Siegbahn, Arkiv f. Fysik (in print) (1951).
S8. G. T. Seaborg and I. Perlman, "Table of isotopes", Rev. Mod. Phy. *20*, 585 (1948).
S9. K. Siegbahn, E. Kondaiah and S. Johansson, Nature *164*, 405 (1949).
S10. E. Shapiro and C. E. Mandeville, Phy. Rev. *78*, 319 (1950).
S11. D. Saxon, Phy. Rev. *74*, 1264 (1948).
S12. W. H. Sullivan, N. R. Sleight and E. M. Gladrow, Phy. Rev. *70*, 778 (1946).
S13. K. Siegbahn and A. Hedgran, Phy. Rev. *75*, 523 (1949).
S14. F. B. Shull and E. Feenberg, Phy Rev. *75*, 1768 (1949).
S15. L. R. Shepherd, Research 1, 671 (1948).
S16. F. B. Shull and E. Feenberg, Phy. Rev. *75*, 1768 (1949).

T

T1. Ter-Pogossian, Cook, Godderd and Robinson, Phy. Rev. *76*, 909 (1949).

W

W1. C. S. Wu, Rev. Mod. Phy. *22*, 386 (1950).
W2. C. F. von Weizsäcker, Naturwiss. *24*, 813 (1936).
W3. Weisskopf and Blatt, private communication.
W4. M. L. Wiedenbeck, Phy. Rev. *67*, 267 (1945).
W5. M. L. Wiedenbeck, Phy. Rev. *68*, 237 (1945).

Z

Z1. E. L. Zimmerman, E. B. Dale, D. G. Thomas and J. D. Kurbatov, Phy. Rev. *80*, 908 (1950).

Å

Å1. B. Åström, Rev. Sci. Instruments, *21*, 323 (1950).
Å2. B. Åström, Report on "scintillation spectrometer" at the Physical conferences at Lund (May 1951).

Tryckt den 13 november 1951

Uppsala 1951. Almqvist & Wiksells Boktryckeri AB

Errata

Art No.	Page No.	Para in Art.	Line No.	Read	for
1.4	88	1	8	(J1)	(G1)
2.9	97	2	Equn. 2.6	$\left[\frac{P\,dW}{\theta\cdot\eta\cdot W}\right]=k\,(W_0-W)^2 dW$	$\left[\frac{P\,dW}{\theta\cdot\eta\cdot W}\right]^{1/2}=k\,(W_0-W)$
2.11	99	5	5	Fig. (4.3)	Fig. (4.2)
2.13	100	2	5	(E2)	(E1)
3.1	102	3	9	**Cancel:** W is the energy of the β-particle	
3.5	104	3	3	$Y =$	$y =$
3.5	105	4	Equn. 3.5	$kp^{2\,(S_1-S_0-1)}$	$kp^2\,S_1-S_0-1)$
3.12	108	1	1	(M11)	(M2)
3.16	110	1	1	(M11)	(M1)
4.2	113	1	6	39.8 ± 0.4	$39.8+0.4$
4.13	121	1	2	Fig. 4.3	Fig. 4.2
4.18	122	2	2	~ 92 %	92 %
4.32	130	1	19	little indication	no indication
4.47	143	1	1	Nd^{147}	Nd^{149}
4.47	143	Table 4.5		522 ± 6	522 ± 8
5.5	147	1	5	γ-rays	γ-rays rays
5.5	147	1	7	agree partly with	agree well with
Fig. 5.3	148			$\beta_1-70\,\%,\ \beta_2-30\,\%$	$\beta_1-30\,\%,\ \beta_2-70\,\%$
6.1	149	1	3	can be	should be
6.1	151	5	3	an allowed	a normal allowed
6.1	151	5	9	belongs	belong
6.2	152	2	1	can	should
6.2	152	3	5	(M9)	(M12)
	155	Ref. E1		635	625
	155	Ref. F2		(1934)	(134)
	155	Ref. F5		Phil. Soc.	Phy. Soc.
	155	Ref. H6		*63 A*	*63*
	156	Ref. M1		235	1235
4.20	124	2	5	Lanthanum	Lactinium
Fig. 5.5	150			$Sm^{147}-f_{5/2}$ (?)	$Sm^{147}-5/2$?)

ARKIV FÖR FYSIK Band 4 nr 3

Communicated 6 June 1951 by Axel E. Lindh and Harald Norinder

---

Two-Directional focusing with short uniform magnetic fields

By Carl Reuterswärd

With 4 figures in the text

Abstract

The three-dimensional ion optic properties of the uniform magnetic fields with boundaries are investigated in the case of ion paths near the plane of symmetry, and the results are given in terms of the dioptrics of ion lenses. The conditions of simultaneous focusing of pencils of rays perpendicular and parallel to the lines of flux are stated in a somewhat specialized class of fields. The second-order aberrations in planes parallel to the plane of symmetry are given. The existence of fields in which these cancel in points of the optic axis is pointed out. The same second-order aberrations due to the fringing fields are calculated to the first approximation.*

1. Introduction

It has been observed, when using a short transverse magnetic field for analyzing ion beams, that there occurs an ion optical effect on the lines of the mass spectrum, causing them to vary in length, as the angle of incidence of the beam on the field boundary is changed [1]. Since this effect is very marked and could be used of advantage to increase the current density in the spectrum, it seems to be a matter of interest to investigate its theoretical background.

The ion optics of these fields have been treated by several investigators. Thus, the case of the ion beams entering and emerging at right angles to the field boundary was analyzed by Stephens [2], who gave the conditions of first-order focusing and the second-order terms responsible of the image errors. Herzog [3] investigated the first-order terms of focusing in the more general case of ion beams at oblique angles to the boundary.

These theories, however, are exclusively two-dimensional, considering ion tracks in the plane of symmetry only and pay no regard to the effects of the non-uniform fields which by necessity limit the supposedly uniform main parts of the fields. In the following, the ion optic theory will be extended so as to account for ion paths near the plane of symmetry (the median plane), resulting

---

* After completing this investigation the author was informed of the substance of the paper by Sturrock [9] in which are found the same conclusions as those numbered 1—3 in the summary of the present paper. Also, a recent paper by Glaser [10] is reported to deal with the same subject.

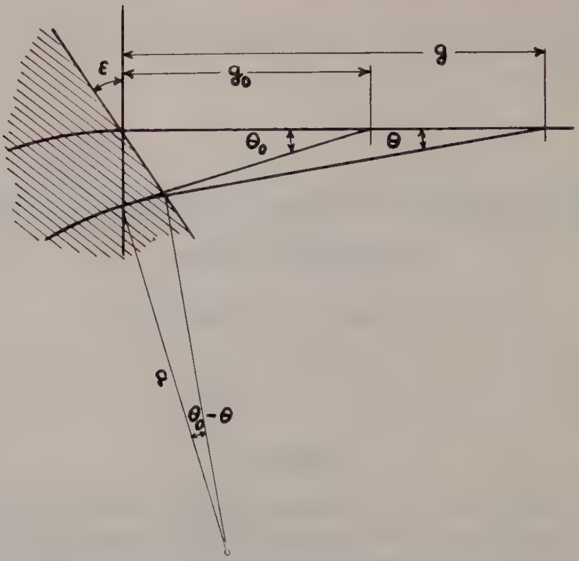

Figure 1. Median plane dioptrics of the field boundary.

in the three-dimensional gaussian dioptrics of the field boundaries in the limiting case of small fringing field extensions. In order to give a basis of experimental application, second-order aberrations and fringing field corrections will be discussed.

2. Transverse dioptrics of the field boundary

We will consider here the projection of the ion path onto the median plane, or that component of the motion of the ions which is *transverse to the flux* of the uniform field. If the fringing field be neglected, the action of the magnetic field on the ion beam — besides bending it through an angle Φ — may be considered as that of a cylindrical lens on a beam of light. Quoting HERZOG [3], the focal distance f, and the distance g'' of the back focus from the back field boundary, are:

$$f = a \cos \varepsilon' \cos \varepsilon'' \operatorname{cosec} (\Phi - \varepsilon' - \varepsilon'') \tag{1}$$

$$g'' = a \cos \varepsilon'' \cos (\Phi - \varepsilon') \operatorname{cosec} (\Phi - \varepsilon' - \varepsilon'') \tag{2}$$

Here, a is the radius of curvature of the ion paths, and ε' (ε'') is the angle of incidence (emergence). Previously it has been pointed out [4], that the focusing effect of the field may be localized to three thin lenses, one of which is situated in the interior of the field, having the focal distance

$$f_{\Phi} = a \operatorname{cosec} \Phi \tag{3}$$

and the other two located one at each field boundary intersection, having the focal distances

$$f_{\varepsilon}^{(i)} = -a \operatorname{ctan} \varepsilon^{(i)} \tag{4}$$

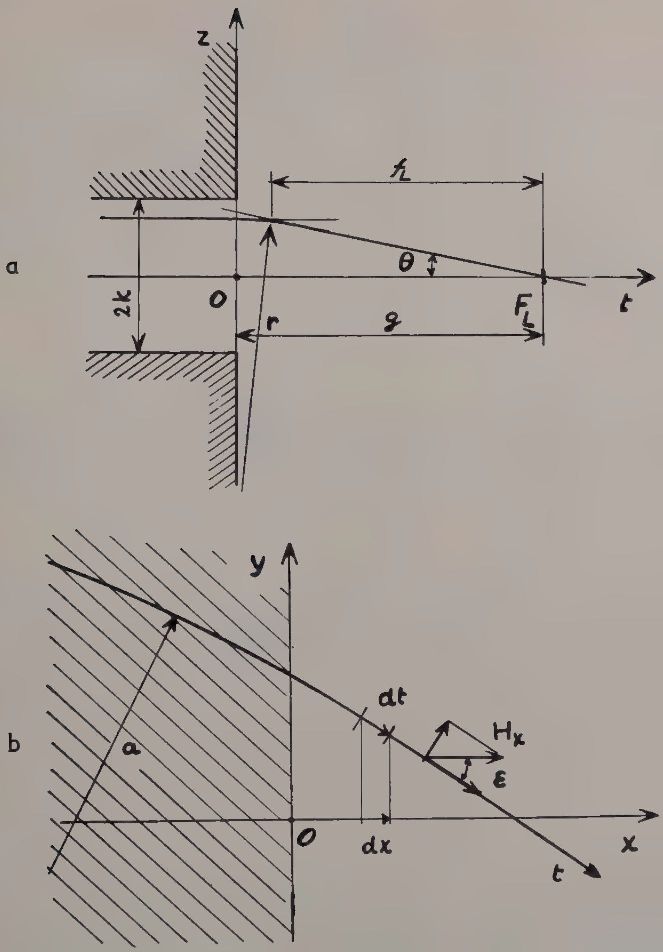

Figure 2. The geometry of ion paths near the median plane. a. The ion path in the (t, z) surface. b. The projection of the path onto the median or (x, y) plane.

(3) gives simply the focal distance of the sector field with $\varepsilon' = \varepsilon'' = 0$. The expression (4) is deduced from the geometric relations displayed in figure 1.

The optic axis ray and one paraxial ray of sloping angle θ_0 are shown, emerging from the field with $\varepsilon = 0$. By rotating the field boundary to the angle ε, the slope is changed to θ. To the first order of approximation,

$$a\,(\theta - \theta_0) = -\,\theta_0\, g_0 \,\tan \varepsilon$$

$$\frac{\theta}{\theta_0\, g_0} = \frac{1}{g} = \frac{1}{g_0} - \frac{1}{a} \tan \varepsilon$$

Thus, parallel to the median plane the field boundary acts as a cylindrical lens of focal distance $-\,a \operatorname{ctan} \varepsilon$.

3. Longitudinal dioptrics of the field boundary

Consider the case of ions in paths parallel to the median or (x, y) plane, emerging from the uniform field between the plane-parallel pole-faces (figure 2 a). In the fringing field the lines of flux will no longer cut the paths at right angles. There will now be an X component, H_X, although the Z component, H_Z, will remain essentially the same (to the second order of z) as in the corresponding points of the median plane. Limiting the attention to paraxial ion optic rays, one finds the component H_X proportional to the distance from the median plane:

$$\mathbf{curl}\ \boldsymbol{H} = 0; \quad H_X \approx z \cdot \frac{\partial H_Z}{\partial x}$$

The component of H_X effective in bending the ray is $H_X \sin \varepsilon$ (figure 2 b), giving a radius of curvature $r = a\,(h_X \sin \varepsilon)^{-1}$, if $h_X = H_X/H_0$, H_0 being the uniform field strength. The angular deflection, Θ_L, of the ray is then

$$\theta_L = \int d\theta_L \approx -\int \frac{dt}{r} \approx -\frac{1}{a} \cdot \int \tan \varepsilon \cdot z\, d h_Z \tag{5}$$

Here t is a curvilinear coordinate of the central ion path.

The falling-off of the field strength occurs mainly in the vicinity of the pole-piece edges. The ion paths are, then, essentially broken at some point near $x = 0$, giving effectively straight lines in the (t, z) surface. The real or virtual intersection of the emerging rays with the median plane will occur at the point F_L, at the track length f_L from the pole-piece edges. Here $h \approx 0$. Thus, when the width of the fringing field may be neglected, one has $\theta_L = z/a \cdot \tan\ \varepsilon$, and

$$f_L = a \cdot \mathrm{ctan}\ \varepsilon. \tag{6}$$

Index L is throughout this paper used to indicate *longitudinal* dioptrics, i.e., *focusing parallel to the flux* of the uniform field.

As the deflection (5) is independent of the slope of the ray but proportional to the heigth z at the field boundary, (6) gives the focal distance of a two-dimensional (cylindrical) lens at the field boundary, acting in a surface perpendicular to the median plane.

4. Two-directional focusing

Two-directional focusing implies the coincidence of the image points of the transverse and the longitudinal dioptric systems. It may be brought about by proper choice of the angles ε', ε'', and Φ. The general expressions of the image positions may easily be derived from the optical constants of (1), (2), and (6), using the conventional methods of geometrical optics. They will not be given here.* In consideration of experimental problems to which two-directional analyzers are to be adapted, the multitude of variations will be restricted by individual specifications. Here only one such class of solutions will be considered,

---

* Recently CAMAC [5] has developed this theory in great detail.

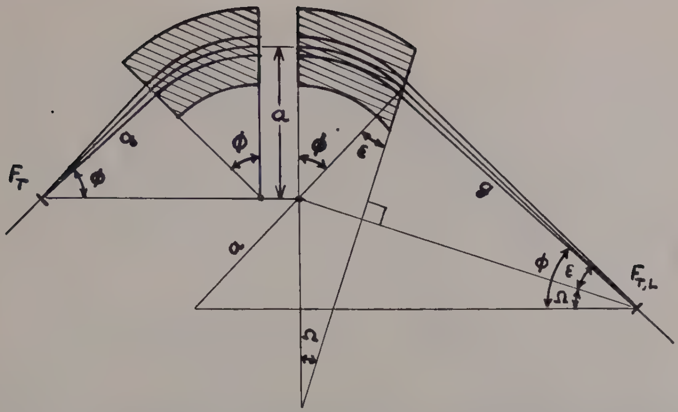

Figure 3. Example of symmetrical focusing analyzers. Left: left half of conventional focusing analyzer. $\Phi = 45°$; $g = a$. Right: right half of two-directional focusing analyzer. $\Phi = 43.54°$; $\varepsilon = 25{,}42°$; $\Omega = 18.12°$; $g = g_L = 2.11\ a$. For second-order focusing, the right boundary of the latter field should be convex, with a radius of curvature equal to $2.33\ a$.

viz., those in which the source and the image coincide, respectively, with the longitudinal foci of the field boundary lenses. In this arrangement the aperture of the longitudinal system is a maximum at any given ε' and gap width. This will be a favourable arrangement for obtaining a maximum ion current at the image (the spectrum).

Consider, first, a field with $\varepsilon' = 0$ and the object at infinity. The condition of two-directional focusing is then:

$$g'' = a \cos \varepsilon'' \cos \Phi \operatorname{cosec} (\Phi - \varepsilon'') = a \operatorname{ctan} \varepsilon'' = f_L'' \tag{7}$$

With the angular deflection Φ fixed, g'' and f_L'' may be changed by varying ε''. As will be seen from (4) and (5), the field boundary is a *negative* lens in *transverse* focusing, when it is a *positive* lens in *longitudinal* focusing, *and vice versa.* A real two-dimensional focus can be obtained, then, only by increasing the deflection Φ or the distance of the focus, g'', as compared to arrangements with $\varepsilon'' = 0$ and mere transverse focusing.

From (7) one obtains the equation

$$\tan \Phi = 2 \tan \varepsilon'' \tag{8}$$

The more general case of focusing with source and image at finite distances, l', l'', is brought back to the one already treated by splitting the field up in two halves of the same character, one with $\varepsilon' = 0$, and the other one with $\varepsilon'' = 0$, having the source in the front and the image in the rear focus, respectively. To each field a condition of the type (8) is applied. The result is:

$$\left.\begin{aligned} &\varepsilon' = \arctan \frac{a}{l'}; \quad \varepsilon'' = \arctan \frac{a}{l''}; \\ &\Phi = \arctan \frac{2a}{l'} + \arctan \frac{2a}{l''} = \arctan \frac{2a\,(l' + l'')}{l'\,l'' - 4a^2} \end{aligned}\right\} \tag{9}$$

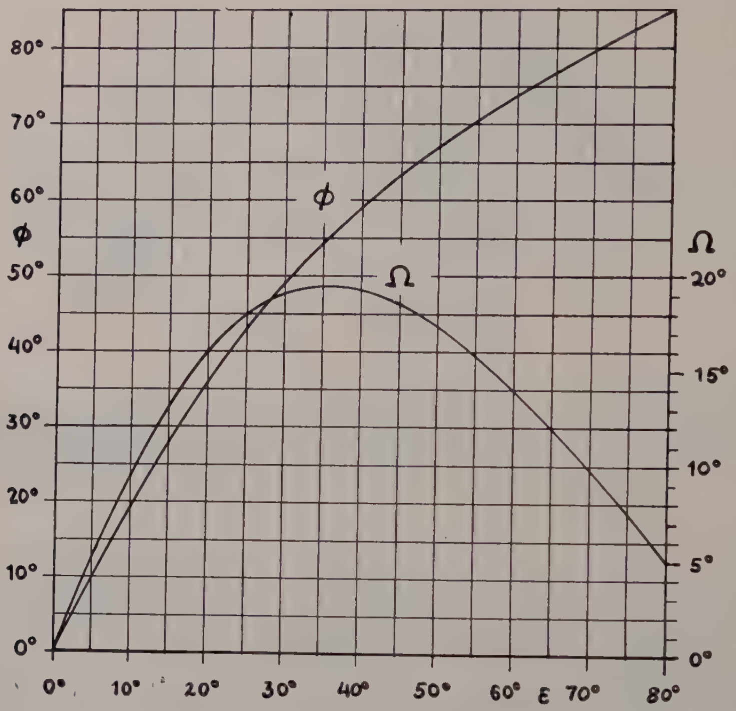

Figure 4. Graph of equation (8).

In figure 3 an example of two-directional focusing is visualized.

The image-to-source scale is different in the directions perpendicular to and parallel to the flux lines:

$$\text{Transverse magnification } V = \left[1 + \left(\frac{l''}{2a}\right)^2\right]^{\frac{1}{2}} \cdot \left[1 + \left(\frac{l'}{2a}\right)^2\right]^{-\frac{1}{2}} \tag{10}$$

$$\text{Longitudinal magnification } V_L = \frac{l''}{l'} \tag{11}$$

When using the magnetic field for focusing inhomogeneous ion beams, the momentum dispersion is of importance. It may be defined as the transverse displacement of the image divided by the fractional change in radius a. Then, according to the HERZOG theory, this dispersion will be:

$$D = a\,(1 + V) \tag{12}$$

If the transverse width of the source is b', then the corresponding width of the image is Vb'. From this, the resolving power due to the finite source (or image) width is found:

$$M = \frac{a}{b''} \cdot (1 + V) = \frac{a}{b'} \cdot \left(1 + \frac{1}{V}\right) \tag{13}$$

In reality, the second-order aberrations due to the finite beam width may limit the resolution (see below).

In order to achieve maximal resolution, according to (13), the magnification V should be small, that is, the source distance l' large. This however makes the longitudinal aperture of the ion lens small, which may reduce the beam current. Therefore a rather small ratio l'/a will usually be chosen, i.e., ε' (and ε'') will be made fairly large. Figure 4 gives a survey of the variations of the angles ε, Φ and Ω, satisfying (8). Ω is the angle between the field boundaries ($\Omega = \Phi - \varepsilon$).

5. Fringing-field effects and second-order aberrations

In order to attain a high intensity in the spectrum of a magnetic analyzer, the magnetic gap width should be made sufficiently large, considering the angular intensity distribution of the ion source. This may give a wide fringing field, making corrections for this advisable. It has been shown [4], that the effects of the fringing field can, for the greater part, be allowed for by displacing the pole-face boundary inwards so as to make the total angular deflexion of the ion beam equal that of the ideal field geometry. Knowing the fringing flux distribution, one can calculate this pole-face boundary displacement, ξ, from

$$\xi(x_F) = \int_0^{x_F} h\,dx - \int_{x(1)}^{0} (1-h)\,dx. \tag{14}$$

x being the perpendicular distance to the pole-face boundary, and $x(1)$ a point near the boundary, having $h \approx 1$.

However, when corrected in this way, the flux distribution will still not be identical with the ideal, with the result that the transverse ion optic image will not coincide with the ideal image. The difference is dependent on the configuration of the magnet and will generally not be known without measurements. It is rather small, of the order of magnitude of the gap width, or less, in conventional shapes of the magnet, being generally quite negligible.

The same may be said about the longitudinal ion optics. In fact, from a more accurate treatment of the integral (5), considering the variations of ε and z in the fringing field, it follows that the bending of the paths in the fringing field is equivalent with breaking them at the distance ξ perpendicular to the pole-face boundaries, i.e., at the point where the equivalent ideal field has its boundary.

Second-order corrections to the theory of transverse focusing in a short magnetic field analyzer have been discussed by PLOCH & WALCHER [6] in the case of $\varepsilon' = \varepsilon'' \approx 0$. Their methods are easily adapted to the present case of arbitrary angles of incidence. If, firstly, only the aberrations due to one field boundary are considered, the following results are found.

1. The θ_L^2-error.

This error is common to all deflecting fields and arises from ion paths near to but inclined to the median plane. In these the velocity component perpendicular to the flux is reduced in the same relation as $\cos \theta_L$, θ_L being the inclination to the median plane (the sign given by figure 2 a):

$$\delta b'' = -\tfrac{1}{2} \cdot (\tfrac{1}{2}\, a\, \Phi^2 + l\, \Phi) \cdot \theta_L{}^2 \tag{15}$$

2. The $z\,\theta_L$-error.

This error is the result of the X component of the fringing flux acting upon the Z component of the ion velocity, causing a transverse bending of the path. As in the case of $\varepsilon = 0$, the $z\,\theta_L$-error is*

$$\delta b'' = \frac{l}{a} \cdot \overline{z\,\theta_L} \tag{16}$$

3. The θ^2-error.

This is the aperture error in the two-dimensional transverse ion optics. It is most readily calculated by using the formulae of HINTENBERGER [7], which give the curvature of an aberration-less field boundary. If the actual boundary is a straight line, and the centre of curvature of the correcting boundary line of radius R_i, is to the inside of the boundary, then non-central ion paths will be longer in the field than is correct for perfect focusing and will acquire too large a deflection. If the boundary be curved to the radius R, then the effect will be modified correspondingly. The resulting shift of the image is:

$$\delta b'' = -\tfrac{1}{2} \sec^3 \varepsilon \cdot \frac{l^3}{a} \cdot \left(\frac{1}{R_i} - \frac{1}{R}\right) \cdot \theta^2 \tag{17}$$

4. The z^2-error.

When the field boundary is curved, the Z component of the flux will be a function of z^2. The variation by z^2 is evaluated by means of the conditions **curl** $\boldsymbol{H} = 0$ and $\Delta \boldsymbol{H} = 0$, with the following result:

$$\delta b'' = -\tfrac{1}{2} \sec \varepsilon \cdot \frac{l}{a\,R} \cdot \overline{z^2} \tag{18}$$

5. The fringing-field errors.

To conclude this listing of second-order effects on the transverse focusing, the image errors due to the fringing field will be calculated.

(a) The $\xi\,\theta_L{}^2$-error.

Due to the longitudinal refraction of paths at the field boundary, the value of $\theta_L{}^2$ in the interior of the field will be different from the mean, $\overline{\theta_L{}^2}$, in the fringing field. In the case when the first-mentioned value is zero, this error will be a maximum:

---

* In equation (21) of reference [6] the equivalent of this equation (16) appears with the wrong sign.

$$\delta b'' = -\tfrac{1}{2}\sec\varepsilon\cdot\frac{\xi}{a}\cdot l\,\overline{\theta_L^2} \tag{19}$$

θ_L being here the slope of the ray *outside* the fringing field.

(b) The $\Psi\,\theta^2$-error.

This error may be evaluated to the first approximation from the focus displacement formulae given in a previous paper [4]. In this the position of the focus relative to the ideal one is given in terms of the angle ε and a quantity $\Psi(x_F, \xi(x_F))$, which is a double integral of the fringing flux distribution between the magnet and the focus:

$$\left.\begin{aligned} x_F - x_{F,i} &= 3\sin\varepsilon\sec^2\varepsilon\cdot\frac{\Psi}{a} \\ y_F - y_{F,i} &= \sec^3\varepsilon\cdot(1-3\sin^2\varepsilon)\cdot\frac{\Psi}{a} \end{aligned}\right\}$$

θ is identical to a variation of ε. Thus by analyzing the locus of the focus at varying ε, the width of the caustic is found:

$$\delta b'' = \tfrac{3}{2}\sec^4\varepsilon\cdot(1+\sin^2\varepsilon)\cdot\frac{\Psi}{a}\cdot\theta^2 \tag{20}$$

By comparison with equation (17) it will be seen, that the fringing flux in this respect is equivalent to curving the straight boundary to the radius

$$R = \tfrac{1}{3}\,l\cdot\frac{\cos\varepsilon}{1+\sin^2\varepsilon}\cdot\frac{l^2}{\Psi}$$

This radius is large in the same ratio to l, as l^2 to Ψ.

In conventional magnet design, the fringing field effects on the second-order focusing errors usually are negligible.

6. Elimination of the second-order aberrations

In the case of two-directional focusing in points of the optic axis, the aberrations are only aperture errors. Thus they can all be given in terms of θ and θ_L. When considering the specialized conditions (9), the treatment of these second-order errors becomes simple.

The θ_L^2-error (15) vanishes, because in the uniform field $\theta_L = 0$. In (16), (18), and (19), $\bar{z} = l\,\theta_L$, $\overline{\theta_L} \approx \tfrac{1}{2}\,\theta_L$, and $\overline{\theta_L^2} \approx \tfrac{1}{3}\,\theta_L^2$. In (17) the HINTENBERGER radius for conditions (9) is given by

$$\frac{a}{R_i} = 4\tan^3\varepsilon$$

As ξ is usually small in relation to l, and Ψ small in relation to l^2, the fringing field terms (19) and (20) can be left out of consideration. The aperture error in the median plane becomes then:

$$\delta b'' = \tfrac{1}{2} \operatorname{ctan}^2 \varepsilon \cdot \left(1 - \operatorname{cosec} \varepsilon \cdot \frac{a}{R}\right) a\, \theta_L{}^2 - 2 \sec^3 \varepsilon \cdot \left(1 - \tfrac{1}{4} \operatorname{ctan}^3 \varepsilon \cdot \frac{a}{R}\right) a\, \theta^2 \qquad (21)$$

This whole second-order error vanishes if simultaneously

$$\frac{a}{R} = \sin \varepsilon, \text{ and } \frac{a}{R} = 4 \tan^3 \varepsilon \qquad (22)$$

This determines $\varepsilon = 25.42°$, thus $\Phi = 43.54°$, the geometry of which appears at the right of figure 3. The correcting radius of curvature (not shown) is $R = a \operatorname{cosec} \varepsilon = 2.33\, a$.

7. The gain of intensity

The question as to which factors determine the gain of image intensity attainable through application of two-directional focusing of the kind considered in the preceding sections, will now be studied in a specific case.

Consider a conventional magnetic analyzer, e.g., the field of PLOCH & WALCHER [6]: field A. It is symmetrical and has the total angle of deflection $2\,\Phi = 90°$, with $\varepsilon = 0$ and the radius $a = 25$ cm. The source and image distances are equal to a. The corresponding two-directionally focusing analyzer, field B, is symmetrical, too, and has the same deflection and the same radius. ε is determined by (9) as 26.56°, and the image distance is equal to $2\,a$. The source and image slits are taken to be of the same length, c, and the angular spread of the ion beam at the source is θ_0.

A rough estimate of the gain in integral image current may be had by supposing the current density uniform in the cone of aperture $2\,\theta_0$. In the B field the total object current is focused into the image slit (if the optic aberrations may be neglected), but in the A field only the fraction

$$\frac{c}{4\,(1 + \Phi)\,\theta_0} = \frac{c}{7.14\,\theta_0} \qquad (26)$$

is collected. Thus, if the image errors are of a magnitude not in any way affecting the resolution, then the introduction of two-directional focusing will result in an increase of integral image current which will be larger the smaller the length of the image slit. The gain in current density at the image is simply proportional to the angular spread θ_0 at the source.

This result, however, no longer holds when θ_0 must be limited with regard to the resolving power. The transverse aberrations at the image are the sum of equal errors due to each boundary or half-field, as calculated in section 5. If the field boundaries are taken as straight, the image broadening becomes in the A field:

$$\Delta b''_A = a\,\theta_0^2 + \frac{\frac{1}{2}\,a\,\Phi^2 + 3\,a\,\Phi}{4\,(1+\Phi)^2}\left(\frac{c}{a}\right)^2 = a\,\theta_0^2 + 0.21\left(\frac{c}{a}\right)^2 \tag{24}$$

and in the B field:

$$\Delta b''_B = (\text{ctan}^2\,\varepsilon + 4\,\sec^3\,\varepsilon)\;a\,\theta_0^2 + \tfrac{1}{2}\,\text{ctan}\,\varepsilon\cdot a\,\theta_0\cdot\frac{c}{a} + \tfrac{1}{4}\,(\tfrac{1}{2}\,a\,\Phi^2 + 2\,a\,\Phi)\left(\frac{c}{a}\right)^2 =$$

$$= 9.6\,a\,\theta_0^2 + a\,\theta_0\,\frac{c}{a} + 0.47\left(\frac{c}{a}\right)^2 \tag{25}$$

The consequence of introducing longitudinal focusing is a considerable enlargement of the aberrations, particularly the aperture errors. This fact is due to the occurrence of the factor $\sec^3\varepsilon$ in the transverse-aperture error, and the factor $\text{ctan}^2\,\varepsilon$ in the longitudinal-aperture error, which is an $z\,\theta_L$-error. If the desired resolution is found to be limited by the second-order aberrations, the longitudinally focusing field will have to work with reduced beam widths, and there will be hardly any gain of image current. Inserting typical values of $c = 1$ cm and $\theta_0 = 0.02$ rad., we find:

$$\Delta b''_A = 0.018 \text{ cm},\; M_A \leq 2\,800; \quad \Delta b''_B = 0.135 \text{ cm},\; M_B \leq 370;$$

$$\text{solid angles: } \omega_A = 1.12\cdot 10^{-4} \text{ sterad.},\; \omega_B = 16\cdot 10^{-4} \text{ sterad}$$

In the case of mass spectrometry of the heavy elements, this two-directionally focusing analyzer has a rather low resolving power, and it is expected that the adoption of longitudinal field boundary focusing to such work will entrain the elimination of the second-order aberrations at the optic axis, by choosing the conditions of equation (22). This arrangement is rather similar to the field B of this section, the angles differing by amounts of about one degree only.

The remaining errors will then be the extended-image aberrations, the fringing field aberrations, and those of degree higher than the second. The first-mentioned are, to the second order

$$\Delta b''_A = 0.21\cdot a\left(\frac{c}{a}\right)^2$$

$$\Delta b''_B = a\,\theta_0\cdot\frac{c}{a} + 0.47\,a\left(\frac{c}{a}\right)^2$$

Numerically we find $\Delta b''_A = 0.008$ cm, $M_A \leq 6\,000$, $\Delta b''_B = 0.04$ cm, and $M_B \leq$ $\leq 1\,300$, which appears sufficient to many purposes.

If long source or image slits can be used, as often is the case with mass spectroscopes using electrometric measuring of the focused ion current, then the gain of current will be rather small, and the chief advantage of two-directional focusing may be the elimination of the mass discrimination occurring when the mass spectrum is recorded by varying the accelerating voltage. In application of detecting methods where the current density is of importance as in the case photographic recording, however, the gain of intensity will be large and advantageous.

Finally the effects of the fringing flux will now be stated in short, adopting the measurements on the analyzer of PLOCH & WALCHER [6]. From their paper, the values of ξ and Ψ may be estimated as 1.35 cm and 1.8 cm^2, respectively (the gap = 2 cm). Thus:

1) proper displacement of pole-face boundary: $\xi = 1.35$ cm.
2) transverse displacement of beam at image: $\sec \varepsilon^3 \cdot \Psi/a = 0.09$ cm.
3) displacement of transverse image: $x_F - x_{F,i} = 0.135$ cm.
4) $\xi \theta_L^2$-error: $\frac{1}{2} \sec \varepsilon \cdot \frac{\xi}{a} \overline{l \theta_L^2} \approx \frac{1}{6} \operatorname{cosec} \varepsilon \cdot \xi \theta_0^2 = 0.0002$ cm.
5) $\Psi \theta^2$-error: 0.00003 cm.

8. Summary of results

1. The boundaries of the short uniform magnetic analyzing fields act upon ion beams as lenses with focal distances different to the pencils of rays *transverse* to and *longitudinal* to the main *magnetic flux.*

2. These focal distances are, practically, determined exclusively by the radius of curvature (a) in the uniform field, and by the angle of incidence (ε) of the beam, but independent of the pole-piece spacing and the fringing flux distribution of conventional magnet designs: $f = -a \operatorname{ctan} \varepsilon$; $f_L = a \operatorname{ctan} \varepsilon$, respectively, the sign of ε being positive if the center of curvature is located to the inside of the tangent of the field boundary.

3. The principal points of these lenses are close to the mouth of the magnetic gap, or the effective boundary of the uniform field.

4. Analyzers giving two-directional focusing at specified object and image distances (l', l'') may be constructed according to the formula (9). In these the ion paths corresponding to the axis points of the object and image are parallel to the pole-faces of the magnet, and the longitudinal aperture is a maximum at given radius a and magnetic gap width.

5. The transverse second-order image errors in axis points of the two-directionally focusing fields may be made to disappear through a specific choice of the angle of deflection (close to 90°) and giving the boundaries of the field the proper curvature.

6. The fringing field part of second-order image errors is negligible.

7. The introduction of the longitudinal focusing effects considered, will increase the second-order aberrations and will result in a gain of intensity of magnetic spectra only if the image errors, at the angular spread of the ion beam given, are far from interfering with the desired spectral resolution. This gain will be larger the greater the angular spread.

9. Discussion

Recently the properties of non-uniform sector fields have been investigated and the conditions of two-directional focusing worked out [8]. Although these methods appear to be much more powerful than the present one, there are some features to the credit of the latter. The correct shaping of the pole-faces necessary in order to obtain the desired flux distribution is not easy and may require controlling by flux measurements with subsequent reworking. In contrast herewith, the uniform field presents no problems for the designer and the workshop, and the shaping of the pole-piece ends to the desired angles and curvature should become a rather simple matter, if the ends of the pole-pieces are designed as separate plates, which if necessary can be removed for reshaping without diassembling the spectrometer proper. If no stress is laid upon second-order focusing, the use of a cylindrical magnet will allow the conditions of two-directional focusing to be attained by experimental adjustment of the spectrometer tube alone (cf. [1]).

Fysiska Institutionen, Uppsala Universitet, May, 1951.

REFERENCES. [1] **Koch,** Diss., p. 72 (Copenhagen, 1942). — [2] **Stephens,** 1934, Phys. Rev., *45*, 513. — [3] **Herzog,** 1934, Z. Physik, *89*, 447. — [4] **Reuterswärd,** 1951, Arkiv f. Fysik, *3*, 53. — [5] **Camac,** 1951, Rev. Sc. Instr., *22*, 197. — [6] **Ploch & Walcher,** 1950, Z. Physik, *127*, 274. — [7] **Hintenberger,** 1949, Rev. Sc. Instr., *20*, 748. — [8] **Svartholm,** 1950, Arkiv f. Fysik, *2*, 115. — **Judd,** 1950, Rev. Sc. Instr., *21*, 213. — **Rosenblum,** 1950, Rev. Sc. Instr., *21*, 586. — [9] **Sturrock,** 1951, Proc. Phys. Soc. London, *63*, 954. — [10] **Glaser,** 1950, Öst. Ingen. Arch., *4*, 354.

Tryckt den 10 december 1951

Uppsala 1951. Almqvist & Wiksells Boktryckeri AB

ARKIV FÖR FYSIK Band 4 nr 4

Read 6 June 1951

Calorimetric study of the precipitation of carbon dissolved in α-iron

By G. Borelius and Stig Berglund

With 6 figures in the text

1. Summary

Specimens of technically pure iron with small carbon contents have first been heated at various temperatures between 350 and 700 °C in order to obtain the corresponding equilibrium between carbon in solution in α-Fe and in cementite Fe_3C, and they have then been quenched to 0 °C and aged at temperatures between 80 and 130 °C. During ageing, the power of the heat evolved by precipitation of carbon as carbide has been measured as a function of time, and by integrating the power-time curves, the total amounts of heat have been computed. From this heat and its dependence on temperature, thermodynamic calculations have given the heat of solution per mol and the solubilities of carbon at various temperatures.

2. Experimental method

The experimental method has been the same as that used in a recently published investigation on the precipitation of nitrogen dissolved in α-iron (1). The specimens were cylinders with a diameter of 18 mm and a height of 50 mm. They were put in from above into a well-fitting glass tube placed in the centre of a vapour thermostat with an inner diameter of 50 mm. For temperatures from 60 to 100 °C a thermostat was used with water boiling at various suitable pressures, and for temperatures above 100 °C a brombenzene thermostat was employed. In order to obtain a very constant temperature the same precautions were taken as described in the earlier paper. Between the glass tube, just outside the specimen, and the wall of the thermostat, were arranged a number of copper-constantan thermocouples in series, with odd junctions near the glass tube and even junctions near the wall. These thermocouples were connected over a commutator to a galvanometer. The galvanometer deflection was then proportional to the temperature difference between the specimen and the thermostat, and under usual circumstances proportional to the power of heat evolved in the specimen. Absolute values were obtained by calibration by means of Peltier heat evolved in a junction of a Pt-PtRh thermocouple put into a central boring in the specimen. In the water thermostat the arrangement

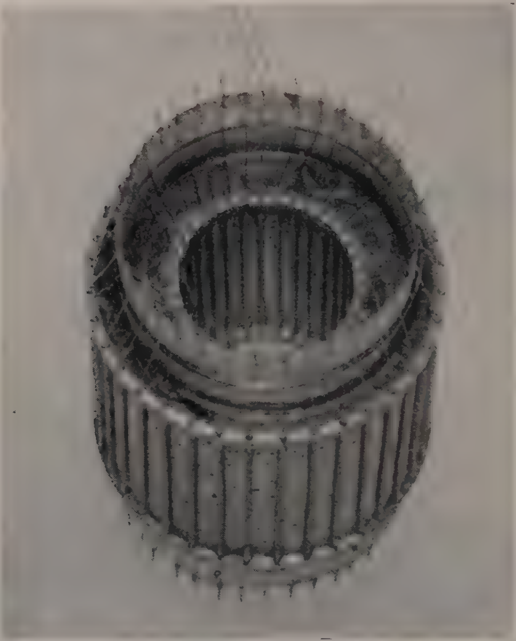

Fig. 1. Arrangement of thermocouples.

of the thermocouples between the glass tube and the wall of the thermostat was exactly the same as described earlier (1). In the brombenzene thermostat we used an improved arrangement shown in fig. 1. It consists of two thin cylinders of aluminium kept together by rings of mica. Thirty capillary tubes of steatite, in which the thermocouples were threaded with their junctions halfway between the ends, were mounted on the inside of this inner cylinder and thirty also on the outside of the outer one. The whole arrangement had a weight of only 20 grams and thus a very small heat capacity.

3. The specimens and their heat treatment

The total carbon content and other impurities of the specimens used are shown in table 1. The contents of nitrogen were determined from our own measurements as described later. Specimens 3, 4, 5, and 7 were taken directly from three bars of pure technical iron from Sandvikens Jernverks A. B., placed to our disposal by Mr. Torkel Berglund. No. 11 had been heat-treated in dry hydrogen at 585 °C in order to reduce the nitrogen content. No. 12 had been treated for some time in moist hydrogen at 720 °C in order to lower the carbon content as well. In this case, also, the remaining carbon was determined by our own measurements.

Before each measurement, the specimen was heated for half an hour at 718 °C and slowly cooled to the test temperature, where it was kept from one day to the next, or about 16 hours, in order to obtain equilibrium of solution.

Table 1.

Specimen No.	Weight % of					
	C	Si	Mn	P	S	N
3	0.070	0.18	0.15	0.004	0.007	0.003
4	0.070	0.18	0.15	0.004	0.007	0.003
5	0.024	0.06	0.11	0.007	0.007	0.003
7	0.017	0.01	0.07	0.002	0.007	0.003
11	0.017	0.01	0.07	0.002	0.007	<0.002
12	0.006	0.01	0.07	0.002	0.007	<0.002

It was then quenched in icecooled water and rapidly, in a few minutes, heated in an oven, the temperature of which was about 300 °C, up to the temperature of the thermostat, the temperature of the specimen being controlled by means of the thermocouple placed in its central hole. The moment the specimen passed the temperature of the thermostat (80, 100 or 130°) it was quickly put into the glass tube in the thermostat and the readings were started.

In order to increase the rate of quenching we made six broad cuts in specimen No. 3 to a depth of 5 mm, and we made eight borings with a diameter of 3 mm in specimens No. 11 and No. 12 about halfway between the outer surface and the central hole. The results for these specimens, however, do not show any difference from the results obtained with the other specimens.

4. The measurements

The procedure of the measurements and corrections were the same as described in the earlier paper already referred to (1).

Before making the final measurements giving the results collected in table 2, we had to make many trials in order to find out the most suitable temperature for the different contents of carbon in solution. From these preliminary runs, fig. 2 shows three curves for specimen No. 3, pre-heated at about 700 °C and measured at about 60, 70 and 80 °C. This figure shows the dependence of the rate of evolution of heat on the temperature. The integrated areas, i.e. the total amount of heat evolved, is about the same for the three curves. 80 °C appeared to be a suitable temperature for the measurements in this case. For specimens heat-treated at lower temperatures and thus containing less carbon in solution, it was convenient to choose a higher measuring temperature, 100 or 130 °C.

The disturbances from the evolution of heat due to precipitation of dissolved nitrogen were small and could be separated from the heat due to carbon by suitable choice of measuring temperature. Fig. 3 shows an example from a preliminary run with specimens No 7, pre-heated at 452 °C and measured at 80 °C. In this case the nitrogen is precipitated during the first few hours, whereas the carbon precipitates much more slowly during a few days. From such measurements and from the knowledge of the heat of solution of nitrogen from the previously published investigation, the content of nitrogen in the specimen could be determined.

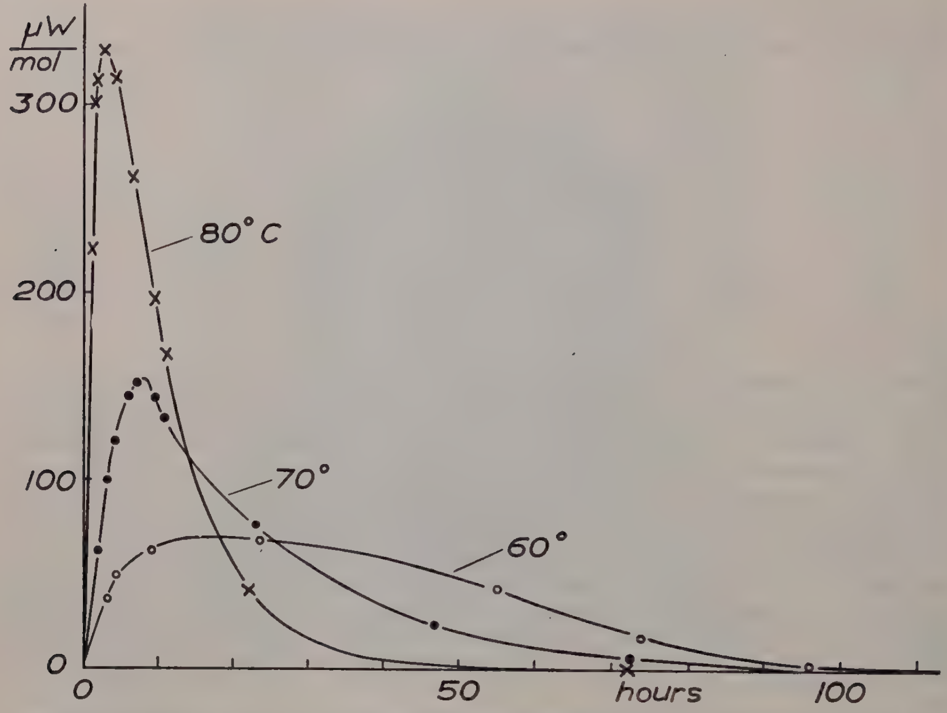

Fig. 2. Evolution of heat at 60, 70 and 80 °C in a specimen quenched from 700 °C.

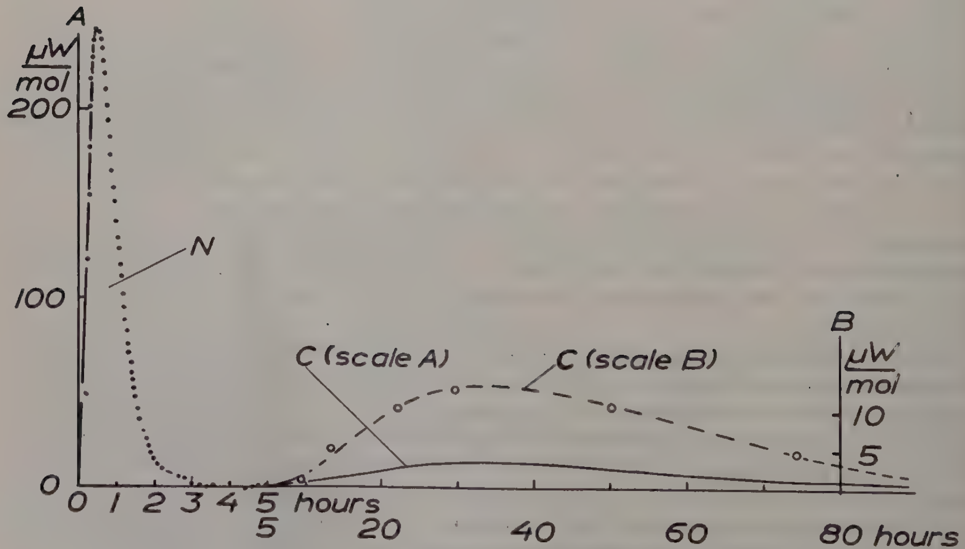

Fig. 3. Precipitation of nitrogen and carbon in the same specimen.

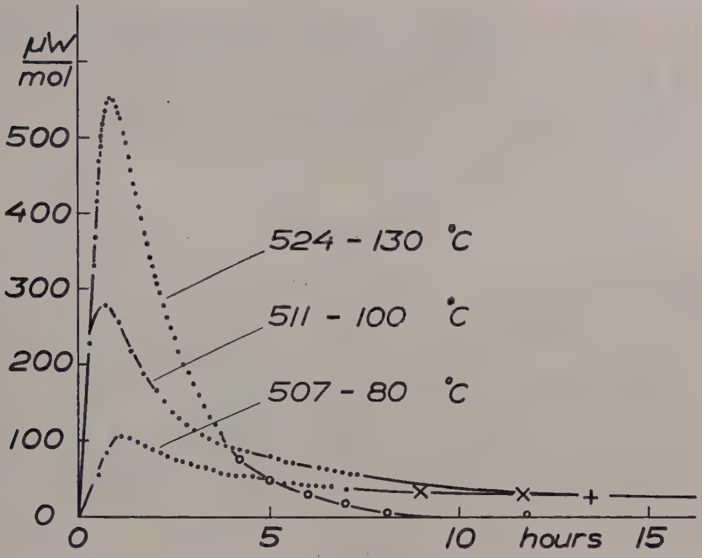

Fig. 4. Three examples of the power-time curves. Measured at 80, 100 and 130 °C.

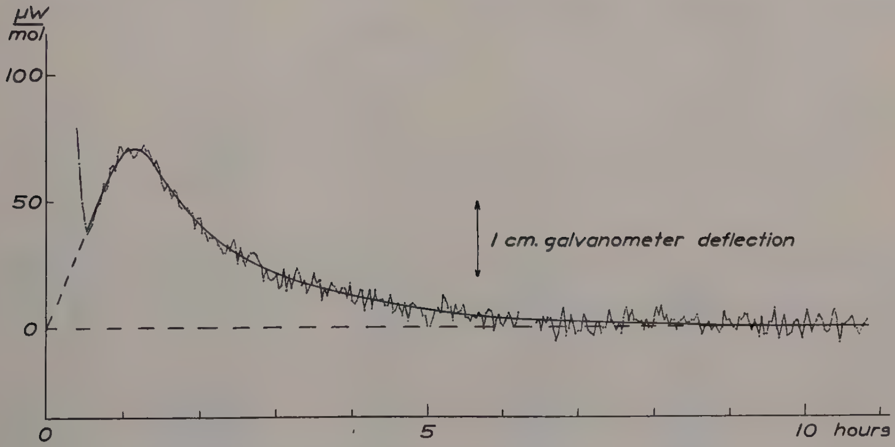

Fig. 5. An experimental power-time curve for a very small evolution of heat. Precipitation at 130 °C after quenching from 348 °C.

Fig. 4 shows three examples from the final runs (see table 2), where the specimens were pre-heated at temperatures somewhat above 500 °C and measured at 80, 100 and 130 °C.

Fig. 5 gives an idea of the present limits of the experimental possibilities of the calorimetric method. Specimen No. 7 had been heated at 348 °C and measured during ageing at 130 °C, where the precipitation is completed in one day. Whereas in the other figures the points are often mean values of measurements during a suitable time, all observed points are given in this figure.

There is also shown the constant deflection depending on non-compensated e.m.f.:s in the galvanometer circuit. This quantity is already substracted from the curves on figs. 2–4. The total amount of heat is obtained by integration as 0.59 Ws/mol and this means that if the specimen had been kept fully thermally insulated during the precipitation, the total increase of temperature would only have been 0.02 °C.

5. Results

The final results are given in table 2. The four first columns of this table give in order: the number of the specimens, the measuring temperatures which were 80, 100 or 130 °C within ± 0.1 °C, the temperatures of preceding heat-treatment, and the total amounts of heat Q, which are obtained by integration of the experimental power-time curves and are given in Ws per gram atom of Fe in the specimen. From these Q-values the corresponding values of the solubility of carbon have been derived under the following assumptions: 1:o, that no dissolved carbon has precipitated during quenching; 2:o, that the

Table 2.

Specimen No.	Measuring temperature °C	Equilibrium temperature °C	Q Ws/mol	$z = \frac{Q}{L} = \frac{C}{Fe}$	Weight % C
3	80	695	19.3	0.000383	0.0082
3	80	703	23.5	0.000467	0.0100
5	80	711	17.8	0.000353	0.0076
7	80	701	19.2	0.000381	0.0082
7	80	680	17.8	0.000353	0.0076
3	80	599	11.2	0.000222	0.0048
5	80	601	9.4	0.000187	0.0040
7	80	605	11.7	0.000232	0.0050
11	100	622	10.6	0.000211	0.0045
3	100	511	4.93	0.000098	0.0021
5	80	507	3.53	0.000070	0.0015
7	80	512	5.84	0.000116	0.0025
7	130	524	4.74	0.000095	0.0020
11	100	506	3.95	0.000077	0.0017
11	100	530	4.46	0.000089	0.0019
3	100	437	2.84	0.000057	0.00123
4	130	421	1.00	0.000020	0.00043
5	130	448	2.29	0.000046	0.00099
7	80	454	2.31	0.000017	0.00037
7	130	413	0.98	0.000020	0.00043
11	100	444	1.32	0.000026	0.00056
4	130	350	0.36	0.000007	0.00015
5	130	344	0.52	0.000010	0.00022
7	130	348	0.59	0.000012	0.00026
12	130	352	0.59	0.000012	0.00026

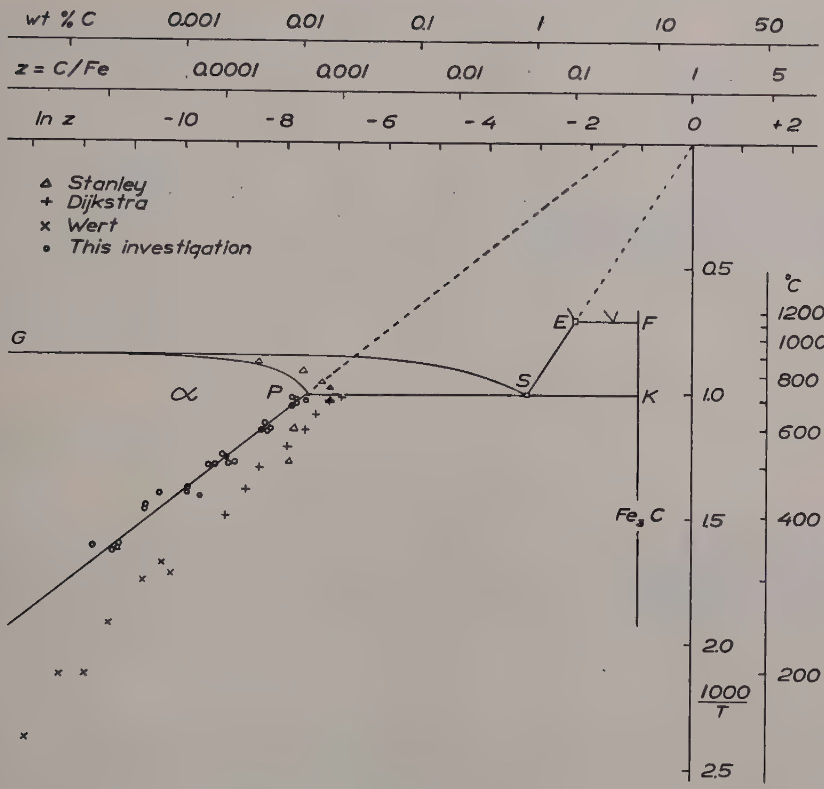

Fig. 6. Part of the logarithmic equilibrium diagram Fe — C.

observed evolution of heat leads to equilibrium at the measuring temperature, which means that the carbon still in solution should be less than 10^{-5} weight percent and thus negligible; 3:o, that the heat of solution at 80, 100 and 130 °C does not appreciably differ from a mean value which we will denote as L_{100} Ws per gram atom C; 4:o, that this heat of solution is independent of the concentration of C at the small concentrations concerned. Under these assumptions the atomic ratio z of C to Fe is obtained by dividing the Q-values by L_{100}, that is

$$z = \frac{\mathrm{C}}{\mathrm{Fe}} = \frac{Q}{L_{100}}. \tag{1}$$

Using the value $L_{100} = 50200$ Ws/mol, which is obtained from the thermodynamic discussion in the following section, we obtain the values of z in the table, which in turn allow the calculation of the weight percentage of dissolved carbon given in the last column of the table.

The results are shown in the logarithmic equilibrium diagram of fig. 6, in which the temperature scale is proportional to $1/T$ and the concentration scale to ln C/Fe. In this diagram the solubility line for small concentrations is approximately a straight line. In the diagram are also included some of the other boundary lines of the system FeC as well as results on the solubility of C in α-Fe obtained by the damping method by DIJKSTRA (2) and WERT (3) and by a diffusion method by STANLEY (4). The discrepancy of our results with the results of these authors is outside the limits of the accidental errors of our measurements, and there must be some methodical error in the way of measuring or computing the solubility either in our investigation or in the earlier ones. Our measurements are within the limits of accidental errors described by the empirical formula

$$\ln z = -6\,300 \frac{1}{T} - 1.3 \tag{2}$$

where z is the atomic ratio C/Fe.

6. Thermodynamic discussion

The equilibrium of solubility at constant pressure and temperature is obtained by minimising the Gibbs thermodynamic potential G. In a solid, the influence of ordinary atmospheric pressure is negligible and G may be approximately replaced by the free energy F

$$G = F = U - T S \tag{3}$$

where U is the internal energy, and S the entropy per gram molecule, and T is the absolute temperature. The condition for G being a minimum gives

$$\left(\frac{\partial U}{\partial x}\right)_T - T \left(\frac{\partial S}{\partial x}\right)_T = 0. \tag{4}$$

If x is the fraction of a mol of C in solution in one mol of Fe + C, the first term is the heat of solution per mol

$$\left(\frac{\partial U}{\partial x}\right)_T = L. \tag{5}$$

In the second term $\partial S / \partial x$ is partly due to the increase of the energy arising from the disordered distribution of the carbon atoms on the available sites in the Fe lattice. For this part of the increase of S statistical mechanics give the value $-R \ln z$, where R is the gas constant and $z = x : (1 - x)$ is the ratio of C to Fe. Besides this part there are, however, also other parts depending on thermal vibrations, the distribution of electron spin directions, etc., which, as recently emphasized by ZENER (5), though generally small, in some cases may be appreciable. If we denote this part $\varDelta S$, we have

$$\left(\frac{\partial S}{\partial x}\right)_T = -R \ln z + \varDelta S. \tag{6}$$

Inserting (5) and (6) in (4) we obtain

$$\ln z = -\frac{L}{R} \cdot \frac{1}{T} + \frac{\Delta S}{R} \tag{7}$$

L/R can be determined from our measurements as the slope of the empirical curve in a $\ln Q$–$1/T$ diagram. As Q, according to eq. (1), differs from z only by a constant factor, the $\ln Q$–$1/T$ diagram differs from the solubility line of fig. 6 only by a parallel displacement in the direction of the $\ln z$ axis. The empirical points are compatible with a straight line described by eq. (2) and giving the slope 6300 at a mean temperature of 500 °C. We thus obtain the heat of solution at 500 °C.

$$L_{500} = 6\,300\ R = 52\,400\ \text{Ws/mol}. \tag{8}$$

The equilibrium we have to consider in our case is that of

$$3\ \text{Fe} + \text{C} = \text{Fe}_3\text{C} \tag{9}$$

where C is carbon dissolved in Fe. The case is complicated by the fact that the α-iron and the carbide (cementite), are ferromagnetic, which means anomalies in the specific heat and consequently in the internal energy and entropy below the Curie point. We denote by ΔC the difference in molar heat between 3 Fe and C in dilute solution on one side and F_3C on the other, so that

$$\Delta C = 3\,C_{\text{Fe}} + C_{\text{C}} - C_{\text{Fe}_3\text{C}}. \tag{10}$$

In the range of temperature considered, the specific heat of α-Fe is known from several measurements; we have used the values selected by AUSTIN (6). The specific heat of the carbide is determined by NAESER (7). The atomic heat of carbon dissolved in iron is unknown. For a rough orientation we have assumed for C_{C} the Dulong-Petit value $C_{\text{C}} = 3\,R$. The values of ΔC thus computed, with the gas constant R as unit, are

for	100	190	300	500	700	760 °C
$\Delta C/R$	-0.9	-2.6	0.9	2.6	8.0	15.6

with a minimum approximately at the Curie point of Fe_3C (190 °C) and a maximum at the Curie point of Fe (768 °C). We are thus able to calculate the heat of solution at 100 °C (L_{100}) from the empirical value $L_{500} = 6\,300\ R$ at 500 °C and obtain

$$L_{100} = L_{500} - \int_{100}^{500} \Delta C\, dt = 6\,300\ R - 260\ R \tag{11}$$

or $L_{100} = 50200$ Ws/mol, which was the value used for the calculation of the solubilities in table 2. We learn from this calculation that the correction, which is of course rather uncertain, is small and within the experimental uncertainty of the determination of L_{500} itself.

With certain assumptions we are also able to calculate from the ΔC values the entropy difference ΔS occurring in eqs. (6) and (7), the empirical value of which can be obtained from a comparison of the empirical formula (2) and eq. (7) as.

$$\Delta S = -1.3\,R. \tag{12}$$

The fact that ΔS seems to be small or zero for solutions of carbon in γ-iron (the extrapolation of the solubility line SE in the logarithmic equilibrium diagram of fig. 6 points to the origin) makes it the more probable that the appreciable value of ΔS for solutions of C in α-Fe is due to the ferromagnetic anomalies. It is then near at hand to assume that ΔS should be zero at and above the Curie point at 768 °C (1041 °K). This would give for the temperature 500 °C (773 °K)

$$\Delta S = \int_{1041}^{773} \frac{\Delta C}{T}\,d\,T = -1.5\,R \tag{13}$$

in fairly good agreement with the empirical value $-1.3\,R$.

The investigation has been supported by a grant from the Swedish Council for Technical Research.

Stockholm, Royal Institute of Technology, Department of Physics.

LITERATURE: (1) **G. Borelius, S. Berglund** and **O. Avsan,** Arkiv f. fysik *2* (1950—51) 551. — (2) **L. J. Dijkstra,** Journal of Metals *1* (1949) 252. — (3) **C. A. Wert,** Journal of Metals *188* (1950) 1242. — (4) **J. K. Stanley,** Journal of Metals *1* (1949) 752. — (5) **C. Zener,** Thermodynamics in Physical Metallurgy, Amer. Soc. for Metals, Cleveland, Ohio (1950). — (6) **J. B. Austin,** Journ. Ind. Eng. Chemistry *24* (1932) 1225. — (7) **G. Naeser,** Mitt. Kais. Wilh.-Inst. f. Eisenf. *16* (1934) 207.

Tryckt den 6 december 1951

Uppsala 1951. Almqvist & Wiksells Boktryckeri AB

ARKIV FÖR FYSIK Band 4 nr 5

Read 7 June 1950

On neutron diffraction phenomena according to the kinematical theory. I

By I. Waller and P. O. Fröman

With 1 figure in the text

The purpose of the present paper is to give for single crystals some furthee discussion of the diffuse temperature scattering of slow neutrons, when th- Laue interference condition is approximately satisfied. Some interesting qualir tative results have already been given by Seeger and Teller.[1] We think it, however, worth while to give the basis of a quantitative theoretical treatment of the problem. The methods used are similar to those in the corresponding theory for the X-ray case which was developed by one of us.[2] This theory has been verified by experiments. For neutrons we do not take into account the influence of spin dependent interactions with the nuclei which in principle involves only a minor change. We shall return to this question and more complete calculations in another paper. For the notations and for the derivation of our starting formula we refer to part II of this paper.[3]

The main terms (i.e., those of "zero" order) are similar to those occurring in the X-ray case. They lead to the sharp interference points. In the immediate neighbourhood of such points, there is a diffuse temperature scattering, the main part of which is due to the first order terms.[4] The contribution from these terms to the differential scattering cross section can be written as[5]

$$\sigma_1(\boldsymbol{k}, \boldsymbol{K}) = \sum_{\boldsymbol{\tau}} \sum_{\boldsymbol{\varkappa}} \sum_{j} \sum_{\varepsilon} \frac{k'}{k} \sum_{pp'} f_p^* f_{p'} \, e^{i(\boldsymbol{k}'-\boldsymbol{k}) \cdot (\boldsymbol{R}_p - \boldsymbol{R}_{p'})} \, e^{-M_p(\boldsymbol{k}'-\boldsymbol{k})} \, e^{-M_{p'}(\boldsymbol{k}'-\boldsymbol{k})} \, \cdot$$

$$\cdot \tfrac{1}{2} [(\boldsymbol{k}' - \boldsymbol{k}) \cdot \boldsymbol{C}_{p\boldsymbol{\varkappa}j}] [(\boldsymbol{k}' - \boldsymbol{k}) \cdot \boldsymbol{C}^*_{p'\boldsymbol{\varkappa}j}] \tfrac{1}{2} \left(g(\omega_{\boldsymbol{\varkappa}j}) + \frac{\varepsilon \hbar}{2\,\omega_{\boldsymbol{\varkappa}j}} \right) 8\pi^3 N \delta_\Omega(\boldsymbol{X}), \quad (1)$$

where the components of $\boldsymbol{X}$ are

$$X_i = (\boldsymbol{k}' - \boldsymbol{k} - 2\pi\boldsymbol{\tau} - \boldsymbol{\varkappa}) \cdot \boldsymbol{a}_i, \qquad i = 1, 2, 3,$$

---

[1] R. J. Seeger and E. Teller, Phys. Rev. 62, 37 (1942).

[2] I. Waller, Interferenz- und Dispersionstheorie der Röntgenstrahlen (Uppsala 1925).

[3] P. O. Fröman, Arkiv för Fysik, Band 3 nr 10.

[4] For the X-ray case the terms of second and higher orders have been estimated by Waller (l.c.).

[5] Fröman (l.c.), eq. (20). We have changed the sign in the definition of $\boldsymbol{\varkappa}$.

and N is the number of unit cells in the crystal.[1] The function $\delta_\Omega(\boldsymbol{X})$ depends on the form, Ω, of the crystal, but it has the character of a δ-function. $\boldsymbol{k}$ is the wave vector of the incident neutron. The summations extend over those $\varkappa$, j, ε that make the wave vector $\boldsymbol{k}'$ of the scattered neutron real. We have

$$\boldsymbol{k}' = \sqrt{1 - \frac{\varepsilon \hbar \omega_{\varkappa j}}{E}}\, \boldsymbol{K}, \tag{2}$$

$\boldsymbol{K}$ being a vector in the direction of scattering having the same length as $\boldsymbol{k}$.

We obtain the formula valid for the X-ray case by neglecting $\frac{\hbar \omega_{\varkappa j}}{E}$ in comparison to 1. For X-rays therefore $\boldsymbol{k}' = \boldsymbol{K}$.

In (1) we replace the sum over $\varkappa$ by an integral and then change to an integration over the $\boldsymbol{X}$-space. We have, then, to multiply by the Jacobian $\frac{1}{|J|}$, where[2]

$$J = -\frac{d(X_1, X_2, X_3)}{d(\varphi, \psi, \chi)} = 1 + \varepsilon \frac{\boldsymbol{K}}{k'} \cdot \frac{\boldsymbol{c}_{gj}}{v}, \tag{3}$$

$v = \frac{\hbar k}{\mu}$ being the velocity of the incident neutron and $\boldsymbol{c}_{gj} = \operatorname{grad}_{\varkappa} \omega_{\varkappa j}$ being the group velocity of the elastic wave corresponding to $(\varkappa, j)$. Choosing a special $\boldsymbol{\tau}$ we find

$$\begin{aligned} \sigma_1(\boldsymbol{k}, \boldsymbol{K}) = N^2 & \sum_{\substack{\varkappa j \varepsilon \\ (\boldsymbol{k}' - \boldsymbol{k} - 2\pi\boldsymbol{\tau} - \boldsymbol{\varkappa} = 0)}} \frac{k'}{k} \sum_{p p'} f_p^* f_{p'}\, e^{i(2\pi\boldsymbol{\tau} + \boldsymbol{\varkappa}) \cdot (\boldsymbol{R}_p - \boldsymbol{R}_{p'})} \cdot \\ & \cdot e^{-M_p(2\pi\boldsymbol{\tau} + \boldsymbol{\varkappa})}\, e^{-M_{p'}(2\pi\boldsymbol{\tau} + \boldsymbol{\varkappa})}\, \tfrac{1}{2} [(2\pi\boldsymbol{\tau} + \boldsymbol{\varkappa}) \cdot \boldsymbol{C}_{p\varkappa j}] [(2\pi\boldsymbol{\tau} + \boldsymbol{\varkappa}) \cdot \boldsymbol{C}^*_{p'\varkappa j}] \cdot \\ & \qquad \cdot \tfrac{1}{2} \left(g(\omega_{\varkappa j}) + \frac{\varepsilon \hbar}{2\omega_{\varkappa j}} \right) \frac{1}{|J|}. \end{aligned} \tag{4}$$

ε can assume the values ± 1. The other sums in (4) are to be extended over those $\varkappa$ and j that satisfy the equation

$$\boldsymbol{k}' - \boldsymbol{k} - 2\pi\boldsymbol{\tau} - \boldsymbol{\varkappa} = 0, \tag{4'}$$

where $\boldsymbol{k}'$ is given by (2). We have

$$g(\omega) = \frac{1}{\omega^2} \left(\frac{\hbar\omega}{e^{\frac{\hbar\omega}{k_B T}} - 1} + \frac{\hbar\omega}{2} \right) = \frac{k_B T}{\omega^2} \left\{ 1 + \frac{B_2}{\underline{|2}} \left(\frac{\hbar\omega}{k_B T} \right)^2 + \frac{B_4}{\underline{|4}} \left(\frac{\hbar\omega}{k_B T} \right)^4 + \cdots \right\} \tag{5}$$

---

[1] In part II of this paper N has a somewhat different meaning.

[2] The quantities φ, ψ, χ are defined in part II.

the series being convergent for $\frac{\hbar\,\omega}{k_B\,T} < 2\,\pi$. $B_2, B_4, \ldots$ are the Bernoullian numbers. Because of the appearance of the function $g\,(\omega_{\boldsymbol{\varkappa} j}) + \frac{\varepsilon\,\hbar}{2\,\omega_{\boldsymbol{\varkappa} j}}$ in (4), we get a particularly large contribution if (4′) has roots $\varkappa$ which are small compared with the basic vectors of the reciprocal lattice. If we assume that $\varkappa$ has been chosen in this way and also that $\varkappa$ is so small that $\hbar\,\omega_{\boldsymbol{\varkappa} j} << E$, (4) gives in the first approximation

$$\sigma_1\,(\boldsymbol{k},\,\boldsymbol{K}) = N^2 \sum_{p\,p'} f_p^*\,f_{p'}\,e^{i\,2\,\pi\,\boldsymbol{\tau}\cdot(\boldsymbol{R}_p - \boldsymbol{R}_{p'})}\,e^{-M_p(2\,\pi\,\boldsymbol{\tau})}\,e^{-M_{p'}(2\,\pi\,\boldsymbol{\tau})}\,\cdot$$

$$\cdot \sum_{\substack{\boldsymbol{\varkappa}\,j\,\varepsilon \\ (\boldsymbol{k}'-\boldsymbol{k}-2\,\pi\,\boldsymbol{\tau}-\boldsymbol{\varkappa}=0)}} \tfrac{1}{2}\,[2\,\pi\,\boldsymbol{\tau}\cdot\boldsymbol{C}_{p\boldsymbol{\varkappa} j}]\,[2\,\pi\,\boldsymbol{\tau}\cdot\boldsymbol{C}^*_{p'\boldsymbol{\varkappa} j}]\,\tfrac{1}{2}\left(g\,(\omega_{\boldsymbol{\varkappa} j}) + \frac{\varepsilon\,\hbar}{2\,\omega_{\boldsymbol{\varkappa} j}}\right)\frac{1}{|\,J\,|} \tag{6}$$

if $\boldsymbol{\tau} \neq 0$.

In the X-ray case we have $J = 1$ and one can express the result of the summation over j in terms of the elastic constants by taking together the terms corresponding to $\varepsilon = +1$ and $\varepsilon = -1$ and using the series expansion (5) of $g\,(\omega_{\boldsymbol{\varkappa} j})$. For X-rays it has further been found[1] that the terms of the second and higher orders give a scattering in the neighbourhood of the interference points, which is much more diffuse than that corresponding to the first order terms.

To get some idea about the character of $\sigma_1\,(\boldsymbol{k},\,\boldsymbol{K})$ we shall treat the idealized case that the crystal has a simple lattice and that $\omega_{\boldsymbol{\varkappa} j} = c_s\,\varkappa$, where c_s means a constant sound velocity, independent of the direction. Then

$$\boldsymbol{c}_{gj} = \mathrm{grad}_{\boldsymbol{\varkappa}}\,\omega_{\boldsymbol{\varkappa} j} = c_s\,\frac{\boldsymbol{\varkappa}}{\varkappa}\cdot$$

For a simple lattice we have

$$\boldsymbol{C}_{\boldsymbol{\varkappa} j} = \sqrt{\frac{2}{N\,\mu_0}}\,\boldsymbol{e}_{\boldsymbol{\varkappa} j}, \qquad j = 1,\,2,\,3,$$

$\boldsymbol{e}_{\boldsymbol{\varkappa}1}, \boldsymbol{e}_{\boldsymbol{\varkappa}2}, \boldsymbol{e}_{\boldsymbol{\varkappa}3}$ being three mutually orthogonal unit vectors, and μ_0 being the masses of the crystal nuclei. Using this, we find that (6) can be written

$$\sigma_1\,(\boldsymbol{k},\,\boldsymbol{K}) = N\,|\,f\,|^2\,e^{-2\,M(2\,\pi\,\boldsymbol{\tau})}\,\frac{(2\,\pi\,\tau)^2}{2\,\mu_0} \sum_{\substack{\boldsymbol{\varkappa}\,\varepsilon \\ (\boldsymbol{k}'-\boldsymbol{k}-2\,\pi\,\boldsymbol{\tau}-\boldsymbol{\varkappa}=0)}} \left(g\,(c_s\,\varkappa) + \frac{\varepsilon\,\hbar}{2\,c_s\,\varkappa}\right)\frac{1}{|\,J\,|}\cdot \tag{6′}$$

An important difference, between our case and the X-ray case, is the appearance of the factor $\frac{1}{|\,J\,|}\cdot$ The idealization just mentioned gives in the first approximation

$$J = 1 + \varepsilon\,\beta\,\frac{\varkappa_{\parallel}}{\varkappa}\cdot \tag{7}$$

---

[1] WALLER, l.c.

The notations $\|$ and $\perp$ refer to the direction of $\boldsymbol{K}$, and $\beta = \frac{c_s}{v}$. Also

$$\boldsymbol{k}' = \sqrt{1 - \frac{\varepsilon \hbar c_s \varkappa}{E}}\,\boldsymbol{K} = \sqrt{1 - 2\varepsilon\beta\frac{\varkappa}{k}}\,\boldsymbol{K}.$$

Substituting the expansion

$$\boldsymbol{k}' = \boldsymbol{K} - \varepsilon\beta\varkappa\frac{\boldsymbol{K}}{k}$$

into (4′), we get

$$\boldsymbol{\varkappa} = \boldsymbol{\eta} - \varepsilon\beta\varkappa\frac{\boldsymbol{K}}{k} \tag{8}$$

$$\varkappa_\perp = \eta_\perp, \quad \varkappa_\| = \eta_\| - \varepsilon\beta\varkappa \tag{8'}$$

if

$$\boldsymbol{\eta} = \boldsymbol{K} - \boldsymbol{k} - 2\pi\boldsymbol{\tau}. \tag{9}$$

$\boldsymbol{\eta}$ is a measure of the deviation from the exact Laue-Bragg condition. We get the following equation for $\varkappa$ by squaring (8)

$$\varkappa^2 = \beta^2\varkappa^2 - 2\varepsilon\beta\varkappa\eta_\| + \eta^2. \tag{10}$$

Now it is convenient to treat the two cases $v > c_s$ and $v < c_s$ separately.

Case I. $v > c_s$, i.e., $\beta < 1$.

The solution of (10) is

$$\varkappa = \frac{-\varepsilon\beta\eta_\| + \sqrt{\eta^2 - \beta^2\eta_\perp^2}}{1 - \beta^2}.$$

In order that $\varkappa$ shall be > 0 we have to choose the positive square-root. With this value of $\varkappa$, (7) and (8′) give

$$J = 1 - \beta^2\left(\frac{\eta_\perp}{\eta}\right)^2 + \varepsilon\beta\frac{\eta_\|}{\eta}\sqrt{1 - \beta^2\left(\frac{\eta_\perp}{\eta}\right)^2}.$$

J can of course be expressed as a function of the single variable $\frac{\eta_\|}{\eta}$. We easily find that:

if $\varepsilon = +1$, J increases monotonically from $1 - \beta$ to $1 + \beta$, when $\frac{\eta_\|}{\eta}$ increases from -1 to $+1$.

if $\varepsilon = -1$, J decreases monotonically from $1 + \beta$ to $1 - \beta$, when $\frac{\eta_\|}{\eta}$ increases from -1 to $+1$.

Hence we have

$$0 < 1 - \beta \leq J \leq 1 + \beta,$$

and the factor $\frac{1}{|J|}$ cannot cause an extreme increase in the intensity.

Case II. $v < c_s$, i.e., $\beta > 1$.

The solution of (10) is

$$\varkappa = \frac{\varepsilon \beta \eta_{\parallel} \pm \sqrt{\eta^2 - \beta^2 \eta_{\perp}^2}}{\beta^2 - 1}.$$

The requirement that $\varkappa$ shall be real gives

$$\left|\frac{\eta_{\perp}}{\eta}\right| \leq \frac{1}{\beta}, \tag{11}$$

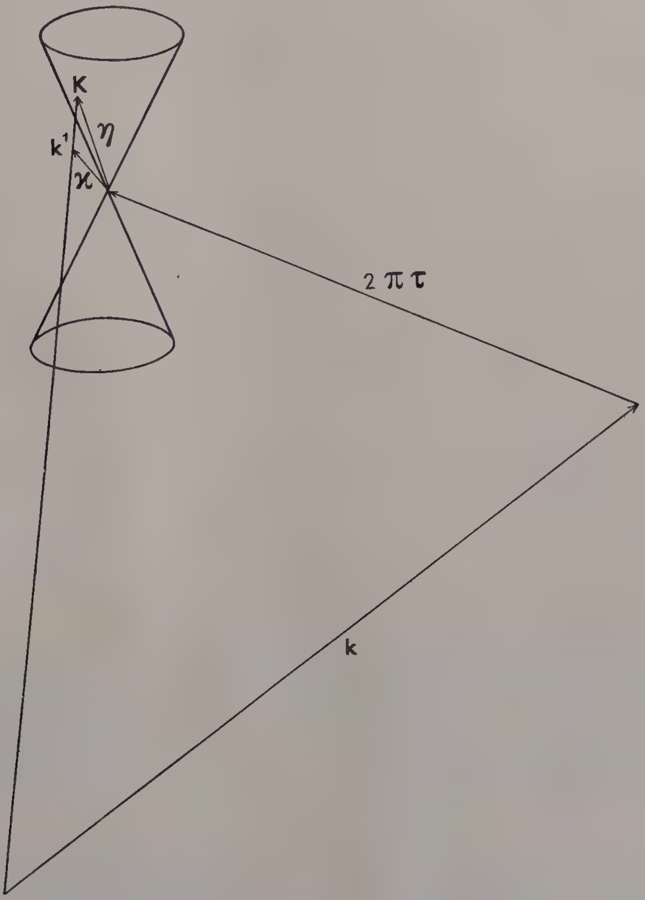

Fig. 1. The proportions in this figure are exaggerated.

and then the requirement that $\varkappa$ shall be positive gives

$$\varepsilon = \frac{\eta_{\parallel}}{|\eta_{\parallel}|}. \tag{12}$$

In the reciprocal lattice we can give the following interpretation of (11) and (12). In the immediate neighbourhood of the interference point $2\pi\boldsymbol{\tau}$, we can have diffuse temperature scattering only if the end point of $\boldsymbol{\eta}$ (cf. (9)) lies within a circular cone with the vertex in the point $2\pi\boldsymbol{\tau}$ and the axis along the direction of $\boldsymbol{K}$. The angle between the axis and the generatrices is $\arcsin\frac{1}{\beta}$. That part of the cone where $\eta_{\parallel} > 0$ corresponds to $\varepsilon = +1$ (the neutron gives energy to the crystal), and that part of the cone where $\eta_{\parallel} < 0$ corresponds to $\varepsilon = -1$ (the neutron receives energy from the crystal). See fig. 1.

With the above expressions for $\varkappa$ and ε, (7) and (8′) give

$$J = 1 - \beta^2 \left(\frac{\eta_{\perp}}{\eta}\right)^2 \mp \beta \left|\frac{\eta_{\parallel}}{\eta}\right| \sqrt{1 - \beta^2 \left(\frac{\eta_{\perp}}{\eta}\right)^2}.$$

This can be written as a function of the single variable $\left|\frac{\eta_{\parallel}}{\eta}\right|$. We easily find that:

if we choose the upper sign, J decreases monotonically from 0 to $-(\beta - 1)$, when $\left|\frac{\eta_{\parallel}}{\eta}\right|$ increases from $\sqrt{1 - \frac{1}{\beta^2}}$ to 1.

if we choose the lower sign, J increases monotonically from 0 to $\beta + 1$, when $\left|\frac{\eta_{\parallel}}{\eta}\right|$ increases from $\sqrt{1 - \frac{1}{\beta^2}}$ to 1.

Hence the factor $\frac{1}{|J|}$ causes an extreme increase of the intensity on the conical surface.

From the expansion $\boldsymbol{k}' = \boldsymbol{K} - \varepsilon\beta\varkappa\frac{\boldsymbol{K}}{k}$, previously found, it follows that we obtain the end point of the vector $\boldsymbol{k}'$ by adding the vector $-\varepsilon\beta\varkappa\frac{\boldsymbol{K}}{k}$ to $\boldsymbol{K}$. If the end point of $\boldsymbol{K}$ lies within that part of the cone where $\eta_{\parallel} > 0$, we find $\boldsymbol{k}'$ by shortening the length of $\boldsymbol{K}$ by the quantity $\beta\varkappa$. If the end point of $\boldsymbol{K}$ lies within that part of the cone where $\eta_{\parallel} < 0$, the corresponding construction is to lengthen $\boldsymbol{K}$ by $\beta\varkappa$. For every vector $\boldsymbol{\eta}$ lying within the cone, we have two possible values for $\varkappa$ and hence two vectors $\boldsymbol{k}'$. The equation

$$\boldsymbol{k}' - \boldsymbol{k} - 2\pi\boldsymbol{\tau} - \boldsymbol{\varkappa} = 0$$

or $\boldsymbol{\varkappa} = \boldsymbol{k}' - \boldsymbol{k} - 2\pi\boldsymbol{\tau}$ shows that $\boldsymbol{\varkappa}$ is the vector connecting $2\pi\boldsymbol{\tau}$ with the end point of $\boldsymbol{k}'$.

For room temperatures it is natural and also consistent with our approximations to retain only the term of highest order in $\frac{1}{\varkappa}$ in the expansion of the function $g(c_s \varkappa) + \frac{\varepsilon \hbar}{2 c_s \varkappa}$ appearing in (6′). In this way we get from (6′) after some calculations

$$\sigma_1(\boldsymbol{k}, \boldsymbol{K}) = N\,|f|^2\, e^{-2M(2\pi\boldsymbol{\tau})} \frac{(2\pi\boldsymbol{\tau})^2}{\mu_0} \frac{k_B T}{c_s^2} \frac{1}{\eta^2} \quad \text{in case I}$$

$$\sigma_1(\boldsymbol{k}, \boldsymbol{K}) = N\,|f|^2\, e^{-2M(2\pi\boldsymbol{\tau})} \frac{(2\pi\boldsymbol{\tau})^2}{\mu_0} \frac{k_B T}{c_s^2} \frac{\beta}{\eta^2 \sqrt{1-(\beta^2-1)\left(\frac{\eta_\perp}{\eta_\parallel}\right)^2}} \quad \text{in case II.}$$

It would be of interest to generalize the treatment, given here, to real crystals. A possible method to perform the calculations has been found, but the numerical work has not yet been performed.

Institute for Mechanics and Mathematical Physics, University of Uppsala, Uppsala.

Tryckt den 9 januari 1952

Uppsala 1952. Almqvist & Wiksells Boktryckeri AB

Errata

Read Band 4 nr 6 instead of Band 3 nr 10 in footnote 3.

ARKIV FÖR FYSIK Band 4 nr 6

Communicated 7 June 1950 by OSKAR KLEIN and IVAR WALLER

On neutron diffraction phenomena according to the kinematical theory. II

By PER OLOF FRÖMAN

The present paper treats the influence of the heat vibrations on the scattering of slow neutrons by small single crystals. As is well known the problem is closely connected with the corresponding problem for X-rays, both as to methods and results, but is more complicated because the frequency of the scattered neutron is in general not equal to that of the incident neutron. For the sake of simplicity, magnetic interaction, isotopic disorder and spin dependence are not taken into account in this paper. The same problem has already been treated by several authors[1], but we thought it to be of some value to give a simpler and more rigorous treatment of it, using chiefly methods from the theory of X-ray scattering.

We consider a single crystal containing N atomic nuclei with the fixed equilibrium positions $\boldsymbol{R}_l$ and the instantaneous positions $\boldsymbol{r}_l = \boldsymbol{R}_l + \boldsymbol{u}_l$, $l = 1, 2, \ldots N$. Putting

$$\boldsymbol{u}_l = \sum_s \boldsymbol{b}_{ls} q_s,$$

we can determine the $\boldsymbol{b}_{ls}$ so that $q_1, q_2, \ldots q_{3N}$ are normal coordinates. Then the Hamiltonian is

$$\sum_s \left(-\frac{1}{2} \hbar^2 \frac{\partial^2}{\partial q_s^2} + \frac{1}{2} \omega_s^2 q_s^2 \right)$$

if we neglect in the expression for the potential energy third and higher order terms in $\boldsymbol{u}_l$. The ω_s are the fundamental frequencies. The eigen function corresponding to the energy eigen value $\sum_s (n_s + \frac{1}{2}) \hbar \omega_s$ is

$$\Phi_n(q) = \prod_s \left(\frac{\omega_s}{\hbar} \right)^{\frac{1}{4}} \varphi_{n_s} \left(\sqrt{\frac{\omega_s}{\hbar}} q_s \right),$$

where the φ_{n_s} are the normalized Hermitian orthogonal functions.

The wave functions of the system, crystal-plus-neutron, without interaction, are

$$\Psi_{n,k}(q, \boldsymbol{r}) = \Phi_n(q) e^{i \boldsymbol{k} \cdot \boldsymbol{r}},$$

---

[1] See the references in R. WEINSTOCK, Phys. Rev. 65, 1 (1944).

where $\boldsymbol{k}$ is the wave vector of the neutron and $\boldsymbol{r}$ its position vector. As has been shown by FERMI[1], the scattering of slow neutrons by bound nuclei can be treated with the use of the δ-function interaction between the neutron and the nuclei coupled with Born's approximation. Thus we put for the interaction potential

$$V(q, \boldsymbol{r}) = -\frac{2\pi\hbar^2}{\mu}\sum_l f_l\,\delta(\boldsymbol{r}-\boldsymbol{r}_l),$$

where μ is the mass of the neutron, and $-f_l$ is the scattering length[2] of the nucleus l. In Born's approximation the quantities f_l are real. For formal reasons, however, it is convenient to use both f_l and $f_l^*\,(=f_l)$ in the formulae. The differential scattering cross section for the single quantum transition $\boldsymbol{k}\rightarrow\boldsymbol{k}'_\nu$, $n_s \rightarrow n_s + \nu_s$ (all s) is

$$\frac{\mu^2}{4\pi^2\hbar^4}\frac{k'_\nu}{k}\,|(n+\nu, \boldsymbol{k}'_\nu\,|\,V\,|\,n, \boldsymbol{k})|^2, \tag{1}$$

where

$$(n+\nu, \boldsymbol{k}'_\nu\,|\,V\,|\,n, \boldsymbol{k}) = \int\!\!\int \Psi^*_{n+\nu, \boldsymbol{k}'_\nu}(q, \boldsymbol{r})\,V(q, \boldsymbol{r})\,\Psi_{n, \boldsymbol{k}}(q, \boldsymbol{r})\,dq\,d\boldsymbol{r} =$$

$$= -\frac{2\pi\hbar^2}{\mu}\sum_l f_l\,e^{-i(\boldsymbol{k}'_\nu-\boldsymbol{k})\cdot\boldsymbol{R}_l}\prod_s A_{n_s+\nu_s,\,n_s}(-(\boldsymbol{k}'_\nu-\boldsymbol{k})\cdot\boldsymbol{B}_{ls}), \tag{2}$$

$$A_{m,n}(x) = \int_{-\infty}^{+\infty} e^{2ix\xi}\,\varphi_m(\xi)\,\varphi_n(\xi)\,d\xi \tag{3}$$

and

$$\boldsymbol{B}_{ls} = \frac{1}{2}\sqrt{\frac{\hbar}{\omega_s}}\,\boldsymbol{b}_{ls}.$$

The wave vector of the incident neutron is $\boldsymbol{k}$. If, during the scattering process, the crystal passes over from the state n into the state $n+\nu$, the wave vector of the neutron after the collision becomes[3]

$$\boldsymbol{k}'_\nu = \sqrt{1-\frac{1}{E}\sum_s \nu_s\hbar\,\omega_s}\;\boldsymbol{K},$$

where

$$E = \frac{\hbar^2 k^2}{2\mu},$$

because the energy equation gives

$$\frac{\hbar^2 k^2}{2\mu} = \frac{\hbar^2 k'^2}{2\mu} + \sum_s \nu_s\hbar\,\omega_s.$$

---

[1] E. FERMI, Ric. Scient. VII—II, 13 (1936).
[2] E. FERMI and L. MARSHALL, Phys. Rev. 71, 666 (1947).
[3] $\boldsymbol{K}$ is defined on the following page.

We shall now calculate the statistically averaged differential cross section $\sigma(\boldsymbol{k}, \boldsymbol{K})$ for scattering in the direction of a vector $\boldsymbol{K}$ which we normalize so that $|\boldsymbol{K}| = k$. The probability that before the collision the crystal is in the state $n = (n_1, n_2, \ldots, n_{3N})$ is $\prod_s (1-\alpha_s)\alpha_s^{n_s}$. Here $\alpha_s = e^{-\frac{\hbar\omega_s}{k_B T}}$ and k_B is the Boltzmann constant. The processes in which the quantum numbers of the crystal are changed by $\nu = (\nu_1, \nu_2, \ldots, \nu_{3N})$ therefore give the following average differential scattering cross section:

$$\sigma(\boldsymbol{k}, \boldsymbol{K}; \nu) = \sum_{n_1} \cdots \sum_{n_{3N}} \left\{ \prod_s (1-\alpha_s)\alpha_s^{n_s} \right\} \frac{\mu^2}{4\pi^2\hbar^4} \frac{k'_\nu}{k} |(n+\nu, \boldsymbol{k}'_\nu | V | n, \boldsymbol{k})|^2. \tag{4}$$

Here, and in the following, the summation over n_s is to be extended from $n_s = \frac{1}{2}(|\nu_s| - \nu_s)$ to $n_s = \infty$. To obtain $\sigma(\boldsymbol{k}, \boldsymbol{K})$ (cf. above) we have to sum $\sigma(\boldsymbol{k}, \boldsymbol{K}; \nu)$ over those ν that make $\boldsymbol{k}'_\nu$ real.

From (2) and (4) we obtain

$$\sigma(\boldsymbol{k}, \boldsymbol{K}; \nu) = \frac{k'_\nu}{k} \sum_{ll'} f_l^* f_{l'} e^{i(\boldsymbol{k}'_\nu - \boldsymbol{k})\cdot(\boldsymbol{R}_l - \boldsymbol{R}_{l'})} \cdot$$

$$\cdot \prod_s \sum_{n_s} (1-\alpha_s)\alpha_s^{n_s} A_{n_s+\nu_s, n_s}((\boldsymbol{k}'_\nu - \boldsymbol{k})\cdot \boldsymbol{B}_{ls}) A_{n_s+\nu_s, n_s}(-(\boldsymbol{k}'_\nu - \boldsymbol{k})\cdot \boldsymbol{B}_{l's}). \tag{5}$$

Using a formula, given in the appendix, together with the definition of α_s, one can write (5) as follows

$$\sigma(\boldsymbol{k}, \boldsymbol{K}; \nu) = \frac{k'_\nu}{k} \sum_{ll'} f_l^* f_{l'} e^{i(\boldsymbol{k}'_\nu - \boldsymbol{k})\cdot(\boldsymbol{R}_l - \boldsymbol{R}_{l'})} \cdot$$

$$\cdot \prod_s e^{-\frac{1}{2}((\boldsymbol{k}'_\nu - \boldsymbol{k})\cdot \boldsymbol{b}_{ls})^2 g(\omega_s)} e^{-\frac{1}{2}((\boldsymbol{k}'_\nu - \boldsymbol{k})\cdot \boldsymbol{b}_{l's})^2 g(\omega_s)} \tag{6}$$

$$e^{\frac{\nu_s\hbar\omega_s}{2k_B T}} (-i)^{\nu_s} J_{\nu_s}\left(i[(\boldsymbol{k}'_\nu - \boldsymbol{k})\cdot \boldsymbol{b}_{ls}][(\boldsymbol{k}'_\nu - \boldsymbol{k})\cdot \boldsymbol{b}_{l's}] \frac{\hbar}{\omega_s} \frac{e^{\frac{\hbar\omega_s}{2k_B T}}}{e^{\frac{\hbar\omega_s}{k_B T}} - 1} \right)$$

where

$$g(\omega) = \frac{1}{\omega^2}\left(\frac{\hbar\omega}{e^{\frac{\hbar\omega}{k_B T}} - 1} + \frac{\hbar\omega}{2} \right). \tag{7}$$

For $\nu_s = 0$ (all s) the formula (6) was derived by OTT[1].

The quantities $\boldsymbol{b}_{ls}$ are very small. In fact we have

$$\boldsymbol{b}_{ls} = O\left(\frac{1}{\sqrt{N}}\right). \tag{8}$$

---

[1] H. OTT, Ann. d. Phys., Folge 5, Bd. 23, 169 (1935).

Neglecting terms that tend rapidly to zero as the dimensions of the crystal tend to infinity, we get[1]

$$e^{\frac{\nu_s \hbar \omega_s}{2 k_B T}} (-i)^{\nu_s} J_{\nu_s}\left(i\,[(\boldsymbol{k}'_\nu - \boldsymbol{k}) \cdot \boldsymbol{b}_{l s}]\,[(\boldsymbol{k}'_\nu - \boldsymbol{k}) \cdot \boldsymbol{b}_{l' s}]\, \frac{\hbar}{\omega_s}\, \frac{e^{\frac{\hbar \omega_s}{2 k_B T}}}{e^{\frac{\hbar \omega_s}{k_B T}} - 1} \right) = \tag{9}$$

$$= \begin{cases} 1 \text{ if } \nu_s = 0 \\ \frac{1}{2}\,[(\boldsymbol{k}'_\nu - \boldsymbol{k}) \cdot \boldsymbol{b}_{l s}]\,[(\boldsymbol{k}'_\nu - \boldsymbol{k}) \cdot \boldsymbol{b}_{l' s}]\, \frac{\hbar}{\omega_s}\, \frac{e^{\frac{(1+\varepsilon_s)\hbar \omega_s}{2 k_B T}}}{e^{\frac{\hbar \omega_s}{k_B T}} - 1} & \text{if } \nu_s = \varepsilon_s = \pm 1 \\ 0 \text{ if } |\nu_s| > 1. \end{cases}$$

Using this result, we easily get (in the same approximation as (9) is valid)

$$e^{-\frac{1}{2}((\boldsymbol{k}'_\nu - \boldsymbol{k}) \cdot \boldsymbol{b}_{l s})^2 g(\omega_s)}\; e^{-\frac{1}{2}((\boldsymbol{k}'_\nu - \boldsymbol{k}) \cdot \boldsymbol{b}_{l' s})^2 g(\omega_s)} \cdot e^{\frac{\nu_s \hbar \omega_s}{2 k_B T}} (-i)^{\nu_s} J_{\nu_s}\left(i\,[(\boldsymbol{k}'_\nu - \boldsymbol{k}) \cdot \boldsymbol{b}_{l s}]\,[(\boldsymbol{k}'_\nu - \boldsymbol{k}) \cdot \boldsymbol{b}_{l' s}]\, \frac{\hbar}{\omega_s}\, \frac{e^{\frac{\hbar \omega_s}{2 k_B T}}}{e^{\frac{\hbar \omega_s}{k_B T}} - 1} \right) = \tag{10}$$

$$= \begin{cases} e^{-\frac{1}{2}((\boldsymbol{k}'_\nu - \boldsymbol{k}) \cdot \boldsymbol{b}_{l s})^2 g(\omega_s)}\; e^{-\frac{1}{2}((\boldsymbol{k}'_\nu - \boldsymbol{k}) \cdot \boldsymbol{b}_{l' s})^2 g(\omega_s)} & \text{if } \nu_s = 0 \\ [(\boldsymbol{k}'_\nu - \boldsymbol{k}) \cdot \boldsymbol{b}_{l s}]\,[(\boldsymbol{k}'_\nu - \boldsymbol{k}) \cdot \boldsymbol{b}_{l' s}]\, \frac{1}{2} \left(g(\omega_s) + \frac{\varepsilon_s \hbar}{2 \omega_s} \right) & \text{if } \nu_s = \varepsilon_s = \pm 1 \\ 0 \text{ if } |\nu_s| > 1. \end{cases}$$

From (5) and (10) we see that only those processes in which $|\nu_s| \leq 1$ for all s give essential contributions to the cross section.

Now it is convenient to alter the symbols so that the lattice structure is made apparent. We let p be the basic index and $l = (l_1, l_2, l_3)$ the cellular index. The basic index p can take on as many values as there are nuclei in the unit cell, and l_i runs from 1 to a large number L_i. $L_1 L_2 L_3$ is the number of unit cells in the crystal. We replace $\boldsymbol{R}_l$ by $\boldsymbol{R}^l + \boldsymbol{R}_p$ and f_l by f_p, where $\boldsymbol{R}^l = \sum_{i=1}^{3} l_i \boldsymbol{a}_i$ and $\boldsymbol{a}_1, \boldsymbol{a}_2, \boldsymbol{a}_3$ are the basic vectors of the lattice. (The basic vectors of the reciprocal lattice are called $\boldsymbol{b}_1, \boldsymbol{b}_2, \boldsymbol{b}_3$.) In the approximate treatment of an ideal single crystal given by Born and v. Kármán and supplemented by Waller, the fundamental frequencies are equal in pairs. The two frequencies in each pair can be distinguished from one another by the fact that one belongs to what may be called a P oscillator and the other to a Q oscillator. (We can also speak of P and Q coordinates.) The pairs of fundamental frequencies are characterized by the symbol $(\varkappa, j)$, where $\varkappa$ takes on

---

[1] Professor WALLER has pointed out that the approximations in (9) and (10) are allowed and that estimates of error in corresponding expressions in WEINSTOCK's paper are not quite correct.

$\frac{1}{2} L_1 L_2 L_3$ values, uniformly distributed in half the phase parallelopiped, and j takes on three times as many values as there are nuclei in the unit cell. (The phase parallellopiped is defined as the region in the reciprocal lattice for which $\varkappa = \varphi \boldsymbol{b}_1 + \psi \boldsymbol{b}_2 + \chi \boldsymbol{b}_3$, $-\pi \leq \begin{matrix} \varphi \\ \psi \\ \chi \end{matrix} \leq \pi$.) If we consider an arbitrary $(\varkappa, j)$ and fix an oscillator type (P or Q), this corresponds to a certain s. (s is here one of our earlier symbols.) From the general theory[1] of the normal coordinates of a single crystal it is clear that we shall replace $\boldsymbol{b}_{ls}$ by

$$\boldsymbol{v}_{pj}^{l\varkappa} \qquad \text{for a } P\text{-oscillator}$$

and by

$$\boldsymbol{w}_{pj}^{l\varkappa} \qquad \text{for a } Q\text{-oscillator.}^2$$

We also replace our earlier $\nu = (\ldots \nu_s \ldots)$ by $\nu = (\ldots \nu'_{\varkappa j} \ldots; \ldots \nu''_{\varkappa j} \ldots)$, where $\nu'_{\varkappa j}$ belongs to a P oscillator and $\nu''_{\varkappa j}$ to a Q oscillator. $\boldsymbol{v}_{pj}^{l\varkappa}$ and $\boldsymbol{w}_{pj}^{l\varkappa}$ are real quantities defined by

$$\boldsymbol{v}_{pj}^{l\varkappa} + i\, \boldsymbol{w}_{pj}^{l\varkappa} = \boldsymbol{C}_{p\varkappa j}\, e^{i(l_1\varphi + l_2\psi + l_3\chi)}$$

where $\sqrt{\mu_p}\, \boldsymbol{C}_{p\varkappa j}$ are the amplitudes of the lattice vibrations.
In the new symbols (6) can be written

$$\sigma(\boldsymbol{k}, \mathbf{K}; \nu) = \frac{k'_\nu}{k} \sum_{pp'} \sum_{ll'} f_p^* f_{p'}\, e^{i(\boldsymbol{k}'_\nu - \boldsymbol{k}) \cdot (\boldsymbol{R}^l + \boldsymbol{R}_p - \boldsymbol{R}^{l'} - \boldsymbol{R}_{p'})} .$$
$$\cdot \prod_{\varkappa}{}' \prod_{j} e^{-\frac{1}{2}((\boldsymbol{k}'_\nu - \boldsymbol{k}) \cdot \boldsymbol{v}_{pj}^{l\varkappa})^2 g(\omega_{\varkappa j})}\, e^{-\frac{1}{2}((\boldsymbol{k}'_\nu - \boldsymbol{k}) \cdot \boldsymbol{v}_{p'j}^{l'\varkappa})^2 g(\omega_{\varkappa j})}$$
$$e^{\frac{\nu'_{\varkappa j} \hbar \omega_{\varkappa j}}{2 k_B T}} (-i)^{\nu'_{\varkappa j}} J_{\nu'_{\varkappa j}} \left(i [(\boldsymbol{k}'_\nu - \boldsymbol{k}) \cdot \boldsymbol{v}_{pj}^{l\varkappa}]\, [(\boldsymbol{k}'_\nu - \boldsymbol{k}) \cdot \boldsymbol{v}_{p'j}^{l'\varkappa}]\, \frac{\hbar}{\omega_{\varkappa j}}\, \frac{e^{\frac{\hbar \omega_{\varkappa j}}{2 k_B T}}}{e^{\frac{\hbar \omega_{\varkappa j}}{k_B T}} - 1} \right) \tag{6'}$$
$$e^{-\frac{1}{2}((\boldsymbol{k}'_\nu - \boldsymbol{k}) \cdot \boldsymbol{w}_{pj}^{l\varkappa})^2 g(\omega_{\varkappa j})}\, e^{-\frac{1}{2}((\boldsymbol{k}'_\nu - \boldsymbol{k}) \cdot \boldsymbol{w}_{p'j}^{l'\varkappa})^2 g(\omega_{\varkappa j})}$$
$$e^{\frac{\nu''_{\varkappa j} \hbar \omega_{\varkappa j}}{2 k_B T}} (-i)^{\nu''_{\varkappa j}} J_{\nu''_{\varkappa j}} \left(i [(\boldsymbol{k}'_\nu - \boldsymbol{k}) \cdot \boldsymbol{w}_{pj}^{l\varkappa}]\, [(\boldsymbol{k}'_\nu - \boldsymbol{k}) \cdot \boldsymbol{w}_{p'j}^{l'\varkappa}]\, \frac{\hbar}{\omega_{\varkappa j}}\, \frac{e^{\frac{\hbar \omega_{\varkappa j}}{2 k_B T}}}{e^{\frac{\hbar \omega_{\varkappa j}}{k_B T}} - 1} \right),$$

where

$$\boldsymbol{k}'_\nu = \sqrt{1 - \frac{1}{E} \sum_{\varkappa}{}' \sum_{j} (\nu'_{\varkappa j} + \nu''_{\varkappa j})\, \hbar\, \omega_{\varkappa j}}\, \mathbf{K}.$$

---

[1] I. Waller, Interferenz- und Dispersionstheorie der Röntgenstrahlen; Erster Teil, § 1 (Uppsala 1925).

[2] Our $\boldsymbol{v}_{pj}^{l\varkappa}$ corresponds to Waller's (l. c.) $\frac{\boldsymbol{v}_{pj}^{l\varkappa}}{\sqrt{\mu_p}}$, where μ_p is the mass of the nucleus p. Similarly for $\boldsymbol{w}$ and $\boldsymbol{C}$.

By using the primed symbols $\prod\limits_{\varkappa}{}'$ and $\sum\limits_{\varkappa}{}'$ we indicate that $\varkappa$ runs through half the phase parallelopiped. To indicate that it runs through the whole phase parallelopiped we write $\prod\limits_{\varkappa}$ and $\sum\limits_{\varkappa}$.

In the same way (10) is to be replaced by

$$e^{-\frac{1}{2}\left((\boldsymbol{k}'_\nu-\boldsymbol{k})\cdot\boldsymbol{v}^{l\varkappa}_{pj}\right)^2 g(\omega_{\varkappa j})}\; e^{-\frac{1}{2}\left((\boldsymbol{k}'_\nu-\boldsymbol{k})\cdot\boldsymbol{v}^{l'\varkappa}_{p'j}\right)^2 g(\omega_{\varkappa j})}\,\cdot$$

$$\cdot\, e^{\frac{\nu'_{\varkappa j}\hbar\,\omega_{\varkappa j}}{2k_B T}}\,(-i)^{\nu'_{\varkappa j}} J_{\nu'_{\varkappa j}}\left(i\,[(\boldsymbol{k}'_\nu-\boldsymbol{k})\cdot\boldsymbol{v}^{l\varkappa}_{pj}]\,[(\boldsymbol{k}'_\nu-\boldsymbol{k})\cdot\boldsymbol{v}^{l'\varkappa}_{p'j}]\,\frac{\hbar}{\omega_{\varkappa j}}\,\frac{e^{\frac{\hbar\,\omega_{\varkappa j}}{2k_B T}}}{e^{\frac{\hbar\,\omega_{\varkappa j}}{k_B T}}-1}\right)=$$

$$=\begin{cases} e^{-\frac{1}{2}\left((\boldsymbol{k}'_\nu-\boldsymbol{k})\cdot\boldsymbol{v}^{l\varkappa}_{pj}\right)^2 g(\omega_{\varkappa j})}\; e^{-\frac{1}{2}\left((\boldsymbol{k}'_\nu-\boldsymbol{k})\cdot\boldsymbol{v}^{l'\varkappa}_{p'j}\right)^2 g(\omega_{\varkappa j})} & \text{if } \nu'_{\varkappa j}=0 \\ [(\boldsymbol{k}'_\nu-\boldsymbol{k})\cdot\boldsymbol{v}^{l\varkappa}_{pj}]\,[(\boldsymbol{k}'_\nu-\boldsymbol{k})\cdot\boldsymbol{v}^{l'\varkappa}_{p'j}]\,\frac{1}{2}\left(g(\omega_{\varkappa j})+\frac{\varepsilon_{\varkappa j}\hbar}{2\,\omega_{\varkappa j}}\right) & \text{if } \nu'_{\varkappa j}=\varepsilon_{\varkappa j}=\pm 1 \\ 0 \text{ if } |\nu'_{\varkappa j}|>1 \end{cases} \tag{10'}$$

and (10″), where (10″) is the same equation as (10′) with $\boldsymbol{v}$ replaced by $\boldsymbol{w}$ and $\nu'_{\varkappa j}$ by $\nu''_{\varkappa j}$. Using (6′), (10′) and (10″), we find $\sigma(\boldsymbol{k}, \boldsymbol{K}; \nu)$, and then by summing this over ν we obtain $\sigma(\boldsymbol{k}, \boldsymbol{K})$.

The terms of zero order

Those terms, in which all $\nu'_{\varkappa j}$ and $\nu''_{\varkappa j}$ are equal to zero, are said to be of the order zero. They constitute the main part of the expression for the cross section.

Using (6′), (10′), (10″) and the relations[1]

$$(\boldsymbol{h}\cdot\boldsymbol{v}^{l\varkappa}_{pj})^2+(\boldsymbol{h}\cdot\boldsymbol{w}^{l\varkappa}_{pj})^2=|\boldsymbol{h}\cdot\boldsymbol{C}_{p\varkappa j}|^2, \text{ valid for any real vector } \boldsymbol{h} \tag{11}$$

and[2]

$$\begin{cases}\omega_{-\varkappa j}=\omega_{\varkappa j}\\ \boldsymbol{C}_{p-\varkappa j}=\boldsymbol{C}^*_{p\varkappa j},\end{cases} \tag{12}$$

we find after some calculation that the terms of zero order give the following contribution to the differential scattering cross section:

$$\sigma_0(\boldsymbol{k},\boldsymbol{K})=\left|\sum_p f_p\, e^{-i(\boldsymbol{K}-\boldsymbol{k})\cdot\boldsymbol{R}_p}\, e^{-M_p(\boldsymbol{K}-\boldsymbol{k})}\right|^2 \prod_{i=1}^{3}\left(\frac{\sin\frac{1}{2}L_i(\boldsymbol{K}-\boldsymbol{k})\cdot\boldsymbol{a}_i}{\sin\frac{1}{2}(\boldsymbol{K}-\boldsymbol{k})\cdot\boldsymbol{a}_i}\right)^2, \tag{13}$$

---

[1] It ought to be pointed out that (11) is a special case of (19). Both expressions are easily obtained from the equation connecting $\boldsymbol{v}$, $\boldsymbol{w}$ and $\boldsymbol{C}$.

[2] WALLER, l. c., eq. 8, p. 13.

where

$$M_p(\boldsymbol{K}-\boldsymbol{k}) = \tfrac{1}{4}\sum_{\varkappa}\sum_{j} |(\boldsymbol{K}-\boldsymbol{k})\cdot \boldsymbol{C}_{p\varkappa j}|^2 g(\omega_{\varkappa j}),$$

the summation over $\varkappa$ running throughout the whole phase parallelopiped. (13) is in complete agreement with the corresponding expression for X-rays[1].

We define a function $\delta_L(x)$ according to

$$\delta_L(x) = \begin{cases} \dfrac{1}{2\pi L}\left(\dfrac{\sin\frac{1}{2}Lx}{\sin\frac{1}{2}x}\right)^2 & \text{if } -\pi < x \leq \pi \\ 0 \text{ for all other } x. \end{cases} \tag{14}$$

Then we obviously have

$$\left(\frac{\sin\frac{1}{2}Lx}{\sin\frac{1}{2}x}\right)^2 = \sum_{m=-\infty}^{+\infty} 2\pi L\,\delta_L(x-2\pi m). \tag{15}$$

By means of this formula, (13) can be written

$$\sigma_0(\boldsymbol{k},\boldsymbol{K}) = \sum_{\boldsymbol{\tau}}\left|\sum_p f_p\, e^{-i(\boldsymbol{K}-\boldsymbol{k})\cdot \boldsymbol{R}_p}\, e^{-M_p(\boldsymbol{K}-\boldsymbol{k})}\right|^2 \prod_{i=1}^{3} 2\pi L_i\,\delta_{L_i}((\boldsymbol{K}-\boldsymbol{k}-2\pi\boldsymbol{\tau})\cdot \boldsymbol{a}_i), \tag{16}$$

where

$$\boldsymbol{\tau} = \sum_{i=1}^{3} \tau_i \boldsymbol{b}_i$$

and τ_1, τ_2, τ_3 take on all integral values from $-\infty$ to $+\infty$ when we sum over $\boldsymbol{\tau}$.

We shall now give some important properties of the function $\delta_L(x)$. From its definition it follows that

$$\lim_{L\to\infty}\delta_L(x) = \begin{cases} 0 & \text{if } x \neq 0 \\ \infty & \text{if } x = 0. \end{cases}$$

Further, we have

$$\lim_{L\to\infty}\int_a^b \delta_L(x)\,dx = \begin{cases} 1 \text{ if } a < 0 < b \\ 0 \text{ if } a < b < 0 \text{ or } 0 < a < b. \end{cases}$$

To prove this, it is obviously sufficient to show that $\int_{-\pi}^{\pi}\delta_L(x)\,dx = 1$. A simple proof is as follows[2]:

$$\int_{-\pi}^{\pi}\delta_L(x)\,dx = \int_{-\pi}^{\pi}\frac{1}{2\pi L}\left(\frac{\sin\frac{1}{2}Lx}{\sin\frac{1}{2}x}\right)^2 dx = \frac{1}{2\pi L}\int_{-\pi}^{\pi}\left|\sum_{l=1}^{L} e^{ilx}\right|^2 dx =$$

$$= \frac{1}{2\pi L}\sum_{l=1}^{L}\sum_{l'=1}^{L}\int_{-\pi}^{\pi} e^{i(l-l')x}\,dx = 1.$$

---

[1] WALLER, l. c., eq. (35), p. 24.

[2] WALLER, l. c., eq. (69′), p. 40.

For any continous function $f(x)$ it can easily be shown that

$$\lim_{L\to\infty} \int_a^b \delta_L(x)\, f(x)\, dx = \begin{cases} f(0) & \text{if } a<0<b \\ 0 & \text{if } a<b<0 \text{ or } 0 \leqslant a<b. \end{cases}$$

The terms of first order

We shall now treat the terms in which one of the quantities $\ldots \nu'_{\varkappa j} \ldots$; $\ldots \nu''_{\varkappa j} \ldots$ is equal to ± 1, and all the others are equal to 0. These terms are said to be of the first order. It is convenient to define

$$\boldsymbol{k}'_{\varkappa j \varepsilon} = \sqrt{1 - \frac{\varepsilon \hbar \omega_{\varkappa j}}{E}}\, \boldsymbol{K}. \tag{17}$$

This wave vector corresponds to a scattering process in which the quantum number of one of the two $(\varkappa, j)$-oscillators is increased by ε, while all the other quantum numbers remain unchanged.

From (6′), (10′) and (10″) it is easily seen that the first order terms give the following contribution to the differential scattering cross section:

$$\begin{aligned}
\sigma_1(\boldsymbol{k}, \boldsymbol{K}) = {} & \sum_{\varkappa_1}{}' \sum_{j_1} \sum_{\varepsilon_1} \frac{k'}{k} \sum_{pp'} \sum_{ll'} f_p^* f_{p'}\, e^{i(\boldsymbol{k}'-\boldsymbol{k})\cdot(\boldsymbol{R}^l+\boldsymbol{R}_p-\boldsymbol{R}^{l'}-\boldsymbol{R}_{p'})} \cdot \\
& \cdot [(\boldsymbol{k}'-\boldsymbol{k})\cdot \boldsymbol{v}_{p j_1}^{l \varkappa_1}]\,[(\boldsymbol{k}'-\boldsymbol{k})\cdot \boldsymbol{v}_{p' j_1}^{l' \varkappa_1}]\, \tfrac{1}{2}\left(g(\omega_{\varkappa_1 j_1}) + \frac{\varepsilon_1 \hbar}{2\,\omega_{\varkappa_1 j_1}}\right) \cdot \\
& \cdot \underbrace{\prod_{\varkappa}{}' \prod_{j}}_{(\varkappa, j) \neq (\varkappa_1, j_1)} e^{-\frac{1}{2}((\boldsymbol{k}'-\boldsymbol{k})\cdot \boldsymbol{v}_{pj}^{l\varkappa})^2 g(\omega_{\varkappa j})}\, e^{-\frac{1}{2}((\boldsymbol{k}'-\boldsymbol{k})\cdot \boldsymbol{v}_{p'j}^{l'\varkappa})^2 g(\omega_{\varkappa j})} \\
& \cdot \prod_{\varkappa}{}' \prod_{j} e^{-\frac{1}{2}((\boldsymbol{k}'-\boldsymbol{k})\cdot \boldsymbol{w}_{pj}^{l\varkappa})^2 g(\omega_{\varkappa j})}\, e^{-\frac{1}{2}((\boldsymbol{k}'-\boldsymbol{k})\cdot \boldsymbol{w}_{p'j}^{l'\varkappa})^2 g(\omega_{\varkappa j})} + \\
& + \text{the same expression, with } \boldsymbol{v} \text{ and } \boldsymbol{w} \text{ interchanged.}
\end{aligned} \tag{18}$$

In this sum we have the restriction that $\boldsymbol{k}'$ (abbreviation for $\boldsymbol{k}'_{\varkappa_1 j_1 \varepsilon_1}$) shall be real.

As $\boldsymbol{v}$ and $\boldsymbol{w}$ are both of the same order of magnitude as $\dfrac{1}{\sqrt{L_1 L_2 L_3}}$, we can neglect the error that we get by extending the products in (18) to contain also the factors corresponding to $(\varkappa, j) = (\varkappa_1, j_1)$.

From the relation between $\boldsymbol{v}$, $\boldsymbol{w}$, and $\boldsymbol{C}$ we obtain

$$\begin{aligned}
& (\boldsymbol{h}\cdot \boldsymbol{v}_{pj}^{l\varkappa})\,(\boldsymbol{h}'\cdot \boldsymbol{v}_{p'j}^{l'\varkappa}) + (\boldsymbol{h}\cdot \boldsymbol{w}_{pj}^{l\varkappa})\,(\boldsymbol{h}'\cdot \boldsymbol{w}_{p'j}^{l'\varkappa}) = \\
& = \tfrac{1}{2}\left\{(\boldsymbol{h}\cdot \boldsymbol{C}_{p\varkappa j})\,(\boldsymbol{h}'\cdot \boldsymbol{C}^*_{p'\varkappa j})\, e^{i\boldsymbol{\varkappa}\cdot(\boldsymbol{R}^l-\boldsymbol{R}^{l'})} + (\boldsymbol{h}\cdot \boldsymbol{C}^*_{p\varkappa j})\,(\boldsymbol{h}'\cdot \boldsymbol{C}_{p'\varkappa j})\, e^{-i\boldsymbol{\varkappa}\cdot(\boldsymbol{R}^l-\boldsymbol{R}^{l'})}\right\},
\end{aligned} \tag{19}$$

valid for all real vectors $\boldsymbol{h}$ and $\boldsymbol{h}'$.

Using (11), (12), (18) and (19), we get after some simplification

$$\sigma_1(\mathbf{k},\mathbf{K}) = \sum_{\boldsymbol{\tau}} \sum_{\boldsymbol{\varkappa}} \sum_{j} \sum_{\varepsilon} \frac{k'}{k} \sum_{pp'} f_p^* f_{p'}\, e^{i(\mathbf{k}'-\mathbf{k})\cdot(\mathbf{R}_p-\mathbf{R}_{p'})}\, e^{-M_p(\mathbf{k}'-\mathbf{k})}\, e^{-M_{p'}(\mathbf{k}'-\mathbf{k})}\,\cdot$$

$$\cdot\, \tfrac{1}{2}\,[(\mathbf{k}'-\mathbf{k})\cdot\mathbf{C}_{p\boldsymbol{\varkappa}j}]\,[(\mathbf{k}'-\mathbf{k})\cdot\mathbf{C}^*_{p'\boldsymbol{\varkappa}j}]\,\tfrac{1}{2}\left(g(\omega_{\boldsymbol{\varkappa}j}) + \frac{\varepsilon\hbar}{2\,\omega_{\boldsymbol{\varkappa}j}}\right)\cdot \qquad (20$$

$$\cdot \prod_{i=1}^{3} 2\pi L_i\, \delta_{L_i}((\mathbf{k}'-\mathbf{k}+\boldsymbol{\varkappa}-2\pi\boldsymbol{\tau})\cdot\mathbf{a}_i),$$

where we shall sum only over those $\boldsymbol{\varkappa}$, j, ε that make $\mathbf{k}'$ (now abbreviation for $\mathbf{k}'_{\boldsymbol{\varkappa}j\varepsilon}$) real.

It ought to be mentioned also that if we formally replace $\mathbf{k}'$ by $\mathbf{K}$ in (20) (i. e., neglect the change of frequency), we obtain agreement with the corresponding expression in the theory of X-ray diffraction.[1]

The terms of higher orders

The terms of order r are those in which r of the quantities $\ldots\nu'_{\boldsymbol{\varkappa}j}\ldots$; $\ldots\nu''_{\boldsymbol{\varkappa}j}\ldots$ are equal to $\varepsilon_1 = \pm 1$, $\varepsilon_2 = \pm 1$, $\ldots$, $\varepsilon_r = \pm 1$, respectively, and all others are 0. We define

$$\mathbf{k}'_{\boldsymbol{\varkappa}_1 j_1 \varepsilon_1,\ldots,\boldsymbol{\varkappa}_r j_r \varepsilon_r} = \sqrt{1-\frac{1}{E}(\varepsilon_1\hbar\,\omega_{\boldsymbol{\varkappa}_1 j_1} + \cdots + \varepsilon_r\hbar\,\omega_{\boldsymbol{\varkappa}_r j_r})}\,\mathbf{K}. \qquad (21)$$

The calculations needed here are analogous to those for $\sigma_1(\mathbf{k},\mathbf{K})$, but require more space. Therefore we shall give only the result:

$$\sigma_r(\mathbf{k},\mathbf{K}) = \sum_{\boldsymbol{\tau}} \sum_{\boldsymbol{\varkappa}_1\ldots\boldsymbol{\varkappa}_r} \sum_{j_1\ldots j_r} \sum_{\varepsilon_1\ldots\varepsilon_r} \frac{k'}{k} \sum_{pp'} f_p^* f_{p'}\,\cdot$$

$$\cdot\, e^{i(\mathbf{k}'-\mathbf{k})\cdot(\mathbf{R}_p-\mathbf{R}_{p'})}\, e^{-M_p(\mathbf{k}'-\mathbf{k})}\, e^{-M_{p'}(\mathbf{k}'-\mathbf{k})}\, \frac{1}{\underline{|r}}\left(\frac{1}{2}\right)^r\cdot \qquad (22)$$

$$\cdot \prod_{i=1}^{r}\left\{[(\mathbf{k}'-\mathbf{k})\cdot\mathbf{C}_{p\boldsymbol{\varkappa}_i j_i}]\,[(\mathbf{k}'-\mathbf{k})\cdot\mathbf{C}^*_{p'\boldsymbol{\varkappa}_i j_i}]\,\frac{1}{2}\left(g(\omega_{\boldsymbol{\varkappa}_i j_i}) + \frac{\varepsilon_i\hbar}{2\,\omega_{\boldsymbol{\varkappa}_i j_i}}\right)\right\}\cdot$$

$$\cdot \prod_{i=1}^{3} 2\pi L_i\, \delta_{L_i}((\mathbf{k}'-\mathbf{k}+\boldsymbol{\varkappa}_1+\cdots+\boldsymbol{\varkappa}_r-2\pi\boldsymbol{\tau})\cdot\mathbf{a}_i),$$

where we shall sum only over those $\boldsymbol{\varkappa}_1, j_1, \varepsilon_1; \ldots; \boldsymbol{\varkappa}_r, j_r, \varepsilon_r$ which make $\mathbf{k}'$ real, k' being an abbreviation for the vector $\mathbf{k}'_{\boldsymbol{\varkappa}_1 j_1 \varepsilon_1,\ldots,\boldsymbol{\varkappa}_r j_r \varepsilon_r}$ defined in (21).

Finally, we mention that if we formally replace $\mathbf{k}'$ by $\mathbf{K}$ in (22) (i. e., neglect the change of frequency), we get complete agreement with the terms of the order r for X-ray diffraction.[1]

---

[1] WALLER, l. c., eq. (37), p. 25.

The author wishes to express his gratitude to Professor IVAR WALLER for suggesting this investigation and for much good advice during the work.

Institute for Mechanics and Mathematical Physics, University of Uppsala, Uppsala.

Appendix

We shall prove that

$$\sum_{n=\frac{1}{2}(|\nu|-\nu)}^{\infty}(1-\alpha)\,\alpha^n A_{n+\nu,n}(x)\,A_{n+\nu,n}(-x') = (\sqrt{\alpha})^{-\nu}\,e^{-(x^2+x'^2)\frac{1+\alpha}{1-\alpha}}(-i)^{\nu}J_{\nu}\left(2\,i\,x\,x'\,\frac{2\sqrt{\alpha}}{1-\alpha}\right).$$

This is a generalization of the formulae (IV) and (VII) in OTT's[1] "Anhang". Our argument is analogous to that of OTT, but somewhat simpler.

If $x = x' = 0$, the formula is evident, for $A_{n+\nu,n}(0) = \delta_{\nu 0}$ and $J_\nu(0) = \delta_{\nu 0}$. Therefore we may suppose in the following, e. g., $x \neq 0$.

Case I: $x \neq 0$ and $\nu \geq 0$.

In the definition (3) we substitute for the Hermitian polynomials

$$H_n(\xi) = \frac{\underline{|n}}{2\pi i}\oint \frac{e^{-u^2+2\xi u}}{u^{n+1}}\,du$$

$$H_m(\xi) = \frac{\underline{|m}}{2\pi i}\oint \frac{e^{-v^2+2\xi v}}{v^{m+1}}\,dv$$

and integrate first over ξ and then over u. Substituting $v = i\,x\,z$, we get

$$A_{m,n}(x) = A_{n,m}(x) = \frac{2^n\,\underline{|m}\,\sqrt{\pi}\,e^{-x^2}}{\sqrt{2^n\,\underline{|n}\,\sqrt{\pi}\,2^m\,\underline{|m}\,\sqrt{\pi}}}\;\frac{(i\,x)^{n-m}}{2\pi i}\oint\frac{(1+z)^n\,e^{-2x^2z}}{z^{m+1}}\,dz, \tag{a}$$

valid for $x \neq 0$.

Analogously, we get

$$A_{n,m}(-x') = A_{m,n}(-x') = \\ = \frac{2^m\,\underline{|n}\,\sqrt{\pi}\,e^{-x'^2}}{\sqrt{2^m\,\underline{|m}\,\sqrt{\pi}\,2^n\,\underline{|n}\,\sqrt{\pi}}}\;\frac{(-i\,x')^{m-n}}{2\pi i}\oint\frac{(1+w)^m\,e^{-2x'^2w}}{w^{n+1}}\,dw, \tag{b}$$

valid for $x' \neq 0$. If $m \geq n$, (b) is valid also for $x' = 0$.

With $m = n + \nu\,(\nu \geq 0)$, (a) and (b) give

$$A_{n+\nu,n}(x)\,A_{n+\nu,n}(-x') = \\ = e^{-(x^2+x'^2)}\left(-\frac{x'}{x}\right)^{\nu}\frac{1}{2\pi i}\oint\frac{(1+z)^n\,e^{-2x^2z}}{z^{n+\nu+1}}\,dz\;\frac{1}{2\pi i}\oint\frac{(1+w)^{n+\nu}\,e^{-2x'^2w}}{w^{n+1}}\,dw, \tag{c}$$

valid for $x \neq 0$ and $\nu \geq 0$.

---

[1] OTT, l. c.

Using (c), we get

$$\sum_{n=0}^{\infty}(1-\alpha)\,\alpha^n A_{n+\nu,n}(x)\,A_{n+\nu,n}(-x') =$$

$$= \sum_{n=0}^{\infty}(1-\alpha)\,e^{-(x^2+x'^2)}\left(-\frac{x'}{x}\right)^{\nu}\frac{1}{2\pi i}\oint dz\,\frac{e^{-2x^2z}}{z^{\nu+1}}\cdot \tag{d}$$

$$\cdot\frac{1}{2\pi i}\oint dw\,\frac{(1+w)^{\nu}e^{-2x'^2w}}{w}\left(\alpha\frac{1+z}{z}\,\frac{1+w}{w}\right)^{n}.$$

We suppose that $|\alpha| < 1$. The contours can be replaced by circles with arbitrarily large radii. Then $\left|\alpha\frac{1+z}{z}\,\frac{1+w}{w}\right| < 1-\varepsilon,\ \varepsilon > 0$, for every z and w on the circles, and we can perform the summation in (d) before the integrations, obtaining

$$\sum_{n=0}^{\infty}(1-\alpha)\,\alpha^n A_{n+\nu,n}(x)\,A_{n+\nu,n}(-x') =$$

$$= (1-\alpha)\,e^{-(x^2+x'^2)}\left(-\frac{x'}{x}\right)^{\nu}\frac{1}{2\pi i}\oint dz\,\frac{e^{-2x^2z}}{z^{\nu}[(1-\alpha)z-\alpha]}\cdot \tag{e}$$

$$\cdot\frac{1}{2\pi i}\oint\frac{(1+w)^{\nu}e^{-2x'^2w}}{w-\dfrac{\alpha(z+1)}{(1-\alpha)z-\alpha}}\,dw.$$

Performing the integration with respect to w and then putting

$$z = \frac{\alpha}{1-\alpha} - \frac{\zeta}{2x^2},$$

we get

$$\sum_{n=0}^{\infty}(1-\alpha)\,\alpha^n A_{n+\nu,n}(x)\,A_{n+\nu,n}(-x') =$$

$$= (\sqrt{\alpha})^{-\nu}e^{-(x^2+x'^2)\frac{1+\alpha}{1-\alpha}}(-i)^{\nu}\left(2ixx'\frac{\sqrt{\alpha}}{1-\alpha}\right)^{\nu}\cdot \tag{f}$$

$$\cdot\frac{1}{2\pi i}\oint\zeta^{-\nu-1}e^{\zeta-\left(2ixx'\frac{\sqrt{\alpha}}{1-\alpha}\right)^{2}\frac{1}{\zeta}}\,d\zeta =$$

$$= (\sqrt{\alpha})^{-\nu}e^{-(x^2+x'^2)\frac{1+\alpha}{1-\alpha}}(-i)^{\nu}J_{\nu}\left(2ixx'\frac{2\sqrt{\alpha}}{1-\alpha}\right),$$

where $\sqrt{\alpha}$ denotes the same number in both places of (f). J_{ν} is the Bessel function of order ν.

Case II: $x \neq 0$, $\nu < 0$.

As $A_{m,n}$ is symmetric in m and n, it follows from (f) that

$$\sum_{n=\frac{1}{2}(|\nu|-\nu)}^{\infty} (1-\alpha)\,\alpha^n A_{n+\nu,n}(x)\,A_{n+\nu,n}(-x') =$$

$$= \alpha^{|\nu|} \sum_{n=0}^{\infty} (1-\alpha)\,\alpha^n A_{n+|\nu|,n}(x)\,A_{n+|\nu|,n}(-x') =$$

$$= (\sqrt{\alpha})^{-\nu}\, e^{-(x^2+x'^2)\frac{1+\alpha}{1-\alpha}} (-i)^{\nu} J_{\nu}\left(2\,i\,x\,x'\,\frac{2\sqrt{\alpha}}{1-\alpha}\right).$$

Note added in proof: The author is aware of the fact that the treatment can be formally simplified by taking together the terms which correspond to the same $\omega_{\varkappa j}$ using the addition theorem for the Bessel functions. However, this treatment could not be included because of lack of time when writing the manuscript.

Tryckt den 10 december 1951

Uppsala 1951. Almqvist & Wiksells Boktryckeri AB

ARKIV FÖR FYSIK Band 4 nr 7

Communicated 6 June 1951 by AXEL E. LINDH and HARALD NORINDER

The isotopic abundance of K^{40}

By CARL REUTERSWÄRD

With 1 figure in the text

The isotopic abundance of K^{40} has attracted a good deal of interest on account of the rôle which this isotope is supposed to have in the thermal balance of the earths crust (1). The earlier measurements of this abundance (2, 3), however, are few and exhibit a rather large degree of uncertainty. The difficulties have been two: (1) in the mass spectrum of K the very small peak at 40 is always superposed on the fringes of the high neighbours at 39 and 41, rendering it difficult to assess the correct height of K^{40}; (2) all absolute measurements of isotopic abundance have been impaired by unsufficient knowledge concerning the systematic errors of the instruments. Recently NIER (4) has removed the latter uncertainty in principle by calibrating the mass spectrometer with artificial isotopic mixtures of known composition, a method which has become practical through the recent advances in the technique of separation in quantity of the natural isotopes. By this means, there is now the possibility of calibrating mass spectrometers by the natural isotopic ratios standardized by Nier.

Regarding the specific difficulty (1) connected with the measurement of the isotopic abundance of K^{40}, it will be of value to apply the above method in order to confirm the new data of Nier himself. For the evaluation of the mass discrimination one uses the ratio of $K^{39} : K^{41}$, as this is established to a higher accuracy. In this respect, there are the old investigation by BREWER (3) and some recent measurements made at this laboratory. Both of them refer to a type of ion source fundamentally different from that used by Nier, viz. the thermionic emission of positive ions from a platinum surface impregnated with potassium (by heating in contact with potassium salts), or ions from certain compounds of potassium. A definite advantage is thereby gained in that no alkali hydride ions have ever been found in such ion sources.

The new determination of $K^{39} : K^{40}$ presented here is the result of 60 individual measurements taken with two different slit widths in order to detect possible systematic errors in the evaluation of the spectra. Typical samples of such records appear in the adjoining figure. The records were taken partly with a Brown potentiometric recorder (right-hand record) partly with an Esterline-Angus recording mA-meter (left-hand records). The recorder scales were calibrated immediately after each run. The results obtained with different spectral resolutions, with different recorders and different recording speeds all agree

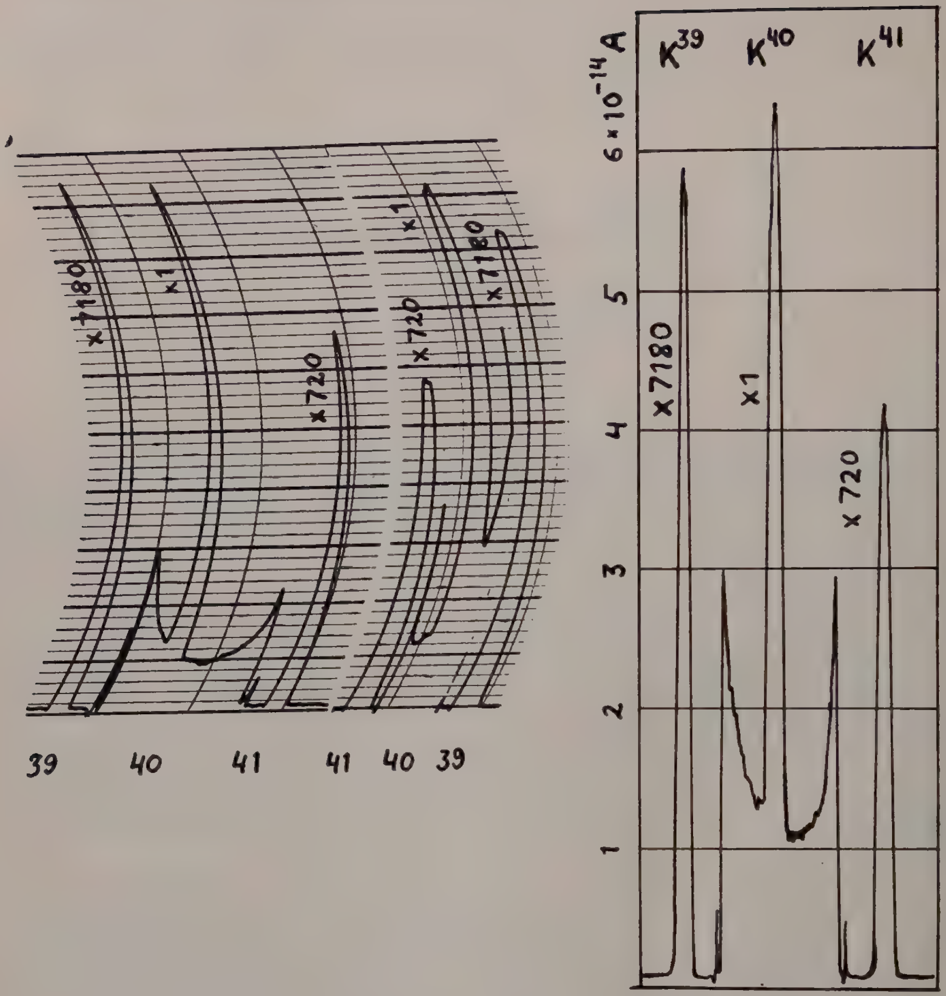

Fig. 1.

within 0.25 percent. The measuring amplifier used is direct-coupled, employing a large amount of negative feedback. Welwyn resistors in the range of 10^{10}–$10^{12}\,\Omega$ were used at the input. It proved necessary to house the resistors in a thermostat. The resistors were repeatedly calibrated internally, and tests for non-linearity did not show any deviation exceeding 0.1 percent in a range of 10 V. The spectrum was scanned by changing the accelerating voltage. The mass discrimination introduced by this method will be superposed on the unknown discrimination active in the thermionic emission of the ion source, a platinum filament coated with potassium phosphate. A more detailed account of these investigations will appear in a subsequent communication.

The (39, 41) ratio is used to determine the mass discrimination in the different spectra, the recent result of Nier being taken as correct. Then the (39, 40) ratios, corrected correspondingly, should become comparable as absolute determinations, the only systematic error remaining being the absolute error of Nier's determination of the (39, 41) ratio. In fact, as shown by the following table, the differences between the various determinations of the (39, 40) ratio (all except Nier's former one) are but a few percent.

Table 1.

Author	$K^{39}:K^{41}$ measured	$K^{39}:K^{40}$ measured	Correction for mass ratio 39 : 40	$K^{39}:K^{40}$ corrected
Nier, 1935	13.96 ±.10	8600 ± 860	− 1.7 %	8450 ± 850
Brewer, 1935	14.25 ±.04	8300 ± 100	− 2.7 %	8080 ± 100
Nier, 1950	13.48 ±.07	7800 ± 80	± 0.0 %	7800 ± 80
Reuterswärd, 1951	14.32 ±.05	8140 ± 40	− 3.0 %	7900 ± 40

The agreement of the new measurements with both the earlier ones of Brewer and the recent ones of Nier appears satisfactory, the error limits given being the median deviation of the individual determinations. The corresponding isotopic abundance of K^{40} is $1.18 \cdot 10^{-4} \pm 1\ \%$, the error including the average deviation of Nier's absolute determination of the isotopic ratio $K^{39} : K^{41}$.

Uppsala, in April, 1951.

REFERENCES. (1) **T. Graf,** 1947, Phys. Rev. *72,* 641. — (2) **A. O. Nier,** 1935, Phys. Rev. *48,* 283. — (3) **A. K. Brewer,** 1935, Phys. Rev. *48,* 640. — (4) **A. O. Nier,** 1950. Phys. Rev. *77,* 789.

Tryckt den 10 december 1951

Uppsala 1951. Almqvist & Wiksells Boktryckeri AB

ARKIV FÖR FYSIK Band 4 nr 8

Communicated 12 September 1951 by MANNE SIEGBAHN and BENGT EDLÉN

Determination of the self-absorption and relative efficiency of some important liquid scintillators*

By HOLGER SKÖLDBORN

With 4 figures in the text

Preliminary experiments with fluorescent liquids and solutions

Studies with scintillation counters have been conducted at this Institute during the past three years. As phosphors, crystals of thallium-activated sodium iodide were used. In October 1949, the present author started an investigation on the gamma-radiation fluorescence of liquids. The primary aim was to find a liquid which, either in the pure state or after suitable mixing, gave pulses sufficiently strong to enable it in certain cases to replace the crystal of a scintillation counter.[1] The main advantage of such a liquid scintillator is that it can easily be given the shape and extension desired, which is not possible with crystal phosphors.

It was difficult to find any clues in the literature as to which liquids would be suitable for our purpose. However, a thirty year old report by H. S. NEWCOMER, The X-ray fluorescence of certain organic compounds[2], proved valuable. In this work about 500 substances were described that had been examined for X-ray fluorescence, chiefly visually, but partly photographically.

On the basis of NEWCOMER'S work a number of those liquids which according to him had the most powerful fluorescence, were examined. The investigation was carried out by means of a photometric device, consisting of a liquid container, a photomultiplier tube (type RCA, 1P21), and a galvanometer. The container was made of brass and was nickelplated on the inside. It was cylindrical and so constructed that it completely enclosed the photomultiplier. As source of radiation a 4 mg. radium container was used at a suitable, fixed distance. The sensitivity attained with this apparatus was so high that even the faint fluorescence present in distilled water could be recorded.

Among the pure liquids studied, xylene and dimethyl aniline proved to be most effective. It soon became apparent, however, that the light emission could be im-

---

* A short account of this work was given at the Conference of the Swedish National Committee of Physics, June 1951.

[1] The first publication on liquid scintillators appears to be Sulla nuova tecnica dei contatori a scintillazione, by AGENO, M., CHIOZZOTTO, M. & QUERZOLI, R. Accad. Naz. Lincei *6*, 626 (1949). Among other things, certain results are reported which were obtained by gamma-radiation of a solution of naphthalene in xylene. The present author did not become acquainted with the paper in question until May 1950.

[2] NEWCOMER, H. S., J. Amer. Chem. Soc. *42*, 1947 (1920).

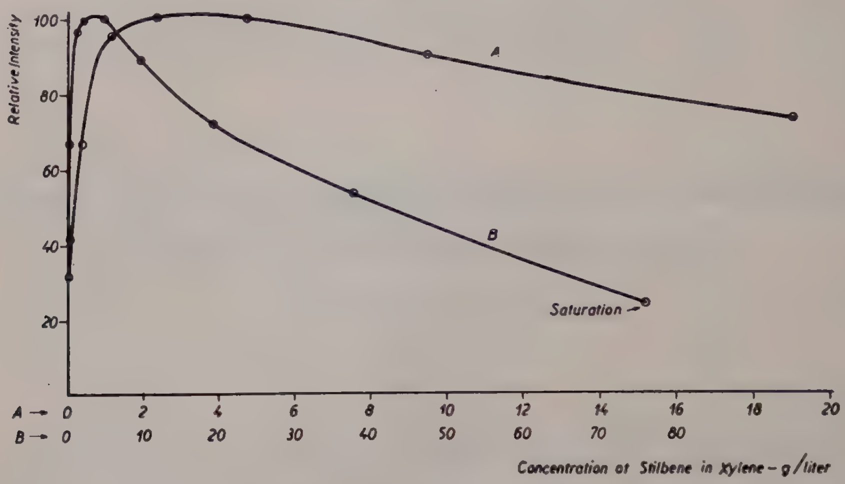

Fig. 1. Stilbene in xylene.

proved by a factor of ten by using instead solutions of fluorescent organic crystals. Of the two-component solutions examined, anthracene in xylene gave the highest light intensity. Optimal concentration was obtained with 1: 6 dilution of a solution saturated at 20° C., corresponding to approximately 1.5 grams per litre. Somewhat better results were obtained when this solution was saturated with naphthalene. An equally effective combination was a solution of β-methyl naphthalene in xylene in a dilution of 1: 40, containing 1.5 grams of anthracene per litre. The curve in Fig. 1 shows the variations in the light intensity with increasing concentration of the fluorescent substance for a solution of stilbene in xylene; similar curves were obtained for anthracene and β-methyl naphthalene. For naphthalene the same steep rise was observed at low concentrations; the light intensity rose slightly with increased concentration up to saturation.

In experiments using dimethyl aniline as the solvent for anthracene and similar fluorescent substances, the effect was quite the opposite to that observed with xylene: there was a powerful quenching of the intensity instead of an increase.

In addition, it may be mentioned that fluorescein and some uranyl-compounds, which showed strong fluorescence on ultraviolet irradiation, all gave negative results on gamma-excitation. The same applied to a solution of approximately 0.5 grams per litre of the compound salicylaldehyde-o-phenylene-diimine uranyl in xylene. The addition of this substance to an optimal solution of anthracene in xylene produced a reduction in the intensity of approximately 10 per cent. In this connection the possibility was considered of employing a liquid scintillator as a neutron detector by utilizing the fission pulses from a uranium compound. A calculation showed conditions to be hardly favourable, however, partly on account of the small cross section of the reaction and partly because of the difficulty in obtaining a uranium compound which was sufficiently soluble in an organic liquid scintillator without causing too great a reduction of the fluorescence effect.

In order to get an idea of the magnitude of the light pulses and the time constant for light emission in these liquid scintillators, the course of the pulses was studied by means of an oscillograph (Tektronix, type 511 A). From this it was apparent that the time constant for a solution of anthracene in xylene was less than 10^{-7} second. The light emission thus occurs very rapidly, which is a great advantage. The pulse height, however, was between 5 and 10 times smaller than that for a naphthalene crystal (γ-radiation, equivalent light collimation).

It was evident from the results of these first studies that liquid scintillators could be employed as phosphors in scintillation counters. It would, however, be of more practical value if a solution could be found with a considerably greater light emission than anthracene in xylene. For this purpose, and also in order to study the mechanism of energy transport in liquids and solutions fluorescent on γ-irradiation, a comprehensive investigation would be required, as well as an ample supply of substances which at present can be obtained in this country only after a long time of delivery.

Shortly after these preliminary experiments had been completed, a few articles were published in Phys. Rev. and Nucleonics with reports of investigations with liquid scintillators[3, 4, 5]. In his first article, KALLMANN mentions anthracene in xylene together with some other solutions, which are said to be equally effective. REYNOLDS et al. were the first to use terphenyl (p-diphenylbenzene) for this purpose; an optimal solution of terphenyl in xylene gives approximately a tenfold increase in light efficiency over that of the corresponding anthracene solution and about half as large light flashes as an anthracene crystal. Terphenyl is still unsurpassed as a light-emitting substance in liquid scintillators. During the past year about ten reports have been published concerning the fluorescence of liquids and solutions on α-β-n-γ-radiation[6, 7, 8, 9, 10, 11]. In their last article, KALLMANN and FURST submit data on the relative effectiveness of more than 400 liquids and solutions measured with a photomultiplier tube, type RCA, 1P28. Since practically all liquids and solutions, which have been measured by the present author, are tabulated by these investigators, the results of the earlier experiments will not be given here. On the basis of their experimental results, KALLMANN and FURST in two longer articles have also attempted an explanation of the complicated transport of energy which occurs from the molecules of the solvent to those of the solute in such fluorescent solutions. The main part of the light emission in all probability takes place from the molecules of the solute.

Absorption

For the practical use of liquid scintillators it is often very valuable to know or to be able to determine easily the self-absorption of the solution for the fluorescent light emitted. This is particularly true when it is desired to make use of one of the special advantage possessed by the liquid scintillator as compared with a crys-

---

[3] REYNOLDS, G. T., HARRISON, F. B. & SALVINI, G., Phys. Rev. *78*, 488 (1950).
[4] REYNOLDS, G. T., Nucleonics *6*, No 5, 68 (1950).
[5] KALLMANN, H., Phys. Rev. *78*, 621 (1950).
[6] KALLMANN, H. & FURST, M., Nucleonics *7*, No. 1, 69 (1950).
[7] AGENO, M., CHIOZZOTTO, M. & QUERZOLI, R., Phys. Rev. *79*, 720 (1950).
[8] HARRISON, F. B. & REYNOLDS, G. T., Phys. Rev. *79*, (1950).
[9] KALLMANN, H. & FURST, M., Phys. Rev. *79*, 857 (1950).
[10] KALLMANN, H. & FURST, M., Phys. Rev. *81*, 853 (1951).
[11] KALLMANN, H. & FURST, M., Nucleonics *8*, No. 3, 32 (1951).

tal phosphor, viz. the possibility of working with a large liquid container in order to count a large number of pulses per unit time. Liquid scintillators have already been used in this way in studies of cosmic radiation. The absorption together with the reflection losses play a decisive part in the determination of the optimal size of the container for the investigation of a certain kind of radiation. The present author has therefor worked out a method which enables a fairly accurate determination of the self-absorption of liquid scintillators.

On account of the small range of alpha-particles in a liquid (< 0.1 mm.), the author chose to work with an α-emitting polonium source. When placed in a fluorescent solution a small source produces an almost point-source of light with a spectrum that is characteristic for the solution in question. When absorption occurs (due to small amounts of impurities) the spectrum changes its character at a greater distance from the light source. It was assumed that excitation with roentgen- or gamma-radiation would give fluorescent spectra in close agreement with those of alpha-particles. This theory was recently confirmed by KALLMANN and FURST (ref. 10, p. 858).

The principle of the measuring device used is evident from Fig. 2. (A) is a cylindrical liquid container made of nickel-plated brass in light-tight connection with the bakelite cylinder enclosing the photomultiplier (B). The bottom of the container has a quartz window, a few millimeters from the photo-cathode. Through the lid runs a screw, 120 mm. long (3 mm. pitch), the lower part of which carries a metallic paraboloidal mirror (16 mm. parameter). The latter is provided with a narrow cross bar with a hole in the middle, in which a small source holder (C) can be fastened so that the polonium source, which is deposited on the upper level silver surface of the holder (0.6 mm. diameter), will be in the centre of the focal plane of the mirror. During the precipitation of the polonium source (from a RaD-solution) the holder, with the exception of the upper surface, was covered with glyptal. In order to make the source more stable it was covered by vacuum evaporation with a layer of aluminium 1000 Å thick. This proved to be very satisfactory.

The channel running through the screw serves two purposes: to prevent the formation of air bubbles under the mirror and to make possible a test of the accuracy of the mirror. The parallel, downwardly directed rays of light are delimited by an oxidized, non-reflecting brass diaphragm.

For the purpose of testing the mirror (without liquid), a source holder was prepared identical to the one described above but with a layer of magnesium oxide in place of the polonium preparation. The diffusely reflecting surface in the focal plane thus obtained was illuminated by means of the channel from the constant light source (D). The light emission from the focus obtained in this manner can be assumed to be almost analogous to that emitted by the polonium source, surrounded by a fluorescent liquid. A photographic recording showed that the diameter of the light beam reflected from the mirror increased somewhat with the distance from the mirror. This would be immaterial if the average sensitivity of the photo-cathode were constant along a diameter which, however, was not the case.

The photomultiplier employed was of the type EMI, 5311. (At first another tube, RCA 5819, was used.) An examination of the variation in sensitivity of these two types of tubes along a number of different diameters of the photo-cathode (chosen at random), gave the following results. With the EMI-tubes, the sensitiv-

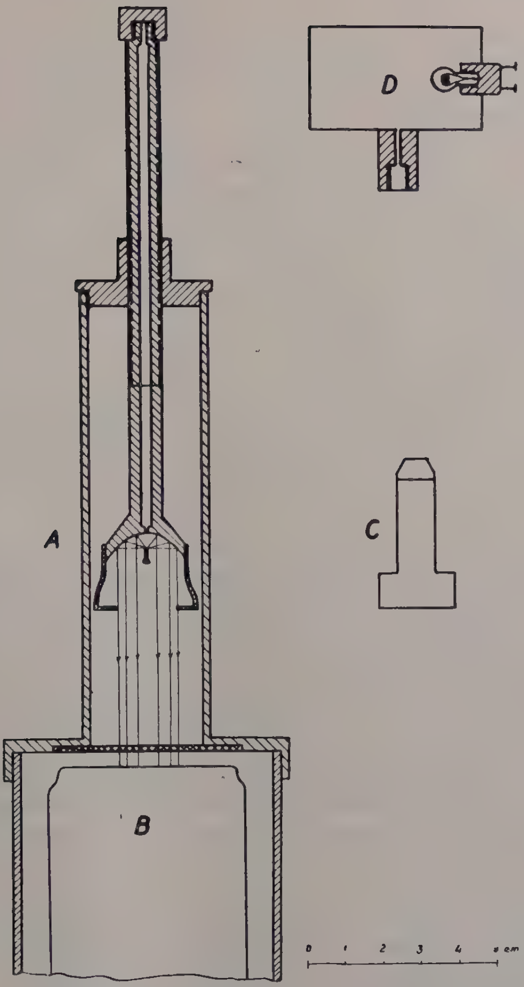

Fig. 2. Experimental arrangement for absorption measurements.

ity diminished approximately 50 per cent at a distance from the centre of 1 cm. Two tubes were examined and both showed the same tendency. With the RCA-tube, the sensitivity increased approximately 50 per cent 1 cm. from the centre; only one tube was available.

This variation in sensitivity necessitated a correction curve for the apparatus (fig. 3). The curve was determined with a constant light source as described above and the anode current was read on a galvanometer for different settings of the mirror. The curve was reproducible within 1 per cent, provided the EMI-tube was not moved from its position.

The apparatus was then ready for absorption measurements. The container was filled with the solution in question and the pulses from the photomultiplier were

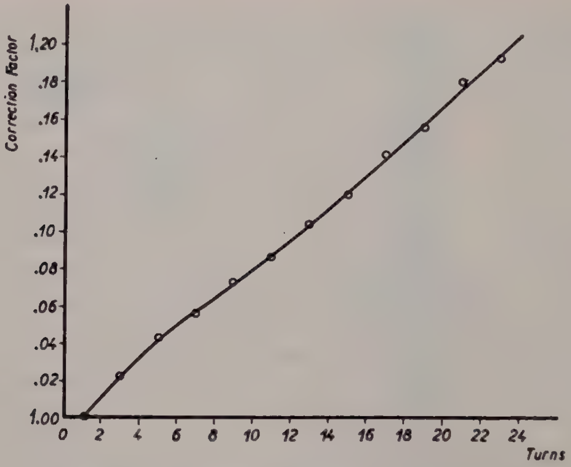

Fig. 3. Corrections for different positions of the parabolic mirror.

studied by means of a one channel differential discriminator.[12] For a certain adjustment of the mirror a pulse hight distribution was obtained in the form of a Gaussian curve, the peak of which could be determined with good accuracy. When the mirror with the alpha-source was moved higher up in the container the depth of the liquid layer increased, through which the excited fluorescent light had to pass before striking the photocathode. If part of the light was then absorbed the average pulse height decreased correspondingly and the distribution curve was displaced towards lower values on the discriminator scale. By determining the location of the peak of the curve for two adjustments, one could calculate the absorption of the layer depth in question. Two typical curves are given in Fig. 4. They were obtained by measuring the absorption in a solution of terphenyl in xylene, 5 grams per litre.

The method is less suitable for solutions with low light efficiency, owing to the fact that alpha-particles in liquid scintillators give 3 to 5 times smaller light flashes than gamma-radiation of the same energy. When the flashes are too small, the typical Gaussian distribution is not obtained; the curves flatten out and the peak cannot be determined with sufficient accuracy.

Table I shows the results from some absorption determinations carried out with the method described above. The absorption coefficients (k) given, which are calculated according to the formula $I = I_0 \cdot e^{-kx}$ refer to solutions of substances with stated quality and layer depth. They depend also on the spectral sensitivity curve of the photomultiplier tube (type S-9). The distance between the polonium preparation and the quartz window was approximately 23 mm. with the mirror in its lowest position, which was the same in every measurement.

An idea of the accuracy of the method was obtained by measurements made on the same solution with different polonium preparations and by other variations in the experimental conditions. The most important source of error was found to

---

[12] The apparatus used has been described by SVEN A. E. JOHANSSON, Arkiv för fysik, *3*, 533 (1951). In this connection I should like to thank Mr. S. JOHANSSON and Dr. L. STIGMARK for their valuable help during the course of my investigations.

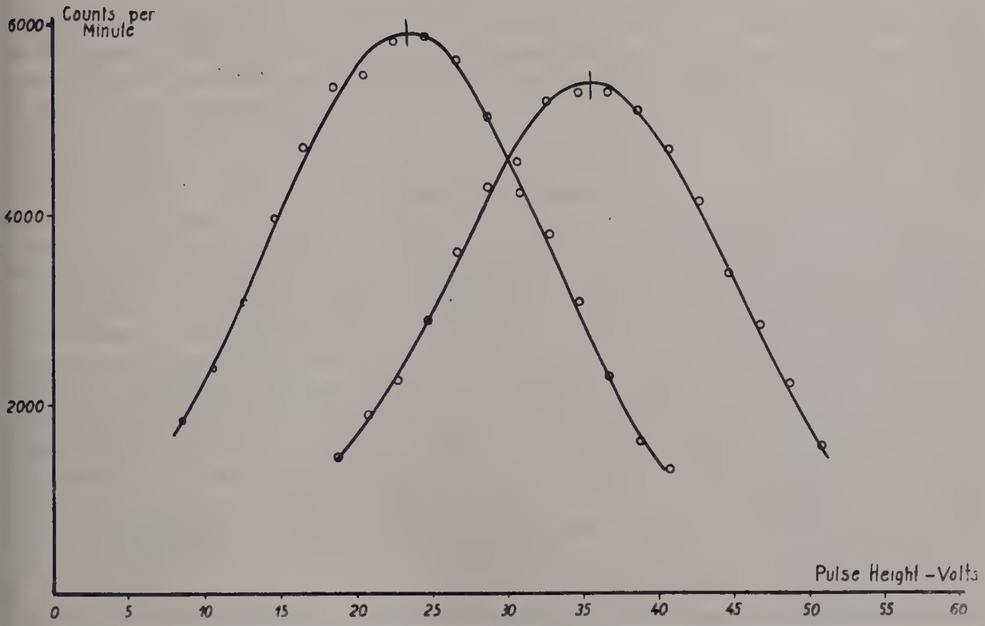

Fig. 4. Pulse height distribution curves for alpha-rays from polonium obtained for two positions of the mirror (fig. 2) in a solution of 5g/l terphenyl in xylene.

Table I.

Absorption coefficients (k) of some liquid scintillators at given depth of the solution.

Solvent	Quality	Solute	Quality	Conc. g/l	Depth cm.	k %/cm.
Xylene	"DAB"	Terphenyl	"Eastman"	5	0.9	14.4
Xylene	"DAB"	Terphenyl	"Eastman"	5	5.4	9.6
Phenylcyclohexane	"Eastman"	Terphenyl	"Eastman"	3	4.5	18.5
p-Cymene	"Eastman"	Terphenyl	"Eastman"	3	2.1	24.3
Xylene	"DAB"	Anthranilic Acid	"Kebo", p. a.	3	2.1	6.7
Phenylcyclohexane	"Eastman"	α-Naphthylamine	"Eastman"	1	2.1	15.5

be small changes in the zero position of the discriminator. This, however, can be practically eliminated. The absorption values given in the table were reproducible within approximately 10 per cent, which was sufficiently accurate for our purpose.

As shown by Kallmann and Furst, among others, the absorption can be considerably reduced in certain cases by further purification of the substances. In one of their recent works[10], these authors have reported approximate measurements of the absorption in many liquids and solutions. The method employed was quite different from the one described in this paper: it appears to be more rapidly carried out but it is probably less accurate. For this reason and in consideration of the decisive role played by the degree of purity of the substances in determining the absorption, it is hazardous to compare the results reached. KALLMANN and FURST found their solution of terphenyl in xylene to be almost free from absorption and used this solution as a standard when measuring the absorption in other solutions.

Relative efficiency

The relative efficiency of the solutions included in table I (together with a few others) was measured with the same EMI-tube as before and a galvanometer, in the following manner. On the top of the photomultiplier a piece of white cardboard was attached, which had a circular hole, 22 mm. in diameter, immediately over the photo-cathode. In this hole, directly on the glass, was placed a cylindrical container of perspex (with inside measurements of 20 mm. × 20 mm. and a wall thickness of 1 mm.), filled with the solution in question. The container was then covered with a brass hood, with a highly reflective layer of magnesium oxide on the inside. In this manner a very effective concentration of light was obtained. A light-tight cover of bakelite was placed over the entire apparatus and a little higher up a 1 mC RaTh-preparation. The reading of the galvanometer (after subtraction of the zero reading) was then a measure of the integrated light intensity emitted from the various solutions on gamma-excitation.

The results of the measurements appear from table II. The values are recalculated in per cent of the reading for the 5 grams per litre solution of terphenyl ("Eastman") in xylene ("DAB"). As appears from the table the product from another firm showed a 34 per cent greater light emission. By way of comparison, the relative values (recalculated) obtained by KALLMANN and FURST[11] using a similar method of measurement but with a photomultiplier of the type RCA, 1P28 (spectral sensitivity curve of the type S-5), are given in column 7. In those instances where very dissimilar values were reached, this is probably largely due to the varying degree of purity of the substances in the solutions. The same concentrations were

Table II.

Relative Efficiencies of Some Highly Fluorescent Solutions.

Solvent	Quality	Solute	Quality	Conc. g/l	Relative Intensity	Relative Intensity according to KALLMANN & FURST
Xylene	"DAB"	Terphenyl	"Eastman"	5	100	100
Xylene	"DAB"	Terphenyl	"Light & Co"	5	134	
Phenylcyclohexane	"Eastman"	Terphenyl	"Eastman"	3	128	113
p-Cymene	"Eastman"	Terphenyl	"Eastman"	3	60	52
p-Dioxane	"Eastman"	Terphenyl	"Eastman"	10	57	50
Xylene	"DAB"	Anthranilic Acid	"Kebo", p. a.	3	54	50
Phenylcyclohexane	"Eastman"	α-Naphthylamine	"Eastman"	1	45	72
Phenylcyclohexane	"Eastman"	Carbazole	"Eastman"	1	42	43
Diphenyl Oxide	"Kebo"	Terphenyl	"Eastman"	3.5	40	113
Tetrahydronaphthalene	"Grave"	Terphenyl	"Eastman"	8	10	50

used throughout. This series of measurements was reproducible within 3 per cent. Some of the solutions showed a tendency to dissolve the material of the container, but there was no noticeable effect on the reading.

The following simple experiment showed in a striking manner the effect of absorption observed according to table I on the total light yield and thus also on the effective pulse height. Solutions 1 and 6 in table II were measured without the reflecting hood; the container of perspex was then enclosed in dark bakelite with little reflecting power. The value of the intensity for the solution of anthranilic acid in xylene was then only 28 per cent of the value for the solution of terphenyl in xylene, against 54 per cent according to table II (with hood). It appears that, due to less absorption (table I), the relative value of solution no. 6 is improved by a factor of nearly 2 in comparison with no. 1 when a liquid container with highly reflective walls is used. A slight change in the reflection factor with the wavelength of the emitted light may have contributed to some slight extent to the result. It is also evident from this experiment that, when employing large liquid containers, it may be more expedient to use a fluorescent solution of relatively low effectiveness, if only the absorption is sufficiently insignificant, rather than to choose a solution, which gives a satisfactory pulse height in a small container, but whose light intensity at greater distances is effectively weakened by too great self-absorption.

The author wishes to express his sincere gratitude to Prof. S. von Friesen for suggesting these experiments and for valuable support during the course of the work.

Department of Physics, University of Lund, June 1951.

Tryckt den 11 december 1951

Uppsala 1951. Almqvist & Wiksells Boktryckeri AB

ARKIV FÖR FYSIK Band 4 nr 9

Communicated 6 June 1951 by OSKAR KLEIN

A differential equation for the phase shifts in scattering problems

By P. O. OLSSON

With 1 figure in the text

In the phase method in scattering theory the phase shifts are usually calculated from the asymptotic behaviour of the solution of the wave equation. As the cross-sections can be calculated from the values of the phase shifts entirely it is natural to try to obtain the phase shifts directly as solutions of a certain differential equation. In order to find such an equation the phase has to be defined for finite values of the argument as it is usually not defined but asymptotically. This may be done in several ways. One may e.g. study the change of the wave number but this was found to lead to inconvenient equations and the investigations were soon abandoned. Another approach that seems more natural from the mathematical point of view and also gives useful results is presented below.

Consider the wave equation

$$L\,u(x) = \left[\frac{d^2}{d\,x^2} + k^2 - \varrho(x)\right] u(x) = V(x)\,u(x) \tag{1}$$

where we assume $x^2\,\varrho(x)$ and $x\,V(x)$ to be integer functions. Further we assume for $x \to +\infty$

$$\varrho(x) = \frac{\text{const.}}{x} + 0\,[x^{-(1+p')}] \qquad p' > 0$$

$$V(x) = 0\,[x^{-(1+p'')}] \qquad p'' > 0$$

where the const. may be zero, and for $x = +0$

$$x^2\,\varrho(x) = \beta \geq 0.$$

Then the differential equation

$$L\,v(x) = 0 \tag{2}$$

has two fundamental solutions $v_1(x)$ and $v_2(x)$ satisfying the conditions

$$\begin{aligned} & v_1(0) = 0 \\ & v_2(x) = 0\left(x^{\frac{1}{2}-\sqrt{\frac{1}{4}+\beta}}\right) && x \to +0 \\ & v_1(x) \sim \sin(kx - \alpha \ln 2kx + \gamma) \\ & && x \to +\infty \\ & v_2(x) \sim \cos(kx - \alpha \ln 2kx + \gamma) \end{aligned} \tag{3}$$

where α and γ are constants. In the following we assume these solutions to be known.

The solution of (1) with the usual boundary condition $u(0) = 0$ satisfies the integral equation

$$u(x) = C\, v_1(x) + \frac{1}{k} \int_0^x [v_1(x)\, v_2(t) - v_1(t)\, v_2(x)]\, V(t)\, u(t)\, dt \tag{4}$$

where C is an arbitrary constant. With the assumptions made we have

$$u(x) \sim \text{const} \sin(kx - \alpha \ln 2kx + \gamma + \delta) \quad x \to +\infty,\ \delta = \text{const}.$$

The problem is to calculate the phase shift δ.

Put

$$\begin{aligned} A_1(x) &= C - \frac{1}{k} \int_0^x v_2(t)\, V(t)\, u(t)\, dt \\ A_2(x) &= \frac{1}{k} \int_0^x v_1(t)\, V(t)\, u(t)\, dt \\ A_0(x) &= \sqrt{A_1^2(x) + A_2^2(x)} \end{aligned} \tag{5}$$

and introduce an angle $\delta(x)$ defined by

$$\cos \delta(x) = \frac{A_1(x)}{A_0(x)}, \quad \sin \delta(x) = \frac{A_2(x)}{A_0(x)}, \quad \delta(0) = 0. \tag{6}$$

Noting that

$$u(x) = A_1(x)\, v_1(x) + A_2(x)\, v_2(x)$$

the following differential equation[1]

$$\delta'(x) = -\frac{V(x)}{k}\left[v_1(x)\cos\delta(x) + v_2(x)\sin\delta(x)\right]^2 \tag{7}$$

for $\delta(x)$ is easily obtained by differentiating (6) and observing (5).

The limits

$$\lim_{x\to+\infty} A_i(x) = A_i \qquad (i = 0, 1, 2)$$

exist and are finite. From

$$u(x) = A_0(x)\left[\cos\delta(x)\,v_1(x) + \sin\delta(x)\,v_2(x)\right] \sim A_0 \sin(k\,x - \alpha\ln 2\,k\,x + \gamma + \delta)$$

it then follows

$$\delta = \lim_{x\to+\infty}\delta(x).$$

The phase shift is thus obtained as the value at infinity of the solution of (7) if $\delta(0) = 0$.

Substituting $y(x) = \operatorname{tg}\delta(x)$ or $z(x) = \cot\delta(x)$ into (7) we obtain respectively

$$y'(x) = -\frac{V(x)}{k}\left[v_1(x) + y(x)\,v_2(x)\right]^2 \tag{8}$$

$$z'(x) = \frac{V(x)}{k}\left[z(x)\,v_1(x) + v_2(x)\right]^2. \tag{9}$$

In these forms the equation is better adapted for numerical treatment. If the interaction is strong the phase $\delta(x)$ may pass $\pi/2$ or $-\pi/2$ for some value of x and the solution of (8) becomes singular. This difficulty is easily avoided by continuing the integration with equation (9) when the solution of (8) becomes inconveniently large.

Wave functions for

$$L\,v(x) = \left[\frac{d^2}{d\,x^2} + 1 - \frac{2\,\alpha}{x}\right] v(x) = 0 \tag{10}$$

have recently been tabulated.[2] The asymptotic forms of these solutions are

$$v_1(x) \sim \sin\left[x - \alpha\ln 2\,x + \arg\Gamma(i\,\alpha + 1)\right]$$

$$v_2(x) \sim \cos\left[x - \alpha\ln 2\,x + \arg\Gamma(i\,\alpha + 1)\right].$$

---

[1] For $\varrho(x) \equiv 0$ equation (7) becomes $\delta'(x) = -\frac{V(x)}{k}\sin^2(k\,x + \delta)$. This equation is derived in COURANT–HILBERT, Mathematische Physik I, p. 287, and has also been used by HOLMBERG, Kungl. Fysiogr. Sällsk. i Lund Förh. Bd. 18 Nr. 7 (1948) as has been pointed out to the author.

[2] The regular wave functions have been tabulated by A. N. LOWAN, Math. Tables Project, New York. The irregular functions have been computed on BARC. FRÖBERG, Ark. f. Fys. Bd. 3 Nr. 1 (1951).

If in (10) there is beside the Coulomb force also a nuclear force the phase shift caused by the latter may be obtained with the aid of (8) or (9) with no more labour than in the case where no Coulomb interaction is present.

Without Coulomb interaction we may put in (1)

$$\varrho(x) = \frac{L(L+1)}{x^2}$$

and equation (1) is the well-known radial part of the Schroedinger equation for two particle scattering with the interaction potential $V(x)$. In this case the functions $v_1(x)$ and $v_2(x)$ are[1]

$$v_1(x) = \sqrt{\frac{\pi k x}{2}}\, J_{L+1/2}(kx) = j_{L+1/2}(kx)$$

$$v_2(x) = \sqrt{\frac{\pi k x}{2}}\, J_{-L-1/2}(kx) = j_{-L-1/2}(kx)$$

and equation (8) will be

$$y'_L(x) = -\frac{V(x)}{k}\left[j_{L+1/2}(kx) + y_L(x)\, j_{-L-1/2}(kx)\right]^2. \tag{11}$$

Putting in (11) for $L = 0$ $y_0(x) = -k\,a(x)$ we obtain in the limit as $k \to 0$

$$a'(x) = V(x)\,[x - a(x)]^2. \tag{12}$$

As we have

$$\lim_{x \to +\infty} a(x) = a = -\lim_{k \to 0} \frac{y_0(\infty)}{k}$$

where the limit at the right is the scattering length, equation (12) may be used to determine this quantity.

Equation (11) has been integrated numerically in a few cases to check results obtained by variational methods. Graphs of the solutions and values obtained are given below.

Potential $V(x)$		L	k	b	$y_0(\infty)$
I	$-b\,\frac{e^{-x}}{x}$	0	1.0	1.5	0.9814
II	,,	0	2.0	1.5	0.6540
III	$-b\,e^{-x}$	0	0.5	1.3477	1.053

---

[1] For tables see Math. Tables Project, National Bureau of Standards, Tables of spherical Bessel functions, Vol. I. New York (1947).

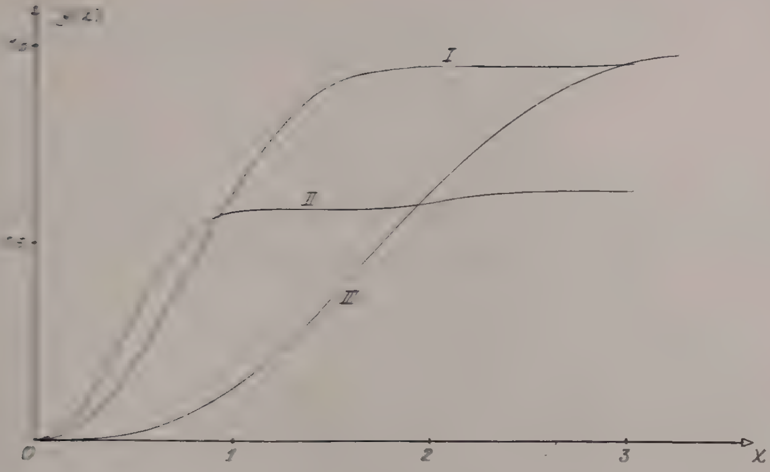

The case of coupled equations as obtained for tensor forces has also been considered. The equations obtained are not written down as the use of them does not seem to be an improvement in comparison with standard methods.

Finally I wish to thank Professor O. KLEIN for the kind interest he has shown in my work and to thank him and Dr. B. ANDERSSON for most valuable discussions.

Tryckt den 11 december 1951

Uppsala 1951. Almqvist & Wiksells Boktryckeri AB

ARKIV FÖR FYSIK Band 4 nr 10

Communicated 12 September 1951 by Erik Hulthén and Gustaf Ising

---

A β-spectro-goniometer for coincidence and angular correlation measurements

Design and applications

By Kai Siegbahn

With 34 figures in the text

Contents

Page

Section 1. *Introduction* 224

Section 2. *Design of the Spectrogoniometer* 227
A. The lenses 228
B. Baffle system 229
C. Counter equipment 231
D. Iron rings and iron shields 232
E. Compensation coils 232
F. Measurement of the effect of mutual disturbance on the resolving power and peak height 233
G. The bellows system 235
H. Neutralization of earth's magnetic field 236

Section 3. *General procedure and expected coincidence rates* 237
A. Coincidences between two conversion lines 237
B. Expected coincidence rate between two lines 238
C. Expected coincidence rate between a line and the continuum 239
D. Generalization of some coincidence rate formulas 241

Section 4. *Some general considerations about angular correlations between electrons* 243

Section 5. *Investigation of Ga^{67}* 245
A. Spectrometer measurements 246
B. Coincidence measurements in the goniometer 247
C. Revised scheme 247

Section 6. *Angular correlation measurements between the F-line and the continuous spectrum of ThB* 248

Section 7. *Investigation of Tm^{170}* 250
A. Source preparation 250
B. Spectrometer measurements 250
C. Determination of source strength 251
D. Measurements of the angular correlation 252

Page

Section 8. *Investigation of Au^{199}* 253
A. Source preparation 253
B. Spectrometer measurements 254
C. The revised scheme 258
D. Conversion coefficients 258
E. Slow neutron cross section of Au^{198} 259
F. Coincidence and angular correlation measurements in the goniometer 260

Section 9. *Investigation of Sm^{153}* 261
A. Source preparation 261
B. Spectrometer measurements 261
C. Revised scheme 263
D. K series fluorescence yield at Z = 63 264
E. Coincidence and angular correlation measurements in the goniometer 265

Section 10. *Angular correlation between internally created positrons and electrons in Na^{24}* 266
A. Positron-electron angular correlation and multipole order 266
B. Experimental procedure 267
C. Experimental proof of the simultaneous emission of electrons and positrons in pairs 268
D. Results of the angular correlation measurements 268
E. Comparison with theory 268

Acknowledgements 271

1. Introduction

As is well known, the coincidence method introduced by BOTHE and applied to nuclear physics problems by BOTHE and v. BAEYER in 1935[1] has gradually become one of the most important tools for studying the coupling between particles and (or) quanta emitted in nuclear phenomena, such as radioactive disintegration processes. In its general performance, however, this method can only to a limited extent discriminate between different kinds of radiations and also between energy components within the same type of radiation. Even in comparatively simple cases the interpretation of a measured coincidence effect may therefore be rather intricate.

As an example we may take a simple K-capture decay, followed by two partially converted γ-rays in a cascade transition according to Fig. 1. Such a decay (In^{111}) has for example been treated by a Swiss group.[2] In the emitted radiation there are X quanta (of different kinds) from the K-capture and also from the internal conversion of both lines. There are also conversion electrons (mostly K and L electrons) and Auger electrons. In fact these quanta and particles are coupled together so as to give a combined coincidence effect from at least 17 different partial couplings. The general procedure is to try to single out the different types of coupling by selecting suitable particle and quanta detectors, the efficiences of which vary with the different types of radiation, and furthermore to use a set of absorbers in the coincidence-arrangement in

---

[1] W. BOTHE and H. v. BAYER, Göttinger Nachr. (II) (N. F.) *1*, 195, 1935.

[2] F. BOEHM, O. HUBER, R. MARMIER, P. PREISWERK a. R. STEFFEN. Helv. Phys. Acta XXII, 69, 1949.

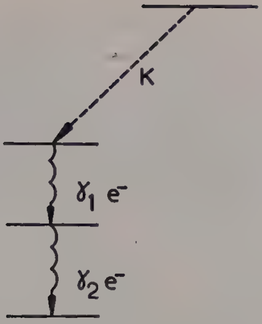

Fig. 1. Simple K capture decay followed by two converted γ-rays.

order to discriminate against one or another kind of radiation. By varying the thickness of the absorbers one can, at least in principle, study the coincidence effect as a function of the energy of the radiation. Such measurements are still uncertain in interpretation because the absorption will affect the whole energy spectrum (which is particularly awkward if this is unknown) and normally also other types of radiation as well.

Though in many cases a careful choice of absorber material, absorber-thicknesses and radiation detectors may help in solving a given problem, other more complicated cases make a refinement in the technique necessary. A natural extension of the original coincidence method would be to combine it directly with the spectrometer method, so that the coincidence effect may be studied under more controlled conditions. The first attempt along these lines was made already in 1937 by BOTHE and MAIER-LEIBNITZ[1], who studied the βγ coincidence effect in the decay of RaC → RaC′. This is a complicated case, which could be studied only by the use of a β-spectrometer to select different well-defined β energy bands in the βγ coincidence arrangement.

We may call this technique "one channel βγ coincidence spectrometry", referring to the fact that there is an energy *band* selecting system only for one of the two kinds of radiation, in this case for the β radiation. This arrangement has the further advantage that the β-counter may be effectively shielded for X and γ radiation, thus eliminating a number of coincidence possibilities. This technique has already been further developed and discussed in the literature.[2–4]

If absorbers are inserted between the source and the γ-counter still more detailed information may be obtained. It would even be possible with present scintillation-detector technique to convert the above βγ coincidence arrangement into a two channel system by using a phosphor such as *NaI* as γ detector and an electronic channel to select the different γ-lines (i.e. as photo lines produced in the crystal). This two channel βγ coincidence spectrometer would certainly be an extremely useful device and will no doubt in the near future be tried by several workers.

If we replace the γ detector by a β detector such as a thin-window GM counter (with or without absorbers) we may study eβ coincidences with a selected energy band of electrons (usually a conversion line). We may also get coincidences between X radiation registered in the β counter and electrons focussed in the spectrometer. In terms of the above classification this device should be a one channel eβ coincidence spectrometer. This arrangement has been used on several occasions, e.g. to determine conversion coefficients[1, 2], or to localize the position of metastable[2] or ordinary[3, 4] levels in disintegration schemes etc.

---

[1] W. BOTHE and H. MAIER-LEIBNITZ, Z. S. f. Phys. *104*, 604, 1937.

[2] M. DEUTSCH, J. DOWNING, L. ELLIOTT, J. IROINE, A. ROBERTS, Phys. Rev. *62*, 3, 1942.

[3] K. SIEGBAHN and A. JOHANSSON, Ark. f. Mat. Astr. o. Fysik *54 A*, Nr. 10, 1946.

[4] K. SIEGBAHN and H. SLÄTIS, Ark. f. Fysik, *2*, Nr. 2, 1950.

It is conceivable that a two channel eβ coincidence spectrometer could be constructed if a thin sheet of some phosphor such as stilbene were used as a β detector and placed behind the source in the spectrometer, the electronic arrangement being the same as for the corresponding βγ two channel system. At the present time it is doubtful, however, whether such an arrangement is capable of measuring ee coincidences, i.e. coincidences between two specified conversion lines, except in some particularly favourable cases.

The most straightforward arrangement for doing this would be a two channel system consisting of two independent β-spectrometers, the coincidence-coupled detectors of which could simultaneously accept electrons from the common β source. This idea was first suggested by FEATHER[5] in 1940 and more recently[6] an actual design of a spectrometer for this purpose was described by him together with experiments on coincidences between the F-line of ThB and its continuous spectrum. In Feather's design a perpendicular homogeneous magnetic field is used in common for both spectrometers, making use of the semicircular focussing principle. The selected electron energy band is varied by changing the radius of curvature, i.e. by changing the position of the detector slit. This means that the band-width and transmitted solid angle of the electrons change with energy. These matters are fully discussed in Feather's papers.

In the present paper a different type of two channel eβ or ee coincidence spectrometer will be described, which has been designed specially to have the additional facility of being able to measure angular correlations between emitted electrons. The instrument[7] could for convenience be called a *β-spectrogoniometer*. In section 2 the design of the instrument will be given, including some magnetic field considerations and its focussing properties. In section 3 the general procedure for two channel eβ and ee coincidence measurements is outlined, and some basic formulas given which are useful in this kind of coincidence spectroscopy. Some experimental conditions for angular correlation measurements between electrons are discussed in section 4. In subsequent sections a number of applications are presented, in which the instrument has been used together with ordinary spectrometer technique. The examples have been chosen at random; many other problems, in particular the angular correlation between conversion electrons, will doubtless arise later.

---

[1] J. DOWNING, M. DEUTSCH and A. ROBERTS, Phys. Rev. *61*, 686, 1942.

[2] K. SIEGBAHN, Phys. Rev. *77*, 233, 1950.

[3] H. SLÄTIS, S. DU TOIT and K. SIEGBAHN, Ark. f. Fysik *2*, Nr. 30, 1950.

[4] H. SLÄTIS and K. SIEGBAHN, Ark. f. Mat. Astr. o. Fysik *36 A*, Nr. 21, 1949.

[5] N. FEATHER, Camb. Phil. Soc. *36*, 244, 1940.

[6] N. FEATHER, J. KYLES and R. PRINGLE, Proc. Phys. Soc. *61*, 466, 1948. R. KATZ, R. HILL and M. GOLDHABER, Phys. Rev. *78*, 9, 1950. C. FOWLER and R. SHREFFLER, Rev. Scient. Instr. *21*, 740, 1950.

[7] A description of the instrument and of some coincidence measurements (Hf^{181}) made with it, was given at the Oxford-Harwell conference, Sept. 1950.

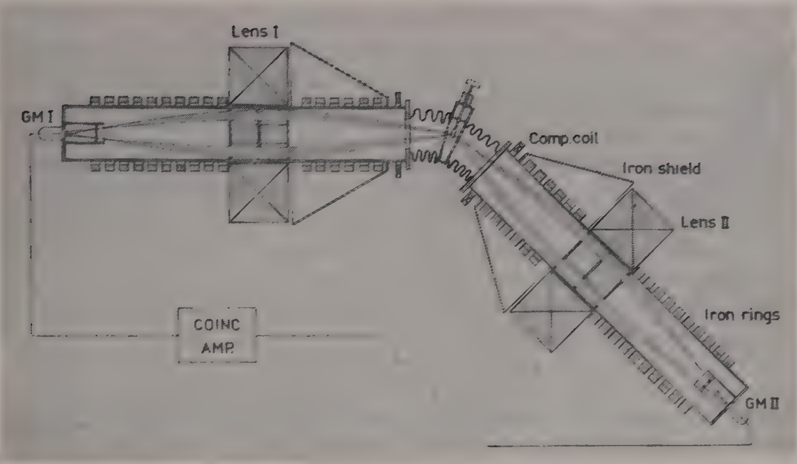

Fig. 2. Schematic cross section of the β-spectrogoniometer.

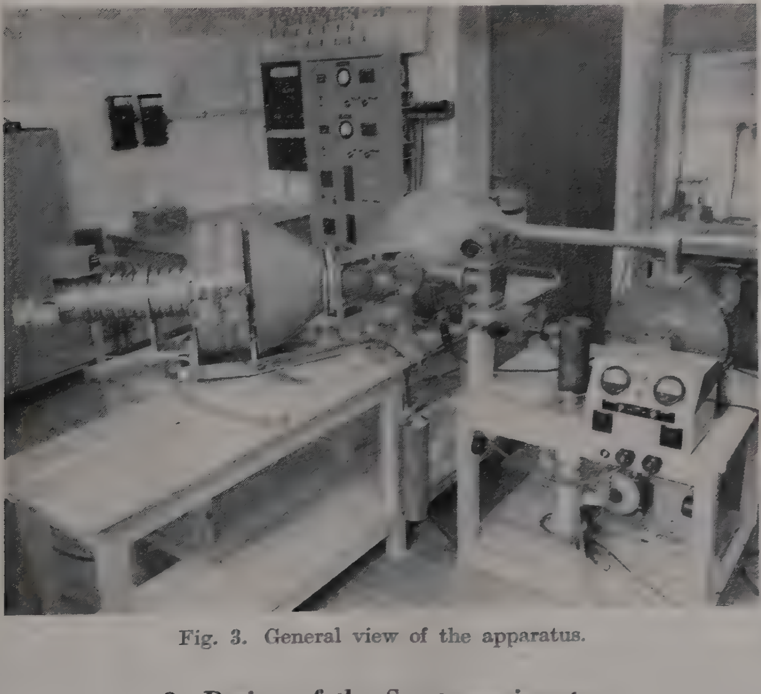

Fig. 3. General view of the apparatus.

2. Design of the Spectrogoniometer

The instrument consists essentially of two short magnetic lens spectrometers, one spectrometer arm being movable, relative to the other, around the β source as a center. Fig. 2 is a schematic cross section of the instrument. The distance between the source and the detectors is 96 cm. By means of two bellows it is possible to turn one spectrometer from the 180° position to the 90° position.

Fig. 3 is a photograph of the whole installation.

One of the main difficulties in the design is to get the two spectrometer arms magnetically independent of each other, so that the stray field from one arm will not appreciably distort or even destroy the focussing action in the other. This difficulty is particularly serious when the axes of the spectrometer arms are making an angle relative to each other, and is especially pronounced near the 90° position. In this case there are mutual field components present which tend to bend the rays sideways from the optical axes of the lenses. When ring-focussing is used, which requires a careful alignment of the spectrometer, the system is quite sensitive to such an effect, since then a sideways deflection of only a few mm may cause the focussed beam to miss the slit completely. Without ring-focussing, and when the spectrometer is adjusted for moderate resolution, the effect of a sideways deflection is not as serious, but it is still a problem which must be considered in the design of the instrument.

In order to meet this difficulty several independent precautions have been taken in the actual construction, which will be described in the following.

A. **The lenses.** To reduce the stray fields from the lenses, these have been made as "short" as possible, i.e. flat coils ($d = 15$ cm) with comparatively small internal diameters ($\Phi_{\text{int.}} = 15$ cm; $\Phi_{\text{ext.}} = 45$ cm) have been used, so that the field is highly concentrated in comparison with the distance to the source. This tends to increase the spherical abberation, which necessitates the use of the ring focus[1] arrangement (see Fig. 2) when good resolving power is required. Each coil consists of 2823 turns 2.30 mm diameter cotton covered copper wire (F. D. B.). The resistance of each coil is 11 Ω. The coils are water-cooled.

The magnetic field distribution along the lens axis as measured by a flux-meter and a search coil (calibrated by the use of the proton resonance) is given in Fig. 4. As is well known one can deduce from this curve the electron optical properties of the lens. We may for example calculate the coil current necessary to focus β-particles of $H\varrho = 1\,000$. This is the calibration constant of the spectrometer and may naturally be determined with higher precision directly by experiment. We may, however, use the approximate formula[2] for the focal distance:

$$f = \frac{2\,a}{\pi \cdot k^2} \tag{1}$$

where a = half the half-width of the field distribution curve, and

$$k = \frac{H_0 \cdot a}{2 \cdot H\varrho} \tag{2}$$

where H_0 = the field at the maximum of the curve and $H\varrho$ the momentum of the focussed electrons.

We then get $I \sim 0.80$ amp at $H\varrho = 1\,000$. The experimentally found value is $I = 0.87$ amp. It should be remarked, however, that the above simple formula for a short lens is developped under certain assumptions as to the form of the

---

[1] E. PERSICO and C. GEOFFRION, Rev. Sci. Inst. *21*, 945, 1950.

[2] W. GLASER, Zs. f. Phys. *117*, 285, 1941. K. SIEGBAHN, Ark. f. Mat. Astr. o. Fysik *28 A*, Nr. 17, 1942.

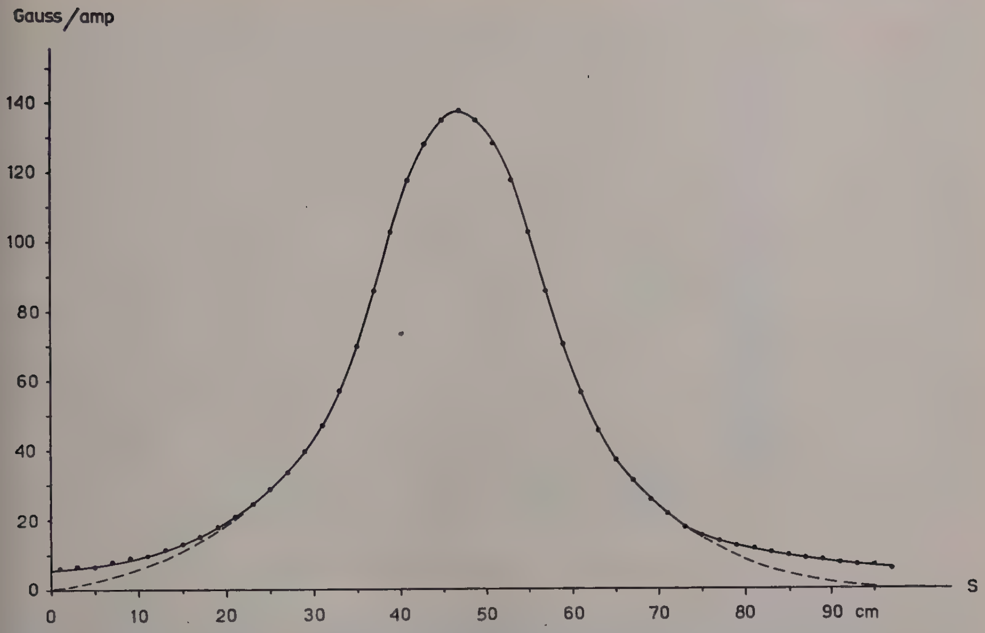

Fig. 4. Magnetic field distribution along the lens axis.

field curve, and for $k \to 0$, and is only meant as a convenient guide, for example for design purposes. The rotation of the image is given by

$$\theta = \frac{k}{H_0 \cdot a} \int_{z_1}^{z_2} H(z)\, dz. \tag{3}$$

Using the same approximations as before we get for the total rotation:

$$\theta = \frac{\pi k}{\sqrt{k^2 + 1}}. \tag{4}$$

From this formula θ is ~ 80°, whereas the experimentally determined value is $\theta = 82°$.

B. **Baffle system:** We may use the field curve in Fig. 4 to plot the rotation of the particle in the lens. According to (3) we obtain the rotation by integrating the field curve and adjusting the ordinate axis so that the total image rotation is equal to that found experimentally. Fig. 5 shows this curve. There is a region in the center of the lens where the rotation is rather constant $\left(\frac{\Delta\theta}{\Delta S} = 47°/18.5 \text{ cm}\right)$. A twisted baffle system was then constructed, consisting of 5 equally-spaced 2 mm thick brass sheets arranged so as to follow the paths of the electrons according to Fig. 5. A solid lead cylinder, of length 15 cm and diameter 5 cm, stops the direct radiation along the lens axis.

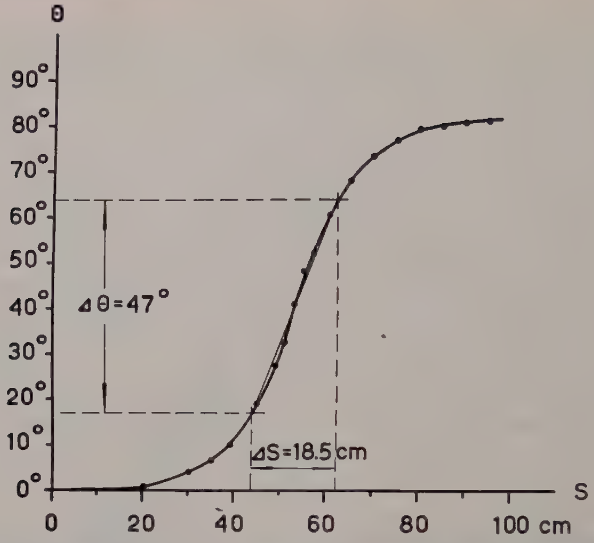

Fig. 5. Integrated field curve for obtaining image rotation.

The transmission factor of the shutter system is 3.0×10^{-3}. This is rather small for a lens and this choice should be regarded as a compromise because of the above-mentioned difficulties due to the stray fields. From the following it will be apparent, however, that one can make other alternative arrangements to eliminate such effects, and it therefore seems that it will be possible in future designs to increase the transmission factor, probably by a factor of two or more.

Because of the twisted baffle system one can effectively separate positrons and negatrons, as first suggested by DEUTSCH et. al.[1] It was found that the intensity of particles of the "wrong" sign dropped by a factor of 10^4 when the twisted system was introduced, whereas more than 90 % of the right sign particles were still transmitted. This efficient separation made it possible to study the angular correlation between internally created positrons and electrons from Na^{24}, as is reported later in this paper.

The ring focus shutter in each lens is mounted together with the GM-tube on the front piece of the spectrometer tube and can easily be changed to correspond to different source conditions. When sources are used of very small diameters ($\Phi = 3$ mm) and high specific activities (e.g. ThB) the ring slit is 3 mm wide. Its mean diameter is 21 mm and the distance from the GM window is 10 cm. The resolving power is then 2.2 %. The correct position of the ring focus was found by exposing a number of photographic plates at right angle to the axis and observing the sharpness of the ring focussed image. This procedure was particularly suitable in the present case since the presence of the iron rings (described below) around the spectrometer tube introduced a slight astigmatic lens error, which could thus be observed. A careful alignment of the rings reduced this error.

---

[1] M. DEUTSCH, L. ELLIOTT, and R. EVANS, Rev. Sci. Inst. *15*, 178, 1944.

C. **Counter equipment:** Although stilbene scintillation detectors and fast coincidence amplifiers ($\tau < 10^{-8}$ sec.) have been designed to be used for further work with the goniometer, only GM counters have yet been tried in the investigations to be described in the present paper. The counters are of the conventional end-window bell type, with a diameter of 30 mm. The window is mounted on a circular frame which can easily be replaced by others of different inside diameters and window thicknesses. Normally the window diameter is 15 mm. The window is usually made of nylon film (Du Pont type 6 A), stretched by treatment with diluted alcohol. The cut-off of the window will then be at 6–8 keV. When softer radiation is investigated (for example Auger electrons), a procedure for preparing thin nylon films very similar to that of Brown et. al.[1] has been adopted. Four layers, each of $10\,\mu g/\mathrm{cm}^2$, is a practical thickness having a cut-off at 4–5 keV, though thinner windows may be prepared in extreme cases. A few cotton meshes are required as support for the window. As a crucial test of the window absorption the well known particularly soft β lines of ThB, discovered by FLAMMERSFELD[2, 3], where studied.

The two counters are evacuated simultaneously with the spectrometer and are subsequently connected to a large common bottle containing the filling gas (60 % argon and 40 % propane).

The transmission of the spectrometer is once and for all set by the central baffle system, and the 15 mm GM aperture is more than enough to accept the monoenergetic electrons from the ring focus baffle. If the latter is removed the transmission will not increase (provided the source dimensions are small enough for the ring focus used). The accepted $H\varrho$ interval will increase, however, and the resolving power at 15 mm is then ~ 8 %. If the counter is fully opened ($\Phi = 30$ mm) the $H\varrho$ interval is increased still more, to give a resolving power of ~ 15 %. In section 3 it will be shown that in most cases when the coupling between conversion electrons and the continuous spectrum is studied optimum conditions are dependent on the magnitude of the selected $H\varrho$ band. An easy adjustment of this quantity is therefore desirable.

The coincidence amplifier has a resolving power of 3.6×10^{-7} sec. The GM tubes are directly connected to cathode followers mounted on each spectrograph near the GM tube. Well shielded cables connect these to the coincidence amplifier. Since even very small coincidence effects, of the order of 5 or 10 per hour, are often quite enough to allow rather definite conclusions to be drawn about the mode of coupling, a considerable amount of work has been done to minimize false coincidences resulting from disturbances. The coincidence background due to cosmic radiation is completely negligible because of the great distance between the tubes. Careful shielding and other precautions (e.g. working with rather low gas pressure in the GM tubes so as to have low anode voltages in the GM tubes) have reduced the total coincidence background to < 1 per hour. This background has been checked at regular intervals.

If we regard 5 coincidences per hour as a lower limit for a definite coincidence effect we observe that this number of accidental coincidences is obtained at a counting rate of ~ 2 600 counts per minute in each channel, because of the finite resolving power. This number goes as the square of the source strength.

---

[1] J. BROWN, F. FELBER, J. RICHARDS and D. SAXON, Rev. Sci. Inst. *19*, 818, 1948.

[2] A. FLAMMERSFELD, Z. S. f. Phys. *114*, 227, 1939.

[3] D. BUTT, Proc. Phys. Soc. *63*, 986, 1950.

The use of stilbene scintillation detectors and a faster amplifier as mentioned earlier will therefore greatly improve the sensitivity of the method. This will also enable one to measure life times of short lived single levels (e.g. 10^{-8}—10^{-9} sec.).

D. **Iron rings and iron shields.** In order to shield the two spectrometer arms from each other's stray fields a number of soft iron rings has been placed along the spectrometer tubes (16 on each tube. Int. diam. = 152 mm. Ext. diam. 165 mm. Width = 23 mm. Distance between the rings 11 mm.) This system has been used before by Alburger[1] to shield a short-lens β-spectrometer from the strong stray field of a cyclotron. The idea is that spaced iron ring will more or less short circuit outer fields perpendicular to the lens axis, whereas the field along the axis of the lens itself will be practically unaffected, due to the high reluctance in this direction. Since the perpendicular external fields are the most dangerous, because they deflect the electrons sideways, this arrangement is very convenient in our case. It also provides shielding against the earth's magnetic field.

An additional shielding is provided by two soft iron sheets of conical form.

Naturally the system adopted here cannot completely eliminate outer fields. The lenses themselves are not iron covered, so the system is not all well shielded. It is also difficult to shield the rather extended region around the source, because of the particular mechanical arrangement necessary in our case.

Magnetic measurements performed at different angles between the lenses showed, however, a surprisingly good magnetic shielding, even in the 90° case.

E. **Compensation coils.** It is nevertheless doubtful whether the above iron shieldings would be completely sufficient for our purpose. In particular, the unshielded region around the source requires additional arrangements. From the field curve in Fig. 4 it is clear that the magnetic field drops down rather quickly along the lens axis. At about 10 cm from the sample position the decrease in field is getting slower, however, and its magnitude is by no means negligible at and beyond the sample, and it thus influences the focussing in the other lens.

In Fig. 6 the upper dotted curve is a reproduction of Fig. 4. If we place an auxiliary coil at some distance from the sample and then give the field an opposite direction relative to the main field (lower dotted curve) we may adjust the number of ampère turns through the small coil so as to compensate the field at the sample and beyond it, over a fairly long distance. The resultant field is shown by the full curve in Fig. 6. After the necessary number of ampère turns and also the form of the auxiliary field had been determined from experiments, the number of turns was chosen so that the same current could go through both coils, i.e. so that the two coils could be coupled directly in series with each other.

These compensation coils have proved to be extremely effective in diminishing the mutual influence of the two spectrometer arms. The final adjustments can be made by turning the arms at different angles relative to each other and by measuring the field component perpendicular to the axis in the one arm if current is going through the other spectrometer coil and compensation coil. In

---

[1] D. ALBURGER, Rev. Sci. Inst. *19*, 474, 1948.

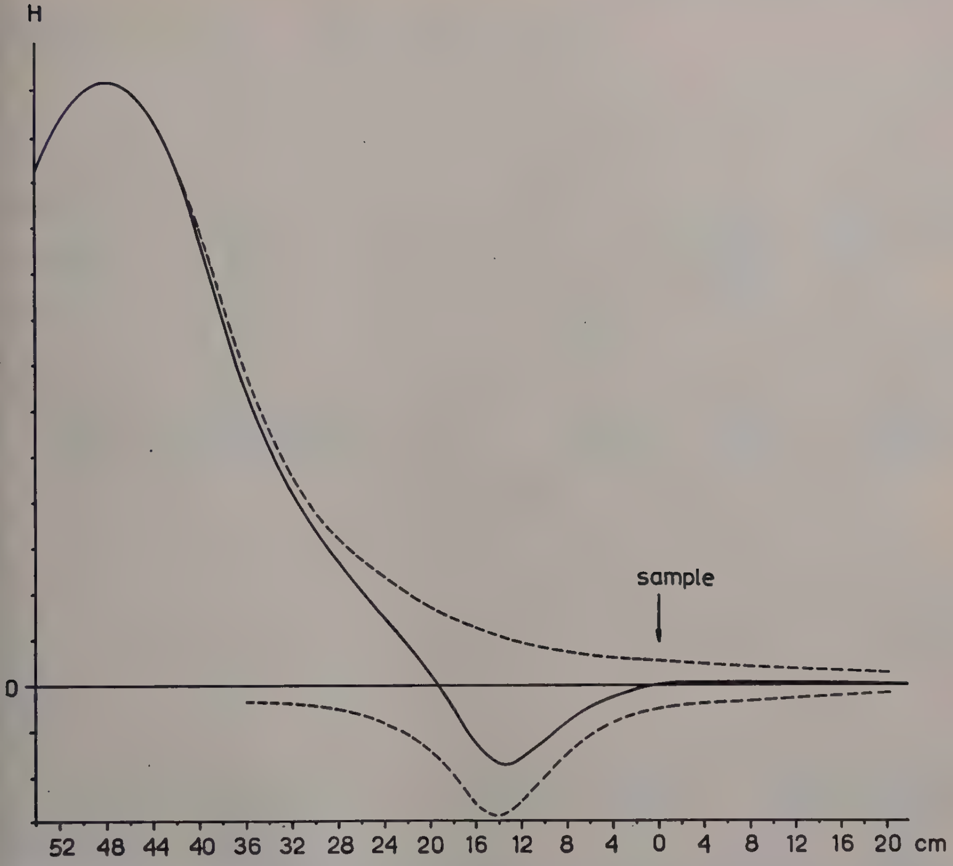

Fig. 6. Magnetic lens field with compensation coil (full curve). Dotted curves: Lens field without compensation coil (upper curve) and with compensation coil field alone (lower curve).

the present case the compensation coils each consists of 335 turns of 1 mm enamelled copper wire (E. E.) with a resistance of 3.8 Ω. The internal diameter is 15 cm, external diam. 23 cm, and width 1 cm.

F. Measurement of the effect of mutual magnetic disturbance on the resolving power and peak height. As pointed out above the goniometer is most sensitive to magnetic disturbances when a narrow ring focus baffle is used, and the following tests have therefore all been performed under these conditions. In many practically occuring cases one may, however, have the freedom of choosing the less critical conditions associated with more moderate resolution.

The F line of ThB was focussed in one spectrometer arm (field = H_0) and a "disturbing field" of H_1 applied in the other arm. The lines were investigated for $\frac{H_1}{H_0} = 0;\ 0.40;\ 0.80;\ 1.20;\ 1.40$ and 2.40 at the angles 180°, 165°, 135°, 120°, 105° and 90° between the lens axes.

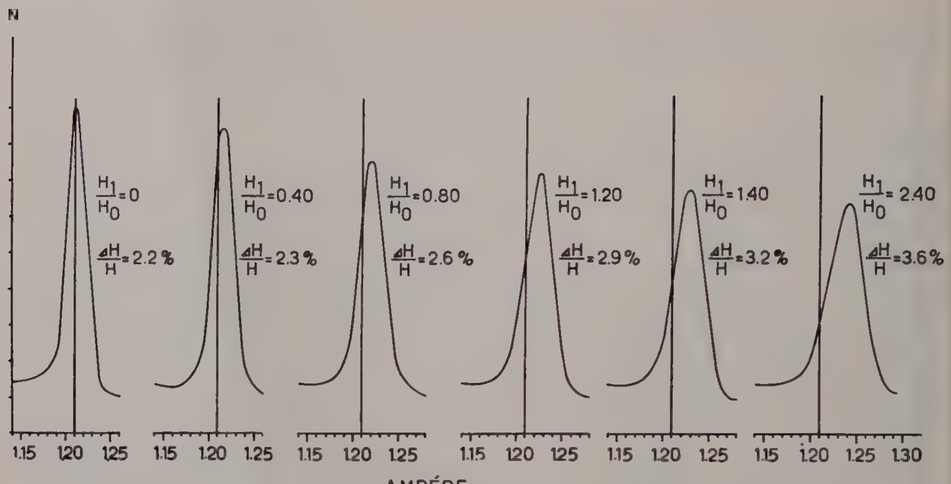

Fig. 7. Change of line profile due to mutual magnetic influence.

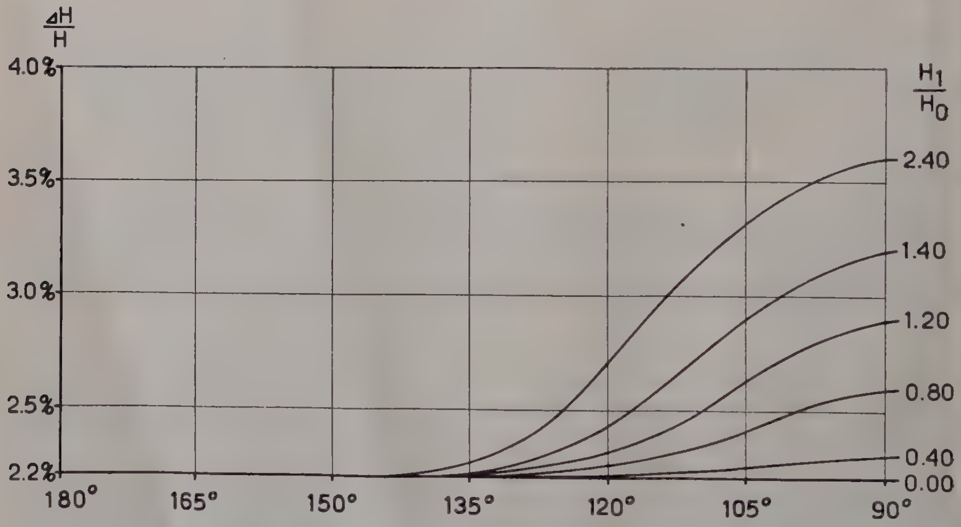

Fig. 8. Relative line width as a function of angle. Magnetic stray field as a parameter.

Fig. 7 shows the line profiles at 90°, where the magnetic disturbance is the greatest. One can notice a slight shift of the line when $\frac{H_1}{H_0}$ increases and also a decrease in peak height and resolution $\left(\frac{\Delta H}{H} \text{ increases}\right)$.

Fig. 8 shows the relative half width of the line as a function of the angle,

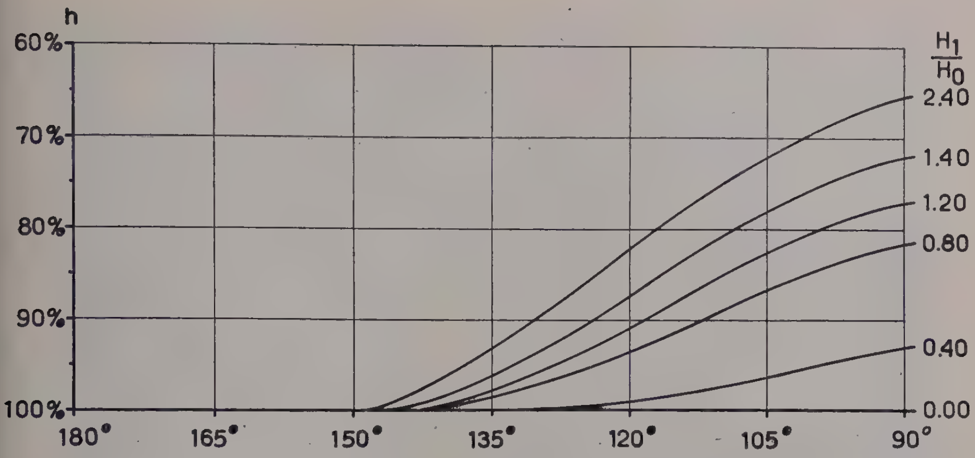

Fig. 9. Height of line as a function of angle. Magnetic stray field as a parameter.

with $\frac{H_1}{H_0}$ as a parameter. According to this plot the goniometer arms are completely independent between 180° and ~ 140°, whereafter $\frac{\Delta H}{H}$ goes from 2.2 % up to 3.6 % for $\frac{H_1}{H_0} = 2.40$.

Fig. 9 shows the same plot for the peak height. At 90° and $\frac{H_1}{H_0} = 2.40$ the peak height has decreased to ~ 65 % of its original value. In section 3 B it will be discussed how this effect may be corrected for in actual experiments.

G. **The bellows system.** Two different main designs have been considered in solving the mechanical problem of being able to turn continuously the one goniometer arm from 180° to 90° without changing the exact position of the sample or screening off any part of the electrons passing the central baffle. The first design consisted of a rather elaborate system of wide cones movable inside each other. There are considerable vacuumtechnical and other difficulties connected with this type of construction. It was therefore later abandoned in favour of a rather simple bellows construction (see Fig. 10) since it was found that a particular type of highly flexible bellows[1] made it just possible to bend one arm through the required angle without breaking the bellows or cutting off the beam. The outer and inner diameters of the bellows are $4\frac{1}{2}''$ and $3''$ respectively and the material has a thickness of only $0.007''$.

The right part of Fig. 10 is a horizontal section of the construction when the goniometer arms are in the 90° position, and the left part is a vertical section, also in the 90° position. The source S, situated on an ebonite ring, is introduced by means of a rod into the vacuum through a lock device as has

---

[1] Type A ("extra flexible hydroflex bellows"): The Drayton Regulator & Instrument Company, Ltd, West Drayton, Middlesex, England.

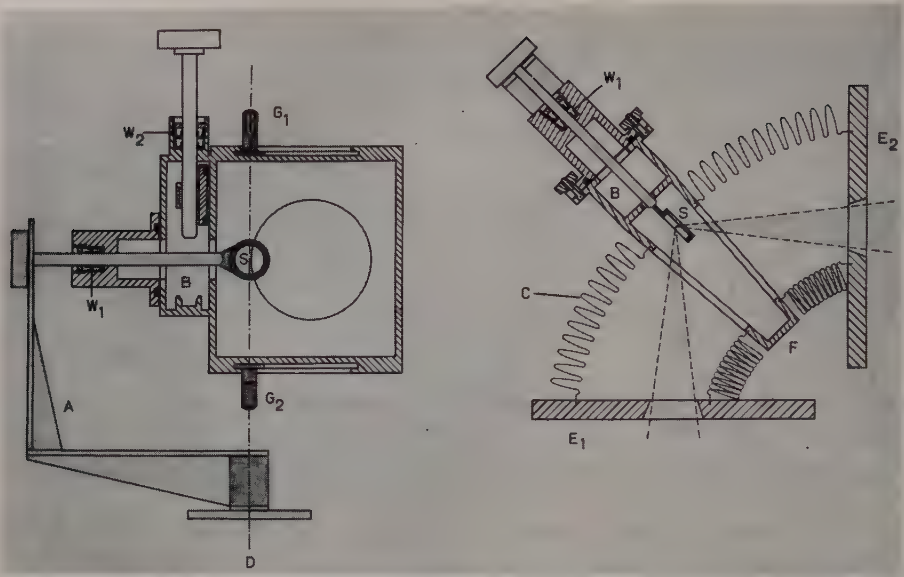

Fig. 10. The bellows construction. Left: vertical section in 90° position; right: horizontal section in 90° position. S = source. B = source rod. W_1 and W_2 = Wilson seals. C = bellows. E_1 and E_2 = ends of goniometer tubes. D = axis of rotation. G_1 and G_2 = pegs, directing the movement. A = arm for keeping the source at correct position. F = box, connecting the pair of bellows, on which the lock device is mounted.

been of the "excenter" type, used on several spectrometers at the Institute before. The lock device is mounted on a box F, the horizontal cross section of which is slightly prismatic so that the two bellows are not pressed together at F in the 90° position more than the bellows can stand. The two bellows are soldered to this box and to the end plates E_1 and E_2 of the goniometer arms. The position of the source S is always kept in the correct position, i.e. at the center of rotation of the goniometer D, by means of the arm A and the Wilson seal W_1. When turning the goniometer arm around D the box will move sideways along the slides G_1 and G_2 but not the source rod D. The pegs directing this movement are also situated on the axis of rotation. Two stop screws (not shown in the figure) acting on the end wall of the box at F prevent the box and bellows from moving more than is compatible with their natural positions without the additional sideways pressure due to the inside vacuum.

In the first bellows construction one of the bellows broke along the edge of a convolution after it had been used several times. Flat ring-shaped rubber gaskets were therefore introduced between the convolutions inside the bellows to prevent the air pressure from flattening the egdes of the thin convolutions. Since then no troubles have been encountered with the bellows arrangement.

H. **Neutralization of earth's magnetic field.** Although the iron shieldings certainly diminish the effect of the earth's magnetic field, the previously discussed unshielded regions require a special arrangement to neutralize this field

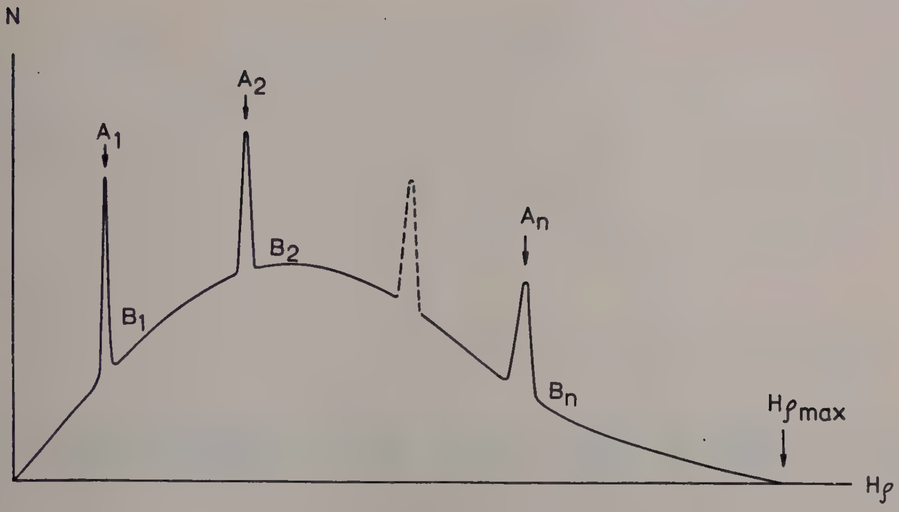

Fig. 11. β-lines superimposed on a continuous spectrum.

when work in the very low energy region in performed. Usually this is accomplished by means of several long rectangular coils mounted along the spectrometer tube. Because of the small dimensions of such a coil system it has to be calculated and designed with some care if a good neutralization over the entire spectrometer region is required[1]. Even so an arrangement of this type could not be used here since one spectrometer arm has to be moveable in the obliquely directed earth field. It was found that a much simpler solution to this problem was to neutralize the whole room by means of rectangular coils following the sides of the walls, roof and floor. It turns out that a total power of ~ 680 watts is sufficient to demagnetize the room (5.0 × 5.3 × 3.3 m). The residual field over the whole volume occupied by the instrument (a few percent of the earth field) is primarily due to small variations in the voltage of the mains supply, which provides the current for this compensation arrangement. The room is oriented in the north-south direction. The vertical component of the earth's magnetic field is neutralized by means of two coils, each having 130 turns of 0-60 mm copper wire (EBD), carrying a current of 1.0 amp. For the horizontal component two coils with 46 turns each have been used. The current is 1.65 amp.

3. General procedure and expected coincidence rates

A. Coincidences between two conversion lines. Suppose that we have a β line spectrum superimposed on a continuous spectrum as shown in Fig. 11. In order to investigate whether a line A_p is in coincidence with A_q the following procedure should generally be used. The coincidence rates are taken between:

I: A_p and A_q
II: A_p and B_q
III: A_q and B_p.

---

[1] See e. g. S. HAYNES and J. WEDDING, Rev. Sci. Inst. *22*, 97, 1951.

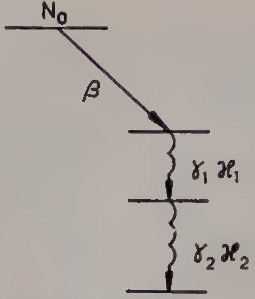

Fig. 12. One continuous β-spectrum followed by two partly converted γ-rays.

After corrections for decay and accidentals one forms the difference I − (II + III). If this difference is $\neq 0$ then there is a coupling between A_p and A_q (i.e. the lines are emitted within a time comparable to or less than the resolving time of the coincidence amplifier). Thus it is not sufficient to measure the coincidence effect only between A_p and A_q since this may be due to a coupling between A_p and the continuum B_q under A_q or vice versa.

B. **Expected coincidence rate between two lines.** Fig. 12 illustrates a simple case, where two partly converted γ-rays are emitted in cascade after the continuous spectrum. The following equations hold:

$$N_{e_1} = N_0 \cdot \varkappa_1 \cdot T_1 \tag{5}$$

$$N_{e_2} = N_0 \cdot \varkappa_2 \cdot T_2 \tag{6}$$

$$C_{e_1 e_2} = N_0 \cdot \varkappa_1 \cdot \varkappa_2 \cdot T_1 \cdot T_2 \cdot f(\theta) \tag{7}$$

N_0 is the number of disintegrating nuclei per time unit; N_{e_1} and N_{e_2} are the number of conversion-electrons registered in each channel per time unit, and $C_{e_1 e_2}$ the $e_1 e_2$ coincidence rate (which according to the previous discussion is not equal to the observed coincidence rate). $\varkappa_1$ and $\varkappa_2$ are the conversion "probabilities"[1] of the lines and $f(\theta)$ the angular correlation function. T_1 and T_2 are the transmission factors of the two lenses, defined as the fraction of emitted monoenergetic electrons from the source, which is accepted by the counter. In the present arrangement T is generally kept constant and is equal in the two channels ($T = 3.0 \times 10^{-3}$). The transmissions in the two channels may, however, be slightly affected by stray magnetic fields, when the lenses are turned through a large angle relative to each other. This dependence on the transmis-

---

[1] According to current notation the (electric) conversion "coefficient" is denoted by α and is defined by $\alpha = N_e / N_q$ where N_q is the number of quanta emitted. Thus α goes from 0 to ∞. The conversion "probability" $\varkappa$, which has been introduced here because of formal convenience, corresponds to the old but now abandoned definition of conversion coefficient. We define $\varkappa = \dfrac{N_e}{N_q + N_e}$ · $\varkappa$ goes from 0 to 100 %. The following relation exists between $\varkappa$ and α:

$$\varkappa = \frac{\alpha}{\alpha + 1}\,.$$

sion of the angle between the two lenses was shown in Fig. 9 and discussed in section 2 F. The narrower the slits (i. e. the better the resolution) the more sensititive is the transmission to external influences. Naturally a very great ratio between the focussed electron energies in the two lenses tends to increase the magnitude of this effect. Since the effect is angularly dependent there will in general be an angular correlation effect due to this cause alone, which might disturb the true angular correlation effect. This difficulty is eliminated, however, if we always plot the experimentally obtained quantity $\frac{C_{e_1 e_2}}{N_{e_1} \cdot N_{e_2}}$ against θ. According to Eq:s 5–7 we have

$$\frac{C_{e_1 e_2}}{N_{e_1} \cdot N_{e_2}} = f(\theta) \cdot \frac{1}{N_0} \tag{8}$$

which is independent of T_1 and T_2. If the distribution is isotropic $f(\theta) = 1$, and the source strength can then be determined from

$$N_0 = \frac{N_{e_1} \cdot N_{e_2}}{C_{e_1 e_2}}. \tag{9}$$

C. **Expected coincidence rate between a line and the continuum.** It is often useful to investigate the coupling between a conversion line and electrons belonging to the continuous spectrum. In a complex spectrum one can for example find the particular β component that is responsible for the subsequent emission of a line simply by investigating the coincidence effect between this line and a number of points on the continuous spectrum.[1]

Since generally the counting rate in the channel accepting electrons from the continuous spectrum is lower than in the other the best disposition in this case is to increase the $H\varrho$ interval in the former channel, i. e. to decrease the resolving power by leaving out the ring focus baffle and using a larger diameter for the counter aperture.

This arrangement is in fact under all circumstances better than to increase the source strength in order to get the same number of coincidences. Suppose for example that we measure the coincidences between e_1 and β in the case illustrated in Fig. 12. We then have

$$N_{e_1} = N_0 \cdot \varkappa_1 \cdot T_1 \tag{10}$$

$$N_\beta = N_0 \cdot \eta \cdot T_2 \tag{11}$$

$$C_{e_1 \beta} = N_0 \cdot \varkappa_1 \cdot \eta \cdot T_1 \cdot T_2 \cdot f(\theta). \tag{12}$$

η measures the fraction of the total continuous spectrum accepted by the β counter. It is a function of the resolving power $\left(R = \frac{\Delta H\varrho}{H\varrho}\right)$ and the $H\varrho$ value of the focussed β particles. We then notice from the last equation that the coincidence rate will increase linearly with *both* N_0 (strength of sample) *and* η.

---

[1] Such an investigation has for example recently been performed by Civ.Ing. S. THULIN using the goniometer on the complex decay of I^{131}. This investigation will later be published.

The number of accidental coincidences, however, will go up as the *square* of $N_0 \, (Z = 2 \cdot \tau \cdot N_0^2 \cdot \varkappa_1 \cdot \eta \cdot \tau_1 \cdot \tau_2)$ but only *linearly* with η.

The quantity $\frac{C_{e_1\beta}}{N_{e_1} \cdot N_\beta}$ takes the same form as in the previous case.

In order to calculate the expected number of coincidences we must express η in terms of known quantities. We have

$$\eta = \int\limits_{H\varrho}^{H\varrho + \Delta H\varrho} N(H\varrho)\, d\,H\varrho \Bigg/ \int\limits_{0}^{H\varrho\,\mathrm{max}} N(H\varrho)\, d\,H\varrho \tag{13}$$

The exact form of the spectrum $N(H\varrho)$ is a fairly complicated function and is therefore inconvenient for making a rough calculation. We may use a simple symmetric funtion like $N(H\varrho) = \alpha \cdot \sin^2 \left(H\varrho \frac{\pi}{H\varrho_{\mathrm{max}}} \right)$ which at least for light elements is a sufficiently good approximation for our purpose.

If we introduce

$$R = \frac{\Delta H\varrho}{H\varrho}$$

$$k = \frac{H\varrho}{H\varrho_{\mathrm{max}}}$$

and observe that $R \ll 1$ we get after integration

$$\eta_k = 2\,k \cdot R \cdot \sin^2 \pi\, k. \tag{14}$$

In order to get an idea of the behaviour of η we may calculate $\eta_{1/2}$ i. e. when the maximum of the continuous spectrum is focussed in the one channel. This is a case often occurring in practice since then the coincidence rate will be high (though not a max.). From (14) we find that $\eta_{1/2}$ is simply equal to the resolving power R. As expected, η_k varies as the "undivided" form of the spectrum itself. We may therefore determine η from the β spectrum as it is obtained in the spectrometer (i. e. before division by $H\varrho$) by multiplying R by the ratio of the number of counts at $H\varrho$ to that at $\frac{1}{2}H\varrho_{\mathrm{max}}$ for a simple spectrum.

The following typical example may illustrate the use of the above discussion. Suppose that we investigate a source having a strength of 4 μC. The conversion probability of the β line is 0.05 and the transmission 3×10^{-3}. The e tube will then accept about 1 300 conversion electrons per minute. If we wish to get 30 coincidences in one hour in the middle of the continuous spectrum the resolution should be set at ~ 12 %. In this part of the spectrum there will be a counting rate of ~ 3 200/min. If the line is situated here then the total counting rate in the e tube (including the electrons from the continuous spectrum) is ~ 2 100, if the resolution is set to be 3 % in this lens. The number of accidentals in one hour (if $\tau = 3.6 \times 10^{-7}$ sec.) will then be 5. The resolution in the conversion electron lens should naturally be set at a value which is just appropriate to the full utilization of the total surface of the sample (or,

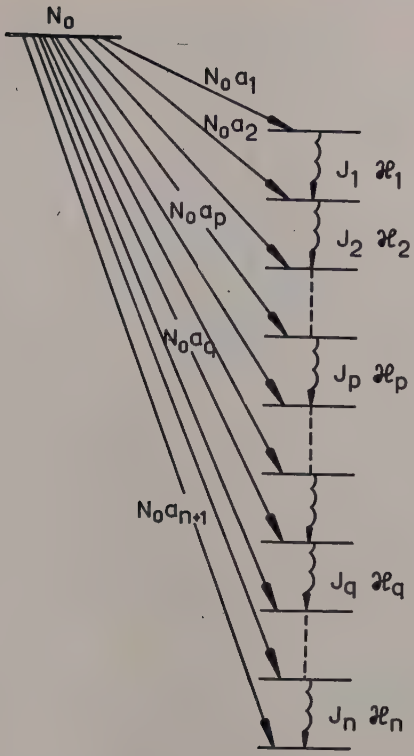

Fig. 13. Generized scheme *without* cross-over γ-rays.

if the sample is thick, to its "natural" line width) and to the spectrometer transmission. A larger R value in this lens will only increase the number of accidentals but not the real coincidence effect.

D. **Generalization of some coincidence rate formulas.** The above simple cases may easily be generalized to include more complicated modes of disintegration. Suppose that we have a scheme of the general type illustrated in Fig. 13. There are n γ-transitions between $n+1$ levels (including the ground state). Let us assume that there are no cross-over γ rays and no metastable levels. The intensities of the different transitions are denoted by $I_1 \ldots I_n$ and the corresponding conversion probabilities by $\varkappa_1 \ldots \varkappa_n$.

We want to investigate the coupling between two arbitrarily chosen p and q converted γ-rays, where $p < q$. The single counting rate in each channel is (conversion electrons only):

$$N_{e_p} = I_p \cdot \varkappa_p \cdot T_1 \tag{15}$$

and

$$N_{e_q} = I_q \cdot \varkappa_q \cdot T_2. \tag{16}$$

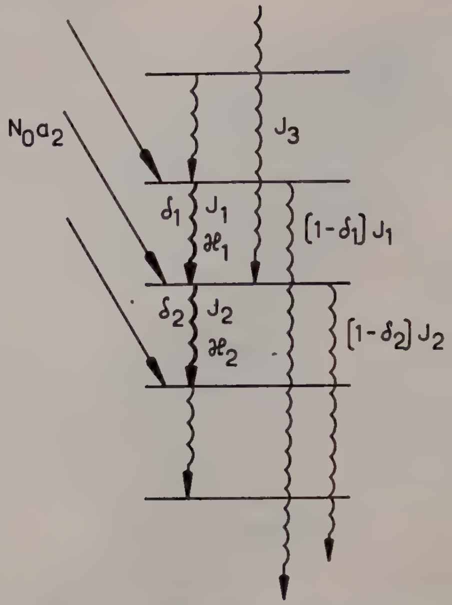

Fig. 14. Scheme *with* cross-over γ-rays.

Then the coincidence rate is

$$C_{e_p e_q} = I_p \cdot \varkappa_p \cdot \varkappa_q \cdot T_1 \cdot T_2 \cdot f(\theta) \tag{17}$$

I_p may be expressed in terms of the intensities of the β components, which in most cases are experimentally easier to measure, i. e.

$$I_p = N_0 \sum_1^p a_r \qquad \left(\sum_1^{n+1} a_r = 1\right). \tag{18}$$

If there are cross-over γ-rays in the scheme, the situation may be much more complicated. We will not consider the general case here but will instead limit the discussion to an important sub-case, i. e. a scheme including two neighbouring cascade transitions with cross-over transition (see Fig. 14).

Let us denote the branching ratio in the first level by δ_1, and in the second level by δ_2. The second level is also fed by a β component (intensity $N_0 \cdot a_2$) and one or more γ-components (I_3).

The single counting rate in each channel is then:

$$N_{e_1} = \delta_1 \cdot I_1 \cdot \varkappa_1 \cdot T_1 \tag{19}$$

and

$$N_{e_2} = \delta_2 \cdot I_2 \cdot \varkappa_2 \cdot T_2. \tag{20}$$

The quantity I_2 is made up from three different contributions, namely:

$$I_2 = \delta_1 I_1 + I_3 + N_0 \cdot a_2. \tag{21}$$

Only the fraction of I_2 represented by the first term is able to produce coincidences. Furthermore, the presence of the cross-over transition of intensity $(1 - \delta_2) I_2$ reduces the coincidence effect still more. We get:

$$C_{e_1 e_2} = I_1 \cdot \delta_1 \cdot \delta_2 \cdot \varkappa_1 \cdot \varkappa_2 \cdot T_1 \cdot T_2 \cdot f(\theta). \qquad (22)$$

Although the general treatment of this problem (e. g. when there are one or more transitions between I_1 and I_2) is considerably more complicated it may not be too difficult in practically occuring cases to find the appropriate expressions if arguments similar to those given in the above example are used.

It may be noticed that though the last given formulas have no analogue to those used in ordinary βγ or γγ coincidence measurements there is a close formal resemblance between the simple formulas given in section 3, B and C, and those commonly used in the more classical coincidence measurements[1]. The expression for the source activity N_0 (eq. (9)) obtainable from ee coincidence measurement in the spectrometer (the same formula applies also to the eβ coincidence measurement if N_{e_2} is changed to N_β) equals the well-known expression obtained from βγ coincidence measurements of source strengths. In some cases, as when for example there is a very strong conversion, it may even be preferable to determine the source strength by eβ measurements instead of βγ measurements. In one case in the following (Tm^{170}) we will use this method for a source strength determination.

4. Some general considerations about angular correlations between electrons

During the last few years a number of papers both experimental and theoretical have appeared dealing with angular correlations between γ rays. Though the basic theoretical aspects[2] had been known for some time the first experimental evidence for γγ angular correlations was given only a few years ago by DEUTSCH and his collaborators.[3] The development of scintillation counter technique has naturally greatly improved the experimental possibility of making this kind of angular correlation experiment.

If we examine the experimental conditions for angular correlation measurements between electrons we are faced particularly by one very serious difficulty, namely the electron scattering in the source and also in the surroundings. This last type of scattering is especially awkward if experiments are performed with closely placed counters, and will generally require rather intricate corrections. Only in one particularly well chosen case[4] (Hg^{197}) has an experiment of this type led to conclusive results.

The goniometer is for obvious reasons practically free from disturbances due to the latter type of scattering. Another essential feature of this instrument is that it is possible to perform electron angular correlation measurements even if the radiation is complex (e. g. consisting of one or several continuous spectra as well as several conversion lines, Auger lines, X-radiations etc.). A good illustration of the potentialities in this respect is given later in this paper and concerns the internal pairs in Na^{24}. It will then be shown that the angular correlation between internally created positrons and electrons of selected energies can be measured, even though this radiation is emitted simultaneously with a γ and β radiation, which is more than 1 000 times as strong.

---

[1] See e. g. J. DUNWORTH, Rev. Sci. Inst. *11*, 167, 1940.

[2] D. HAMILTON, Phys. Rev. *58*, 122, 1940. G. GOERTZEL, Phys. Rev. *70*, 897, 1946.

[3] L. BRADY and M. DEUTSCH, Phys. Rev. *72*, 870, 1947; *74*, 1541, 1948; *78*, 558, 1950.

[4] H. FRAUENFELDER, M. WALTER and W. ZÜNTI, Phys. Rev. *77*, 557, 1950.

The multiple scattering within the source still remains as the main problem. The scattered electrons are deviated according to a Gaussian distribution with a certain mean deflexion angle $\bar{\alpha}$, which tends to destroy any primary existent angular correlation effect. Naturally $\bar{\alpha}$ increases with source thickness and decreasing electron energy. In dealing with βγ coincidences the electron scattering may not be so difficult to handle since the most pronounced correlations, if any, in this case occur at the high energy side of the β-spectrum. Conversion lines convenient for electron coincidences are, however, usually of energy lower than 100 keV.

We may quote WILLIAM's formula[1] for $\bar{\alpha}$ in order to get a figure of the allowable source thicknesses at different electron energies:

$$\left\{\begin{aligned} \bar{\alpha} &= \{3.69 + 0.28 \log_{10} (Z^{4/3} \cdot \varrho \cdot t / W \beta^2)\}\, \delta \\ \delta &= \sqrt{k/\pi} \\ k &= 4\pi \cdot N \cdot t \cdot Z^2 \cdot e^4 / M^2 \cdot C^4 \beta^4 \xi^2 \end{aligned}\right. \tag{23}$$

where N = number of nuclei / cm^3
t = thickness of absorber
Z = atomic number
e = electronic charge
M = mass of electron
$\beta = v/c$
$\xi = \dfrac{1}{\sqrt{1-\beta^2}}$
ϱ = specific weight
W = atomic weight.

According to this formula a β line for example 80 keV, which passes through a 0.1 mg/cm^2 Al foil, will have a mean deflexion angle $\bar{\alpha}$ of ~ 6°. In general a mean angle of ~ 10° can be tolerated in order not to smear out a primary correlation effect. The maximum source thickness has to be calculated from case to case. A convenient monogram for this purpose has been given in a recent survey by WALTER, HUBER and ZÜNTI[2], based on a similar formula by BOTHE.[3] This article also includes a complete list of references regarding angular correlation between nuclear radiations.

The important practical problem of preparing a thin *uniform* source is still

---

[1] E. WILLIAMS, Proc. Roy. Soc. *169*, 531, 1939.

[2] M. WALTER, O. HUBER and W. ZÜNTI, Helv. Phys. Acta *XXIII*, 697, 1950.

[3] W. BOTHE, Handb. d. Physik Bd, 22/2, Springer, Berlin (1933).

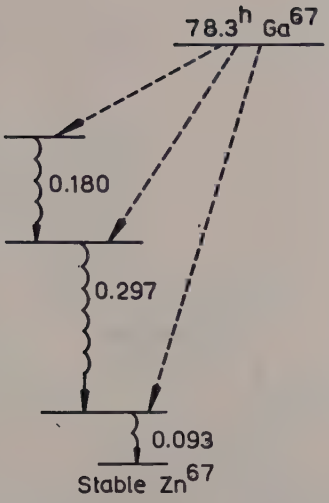

Fig. 15. Previous scheme of Ga^{67} disintegration.

not completely solved. As observed by LANGER et.al.[1], sources prepared from chemical solutions may in some cases show variations in thickness which differ by as much as a factor of 100 from the average thickness. If otherwise possible, evaporation technique is preferable[2], but other methods may in many cases be sufficiently good. The uncertainty regarding the effective source thickness is still a serious obstacle, which should be closer investigated.

The theoretical interpretation of angular correlations between internal conversion electrons, considering the angular momenta of the states involved, has been treated in two recent papers by GARDNER.[3,4] Though the experiments certainly are hard to perform it is promising to notice that the expected anisotropics are generally greater than those encountered in $\gamma\gamma$ correlations.

5. Investigation of Ga^{67}

This isotope is of particular historical interest since ALVAREZ[5] in 1938 made the experimental discovery of the K-capture phenomenon on Ga^{67} and V^{48}. He found that 78.3^h Ga^{67} decays by K-capture with the emission of X-rays and γ-radiation of ~ 250 keV and 100 keV. The latter γ-line was converted to a high extent (according to ALVAREZ ~ 40 %) which was the first example of internal conversion in artificially active atoms.

It was later found by HELMHOLZ[6] that the γ-radiation consisted of three lines at 93 keV, 180 keV and 297 keV. HELMHOLZ suggested a scheme for the disintegration[7] which is reproduced in Fig. 15. According to this scheme all

---

[1] L. LANGER, R. MOFFAT and H. PRICE, Phys. Rev. *76*, 1725, 1949.

[2] An excellent method has been developed recently by H. FRAUENFELDER, Helv. Phys. Acta XXIII, 347, 1950.

[3] J. GARDNER, Proc. Phys. Soc. *62*, 763, 1949.

[4] J. GARDNER, Proc. Phys. Soc. *64*, 238, 1951.

[5] L. ALVAREZ, Phys. Rev. *54*, 486, 1938.

[6] A. HELMHOLZ, Phys. Rev. *60*, 415, 1941.

[7] Adopted in Nuclear Data, National Bureau of Standards.

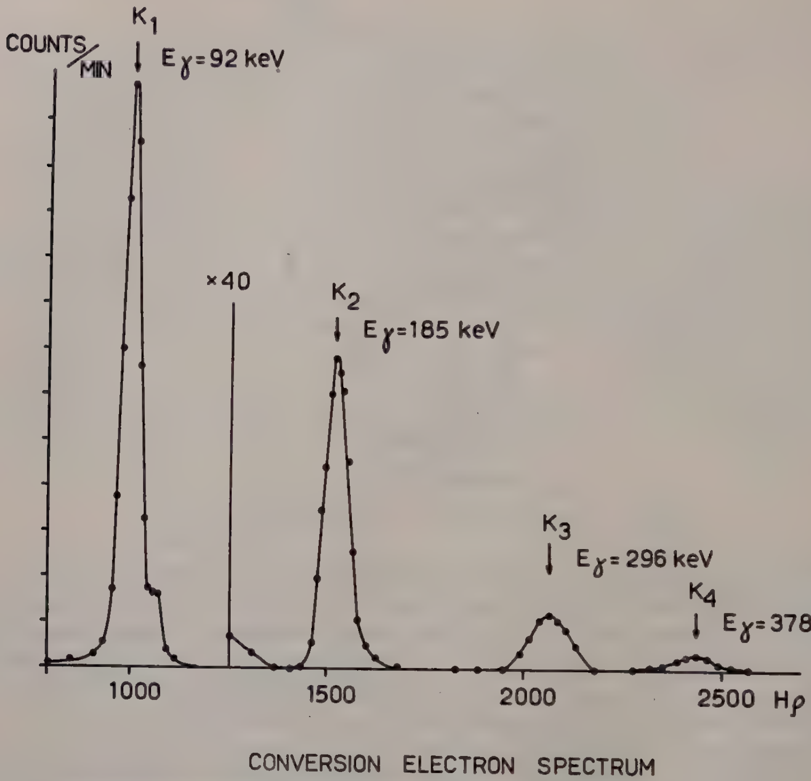

Fig. 16. Ga^{67} conversion electron spectrum.

three lines should be emitted in cascade transitions. The conversion coefficient for the 93 keV line could be accounted for by the assumption of an electric quadrupole transition, whereas the small conversion of the other two lines made any multipole assignments there rather difficult. $l = 1$ seemed to be probable.

The scheme given in Fig. 15 can be tested easily in the spectrogoniometer. Ga^{67} was produced in the cyclotron by means of the reaction Zn^{66} (dn) Ga^{67} and the active Ga was extracted essentially carrier-free by ethyl ether from 6 *N* hydrochloric acid.[1]

A. **Spectrometer measurements.** The β spectrum obtained in the spectrometer is given in Fig 16. The high K/L ratio[2] for the 92 keV lines certainly excludes any higher multipole order than $l = 2$ for this transition, in agreement with HELMHOLZ. A careful run was made in the higher energy region in order to find any other weak lines, and one new line was actually found, corresponding to $E_\gamma = 378$ keV. The half life has been followed in the spectrometer

---

[1] D. GRAHAME and G. SEABORG, J. Am. Chem. Soc. *60*, 2524, 1938.
[2] M. HEBB and E. NELSON, Phys. Rev. *58*, 486, 1940.

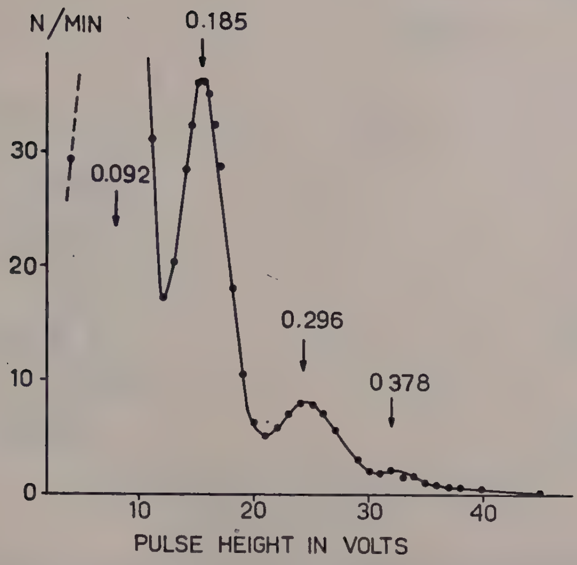

Fig. 17. Scintillation spectrum of Ga^{67} γ-rays.

and is found to be the same as for the others. The relative intensities of the four conversion lines are ~ 75 : 1 : 0. 18 : 0.03.

The γ spectrum taken in the scintillation spectrometer is shown in Fig. 17. As can be seen, no other γ-lines exist except those already obtained as conversion lines in Fig. 16.

B. **Coincidence measurements in the goniometer.** If we assume, in accordance with experimental findings, that the 92 keV line is a quadrupole transition, we may use the theoretical value for $\varkappa$ (45 %) to calculate (see 3 D) the number of expected coincidences. We then get $(C_{92;185})_{\text{expected}} = 30/\text{hour}$.

Experimentally the number of coincidences was found to be 10 / hour. The accidentals were then 7 / hour. Consequently the net effect is 3 ± 3 and therefore certainly disagrees with the number expected, if the scheme given in Fig. 15 were correct. The expected coincidence effect between the 296 keV and 92 keV lines according to the same scheme would be 5 / hour. Experimentally one obtains 2 / hour. The accidentals are 2 / hour and the net effect is thus zero, which also disagrees with the scheme.

It was found, however, that there was a strong $\gamma\gamma$ coincidence effect if the sample was investigated in an ordinary $\gamma\gamma$ coincidence set up (with calibrated gold-γ-tubes.

C. **Revised scheme.** These facts together with the existence of the new line can be accounted for by a revision of the scheme according to the two alternatives given in Fig. 18. The number of K-capture branches in Fig. 18 is the minimum required by the experiments. It seems likely that if any K capture transition at all leads directly to the 296 keV excited level in Zn^{67} it must

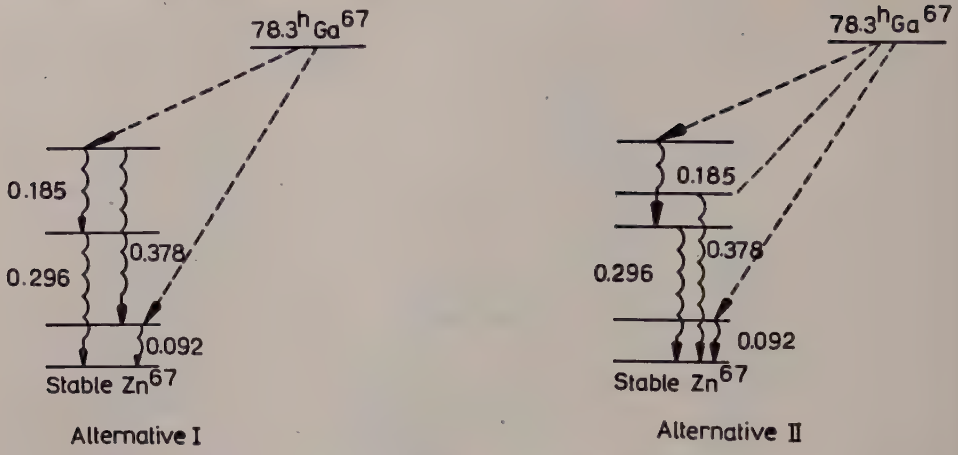

Fig. 18. New scheme of Ga^{67} disintegration.

have a small intensity. If the intensities of the conversion lines due to the 185 keV and 296 keV transitions are compared ($I_2 : I_3 = 5.5$) one finds that they are in the same proportion as the theoretical values for the conversion coefficients appropriate to electric quadrupole transitions at the two energies. In fact $\alpha_{185} : \alpha_{296} = 0.059 : 0.011 = 5.3$. It is therefore tempting to assume that the two transitions are of the same intensities and of the same multipole type.

If the three softer γ-rays are of electric quadrupole type one can furthermore conclude from the conversion spectrum that the 92 keV transition in the scheme is almost 10 times more probable than the left two-step branch. If the two harder γ-rays were of electric dipole type this ratio would of course be much smaller. At the present stage it is not possible to decide between alternatives I and II because of the very small intensity of the 387 keV line. With scintillation detectors, as discussed before, it should be possible.

6. Angular correlation measurements between the *F*-line and the continuous spectrum of ThB

The 10.6^h activity of ThB has been studied frequently from different aspects. Its decay scheme is rather well known.[1] There is a 90 % branching ($E_\beta = 331$ keV) in the β spectrum leading to an excited level of 238 keV. This level is deexcited to the ground state through the emission of the well-known *F* line of $1388.56\, H\varrho$[2], extensively used as a standard in β spectroscopy because of its high intensity. Its conversion factor has been measured[3] to be 0.377, whereas α_K for a magnetic dipole transition according to theory is 0.325.

The angular correlation between the electrons of the *F* line and the continuous spectrum near the *F*-line was investigated in the goniometer with the

---

[1] Nuclear Data, loc. cit.

[2] G. LINDSTRÖM, Phys. Rev. 1951.

[3] D. MARTIN and H. RICHARDSON, Proc. Roy. Soc. *195*, 287, 1948.

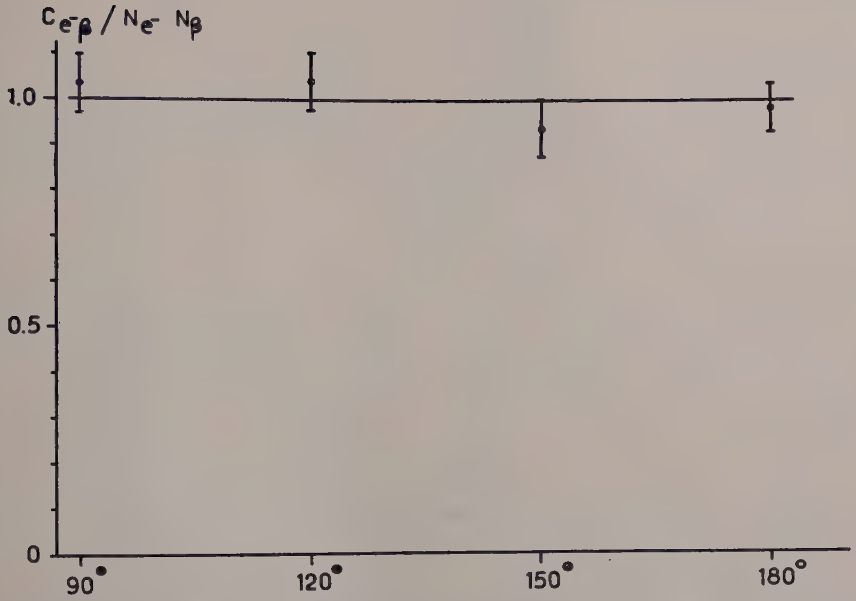

Fig. 19. Angular correlation between the *F*-line in the ThB spectrum and continuum at $H\varrho = 1\,500$.

result given in Fig. 19. The statistical accuracy is between ± 4 and 7 %. Since the source and backing are of completely negligible weight systematic errors due to electron scattering are absent. As can be seen the angular distribution is isotropic within the statistical errors.

Falcoff and Uhlenbeck[1] have given a theoretical treatment of the expected $\beta\gamma$ angular correlations. They find that, irrespective of the type of β interaction, an allowed β transition followed by any other radiation should give rise to no angular correlation. Furthermore, if the β transition is forbidden but still has an allowed shape then there will be no angular correlation with any radiation following the β transition. For forbidden shape spectra there will be angular correlations of different kinds.

Though Falcoff and Uhlenbeck's conclusions apply to $\beta\gamma$ correlations it seems reasonable that similar relations exist for βe correlations. At least, our result on ThB is not inconsistent with this view, since the ft value of the 331 keV β transition is 10^5 which definitely classifies this transition as an allowed one, and the distribution is isotropic.

As yet there are no other βe angular correlation experiments reported. In particular the case of Tm^{170} where a strong $\beta\gamma$ angular correlation has been reported[2], constitutes a favourable object for closer study, since the γ-transition emitted after the forbidden shape spectrum is highly converted. This case will be examined in the next section.

---

[1] D. Falcoff and G. Uhlenbeck, Phys. Rev. *79*, 323, 1950; *79*, 334, 1950.
[2] T. Novey, Phys. Rev. *78*, 66, 1950.

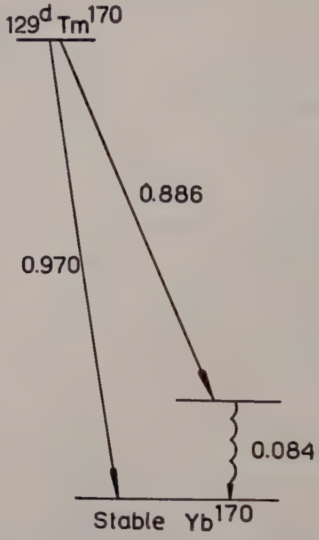

Fig. 20. Disintegration scheme of Tm^{170}.

7. Investigation of Tm^{170}

Earlier investigations on the 129^d Tm^{170} indicated several β and γ components, but according to recent results[1] only one highly converted γ is emitted, with the energy of 84 keV. The β spectrum has two components, with the energies 970 keV and 886 keV. The accepted scheme[2] is reproduced in Fig. 20. The 886 keV component should have a relative intensity of 10 %. The life time of the 84 keV excited state has been measured[3] by the delayed coincidence method to be $T_{1/2} = (1.6 \pm 0.2) \times 10^{-9}$ sec.

A. **Source preparation.** Tm in the form of finely powdered Tm_2O_3 was activated in the pile "Bepo", at Harwell. Since the cross section is very high (106 barns) the specific activity was extremely good. The water suspension method was used (see section 9 A) to transfer the activity onto the thin nylon foil. The sample was invisible and had a weight smaller than 0.1 mg/cm².

B. **Spectrometer measurements.** The β spectrum taken in one goniometer arm is given in Fig. 21. The resolution is set to be low (ring focus baffle removed) and the L and M lines are not resolved.

The intensities of the K and $(L + M)$ lines compared to the whole continuum are 0.013 and 0.13 respectively. This means a $K/(L + M)$ ratio of 0.1 which is in good agreement with FRASER's value ($K : L : M = 0.4 : 2.75 : 0.83$) but deviates markedly from that of SAXON et al.[4] and GRANT et al.[5], who report

---

[1] For references see: Nuclear Data, loc. cit.

[2] J. FRASER, Phys. Rev. *76*, 1540, 1949.

[3] R. BELL and R. GRAHAM, Phys. Rev. *78*, 490, 1950.

[4] D. SAXON and J. RICHARDS, Phys. Rev. *76*, 186, 1949.

[5] P. GRANT and R. RICHMOND, Proc. Phys. Soc. *62*, 573, 1949.

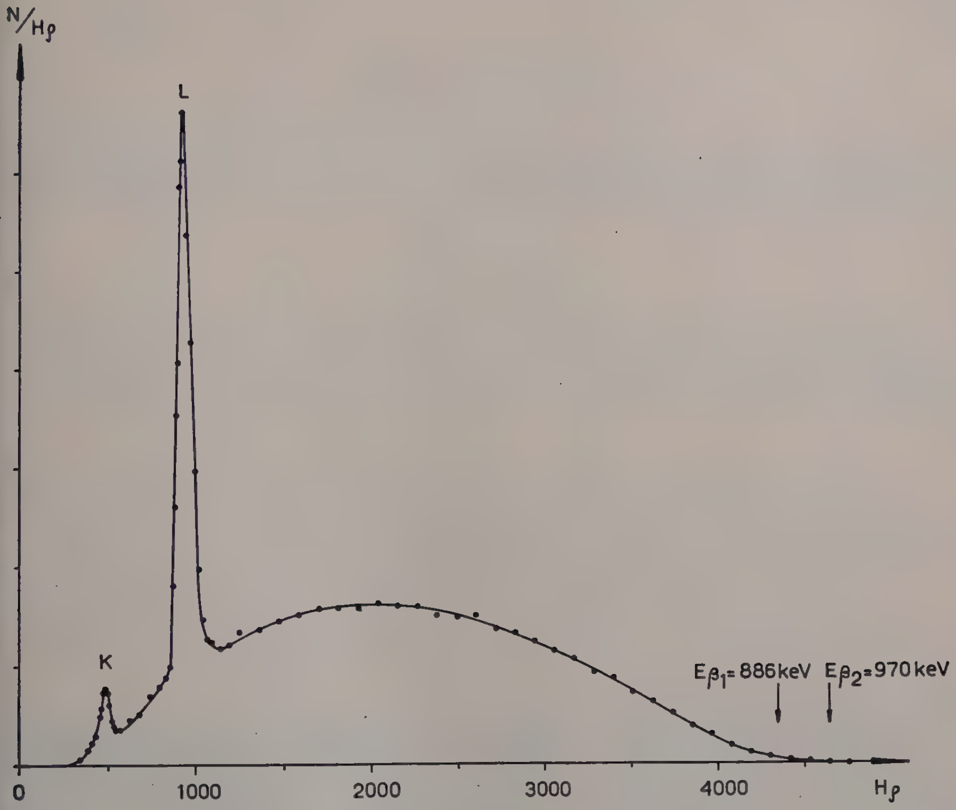

Fig. 21. β-spectrum of Tm^{170}.

$K/L = 0.71$ and 0.9 respectively. Our figure is also consistent with a total conversion probability of more than 90 % if the branching in the β spectrum is ~ 10 % as concluded by FRASER.

γ rays other than the one at 84 keV were looked for in the scintillation spectrometer, but none were found.

C. **Determination of the source strength.** Let us assume that $a \cdot N_0$ transitions go to the 84 keV excited state. We focus the strong $(L + M)$ line in one arm and some part of the continuum in the other. η_1 denotes the fraction of the *total* β spectrum focussed and η_2 the fraction of the *softer* component of the spectrum. We then have:

$$N_e = N_0 \cdot a \cdot \varkappa \cdot T_1 \tag{24}$$

$$N_\beta = N_0 \cdot \eta_1 \cdot T_2 \tag{25}$$

$$C_{e\beta} = N_0 \cdot a \cdot \varkappa \cdot \eta_2 \cdot T_1 \cdot T_2 \cdot f(\theta). \tag{26}$$

Thus

$$\frac{N_e N_\beta}{C_{e\beta}} = \frac{\eta_1}{\eta_2} \cdot N_0 \cdot f(\theta). \tag{27}$$

The upper limits of the two spectra are in this case very close together and we may to a good approximation put $\eta_1 = \eta_2$. $F(\theta) = 1$ according to next paragraph. We then get

$$\frac{N_e N_\beta}{C_{e\beta}} = N_0. \tag{28}$$

Two different measurements were performed with the same sample at two different $H\varrho$ values in the continuous spectrum. The resolving power was also changed in the two cases. Table I gives the result from the two series.

Table I.

Nr. of series	$H\varrho$	N_e/min	N_β/min	$C_{e\beta}$/min	$\frac{N_e\ N_\beta}{C_{e\beta}}$	N_0 in μC
1	2 400	6 910	5 100	1.50 ± 10 %	2.35×10^7	10.6 ± 1.2
2	3 430	6 730	7 630	1.88 ± 5 %	2.73×10^7	12.3 ± 0.7

The agreement between the two series is inside the statistical errors.

The source strength was also measured[1] by a completely independent method in order to check our result. Another source, scaled down in intensity by a known factor was measured in a standard β counter arrangement, which was calibrated in μC as a function of the maximum β energy by means of several β standards. The window was thick enough to absorb most of the strong β line. According to this measurement the source strength was found to be (11.8 ± 0.9) μC in excellent agreement with the above values.

D. Measurement of the angular correlation. The angular correlation between the strong β line and the continuous spectrum at 3 430 $H\varrho$ is shown in Fig. 22. As can be seen the statistical errors are here quite small (< 5 %). The result is somewhat unexpected. Even in this case the correlation seems to be isotropic, in spite of the fact that NOVEY[2] previously found a strong anisotropy in the corresponding βγ coincidence effect (~ 25 %). NOVEY's result is also theoretically reasonable since the ft value of the soft β component in cascade with the 84 keV γ ray suggests a forbidden shape spectrum. As previously discussed in section 4, the physical state of the source is a very important factor since great variations in density may partly smear out a given anisotropy, because of multiple scattering. In view of the apparently good source conditions in this case, however, it seems somewhat hard to believe that the flat form of the curve is entirely caused by source scattering. At the present

---

[1] This measurement was kindly performed by Fil. mag. STIG JOHANSSON.

[2] T. NOVEY, loc. cit.

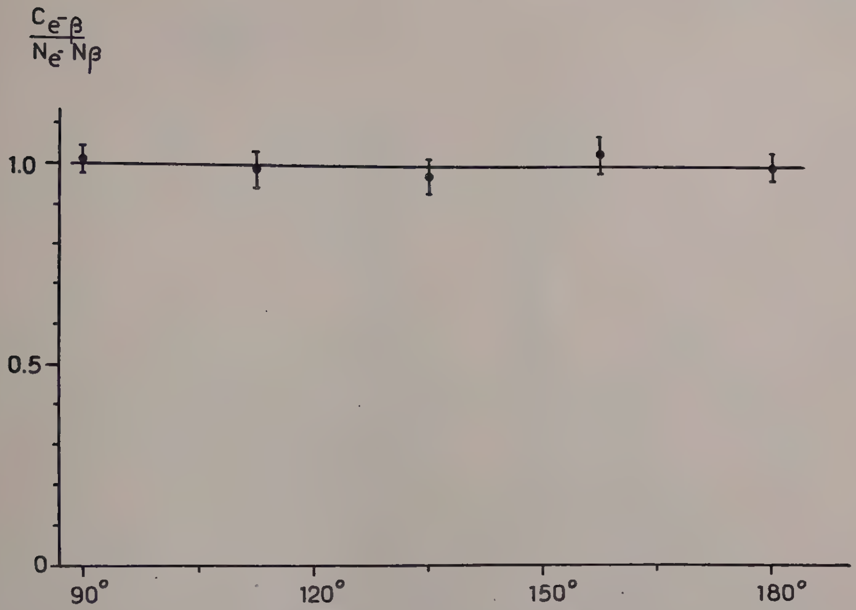

Fig. 22. Angular correlation between the L conversion line and continuum of Tm^{170} at $H\varrho = 3\,400$.

stage of the theory it is hardly worth while entering further into the different theoretically possible alternatives in an attempt to explain the isotropy found. Only one of these may be mentioned here. If the interaction between the nucleus and the electron shell (hfs) is strong and the life time of the intermediate state is sufficiently long the nucleus may reorientate itself before emission of the second quantum. In this case one may expect an influence of the atomic shell on the angular correlations. This has only recently been found by FRAUENFELDER et al.[1]

8. Investigation of Au^{199}

This isotope was selected for a study in the spectrogoniometer since the last published disintegration scheme[2] indicated that a number of relatively strong conversion lines in cascade transitions were present. During the course of the experiments it became apparent, however, that this scheme had to be revised. Several of the same conclusions have also recently been drawn by HILL[3], who made a study of the conversion spectrum in a semicircular spectrometer of high resolving power using photographic registration.

A. **Source preparation.** The sample was obtained by neutron bombardment

---

[1] H. FRAUENFELDER, Phys. Rev. *82*, 549, 1951. H. AEPPLI, A. BISHOP, H. FRAUENFELDER, M. WALTER and W. ZÜNTI, Phys. Rev. *82*, 550, 1951.

[2] L. BEACH, C. PEACOCK, and R. WILKINSON, Phys. Rev. *76*, 1585, 1949, see also Nuclear Data, loc. cit.

[3] R. HILL, Phys. Rev. *79*, 413, 1950.

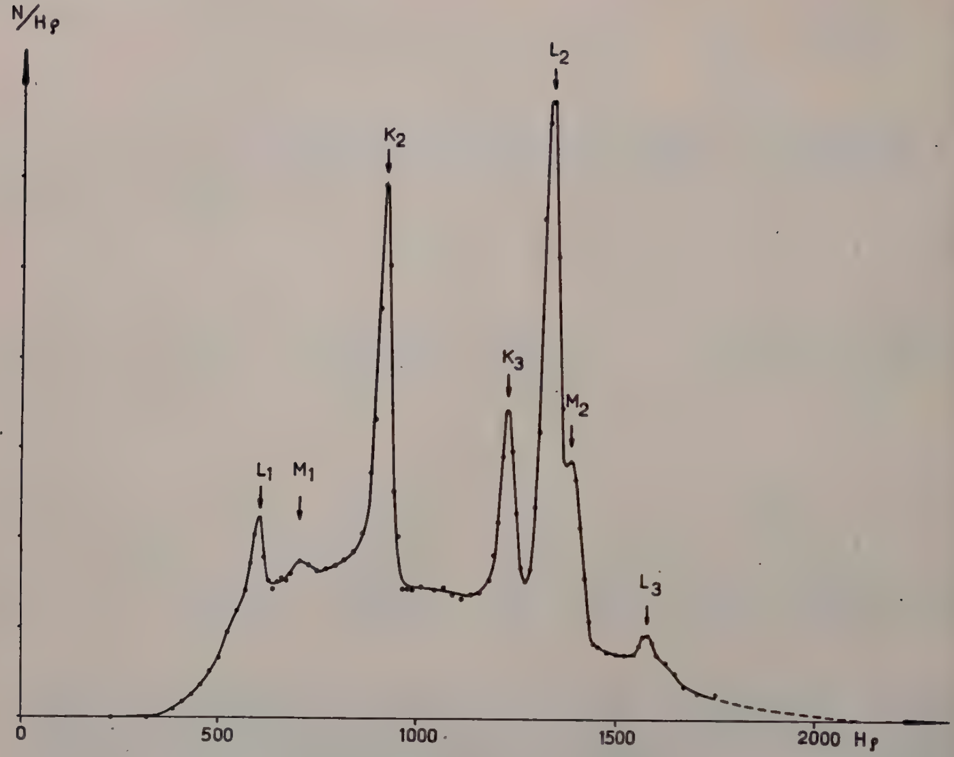

Fig. 23. β-spectrum of Au^{199}.

of Pt in Bepo, at Harwell. 31 min. Pt^{199} which is first formed decays to Au^{199}, which has a half life of 3.3 days. The Pt powder was dissolved in aqua regia. No carrier was added. The solution was shaken with ethyl acetate, which was washed six times with equal volumes of 6 N. hydrochloric acid. The ethyl acetate which contained the active $AuCl_3$ was evaporated to dryness. The residue obtained in this way had very a small weight. A drop of the activity was transferred onto the nylon film ($\sim 10\,\mu g/cm^2$) of the sample holder. In order to get the activity uniformly distributed within a conveniently sized area this part of the nylon foil was first treated with a diluted solution of insulin before the drop was added, according to the procedure given by LANGER.[1]

B. **Spectrometer measurements.** In Fig. 23 the β spectrum is shown. It agrees well with that obtained by BEACH et al. showing the existence of three converted γ-rays with the energies 50 keV, 158 keV and 208 keV. They reported still another very soft β line at 9 keV (just absorbed in our window), which was interpreted as an *L* line of a 24 keV γ-ray. This line is however more probably due to AUGER electrons of the *L X* radiation, which can be expected to occur at this place in the β spectrum. In his recent work HILL

---

[1] L. LANGER, Rev. Sci. Inst. *20*, 216, 1949.

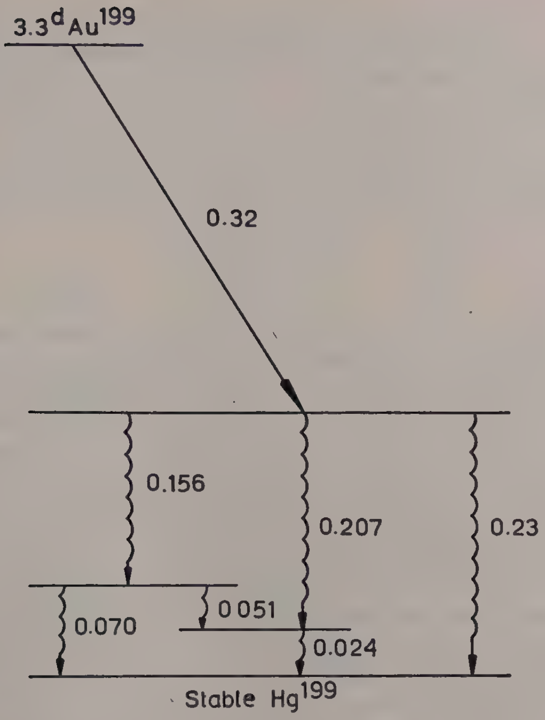

Fig. 24. Previous disintegration scheme of Au^{199}.

actually demonstrated the existence of such Auger lines and also those coming from the K X radiation. In view of these circumstances the 24 keV γ radiation most probably should be left out from the old disintegration scheme (see Fig. 24). If that is done the whole scheme must be revised since both the 50 keV and the 208 keV γ-ray end up in this particular level.

Another γ ray of 70 keV, was also reported before and put into the scheme. This line was not observed as a conversion line, in spite of the fact that the conversion coefficient should be expected to be fairly high at this low energy, but was only found as an L photo line when a lead foil was covering the sample. There are, however, reasons to believe that this radiation is the $K\alpha$ radiation from Hg (68 keV), which must be rather strong because of the K conversion of two of the other γ-lines. The emission of the 70 keV γ line from the scheme means that the 158 keV γ ray cannot reach the ground state, the position of which is fixed because of a reported strong (45 %) γ-ray of 230 keV. The K conversion line corresponding to this γ line should fall on the L line of the 158 keV γ ray and thus cannot be seen in the β spectrum. With his higher resolution Hill was also unable to observe any conversion line corresponding to this γ energy. The evidence for the strong 230 keV line therefore comes entirely from the secondary photoelectron spectrum of the lead foil. A closer analysis of this spectrum shows, however, that the K photo line of the 230 keV γ ray is situated exactly on the place where one should expect to find the L photo line of the 158 keV γ ray. The thickness of the lead converter used in BEACH's investigation (32 mg/cm^2) is of saturation thickness for both the K and the L photoelectrons of the 158 keV γ ray. This explains the abnormal $K:L$ photoelectron intensity ratio, since the intensity of the L line will be very much overrepresented because of the longer range of the L electrons (142 keV) compared to the K electrons (70 keV).

As a rough estimate of this effect we may use the relation given by LIBBY[1] for the range R_β of electrons, valid for $E_\beta < 0.2$ MeV

$$R_\beta = \frac{2}{3} E_\beta^{5/3}. \tag{29}$$

We then get $R_{L\,158}/R_{K\,158} = 3.2$. If we make the somewhat arbitrary assumption that the peak heights represent the intensities of the photo lines from the effectively infinitely thick radiator we get this intensity ratio from BEACH's curve (in undivided form) as $N_K/N_L = 4:3$. If we take into account the above differences in ranges we get as a corrected value for the ratio between the K and L photoelectric cross sections $\sigma_K/\sigma_L = 4.3$, which is sufficiently near to the expected[2] $\sigma_K/\sigma_L \sim 5$, considering the possible errors in our estimate.

We may use the same procedure to get an estimate of the relative intensities of the unconverted 158 keV and 208 keV γ rays from BEACH's photoelectron spectrum. From LIBBY's relation one gets $R_{L\,158}/R_{K\,208} = 1.8$. Taking the heights of the peaks one has $N_{K\,208}/N_{L\,158} \sim 8:30$. The corrected photo lines will then have an intensity ratio of 0.48. The ratio between the photoelectric cross sections for the 208 keV and 158 keV γ radiation is according to GRAY[3] $\sigma_{208}/\sigma_{158} = 0.50$. Using the ratio of $N_K/N_L = 5$ we then get as our result $\text{Int. } \gamma_{158}/\text{Int. } \gamma_{208} = 5 \cdot \frac{1}{0.48} \cdot 0.50 \sim 5$, which naturally must be considered as an estimate only. It is, however, considerably higher than that given by BEACH et al., who estimate the two unconverted γ-rays to be of the same intensity, which seems to be definitely inconsistent with the above considerations.

In order to investigate this question closer a scintillation spectrum of the γ-radiation was run. Fig. 25 shows the result in the high energy part of the spectrum calibrated against the annihilation radiation from Na^{22}. The peak at 158 keV is very clear but there is almost no sign of the 208 keV peak. The dotted curve indicated in the spectrum is merely to show the possible maximum intensity of the 208 keV peak. The intensity ratio between the two peaks is at least 10 and considering the variation in photoelectric cross sections for the two γ rays we may therefore conclude that the intensity ratio between the two γ rays is at least 5, which is consistent with our high value, deduced from BEACH's experimental curve.

Fig. 26 shows the low energy part of the scintillation spectrum. Besides the 158 keV peak it shows the $K\alpha$ X-ray peak from Hg due to the K conversion. The 50 keV peak can also be seen, though less clearly, partly because of its low intensity. Both from the scintillation spectrum and from the conversion spectrum one must conclude that the 50 keV transition is much less frequent than the 158 keV transition.

---

[1] W. LIBBY, Measurements of Radioactive Tracers, Analytical Chemistry, *19*, 2, 1947.
[2] See e. g. W. HEITLER, Quantum Theory of Radiation, Oxford Univ. Press 1944.
[3] L. GRAY, Proc. Camb. Phil. Soc. *27*, 103, 1931.

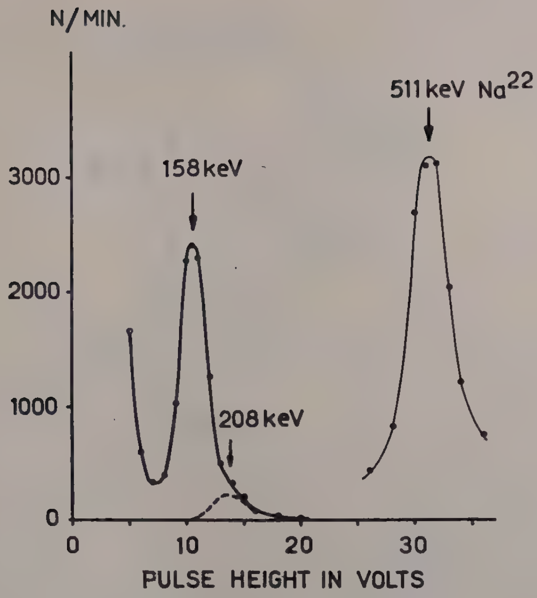

Fig. 25. Scintillation spectrum of harder γ-rays in Au^{199}.

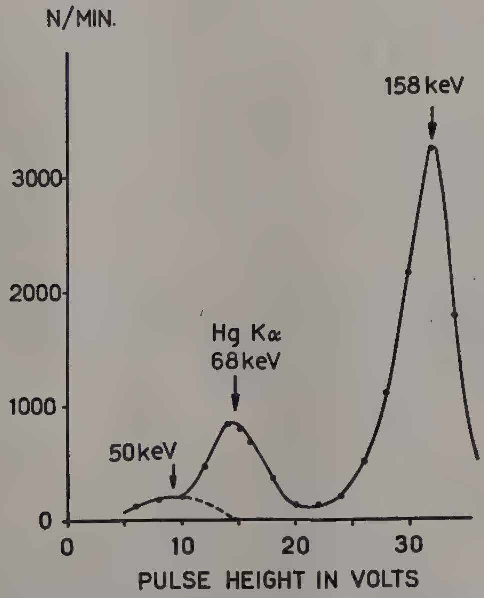

Fig. 26. Scintillation spectrum of softer γ-rays + X-rays in Au^{199}.

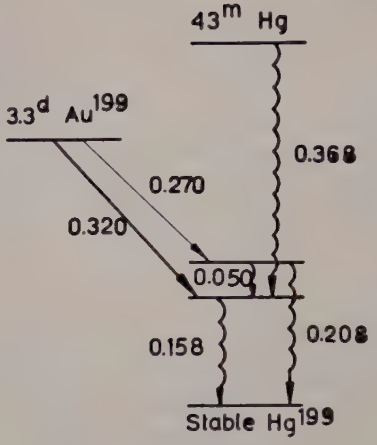

Fig. 27. Revised disintegration scheme of Au^{199}.

C. **The revised disintegration scheme.** A disintegration scheme consistent with our experimental results and also with those obtained by HILL (loc. cit.) is given in Fig. 27. Since the energies of the 50 keV and 158 keV lines add up to the third line of 208 keV one is inclined to regard the latter as a cross-over γ-ray. This point will be discussed below in connection with the coincidence measurements. Both the 50 keV and the 208 keV transitions are definitely much less frequent than the 158 keV transition and the main β component of 230 keV therefore goes directly to the 158 keV excited level.

There is still one more reason to put the 50 keV transition above the 158 keV one, as pointed out by Hill. HOLE[1] investigated the radiation emitted from the 43 min. isomeric state of Hg^{199} (obtained by fast neutrons on Hg). He found two converted γ-rays of the energies 155 keV and 368 keV in cascade transitions. Hole showed that the last line is the one which is responsible for the long life time, and therefore the 155 keV transition goes directly to the ground state in Hg^{199}. Neither the 208 keV γ-ray nor the 50 keV γ-ray was emitted in that decay.

D. **Conversion coefficients.** From Fig. 23 and from the above discussed estimate of the relative intensities of the unconverted γ-rays one can obtain values of the conversion coefficients for the 158 and 208 keV transitions. We thus obtain for the 158 keV transition:

$$\alpha_{K\,158} = 0.24$$

$$\alpha_{L\,158} = 0.33$$

$$\left(\frac{\alpha_K}{\alpha_L}\right)_{158} = 0.73$$

$$\alpha_{M\,158} = 0.10.$$

---

[1] N. HOLE, Ark. f. Mat. Astr. o. Fysik *36 A*, Nr. 9, 1948.

The values of the 208 keV coefficients must be based on the uncertain intensity ratio between $\gamma\,158$ and $\gamma\,208$ and are therefore much less reliable:

$$\alpha_{K\,208} \sim 0.62$$

$$\alpha_{L\,208} \sim 0.11$$

$$\left(\frac{\alpha_K}{\alpha_L}\right)_{208} \sim 5.6$$

$$\alpha_{M\,208} \sim 0.03.$$

E. Slow neutron cross section of Au^{198}. These conversion coefficients have to be used together with the γ-ray intensities, when an estimate is made of the neutron cross section of Au^{198}.

It was first found by LEVY and GRUELING[1] that the conversion spectrum of Au^{198}, obtained by slow neutron bombardment of Au^{197} in a high-flux reactor, contained, as well as the well-known 411 keV γ-ray, some weak conversion lines corresponding to γ-energies of 157 and 208 keV. Other authors reported $\gamma\gamma$ coincidences and it was believed that the Au^{198} had a complex disintegration with a low energy branch of $\leq 15\,\%$. It was later found by SIEGBAHN and HEDGRAN[2] that a Au^{198} sample obtained from the low power reactor in HARWELL (GLEEP) emitted no unconverted γ-rays of measurable intensity at the energies concerned. (The intensity must have been less than 2 % of the 411 keV γ-ray.) LANGER and PRICE[3] furthermore showed that the Au^{198} continuous spectrum had the allowed form for one single component. It was therefore generally concluded that the two γ-rays found by LEVY and GRUELING did not belong to the Au^{198} disintegration but could perhaps be due to some impurity[4], as had been suggested before. The present explanation is, however, another and rather unexpected one which was given recently by HILL and MIKELICH.[5] Due to an exceptionally high neutron cross section ($\sim 10^4$ barns) the primarily formed Au^{198} may occasionally absorb one more neutron during the bombardment, thus forming Au^{199}. HILL et al. derived the formula for the relative populations of Au^{199} and Au^{198} after irradiation. It is found that this ratio increases as the reactor flux increases. In order to observe the additional Au^{199} lines it is therefore necessary to have the irradiation performed in a high power reactor. Furthermore, since these lines are highly converted compared to the 411 keV γ line of Au^{198} a certain intensity ratio between the conversion lines of Au^{199} and Au^{198} will correspond to a much smaller ratio between activated nuclei and between the unconverted γ-rays. By measuring the intensity ratio of the 411 keV conversion line of Au^{198} and the 158 keV conversion line of Au^{199} (31 : 1) HILL was able to calculate the neutron cross section σ of Au^{198}. It is then necessary to know the branching ratio of the 158 and 208 keV transitions, including the different conversion coefficients. As a result HILL et al. obtained $\sigma = 3.5 \times 10^4$ barns. In a later communication[6] this figure was corrected to be 1.6×10^4 barns. In both cases the conversion coefficients had to be estimated from theoretical considerations, which, as stressed by HILL, were partly conflicting. By using the experimentally obtained data we are now able to get a new value of for Au^{198}, namely 3.0×10^4 barns. The greatest uncertainty in this value probably comes from the intricate photographic determinations of the intensity ratio between the Au^{198} and Au^{199} conversion lines (see above).

---

[1] P. LEVY and E. GRUELING, Phys. Rev. *73*, 83, 1948; *75*, 819, 1949.

[2] K. SIEGBAHN and A. HEDGRAN, Phys. Rev. *75*, 523, 1949.

[3] L. LANGER and H. PRICE, *76*, 641, 1949.

[4] See e. g. C. PEACOCK and R. WILKINSON, Phys. Rev. *74*, 297, 1948.

[5] R. HILL and J. MIKELICH, Phys. Rev. *79*, 275, 1950.

[6] R. HILL, Phys. Rev. *79*, 413, 1950.

F. Coincidence and angular correlation measurements in the goniometer. Coincidences (and individual counting rates in the two channels) were taken between:

L_1 and L_2

L_2 and the continuous spectrum at $H\varrho = 1\,100$

L_1 and the continuous spectrum at $H\varrho = 1\,100$

K_2 and the continuous spectrum at $H\varrho = 1\,100$

K_2 and K_3

K_3 and the continuous spectrum at $H\varrho = 1\,100$.

In some cases the results were checked by changing the resolving power. Following the general procedure outlined in section 3 A the coincidence data thus obtained were used to show conclusively that:

1. L_1 is in cascade with L_2
2. L_1 is in cascade with the continuous spectrum at $H\varrho = 1\,100$
3. K_2 is in cascade with the continuous spectrum at $H\varrho = 1\,100$
4. K_3 is in cascade with the continuous spectrum at $H\varrho = 1\,100$
5. K_2 is *not* in cascade with K_3.

Thus the coincidence results all confirm the scheme given in Fig. 27.

The above coincidence investigations were supplemented by measurement of the angular correlation between K_2 conversion electrons and the continuous spectrum electrons (at $H\varrho = 1\,100$) and also between L_2 conversion electrons and the continuous spectrum electrons (at $H\varrho = 1\,100$). The activity of the sample at the time of this investigation was low and the statistical errors are therefore not better than $\sim \pm 12\,\%$. Within this statistical accuracy, however, the angular correlation between both K and L electrons relative the continuous spectrum electrons seems to be isotropic. Fig. 28 shows the results in the case of the K_2 electrons. A similar curve was obtained for the L_2 electrons. The isotropic correlations obtained in both cases are consistent with the fact that the form of the continuous spectrum in this case should be expected to have an allowed shape, according to the general discussion recently given by FALCOFF and UHLENBECK.[1]

---

[1] D. FALCOFF and G. UHLENBECK, loc. cit.

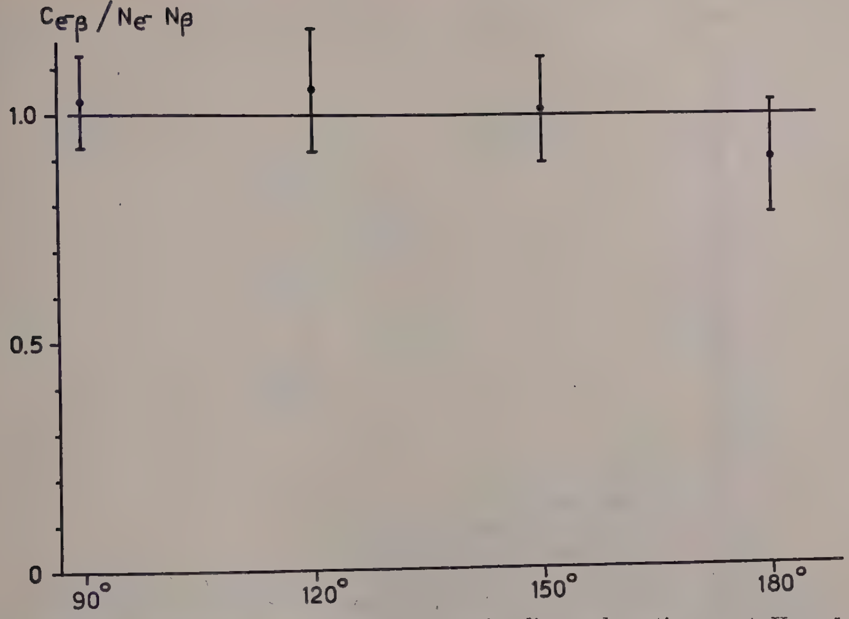

Fig. 28. Angular correlation between K_2 conversion line and continuum at $H\varrho$ = 1 100 in Au^{199}.

9. Investigation of Sm^{153}.

According to the currently accepted scheme[1] for Sm^{153} the main β component ($E_\beta = 0.78$ MeV by absorption) should be followed by two strongly converted γ-rays in cascade (with energies[2] 69.5 keV and 103 keV) and should consequently be well suited for angular correlation measurements. By means of absorption measurements an additional very weak γ-ray of 0.57 — 0.61 MeV has been found.

A. **Source preparation.** Finely powdered Sm_2O_3 was irradiated at HARWELL in BEPO. The powder was suspended in water and after letting the suspension settle down for a while it was possible to extract the small-grains part of it and transfer it to the sample holder. In order to get the activity uniformly distributed the previously mentioned insulin method was used (see section 8 A). The weight of the sample was very small (~ 0.1 mg/cm^2).

B. **Spectrometer measurements.** The β spectrum (in $H\varrho$ divided form) is given in Fig. 29. A FERMI analysis of the continuous spectrum (enlarged 10 times in Fig. 29) gave an upper limit of 700 ± 30 keV. Besides the K_1, L_1 and M_1 conversion lines corresponding to the 70 keV γ line, and the K_2, L_2 and M_2 lines corresponding to the 103 keV γ line, there are two AUGER lines A_1 and A_2. The energies of these lines correspond to $K - 2L$ and $K - L - M$ respectively.

---

[1] Nuclear Data, loc. cit.

[2] R. HILL, Phys. Rev. *74*, 78, 1948.

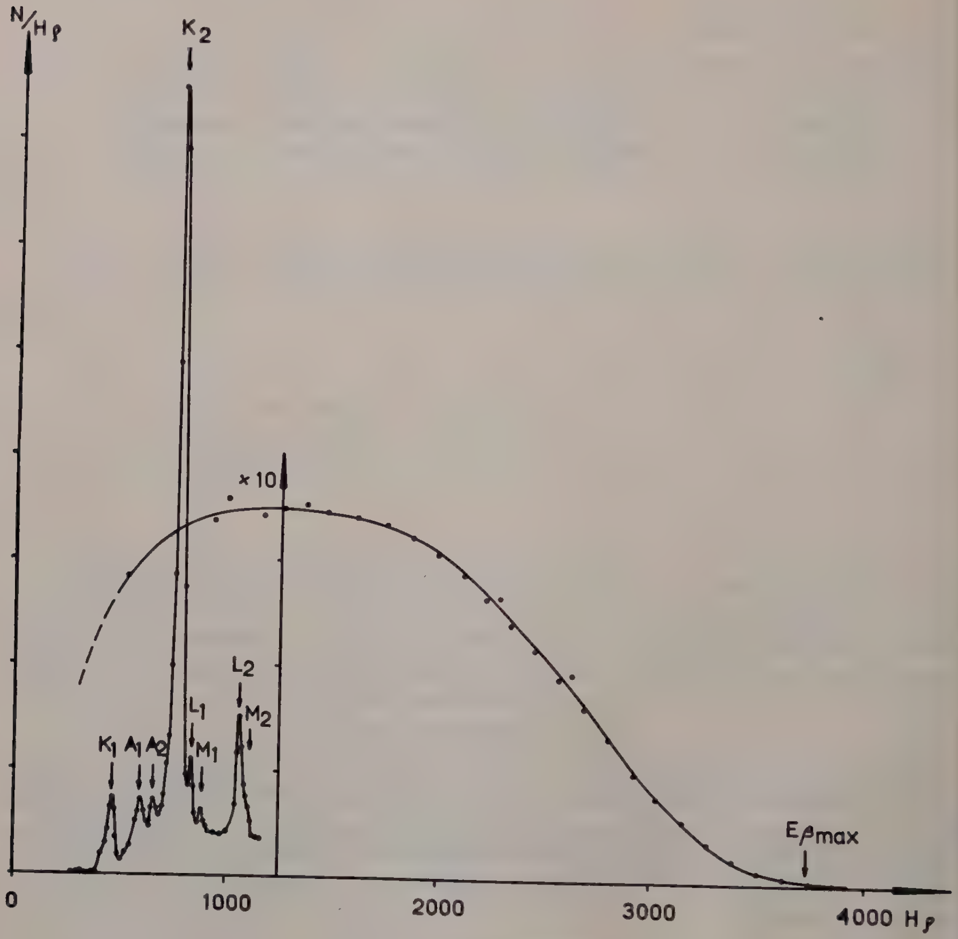

Fig. 29. Sm^{153} β-spectrum.

The accepted scheme would require that the 70 keV and the 103 keV transitions should be of the same intensities. As can be seen from Fig. 29 the 103 keV conversion lines are much stronger than the 70 keV conversion lines. It may be, however, that the 70 keV γ line is much less converted than the 103 keV line. In order to investigate this the (unconverted) γ spectrum was run in the scintillation spectrometer. Fig. 30 shows the low energy region. The 103 keV γ line can easily be recognized, as can the 40 keV $K\alpha$ radiation from Eu (due to the internal conversion). There is, however, no sign of any unconverted 70 keV γ radiation. We must therefore conclude that the 70 keV radiation is converted to a very high extent, which is consistent with MUELHAUSE's figure[1] $\alpha = \infty$. The intensities of the conversion lines then indicate that the 70 keV transition is much less frequent than the 103 keV transition (5 — 10 %)

---

[1] C. O. MUELHAUSE, private communication given in Nuclear Data.

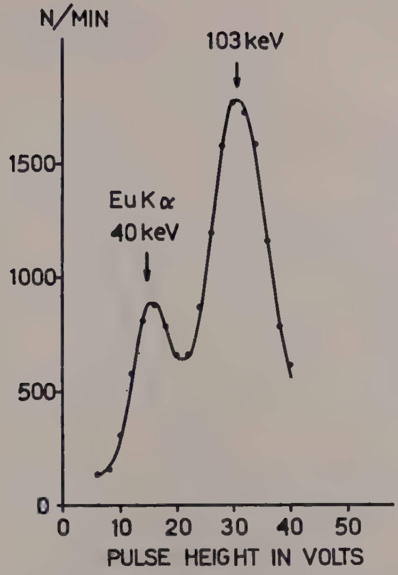

Fig. 30. Scintillation spectrum of softer γ-rays + X-rays in Sm^{153}.

in disagreement with the scheme. The main β component should therefore lead directly to the 103 keV excited level.

The previously found very weak γ-ray of higher energy was further studied in the scintillation spectrometer. Fig. 31 shows the position of it compared to the annihilation line from Na^{22}. According to this measurement the energy of the γ line is 530 keV.

C. **Revised scheme.** Fig. 32 shows a revised scheme. The position of the weak 530 keV γ ray in the scheme is only one of three possible alternatives. The line may also go either to the 103 excited level or to the ground state. If the position is that indicated in the scheme it may be that the β component of 630 keV is absent. In that case the intensities of the 530 keV and the 70 keV lines should be identical. This is very hard to prove experimentally with present techniques, since one of the lines is very much converted and the other only very little, and furthermore both are of small intensity.

The K conversion coefficient of the 103 keV transition can be calculated from Fig. 29 to be $\alpha_K = 0.65$ and $\frac{\alpha_K}{\alpha_L} \sim 6$. For an electric quadrupole transition the theoretical values[1] are $\alpha_K = 1.0$ and $\frac{\alpha_K}{\alpha_L} \sim 2$. If instead a mixture of electric quadrupole and magnetic dipole radiation be assumed, α_K will be smaller and $\frac{\alpha_K}{\alpha_L}$ larger, i.e. in much better agreement with the experimental results. In that case the transition probably involves a spin change of 1 unit without parity

---

[1] See P. Axel and R. Goodrich, Internal Conv. Data (privately distributed).

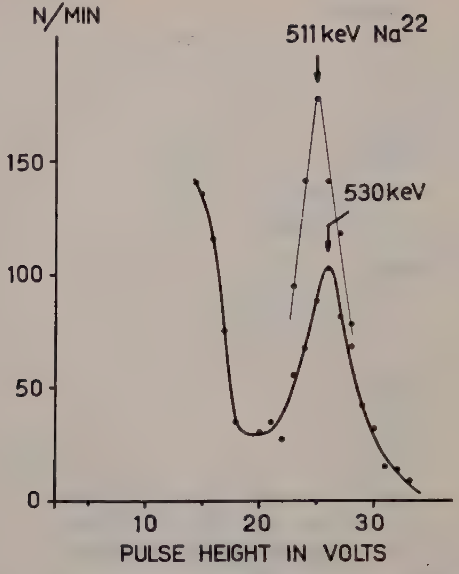

Fig. 31. Scintillation spectrum of hard γ-ray in Sm^{153}.

change. The spin of the Eu^{153} ground state has been measured[1] to be 5/2. According to the spin orbit coupling scheme the ground state would be expected to be a $d_{5/2}$ state. The conversion data then suggest that the 103 keV transition takes place between the two states within the d-doublet, i.e. $d_{3/2} \rightarrow d_{5/2}$.

D. **K series fluorescence yield at $Z = 63$.** If the areas under the AUGER lines A_1 and A_2 are compared to those under $K_1 + K_2$ we obtain a value for the K fluorescence yield $\tilde{\omega}$ at $Z = 63$. We have:

$$1 - \tilde{\omega} = \frac{N_{A_1}}{N_{K_1} + N_{K_2}} + \frac{N_{A_2}}{N_{K_1} + N_{K_2}}$$

$1 - \tilde{\omega}$ is then simply the K series internal conversion coefficient.

The fluorescence yield has been calculated by BURHOP[2] (unrelativistic approximation) and by MASSEY and BURHOP[3] (relativistic approximation). At high Z values (e.g. Au) the latter approximation yields internal conversion values about twice as high as the former approximation. An inspection of the diagram given in MASSEY and BURHOP's paper illustrating the experimental fit to the theoretical curve shows that there exists a remarkably good agreement between experimental results and theory at low and medium Z values ($Z < 40$). For Z between 40 and 50 there is a definite tendency for the experimental values to be higher than those expected from the calculated curve. Above $Z = 50$ there were no precise measurements available for comparison. Recently BERGSTRÖM

---

[1] H. SCHÜLER and T. SCHMIDT, Z. Physik *94*, 457, 1935.

[2] E. BURHOP, Proc. Roy. Soc. *148*, 272, 1935.

[3] H. MASSEY and E. BURHOP, Proc. Roy. Soc. 153, 661, 1936.

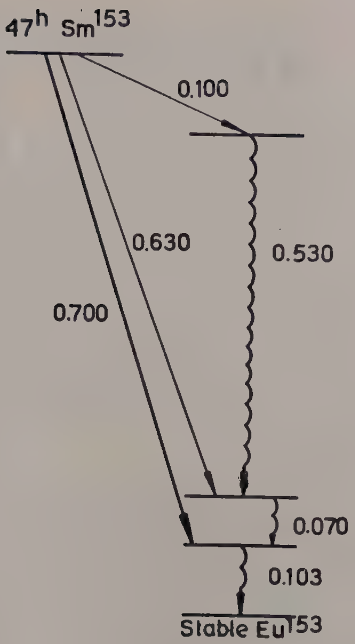

Fig. 32. Revised disintegration scheme of Sm^{153}.

and THULIN[1] however, were able to give a value of $\tilde{\omega}$ at $Z = 55$ in good agreement with the theoretical curve. Since the correction due to relativistic effects is higher for high Z values it might be of some interest to compare the results obtained in our case at $Z = 63$ with the theoretical curve. The experimental results from Fig. 29 yield:

$$1 - \tilde{\omega} = 0.074 + 0.048 = 0.12 \pm 0.02$$

$$\tilde{\omega} = 0.88 \pm 0.02.$$

The theoretical value is 0.90 which agrees very well with our experimental value.

E. **Coincidence and angular correlation measurements in the goniometer.** Following the general procedure outlined in section 3 A it was fount that K_1 and K_2 are in cascade. Coincidences were also demonstrated between the AUGER lines and the K_2 line.

Because of the small intensity of the K_1 line angular correlation experiments between K_1 and K_2 were not performed as originally intended. Instead, the angular correlation between K_2 and the continuous spectrum electrons at $H\varrho = 1\,500$ was investigated. The curve obtained was similar to that for Au^{199}, showing an isotropic distribution within the statistical errors (~ 10 %). This is consistent with FALCOFF and DANCOFF's theory, since the β spectrum is of the allowed type.

---

[1] I. BERGSTRÖM and S. THULIN, Phys. Rev. *79*, 538, 1950.

10. Angular correlation between internally created positrons and electrons in Na^{24}

A nuclear level situated more than 2 m_0c^2 above another level may be de-excited to this level by emitting an electron-positron pair, created in the field of the nucleus. The cross section for this process is, compared to the ordinary γ ray emission, usually very small (the conversion coefficient for pair formation being only $\sim 10^{-3} - 10^{-4}$) and is therefore difficult to observe and measure. In this high energy region and especially for light nuclei the other process of similar origin which might give information about the multipole order of the radiation, i.e. K and L internal conversion, is also, however, very improbable. Furthermore, the latter process decreases rapidly with available excitation energy (and decreasing Z) whereas the pair process increases. For light nuclei and at sufficiently high energies it will therefore occur that it is more convenient to study the pair process than the K or L conversion effect, if a determination of the multipole order is wanted.

A typical example is given by the two γ rays of Na^{24}, having the energies of 1.38 and 2.76 MeV. The conversion line of the 1.38 transition is situated on the continuous spectrum (very near the end-point) and will therefore certainly be hard to observe. The 2.76 conversion line has a conversion coefficient, which is extremely small ($\sim 10^{-6}$). Although this line has actually been observed and the conversion coefficient determined by means of the double focussing spectrometer[1], it is no doubt more convenient to use the internal pair process in this case[1, 2, 3, 4], which has a cross section about 10^3 as big. The results of these cross section measurements (except ref. 3) seem to indicate that this line is due to an electric quadrupole transition, which is also consistent with results of $\gamma\gamma$ angular correlation experiments performed by Deutsch et al.[5]

A. **Positron-electron angular correlation and multipole order.** It has been suggested by Horton[6] and by Rose[7] that the internal pair process may be used in another way to give information about the multipole order of the transition. Thus they have shown that the angular distribution in internal pairs is expected to be dependent on the multipole order. Consequently, an experimental investigation of the angular correlation between simultaneously emitted electrons and positrons (i.e. forming a pair) in principle determines the multipole order of the radiation.

The angular distribution of pairs of all energy combinations between electrons and positrons is shown in Fig. 33, taken from Horton's paper. For Na^{24} $\gamma = 5.4$ and corresponds rather closely to the lower group of curves $\gamma = 5$. The anisotropy is quite pronounced, according to this diagram, particularly for higher multipole order. In the region between 0° and 90° one can discriminate between electric dipole and quadrupole and magnetic dipole radiation, whereas the two latter types coincide in the region 90°—180°. Horton has also drawn similar

---

[1] K. Siegbahn and S. du Toit, Ark. f. Fysik *2*, Nr. 22, 211, 1949.
[2] K. Siegbahn and H. Slätis, Ark. f. Fysik, 1951, in print.
[3] E. Rae, Phil. Mag. *40*, 1155, 1949.
[4] W. Mims, H. Halban and R. Wilson, Nature *166*, 1027, 1950.
[5] E. Brady and M. Deutsch, Phys. Rev. *78*, 558, 1950.
[6] G. Horton, Proc. Phys. Soc. *60*, 457, 1948.
[7] M. E. Rose, Phys. Rev. *76*, 678, 1949.

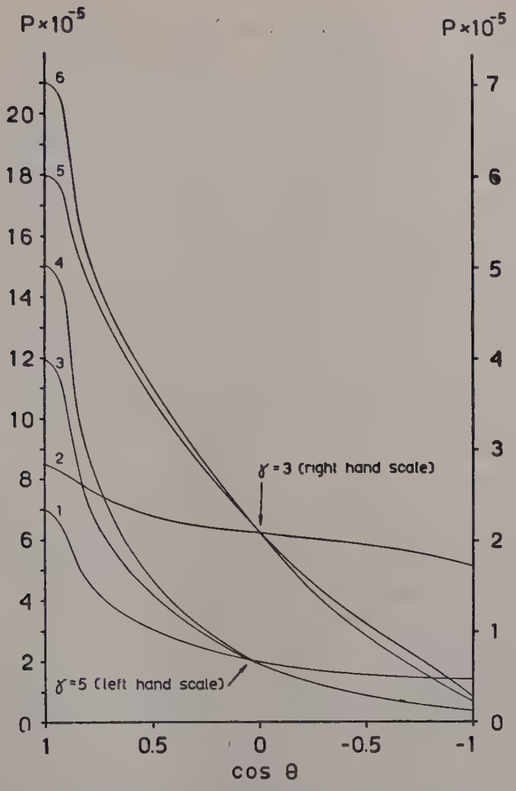

Fig. 33. Overall angular distribution of pairs according to Horton. 1, 2 electric dipole. 4, 6 magnetic dipole. 3, 5 electric quadrupole.

distribution curves when definite energies are given to the electron and positron in the pair. If there is a great difference in energy between the two particles the anisotropy is reduced but it is still always possible to discriminate between electric dipole and electric quadrupole plus magnetic dipole radiation.

B. **Experimental procedure.** Naturally such an experiment meets with considerable technical difficulties and has to our knowledge not yet been tried. First we have the low cross section for the entire pair process. Then the electrons and positrons are distributed in continuous energy spectra. In order to get coincidences one has to select positron and negatron energies within these continuous spectra which add together to give $E_\gamma - 2\ m_0c^2$. The necessary angular resolution furthermore strongly reduces the expected e^+e^- coincidence effect.

In more conventional experimental arrangements for correlation studies it would also be extremely hard to discriminate between the rare internally created electrons superimposed on the 1 000 times stronger continuous β spectrum. Even so it would be quite difficult to avoid the uncertainties caused by coincidences due to other causes, such as γγ, βγ, and scattered radiation.

All these difficulties can be overcome if we select Na^{24} for a study in the goniometer, although the encountered coincidence effects are admittedly very low and the required data tedious to collect.

In making these experiments the twisted baffles described in section 2 B are mounted in the two goniometer arms and the senses of the currents chosen so that only positrons are transmitted in one arm and negatrons in the other.

Since good resolution is not wanted in these experiments the ring focus shutters are removed. Because of this and the fact that we are dealing exclusively with continuous electron spectra the arrangement is very insensitive to mutual magnetic disturbances between the two arms (see sections 2 F and 3 B).

The continuous β^- spectrum has an upper limit of 1.39 MeV. The upper limit of the internally created negatrons and positrons is $2.76 - 1.02 = 1.74$ MeV. If we focus negatrons of 1.46 meV in one arm, in order to get rid of the bulk of electrons from the continuous spectrum, the coinciding positrons still have an energy of $1.74 - 1.46 = 0.28$ MeV, which consequently should be focussed in the other arm in order to get coincidences. Fortunately the energy left over for the positrons is high enough not to cause any particular trouble regarding the source conditions. The multiple scattering (see section 4) will be rather negligible at the source thicknesses used in our experiments (~ 0.5 mg/cm^2). Total activities around 1 mC were found to be convenient since the corrections due to accidentals then were sufficiently small compared to the real $e^+ e^-$ coincidence effects, even in the 180° position.

Due to the large distances between the source and detectors, possible $\gamma\gamma$ and $e\gamma$ coincidence effects between scattered radiation or unabsorbed γ quanta are found to be completely negligible. Possible coincidences between electrons scattered over the energy limit in the β^- arm and internally created β^+ registered in the other arm were also found to be negligible.

C. Experimental proof of the simultaneous emission of electrons and positrons in pairs. In order to make sure that the registered coincidences really were due to electron-positron pairs from the 2.76 MeV transition, and nothing else, coincidence "lines" were taken in the following manner. The current through one lens was set at a fixed value, whereas it was varied step-wise in the other arm around the required value for $e^+ e^-$ coincidences. It was then found that the coincidence rate dropped down to zero on both sides of the calculated correct current value. The same procedure was then repeated with the other lens.

It was noticed that the relative half width of the coincidence line, was appreciably bigger when the current through the e^+ lens was changed than in the other case. This must be expected, since the *high* energy e^- particles selected in the e^- lens may give coincidences with low energy e^+ particles in the other lens extended over the same *absolute* energy range. In view of this η (see section 3 C) in the e^+ lens was increased by replacing the GM aperture by a much wider one. In this way the coincidence effect was doubled without affecting the number of accidentals to the same extent (the single counting rates are largely due to scattered γ-rays).

The simultaneous emission of internally created electrons and positrons in pairs corresponding to the 2.76 MeV transition is thus well demonstrated by the existence of the $e^+ e^-$ coincidence lines discussed above.

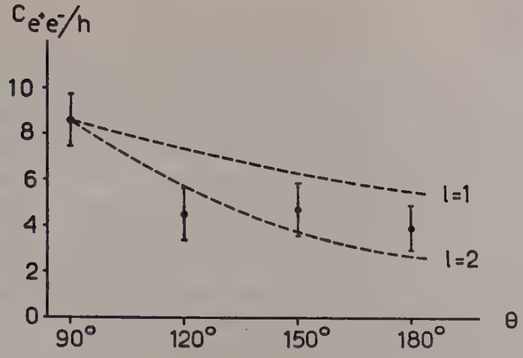

Fig. 34. Angular correlation between e− (e′ = 3.85) and e+ (e″ = 1.55) in Na^{24}.

D. **Results of the angular correlation measurements.** Fig. 34 shows the results of the angular correlation between the internally created positrons (0.28 MeV) and electrons (1.46 MeV) after corrections due to decay and accidentals have been applied. As can be seen the coincidence effects are very small, only 9 per hour at 90°. The experimental points are mean values of a great number of series extended over a long period of time. Though the statistical errors are of necessity large there is a definite decrease in coincidence rate when the angle increases from 90° to 180°. For each new source the relative coincidence rates at 90° and 180° were always first investigated and it was every time found that the 90° emission angle was by far the most favoured.

E. **Comparison with theory.**[1] Angular correlation calculations were first carried out by Rose and Uhlenbeck[2] for the electric dipole and quadrupole case, and by Horton[3] for the magnetic dipole case.

With the goniometer one can only investigate the region 90°—180°. For convenience we may form the expression for the ratio of the number of pairs at $\theta = \frac{\pi}{2}$ to the number at $\theta = \pi$. One then gets:

Electric dipole:

$$Q(e') = \left(1 + \frac{p'\,p''}{1 + e'\,e''}\right)^2 \frac{2 + e'\,e'' + \frac{1}{\gamma^2}(1 - e'^2 e''^2)}{2 + e'\,e'' + \frac{1}{\gamma^2}(1 - e'^2 e''^2) + \left(1 + \frac{2}{\gamma^2}\right) p'\,p'' + \frac{1}{\gamma^2} p'^2 p''^2}.$$

---

[1] The following discussion is based on a correspondence with Dr. G. Horton at the University of Birmingham who has also kindly made the calculations applicable in our particular case.

[2] M. Rose and G. Uhlenbeck, Phys. Rev. *48*, 211, 1933.

[3] G. Horton, loc. cit.

Electric quadrupole:

$$Q(e') = \left(1 + \frac{p'p''}{1+e'e''}\right)^2 \frac{2 + e'e'' - \frac{3}{\gamma^2}(e'e''+1)^2 + \frac{8}{3\gamma^4}(e'e''+1)^2(e'e''-1)}{\left\{\begin{array}{l} 2 + e'e'' - (e'e''+1)^2\left\{\frac{3}{\gamma^2} - \frac{8}{3\gamma^4}(e'e''-1)\right\} \\ + p'p''\{1-(e'e''+1)\}\left\{\frac{4}{\gamma^2} - \frac{8}{3\gamma^4}(e'e''-3)\right\} \\ - p'^2p''^2\left(\frac{1}{\gamma^2} + \frac{8}{\gamma^4} + \frac{8e'e''}{3\gamma^4}\right) - \frac{8}{3\gamma^4}p'^3p''^2 \end{array}\right\}}.$$

Magnetic dipole:

$$Q(e') = \left(1 + \frac{p'p''}{1+e'e''}\right)^2 \cdot$$

$$\cdot \frac{2 + e'e'' - \frac{3}{\gamma^2}(e'e''+1)^2}{2 + e'e'' - \frac{3}{\gamma^2}(e'e''+1)^2 + p'p''\left\{1 - \frac{4}{\gamma^2}(e'e''+1)\right\} - \frac{1}{\gamma^2}p'^2p''^2}$$

where e' and e'' are the energies of electron and positron (including rest energies) in mc^2 units.

$$\gamma = \frac{h\nu}{mc^2} \text{ and } p = \sqrt{e^2 - 1}.$$

In our case $e' = 3.85$ and $e'' = 1.55$. We then get numerically:

Q electric dipole = 1.67

Q electric quadrupole = 3.18

Q magnetic dipole = 3.17.

Thus the anisotropy for the electric quadrupole and the magnetic dipole cases is about twice as big as for the electric dipole case.

In Fig. 34 the dotted lines represent these two cases. The experimental points are consistent with the electric quadrupole curve whereas the electric dipole curve is definitely outside the allowed statistical errors. In view of the exceptionately small effects studied here it is thus very satisfying that the angular correlation measurements check with other findings regarding the multipole nature of the radiation, as discussed above. The statistical errors could naturally be reduced if scintillation detectors and stronger samples were used.

Acknowledgements

It is a great pleasure to acknowledge the valuable cooperation in this work by several of the employees of the Nobel Institute. In particular my former assistant Mr. L. ERIKSSON has been of very great help throughout the whole work. My thanks are further due to Docent L. MELANDER and the Radiochemical Department of the Institute for the radiochemical preparations; to Civ.Ing. B. ÅSTRÖM for kindly putting at my disposal his scintillation spectrometer; and to Fil. Mag. S. JOHANSSON for performing the measurement of the Tm source strength with his calibrated β-counter arrangement. Fil. Lic. H. ATTERLING has given very valuable information about different types of bellows. Finally the kind cooperation of Dr. G. HORTON, Birmingham, regarding the theoretical angular distribution in internal pairs from Na^{24} is very much appreciated. Several of the radioactive sources have been obtained from Harwell, England.

Nobel Institute of Physics, Stockholm 50, Sweden.

Tryckt den 30 januari 1952

Uppsala 1952. Almqvist & Wiksells Boktryckeri AB

ARKIV FÖR FYSIK Band 4 nr 11

Communicated 10 October 1951 by ERIK HULTHÉN and ARNE WESTGREN

The disintegration of As^{73}

By STIG JOHANSSON

With 10 figures in the text

1. Introduction

When germanium is bombarded with deuterons the activities produced include a long-lived arsenic isotope ($\tau = 76$ d (1)), which has been assigned to As^{73} (1). As^{73} decays by K-capture (1, 2), and no positrons have been observed (1, 2). ELLIOTT and DEUTSCH (2) found a strongly-converted γ-ray of energy 52 ± 3 kev. A γ-ray of energy 100 kev has been found by means of absorption measurements in copper (1).

It is of interest to compare the experimental findings with the predictions of the nuclear shell theory for the low-lying levels in Ge^{73}, a nucleus with 41 neutrons. A more detailed investigation has therefore been undertaken.

2. Irradiation and preparation of samples

As^{73} was produced by bombarding a target of copper-germanium alloy (3) with 6 Mev deuterons. After the irradiation the arsenic was separated chemically by a method described by IRVINE (3). The measurements were begun about 3 months after the irradiation at which time the only remaining activities were those of As^{73} and As^{74}.

Samples prepared from solution showed considerable line broadening at the energies of interest for this investigation (10–50 kev), because of self-absorption. In order to resolve the different lines, and to make intensity comparisons and energy measurements, electromagnetically separated samples (4) on thin supports have been used. The separated samples have also the advantage that As^{74} does not disturb the measurements. The 75 kev conversion line could, however, only be studied with an unseparated sample, because of its very low intensity.

3. Separation and determination of mass number

The AsH_3 used for the electromagnetic separation was mixed with hydrogen. A few milligrams of stable As^{75} were used as carrier. The arsenic hydride was in some cases concentrated by freezing it down with liquid air and pumping off most of the hydrogen. When the separation was carried out traces appeared on the collector plate at mass numbers 75, 76, 77 and 78 corresponding to inactive As^{75}, $As^{75}H$,

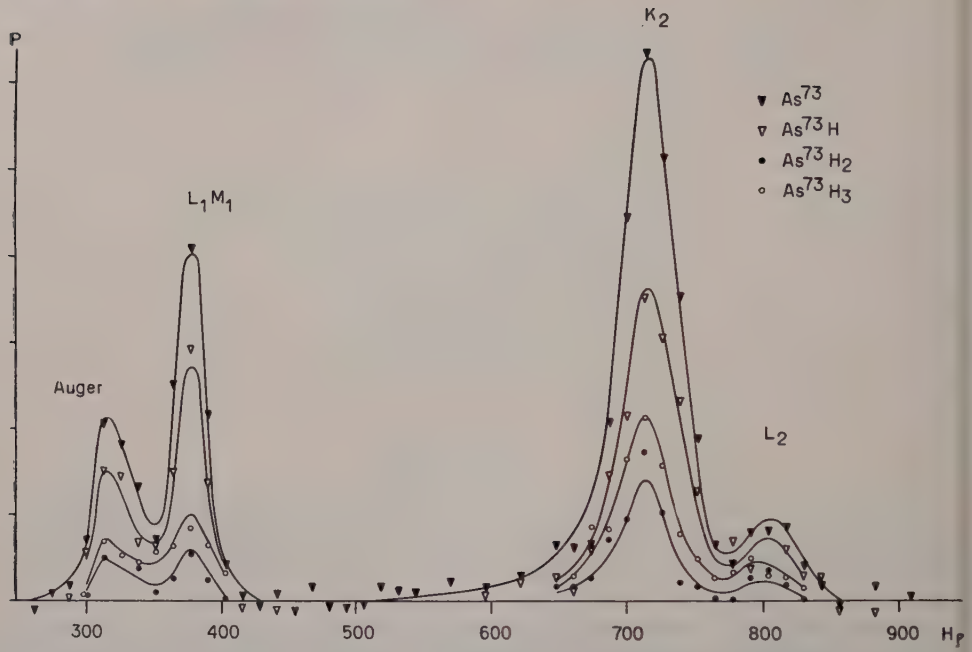

Fig. 1. Conversion electron spectrum of As^{73}. The same spectrum but with different intensity is found for each of the mass numbers 73, 74, 75 and 76. This is because during separation As^{73}, $As^{73}H$, $As^{73}H_2$ and $As^{73}H_3$ are collected.

$As^{75}H_2$ and $As^{75}H_3$. At mass number 75, for example, one can thus expect to find As^{73} from $As^{73}H_2$, As^{74} from $As^{74}H$, and As^{75}.

The relative intensities of As^{75}, $As^{75}H$, $As^{75}H_2$ and $As^{75}H_3$ were measured during the separation (only stable arsenic gives a measurable current).

The activity of the mass numbers 72–77 was investigated in a lens spectrometer (5). For the mass numbers 73–76 the same line spectrum was found in each case, but with different intensities (Fig. 1). The relative intensities of the spectra are the same as the stable arsenic ion currents to the corresponding mass numbers. At the mass numbers 72 and 77 none of the conversion lines were observed. Thus the activity on the collector plate is clearly due to As^{73}, and corresponds to the collection of As^{73}, $As^{73}H$, $As^{73}H_2$ and $As^{73}H_3$ (As^{74} is present at the mass numbers 74–77, but its β-spectrum has such low intensity that it is not noticeable at the low energies in question here). This confirms the mass assignment of McCown et al. (1).

4. Line spectrum

A separated sample collected at mass number 73 on a 0.15 mg/cm² aluminium foil was measured in a lens spectrometer (5) adjusted for ~4.5 % resolution. In the line spectrum (Fig. 2) can be seen the unresolved Auger lines and K_2 and L_2 conversion lines corresponding to a 53.9 kev γ-ray. This value agrees well with that of Elliott and Deutsch.

There is one more line, which is marked L_1M_1 in the figure. It cannot be an Auger line, since its energy is 1 kev greater than the binding energy of the K-shell in ger-

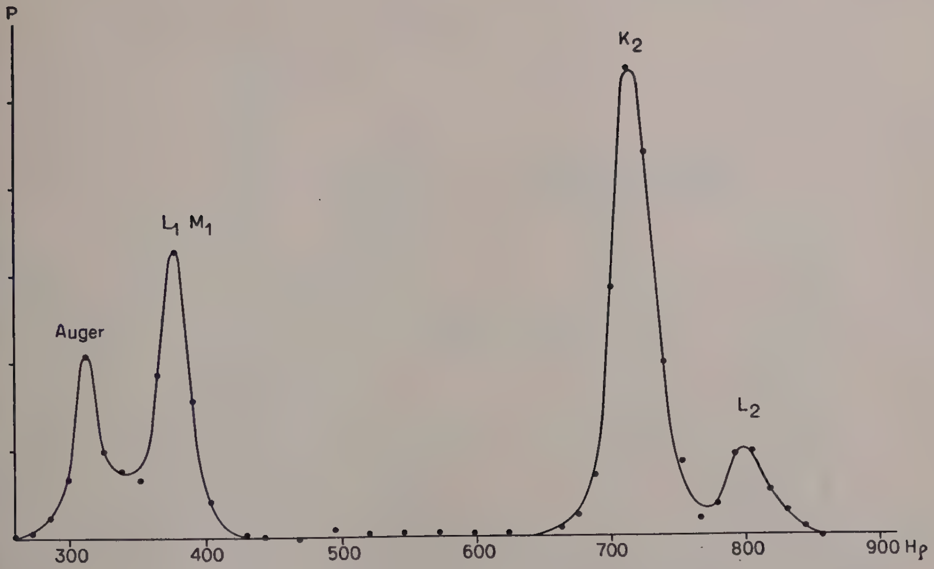

Fig. 2. Conversion electron spectrum of As^{73}.

manium. Neither can it be the K line of a converted γ-ray, since the corresponding L line is not visible. The measurement gives $L < K/20$, which would be unreasonable whatever the multipole order of the γ-ray. Thus there remains only one possibility: the line consists of the unresolved L and M lines of a 13.5 kev γ-ray.

In order to confirm the assumption that the new line is an L line the measurement was repeated with better resolution. The spectrometer was fitted with a ring stop, which improved the resolution to less than 3 %, with negligible loss of intensity.

As can be seen in Fig. 3, the L_1 and M_1 lines are now partly resolved. The Auger lines $A_1 \sim K - L_z - L_{z+1}$ and $A_2 \sim K - L - M$ are shown in Fig. 4. The K_2 and L_2 lines have also been measured with the improved resolution (Fig. 5). There was no noticeable difference between the half-lives of these lines, as was shown by repeating the measurements about three months later.

During measurements on an unseparated sample containing As^{73} and As^{74} a line giving 75 kev conversion electrons was found. Because of the low intensity of this line it was necessary to use a thick sample (mean thickness about 2 mg/cm^2). With this sample the line broadening was so severe that the K and L lines could not be resolved.

The low-energy side of the line is moreover completely obscured by L_2. The line, which is designated $K_3 L_3$, is shown in Fig. 6. The lower curve shows the same line as it appeared when measured again 35 days later. In order to separate the spectrum into two components, one due to As^{73} and the other due to As^{74}, the following procedure was used.

At the time of the first measurement, let $f_1(H\varrho)$ represent the spectrum of As^{73}, and $f_2(H\varrho)$ represent that of As^{74}. The spectrum measured, $F_0(H\varrho)$, is thus the sum of these:

$$F_0(H\varrho) = f_1(H\varrho) + f_2(H\varrho) \qquad (1)$$

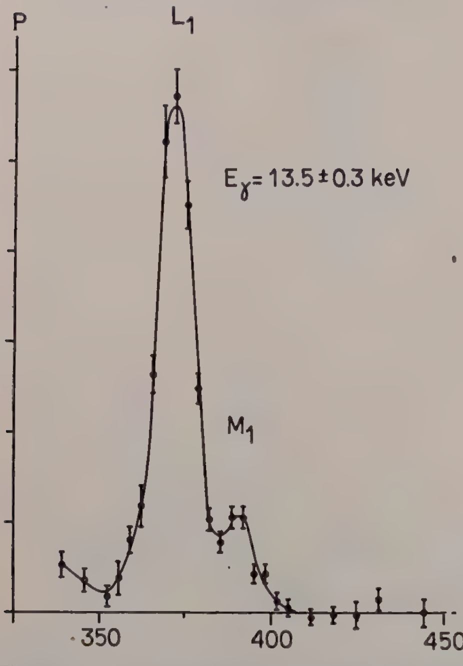

Fig. 3. The partially resolved internal conversion lines L_1 and M_1, corresponding to the γ-energy of 13.5 kev.

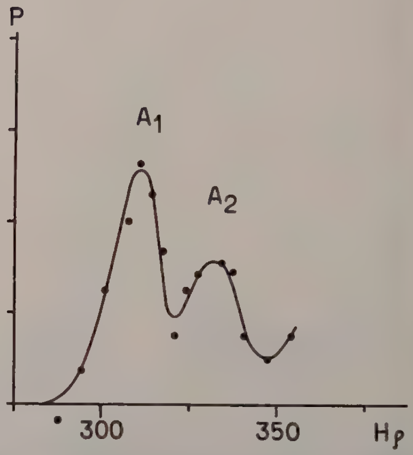

Fig. 4. The Auger lines A_1 and A_2 in the decay of As^{73}.

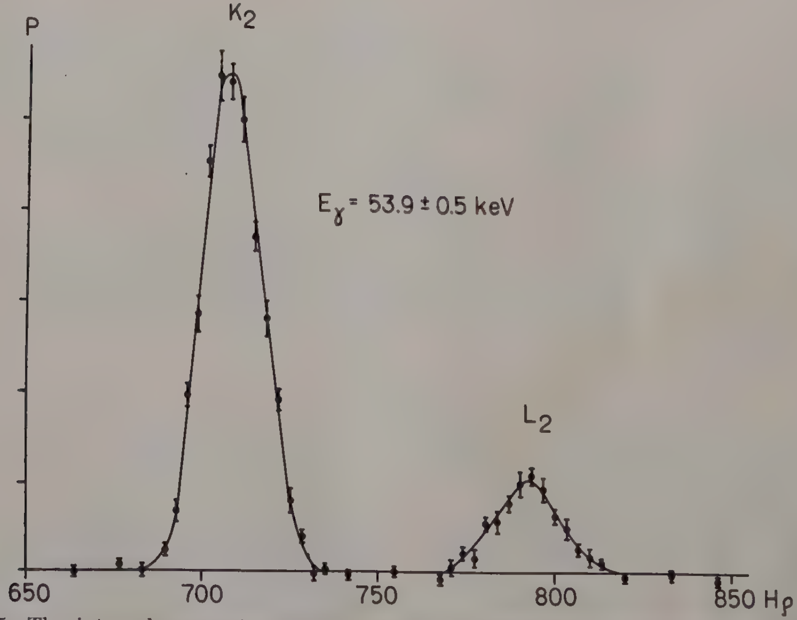

Fig. 5. The internal conversion lines K_2 and L_2, corresponding to the γ-energy 53.9 kev.

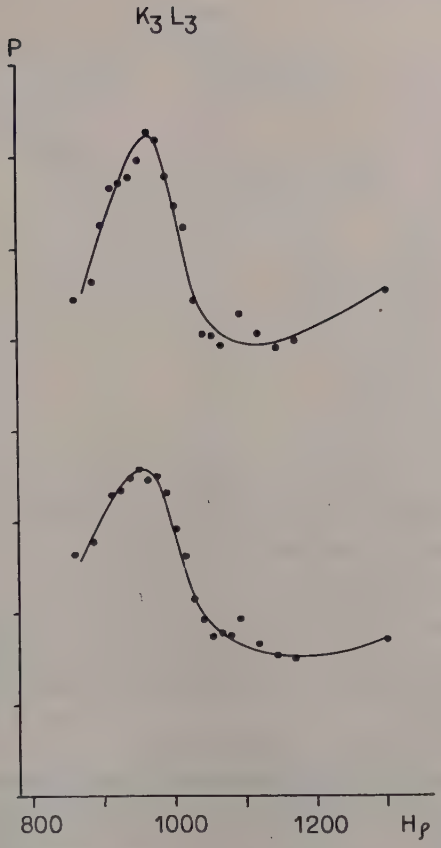

Fig. 6. Part of the electron spectrum of As^{73} and As^{74}. The lower curve was measured 35 days later than the upper curve.

At a later time, remeasurement will give the new spectrum

$$F_1(H\varrho) = k_1 \cdot f_1(H\varrho) + k_2 \cdot f_2 H\varrho) \tag{2}$$

Since k_1 and k_2 are known, from the half-lives of As^{73} and As^{74}, the required functions $f_1(H\varrho)$ and $f_2(H\varrho)$ can be found at once. From their curves, which are given in Fig. 7, it is clear that the line is due to As^{73}, or to some impurity of about the same half-life, but not to As^{74}.

This procedure can of course also be used for a mixture of several isotopes. There is no need for all the half-lives to be known, since the measurements may be repeated until all the unknowns can be determined.

The energy of the γ-ray corresponding to the $K_3 L_3$ line can only be estimated roughly, since conversion in the L shell may be predominant. If the γ-ray is only weakly converted, it may be the same as that which McCown et al. found by the absorption method.

For the energy determinations the *ThF* and *ThA* lines have been used as reference lines. For the energy of the F line the value found by Lindström (6) has been

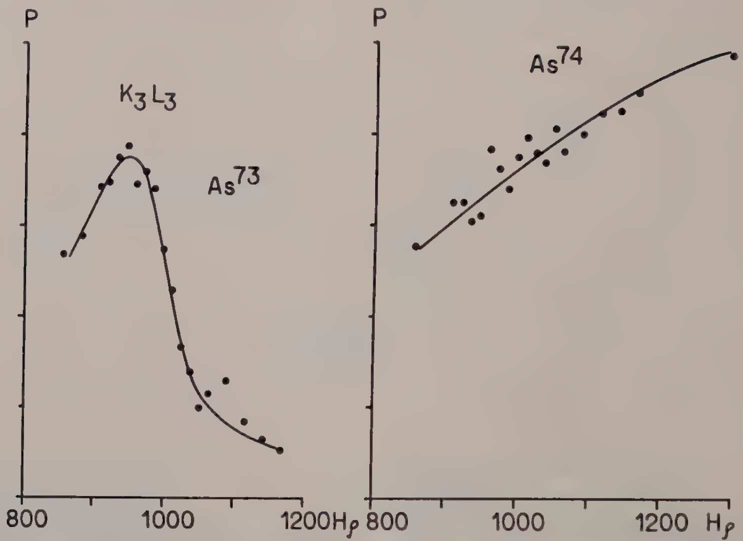

Fig. 7. The parts of the electron spectra in Fig. 6 corresponding to As^{73} and As^{74} drawn separately. The line K_3L_3 is due to As^{73}.

used. The energy of the *A* line has been calculated from that ot the *F* line, making use of earlier $H\varrho$ measurements on the two lines (7). The resulting energy values are given in Table I. The necessary *X*-ray data has been taken from reference (8).

Table I.

Line	Calculated energy (kev)	Measured energy		Final energy
		conversion electrons (kev)	γ-rays (kev)	
A_1	8.2	8.4	—	
A_2	9.6	9.6	—	
L_1	—	12.1	13.5	13.5 ± 0.3
M_1	—	13.3	13.4	
K_2	—	42.64	53.74	53.9 ± 0.5
L_2	—	52.7	54.1	
K_3-L_3	—	75		81 ± 8[1]

5. **Intensity ratios**

The GM counter used for the measurements was operated with several different nylon windows, having cut offs at about 7 kev or less. The intensity ratio $\frac{K_2}{L_2+M_2}$ can be measured accurately. At the energies concerned the window absorption is

---

[1] The large error given is mostly due to the uncertainty whether it is *K* or *L* conversion which predominates.

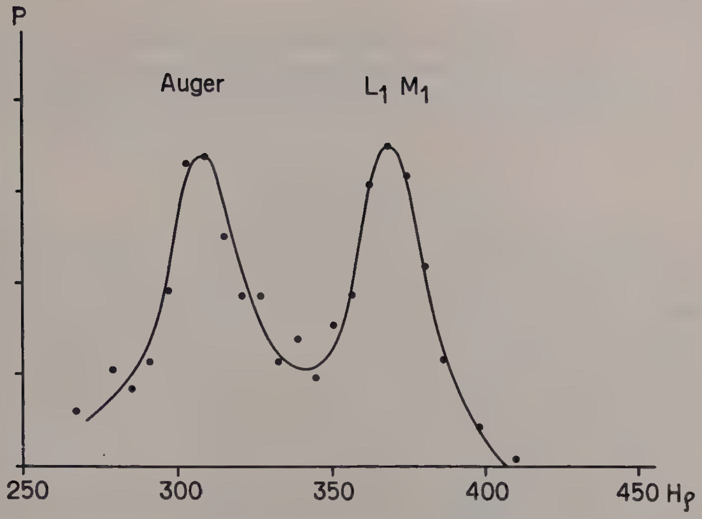

Fig. 8. The Auger lines and the $L_1 M_1$ lines measured with thin (10 μg/cm²) counter window for intensity comparisons.

negligible with the geometry of the counter with which the measurements were made.

The value for $\frac{L_1}{M_1}$ should also be rather good, since the difference between the energies of these lines is small.

Other intensity comparisons between conversion lines in this extremely low energy region are more uncertain. Use has been made only of measurements in which the difference in window absorption for the two lines compared was estimated to be less than 10 %. This has been checked by making measurements with different window thicknesses. No correction has been made for absorption.

The variation with energy of scattering in the sample support (0.15 mg/cm² aluminium) will also disturb the intensity ratios, giving too high intensity to the line with the lower energy. The difference in scattering between the lines compared is, however, certainly less than 10 %. The effects of absorption in the window and scattering in the support tend to compensate each other.

Sometimes $\frac{\Delta H\varrho}{H\varrho}$ has different values for the lines compared, and in such cases a comparison between the heights would give too low intensity for lines with low energies. It is then better to make the comparison between the areas under the lines (in divided form).

In order to compare the intensities of the Auger lines with that of the $L_1 + M_1$ line a special measurement was made using a thin nylon window (9) on the GM counter. This window (thickness 10 μg/cm², cut off = 2 kev) was supported on a copper grid and could withstand a pressure of 20 mm Hg. The GM tube was in this case filled with a mixture of 25 % alcohol and 75 % argon. A gas reservoir was coupled to the tube, to maintain the pressure against the slow leak through the window. The Auger lines (unresolved) and the $L_1 M_1$ line measured in this way are shown in Fig. 8.

Table II.

Lines compared	Experimental intensity ratio
$\frac{K_2}{L_2 + M_2}$	5.6 ± 0.3
$\frac{L_1}{M_1}$	5.4 ± 0.5
$\frac{L_1 + M_1}{\text{Auger}}$	0.77
$\frac{K_2 + L_2 + M_2}{L_1 + M_1}$	1.2
$\frac{K_1}{L_1}$	< 0.5
$\frac{K_3 + L_3}{K_2}$	~ 0.001

With this window an attempt was also made to measure the K_1 line, which has a calculated energy of 2.4 kev. There is considerable absorption in the window of the counter at this energy, but it must certainly be less than 90 %. Although a slight hump on the background was found at the expected place, the line could not be definitely identified. From the known intensity of the L_1 line, this means that K_1/L_1 must be less than 0.5.

The intensity of the K_3L_3 line was so weak, compared even with the L_2 line that it was not possible to measure these two lines with the same source. The value given is therefore very rough.

The intensity ratios are given in Table II. Each ratio is the mean of at least two sets of measurements.

From the intensity relations one can in this case deduce useful informations about the decay scheme and the conversion coefficients.

The values for $\frac{K_2}{L_2+M_2}$, $\frac{L_1}{M_1}$, $\frac{K_2 + L_2 + M_2}{L_1 + M_1}$, and $\frac{L_1 + M_1}{\text{Auger}}$ have been used for the calculations. It is obvious also that the relationships $\frac{K_1 + L_1 + M_1}{K_1 + L_1 + M_1 + Q_1} \leq 1$ and $\frac{K_2 + L_2 + M_2}{K_2 + L_2 + M_2 + Q_2} \leq 1$ hold, where Q_1 and Q_2 are the intensities of the unconverted γ-quanta. For these calculations it is necessary to know the internal conversion probability of K_α X-rays (10) and it has also been assumed that 90 % or more of the capture processes take place by K-capture, which seems reasonable.

From these considerations it is evident that a decay scheme in which both γ-rays correspond to transitions to the ground state of Ge^{73}, after K-capture to different excited levels cannot be correct. For the alternative scheme, with γ-rays in cascade, one finds that both the γ-rays must be strongly converted. The lower limit for the conversion is about 70 %, allowing for the uncertainties in the intensity ratios, and for the possible range of values for the intensity of the K_1 line.

It also follows that if there is K-capture to the lower of the excited states as well as to the upper, it must have low intensity. The intensity of the K_1 line can at the most be about 30 % of that of the L_1 line, which is in agreement with the result of the attempt to measure the K_1 line.

6. Decay scheme

The spectrum of Ga^{73} ($\tau = 5.0$ h (11)) has recently been investigated (12). The internal conversion lines K_2, L_2 and L_1 corresponding to γ-ray energies of 53.9 kev and 13.5 kev respectively, were found in this spectrum also. These excited levels in Ge^{73} are thus common to the disintegration of both As^{73} and Ga^{73}.

It was not possible to measure Ga^{73} using a separated sample, and therefore proper intensity comparisons between the lines could not be made. The lines L_1 and K_2 have, however, been measured with unseparated samples of Ga^{73} and As^{73}, of similar thickness. Very nearly the same line widths and intensity ratios were found for the two samples. The intensity ratios between the lines may thus well be the same in the two cases, although no definite conclusions can be drawn. This gives some support to the view that the lines are emitted in cascade. The half-lives for K_2 and L_1 were about 5 h. Should either of the levels be metastable, this puts an upper limit to the half-life.

In the following an attempt is made to decide the type of the γ-radiation, making use of the experimental values for the K/L ratios, conversion coefficients, and half-lives. It is, however, not possible to arrive at a definite conclusion, chiefly because of the uncertainty in the theoretical values for the K/L and L/M ratios.

Relativistic calculations for the conversion coefficients have not been made for γ-energies so low as those in question here. Internal K-shell conversion coefficients for electric radiation have been taken from the paper of HEBB and NELSON (13) and the values found have been corrected according to the work of AXEL and GOODRICH (14. At low energies the correction is small. The errors in the coefficients thus calculated for the different l-values are too small in this case to influence the discussion.

AXEL and GOODRICH (14) have given curves for the ratio between the internal conversion coefficients of magnetic $l-1$ pole to electric l pole radiation, as a function of energy, extrapolated to low energy values. These have been used to calculate the conversion in the K-shell for magnetic radiation corresponding to a γ-energy of 53.9 kev. The values found in this way are only approximate.

The K/L ratio has been calculated for electric radiation by HEBB and NELSON (13), and for magnetic radiation by TRALLI and LOWEN (15). Very little is known about the accuracy of the curves given by these authors. GOLDHABER and SUNYAR (16) have recently given empirical curves for the K/L ratio. These have been used in the following.

To classify the 53.9 kev γ-line we start from the value $\frac{K_2}{L_2 + M_2} = 5.6$ $\left(\frac{K_2}{L_2}\right.$ is higher, probably between 6 and 7$\left.\right)$. The curves of GOLDHABER and SUNYAR exclude the possibility of pure electric multipole radiation with l value 2 or higher. For $l = 2$ the curves give $K/L \sim 2$, which is much lower than the experimental value. The alternative, electric dipole radiation must also be excluded, since the theoretically

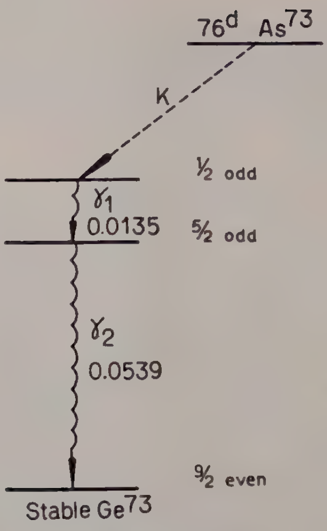

Fig. 9. Proposed decay scheme of As^{73}.

calculated conversion would in that case be much lower than the lowest possible experimental value.

The 53.9 kev γ-line could however, be magnetic multipole radiation. The GOLDHABER-SUNYAR curves are unfortunately less exact for the lower magnetic multipole orders, which are of interest here: magnetic quadrupole radiation seems to fit the experimental K/L ratio best, but magnetic octopole radiation would also be possible. Magnetic dipole radiation can be excluded, as the corresponding theoretical conversion coefficient is too low.

For the 13.5 kev γ-ray the theoretical half-life (16, 17), calculated with $\Delta I = 4$, is more than 10^3 times longer than the longest possible value (5 h). (Correction has been made for decay by internal conversion.) Thus it is very improbable that $\Delta I = 4$ for this γ-ray, even though the calculations are only approximate.

From the attempt to measure the K_1 line it can be estimated that $\frac{K_1}{L_1}$ is less than 0.5. From the intensity comparisons, $\frac{K_1}{L_1} < 0.3$. A consideration of the curves for K/L for magnetic radiation shows that magnetic dipole and quadrupole radiation must both be excluded. Neither is magnetic octopole radiation likely.

The K/L value is, however, consistent with electric radiation. The 13.5 kev γ-ray is in consequence probably electric quadrupole or octopole.

The spin of the ground state of Ge^{73} has been found to be 9/2, by a measurement of TOWNES, MAYS and DAILEY (18).

The level scheme proposed in Fig. 9 is the only one. which is completely consistent with all the experimental data, and with the possible types of γ-radiation.

There are several ways in which the third, very weak, γ-ray could be fitted into the level scheme. Since none of the experimental data is of any use in placing it, no attempt has been made to include it in the diagram. It may be noticed, however, that it can hardly be a cross-over transition, because of its energy-value. Since the K_3L_3 line is very weak, one cannot altogether exclude the possibility that it may be due to some impurity whith $\tau \sim 75$ d.

7. Coincidence measurements

Coincidence measurements have been made in a lens spectrometer (19). A GM tube with a 0.9 mg/cm² window was placed behind the sample. This window thickness was chosen to stop the Auger and L_1M_1 electrons. The K_2 and L_2 electrons had, however sufficient energy to pass through both the source mounting (0.15 mg/cm²) and the counter window. This tube may also count X-rays of various energies, and perhaps some unconverted γ-rays. The efficiency of the counter for these radiations is difficult to estimate, which makes the interpretation of the results more difficult.

The K_2 line, the L_1M_1 line, and the Auger lines, were in turn focused on the usual GM counter of the spectrometer. Coincidences were measured between each of these lines and the K_2L_2 electrons, which were registered by the second GM tube. The resolving time of the coincidence circuit was about $0.4 \cdot 10^{-6}$ sec. The experimental results are given in Table III. The coincidence rate has been corrected for the unimportant background (~ 0.04 coincidences/min.) and for chance coincidences (~ 0.01/min).

No coincidence effect is of course expected between the K_2 and K_2L_2 electrons. The slight effect observed is probably due to coincidences between focused K_2 electrons and X-rays from the conversion of the γ_2-ray, which are registered by the second counter.

There are several indications that the γ_1 and γ_2 lines are in cascade. The low coincidence rate between L_1M_1 and K_2L_2 electrons can therefore only be explained if the 53.9 kev level in Ge^{73} is delayed. The measured coincidence rate can at least partly be accounted for by coincidences between L_1M_1 electrons and X-rays from the conversion of γ_1 (the effect is considerably larger here than before, but the two cases cannot be compared, since the γ_1-line is mostly converted in the L-shell, while the γ_2-line is mostly converted in the K-shell).

Even if the 53.9 kev level is delayed, the K_2L_2 electrons ought to give coincidences with the Auger electrons, which are due to the conversion of γ_2 in the K-shell.

Table III.

Line focused	Calculated coincidence rate per electron registered in the spectrograph counter (error < 30 %)		Measured coinc. rate, per electron registered in the spectrograph counter. (statistical error ~ 10 %)
	No delay at any level	53.9 kev level or both levels assumed to be delayed	
K_2	0	0	$0.11 \cdot 10^{-2}$
$L_1 + M_1$	$9 \cdot 10^{-2}$	0	$0.75 \cdot 10^{-2}$
Auger	$9 \cdot 10^{-2}$	$4 \cdot 10^{-2}$	$2.9 \cdot 10^{-2}$

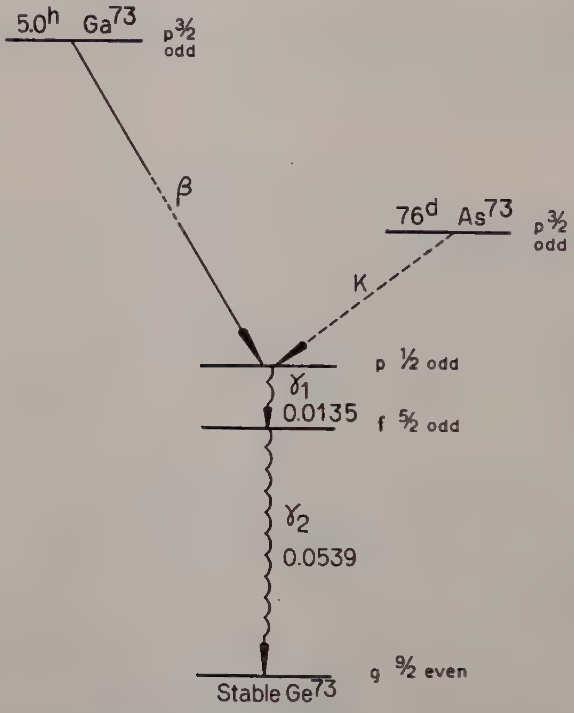

Fig. 10. Proposed term scheme of Ga^{73} and As^{73}.

In this case the largest coincidence effect is in fact observed, and is in satisfactory agreement with the rate calculated on the assumption that the 53.9 kev level is delayed.

Coincidence measurements have also been made between the L_1M_1 electrons and the K_2 electrons, in the goniometer (20). In this case the X-rays or γ-rays cannot disturb the measurements. The calculated coincidence rate in this case was, however, only 6 coincidences per hour, compared with the background coincidence rate of about 1 per hour. The measured rate was equal to the background rate, within the statistical error.

Several different formulae have been given (17, 21, 22) for the calculation of the mean half-life (τ) for γ-decay from metastable states. The calculated values have been corrected for decay by internal conversion, using theoretically calculated values for the conversion coefficients. For the 53.9 kev level one finds values for τ between $\sim 10^{-3}$ and ~ 1 sec. Even if these values must only be regarded as estimates, however, they show that the 53.9 kev level may well be metastable, with a half-life sufficiently long to explain the results of the coincidence measurements.

For the 13.5 kev level also the calculation of the mean half-life ($\tau = 10^{-6}$–10^{-5} sec.) shows that one can expect the level to be metastable. It is thus not impossible that Ge^{73} should have a metastable state with a half-life of the order of milliseconds (16).

8. Level scheme

The level scheme for As^{73} is consistent with the spin-orbit coupling scheme of the nuclear shell model (some levels have crossed) (23, 24). The ground state should then be g 9/2, the first excited level f 5/2, and the second p 1/2.

Ga^{73} (half-life 5.0 h) emits β-rays with maximum energy 1.4 Mev (11). The $f \cdot t$ value shows that Ga^{73} must make an allowed transition (25). This is in good agreement with the prediction of the spin of Ga^{73} by the shell theory.

Fig. 10 shows a level scheme for the decay of Ga^{73} and As^{73}. It is interesting that in Ge^{73} there is no need to assume a 7/2 + level (16, 26).

SUMMARY

The disintegration of As^{73} has been investigated and the mass assignment has been confirmed.

As^{73} decays by K-capture and the resulting Ge^{73} emits two strongly-converted γ-rays, of 13.5 kev $\left(\frac{L}{M}=5.4\right)$ and 53.9 kev $\left(\frac{K}{L+M}=5.6\right)$.

The 53.9 kev γ-ray seems to be magnetic quadrupole radiation and the 13.5 kev γ-ray electric quadrupole. A very weak γ-ray of about 81 kev has also been found.

The first excited level in Ge^{73} (53.9 kev) is metastable, and the second level is probably metastable also. A level scheme is proposed for Ga^{73}, Ge^{73} and As^{73}.

The author wishes to thank Docent L. MELANDER and Fil. mag. W. FORSLING for making the chemical separations. Thanks also are due to Civiling. S. THULIN and Civiling. I. BERGSTRÖM who performed the electromagnetic separations.

Nobel Institute of Physics, Stockholm 50, Sweden

REFERENCES. 1. **D. A. McCown, L. L. Woodward** and **M. L. Pool**, Phys. Rev. *74*, 1315 (1948). — **L. G. Elliott** and **M. Deutsch**, Phys. Rev. *63*, 457 (A) (1943). — 3. **J. Irvine**, J. Phys. Chem. *46*, No. 8 (1942). — 4. **I. Bergström, S. Thulin, N. Svartholm** and **K. Siegbahn**, Ark. f. Fysik *1*, Nr 11, 281 (1949). — 5. **K. Siegbahn**, Phil. Mag. *37*, 162 (1946). — 6. **G. Lindström**, Phys. Rev. *83*, 465 (1951). — 7. **A. Flammersfeld**, ZS. f. Phys. *114*, 227 (1939). — 8. **Y. Cauchois** and **H. Hulubei**, Longueurs d'Onde des Émissions X et des Discontinuités d'Absorbtion X (Hermann et Cie, Paris). — 9. **J. Brown, F. Felber, J. Richards** and **D. Saxon**, Rev. Sci. Inst. *19*, 818 (1948). — 10. **H. S. W. Massey** and **E. H. S. Burhop**, Proc. Roy. Soc. A *153*, 661 (1935—36). — 11. **J. M. Siegel** and **L. E. Glendenin**, National Nuclear Energy Series *9*, paper 53 (1950). — 12. **S. Johansson** and **J. Orring** to be published in Ark. f. Fysik. — 13. **M. H. Hebb** and **E. Nelson**, Phys. Rev. *58*, 486 (1940). — 14. **P. Axel** and **R. F. Goodrich**, Internal Conversion Data, Office of Naval Research Task Contract N 6ori-70 T.O.1. — 15. **N. Tralli** and **I. S. Lowen**, Phys. Rev. *76*, 1541 (1949). — 16. **M. Goldhaber** and **A. W. Sunyar** to be published in Phys. Rev. — 17. **V. F. Weisskopf** and **J. M. Blatt**, privately circulated notes to appear as part of a book on nuclear physics. — 18. **C. H. Townes, J. M. Mays** and **B. P. Dailey**, Phys. Rev. *76*, 700 (1949). — 19. **H. Slätis** and **K. Siegbahn**, Ark. f. Fysik, *1*, Nr 17, 339 (1949). — 20. **K. Siegbahn**, Ark. f. Fysik. *4*, Nr 23, (1951). — 21. **P. Axel** and **S. M. Dancoff**, Phys. Rev. *76*, 892 (1949). — 22. **A. C. Helmholz**, Phys. Rev. *60*, 415 (1941). — 23. **M. G. Mayer**, Phys. Rev. *78*, 16 (1950). — 24. **O. Haxel, J. H. D. Jensen** and **H. E. Suess**, Phys. Rev. *75*, 1766 (1949). — 25. **L. W. Nordheim**, Phys. Rev. *78*, 294 (1950). — 26. **S. A. Moszkowski** to be published in Phys. Rev.

Tryckt den 30 januari 1952

Uppsala 1952. Almqvist & Wiksells Boktryckeri AB

ARKIV FÖR FYSIK Band 4 nr 12

Communicated 14 March 1951 by MANNE SIEGBAHN and ERIK HULTHÉN

A 1.5 MV accelerator for heavy particles with analyzing magnet for use in nuclear research

C. MILEIKOWSKY and R. T. PAULI

With 9 figures in the text

Introduction

In nuclear research there are two main types of generator used in connection with high voltage accelerators, the cascade generator and the electrostatic generator. The former is characterized by technical simplicity and high current output, but its maximum voltage is limited by space requirements. The ripple depends on the capacitance of the condensers, on the frequency, and on the number of steps.

The electrostatic generator has the advantage that if built in a pressure tank, it requires only a moderate amount of space. The voltage fluctuation is generally low and the maximum voltage is limited only by the break-down voltage of the accelerating tube. It is, however, technically more complicated than the cascade generator and usually has a lower current output.

The cost of a high voltage accelerator rises fast with the maximum voltage. Although high voltage accelerators have been used in nuclear research since 1932, there is a rich field for investigations even in the region about one million volts, if the high tension set is combined with precision spectrometers for different kinds of radiations.

For work in this voltage range an accelerating tube fed by an open air cascade generator has many advantages, and a 1.5 million volt apparatus of this type has been built at this institute.

The chosen maximum voltage is about the highest that is practically possible with an unpressurized cascade generator. By using relatively large capacitors and a frequency of 500 p/s the ripple is made low. The use of a large deflecting magnet makes it possible to obtain an ion beam with small energy spread.

The building

The accommodation available for the high tension set contains the main hall, the target room, and the control room. The dimensions of these rooms are indicated in Fig. 2. In this figure the general arrangement of the generator and the accelerating tube is shown. The smallest distance between a top electrode and a grounded surface is 2.70 meter, and the smallest radius of curvature of the top corona shields is 50 cm.

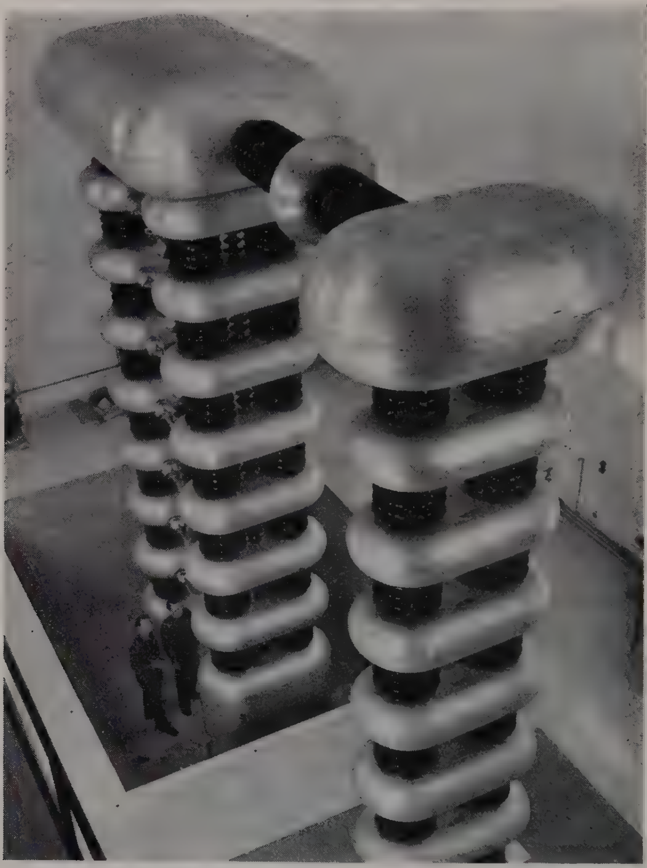

Fig. 1. The cascade generator and accelerating tube.

The generator

The high tension generator is of the cascade type. It is built in seven steps, the maximum voltage over each step being 230 keV.

Each step consists of four porcelain insulators, which serve mechanically as carrying construction and contain a condensor of 40 000 pF. The insulators are filled with transformer oil and are closed at both ends with silumin plates and armed rubber gaskets. Their internal diameter is 300 mm and height 730 mm. The height of each step is 875 mm. The connections between the different porcelain units are surrounded by corona shields of minimum radius 210 mm.

The rectifiers which have been used till now are of the vacuum type. The cathodes are heated by means of generators in each corona shield. Two vertical porcelain axles in seven steps drive the generators for the two sets of rectifiers.

One of these axles is also used to supply power to a 220 V, 1 kVA, Ac generator in the top electrode of the accelerating tube.

This is accomplished by means of a semi-crossed belt drive, which runs inside

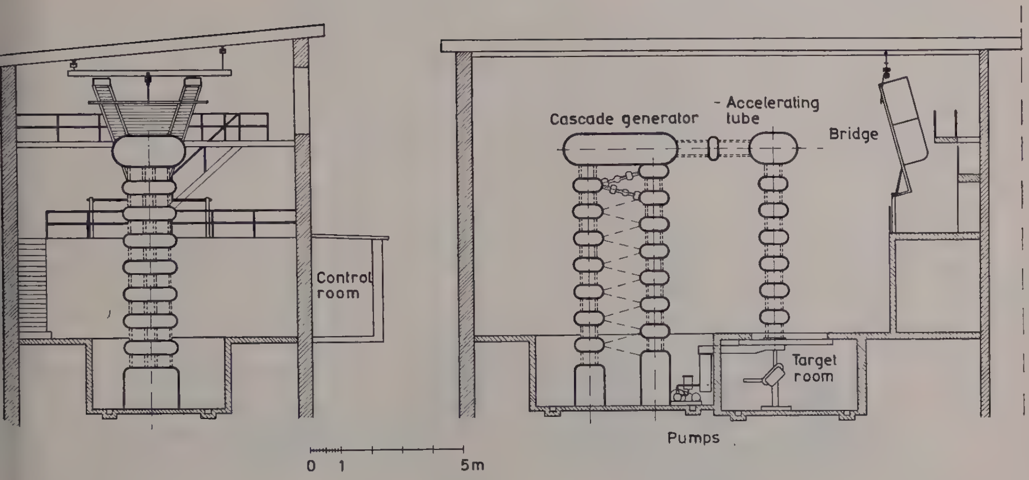

Fig. 2. General arrangement of the high tension set.

the horizontal porcelain insulator connecting the generator top with the top of the accelerating tube. The driving pulley is 25 cm in diameter and is mounted at the top of the vertical axle, the generator pulley being horizontal and 7 cm in diameter. There was no difficulty in holding the belt in place, although the distance between the pulleys is 4 meters, but there was a tendency for torsional vibrations to build up in the different parts of the driving axle. Special attention was therefore paid to the design of the couplings between the different sections of this axle, and it was found that heavy rubber flexible coupling were suitable. A section of the axle is shown in Fig. 3.

The cascade generator is fed by a 500 p/s generator, which delivers 1200 V maximum to the input transformer. The latter is designed for 1200 V 15 A primary and 71 kV 0.14 A secondary.

The value of each capacity in the cascade generator is 0.08 μF, except for the one nearest to the transformer, which is 0.17 μF. (Fig. 4.)

From this value the computed voltage drop is 6 kV per mA and the ripple amplitude (peak to peak), computed to 0.7 kV per mA, was measured to 2 kV per mA.

The electrical circuit of the cascade generator is given in Fig. 4. Fig. 1 shows the accelerating tube and the generator. Fig. 2 gives the general dimension of the whole apparatus.

The general design of the accelerating tube and resistance column

The accelerating tube rests on the roof of the target room. It is built of seven standard porcelains of the same type as those in the cascade generator. Fig. 5 shows the accelerating tube and the porcelain column containing the potential divider and the voltmeter resistor. The joints between the porcelains are made by means of ring-shaped silumin flanges, which are clamped to the porcelains. Each joint contains two flanges, one for the upper and one for the lower porcelain, and between the flanges is inserted a thick silumin ring which has four inside shoulders for carrying a lens electrode. The latter is made of chronium-plated copper

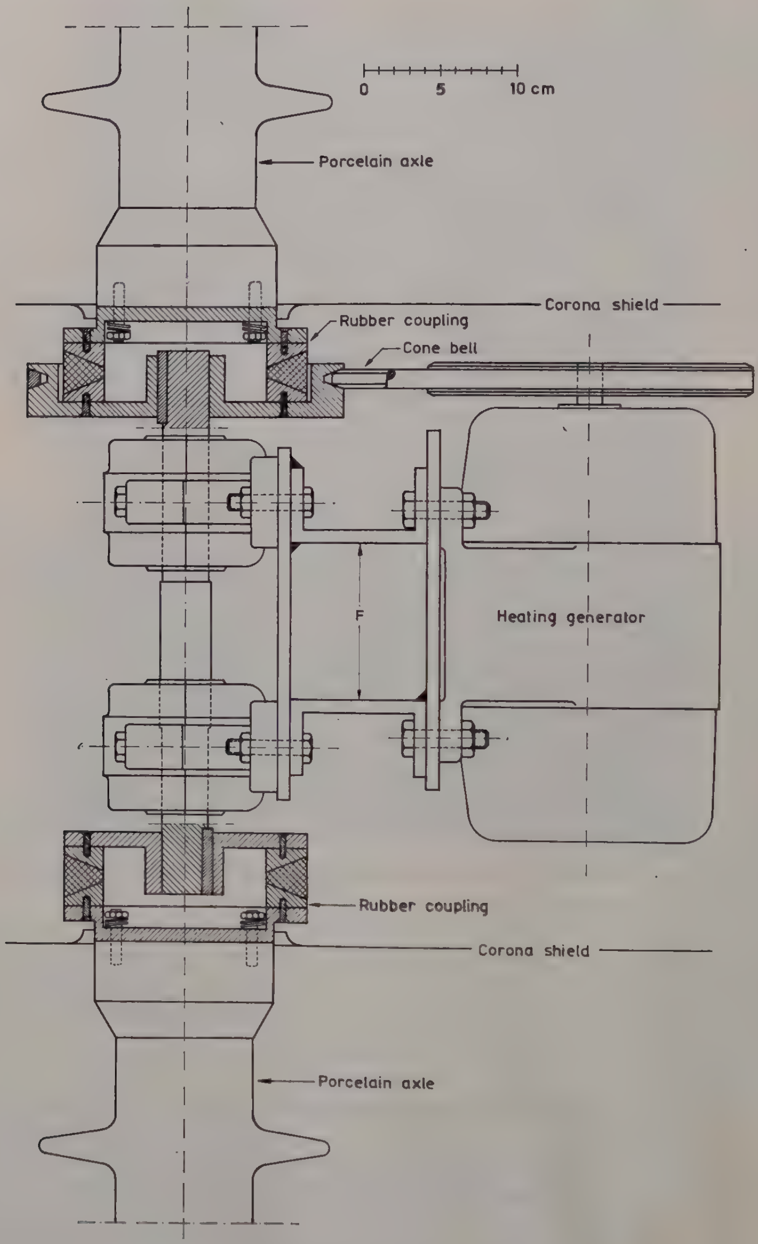

Fig. 3. One section of the vertical axle for driving the heating generators in the cascade generator and for delivering power to the AC generator in the top electrode of the accelerating tube. The assembly is mounted on the frame F, which is bolted to the silumin plates of the condensers (not shown in the figure).

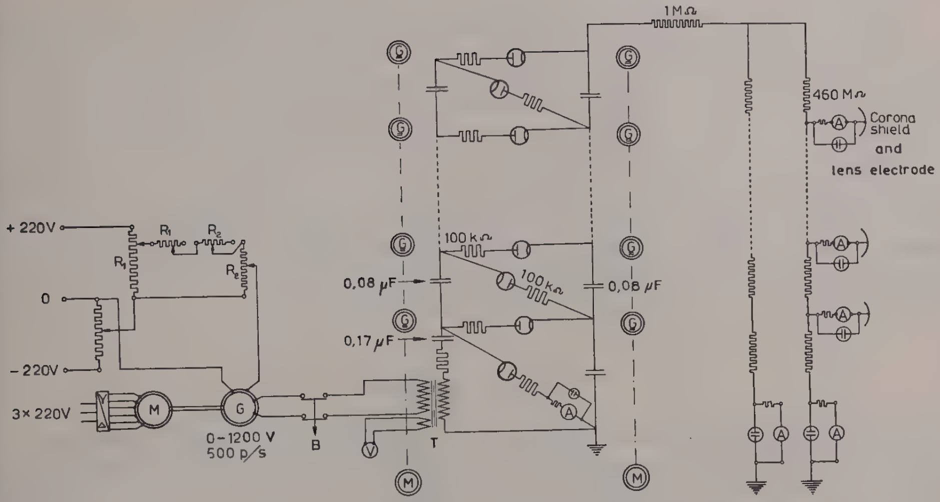

Fig. 4. Circuit diagram of the high tension set.

tube. Seven coaxial lens electrodes form the accelerating path for the ions. (See Fig. 5.) The column is made gas-tight by means of lead-armed rubber gaskets. There are 40 of these in the accelerating tube.

The lens electrodes can be centered by moving the silumin ring with four adjusting screws tapped into the lower silumin flange of each joint. This centering facility is only needed when the tube is first erected.

Each lens electrode has four adjustable screws mounted on it, which rest on the above-mentioned shoulders of the silumin ring, and it is thus possible to align the lens axis. The screws have conical tips which fit into small holes in the shoulders, in order to locate the lens with respect to the silumin ring.

The building of one step of the tube proceeded in the following way. A porcelain with its silumin flanges was put on top of the silumin ring of the preceeding step. Then a gasket, a silumin ring and a lens were put in place. A weight, whose diameter was about 1/2 mm less than the internal diameter of the lenses, was suspended by a wire from the center of the upper end of the lens, and the wire length was adjusted so that the weight was level with the lower end of the lens. A lamp was placed at the bottom of the accelerating tube. When the light ring around the weight, observed from the upper end of the lens, was uniformly thick, the criterion of verticality was reached. With the same point of suspension the weight was lowered into the next lens and the upper lens was then centered. The adjustment screws were locked, and the next step built in the same way. The different silumin rings were slightly turned with respect to each other so that the shoulders carrying the lenses formed a screw line, and thus all the adjusting screws were accessible from the top of the tube.

The voltmeter-resistor and the potential divider are mounted in a special column consisting of seven steps of standard porcelains, each porcelain being filled with oil. This column is erected just alongside the acceleration tube, and is mechanically and electrically connected with it, as is seen in Fig. 5, in order to ensure the mechanical stability of the whole construction.

Both the voltmeter-resistor and the potential divider are mounted on porcelain insulators rated at about 30 keV, fastened to the silumin end plates. (Fig. 5.) At the joint between two column porcelains the potential divider is connected to the corona shield via an instrument (—100 to +400 μA), showing if a lens is hit by the beam, or if corona current leaves any corona shield. These instruments can be read from the control room.

The voltmeter-resistor, which has a total value of about 3400 MΩ, consists of seven parts, one part in each porcelain. Such a part is built of 40 carbon resistances, each of 10 MΩ, 2 W, mounted on a ebonite strip. These resistances have a negative temperature coefficient of $4 \times 10^{-4}/^\circ$ C.

The potential divider is made in the same way with the same type of resistances.

Vacuum system

The volume of the vacuum system is about 1000 litres, comprising the accelerating tube and the pumping system. The large diameter of the tube (300 mm) and the "transparent" construction of the lenses and their suspensions (Fig. 5) admits a high pumping speed. The pumping line connecting the bottom of the accelerating tube with the pumps can be seen in Fig. 5. It is 2 m long and is mounted as near the ceiling of the target room as possible. It has a large cross section, 0.5×0.25 m^2, to allow a high pumping speed. In the pumping line there is a baffle.

The diffusion pump is a Distillation Products Mc 3000 with a pumping speed of 3000 l/s at 10^{-4}—10^{-5} mm Hg. Its heater requires 4 kW. The fore-pump is a Kinney-pump with a volumetric displacement of 30 l/s, driven by a 5 horse-power motor.

With the ion source throttled the vacuum in the whole tube is better than 10^{-5} mm Hg. With the ion source working, the pressure is lower than 10^{-5} mm Hg in the lower end of the tube and lower than 10^{-4} mm Hg in the upper end of the tube.

The calculated pumping speed without baffle is 100 l/s at the top of the accelerating tube and 1000 l/s at the bottom of the tube. It was measured to be 150 l/s and 1000 l/s respectively, for air.

A slide valve is mounted below the pumping line (Fig. 5) so that one can work on the target part of the tube without letting air into the accelerating tube. At the top of the tube there is also a valve arrangement which permits a change of the ion source while the tube remains under vacuum (Figs. 5 and 6).

The ion source

The ions are produced in a radiofrequency ion source of the Thoneman type.[1] The vessel is made of Pyrex glass, to prevent recombination. Its shape, which is shown in Fig. 6, is chosen so that the recombination of atomic ions is at a minimum. For this reason the aluminum probe is surrounded with a glass tube, and the tungsten electrode, which gives the plasma its potential, is mounted in a volume separated from the main vessel by a comparatively narrow passage.

The upper end of the glass tube surrounding the probe is ground so that it is plane, and is perpendicular to the longitudinal axis of the probe. The glass vessel can be centered with respect to the probe during operation.

---

[1] THONEMANN, P. C., Proc. Phys. Soc. 61, p. 483, (1948).

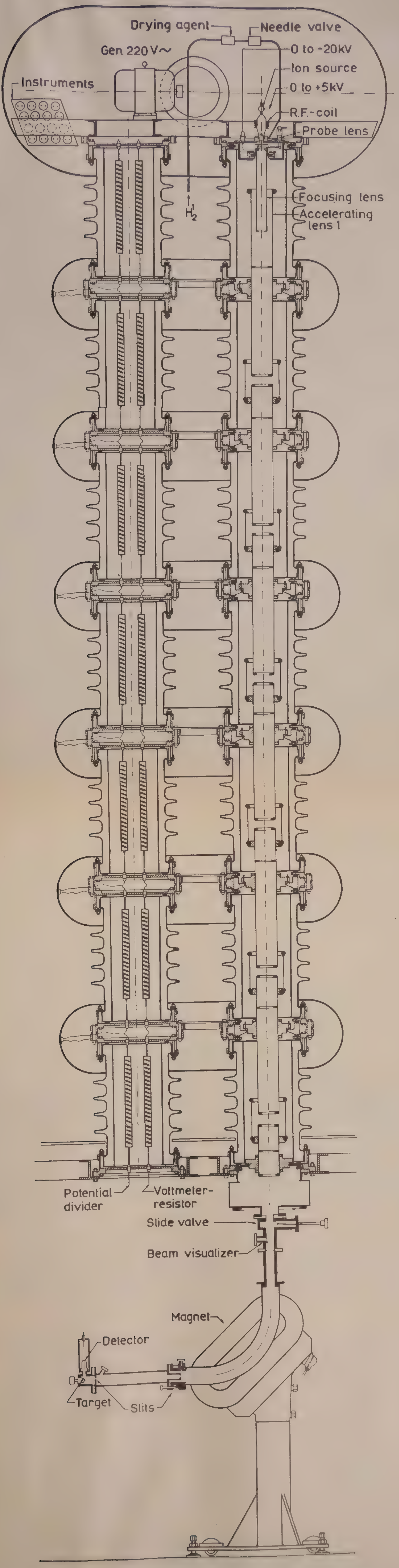

Fig. 5. The accelerating tube and the porcelain column containing the potential divider and voltmeter resistance.

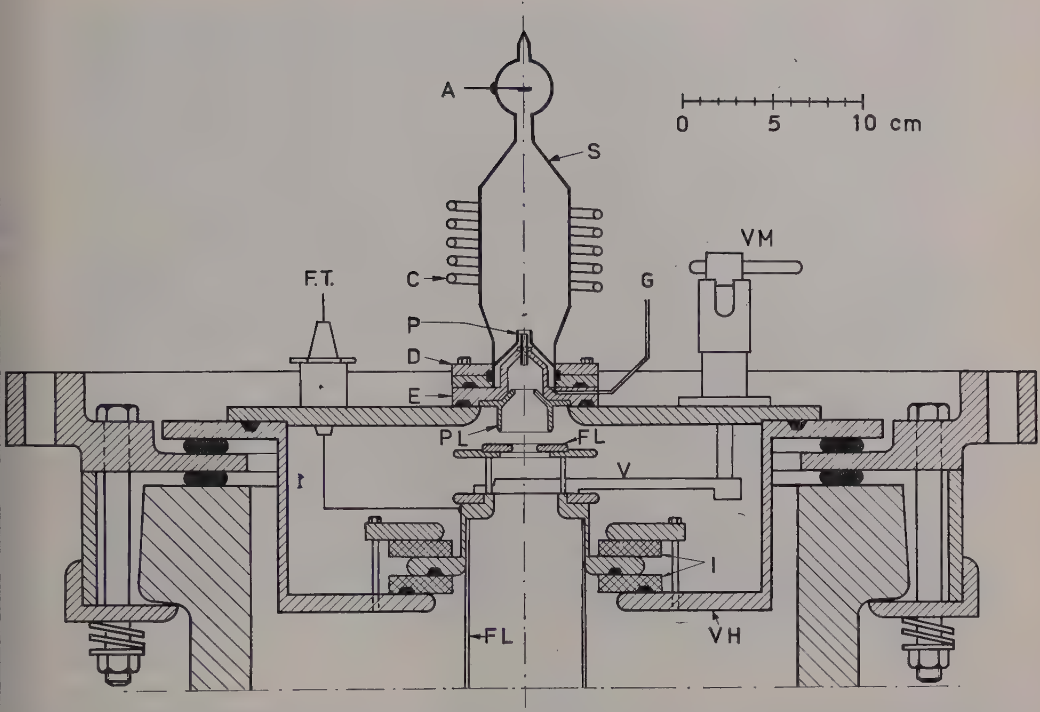

Fig. 6. Radiofrequency ion source. A = anode. C = RF. coil. D and E = flanges permitting centering of ionization vessel about probe and of probe about axis of accelerating tube. FL = focusing lens electrode. G = gas inlet. I = insulators, micalex rings. P = probe. PL = probe lens electrode. S = pyrex vessel. V = valve plate. VH = valve house. VM = valve handle.

These arrangements are necessary to obtain an optimum beam current from the ion source. The reason for this is that the plasma surface takes a dome-like form over the glass tube and probe. The ions emitted at right angles to the plasma surface are thus focused somewhere in the probe canal, but because of the electrostatic repulsion between them the beam will broaden again. Optimum conditions are reached when the beam axis and probe axis coincide, and when the narrowest section of the beam occurs at the half-way point of the probe canal.

The whole ion source can be centered with respect to the focusing system during operation at high tension. This is accomplished by glass-spun cotton cords passing from the top electrode of the acceleration tube to earth. The gas flow to the ion source and thus the pressure in it can be adjusted with a needle valve, which can be operated from the control room.

The 20 Mc radiofrequency power necessary to drive the ion surce is generated by a Hartley oscillator giving approximately 100 Watts RF. The power is coupled from the oscillator circuit via a coil and a coaxial cable to another oscillating circuit consisting of a coil of seven turns and a variable condenser. This coil surrounds the ion source. The frequency and coupling of the oscillator can be regulated from the control room.

The 220 V AC generator of 1 kVA in the top electrode of the accelerating tube is used to feed a) the above mentioned oscillator (300 W), b) the two rectifiers for the probe voltage (0—5 keV) and for the first focusing voltage (0—20 keV), c) the fans for cooling the ion source and the oscillator tube and d) the lamps for illuminating the instruments in the electrode, which can be read from the control room with a telescope. The top electrode is shown in Fig. 7.

Ion optics of the accelerating tube

The accelerating path inside the tube is formed by eight coaxial cylinders, lens electrodes, or simply "lenses," which distribute the potential rise equally along the tube. They form an ion optical system focusing the ions emerging from the ion source into a well collimated beam.

The cylinder nearest to the ion source is here called focusing lens electrode. It is connected to a variable high tension set of 20 kV max., thus permitting adjustment of the beam focusing. The other seven cylinders, the accelerating lens electrodes, are connected to the corona shields, and their voltages are determined by the resistive potential divider described above.

The accelerating lens electrodes are made of chromium-plated copper tubes each 81.5 cm long and of 13 cm external diameter. In both ends there are inserted chromium plated brass diaphragms of 8 cm internal diameter, giving a smooth shape to the ends.

The gaps between the accelerating lens electrodes are 5 cm, and are shielded from the tube walls by short, wide cylinders (length = 25 cm, internal diameter = 20 cm) resting on four spokelike holders connected to the lower cylinder of each gap. (See Fig. 5.) The gaps between the accelerating electrodes form six lenses with the voltage ratio 2: 1 in the first (uppermost) gap, 3: 2 in the second, and so on, being 7: 6 in the last (lowest) gap. The resulting refracting power of this system has been calculated with the help of the approximate formula[2] for a lens formed by two coaxial cylinders

$$\frac{D}{f_1} = 0.658 \left(\frac{V_2}{V_1}\right)^{\frac{1}{4}} \left(\frac{V_2 - V_1}{V_2 + V_1}\right)^2; \quad \frac{D}{f_2} = 0.658 \left(\frac{V_1}{V_2}\right)^{\frac{1}{4}} \left(\frac{V_2 - V_1}{V_2 + V_1}\right)^2$$

where D is the internal cylinder diameter (8 cm), V_1 and V_2 the potential of the cylinders with respect to the ion source, f_1 the focal length on the V_1-side and f_2 focal length on the V_2-side.

In our case an image plane is required to be situated 640 cm below the ion source —for a convenient use of the analyzing magnet. By calculating upwards from the required image plane (I_2I_2 in fig. 8), using the above mentioned voltage ratios in the given formula, one finds that the object plane (0_2-0_2 in fig. 8) has to lay 57 cm below the ion source. The magnification is about 1.3.

Thus it is clear that one has to produce an intermediate image of the ion source outlet in the 0_2-0_2-plane.

This focusing of the ion beam is regulated by two lenses, (1) the gap between the probe electrode and the focusing electrode, and (2) the gap between this latter and

---

[2] See for ex. ZWORYKIN, V. K. ET AL.: *Electron optics and the electron microscope.* J. Wiley and Sons Inc. N.Y. 1945. p. 612.

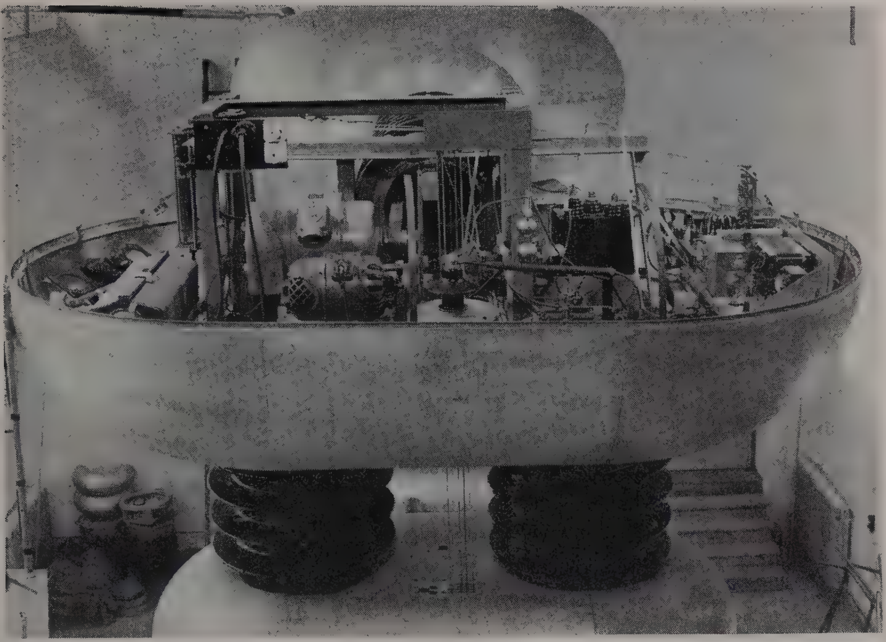

Fig. 7. Top electrode of accelerating tube.

the first accelerating lens. If the voltage of the focusing electrode is adjusted so that the smallest ion beam diameter near the ion source outlet is focused in a crossover in the O_2O_2 plane, the beam spot diameter on the target has its minimum value. By changing the focusing electrode voltage it is possible to move the first beam crossover below the plane O_2O_2, thus enlarging the target spot.

The gap between the focusing lens electrode and the first accelerating lens electrode must obviously be placed between the O_2O_2 plane and the ion source. The voltage ratio in this gap depends both on the voltage of the focusing electrode and on that of the first accelerating electrode, which is 1/7 of the total accelerating tension. The diameter and place of this gap are therefore determined by (1) the available focusing electrode voltage and (2) the range of the total accelerating voltage within which it must be possible to focus the ion beam to a spot of minimum diameter on the target.

In the present arrangement a small diameter of the focusing lens (4 cm) is used and the lens plane is placed near the O_2O_2 plane (lens plane 57 cm below ion source). The lens formed by the gap between probe electrode and focusing electrode is 2.0 cm in diameter and is situated 5 cm below the ion source. With this arrangement it has been possible to focus the beam at total voltages between 250 and 1000 kV, with a focusing voltage variable up to 20 kV.

In order to verify the above mentioned calculations of the object plane in the accelerating system, the voltages of probe and focusing electrode giving minimum target spot diameter were determined at different total voltages. Knowing the dimensions and voltage ratios of the two gaps (1) probe-focusing electrode and (2) focusing electrode—accelerating electrode, it was possible to calculate where these

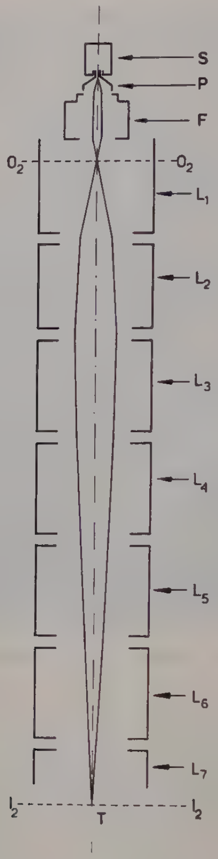

Fig. 8. Schematic view of focusing system.

S = Ion source
P = Probe electrode
F = Focusing electrode
$L_1 - L_7$ = Accelerating lens electrodes

T = Target
O_2—O_2 = Object plane
I_2—I_2 = Image plane.

two lenses should give an image of the ion source outlet. When minimum target spot size was obtained this image fell between 59 and 68 cm below the ion source, as calculated from the measured voltage ratios of the gaps (1) and (2). Considering the crude method and the difficulty of deciding when minimum spot size was obtained, because of spherical aberration, the result must be considered as satisfactory.

Due to spherical aberration each point in the object plane corresponds to a small circular surface in the image, and the radius of the "circle of confusion" depends on the third power of $\frac{x}{D}$ where x is the diameter of the imaging ray pencil in the lens plane and D the lens diameter.

Because of the small diameter of the lens gap between focusing and first accelerating electrode, the ion beam fills a large part of the gap and some spherical aberra-

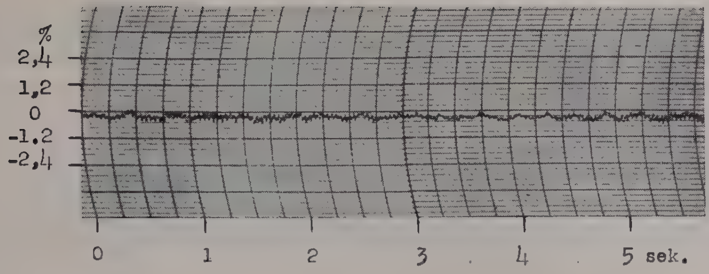

Fig. 9. Fluctuation of the stabilized current of the analyzing magnet.

tion is therefore unavoidable in this lens. If a high current density is desired it is necessary to suppress spherical aberration in the ion optical system. It is then required to enlarge the diameter of this lens.

The analyzing magnet

After having left the accelerating tube the beam passes a magnetic field. The magnet is constructed so that it can be used as beam analyzer, energy selector or energy stabilizer. It is shown in Fig. 5.

The field is homogeneous, the deflection of the beam is 90°, the mean radius 40 cm, the gap 3 cm and the width of the field is 10 cm. There are altogether 2376 turns of cotton-covered enamelled copper wire in the coils. The windings of each coil are made in sections, separated by parallel copper flanges, to the outer edges of which are soldered copper tubes for water cooling of the coils.

The magnet is fed by a special motor-driven generator of 3.4 kVA, 340 V. The current is electronically stabilized to $\pm 0.2\,\%$. A typical record of the current fluctuations is given in the graph, Fig. 9, which was taken with a Brush recorder.

The magnet and deflection chamber can be rotated about the axis of the incoming beam without breaking the vacuum. The horizontal analyzed beam can thus be directed to any part of the target room. This is important for an effective use of the accelerating tube. The beam is not locked to only one heavy piece of apparatus, but can easily be used for other experiments during the development or change of the auxiliary apparatus for one experiment.

Regulating devices

The following operating conditions for the ion source and the focusing system can be regulated from the control board:

a) the gas flow
b) the oscillator frequency
c) the oscillator coupling factor
d) the centering of the ion source
e) the probe voltage, 0—5 keV
f) the focusing voltage, 0—20 keV.

These regulations are made with cords passing down through holes in the corona shields to small motors in the target room. Only in case d) are the cords regulated by hand.

The high voltage and magnet current can be regulated and read from both the target room and the control room.

The following operating conditions in the top electrode are shown on instruments which can be read by a telescope from the control room: probe voltage, probe current, focusing voltage, focusing current, oscillator anode current, oscillator grid current, potential divider current, AC generator voltage.

With a mirror arrangement it is also possible to see the colour of the ion source discharge, which is a useful indicator (e.g. a leak in the ion source can immediately be detected).

Little attention has generally to be paid to the above mentioned instruments after the tube has been started.

Performance

Immediately after the tube was put into operation nuclear investigations were started on (p, α)-reactions.[3] During this work currents not greater than a few microamps were allowable, because of the targets. The required currents were obtained without trimming on a convenient spot size (7×3 mm^2). Since the α-detectors used did not permit efficient discrimination against scattered protons of energies higher than 950 keV, the maximum voltage was restricted to this value during the investigations. There has thus been no reason hitherto to adjust the apparatus to the limits of its performance.

However, currents of 100 μA protons to the target have been obtained (up to 800 keV), of which 50 μA could be focused to a spot of less than 1 cm^2. (Due to spherical aberration there is a certain loss of current when focusing to small spots.)

The maximum tension used until now is 1.1 MV.

Magnetic analysis of the beam shows that it contains atomic ions to 85 % of the total hydrogen ion current. A palladium leak gives the same atomic ion percentage as a needle valve, although the hydrogen gas is purer in the former case.

It is possible to get a well focused beam spot on the target from the highest voltages down to 200 kV. By letting a small amount of air into the ion source it is possible to increase the percentage of hydrogen molecular ions in the beam, and by using H_2^+ and H_3^+ ions at 200 keV one can thus extend the range in which the beam is well focused down to proton energies of 66 keV.

Some of the performance data under the conditions necessary for nuclear research will be given elsewhere.[3]

Acknowledgements

We wish to express our thanks to professor M. Siegbahn, who initiated this work, for his encouraging interest and skilled guidance.

The design of the generator stack was mainly made by överingenjör R. Nordell at Sieverts Kabelverk, where the stack was also manufactured.

We are due to Dr. L. Dreyfus, ASEA, for help with the design of the magnet, to civilingenjör B. Åström, civilingenjör A. Hult and civilingenjör K. Kraft-Ahnlund for assistance during different phases of the work, and to Mr. B. Rogander and Mr. R. Selén, among others, for technical assistance.

Svenska Atomkommittén granted this work.

Nobel Institute of Physics, Stockholm 50, Sweden.

---

[3] Mileikowsky, C. and Pauli, R. T., Ark. f. Fysik, Bd 4 nr 13 (1951).

Tryckt den 5 februari 1952

Uppsala 1952. Almqvist & Wiksells Boktryckeri AB

ARKIV FÖR FYSIK Band 4 nr 13

Communicated 14 March 1951 by Manne Siegbahn and Erik Hulthén

Some investigations of (p, α) reactions on thin separated O^{18} and N^{15} targets. Techniques and results

C. Mileikowsky and R. T. Pauli

With 18 figures in the text

1. Earlier knowledge of the reactions $O^{18}(p, \alpha)N^{15}$ and $N^{15}(p, \alpha)C^{12}$

The two (p, α) reactions on O^{18} and N^{15} were discovered by Burcham and Smith[1] in 1939. When bombarding with protons, they found α-particles from apparently clean metal target backings. They attributed these α-particles to impurities of oxygen and nitrogen, whose isotopes 18 and 15 respectively would give (p, α) reactions with Q-values of 3.95 MeV and 5.00 MeV as calculated from the known masses of the reactants.

To investigate the correctness of this assumption they used gas targets of oxygen and nitrogen, and got α-particles with ranges corresponding to Q-values of 3.9 and 5.0 MeV respectively. They thus established the reactions $O^{18}(p, \alpha)N^{15}$ and $N^{15}(p, \alpha)C^{12}$.

In 1949 Burcham and Freeman[2] remeasured the Q-values of the two reactions with a better accuracy, again using gas targets of natural oxygen and nitrogen. They used a refined technique for the range measurement, evaluating the results by means of the latest energy-range relation curve. For $O^{18}(p, \alpha)N^{15}$ they got the Q-value 3.97 ± 0.05 MeV, and for $N^{15}(p, \alpha)C^{12}$, the value $Q = 4.96 \pm 0.05$ MeV.

The above-mentioned Q-value was the only known fact about the $O^{18}(p, \alpha)N^{15}$ reaction when our investigations were carried out.

In figures 1 and 2 the usual energy level notation of Lauritsen is used. The ground state of the compound nucleus, F^{19}, is represented as a line in the centre column of the figure, and is used as zero level for the energy scale. Because of the mass difference $(O^{18}+p)$—F^{19} the excitation energy of the system $O^{18}+p$ is 7.9 MeV at proton energy zero (the line to the right), and $7.9+\frac{18}{19}\cdot E$ MeV at proton energy E MeV. The compound nucleus F^{19} decays into an α-particle and a N^{15} nucleus in its ground state, which has an excitation energy of 3.99 MeV (at kinetic energy zero). The difference between 7.9 MeV and 3.99 MeV should be equal to the Q-value of the reaction.

The reaction $N^{15}(p, \alpha)C^{12}$ has attracted special attention, since it is the last reaction of the carbon cycle in the sun. Thus Holloway and Bethe[3] have measured

---

[1] Burcham, W. E., and Smith, C. L., Nature *143*, 795 (1939).

[2] Freeman, J. M., Proc. Phys. Soc. *63*, 668 (1950).

[3] Holloway, M. G. and Bethe, H. A., Phys. Rev. *57*, 747 (1940).

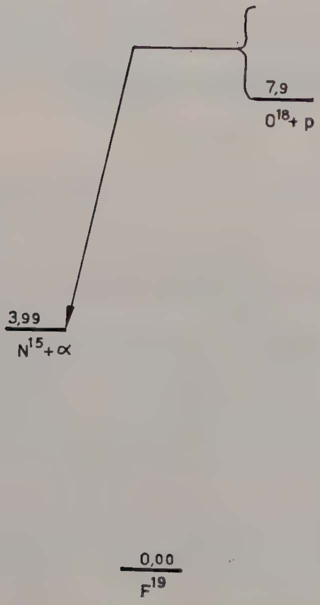

Fig. 1. Level scheme of the reaction O^{18} (p, α) N^{15}.

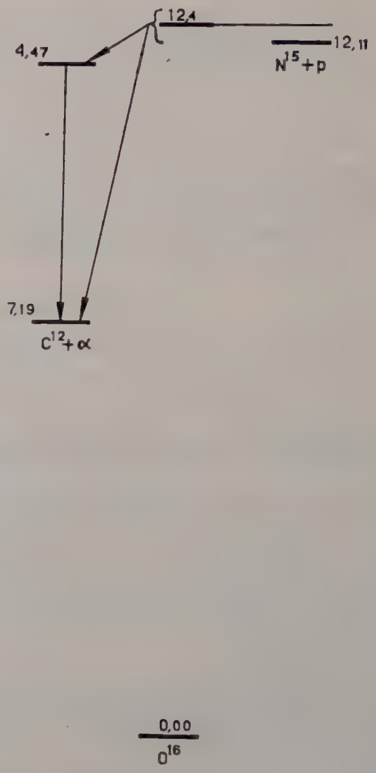

Fig. 2. Level scheme of the reaction N^{15} (p, α) C^{12}.

its absolute cross section at one single bombarding proton energy, 350 keV. They got the cross section $= 1.3 \times 10^{-26}$ cm^2, which they regarded as a remarkably high value. COCHRANE and HESTER[4] found in 1949 a resonance in the N^{15} (p, α) C^{12} reaction at about 400 keV.

LAURITSEN et. al.[5] have found a γ-radiation from a reaction which they supposed to involve the known 4.4 MeV level in the residual nucleus, C^{12}. Three resonances in the γ-yield appeared, namely at the proton bombarding energies 0.88 MeV, 1.03 and 1.2 MeV. The (p, α) reactions on N^{15} are given in Fig. 2.

2. The choice of reactions

For O^{18} (p, α) N^{15} neither excitation curves nor angular distributions had been studied before. The reason for this was the rather low abundance of the target nucleus, 0.20 % for O^{18}. For N^{15} the abundance is 0.38 %.

---

[4] COCHRANE, W. and HESTER, A. G., Proc. Roy. Soc. A *199*, 458 (1949).

[5] LAURITSEN, T., LAURITSEN, C. C. and FOWLER, W. A., Phys. Rev. *59*, 241 (1941).

With the electromagnetic isotope separator[6] available at this institute, however, we thought it would be possible to produce isotopically pure thin gas targets containing a number of target nuclei large enough for work on excitation curves and angular distributions.[7]

Certain other points favoured this choice of reactions. From the experimental point of view the Q-values 3.97 MeV and 4.96 MeV are high enough to make it possible to differentiate between scattered protons and the α-particles from the reaction, without a magnetic analyzer, thus simplifying the experimental arrangement, and allowing large solid angles to be used.

The yields of the reactions could be expected to be sufficient to give adequate counting rates: the cross section for the N^{15} reaction was known at one energy, as mentioned above, being 1.3×10^{-26} cm², which is comparatively large. Because of the comparatively high Q-values and the rather low Z-values of both the target nuclei, one could expect that the Gamow penetration factors of the incoming and outgoing particles would give rise to a high yield for both reactions. One gets the following values of penetration factors at 500 keV:

	Q MeV	$E_{B_{\text{in}}}$	P_{in}	$E_{B_{\text{out}}}$	P_{out}	$P_{\text{in}} \times P_{\text{out}}$
$O^{18}(p, \alpha)N^{15}$	3.97	2.64	0.0043	4.88	0.87	0.0037
$N^{15}(p, \alpha)C^{12}$	4.96	2.44	0.0094	4.45	1	0.0094

From this table it is seen that one would expect a yield of about the same order of magnitude from comparable targets of N^{15} and O^{18}.

Another reason for taking these two reactions as objects of the first investigations with the new acceleration tube[8] was the fact that O^{18} and N^{15} are in many cases inevitable target contaminants. Thus for further work it will be useful to know as much as possible about these two reactions, so as to be able to predict and correct for possible disturbing effects.

3. The target system

After leaving the acceleration tube the beam passes a slide valve, a tungsten visualizer, the chamber of the analyzing magnet, a limiting slit, the target tube, the defining slit, the secondary electron screen, and so strikes the target surface (see Fig. 3).

The slide valve is of course used to maintain the high vacuum in the tube when the target vacuum system is opened for changing targets or target arrangements. When the target system is closed again it is evacuated via a direct line from the forepump before the slide valve is reopened.

The tungsten visualizer is used as indicator of several important beam properties, such as the form of the beam cross section, its symmetry and its intensity homogeneity. It consists of a tungsten plate, which can be turned into the beam (at

---

[6] BERGSTRÖM, I., THULIN, S., SVARTHOLM, S. and SIEGBAHN, K., Ark. f. Fysik Bd 1 nr 11, 281, (1949).

[7] KOCH and others in Copenhagen have earlier used electromagnetically separated gas targets.

[8] MILEIKOWSKY, C. and PAULI, R. T., Ark. f. Fysik Bd 4 nr 12 (1951).

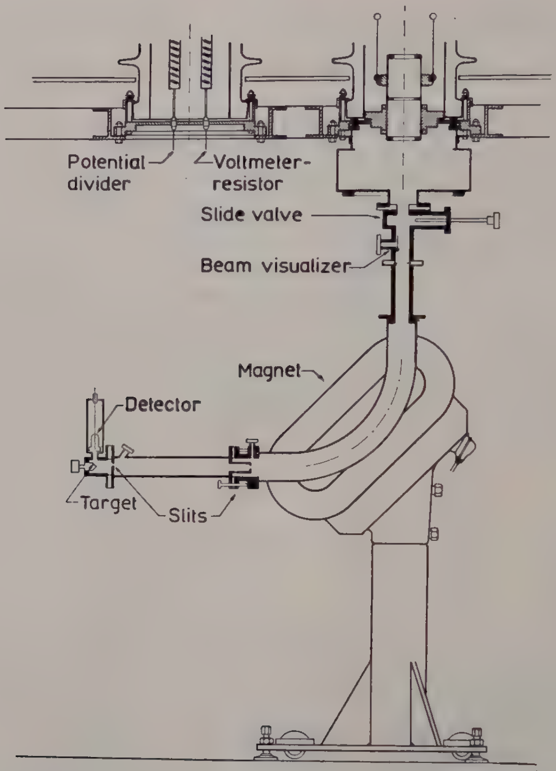

Fig. 3. Selecting magnet, slits and target system.

45° to the beam). The flourescent spot on the plate can be studied through a window (see Fig. 3).

In case the thin target thickness might vary within the bombarded area—which is difficult to control—it is important to use a beam whose intensity is as homogeneous as possible over it cross section, if a true relative yield curve is to be measured. In such cases it has been found to be important to focus the beam in such a way that the eye cannot see any intensity inhomogeneity on the tungsten visualizer. The beam spot on the defining slit has to be adjusted in the same way. No fluorescent light can be seen from a target free of contaminants, when it is under bombardment.

The beam is analyzed by bending through 90° with radius 40 cm by the magnetic field. In the reactions considered here we are interested in protons. In practice the magnet, with the current adjusted for mass number one, gives a clean beam of protons, although theoretically there could also be deuterons of half the proton energy in the outgoing beam. Such deuterons would have to be produced by ionization of deuterium in the beam in the tube, at a place where the potential is half the top voltage. Taking into consideration the finite resolution of the magnet and the properties of the electrostatic lenses, such deuterons would have to originate in a disc volume of 1 mm height and 4 mm radius, in the middle of the fourth lens gap from the bottom. The pressure in the tube is mainly caused by hydrogen from the ion source. The number of hydrogen ions produced by a proton of, say, 0.5 MeV, in 1 mm path at the pressure 10^{-4} mm, is about 2×10^{-4}. As there is only 1 deuterium atom in 5 000 normal hydrogen atoms, the outgoing proton beam should consist of about 1 deuteron in 10^8 protons. This contamination is negligible even with respect to the possibility of high cross sections for d-reactions. Thus, from the practical point of view, the magnet gives a clean proton beam. The analyzis of the reaction products confirmed this view.

The magnet is electronically stabilized to ± 0.1 %, when properly adjusted. This corresponds to a movement of $\pm$ 1 mm in the beam position at the target plane.

After leaving the analyzing field the beam enters the target tube through a limiting slit. This slit can be examined through a window, which facilitates the adjustment of the magnetic field strength. The tube is connected to the magnet chamber with a bellows. By means of adjusting screws the tube can be aligned as desired.

At the end of the target tube the beam passes the defining slit. This slit is a rectangular hole of height 3.5 mm. and width 7 mm. in a copper disc. (Fig. 4). These dimensions were chosen because they are somewhat smaller than the target surfaces used. This slit is electrically insulated by pieces of perspex from the target chamber and from the secondary electron screening electrode. The copper disc is mechanically mounted on these insulators so as to have a well defined position with respect to the center of the target surface. It is in direct electrical and thermal contact with the target tube, which carries a water-cooled flange at this point. The defining slit can be seen through a window in the target tube.

The target chamber is electrically insulated from the target tube with a glass ring, so that the target current can be measured.

When entering the target chamber through the defining slit the beam has to pass the secondary electron screen. This electrode is insulated from all other parts and is kept at a negative voltage of 250 Volts, compared to the target chamber and the target tube. Thus secondary electrons ejected by the proton beam from the edges of the defining slit are repelled back to the target tube, and those electrons, which are released at the target surface, turn back to the target chamber and so do not influence the measurement of the irradiation current.

The target support is a massive cone of copper. In order to prevent the target temperature from rising too much when it is bombarded by the beam the target backing plate is made of silver (silver is chosen also for several other reasons. See below). The cone has two plane surfaces, making 45° with the symmetry axis. To each surface a target backing plate can be screwed. (Fig. 4.) In this way the target surface makes 45° to the incoming proton beam, which is eccentric to the conical target support. By turning the cone through 180° the other target plate may be put into the path of the beam. This arrangement makes it possible to compare the target with a clean target backing, or with another target for energy calibration, without changing the beam or other parameters.

Between the two target surfaces there is a threaded hole in the copper cone with its axis perpendicular to the symmetry axis of the cone. The hole contains a Po-source of α-particles, half-spherical in shape of 1 mm diameter. Foils of appropriate thickness can be mounted on a frame which is screwed in the hole, and one thus gets a defined solid angle, in which the α-particles have an arbitrary, defined, maximum energy. By turning the cone through 90° this beam of α-particles can be

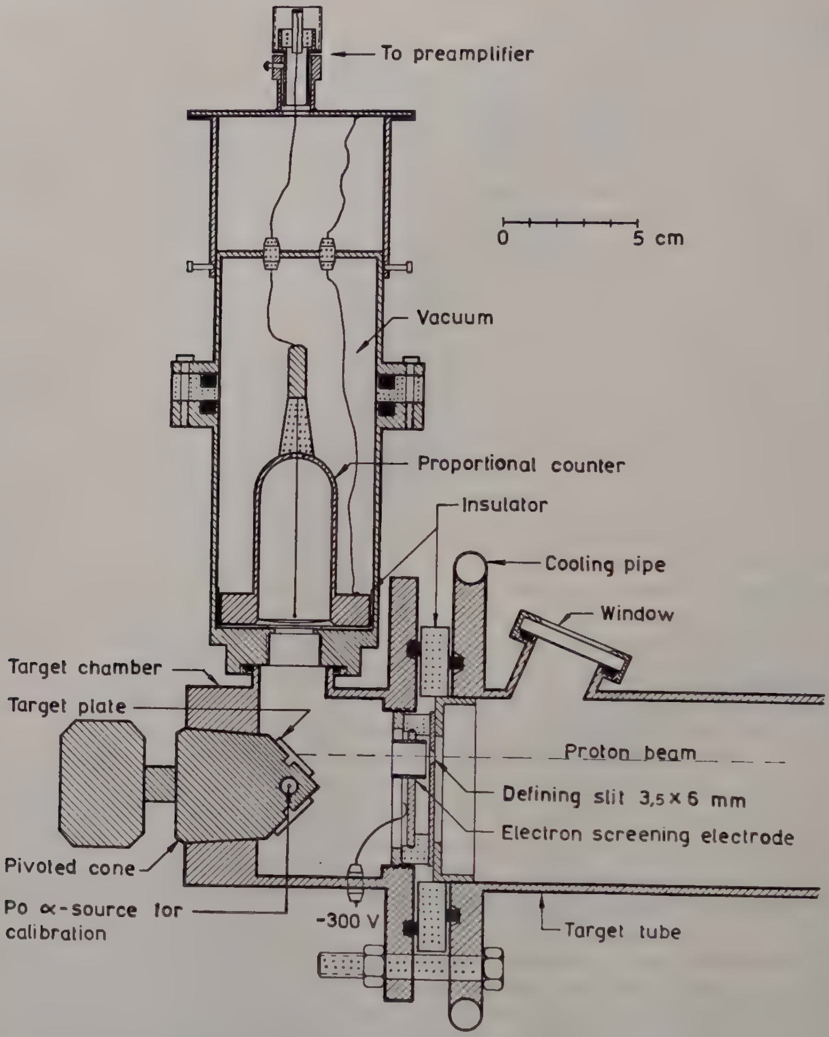

Fig. 4. Details of target arrangement for taking yield curves.

directed into the detector. This arrangement is useful for checking the detector devices for constancy, pulse shape, etc. at the actual α-energies in use.

When changing a target, air is first let in to the target system and the support cone may then be removed quite simply. Vacuum grease must be used very sparingly.

4. The preparation of thin separated targets

The choice of metal for the target backing plates was governed by several requirements.

a) The chosen metal should allow a high number of oxygen or nitrogen atoms to be shot into and stay in the lattice.

b) The chosen metal should be available or producible in a quite clean state.

c) It should be a good heat conductor to facilitate cooling, because a too high temperature, either during production of the target or during measurement on the target, would cause the trapped gas atoms to escape.

d) It should not be easily oxidized.

Silver was found to be a good metal to meet these demands. Copper, for instance, is too easily oxidized.

The silver plates used had a diameter of 20 mm. and a thickness of about 3 mm. They were made of pure silver, and had a mounting screw on the side away from the target surface, which was very carefully turned with a clean steel tool. Such clean surfaces gave, when bombarded with protons, very few α-particles. If such a plate had been slightly touched by a finger, or washed with a solvent such as ether or toluol, it gave a large number of α-counts.

The plates were not exposed to the air for more than a few minutes. As quickly as possible after turning they were put into the vacuum system of the electromagnetic separator or the high tension accelerator. Target plates which were not for immediate use were put at once into a vacuum box, to avoid oxidation or adsorption.

For the production of the O^{18}-targets a small tube containing water was connected to the ion source of the electromagnetic separator, and the water vapour pressure was allowed to develop in the ion source. The target plates were placed in the separator corresponding to the mass number 18, where the beam consisted mainly of H_2O^{16+}, number 19 with H_3O^{16+} and mass number 20 with H_2O^{18+}.

In a typical run the current on mass number 18 was 50—100 μA. This corresponded to a current of 0.1—0.2 μA of H_2O^{18} at mass number 20.

From a rough estimation of the cross section of the reaction O^{18} (p, α) N^{15}, and assuming a detecting solid angle of 0.07 sterad with a maximum allowed proton current of 1 μA (because of the cooling problem), one would require 10^{15} 0^{18}-atoms in the bombarded target area to get about 1 α-pulse/s. Thus, if during the separation all 0^{18}-atoms hitting the mass number 20 plate also stayed there, the time required to get the desired number of target atoms would be about an hour, quite a reasonable time.

The first runs, however, were not successful.

The heat produced in the mass number 18 plate spread to the 20-plate, so that this plate did not catch the 0^{18}-atoms efficiently. The importance of cooling is seen from the fact that a better cooling arangement gave about 50 times more 0^{18}-atoms in the lattice.

The mass number 15 was used for the production of N^{15}-targets. In this case nitrogen gas was let into the ion source. The current on mass number 15 was about 0.1 μA, and a typical separator run took 4 hours which corresponds to a transport of 8×10^{15} N^{15}-atoms to a spot of about 1 cm².

From the known cross section of N^{15} (p, α) C^{12} at resonance, 1×10^{-25} cm², and the number of α-particles from a typical target bombarded with protons of this energy, one gets a number of N^{15}-nuclei, 5×10^{15}/cm² corresponding to 0.1 μg/cm².

5. Current integrating

It is well known that the measurement of true target current is complicated by the presence of secondary electrons, which are formed when the beam strikes various parts of the target system. In the arrangement used here, which was described in section 3, secondary electrons are produced in the defining slit and in the target. The first group of electrons must not reach the target chamber, and the second must not leave it. The above-mentioned electron screening electrode will satisfy these conditions if held at a sufficiently negative potential. It was found that the measured current was independent of the electrode potential if the latter was set lower than —100 Volts. Generally, —250 Volts were used.

It is difficult to avoid a certain fluctuation in the current during the measurement. As it is not the number of protons hitting the target per second that is of interest, but the total number of protons, the current is fed into an integrating device. Many current integrators have been described in the literature; the simple one used here is of a type given by Tangen. The current charges a condenser until it reaches the break down voltage of a glow lamp connected across it. The subsequent discharge quickly lowers the voltage to the extinction voltage and the cycle is repeated again. The discharge pulses operate a counter (Fig. 5). The discharge time in such an arrangement is so short that the maximum current allowable for an accuracy of say 1 % is determined by the mechanical register.

The minimum current allowable, $i_{\min}$, depends on the resistance R between the target chamber and earth, so that $i_{\min} \cdot R \gg V_b$, where V_b = break down voltage of the glow lamp. Evidently, weak currents require careful attention and it is always preferable to keep R as high as possible. A good value of R is 3 000 MΩ. It is an advantage to keep the atmosphere dry in the target room; otherwise moisture condenses on the target chamber insulators, which are cooled by the target tube, and R falls easily to about 100 MΩ.

To minimize the effect of leakage from the target to earth, and in the condenser (which is carefully selected), the condenser is not connected to earth but is biased to a negative variable potential (Fig. 6). These leakages should be eliminated by biasing to a negative potential which is numerically the arithmetic mean value of the breakdown and extinction voltages. By this arrangement the $i_{\min}$ is also lowered.

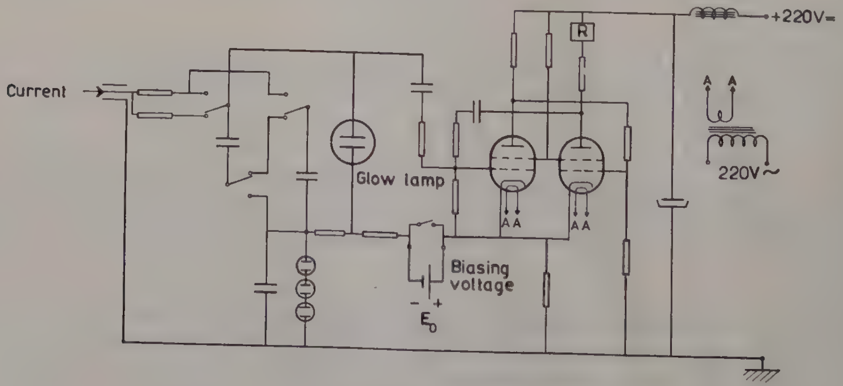

Fig. 5. Circuit diagram of current integrator.

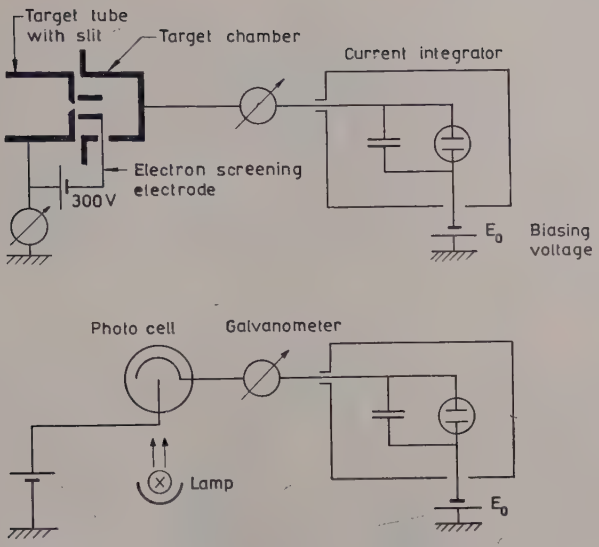

Fig. 6. Connections of integrator: a) Operation b) Calibration

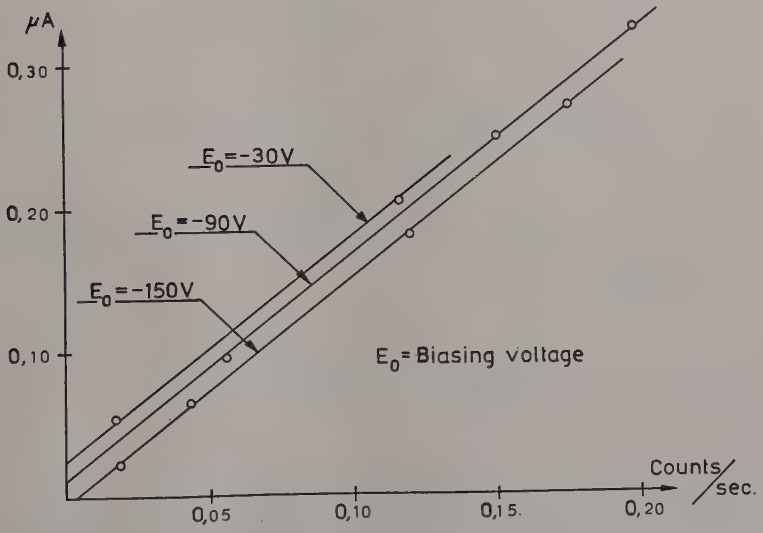

Fig. 7. Calibration curves for current integrator.

For calibration, and the determination of the leakage currents in the integrator, the proton current and the target chamber were replaced by a photocell arrangement (Fig. 6). This device had the desired properties of giving a regulable current (by appropriate illumination), and having a high internal impedance, thus resembling the target system. It has the advantage of good constance, and can be varied down to very small currents (Fig. 7). The current was measured with a mirror galvanometer placed on a ebonite block in order that the insulation should be as good as possible, and the counting rate was determined at different currents. Fig. 7 shows the calibration curves for different condenser biases. The curves are parallel straight lines. As is seen, the leakage currents are not more than some per cents of a micro-ampère. If the bias is set to about —120 Volts, which is between the breakdown and extinction potentials, the line goes through the origin. The slope of the curves corresponds to a calibration constant of 1.63 μC per registered pulse.

The accuracy of relative measurements with the current integrator was found to be 1 %.

6. Detectors.

Proportional counters were used for the identification of the reactions and for the investigation of the excitation curves; some properties of scintillation counters for (p, α) reactions were also studied.

The identification was accomplished with the following range measurement arrangement. The α-particles could leave the target chamber through a mica window (Fig. 8) which had a thickness of 0.8 mg/cm^2 and a diameter of 3.63 mm. The particles then enter an end-window GEC counter with 1.7 mg/cm^2 window thickness. Thus the range of the O^{18}-α-particles allows about 1 mm. distance between the windows, while for N^{15}-α-particles the maximum distance is 7 mms. The solid angle of the outgoing particles was 0.004 sterad. The counter was mounted a little eccentrically, so that the beam of α-particles would neither hit the wall of the tube nor the knob on the end of the central wire. The counter could be moved along its axis with a micrometer screw.

This arrangement is quite simple, but because of the windows a range measurement cannot be trusted to within less than 5 %. For the desired identification this is quite good enough.

The excitation curves were taken with a proportional end window counter (see Fig. 4) permitting a much larger solid angle, 0.07 sterad. Here the window thickness was 2.1 mg/cm^2.

In both arrangements the counters were often checked, using a Ra-γ-source, to ensure that they were working in the proportional region, and did not respond to γ-quanta.

In some other cases the same tube was used in the G.M.-region for counting γ-quanta, for instance at the calibration of the voltage with the Li^7 (*p*, γ) resonance at 442 keV.

As already mentioned a scintillation counter technique was tried for α-particles. A screen of zinc sulphide activated with silver was placed in the vacuum on a glass window (Fig. 9). Scintillations in the semi-transparent screen were detected by a photomultiplier 931-A. To eliminate the effect of scattered protons, and of light from the target spot, an appropriate thin metal foil was put between the target and the screen. The scintillation arrangement, however, could in general be used only up to proton energies of 400 to 450 keV. At higher energies severe disturbances appeared on the oscillograph, many of which were counted by the scaler. It was first supposed that these pulses originated from protons passing through thinner parts of the foil (Al in one case). To diminish this effect a light element should be chosen as target backing material. With Al target plates (instead of Ag) one got more violent disturbances and many more false counts, contrary to expecta-

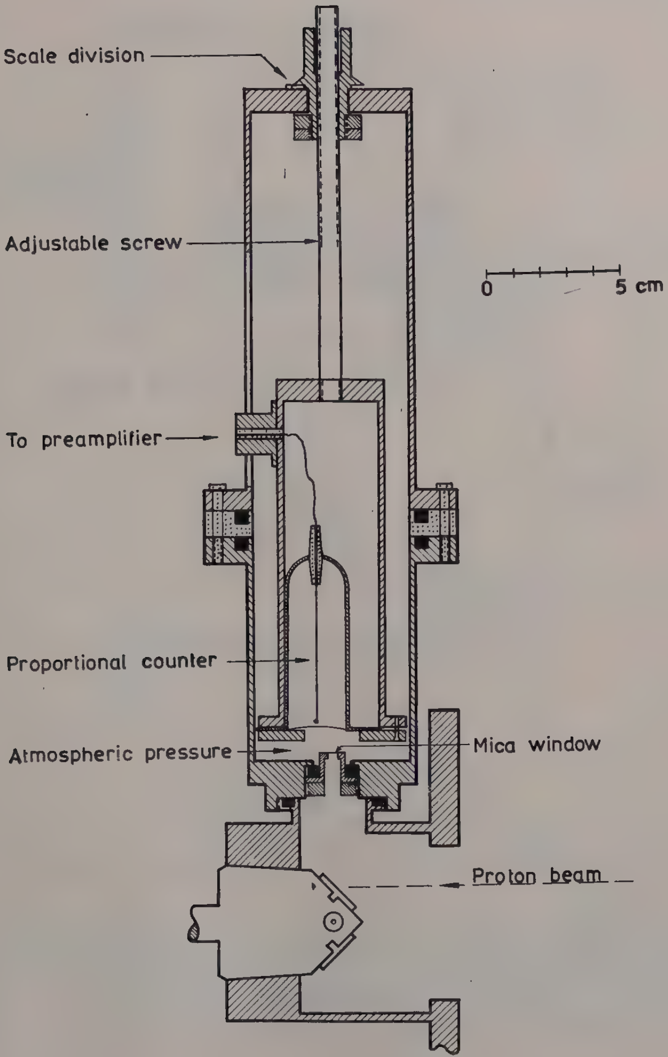

Fig. 8. Device for range measurement.

tion. In general, a choice of the same material in the foil and the backing plate was found to be especially unfavourable. This fact and others could be completely explained if the disturbance was identified with X-rays from the target plate. The characteristic sudden changes of absorption coefficient with changing wave length can be used to minimize X-ray disturbances, by choosing suitable different materials for the target plate and the metal foil.

In practice, experiments showed that combinations chosen from a knowledge of the X-ray emission and absorption spectra largely reduced the disturbances, so that proton energies up to 600 keV could be used. (Such a combination was for instance an Al-foil and a silver target plate.)

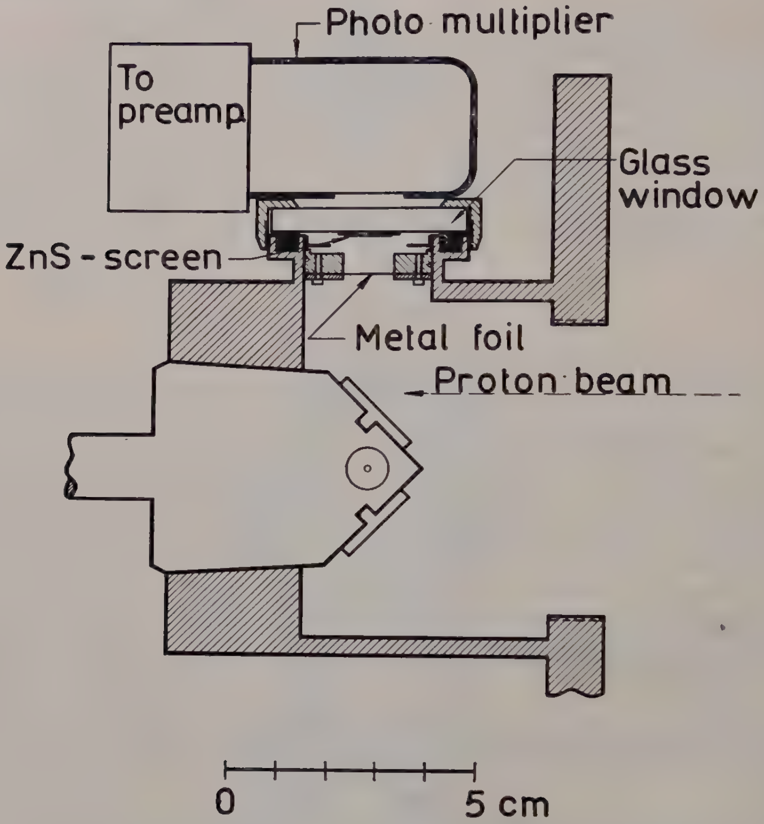

Fig. 9. Arrangement for α-detection by scintillation counter.

A scintillation counter of this type is, of course, not limited to low energies if the path of the charged particles is curved by a magnetic field, care being taken to ensure that the effects of the stray field on the multiplier can be eliminated, which is generally possible. In this case the metal window is not needed.

7. Procedure and results

The energy of the α-particles leaving the separated O^{18}- and N^{15}-targets was studied with the range measurement arrangement. The resulting curves are shown in Fig. 10 and Fig. 11. The micrometer scale was in each case calibrated with α-particles from the Po-source. The calibration agreed well with that expected from the known window thicknesses and the air path. These range curves correspond, within the accuracy of the experiments (some percents), to the expected ranges of the α-particles from the reactions O^{18} $(p, \alpha)N^{15}$ and N^{15} (p, α) C^{12}, as calculated from the Q-values of these reactions. It can be seen from Fig. 11 that in the case of the N^{15}-target a contaminant was present, probably consisting of O^{18}, most

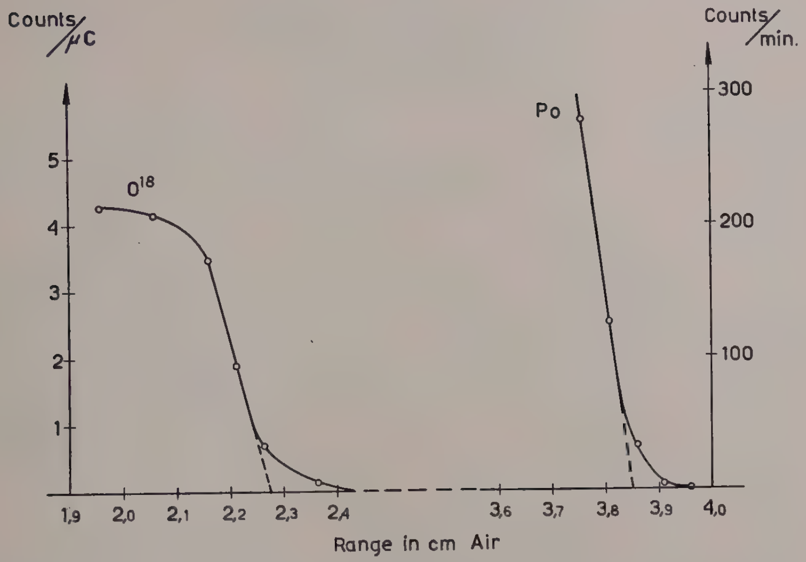

Fig. 10. Number-range curves for α-particles from O^{18} (p, α)N^{15} and from Po.

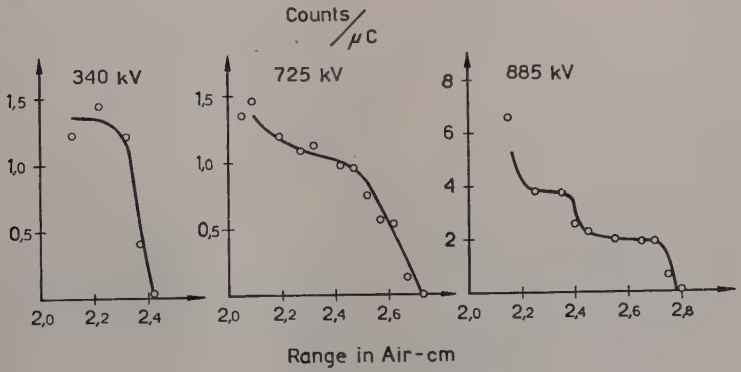

Fig. 11. Number-range curves for α-particles from N^{15} (p, α) C^{12}.

marked at high energies. From these curves, one chose an appropriate window thickness for the counter to be used for the excitation curves.

To replace the range measurement apparatus by the large-angle propotional counter it was necessary to break the vacuum, but only for a very short time. The beam was adjusted to optimum intensity homogeneity with the help of the tungsten visualizer. It was also checked at the plane of the limiting slit by temporarily displacing the spot slightly upwards. The beam cross section was made slightly bigger than the limiting slit. During the measurement of an excitation curve the spot was kept unchanged, as far as possible. The excitation curves are shown in Fig. 12 and Fig. 13. The abscissa gives the energy in keV of the bombarding proton beam; the ordinate gives the number of pulses per microcoulomb of protons.

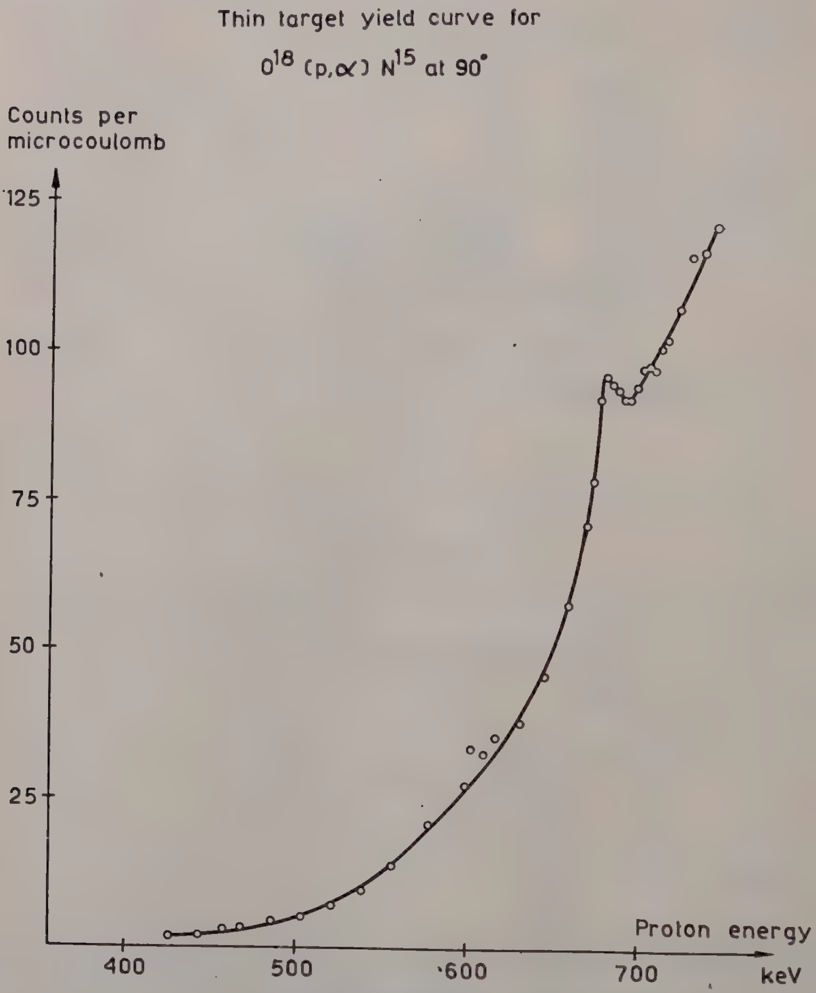

Fig. 12. Thin target yield curve for O^{18} (p, α) N^{15} at 90°.

The high voltage was measured with an oil-insulated resistor column, consisting of 280 carbonized resistors. By electrical methods, and also by using the Li-γ-resonance at 442 keV, the value of the resistor column was found to be 3 400 MΩ. The accuracy of this absolute calibration was within 5 %. The variation over a long run was found to be less than 1 %.

The current through the voltmeter-resistor was read on a carefully calibrated Weston instrument. The high voltage could be held constant manually to within 0.2 % during the measurement of each point of the excitation curve.

The ordinate of the curves is the ratio between the number of counted α-particles and the integrated proton current during the time of measurement of a point. For each point more than 1 000 α-particles were counted (except for a few points at very low voltage) so that a statistical mean deviation of ± 3 % was obtained.

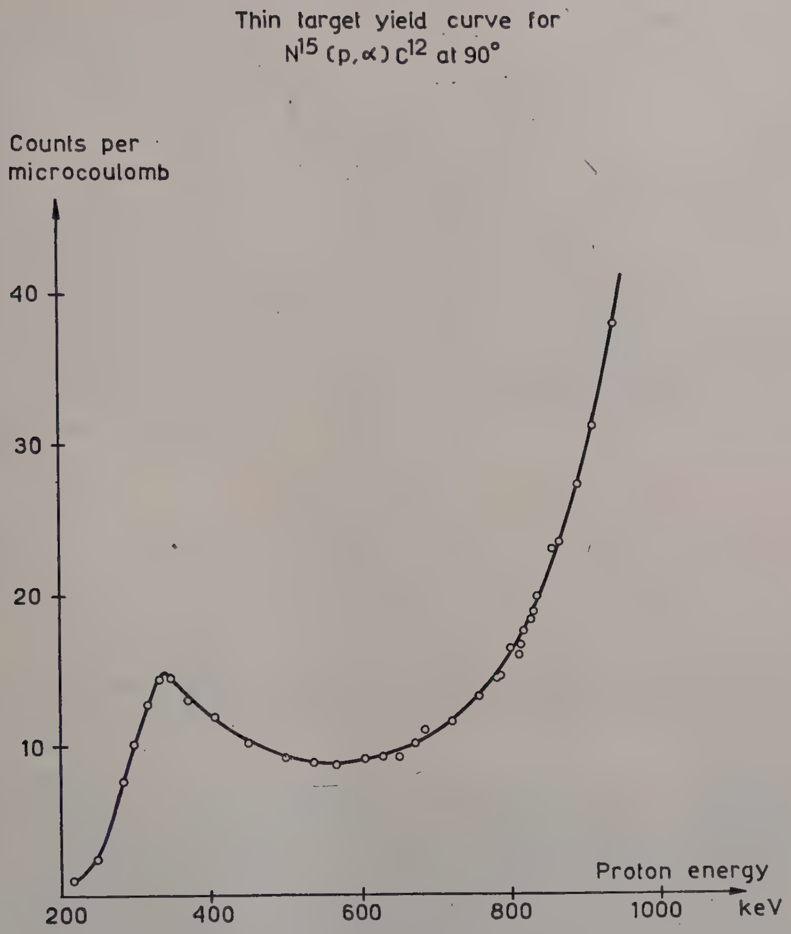

Fig. 13. Thin target yield curve for N^{15} (p, α) C^{12} at 90°.

The resistance between target chamber and earth was repeatedly checked, and low counting rates of the current integrator were not used.

Generally about 50 to 150 integrator pulses were counted during the measurement of one point. The start and finish of the measurement of a point were made to coincide with register pulses of the current integrating set.

In this way the relative accuracy of the integrator was kept to 1 %.

There are especially two factors which could cause errors in the measurements, namely target destruction during bombardment, and formation of a surface film. In the case of N^{15} the number of target atoms slightly decreased with time, 2 % per hour at 1 μA bombarding current. A correction for this decay has been made in Fig. 13. In the case of O^{18}, however, no such target destruction could be observed, so that, for instance, after five hours run the target yield was unaltered. This difference between oxygen and nitrogen is not quite understood, but we suppose it depends on the higher chemical affinity of oxygen to the target backing.

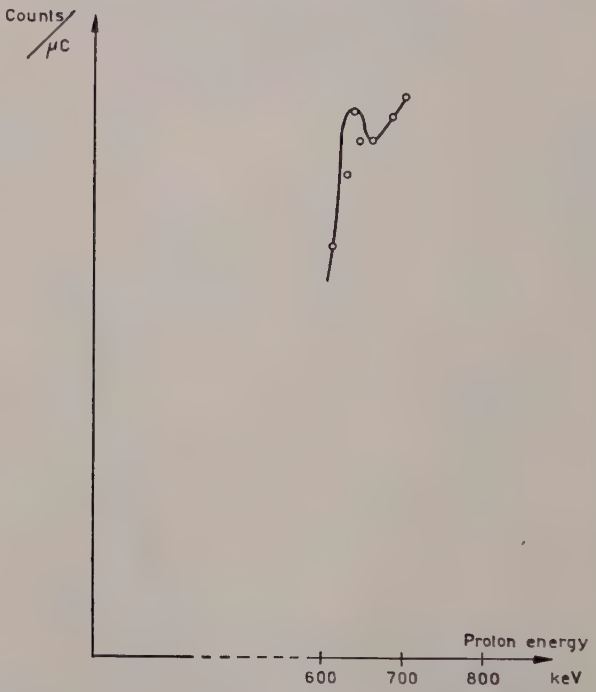

Fig. 14. Yield of α-particles from O^{18} (p, α) N^{15} of range $\geq$ 2,0 cm air.

The possibility of the formation of a thin surface film from small amounts of matter in the vacuum system cannot be excluded. Such a film would have shifted the energy scale. The peak in the O^{18}-curve, however, lay at an energy value which was constant within 1 %. As this variation could be due to the uncertainty in the relative energy measurement, there was no reason to suspect a surface film thicker than 5 keV on the O^{18}-target, unless the surface film had developed and reached a saturation thickness at the very beginning of the measurements. The surface film could, of course, also be much thinner.

As a control, plates of the same material (silver), machined at the same time and with the same steel tool, were exposed to a proton beam without having been put into the isotope separator. Such plates showed a very small α-yield, about 0.1 counts per microcoulomb at 600 keV. Plates cleaned with toluol gave much larger effect.

The yield curve of a plate which had been exposed to a strong beam of mass number 14 in the separator was measured with special care around the energy 680 keV (the O^{18}-resonance). The yield did not exceed 3 counts per microcoulomb, rising slowly with increasing energy. No resonance could be observed. This was done in order to investigate α:s from target contaminations due to the long exposure to residual gases in the isotope separator vacuum. Mass number 14 is suitable for such a test because neither N^{14} nor C^{12} or C^{13} give any (p, α)-reactions at these energies. All these control experiments were made with the large-angle proportional counter.

To be sure that the resonance in the O^{18} (p, α) reaction was not due to any contamination, the more time-taking measurement of the excitation curve with the range energy arrangement adjusted for the actual range is shown in Fig. 14. The curve has the same type of peak as the one in Fig. 12, at the same energy, 680 keV. Therefore, it must be concluded that this resonance belongs to the O^{18} $(p, \alpha)N^{15}$-reaction. There is consequently a level in the intermediate nucleus, F^{19}, at 8.6 MeV. The exact position of the energy level depends on the peak shift caused by the Gamow penetration factor. This influence will be discussed below.

The α-yield curve of N^{15} $(p, \alpha)C^{12}$ has a resonance peak at 340 keV. This resonance was found by COCHRANE and HESTER[4] in 1949 in the neighbourhood of 400 keV. They followed the curve to about 500 keV. Up to 940 keV we have found no other resonance. The corresponding level in the intermediate nucleus, O^{16}, lies at 12.9 MeV, depending somewhat on the peak shift due to the rise of the curve.

After the completion of our work SCHARDT et. al[9] published a value of 0.36 MeV for the resonance in N^{15} $(p, \alpha)C^{12}$. They also found resonances at 1.0 and 1.2 MeV.

8. Discussion

The theory of nuclear reactions gives for the cross section[10]:

$$\sigma = P_P \cdot s \cdot P_Q$$

The cross section is the product of the penetrability for the incident particle, P_P of the internal disintegration probability, s, and of the penetrability for the outgoing particle, P_Q.

For s the dispersion theory gives

$$s = \pi \bar{\lambda}^2 \frac{1}{(2s+1)\ (2i+1)} \sum (2J+1) \left| \sum \frac{w_P{}^r \cdot w_Q{}^r}{E - E_r + \frac{1}{2} i \gamma_r} \right|^2$$

where $\bar{\lambda}$ = wave length of the incident particle, divided by 2π,
s = spin of the incident particle,
i = angular momentum of the incident particle,
J = angular momentum of the compound nucleus,
E_r = resonance energy of the resonance r,
γ_r = total effective width of the level r of the compound nucleus,
$(w_r)^2$ = level widths without barrier.

Now, if one wants to investigate the resonance properties, the formula suggests that the measured cross section should be divided by $P_P \cdot \pi \bar{\lambda}^2 \cdot P_Q$. The curve obtained in this way would represent

$$\frac{\sigma}{P_P \cdot \pi \bar{\lambda}^2 \cdot P_Q} = \frac{s}{\pi \bar{\lambda}^2}, \text{ where } s \text{ is given above.}$$

---

[9] SCHARDT, A. W., FOWLER, W. A., and LAURITSEN, C. C., Phys. Rev. *80*, 136 (1950).
[10] BETHE, H. A., Rev. Mod. Phys. *9—10*, 189 (1937—1938).

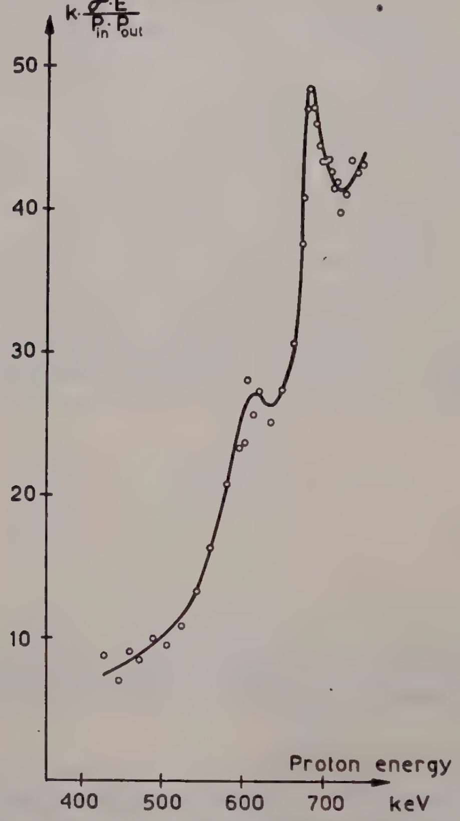

Fig. 15. Semiempirical internal disintegration probability multiplied by energy for the reaction O^{18} (p, α) N^{15}.

The penetrabilities P_P and P_Q used are, according to Bethe,

$$P_P = e^{-2\,C_P} \quad \text{and} \quad P_Q = e^{-2\,C_Q}$$

with

$$C_i = \frac{2\,z_i Z_i e^2}{\hbar} \sqrt{\frac{M_i}{2\,E_i}} \left[\text{arc cos} \sqrt{\frac{E_i}{B_i}} - \sqrt{\frac{E_i}{B_i}} \sqrt{1 - \frac{E_i}{B_i}}\right]$$

where i stands for P or Q.

and $B_i = \frac{z Z e^2}{R}$ = barrier potential,

z = charge of penetrating particle,
Z = charge of barrier-producing nucleus,
R = radius of barrier-producing nucleus,
M = reduced mass.

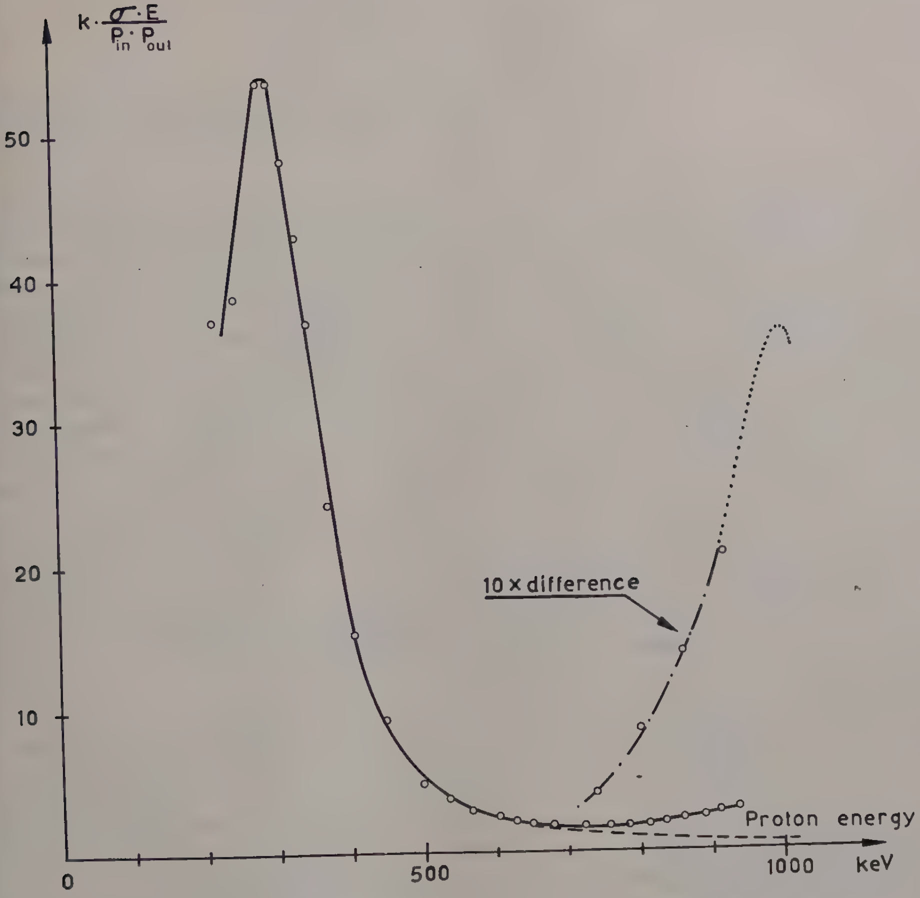

Fig. 16. Semiempirical internal disintegration probability multiplied by energy for the reaction N^{15} (p, α) C^{12}.

The curves $\frac{\sigma}{P_P \cdot \pi \bar{\lambda}^2 \cdot P_Q}$ are drawn in Fig. 15 and Fig. 16.

The resonance peaks, which experimentally occured at 680 keV and 340 keV in the two reactions, are shifted downwards by the mathematical operation to new peak energies, which should be the theoretically more interesting values.

Let us first look at the N^{15} (p, α) C^{12} case. This curve (Fig. 16) first shows the above-mentioned resonance, and then rises again with increasing energy as if there were another resonance at a somewhat larger energy than our maximum energy, 940 keV. This resonance should be the one at 1.0 MeV reported by SCHARDT et al.[9] Thus in the energy region covered by our measurements the curve should be predominently influenced by two resonances. Putting $(w_P^r)^2 = G_{P_r}$, $(w_Q^r)^2 = G_{Q_r}$ we get, for the theoretical formula of $s/\pi\bar{\lambda}^2$:

$$\frac{s}{\pi \bar{\lambda}^2} = \frac{\sum (2J+1)}{(2s+1)\ (2i+1)} \left\{ \frac{G_{P_1} G_{Q_1}}{(E-E_1)^2 + \frac{1}{4}\gamma_1^2} + \frac{G_{P_2} G_{Q_2}}{(E-E_2)^2 + \frac{1}{4}\gamma_2^2} + \right.$$
$$\left. + \frac{2\sqrt{G_{P_1} G_{Q_1}} \cdot \sqrt{G_{P_2} G_{Q_2}}\ [(E-E_1)\ (E-E_2) + \frac{1}{4}\gamma_1 \gamma_2]}{[(E-E_1)^2 + \frac{1}{4}\gamma_1^2]\ [(E-E_2)^2 + \frac{1}{4}\gamma_2^2]} \right\}$$

Here index 1 refers to the first resonance, index 2 to the second resonance.

The total effective widths γ_1 and γ_2 are functions of energy, but they vary only very slowly. They can therefore be regarded as approximately constant, and replaced by the widths at resonance, Γ_1 and Γ_2. The same argument will be relevant for the G_Q:s and to a certain degree also for the G_P:s (if $l = 0$). The solid line in Fig. 16 shows the semiempirical curve for $s/\pi\bar{\lambda}^2$. It has a peak at $\approx$ 290 keV with a half-width of 140 keV. In the 300 keV region the influence of the high energy resonance can be regarded as small. The dashed line represents the contribution of the 290 keV resonance in the energy region 700—1 000 keV. The dash-dotted curve gives the difference between these two curves, magnified 10 times. It can well be identified with a resonance at 1.0 MeV of 200 keV half-width, the peak height of which would be $\approx 1/15$ of the peak height at 290 keV. Thus we may, to a rough approximation, suppose that the relative amplitudes $G_{P_1} G_{Q_1} / G_{P_2} G_{Q_2}$ of the two purely resonance terms are given by the ratio of the two peak heights on the semiempirical curve of Fig. 16, which is about 15: 1. This is allowable because the interference term does not significantly influence the peak heights. In the region between the resonances the interference term should lower the curve. There seems to be no sign of such a lowering in fig. 16.

Our curve therefore roughly corresponds to a $s/\pi\bar{\lambda}^2$ of the form

$$\frac{s}{\pi \bar{\lambda}^2} \approx \frac{\sum (2J+1)}{(2s+1)\ (2i+1)}\ G_{P_1} G_{Q_1} \cdot \left\{ \frac{1}{(E-E_1)^2 + \frac{1}{4}\gamma_1^2} + \frac{1}{15} \frac{1}{(E-E_2)^2 + \frac{1}{4}\gamma_2^2} \right\}$$

where

$$E_1 = 290 \text{ keV} \qquad \qquad E_2 = 1\,000 \text{ keV}$$
$$\text{and}$$
$$\gamma_1 = 140 \text{ keV} \qquad \qquad \gamma_2 = 200 \text{ keV}$$

SCHARDT et. al. give the yield resonance as 360 keV, compared to our value of 340 keV. As the absolute calibration of our voltmeter-resistor was uncertain within 5 %, this difference is perhaps no discrepancy. But SCHARDT et. al. report a width of 100 keV for this resonance, whereas we find 140 keV. As the width depends only on relative accuracy, the experimental errors cannot easily be responsible for this. Moreover, the correction for *s*-wave penetration is about 20 keV for a width of 100 keV, and about 50 keV for a width of 140 keV in this region. Therefore, we get the corrected resonance to 290 keV, while SCHARDT et al. get 340 keV.

Let us now turn to the $O^{18}\ (p, \alpha)N^{15}$ case. The $s/\pi\bar{\lambda}^2$ curve for this reaction is given in Fig. 15. Here the 680 keV resonance is practically not shifted at all, because of the comparatively small half-width, 40 keV. This resonance thus corresponds to a level in the compound nucleus, F^{19}, at $7.9 + \frac{18}{19} \cdot 0.680 \text{ MeV} = 8.6 \text{ MeV}$. This level is shown in Fig. 17.

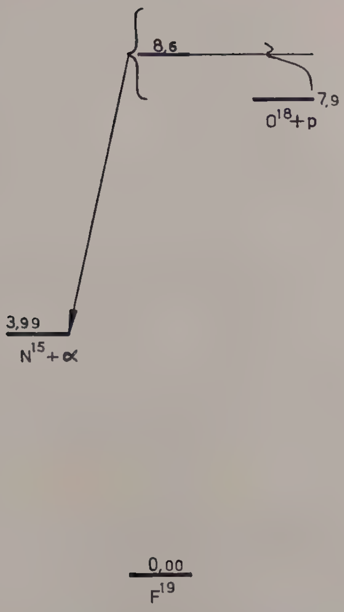

Fig. 17. Level scheme of the reaction O^{18} (p, α) N^{15}.

The 'irregularity' at 600 keV in the yield curve, Fig. 12, becomes more evident in the type of representation used in Fig. 15. It is possible that it is due to a level of roughly 100 keV width in the compound nucleus, corresponding to the proton energy 600 keV.

The further rise of the curve for energies higher than 720 keV indicates another broad resonance at a somewhat higher energy. The possibility of three resonances rather near each other makes the use of the dispersion theory of resonance inconvenient in this case, and therefore no more detailed analysis of this curve has been attempted.

9. Wigners exact resonance theory

The dispersion formula used above, which is due to BETHE, is valid only if the widths are much smaller than the distance between the resonances. The analysis of the excitation curve of N^{15} (p, α) C^{12} gives resonance widths of 150—200 keV, with a separation of 700 keV. One might expect that an exact calculation would be better suited for comparison with experiment in cases such as this, in which it is questionable whether the condition for the validity of the approximation is fulfilled.

WIGNER[11, 12] has treated the resonance phenomenon when there are several levels, paying particular attention to the region between resonances. For the resonant factor of the cross section WIGNER obtains the expression, for the case $l = 0$,

---

[11] WIGNER, E. P., Phys. Rev. 70, 606 (1946).

[12] WIGNER, E. P. and EISENBUD, L., Phys. Rev. 72, 29 (1947).

$$\left| \sum_{\mu\lambda} A_{\mu\lambda} \cdot \gamma_\mu \cdot \gamma_\lambda \right|^2$$

where the matrix elements $A_{\mu\lambda}$ obey the condition

$$A_{\mu\lambda} - \frac{\frac{1}{2} i}{E_\lambda - E} \sum_\nu A_{\mu\lambda} \Gamma_{\nu\lambda} = \frac{\delta_{\mu\lambda}}{E_\lambda - E}$$

Here the indices μ and λ independently take numbers 1, 2, 3, . . . and n, for n resonances, so that this expression gives n^2 equations for determining the $A_{\mu\lambda}$.

The E_λ are the resonance energies.

Since the $A_{\mu\lambda}$ are complex numbers, the summation in the bracket giving the reaction cross section is a vector summation.

The $\Gamma_{\nu\lambda}$ are quantities representing the half width of the resonance λ if $\nu = \lambda$, and mutual transitions if $\nu \neq \lambda$. $\delta_{\mu\lambda}$ is Diracs δ-function. Here $A_{\mu\lambda} = A_{\lambda\mu}$ and $\Gamma_{\nu\lambda} = \Gamma_{\lambda\nu}$, according to WIGNER's theory.

10. A network representation of Wigners exact resonance formula

In order to get a more clear picture we suggest to represent the n^2 equations for the matrix elements by a system of n parallel electric impedances. This network is shown in Fig. 18. It is as well a skizz to an analogy machine, for nuclear resonances. It can be verified that the two representations are identical if we make the identifications

$$E \rightarrow \frac{1}{a_\lambda^2} R \qquad E_\lambda \rightarrow \frac{1}{a_\lambda^2} R_\lambda \qquad \tfrac{1}{2} \Gamma_{\mu\lambda} \rightarrow \frac{w}{a_\mu a_\lambda} L_{\mu\lambda}$$

V is the e.m.f. across the parallel impedances: it is constant in frequency and can be written $V \cdot e^{iwt}$. I_λ is the current vector in the λ:th impedance (negative sign) where the $\frac{1}{a_\lambda^2} R$ are variable resistances, corresponding to the variable energy of the incoming particle, the $\frac{1}{a_\lambda^2} R_\lambda$ are negative resistances (which can be simulated by amplifiers) corresponding to the resonance energies, the $\frac{1}{a_\lambda^2} L_{\lambda\lambda}$ are inductances corresponding to the widths of the resonances $\Gamma_{\lambda\lambda}$, and the mutual inductances between the coils correspond to mutual transition probabilities. The a_λ are amplitude factors, and are constant dimensionless real numbers, the a_λ^2 represent the heights at the different resonances, and the $a_\mu a_\lambda$ represent the amplitudes of the various mutual transitions. The division by a_λ^2 is taken into the transformation to reduce the different resonance heights to an equal value, which of course makes an important simplification without loosing generality. The a_λ correspond to γ_λ in the WIGNER expression for the cross section.

If a_λ is supposed to be proportional to γ_λ one can easily show that the matrix representation and the network representation are connected by the relation

$$\sum A_{\mu\lambda} \cdot \gamma_\mu \cdot \gamma_\lambda = I_\lambda$$

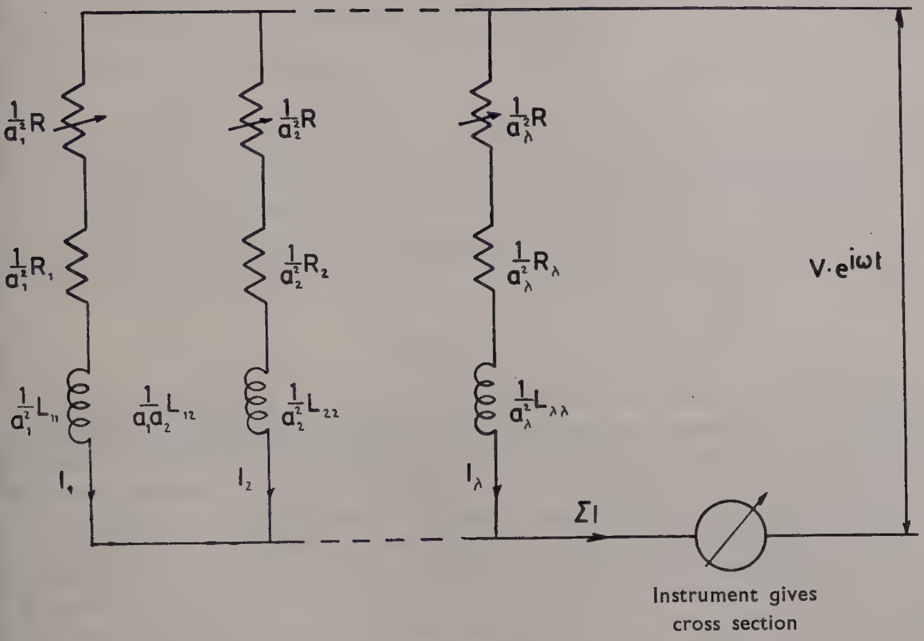

Fig. 18. Network representation of resonance formula.

Thus, we get for the resonance factor of the reaction cross section the simple equivalent expression

$$\left| \sum_{\lambda} I_\lambda \right|^2$$

where the summation inside the bracket is the vectorial summation of the currents in all the branches λ. A current-measuring instrument in series with the parallel-coupled branches will perform this vector addition.

Consequently this instrument, calibrated according to a square law, gives $s/\pi\bar{\lambda}^2$, the internal disintegration probability divided by $\pi\bar{\lambda}^2$, for n resonances.

Thus the simultaneous variation of the variable resistances

$$\frac{1}{a_1^2} R_1, \quad \frac{1}{a_2^2} R_2 \; \ldots \; \frac{1}{a_\lambda^2} R_\lambda$$

gives directly upon the instrument the energy variation of the quantity

$$\frac{\sigma \cdot E}{P_{\text{in}} \cdot P_{\text{out}}} \quad \text{as a function of energy.}$$

It is to be noticed that the Bethe approximation, which is valid if the widths are much smaller than the distances between the resonance levels, i.e. if the $\Gamma_{\lambda\lambda}$ are small, is equivalent to neglecting the mutual inductances in the exact network representation.

The energy variation of the widths, and also the amplitudes, will depend on the l-value.

The exact WIGNER resonance formula, as well as the above-mentioned approximate BETHE formula gives a marked lowering of the excitation curve between the resonances, compared to the purely resonance terms. As was pointed out, no lowering was found in the investigated N^{15} case. This suggests that there is either a small third resonance, or else a non-resonant part of the reaction, if the theory is to be right. It is clear that an extension of the curve to lower and higher energies would be desirable.

11. Conclusion

The different lines of work on nuclear reactions with light nuclei, such as the investigation of Q-values, excitation functions, angular distributions, and angular correlations, are all of great importance. The study of excitation curves has attracted interest from the beginning of nuclear research, and, because finer details of nuclear cross section theory have been developed during the last five years, there has recently been an increased demand for experimental results of high precision. Electromagnetically separated thin targets are a valuable tool for such investigations. They have the evident advantage of being isotopically pure, they show a good stability if used under reasonable conditions, compared to evaporated targets, and the measurement of the bombarding current is easier than for free gas targets. The parallel development of experimental technique and cross section theory during the last few years has given to this field of nuclear research an increased degree of interest.

Acknowledgements

We wish to thank professor M. SIEGBAHN for his continuous interest and encouraging support.

Our thanks are also due to civiling. I. BERGSTRÖM and civiling. S. THULIN for preparing the targets, and to civiling. K. KRAFT-AHNLUND for valuable assistance.

Svenska Atomkommittén granted this work.

Nobel Institute of Physics, Stockholm 50, Sweden.

Tryckt den 1 februari 1952

Uppsala 1952. Almqvist & Wiksells Boktryckeri AB

ARKIV FÖR FYSIK Band 4 nr 14

Communicated 12 September 1951 by MANNE SIEGBAHN and ERIK HULTHÉN

Q-values for (αp)-reactions on fluorine and sodium

By ELIS HJALMAR and HILDING SLÄTIS

With 2 figures in the text

In a previous paper (1) we have published a survey over earlier investigations concerning (αp)-reactions, in particular reactions on aluminium and boron. Methods of determining the Q-values for the (αp)-reactions were described. A new arrangement for measuring the Q-values by means of modern photographic nuclear research emulsions and a polonium α-particle source was developed.

We have now continued these investigations by bombarding fluorine and sodium with α-particles from the same source. The results will be presented in this work.

Earlier investigations. Using the original method of RUTHERFORD (2), RUTHERFORD and CHADWICK (3) in 1921 discovered protons from targets of CaF_2 and Na_2O when these were bombarded with α-particles from RaC′.

Next year the same authors (4) found two proton ranges from fluorine and two ranges from sodium. CHADWICK, CONSTABLE and POLLARD (5) observed that the protons from fluorine consisted of at least three distinct groups. In the experiments with sodium no groups could be established.

POSE (6) slit thin lamina from a crystal of CaF_2 and used them as target. The source was a polonium α-emitter, which, as is known from experiments by RUTHERFORD and CHADWICK is not able to eject protons from the nucleus of Ca. POSE found proton groups with Q-values of 0.8, 0.9 and 1.9 MeV. The two first groups mentioned may be a single group.

Using a stronger polonium source and an improved apparatus CHADWICK and CONSTABLE (7) investigated fluorine and observed three pairs of proton groups. The influence of the energy of the α-particles on the groups was investigated. Two undoubted proton groups were assigned the Q-values 0.99 and 1.67 MeV, respectively. Thus this result is in approximate agreement with the results of POSE.

Sodium was studied by ATTY KÖNIG (8), who used an NaCl target for observations in the backward direction. For observations in the forward direction she evaporated Na onto a gold foil and covered the sodium layer with a sputtered silver film. The energy of the α-particles was varied by means of gold foils. She found four proton groups. The corresponding Q-values were —2.0, —0.80, —0.72 and 2.5 MeV, respectively.

MAY and VAIDYANATHAN (9) utilized the apparatus developed and employed by DUNCANSON and MILLER (10), a Geiger-Klemperer ball counter. The α-particle source was RaC′. They bombarded fluorine and obtained proton groups with the Q-values —3.2, —2.1, —0.1 and 1.4 MeV. The authors recalculated, using a reliable range-velocity curve, the results given by CHADWICK and CONSTABLE to 0.87 and 1.47 MeV, respectively. Only the latter value agrees with their own 1.4 MeV. They suppose that the target used by CHADWICK and CONSTABLE was too thick.

MAY and VAIDYANATHAN studied sodium in the 90° direction. The thickness of the NaOH-target corresponded to 1.25 cm in air. They obtained three proton groups with the Q-values —3.1, —2.0 and —0.6 MeV. When they made observations in an other arrangement in the forward direction they got the Q-values —2.2 and —0.3 MeV. The most energetic protons had a range greater than 63 cm in air but as their number was very small they made no attempt to resolve these particles.

MERHAUT (11) studied the $Na^{23}(\alpha p)Mg^{26}$-reaction by means of photographic emulsions. The thickness of the NaCl-target corresponded to 4 mm in air. Two proton groups were found, the Q-values of which were —0.15 and 1.64 MeV.

POLLARD and HUMPHREYS (12) raised the question of whether the levels of the residual nucleus are independent of the way in which the nucleus is created. They therefore examined the reactions $Na^{23}(\alpha p)Mg^{26}$ and $Mg^{25}(dp)Mg^{26}$. The excited states found from the former reaction were 2.3 and 4.0 MeV, from the latter 1.85 and 3.00 MeV. The authors concluded that the energy levels found depend on the type of reaction. However, in a later experiment the same investigators (13) used 7.4 MeV cyclotron α-particles and observed in the Mg^{26} nucleus excited states at 0.23, 0.60, 1.18, 1.92 and 2.75 MeV. This indicates, according to HUMPHREYS and POLLARD (13), that the level spacing in the moderately light nuclei is much smaller than the generally published figures. ALLAN and CLAVIER (14) did not find the 1.85 and 3.00 MeV Mg^{26} levels, reported by POLLARD and HUMPHREYS, but found some evidence for an excited level at about 5 MeV above the ground state. ALLAN and WILKINSON (15) gave the value 4.45 MeV for this level. However, ALLAN, WILKINSON, BURCHAM and CURLING (16), using separated isotopes of Mg, found no evidence for this (dp)-induced level proposed for Mg^{26}.

SAHA (17) bombarded CaF_2 with α-particles from polonium and found three different proton groups. The Q-values are not reported.

CHAMPION and ROY (18) studied the protons from fluorine bombarded with Po-α by means of a Wilson chamber. 1775 photographs were taken and 67 disintegrations could be observed on them. No effective separation of the protons into discrete groups was possible with the resolution available.

MOTZ and HUMPHREYS (19) finally bombarded an Na-target with 7 MeV α-particles from the Yale cyclotron. They observed four groups, the second (counted from the high energy side) of which is only barely resolved from the ground state and has not been previously reported. They obtained the following Q-values: —1.3, —0.30, 1.12 and 1.44 MeV.

In a monography on nuclear energy levels ALBURGER and HAFNER (20) give the following probable Q-values for the $Na^{23}(\alpha p)Mg^{26}$-reaction: —3.1, —2.1, —1.13, —0.19, 1.28 and 1.72 MeV.

The Q-values previously obtained as well as our Q-values are summarized for comparison in Tables I and II. It is seen, that the measurements made are very unsatisfactory and inconsistent. It would therefore be highly desirable to

Table I

$F^{19}(\alpha p)Ne^{22}$.

Author	Year	Ref. No.	Method	α-source	Q-values (MeV)						
POSE	1931	6	Ionization chamber	Po-α					0.8	0.9	1.9
CHADWICK, CONSTABLE	1932	7	» »	»					0.99 (0.87*)	1.67 (1.47*)	
MAY, VAIDYANATHAN	1936	9	Geiger ball counter	RaC′	−3.2	−2.1		−0.1		1.4	
HJALMAR, SLÄTIS (this paper)	1951		Photographic plate	Po-α			−1.27	0.23		1.0	1.57

* Recalculated by MAY and VAIDYANATHAN.

Table II

$Na^{23}(\alpha p)Mg^{26}$.

Author	Year	Ref. No.	Method	α-source	Q-values (MeV)					
KÖNIG	1934	8	Ionization chamber	Po-α		−2.0	−0.80	−0.72 (−0.2*)		2.5 (1.9*)
MAY, VAIDYANATHAN	1936	9	Geiger ball counter	RaC′	−3.1	−2.1		−0.4		
MERHAUT	1940	11	Photographic plate	Po-α				−0.15		1.64
MOTZ, HUMPHREYS	1948	19	Proportional counter	Cyclotron			−1.3	−0.30	1.12	1.44
ALBURGER, HAFNER	1950	20	Review of previous results	—	−3.1	−2.1	−1.13	−0.19	1.28	1.72
HJALMAR, SLÄTIS (this paper)	1951		Photographic plate	Po-α			−1.17	−0.17	1.15	1.55

* Recalculated by MAY and VAIDYANATHAN.

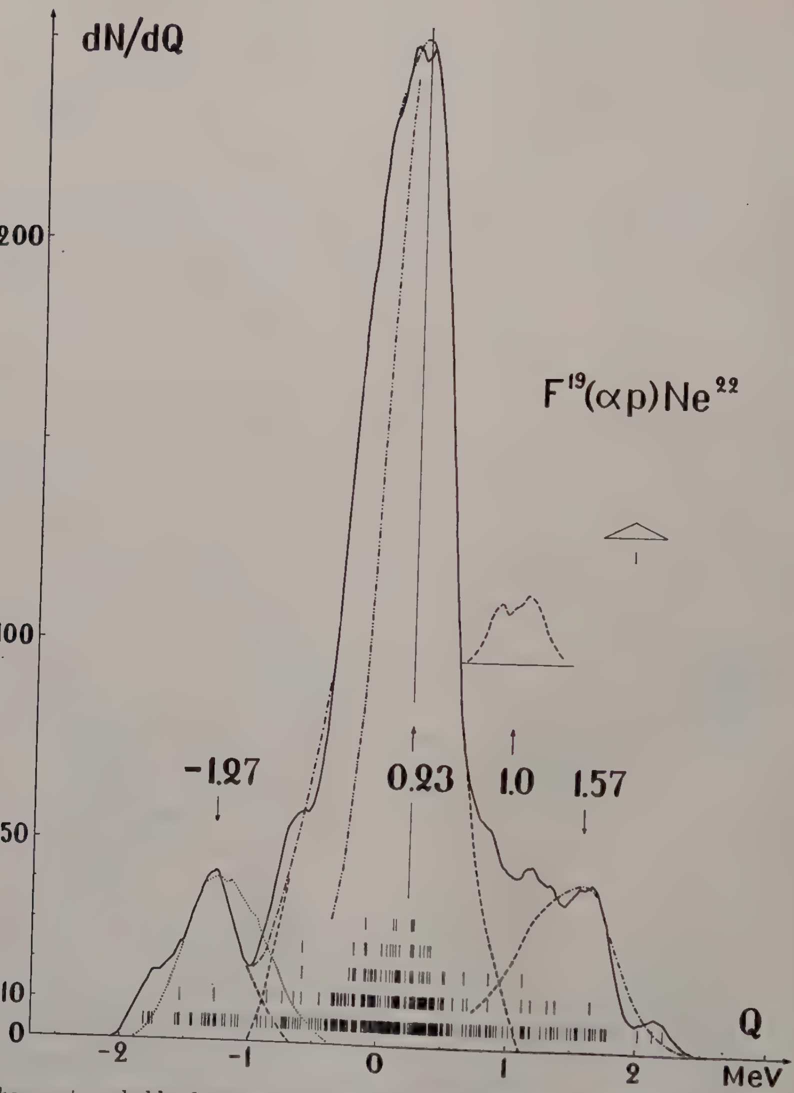

Fig. 1. The most probable Q-values for the $F^{19}(\alpha p)Ne^{22}$-reaction, computed from the Q-values obtained from 177 proton tracks.

get some more informations about the Q-values for (αp)-reactions on fluorine and sodium.

Bombardment of fluorine. The fluorine target consisted of 0.29 mg/cm² FeF_3 on an iron plate. An Ilford Nuclear Research plate type C 2 of 100 μ thickness was exposed to protons from the fluorine target for 24 hours (June 14th 1950). All details in the experimental arrangement, development of the

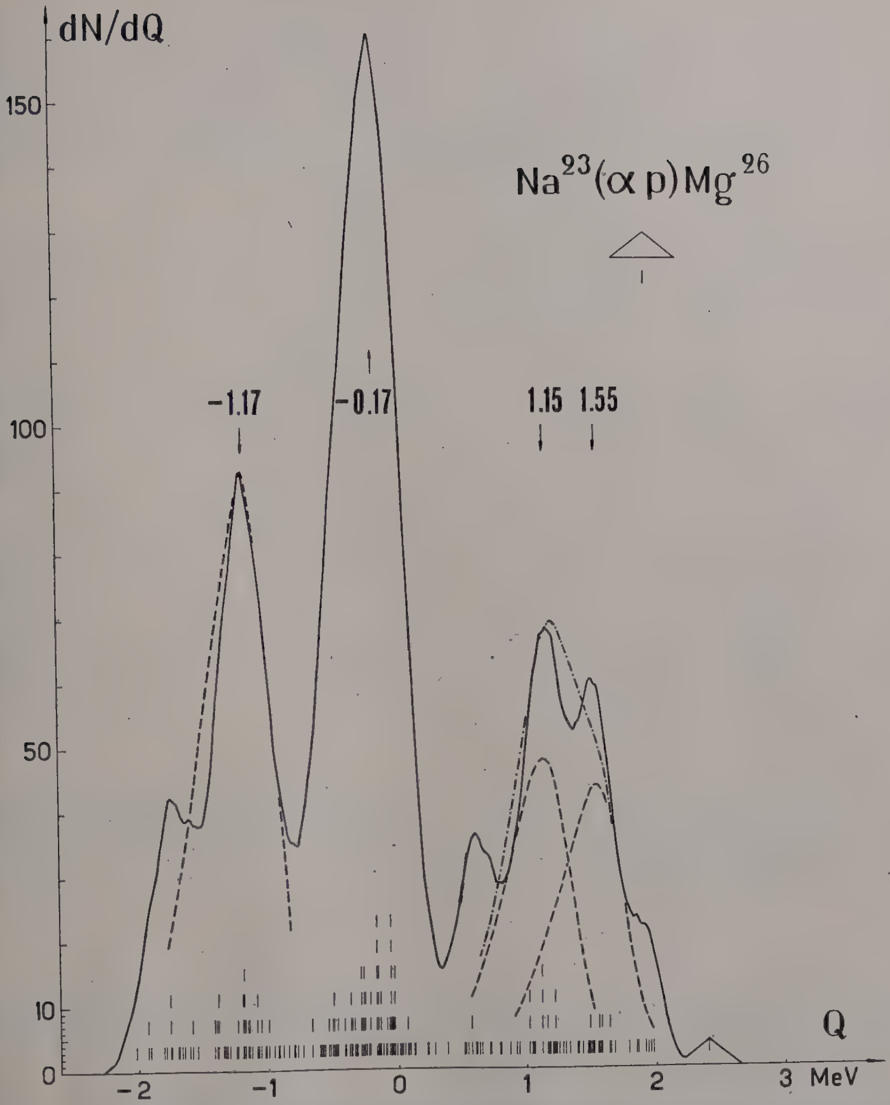

Fig. 2. The most probable Q-values for the $Na^{23}(\alpha\, p)Mg^{26}$-reaction, computed from the Q-values obtained from 235 proton tracks.

plate, scanning of the emulsion, correction for oblique passage through the window, calculation of the Q-values etc. were similar with those described in our earlier paper (1). The Q-values obtained from 177 proton tracks are presented diagrammatically in Fig. 1. The figure shows that there are four groups of Q-values, viz.

$$-1.27, \quad 0.23, \quad 1.0 \text{ and } 1.57 \text{ MeV}.$$

The highest Q-value, 1.57 MeV, is in good agreement with the value 1.50 MeV, computed for a transition to the ground state of the Ne^{22} nucleus and using the nuclear mass values given in (21). A transition from the 1.34 MeV ($Q = 0.23$ MeV) level to the ground state ($Q = 1.57$ MeV) of the Mg^{26} nucleus would give a γ-ray of the same energy, 1.34 MeV. This energy agrees with the upper energy limit for the positron spectrum of Na^{22}, which is 1.28 MeV (22).

Our Q-values lead to the Ne^{22} excited levels

0.57, 1.34 and 2.84 MeV.

This result may be compared with the figures given in the survey by HORNYAK, LAURITSEN, MORRISON and FOWLER (23), viz.

0.6, 1.28, (2.0), 3.4 MeV,

which represent probable level values estimated from measurement of different reactions all leading to the Ne^{22} nucleus. The value in brackets is uncertain.

The Q-components in Fig. 1 are broader than the components found in the aluminium and in the boron bombardments (1). This depends on the thickness of the fluorine target. It is interesting to see that the increase in half width of the Q-lines belong to the low energy side. The high energy side of the Q-lines for fluorine have the same shape as the Q-lines for aluminium and boron in our previous paper (1). This circumstance was of use in the analyse of the curve into different components. The 0.14 line, which we found for aluminium, Fig. 1 in Ref. (1), is for comparison plotted (chain-dotted curve with double dots) in coincidence with the 0.23 MeV line in Fig. 1. There is complete coincidence between the right-hand slopes of the curves. We think this circumstance is an indication of the reliability of our method.

Bombardment of sodium. The sodium target consisted of 0.15 mg/cm² NaOH deposited on a brass plate. The NaOH layer was produced by burning metallic sodium. Exposure was made for 60 hours (August 28th, 1950). The distribution of the Q-values obtained from 235 proton tracks is given in Fig. 2. The figure shows that there are four groups of Q-values, viz.

—1.17, —0.17, 1.15 and 1.55 MeV.

The Q-value for a transition to the ground state of Mg^{26} computed from the data given in (21) is 2.0 MeV. This does not agree with our 1.55 MeV Q-value. On the other hand, our Q-values are in good agreement with the values given by ALBURGER and HAFNER (20) Table II).

Our investigations on (αp)-reactions by means of photographic emulsions are being continued.

SUMMARY

Some Q-values for the reactions $F^{19}(\alpha p)Ne^{22}$ and $Na^{23}(\alpha p)Mg^{26}$ have been measured by means of photographic emulsions, and these values are compared with earlier results obtained by other authors (Tables I and II).

Nobel Institute of Physics, Academy of Sciences, Stockholm.

REFERENCES: 1. **Hilding Slätis, Elis Hjalmar** and **Rune Carlsson,** Arkiv f. Fysik *3,* 315, 1951. — 2. **E. Rutherford,** Phil. Mag. *37,* 537, 1919 and Nature *103,* 415, 1919. — 3. **E. Rutherford** and **J. Chadwick,** Phil. Mag. *41,* 809, 1921. — 4. ——, Phil. Mag. *44,* 417, 1922. — 5. **J. Chadwick, J. E. R. Constable** and **E. C. Pollard,** Proc. Roy. Soc. *A 130,* 463, 1931. — 6. **H. Pose,** Z. f. Ph. *72,* 528, 1931. — 7. **J. Chadwick** and **J. E. R. Constable,** Proc. Roy. Soc. *A 135,* 48, 1932. — 8. **Atty König,** Z. f. Ph. *90,* 197, 1934. — 9. **A. N. May** and **R. Vaidyanathan,** Proc. Roy. Soc. *A 155,* 519, 1936. — 10. **W. E. Duncanson** and **H. Miller,** Proc. Roy. Soc. *A 146.* 549, 1934. — 11. **O. Merhaut,** Phys, Z. *41,* 528, 1940. — 12. **E. C. Pollard** and **R. E. Humphreys,** Phys. Rev. *59,* 466, 1941. — 13. **R. F. Humphreys** and **E. C. Pollard,** Phys. Rev. *59,* 942, 1941. — 14. **H. R. Allan** and **C. A. Clavier,** Nature *158,* 832, 1946. — 15. **H. R. Allan** and **C. A. Wilkinson,** Proc. Roy. Soc. *A 194,* 131, 1948. — 16. **H. R. Allan, C. A. Wilkinson, W. E. Burcham** and **C. D. Curling,** Nature *163,* 210, 1949. — 17. **N. K. Saha,** Z. f. Ph. *110,* 473, 1938. — 18. **F. C. Champion** and **R. Roy,** Phys. Rev. *74,* 5, 1948. — 19. **H. T. Motz** and **R. F. Humphreys,** Phys. Rev. *74,* 1232, 1948. — 20. **D. E. Alburger** and **E. M. Hafner,** Rev. Mod. Phys. *22,* 373, 1950. — 21. **J. Mattauch** and **A. Flammersfeld,** Isotopenbericht, Tübingen 1949. — 22. **P. A. Macklin, L. J. Lidofsky** and **C. S. Wu,** Phys. Rev. *78,* 318, 1950. — 23. **W. F. Hornyak, T. Lauritsen, P. Morrison** and **W. A. Fowler,** Rev. Mod. Phys. *22,* 291, 1950.

Tryckt den 4 februari 1952

Uppsala 1952. Almqvist & Wiksells Boktryckeri AB

ARKIV FÖR FYSIK Band 4 nr 15

Communicated 12 September 1951 by MANNE SIEGBAHN and ERIK HULTHÉN

On the non-existence of a long-lived isomer of Ti^{51}

By WILHELM FORSLING and AMAL GHOSH

With 1 figure in the text

Abstract

Titanium from a pile-irradiated sample was separated in the isotope separator. No activity from Ti^{51} was detected. Radiochemical separation also proved that the activity of the sample did not belong to titanium but to tantalum occurring as impurity. β-spectra of the original sample and that of the chemically separated tantalum showed close similarity to each other and to the spectrum of Ta^{182} reported by others.

Introduction and survey

The present investigation was undertaken with the intention of studying the β- and γ-spectra of 72 day Ti^{51} and to try to formulate the decay scheme therefrom. The sample was pile-irradiated in Harwell for two months in a total quantity of 20 g of titanium(IV)oxide. As the preliminary investigations were proceeding, the remark of MISKEL, DER MATEOSIAN, and GOLDHABER (1) concerning the non-existence of a long-lived isomer of Ti^{51} came to our notice. The stress of the whole problem now shifted from decay scheme investigation to corroboration of Goldhaber's finding.

The first attempt was to separate the titanium sample in the isotope separator (2) of the institute and to see whether any activity is associated with Ti^{51}. No activity was found corresponding to Ti^{51}.

The next problem was to find out which element is responsible for the activity. To settle this point an elaborate scheme of radiochemical separation was adopted. After a protracted investigation the matter appeared to be settled, when the activity was finally concentrated in tantalum, originally occurring as impurity. This conclusion was corroborated by the investigation of the β-spectra in a lens spectrometer. We have not tried to make any further studies on this spectra, as this problem has already been dealt with by other investigators.

Analysis by means of the isotope separator

In order to get a suitable sample for the isotope separator analysis the irradiated titanium(IV)oxide was transformed into titanium(IV)chloride by the method described in Inorganic Syntheses (3) for preparing titanium(IV)bromide. Chlorine vapor was passed over a mixture of titanium(IV)oxide and carbon at a temperature of about 350° C. The distilled product was collected in a glass tube, which was sealed immediately after collection in order to prevent hydrolysis in moist air.

The separation was carried out with the help of Civ.ing. I. BERGSTRÖM and Civ. ing. S. THULIN. The separator (4) was in operation for about 13 hours in order to collect an amount of the isotope in question sufficient for the easy detection of the expected activity. The mass assignment was carefully checked, and there was practically no overlapping of the different lines. The total amount of the titanium separated was about 0.7 mg. The number of counts obtained in a calibrated G.M.-counter arrangement from the separated line of Ti^{51} was just the background. The specific activity of the titanium(IV)chloride was about 7 000 counts/mg min.

Chemical separations and analyses

Separations in earlier works

WALKE, WILLIAMS, and EVANS (4) were the first to report the existence of a long-lived isomer of Ti^{51}. They bombarded titanium by deuterons and made a chemical separation of the sample into calcium, scandium, titanium and vanadium. The separated titanium showed an activity with the half-life of 72 days and was assumed to decay emitting electrons of a maximum energy of 0.36 MeV. SEREN, FRIEDLANDER and TURKEL (5) have measured the thermal neutron cross section of Ti^{50} for the formation of a long-lived isomer, but they have not described any chemical separation of the irradiated titanium(IV)oxide. Nor have HEIN and VOIGT (6) given such an account in their investigations of the activities produced by the bombardment of titanium(IV)oxide with pile neutrons. MANDEVILLE and SCHERB (7) have given a detailed account of a chemical separation carried out after the irradiation of titanium(IV)oxide by neutrons in the Clinton pile. They do not seem, however, to have added carriers for the elements they wanted to separate from titanium. But even if carriers had been added, the method of separation used by them is not sufficiently specific for titanium. Certainly, zirconium, tantalum and tungsten will interfere.

MISKEL, DER MATEOSIAN, and GOLDHABER (1) were able to separate inactive titanium(IV)chloride from titanium(IV)oxide, which had previously been bombarded by slow neutrons at Oak Ridge. They were also able to establish the presence of Hf^{181} and Sb^{124}, though the spectroscopic analysis of the titanium(IV)oxide sample revealed neither Hf nor Sb.

It does not seem that any thorough qualitative chemical analysis has previously been performed on neutron irradiated samples of titanium or any of its compounds. Such an analysis would be much facilitated if the reputed radioactive impurity could first be isolated from the bulk of the titanium.

Principles of our chemical separation and analysis

In an attempt to separate the radioactive element or elements from the bulk of titanium(IV)oxide an anion exchange resin was used. The fact that many elements form negatively charged complexes in solutions containing hydrofluoric and hydrochloric acids was made use of. The resin Amberlite IRA-400 in the chloride form was shaken with such a solution of the irradiated sample. It turned out to be possible to separate almost all the activity in one batch process. The radioactive substance was strongly absorbed by the resin, while nearly all of the titanium remained in the solution. The resin was washed with a solution of hydrochloric and hydrofluoric acids, and the radioactive ions were completely removed from the resin by elution in an ion exchange column. After evaporation of the eluate to dryness, the small residue, most of which consists of impurities from the reagents used, was subjected to chemical analysis. For the β-spectrographic analysis and the adsorption measurements most of these impurities were removed from the sample as described below under the heading Experimental procedure.

The qualitative chemical analysis of the irradiated titanium(IV)oxide was carried out according to two different schemes. In each case a great number of carriers were added in quantities of about ten milligrams.

In order to make it probable that a tracer element in the titanium sample should not exist in an oxidation state different from that of the carrier added for that element, the sample and the carriers together had to be subjected to a strong oxidation or reduction process. Obviously this procedure is not always adequate. Two quite different ways for the chemical analysis have therefore been used, and the agreement between them taken as a test of the reliability of the method.

The qualitative analysis was first carried out according to the classical scheme, given for example by VOGEL (8). Secondly, it was done according to the system given by NOYES and BRAY (9) for the rare elements. With the first method an additional analysis of most of the elements in the subgroups IV B, V B and VI B of the periodic table had to be performed. This was made according to a procedure given by HICKS and WILKINSON (10).

Both these ways of analysis gave a clear result. Practically all of the long-lived activity originally present in the sample was recovered in the tantalum fraction.

Experimental procedure

Preparation of the sample. About 0.7 g of the irradiated titanium(IV)oxide powder was fused with about 5 g of potassium pyrosulphate in a platinum crucible. The fused mass was completely dissolved in hot 10 % sulfuric acid, which is possible only when small amounts of earth acids are present. The solution was filtered, and a small excess of ammonia added to the filtrate in order to precipitate insoluble hydroxides. After centrifugation in a Lusteroid tube the inactive supernatant solution was rejected and the precipitate washed three times with portions of about 40 ml of water. Each time the liquid was decanted after centrifugation. About 3 ml of 21 N hydrofluoric acid was added to the hydroxide precipitate, which rapidly dissolved. The volume of the solution was increased to about 35 ml with 4 N hydrochloric acid. This solution was now ready for the batch process with the anion exchanger.

Anion exchange separation. The anion exchange resin used was Amberlite IRA-400 of mesh size 200–300 and in the chloride form. This resin is a strongly basic cross-linked quarternary amine. 1 g of air-dried resin was introduced into the Lusteroid tube containing the solution the preparation of which is described above. The tube was closed with a stopper and shaken mechanically for one hour. The mixture was then centrifuged and the supernatant liquid containing the bulk of titanium decanted. The resin was shaken again with a solution of 4 N hydrochloric and 0.02 N hydrofluoric acid for about half an hour. The resin, which had adsorbed nearly all of the radioactive substance, was separated from the supernatant solution and transferred to the top of an adsorption column, made out of a short polystyrene tube with a cross-sectional area of 2.0 sq.cm. The lower end of the tube was fitted with a polystyrene cap having a capillary tip. A cotton plug was pushed down to the bottom of the column, and a small quantity of pure anion resin washed in, to give a bed length of only 1 cm.

The reason for using a column run process following the batch process is twofold. Firstly, the complex ions of the radioactive element or elements had to be desorbed as completely as possible for the analyses. Secondly, it would be of great advantage if all the remaining impurities of titanium or any other element could be separated from the active substance in this way. The behaviour of this substance in the anion exchange column gave in fact good support to the result of the analyses.

In order to choose suitable concentrations of the influent acids, we made use of experience gained from similar separations performed earlier at this institute, and of the data given by KRAUS and MOORE (11).

When the radioactive resin had formed a narrow layer at the top of the small column, an eluting solution composed of 4 N hydrochloric acid and 0.02 N hydrofluoric acid was added in order to elute any remaining impurities, e.g. titanium, zirconium, hafnium and niobium. About 40 ml of this elutriant was sufficient for that purpose, according to the above-mentioned studies of separations of the same kind. The effluent was quite inactive, suggesting the absence of radioactive impurities of these elements at the time of the separation.

The radioactive substance was eluted by the addition of a solution composed of 9 N hydrochloric acid and 0.01 N hydrofluoric acid. The total volume of the elutriant necessary for eluting all the activity was about 800 ml, in agreement with what could be expected if the active element were tantalum. It must be pointed out that the elutriant had to be composed of just 0.01 N hydrofluoric acid as the elution constant(11) seems to have a maximum at that concentration in 9 N hydrochloric acid solution. The elution can indeed be carried out by a smaller volume of elutriant, but in that case the concentration of hydrofluoric acid must be inconvenientely high. Unfortunately there will usually be present rather much impurities in such large volumes of hydrochloric and hydrofluoric acids, if the acids are not pure to a very high degree.

For the samples used in the physical measurements the residue from the effluent evaporated to dryness was subjected to a purification process, including repeated evaporation to dryness with small amounts of hydrofluoric and sulfuric acids, and precipitations of insoluble hydroxides by ammonia before and after the separation of tantalum according to the procedure of HICKS and WILKINSON (10).

The chemical qualitative analyses. The analyses were carried out exactly according to the systems mentioned on page 251. For that reason this rather extensive work will not be described here. No particular difficulties or ambiguities arose. The elements added as carriers in the beginning of the analyses were: Cu, Ag, Au, Be, Mg, Ca, Sr, Ba, Zn, Cd, Hg, Sc, La, Ce, Y, Al, Zr, Th, Ge, Sn, Pb, V, Nb, Ta, As, Sb, Bi, Cr, W, U, Mn, Fe, Co, Ni, Ru, Pd, Os and Pt.

Other methods tried for the chemical separation. Before the anion exchange separation and the analyses were carried out, some other attempts were made to

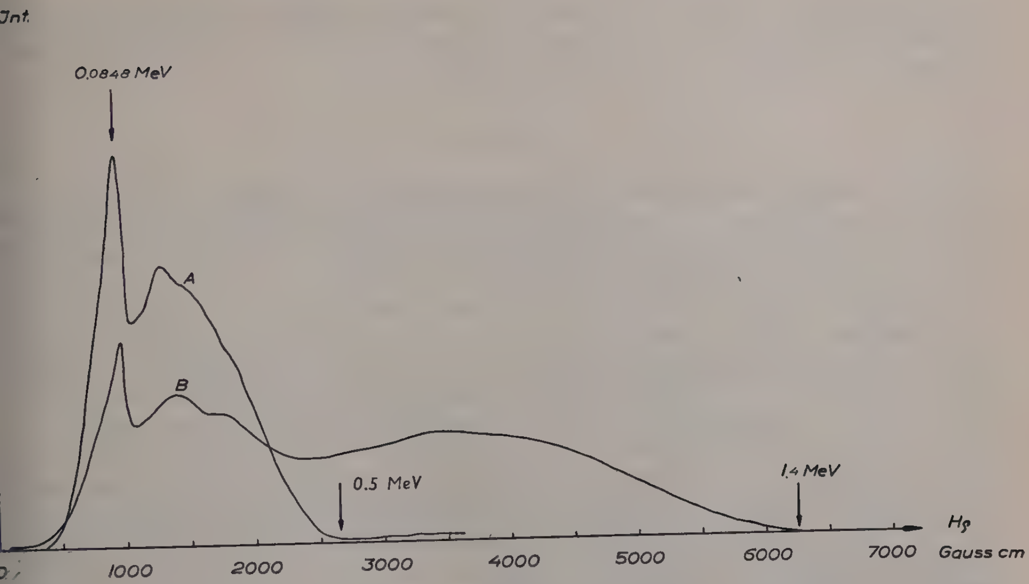

Fig. 1. β-spectra taken with the titanium(IV)oxide sample just after arrival from the pile-irradiation (B), and with the tantalum(V)oxide chemically separated from the titanium (A).

separate the radioactivity from the titanium, including the enrichment of the activity in the residue from the distillation of titanium(IV)chloride, and the separation of the active substance by cation exchanger. The first-mentioned method gave an enrichment factor of about 20. The method was inferior to the anion exchange separation, and for that reason it was abandoned. The experiments with cation exchange separation were unsuccessful.

β-spectrum

The original sample was used without any chemical operation for a preliminary study of the β-spectrum immediately after its arrival from Harwell. Because of low specific activity, a very thick sample had to be used. A conversion line appeared at about 85 KeV. The spectrum turned out to be complex, with maximum energies of 0.5 MeV and 1.4 MeV.

When the chemical method finally isolated the activity, it was thought worth while to study the β-spectrum of the separated activity, which had been shown to belong to tantalum. The spectrum agreed well with that taken 14 months previously except for the absence of the harder component. This component might be due to some other activity of shorter half-life.

The spectrum of the original sample and that of the separated tantalum show the major features of the β-spectrum of Ta^{182} reported by Beach, Peacock and Wilkinson (12), which were the occurrence of the strong line corresponding to conversion electrons of about 85 KeV energy, and the maximum β-energy of about 0.5 MeV. The other lines could not be established because of low intensity and high statistical error. In spite of this it is evident that the curves belong to the activity of Ta^{182}. Fig. 1 shows the β-spectra taken with the titanium (IV)oxide sample just after arrival from the pile-irradiation (B) and with the tantalum (V)oxide chemically separated from the titanium (A).

Remarks

An absorption measurement of separated tantalum(V)oxide gave a value for the maximum β-energy of about 0.40 MeV. The similarity of this value and those found by MANDEVILLE and SCHERB(7, 13) make it probable that the activity reported by them also belonged to impurities of tantalum.

The half-life of the irradiated titanium(IV)oxide sample was studied when 6 months had already elapsed after the bombardment. The decay was followed for 7 months and therefrom the half-life could be roughly established at about 115 days, which is in agreement with the values given in the literature for Ta^{182}.

From the thermal neutron cross section data for Ti^{50} and Ta^{181} given by SEREN, FRIEDLANDER, and TURKEL(5), it is to be expected that an impurity of 0.05 % of tantalum(V)oxide in a titanium(IV)oxide sample would be enough to explain all the activity found in that sample. MISKEL, DER MATEOSIAN, and GOLDHABER got an activity 10 times less than that expected from the cross section data. This would correspond to an impurity of only about 0.005 % of tantalum, which could hardly be detected by spectrographic analysis.

Nobel Institute of Physics, Stockholm 50, Sweden.

REFERENCES. 1. **J. A. Miskel, E. der Mateosian,** and **M. Goldhaber,** Phys. Rev. *79*, 193, 1950. — 2. **I. Bergström, S. Thulin, N. Svartholm,** and **K. Siegbahn,** Arkiv för fysik, *1*, 281, 1949. — 3. Inorganic Syntheses, Vol. II, lst ed., New York, 1946, p. 114. — 4. **H. Walke, E. J. Williams,** and **G. R. Evans,** Proc. Roy. Soc. A *171*, 360, 1939. — 5. **L. Seren, H. N. Friedlander,** and **S. H. Turkel,** Phys. Rev. *72*, 888, 1947. — 6. **R. E. Hein,** and **A. F. Voigt,** Phys. Rev. *74*, 1265, 1948. — 7. **C. E. Mandeville,** and **V. Scherb,** Phys. Rev. *73*. 141, 1948. — 8. **A. J. Vogel,** A Text-book of Qualitative Chemical Analysis, London, 1947. — 9. **A. A. Noyes** and **W. C. Bray,** A System of Qualitative Analysis for the Rare Elements, New York, 1943. — 10. **W. W. Meinke,** Chemical procedures used in bombardment work at Berkeley, Berkeley, 1949, p 73—2. — 11. **K. A. Kraus,** and **G. E. Moore,** Am. Chem. Soc. *73*, 913, 1951. — 12. **L. A. Beach, C. L. Peacock,** and **R. G. Wilkinson,** Phys. Rev. *76*, 1586, 1949. — 13. **C. E. Mandeville,** and **V. Scherb,** Phys. Rev. *73*, 656, 1948.

Tryckt den 6 februari 1952

Uppsala 1952. Almqvist & Wiksells Boktryckeri AB

ARKIV FÖR FYSIK Band 4 nr 16

Communicated 12 September 1951 by MANNE SIEGBAHN and ERIK HULTHÉN

A nuclear spectrometer for heavy particles

By CURT MILEIKOWSKY

With 10 figures in the text

Part 1. Design and construction of the instrument

Purpose and dimensions of the instrument

The need for a heavy particle spectrometer is evident if high precision is desired in the study of reaction products from nuclear transmutations. However, the requirements of an ideal spectrometer are partly contradictory. Broad energy region, high energy resolution and large solid angle are all important properties. It is also desirable to be able to measure the reaction fragments at different angles to the bombarding beam. These different demands introduce limits to each other.

The fragment energies which occur at high voltage proton or deutron bombardment of light nuclei fall in the region 0–20 MeV. Electrostatic deflection is practicable at low energies only. The same is true about the use of a magnetic "lens" for heavy particles, because of the difficulty of getting sufficient field strengths.

The necessary fields can be obtained between not too distant iron pole pieces. Semicircular focusing in homogenous fields can of course be used, with both target and detector in the field (1). Such an arrangement is specially suitable for the measurement of Q-values. As the bombarding beam must not be influenced by the spectrometer field, the beam must enter the field parallel to the lines of force and the Q-values be measured at 90° to the bombarding beam.

If, on the other hand, one wants to vary the angle between the bombarding beam and the outgoing particles to be detected, one can use a sector field with target outside the field, such that the stray field from the spectrometer along the path of the bombarding beam is negligible or can be made negligible by the aid of an iron screening tube. In this case the energy calibration becomes more difficult, because the particles have to pass the entrance and exit fields.

To enlarge the solid acceptance angle the instrument described here is designed to use double directional focusing. This principle was originated by SVARTHOLM and SIEGBAHN (2) in 1946 and has been used by them in a β-spectrometer. The Lauritsen group in Pasadena later applied it to a small heavy particle spectrometer (3) and recently to a large spectrometer.

The ideal pole piece surface would have a radial section lying on a parabola the vertex of which coincides with the axis of the spectrometer. In our instrument, however, where the gap (52 mm) is small compared to the mean radius (400 mm), conical surfaces have been preferred, having the same slope (1.80°) as that of the ideal parabola at mean radius (4). The choice of conical surfaces facilitates the

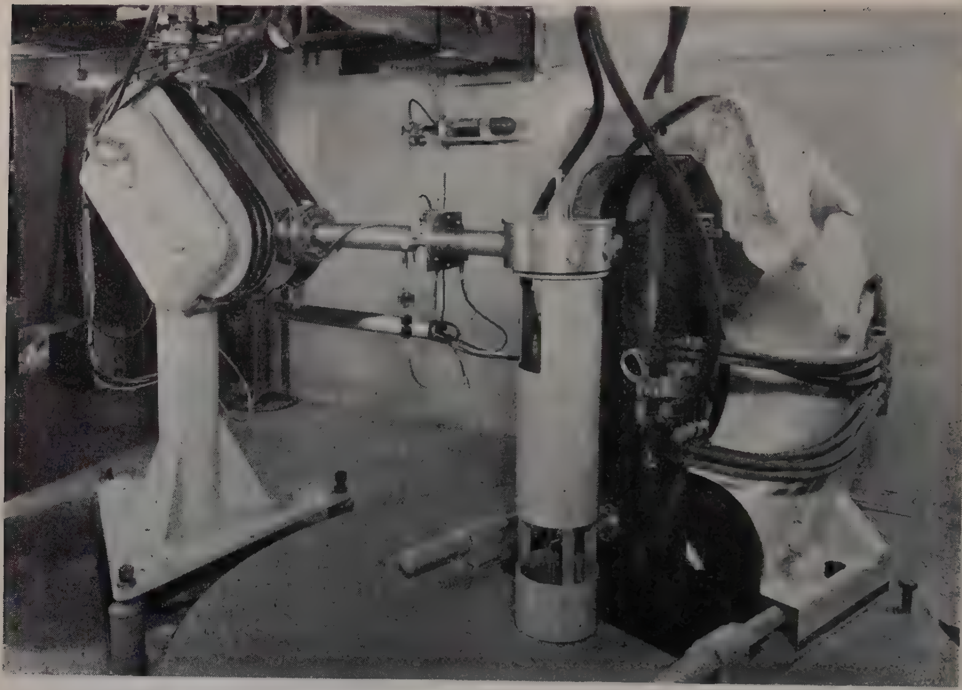

Fig. 1. General view of spectrometer arrangement in target room showing analyzing magnet for bombarding beam (left) and spectrometer connected to target chamber (right).

machining of the pole pieces although even conical surfaces are not easy to make with the accuracy desired.

The sector angle 180° has been chosen to facilitate the machining and mounting of the magnet.

For the purpose of resolution a mean radius of 400–500 mm is desired. To get a reasonable solid acceptance angle within the limits of reasonable cost a 40 to 60 mm gap is necessary, which in turn requires the pole pieces to be 120–150 mm broad. The pole piece surface will thus be 1 500–2 000 cm^2. If high field strengths are desired one cannot use a central core, because in such a case one wuold have to extend the core beyond the vertical diameter of the spectrometer in order to get adequate iron area, and large deviations in the field strength from rotational symmetry within the sector of 180° would occur as a consequence.

For this reason the magnetic circuit in the actual instrument is closed by means of a yoke outside the particle orbit instead of by a central core. Such an external yoke also reduces to a large extent the stray field around the magnet—another important advantage. The external yoke, however, requires more iron than a central core.

A field of 18 000 Gauss in the 5 cm gap requires about 45 000 Ampere-turns from each of the two coils. These coils are placed on the pole pieces inside the yoke, as indicated in Fig. 2. To save material in the yoke and the coils the cross section of the coils should not be larger than necessary. Very efficient cooling is therefore desirable and for this reason the coils are made of water cooled copper tubes. This

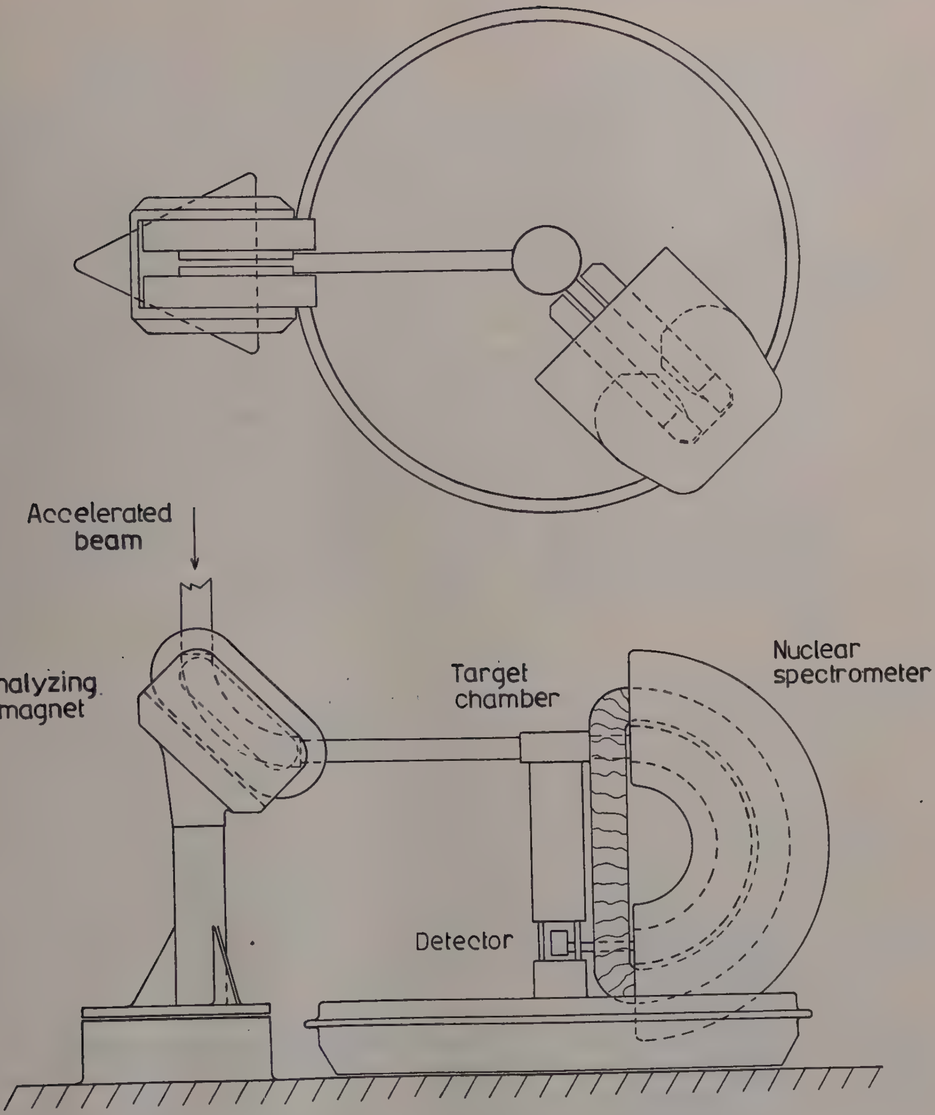

Fig. 2. Schematic diagram of spectrometer arrangement.

leads to a design with comparatively few turns and high current. The actual coils have 76 turns each and are dimensioned for a maximum current of 600 Amps. The resistance of the two coils in series is 0.1 ohm so the total voltage required for maximum current is not more than 60 V, which is an advantage, since it facilitates the insulation of the coil windings.

The magnet is mounted on a rotatable foot plate as indicated in Fig. 1 and Fig. 2, in order to make angular distribution measurements possible.

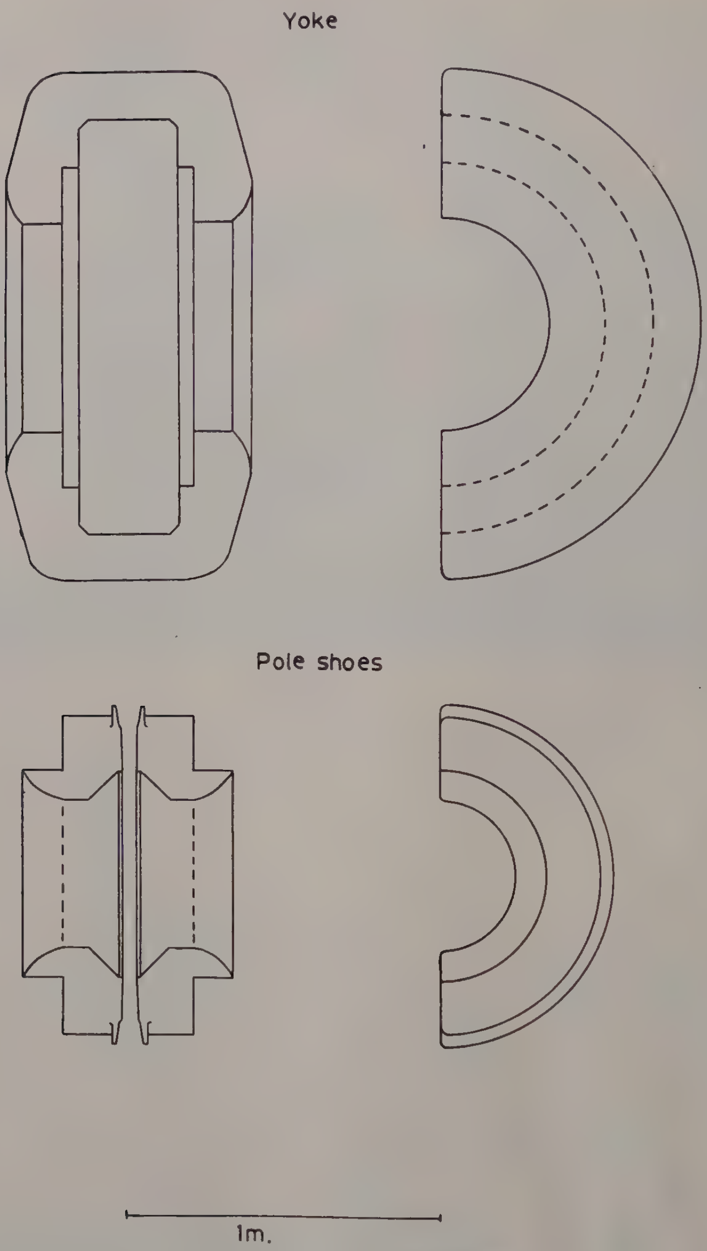

Fig. 3. Yoke and pole pieces.

The spectrometer is fed by a special motor-generator. The current can be varied continuously in the range 10–600 Amps, corresponding to a field range of 300–18 000 Gauss, and is electronically stabilized to ± 0.1 %.

Yoke and pole pieces

The magnet consists of three iron pieces, the yoke (3 300 kg) and the two pole pieces (2×500 kg). The design of the yoke and pole pieces is shown in Fig. 3. The pole pieces can be easily mounted and demounted. The magnet is thus a rather general one which can be modified for different uses in the field of nuclear physics.

The yoke and pole pieces are cast in soft iron (sgj 10 in Surahammar's nomenclature). A good soft iron is required to avoid distortion of the $1/\sqrt{r}$-field. The yoke has been machined in a vertical turning mill to the accuracy of a hundredth or a few hundredths of a millimeter. The pole pieces were planed along their diametral surfaces, then clamped together surface to surface and machined in a vertical turning mill.

The ideal way to finish the pole piece surfaces would be to machine them while screwed into position in the yoke. In that case, however the support of the tool cannot be made sufficiently rigid to avoid vibrations during the machining of the very soft iron, because of the restricted space available in the gap.

Instead, the finishing was done in the above-mentioned set-up with the two pole pieces screwed together forming a complete solid of rotation with one conical surface. This put the turner to a severe test. The result was very satisfactory. With the pole pieces mounted in the yoke the deviation from the "ideal" conical shape of the gap is every-where less than two hundredths of a millimeter. The planed surface of the yoke coincides with those of the pole pieces within a few hundredths of a millimeter. The machining was performed by Atlas Diesel.

Coils

The coils are made of copper tubes of square cross section ($10{,}5 \times 10{,}5$ mm^2) with a central hole of 6 mm diameter. Copper tubes of this kind are usually made in lengths of 7–8 m, but in this case Svenska Metallverken kindly manufactured lengths of 15 m, which reduces the number of joints necessary. The coils need about 400 kg of copper tubing.

The joints were made as indicated in Fig. 4. The holes of the joining ends were bored out so as to make room for a thin-walled internal guide tube 6 cm long. The joining ends were hardsoldered together with "Silfos".

The cross section of the coils is shown in Fig. 4. Each coil consists of five different windings connected in parallel for the cooling water but in series for the electric current.

The tubes, which are wound on a brass frame, are insulated with presspan and bound together with cotton and multiplex tape. The coils have been baked four times at about 120° C each time for 10 hours. During this baking the coils were impregnated with "Quick baking varnish clear" especially resistive against humidity. A fifth baking was performed with "Bakelite Ltd, R 1182" to obtain mechanical rigidity.

A section for baking tests in Fig. 5 shows how a coil is built up.

Each coil has an extra winding of 0.5 mm copper wire corresponding to about 500 extra ampere-turns. These windings are intended to be used for further stabilizing beyond the 0.1 % achieved by the electronical current stabilizer. They have not yet been used.

The coils were wound by SANDBLOM & STOHNE.

At maximum current, 600 Amps, the power to be cooled away from the coils is 36 kW. The total amount of cooling water passing through the coils is 12 l/min. at 2 kg pressure.

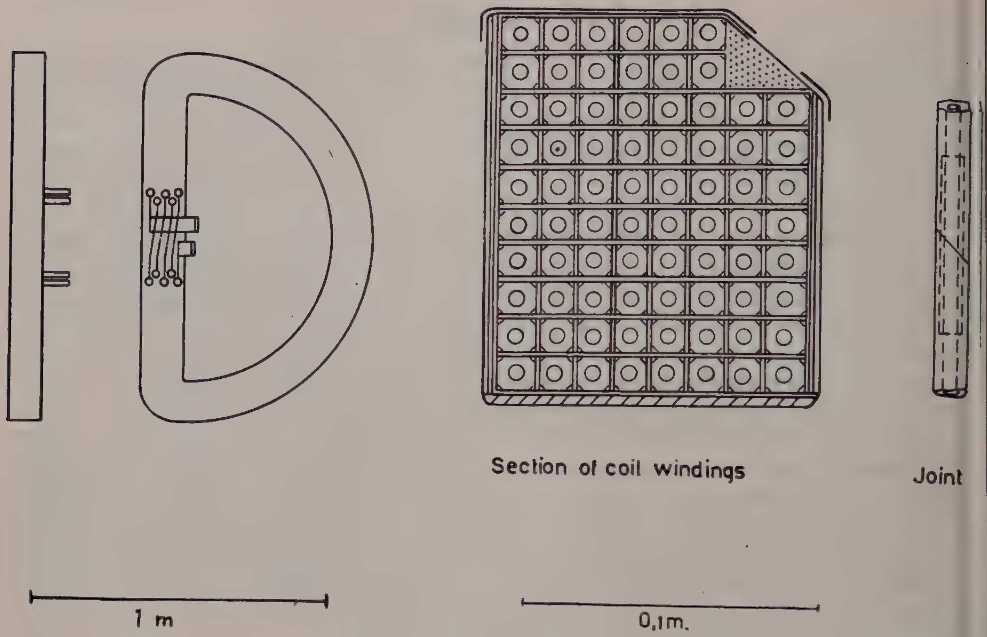

Fig. 4. Cross section of the coils.

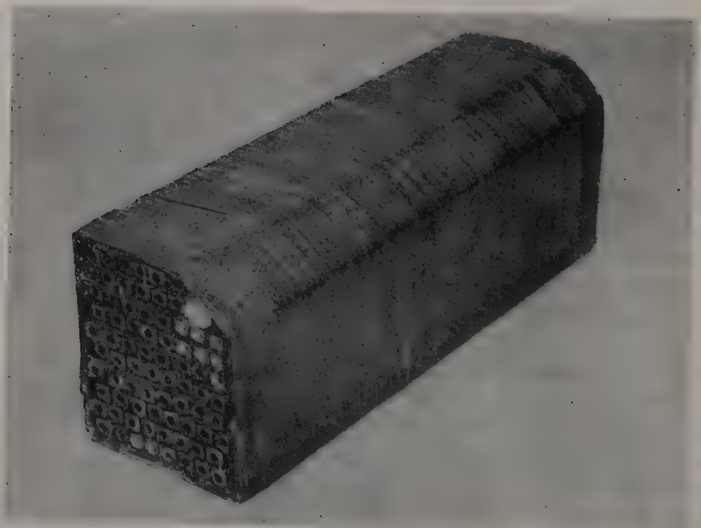

Fig. 5. Coil section for baking tests showing the interior of the coils.

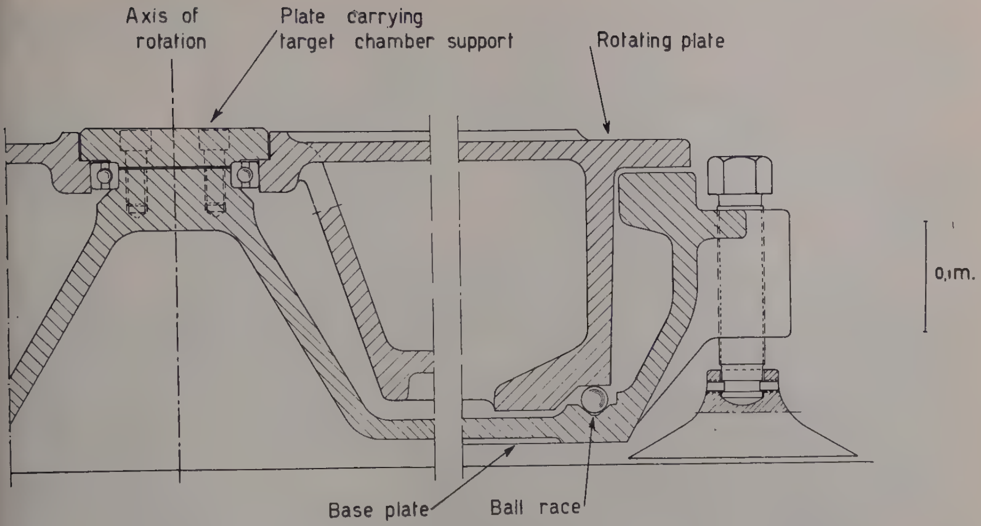

Fig. 6. Section of central and peripheral parts of the rotatable foot.

The rotatable foot plate

The foot consists of the rotatable plate on which the magnet is mounted and the base plate containing a circular ball race of 2 m diameter. Two hundred 1″ nickel balls carry the rotatable plate with the magnet. 1.4 tons of lead serve as counterweight to the spectrometer. This construction is sufficiently rigid, the relative movement between the target spot center and the symmetry plane of the magnet being always less than 0.2 mm, however the magnet is turned.

Both plates are made of cast iron. The magnet supports rest on brass plates, to prevent magnetic short-circuiting of the yoke.

The distance between the magnet and the axis of rotation can be adjusted by horisontal screws, which also serve to orientate the plane of symmetry of the magnet so that the axis of rotation falls in the plane of symmetry.

The axis of rotation can be made vertical by means of six adjusting screws carrying the base plate. A non-rotating plate in the center of the foot carries the brass support for the target chamber. (Fig. 6.)

The motor-generator equipment

The power to the magnet is delivered by a motor-generator constructed by ASEA for this purpose.

The generator is a LB 50 DC generator, 60 V, 600 A, 1465 r/m, with a magnetizing LD 8 DC-generator, 0.5 kW, 115 V.

The motor is a MKB short-circuited 3-phase motor, 42 kW, 220 V, D-coupled, 1465 r/m, 50 c/s.

They are mounted on a common base plate, firmly moulded into the concrete floor of the machine room.

The machine is started by a remote control KDEA 200 star-delta switch.

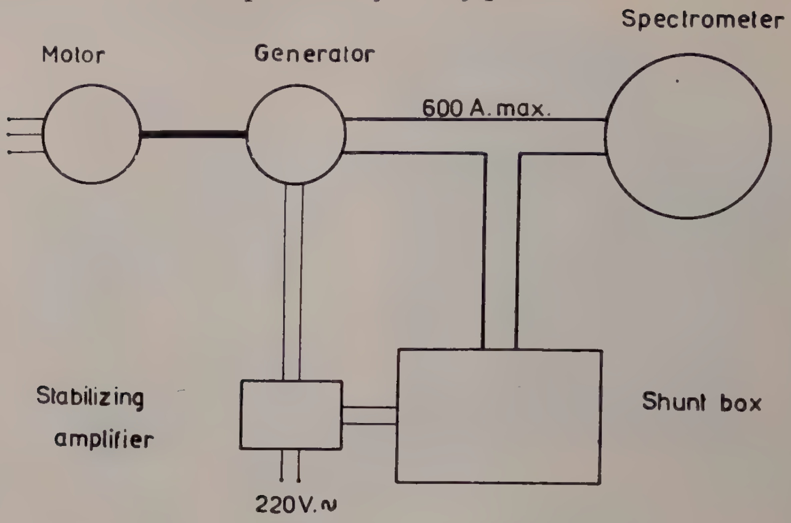

Fig. 7. Block diagram of the electric circuits.

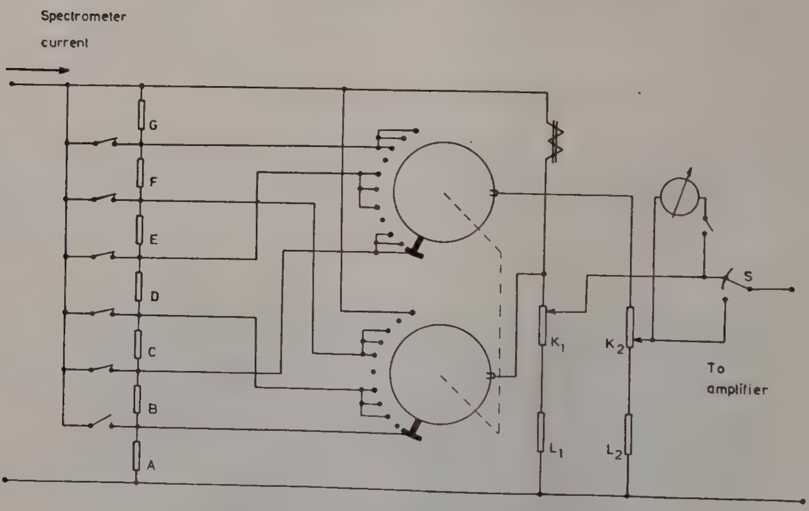

Fig. 8. Circuit diagram of the shunt box.

The regulating and stabilizing device

The block diagram of the regulating device is shown in Fig. 7. The stabilizing amplifier controls the exciter of the generator. The range of current regulation is 10–600 Amps.

The current to the spectrometer passes through seven resistors in series, A, B, C, D, E, F and G in the shunt box, Fig. 8. Each of them has a resistance which is equal to the sum of the preceeding resistances. Each one of the resistors, except A, can be short-circuited by a knife-switch.

In the highest energy region, 600–300 A, all the knife switches are closed and the stabilizing amplifier "feels" the voltage over the resistance A. By varying the

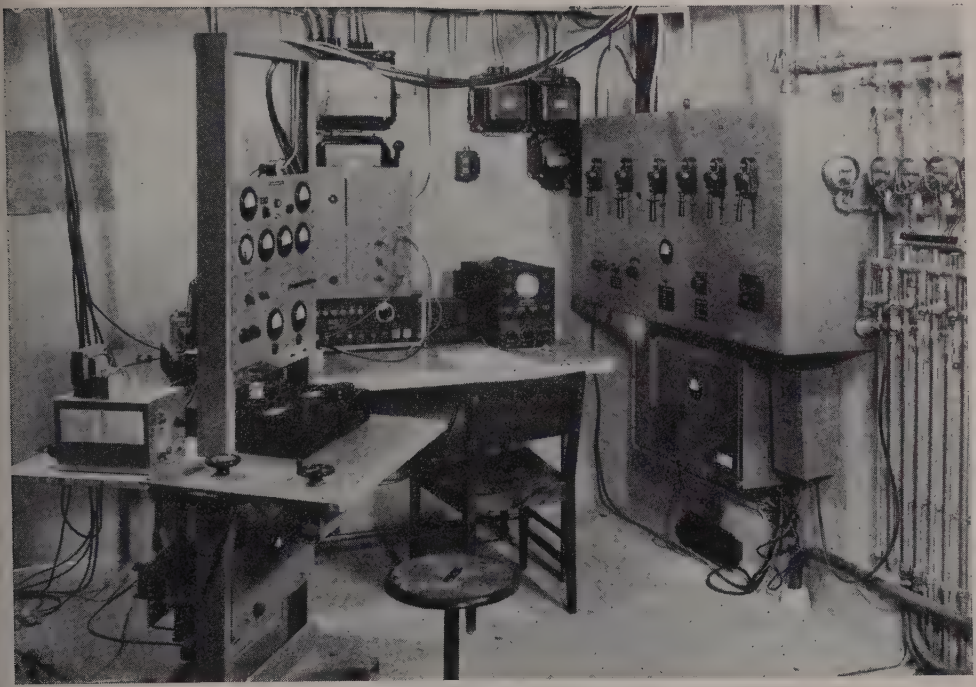

Fig. 9. Control room.

potentiometer K one covers the current range in question. In the next lower current range the stabilizing amplifier feels the voltage over A + B, and so on.

To avoid hysteresis effects in the spectrometer it is necessary to avoid a jump in magnetizing current when switching from one current range to another.

This is achieved by aid of a double potentiometer system as indicated in Fig. 8. The maximum value of K is made slightly greater than L, so that the ranges overlap. The two potentiometers can be set before switching in such a way that both correspond to the same value of magnetizing current, and it is thus possible to use a non-disconnecting switch for the transfer.

Shunt box and amplifier are shown to the right in the picture of the spectrometer control room, Fig. 9.

The stabilizing amplifier has a preamplifier (120 mV input, 45 V output) with vibrator input and strong negative feedback. The output from this amplifier is balanced against a dry battery (45 V) and the voltage difference regulates the output stage which is an ASEA standard amplifier for current stabilizers.

The vacuum chamber

The vacuum chamber, the cross section of which is shown in Fig. 10, is semicircular. It was made in the following way.

Two copper bars of cross section 8 × 54 mm² and 8 × 46 mm² were bent to semicircular form with the radii 460 mm and 340 mm. They form the outer and inner walls of the chamber. A circular 4 mm brass plate (⌀ 920 mm) with a central hole (⌀ 680 mm) was pressed to slightly conical shape and cut along a diameter. The

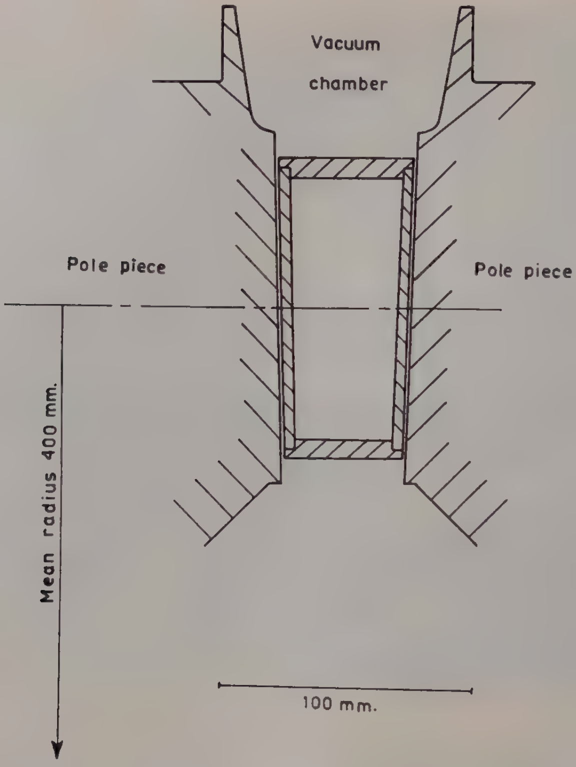

Fig. 10. Cross section of the vacuum chamber.

two halves were hardsoldered to the copper walls. Flanges were soldered to the ends of the chamber and the chamber was electrolytically covered with a 0.1 mm layer of copper.

Acknowledgements. Although the description of the spectrometer is not complete until Part II is published I want to take this opportunity to thank Professor Manne Siegbahn for his interest in this work.

Thanks are also due to ASEA, especially to Dr. L. Dreyfus and Ing. E. Ladell for their important technical contributions and to Surahammar AB, Atlas Diesel AB, Svenska Metallverken AB and Sandblom och Stohne AB for agreeable cooperation. Svenska Atomkommittén granted this work.

Nobel Institute of Physics, Stockholm 50, Sweden.

REFERENCES. 1. **Buechner, W. W., Strait, E. N., Stergiopoulos, C. G., and Sperduto, A.,** Phys. Rev. *74*, 1569 (1948). — 2. **Svartholm, N., and Siegbahn, K.,** Ark. f. Fys. Bd *33 A*, nr 21 (1946). — 3. **Snyder, C. W., Rubin, S., Fowler, W. A., and Lauritsen, C. C.,** Rev. Sci. Instr. *21*, 852 (1950). — 4. **Svartholm, N.,** Ark. f. Fys. Bd *2*, Nr 14 (1950).

Tryckt den 6 februari 1952

Uppsala 1952. Almqvist & Wiksells Boktryckeri AB

ARKIV FÖR FYSIK Band 4 nr 17

Communicated 10 October 1951 by MANNE SIEGBAHN

The motion of electrons in the field of a homogeneously winded toroid

By SVEN GÖSTA NILSSON

With 3 figures in the text

The focusing properties of the toroid are investigated for the use of it as a beta-spectroscope or as a device for space focusing in a more complicated spectroscope.

We assume a winding carrying an electric current to be distributed homogeneously along the whole surface of a toroid. Expressed in cylindrical coordinates in accordance with Fig. 1 the field inside the toroid can be easily determined:

$$B = B_\varphi = \frac{\text{const}}{r} = \frac{B_0\, r_0}{r}.$$

The field is thus constant in the φ- and z-direction as long as we stay inside the toroid.

We further assume a β-radioactive point source to be placed inside the toroid at $r = r_0$, $\varphi = 0$, $z = 0$. The limits for the angles of injection will be determined by an entrance slit. Possible directions inside this entrance slit will be described by the parameters ξ and η, where ξ and η both measure deviations from the tangent at the point of injection, ξ in the z-direction, η in the r-direction. (Fig. 2.)

The relativistic equation of motion reads

$$\frac{d}{dt}\left(\frac{m_0\,\bar{v}}{\sqrt{1-\frac{v^2}{c^2}}}\right) = -e\,\bar{v} \times \bar{B}$$

where $\bar{v}$ is the velocity vector and $-e$ the charge of the electron. From this equation it is immediately apparent that $|\bar{v}| = \text{const.}$ is a solution. (The Lorentz force performs no work.) The relativistic mass $\frac{m_0}{\sqrt{1-v^2/c^2}} = m$ can thus be brought outside the differential operator $\frac{d}{dt}$, and the classical formulae are formally regained.

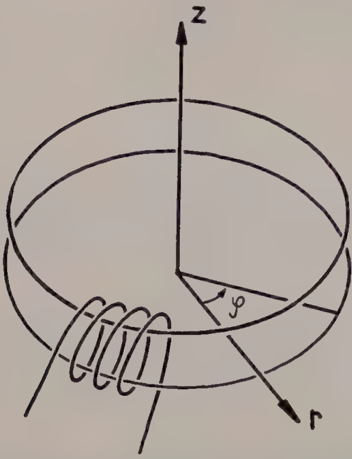

Fig. 1. The orientation of the cylindrical coordinate system in relation to the toroid.

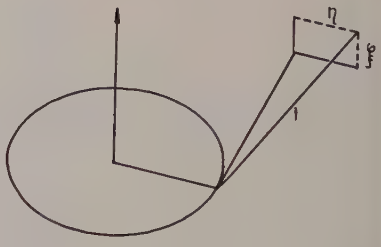

Fig. 2. The significance of the parameters ξ and η as determining the direction of the initial ray.

Introducing new variables

$$\varrho = \frac{r}{r_0}, \quad x = \frac{z}{z_0}, \quad \tau = \frac{e\,B_0}{m} \cdot t, \quad a = \frac{m\,v_0}{e\,B_0\,r_0}$$

the equation (resolved into its components) can be rewritten

$$\ddot{\varrho} - \varrho\,\dot{\varphi}^2 = \frac{1}{\varrho}\dot{x} \tag{1}$$

$$\frac{1}{\varrho}\frac{d}{d\tau}(\varrho^2\,\dot{\varphi}) = 0 \tag{2}$$

$$\ddot{x} = -\frac{\dot{\varrho}}{\varrho} \qquad \text{where } \dot{\varrho} = \frac{d\varrho}{d\tau} \text{ etc.} \tag{3}$$

The initial conditions on those equations are

$$\begin{aligned} \varrho(0) &= 1 & \dot{\varrho}(0) &= \alpha\eta \\ \varphi(0) &= 0 & \dot{\varphi}(0) &= \beta = \alpha\sqrt{1-\xi^2-\eta^2} \\ x(0) &= 0 & \dot{x}(0) &= \alpha\xi. \end{aligned}$$

An equation containing only ϱ and its derivatives with respect to τ, can be obtained by integrating (2) and (3) once and substituting into (1)

$$\ddot{\varrho} = \frac{\beta^2}{\varrho^2} + \frac{\xi\alpha - \log\varrho}{\varrho}. \tag{4}$$

As the right hand side of this equation is the derivative of a function having a single maximum and tending monotonously towards $-\infty$ on both sides of this maximum, it is easily found that the solutions of this equation are *periodic* in τ.

The approximate solution of the differential equation (4).

The periodicity of the solutions proved, we now proceed to look for approximate solutions of the equation. We put

$$\varrho = 1 + f, \tag{5}$$

and assume the field to be strong enough so that $|f| \ll 1$. This condition is equivalent to α being sufficiently small.

We substitute (5) into (4), expand in powers of f, eliminate the constant term in the expansion by a new substitution $f = y + a$, and obtain, admitting terms up to the order y^3 only:

$$\ddot{y} + w^2 y = b y^2 + d y^3 \tag{6}$$

where w^2, b and d are all of order 1 if $|\xi|_{\max} |\eta|_{\max}$ and α are assumed small of order 0.1.

This equation (6) is now tackled by a modification of the Lindstedt-Poincaré method.

The method referred to, is applicable to an equation of the form $\ddot{y} + w^2 y = b y^2$, where, however, $|b|$ is to be $\ll 1$. Apart from the existence of a second term on the right side of the equation the main difficulty is the condition $|b| \ll 1$. This can be fullfilled by an artifice. We can prove $|y|$ to be small of the order α^2 and substitute $y = x q$, where $q \sim \alpha^2 \ll 1$. (6) now takes the form

$$\ddot{x} + w^2 x = b q x^2 + d q^2 x^3. \tag{7}$$

We then write, expanding in powers of q

$$x = x_0 + q x_1 + q^2 x_2 + \cdots$$
$$w^2 = w_0^2 + q w_1^2 + q^2 w_2^2 + \cdots$$

The rapidity with which we obtain satisfactory values on w_0^2 and x depends on the smallness of q.

We admit terms only to the order α^2. The real power of the method, however, is apparent first when higher approximations are aquired.

Determination of the focusing angle Φ.

We use expression (2), integrate once and expand in powers of f, insert the expression found above, and finally integrate over a whole period $\tau = \dfrac{2\pi}{w_0}$. For the integrated expression, we use the notation Φ_τ.

The ray corresponding to the central ray in ordinary lenses is not the "tangential" ray with initial conditions $\xi = 0$, $\eta = 0$. Instead $\xi = -\alpha$, $\eta = 0$ gives the solution $\varrho = \text{const} = 1$, $x = \text{const} \cdot \tau$.

Here the Lorentz force compensates the "centrifugal force". We define the Φ_τ corresponding to this latter ray as the focusing angle Φ.

$$\Phi = 2\pi\alpha\left(1 - \frac{3}{2}\alpha^2\right). \tag{7}$$

The magnitude of the field or the value of α thus essentially determines the magnitude of Φ.

The form of the image in a plane through the z-axis at the angle Φ is then derived.

ϱ and x are determined by Taylor expansions from points on the respective rays corresponding to the respective Φ_τ:s

$$\varrho_\Phi = \varrho_{\Phi_\tau} + \dot{\varrho}\,\Delta\tau + \cdots$$

where $\Delta\tau$ is determined from

$$\Phi - \Phi_\tau = \dot{\varphi}_{\Phi_\tau}\,\Delta\tau + \tfrac{1}{2}\,\ddot{\varphi}_{\Phi_\tau}\,(\Delta\tau)^2$$

x is determined anlogously. The final expression for x is:

$$x_\Phi = \pi\alpha\left[-2\alpha + \alpha^3 + \xi'\left(\xi'^2 + \eta^2 - 2\alpha^2\right)\right], \quad \text{where } \xi' = \xi + \alpha. \tag{8}$$

At this point it is to be noticed that beside the sine-oscillation in x there is a constant drift, to the second order independent of the initial x-velocity. This drift is opposite in direction for electrons and positrons — a property which makes the apparatus useful for instance for the study of γ-rays via pair creation.

Form of entrance slit. The resolving power without regard to the finite dimensions of the source and the counter slit.

x is now considered as function of the parameters ξ and η. The form of the entrance slit determines the limits of variation of the latter. The slit form is chosen to make $T/\Delta x$ maximum, where T signifies the transmission and Δx the total variation in x.

The best form of the entrance slit is shown by the egg-shaped line in Fig. 3. The dotted curves are the locus of rays exactly at focus in Φ. The signs + and — signify the "landscaping" of the $x(\xi, \eta)$-surface.

Under these conditions the transmission $T = \alpha^2\,\%$, and the "base spread"

$$\mu_0 = \frac{\Delta\varrho_0}{\varrho}\left[\text{or } \frac{\Delta(H\varrho)}{H\varrho}\right] \simeq \tfrac{1}{2}\,\alpha^2.$$

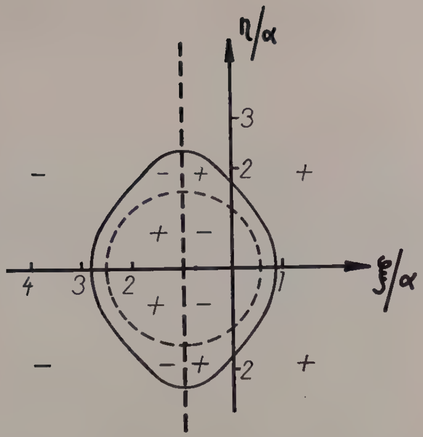

Fig. 3. The eggshaped curve shows the optimal form of the entrance slit as function of the parameters of injection. The dotted curves signify the ξ, η-locus of rays exactly confocal with the central ray. The signs + and − denote the level of x in relation to x_0 of the central ray.

The "spread" μ or the relative half width of the line is of the order $1/2\ \mu_0$, and the resolving power $R = \frac{1}{\mu}$.

Table I.

a	T	μ	R	Φ
0.1	1 %	1/2 %	400	35°
0.2	4 %	2 %	100	68°
0.2[1]	1 %	1 %	200	68°

Calculations are in progress on the problem of combining the toroid with a spectroscope of the flat type for obtaining double focusing of a high order.

My thanks are due to Professor Kai Siegbahn for kindly suggesting the problem and supervising the work.

---

[1] Signifies another entrance slit then the optimal one.

Tryckt den 30 januari 1952

Uppsala 1952. Almqvist & Wiksells Boktryckeri AB

ARKIV FÖR FYSIK Band 4 nr 18

Communicated 12 September 1951 by ARNE WESTGREN and ROLF SIEVERT

Quantitative measurements of low dose-rate roentgen rays in terms of the international *r*-unit by closed ionization chambers

By R. THORÆUS

With 5 figures in the text

In an institute which like the Institute of Radiophysics is officially commissioned to inspect periodically the physical factors of dosage in roentgen therapy, and the protection in radiological work (1), it is of fundamental importance to have reliable instruments for quantitative measurements of the radiation. As far as roentgen rays are concerned, the measurements are based on the international *r*-unit. The use of this unit requires a standard open air ionization chamber designed in accordance with the directions in the definition of the unit. Such a chamber was accordingly designed by the author in 1931 (2). It was provided with a complete 200 kV constant potential roentgen installation. Together they form the fundamental equipment of the standard laboratory. An improved modification of the standard chamber was later designed (3). With such instruments quantitative radiation measurements, and calibrations of other instruments, both in terms of the *r*-unit, can be made to an accuracy of about ± 1 per cent, if all precautions are taken.

Measurements of effective doses or dose-rates are mainly met with in most clinical, experimental and practical radiological work. The use of the *r*-unit in such work thus provides not only a standard open air chamber, but, supplementary to this, secondary standard chambers, usually constructed as closed ionization chambers of various types and sizes. The working principle of closed chambers, however, is not in accordance with the definition of the *r*-unit. For this reason their measuring properties cannot be safely foreseen which in turn makes their design and construction both difficult and time-consuming.

The most difficult problem in constructing closed chambers usually is to get the ionization effect in a constant proportion to that of a standard open air chamber over a wide range of radiation qualities (wavelength independence). During many years, a great amount of research work has been devoted to this problem, yet a generally valid solution, or construction principle, the use of which always guarantees a perfect wavelength independence has not been found. On the other hand, it is long known that many factors, such as the materials used, the geometrical form, and the dimensions of the chamber are included in the problem, and thus must be carefully considered and balanced against each other. As a rule many trials have to be made before an acceptable result finally may be attained.

Another difficult problem in the construction of closed chambers is to get the ionization effect independent of the direction of the incident beam in relation to the longitudinal axis of the chamber. For constructional reasons it has not been possible to construct a closed chamber of complete direction independence for all radiation qualities. Particularly when the chamber is provided with a metal collar or ring at its base, and is irradiated through the base or stem by radiations of low or moderate penetrating power, an increased absorption occurs, and thus reduces the ionization produced in the air volume enclosed. However, in the construction of closed chambers the widest possible direction independence for the range of radiation qualities considered is always strived for, and in most cases reasonable requirements may be satisfied.

The calibration of a closed chamber against a standard open air chamber serves to verify its measuring properties and their constancy, and to define the ranges of radiation qualities and angle in which it is wave length and direction independent, and thus may safely be used. If we take into consideration that roentgen ray qualities of half-value-layers from about 0.02 mm Al in superficial, short-focal distance therapy, up to about 2 mm Cu in ordinary deep therapy, and up to about 9 mm Cu in the supervoltage range of deep therapy are in use today, and that dose-rates from about 10^{-5} to 10^{4} r per minute are to be measured, it may easily be understood that the problem of measuring effective doses and dose-rates in roentgen therapy, and at inspections of the protection in radiological work, sufficiently accurately in terms of the r-unit is very extensive. For these reasons and because of its fundamental importance the problem needs continuous attention. It has, however, not been possible to cover these wide ranges of radiation qualities and dose-rates by a single design of secondary standard chamber, thus various types have been developed.

When the first standard open air chamber of the Institute of Radiophysics had been completed, the next step was to construct an instrument for use as a secondary standard, and to provide it with chambers of suitable types. At that time condenser dose meters of various types, SIEVERT (4), and of satisfactorily high electrostatic insulation, had been in use for some years, and proved both convenient and reliable, if properly constructed for the purpose considered. A specially adapted variant of condenser dose meter was then designed by the author (5). In principle it consists of various types of separate ionization chamber units, provided with a suitable number of interchangeable additional capacitors. The ionization chamber unit is the fundamental part of the measuring instrument. By the construction described each chamber unit may be used separately and, with or without an additional capacitor, calibrated against a standard open air chamber. This in turn makes the experimental investigation of the measuring properties of each unit very convenient. The function of the additional capacitor is simply to reduce the sensitivity of the chamber unit used to the level required by the actual conditions. By this design it was found possible to construct a convenient secondary standard instrument of extensive wavelength and direction independence, the sensitivity of which could easily be changed within wide limits.

Later it was found possible, by using a simple design and easily accessible, pure materials to construct a small, closed chamber unit able to serve as a portable substitute for the standard open air chamber (6). In calibrations, the sensitivity of this chamber unit was found to be $k = 7.3 \times 10^{-3} \pm 2.5$ per cent. This value gives the amount of radiation in r-units producing a drop of one volt in the difference in the electrode potentials of the chamber, and was obtained with roentgen tubes the inherent filtration of which was equivalent to 0.2 mm Al or more, with additional filters from 0 to 4 mm Pb, and with tube-voltages from 10 to 400 kV. This corresponds to roentgen rays of half-value-layers between about 0.04 mm Al and 7 mm Cu. By an additional capacitor the sensitivity may easily be reduced to about 0.4 *r* per volt. For constructional reasons the direction independence of this chamber was expected to be very narrow. From experiments it was, however, found that a zone of 0–15° around the axis of the chamber is perfectly safe. This favourable result makes this chamber a very convenient substitute for a standard open air chamber; it is accordingly used very much, particularly in calibrations.

In studying the absorption of roentgen rays in various materials to determine their efficacy in protective barriers, and in calibrating instruments intended in particular for the measurement of small doses or very low dose-rates of roentgen rays, the sensitivity of the chamber units used must, however, be very high. Since the highest degrees of sensitivity cannot, as a rule, be attained with chambers of the usual size (ionized air volumes of a few cm³), that volume must be more or less increased.

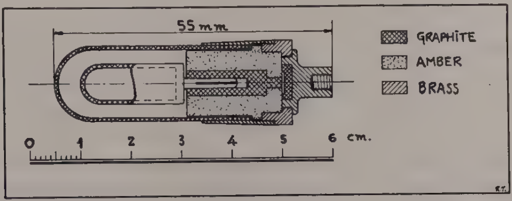

Fig. 1. Construction of small size thimble chamber unit.

In a previous paper (7) the author has described the construction and properties of a rather small thimble graphite chamber unit (ionized air volume about 4 cm³). For the reader's convenience the constructional details of this chamber are illustrated in Fig. 1. In calibrations the average sensitivity of this unit was found to be $k = 9.7 \times 10^{-3} \pm 4$ per cent. This value gives the amount of radiation in *r*-units producing a drop of one volt in the difference in the electrode potentials of the chamber, and was obtained with a roentgen tube the inherent filtration of which was equivalent to 0.6 mm Al, with additional filters of not less than 0.5 mm Al, and with tube-voltages from 50 to 165 kV constant potential. This corresponds to half-value-layers from 1.1 mm Al to about 1.6 mm Cu. Another copy of this chamber unit was later found to be wavelength independent up to 400 kVp, corresponding to a half-value-layer of 4 mm Cu. The calibration result shows that this chamber is sufficiently wavelength independent safely to be used for measuring doses and dose-rates at all radiation qualities met with in ordinary roentgen diagnostics and therapy.

The calibration result given above was obtained with the incident beam directed square to the longitudinal axis of the chamber. To investigate the direction independence, the chamber was positioned at various angles between the direction of the beam and that axis. At each position the entire chamber was irradiated, and the exposure time was always the same. The result obtained is graphically illustrated by the diagram in Fig. 2. As may be seen the direction independence is fairly good

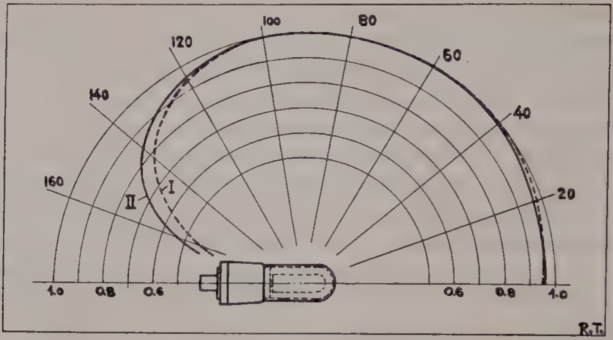

Fig. 2. Direction independence of the thimble chamber unit in Fig. 1.

Curve I obtained with an incident beam of HVL = 1.8 mm Al
» II » » » » » » » = 0.9 mm Cu.

within angles of 0–120° from the top against the base of the chamber. By integration in the diagram an average of 0.98 is obtained for the range 0–140°, and 0.94 for 0–160°. From the result it may be concluded that these measuring properties of the chamber unit are in fairly good accordance with what may be reasonably required for the purpose in question.

This type of chamber unit can easily be provided with an additional capacitor reducing the sensitivity to about 0.3 or 0.6 *r* per volt. Such a unit has proved to be a very suitable secondary standard for dosage measurements in ordinary roentgen therapy, and is accordingly used for this purpose. On the other hand, the sensitivity may be raised to about $10^{-3}\,r$ per volt, by reducing the diameter of the inner electrode, and the length of the insulator.

It was subsequently found, however, that a sensitivity of this order of magnitude was not sufficient for certain purposes, e.g. for inspection measurements behind ordinary protective walls, in which the dose-rate commonly is of the order of magnitude of 10^{-6} *r* per second. It was further considered desirable to construct the instrument of common and easily obtainable materials, to simplify the design as much as possible in order to facilitate the manufacture and so reduce the cost of production, and also to increase the range of direction independence. An instrument adapted to these requirements was first designed early in 1943, but some improvements have since been introduced. The latest design is briefly described below, and its most important measuring properties are demonstrated by the calibration results.

Fig. 3 shows the design and dimensions of this type of chamber Its ionized air volume is about 563 cm³. The hollow aluminium plug at the base of the chamber may be unscrewed to allow the difference in the potentials of the inner electrode and the outer shell to be measured, or charged to a desired value.

The measuring properties were studied by extensive calibrations, and the main result finally attained is given in table 1. Primary radiation as well as secondary radiation scattered from a wax-phantom were both used in the calibration to verify that this instrument can safely be used in special calibrations as well as inspections of the protection in ordinary roentgen therapy and diagnostics.

The calibration result does not show any systematic changes of the sensitivity

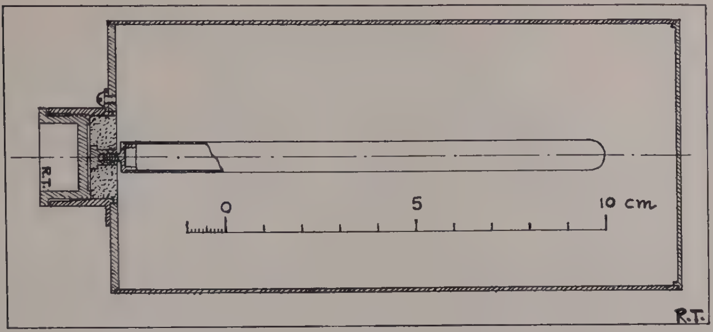

Fig. 3. Construction of high sensitivity chamber unit.

due to quality of the radiation, and we may therefore be justified to use the average value $k = 2.55 \times 10^{-5}$ r per volt. Using this value over the whole range of radiation qualities investigated, the maximum error introduced will be ± 3.5 per cent. The chamber to which the calibration result in table 1 refer, is accordingly used as a sub-standard by which other instruments for routine inspections of protection are calibrated. For example, the calibration of the leakage detector proviously described (Acta Radiol., Vol. 33, 1950, p. 305) was made possible by that sub-standard.

In regard to the wide range of qualities used in the calibration (half-value-layers from about 0.8 mm Al to about 8 mm Cu) the error found may be considered relatively small, and in most cases of no practical significance. Studies of biological reactions of the human body produced by roentgen rays, for instance various degrees of skin

Table 1. Calibration results.

Additional filter[1] mm	Tube-voltage	k (r per volt)	Radiation used
7 Pb	400 kV half-wave	2.63×10^{-5}	Primary radiation obtained with the tube-voltage and filtration given.
1 Pb	165 kV const.pot.	2.57	
Tin-filter	165 »	2.53	
0.5 Cu	165 »	2.57	
4 Al	145 »	2.56	
1 Al	100 »	2.52	
0	70 »	2.56	
0	50 »	2.45	
0	50 kV const.pot.	2.62	Secondary radiation from a wax-phantom irradiated by a primary beam obtained with the tube-voltage and filtration given.
0	40 »	2.50	
Average k-value 2.55×10^{-5} r per volt ± 3.5 per cent.			

---

[1] The inherent filtration of the roentgen tube used at 400 kVp was equivalent to 0.6 mm Cu. At the remaining tube-voltages another tube was used the inherent filtration of which was equivalent to only 0.95 mm Al.

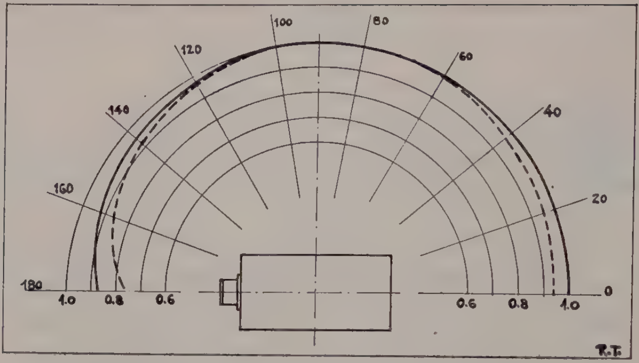

Fig. 4. Direction independence of the chamber in Fig. 3.

erythema, have shown that a change of 5 per cent in the dose received by the skin, other conditions being the same, does not perceptibly affect the reaction.

The calibration result given in table 1 was obtained with the incident beam directed square to the longitudinal axis of the chamber. To investigate the direction independence, the chamber was positioned at various angles between the direction of the beam and that axis. At each position the entire chamber was irradiated, and the exposure time was kept the same. The result obtained is graphically presented in the diagram in Fig. 4. The dotted curve was obtained with the radiation excited by a tube-voltage of 70 kV constant potential and using a total filtration of 5 mm Al, which corresponds to a half-value layer of about 3.4 mm Al. The solid line curve was obtained with the relatively hard radiation excited by a tube-voltage of 170 kV constant potential, and using an additional filter of 1 mm Pb. From the diagram it is seen that the much wider direction independence which, for constructional reasons, may be expected in this type of chamber, is clearly verified by the experiments.

From a large number of observations the total rate of leakage produced by the conduction in the insulator, and the ionization due to the natural radiation was found to be fairly constant, amounting to about 3 volt per hour when the chamber was charged to a difference in the potentials of the electrodes of about 260 volt. Whenever required, that leakage may be corrected for. If the total rate of leakage were entirely due to ionization, it would correspond to a dose-rate of $2.1 \times 10^{-8}\, r$ per second, or about 44 pairs of ions per cm³ per second. A usual value of the natural radiation is about 25 pairs of ions per cm³ per second. As may be expected, the total rate of leakage in the chamber is somewhat higher than that. The leakage produced by the conduction in the insulator is, however, smaller than that produced in the air volume by the natural radiation.

Owing to its simplified design, this chamber is not very expensive, and may easily be manufactured in series of any desired number, all with very nearly identical properties. Years of experience have clearly demonstrated that this chamber is not particularly susceptible to transport vibrations, and may thus be conveniently used both in laboratory measurements and for routine inspection work. No special care need be taken beyond that ordinarily required in handling measuring instruments.

The electrometer used by the author for reading condenser chambers (3) is usually adjusted to the moderate sensitivity of about 2.5 volt per scale division, and allows the difference in the potentials of the chamber electrodes to be read within less than 1 volt. The drop in potential difference between the electrodes of the condenser chamber used should accordingly be at least 30 volts if a measuring result of satisfactory accuracy is to be obtained. In the chamber described here a dose of about $7.6 \times 10^{-4}\, r$ would be required to produce a drop of 30 volts. If the maximum permissible daily dose for workers in radiological work is assumed to be 0.02 r, 2 hours of exposure daily corresponds to a dose-rate of $2.8 \times 10^{-6}\, r$ per second. A drop of 30 volts will thus require an exposure time of 270 seconds or 4.5 minutes. Assuming 4 hours of operation daily, the exposure time required would be 9 minutes. If a number of these chambers are available for routine inspection work, it is convenient to make simultaneous measurements at various points, using exposure times of 2–10 minutes. Under these conditions corrections for leakage are not required.

Assuming the charging potential to be 260 volts, and the residual potential difference to be at least 100 volts, to be sure of having saturation current, a maximum drop of 160 volts is available. This corresponds to a maximum dose of $4 \times 10^{-3}\, r$. If that maximum drop is obtained by exposure times of less than one minute, a charging potential higher than 260 volts may be used. Besides that, the sensitivity of the chamber may be independently and conveniently reduced by unscrewing the aluminium plug and adding a suitable capacitor. The capacitors normally used with the secondary standard ionization chambers for ordinary dosage measurements may also be used for this purpose.

In condenser chamber units intended to be worn by workers in radiological work to measure the amount of radiation received, the demand for sensitivity is not so high as that indicated above. If we assume a maximum permissible daily dose of about 0.02 r, and that the difference in potential between the electrodes of the chamber unit may be read to within 1 volt by an electrometer of average quality, the decrease in this difference produced by 0.02 r should be at least 30 volts to keep the reading accuracy within the usual limits of error in secondary standards, or about ± 3 per cent. Hence, a convenient sensitivity of such chamber units would be about $5 \times 10^{-4}\, r$ per volt. In a unit of the type described this would probably be obtained by reducing the ionized air volume to about 25 cm^3 or less, if the capacitance is kept small.

At the dose-rates usually met with when protection is inspected, saturation current in chambers of the last mentioned sensitivity will probably be attained if the potential difference is about 35 to 50 volt per cm distance between the electrodes. If the chamber unit is charged to a potential difference of 300 volts, a decrease of about 200 volts is thus usually available. This means that a maximum dose of about 0.1 r, *i.e.*, the maximum permissible weekly dose, can be measured. With such a unit, doses down to half the maximum daily permissible dose may be measured to within ± 6 per cent which may be accepted as being sufficiently accurate in this range.

In radiation measurements by condenser chamber units worn by workers in radiological work, it may sometimes happen that the dose received by some of the chambers is too high, and thus that these chambers are too much, or even completely discharged. In such cases the corresponding measuring results are missed, and cannot be obtained unless the conditions of the irradiation can be accurately repro-

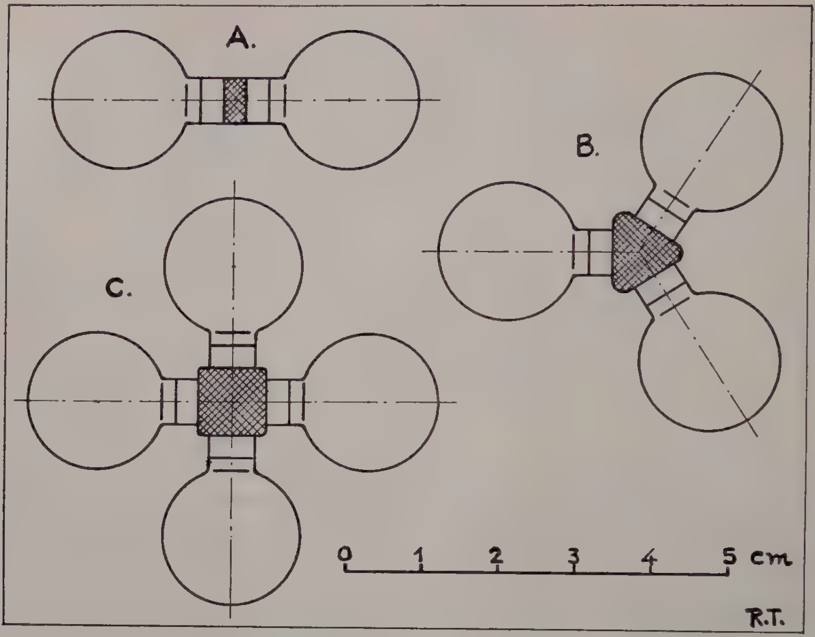

Fig. 5. Multiple measuring units containing various numbers of chamber units of equal or different sensitivity.

duced, and the measurements repeated by chambers of lower sensitivity. Since this is not always possible, and at all events to avoid such complications and time-wasting re-exposures, the author in 1946 developed a method of measuring briefly described below.

As illustrated by Fig. 5, two or more spherical chambers of equal or different sensitivity are symmetrically positioned around, and screwed to a common, central holder, thus forming a multiple measuring unit which may easily be carried in a pocket. The spherical type was adopted as it usually has the most extensive direction independence. A measuring unit designated type *A* refers to a twin-chamber unit, type *B* to a triple-chamber unit, and type *C* to a quadruple-chamber unit. The type *C* containing four chambers may, for instance, be arranged in such a manner that two opposite chambers have about the same sensitivity. This measuring unit will then consist of two pairs of chambers the sensitivities of which may be proportional to a ratio of, for instance, 1:10. The sensitivity of spherical chambers of the same external dimensions may be varied up to such a ratio by providing the chambers with inner electrodes of adequate diameters. If a still higher ratio is required, some chambers may be provided with additional capacitors, be of a larger size, or be charged to a higher potential difference.

The common central holder (connecting head) of each measuring unit is suitably made of aluminium or electron metal. By unscrewing a chamber from the head, the difference in potential between the electrodes of that chamber may be measured, or charged to a desired value. Measuring units of other types, and such ones more complex than those shown in the figure, may, of course, also be developed. As a rule, the symmetrical types using a central connecting head will give the smallest dimensions of the head. In all units other types of suitable chambers, for instance the thimble unit shown in Fig. 1, may be used as well.

Using measuring units of the types described, two or more individual readings will be obtained with each unit, giving a more reliable result. If the most sensitive chambers are discharged below the saturation potential, those of lower sensitivity will, as a rule, give an acceptable result.

When ionization chambers are used for radiation measurements, it should, however, be noticed that correct readings may only be obtained if the dose-rate is fairly constant at least within the volume enclosed by the chamber. If this is not the case, the readings obtained will be some kind of average for that volume, and will thus not indicate the maximum. Nor can a narrow beam of leakage, the cross-section of which is not sufficient to cover the entire chamber, be correctly investigated by that chamber. It may be mentioned that narrow beams of leakage frequently are found at protective doors and lead-glass inspection windows (1).

In consequence of this, the method of wearing ionization chambers, or other measuring device, to check the dose received by individual workers, is of a very limited value, unless the workers are extensively covered with chambers, and undue irradiation of the chambers is effectively prevented by keeping the workers under supervision. It is particularly important to position chambers at sites where the amount of radiation incident upon the blood forming and the generative organs may be satisfactorily measured. Chambers thus positioned will, however, usually be at a higher temperature than the room temperature. For example, chambers in contact with naked or uncovered skin, or put in the trousers-pockets, will normally be at a temperature of about 32° C. Due correction for the difference must be applied, unless the chambers are hermetically sealed (5 and 7). Such sealed chambers are therefore most convenient, not only at inspections of protection in radiological work, but in all kinds of radiation measurements.

The Institute of Radiophysics, Stockholm, Sept. 1951.

SUMMARY

This paper gives a brief survey of the roentgen standard laboratory outfit designed and installed by the author. In particular it discusses the use of closed ionization chambers for quantitative measurements of low dose-rate roentgen rays in terms of the international *r*-unit, and describes the design and properties of some chamber units, one of them having a sufficiently high sensitivity to allow measurements of the radiation behind ordinary protective barriers by exposure times of only a few minutes. The direction independence of this chamber is fairly good, and its wave-length independence is wide enough to cover all qualities of radiation met with in ordinary roentgen therapy and diagnostics within a measuring accuracy of about ± 3.5 per cent. Finally the value of wearing measuring instruments in radiological work to check the amount of radiation received by individual workers is discussed, and in addition an improved method of arranging the instruments is described.

REFERENCES: 1. **Thoraeus:** Acta Radiol., Vol. 33, 1950, p. 253. — 2. —— Acta Radiol., Supplementum XV, 1932. — 3. —— Acta Radiol., Vol. 27, 1946, p. 451. — 4. **Sievert:** Acta Radiol., Supplementum XIV, 1932. — 5. —— Acta Radiol., Vol. 18, 1935, p. 735. — 6. —— Acta Radiol., Vol. 22, 1941, p. 260. — 7. —— Acta Radiol., Vol. 18, 1937, p. 471.

Tryckt den 30 januari 1952.

Uppsala 1952. Almqvist & Wiksells Boktryckeri AB

ARKIV FÖR FYSIK Band 4 nr 19

Communicated 12 September 1951 by Manne Siegbahn and Erik Hulthén

On the decay of $Kr^{88} \rightarrow Rb^{88} \rightarrow Sr^{88}$

By Sigvard Thulin

With 19 figures in the text

Introduction

The study of the radiations of 2.77 hr Kr^{88} entails several difficulties, which explains why the results hitherto reported have been rather fragmentary. Since Kr^{88} is only produced in fission it is always obtained together with several other Kr and Xe activities. It is also difficult to prepare good β-spectrometer samples by conventional methods since Kr is a rare gas. Another complication is the active decay product Rb^{88}, which has a complex decay and a half-life of 17.8 min.

A convenient way to attack the problem is by means of electromagnetic isotope separation. In this way it is possible to prepare β-spectrometer samples of Kr^{88}, deposited on very thin backing foils. Disturbances due to activities of other rare gas isotopes are eliminated. The 17.8 min. Rb^{88} will however also be present in these samples.

In order to investigate the decay of Kr^{88} it is thus necessary to know accurately the β-decay of Rb^{88}. Bunker et al (1) recently published an investigation on Rb^{88} and suggested a decay scheme for this isotope. Our own preliminary β-spectrometer measurements on Rb^{88}, however, showed a definite discrepancy in the shape of the β-spectrum, as compared with that of Bunker et al, and it was therefore considered necessary to reinvestigate the β-spectrum of Rb^{88}. As the author used a quite different sample technique for this measurement the investigation on Rb^{88} will be described in some detail.

Earlier investigations

Rb^{88}

As the present measurements on Rb^{88} concern only the β-continuum, the reader is referred to the more extensive paper by Bunker et al (1) for a study of the whole decay and for references to earlier works. These authors used samples of thickness 26–30 mg/cm² for measurements in a magnetic lens spectrometer, and found three β-groups of energies 5.13 ± 0.03, 3.29 ± 0.10 and 2.04 ± 0.15 MeV, the intensities being 66, 19, and 15 percent respectively. Three γ-rays of energies 0.90, 1.86 and 2.8 MeV were established. The decay scheme suggested by Bunker et al is discussed on page 375.

Later K. Geiger (2) has published a paper on the results of absorption and coincidence measurements on Rb^{88}. Geiger used samples of thickness 50–500 mg/cm² and extrapolated his results to zero thickness. He found three β-components of energies 5.10 ± 0.10, 3.8 ± 0.5 and 1.8 ± 0.2 MeV and of intensities 56, 22 and 22 percent respectively.

Kr^{88}

1939: F. A. HEYN et al (3) reported for the first time a Kr isotope among the fission products. 500 ml of saturated uranyl nitrate solution was irradiated with slow neutrons. Air was bubbled through the solution, dried, and passed through a weak solution of HNO_3. In this solution the authors proved chemically the presence of a 16 min. Rb activity probably identical with the 17 min. activity earlier known from the Rb (n, γ) reaction. Heyn et al therefore suggested the decay chain $Kr^{88} \rightarrow Rb^{88} \xrightarrow{16\ \text{min.}} Sr^{88}$ (stable).

1939: A. LANGSDORF, jr. (4) estimated the half life for Kr^{88} to be about 3 hr.

1939: O. HAHN and F. STRASSMANN (5) also found a Rb activity of half life 15-20 min. in the uranium fission products and estimated the half life of the parent isotope to be of the order of hours.

1940: SEELMANN-EGGEBERT (6) absorbed the fission gases in active carbon and then desorbed them into a gas chamber, in the centre of which was placed a GM-counter. His value for the half life of Kr^{88} was 170 min.

1942: G. N. GLASOE and J. STEIGMAN (7) determined the half life for Kr^{88} indirectly by means of electrostatical deposition of Rb^{88} from an aging fission gas mixture. From activity measurements on successive Rb^{88} samples in a standard geometry they obtained a value 175 ± 10 min. for the half life of Kr^{88}.

1942: G. L. WEIL (8) measured the momentum distribution for the β-particles from Kr^{88} + Rb^{88} and from Rb^{88} with a cloud chamber. As the total number of tracks was small, the results are not accurate. Weil reported $E_{max} = 5.8$ MeV for Rb^{88} and 2.5 MeV for Kr^{88}.

1945, 1948: J. C. JACOBSEN and O. KOFOED-HANSEN (9) used the pair $Kr^{88} + Rb^{88}$ to study the recoil of the nucleus in β-decay. They also determined the maximum β-energy by absorption and reported the value 2,4 MeV.

1949: J. KOCH et al (10) measured the half-life of Kr^{88} with an electromagnetically separated sample and found the value 2.77 hr. Absorption measurements showed that the main part of the Kr^{88} spectrum has an upper limit of 0.5 MeV. The authors also found an intense γ-radiation and concluded that the Kr^{88} decay is complex.

Preparation of the β-spectrometer samples

The Kr^{88} β-spectrum is obtained as a difference between the β-spectrum of Kr^{88} + Rb^{88} and that of Rb^{88}. In the measurements of these two β-spectra, it is necessary to eliminate errors due to differences in the thickness of the β-sources or backing foils. We have in both cases used weightless samples on aluminium backings of thickness 0.15 mg/cm². The $Kr^{88} + Rb^{88}$ samples were prepared by electromagnetic separation of fission gases, and the Rb^{88} samples by electrostatic deposition of Rb^{88} from a fission gas mixture.

The radioactive equilibrium conditions for the pair $Kr^{88} + Rb^{88}$ in a separated Kr^{88} sample must be known, since the activity ratio of these two isotopes must be constant during the β-spectrometer measurements.

The different problems of importance for the preparation of useful β-spectrometer samples in the investigation of Kr^{88} will be discussed in detail below.

a. Preparation of fission gases

The fission gases used for preparation of the Kr^{88} and Rb^{88} samples have been extracted from irradiated uranium by two different methods. Of these, method I was used during the first period, when the general technique of β-spectrometric investigation of separated Kr and Xe isotopes was being worked out.

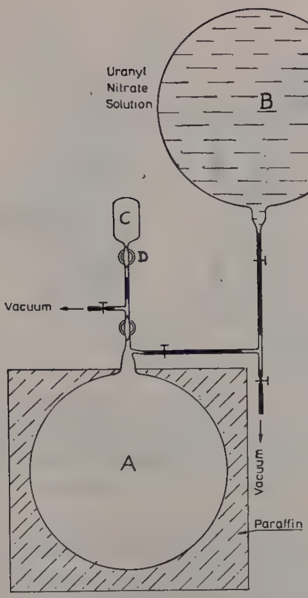

Fig. 1. Apparatus for preparation of fission gas samples from a neutron-irradiated uranyl nitrate solution.

Method I: A sample of uranium oxide with high emanating power was obtained in the following way, suggested by Dr. Melander of this Institute. Small pieces of surface-active alumina were introduced into a suction flask containing saturated uranyl nitrate solution. The air contained in the pores of the alumina was liberated by evacuating the flask. When exposed to atmospheric pressure again, the solution was forced into the pores. The preparation was dried at elevated temperature and finally heated to ~ 600° C for one hour in order to convert the uranyl nitrate into uranium oxide. This sample, containing about 0.5 kg uranium oxide, was then stored in a cylindrical pyrex container with a volume of about 4 l. When surrounded with a moulded paraffin shield of 2–5 cm thickness this cylinder occupied the whole irradiation space of the 80 cm cyclotron at this Institute.

Before irradiation the glass container was evacuated and a small amount of stable Kr was introduced as carrier. Immediately after irradiation the container was connected directly to the ion source of the separator by means of rubber tubing.

Method II: In order to increase the activities of the Kr^{88} and Rb^{88} samples it was necessary to increase the amounts of fissionable material. However, the uranium sample described above already occupied the whole irradiation space of the cyclotron. It was therefore necessary to try another method, and we preferred to use a modification of the classical method of bubbling air through an irradiated uranyl nitrate solution.

A spherical glass bulb with a volume of 1 l was completely filled with saturated uranyl nitrate solution. The bulb was enclosed in a block of paraffin (A Fig. 1). After irradiation in the cyclotron the bulb A was connected with another bulb B of the same size, which contained only a small amount of stable Kr. Half of

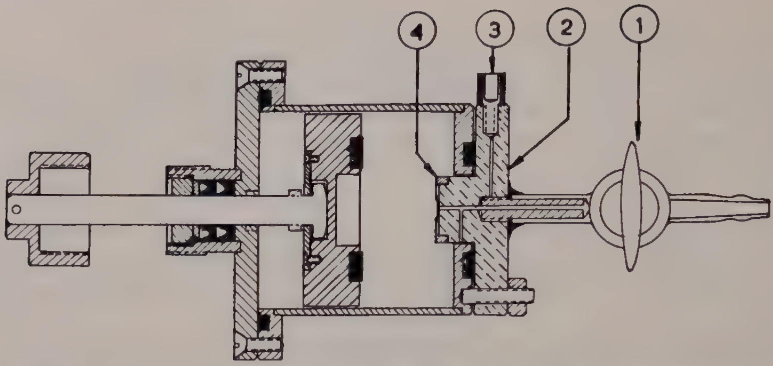

Fig. 2. Device for preparation of Rb^{88} β-samples. The fission gases were introduced through the stop-cock 1, which also was used for pressure compensations during the locking operations. The β-sample holder 4 was placed on the plexiglass flange 2 with the thin backing foil (0.15 mg/cm²) electrically connected to the contact 3, which was held at a potential of 800 V negative with respect to the container.

the solution was transferred into the empty bulb B and the whole system was shaken for about ten minutes. It was found experimentally that most of the active gases were liberated during this time. The whole solution was now transferred to B. With the bulbs in the positions shown in figure 1 the solution was allowed to flow down into A and compress the gas mixture into the evacuated container C. By allowing the liquid to rise to the stopcock D the gas sample was almost quantitatively transferred to the container C. This container was then connected with the ion source of the separator through a needle valve, or else was used to prepare Rb^{88} samples as described below.

With this method it was not possible to begin the separation until about half an hour after irradiation. However, the Kr^{88} activities were about 5 times stronger than those obtained by method I.

The irradiations were performed in the 80 cm cyclotron of the Institute, using a beryllium target for the neutron production. The mean flux of slow neutrons was about $2 \cdot 10^8$ neutrons/cm²sec.

b. Preparation of the Rb^{88} samples

For the preparation of Rb^{88} samples the method of electrostatic deposition from fission gases, described by GLASOE and STEIGMAN (7), was used. These authors have shown that the Rb^{88} will be free from other activities if the gas mixture is left to decay for at least 3 hr before the collection of Rb^{88} begins.

A special brass container was designed (Fig. 2), which is provided with a device for locking standard β-sample holders and is designed to give minimize losses of gas during the locking process. The fission gases were prepared and introduced into the container according to method II described above (cf Fig. 1). Before the collection of the Rb^{88} samples began, the gas mixture was allowed to decay for at least 3 hr. The Rb samples were deposited on aluminium foils of thickness 0.15 mg/cm². The thin foil was mounted over an aperture of 6 mm diameter in the centre of a piece of scotch tape covering the β-sample holder.

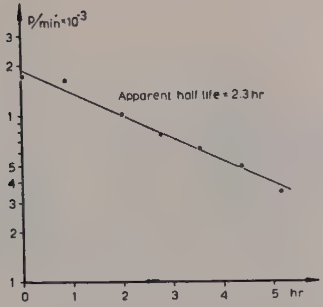

Fig. 3. Apparent half life of Kr^{88}, obtained from measurements on successively deposited Rb^{88} samples. The curve can be used to calculate the gas losses in the locking of Rb^{88} samples.

It was found that the whole β-sample holder became contaminated with the Rb activity when exposed to the gas. In order to obtain a well-defined sample in the centre of the thin aluminium foil the sample holder was shielded by means of an earthed "electrode". This was made of a ring-shaped aluminium foil, covered with tape and provided with a copper tongue to give electrical contact with the earthed container. This "electrode", which covered the whole sample holder except for a central spot (diameter 5 mm), remained fixed on the tape of the sample holder while the electrostatic collection was in progress. Before the sample was introduced in the β-spectrometer the "electrode" was teared off.

The activity of the fresh Rb^{88}-samples corresponded to ~ 12 000 counts/min when measured at the energy 4 MeV in a spectrometer with 7 % resolution and a transmission of 1 %.

Because of the rather tedious work necessary before a sample of fission gases for preparing Rb sources was ready (5–6 hours cyclotron irradiation, shaking of the solution, waiting for three hours, and collection of the sample), it was desirable to obtain several strong Rb^{88} samples from one Kr sample. Thus the locking losses had to be small. A rough estimate of these was obtained by measuring the half life of the parent isotope Kr^{88} indirectly from the activity of successive Rb^{88} samples, obtained by collection during the same time interval and measured in a standard position. Fig. 3 shows the decay curve obtained in this way. We find the apparent half life 2.3 hr. The discrepancy between this value and the value 2.77 hr determined by KOCH et al (10), with electromagnetically separated Kr^{88}, is due to gas losses in the container. These can be roughly calculated to be 23 % after 6 lockings.

c. Electromagnetic separation technique

In an earlier work (17) it has been shown that β-spectrometer samples of a radioactive gas can be conveniently prepared by electromagnetic separation.

The fission gases to be separated were extracted from the uranium and mixed with inactive Kr as described above. The sample container was then connected with the ion source of the separator and the gas flow regulated by a needle valve. The target arrangement is shown in figure 4 (a) and (b). When the target disc 2 is in the position A the mass spectrum of the stable isotopes is visible on the fluorescent screen 1. The line shape is then adjusted by means of the electrostatic focusing

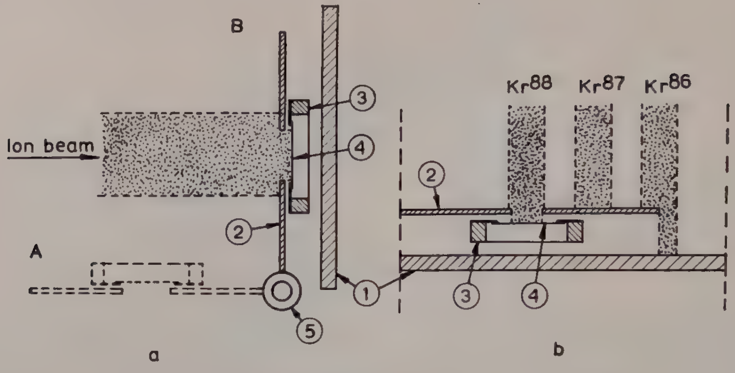

Fig. 4. Target arrangement for separation of Kr^{88}:
a) side wiew, b) seen from above.

system of the separator. When the lines have the desired shape and position, the target is turned into position B. The aluminium disc 2 was provided with a 6×10 mm aperture at the calculated position of the mass number 88. Behind this aperture was placed a standard β-sample holder 3, covered with a thin backing foil 4 (0.15 mg/cm^2). The shaft 5 is watercooled and electrically insulated to permit continuous measurement of the ion current striking the aluminium disc. The separation is simply controlled by means of one of the stable mass numbers, which is continuously held at the edge of the aluminium disc (Fig. 4 (b)) or at some other fixed position on the part of the fluorescent screen not covered by the target disc.

The separation time was 1–2 hours and the total Kr ion current about 2 μ A.

d. Separation of active isotopes

When separating an active isotope the growth of the target activity is a certain function of time. A knowledge of this function is necessary to find the proper separation time for each case.

Suppose we separate an active isotope with decay constant λ_1. If the ion current is constant, the target will in each time interval dt receive an amount $c_0 e^{-\lambda_1 t} dt$ of the isotope, where c_0 is a constant. Neglecting losses due to sputtering, the increase of active atoms on the target during the time dt is then

$$d A_t = c_0 e^{-\lambda_1 t} dt - \lambda_1 A_t dt, \tag{1}$$

where A_t is the number of active atoms on the target at the time t. Integration of equation (1) gives the amount A_T after the separation time T:

$$A_T = c_0 T e^{-\lambda_1 T}.$$

This function has a maximum $A_{\max}$ for

$$T = \frac{1}{\lambda_1} = 1.44\, T_{1/2}.$$

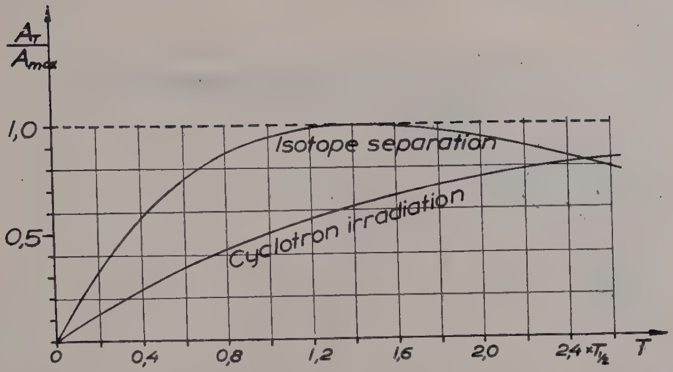

Fig. 5. The intensity ratio $A_T/A_{\max}$ as a function of the time T in units of the half-life. A_T = the amount of isotope A separated during a time T. $A_{\max}$ = the maximal amount of A obtainable.

Fig. 5 shows $A_T/A_{\max}$ as a function of T in units of the half-life. For comparison the corresponding curve for constant activity production (for example cyclotron irradiation) is also shown. It is seen from the figure that ~ 80 % of the maximum activity is obtained already after a separation time $T = 0.7\ T_{1/2}$.

e. Separation of genetic activities

Assume that in the Kr^{88} separations the ion beam contains no Rb^{88}. The target activity of mass number 88 will then for the first moment contain pure Kr^{88}, but will soon be mixed with an increasing amount of Rb^{88}. For the β-spectrometer investigation it is necessary to know the ratio of these two activities at every moment after the separation is finished. An expression for this ratio can be derived as shown below.

Assume we separate an active isotope A, which decays to the active isotope B on the target. The equation (1) is still valid for the isotope A. The increase of the isotope B on the target during the time interval dt is

$$d B_t = \lambda_1 A_t\, dt - \lambda_2 B_t\, dt. \tag{2}$$

This gives the amount B_T at the end of the separation:

$$B_T = \frac{c_0 \lambda_1 T}{\lambda_2 - \lambda_1} e^{-\lambda_1 T} + \frac{\lambda_1 c_0}{(\lambda_2 - \lambda_1)^2} (e^{-\lambda_2 T} - e^{-\lambda_1 T}).$$

Substituting $\tau = T + t$, we have for the time t after the end of the separation

$$d B_\tau = \lambda_1 A_\tau\, dt - \lambda_2 B_\tau\, dt \tag{2 a}$$

where $A_\tau = A_T e^{-\lambda_1 t}$.

Equation (2 a) has the solution

$$B_\tau = B_T e^{-\lambda_2 t} + \frac{A_T \lambda_1}{\lambda_2 - \lambda_1} (e^{-\lambda_1 t} - e^{-\lambda_2 t}).$$

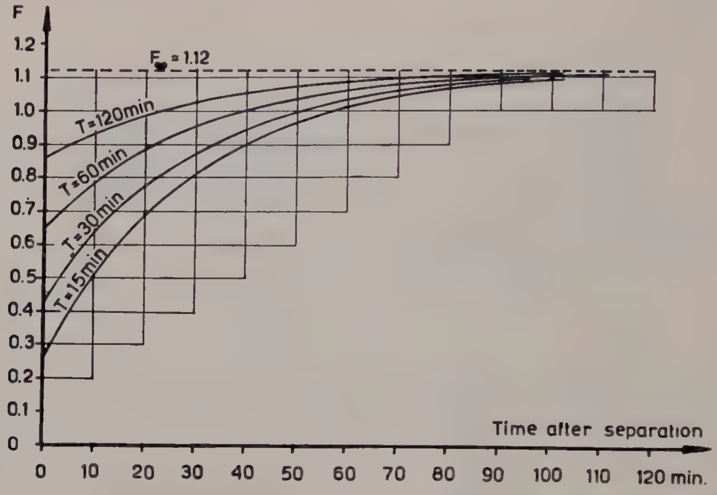

Fig. 6. The intensity ratio $F = \frac{Rb \text{ activity}}{Kr \text{ activity}}$ as a function of the time after separation and with the separation time T as parameter.

The ratio of the activities of isotope B and A at the time $\tau = T + t$ after the beginning of the separation is

$$F_\tau = \frac{\lambda_2 B_\tau}{\lambda_1 A_\tau}$$

and hence

$$F_\tau = \frac{\lambda_2 e^{(\lambda_1 - \lambda_2) t}}{(\lambda_2 - \lambda_1)^2 T} (e^{(\lambda_1 - \lambda_2) T} - 1) + \frac{\lambda_2}{\lambda_2 - \lambda_1}.$$

For very long times after the end of the separation we have

$$\lim_{\substack{t \to \infty \\ \lambda_1 > \lambda_2}} F_\tau = \frac{\lambda_2}{\lambda_2 - \lambda_1} = F_\infty$$

and consequently

$$d B_\tau = \text{const} \cdot d A_\tau$$

i.e. the isotope B decays apparently with the same half-life as A. This is important for the decay correction of the β-spectrum of the isotope mixture.

In practice, it is not convenient to wait too long before the measurements begin, because of the decrease of the activity. We therefore want to know the errors introduced when the β-measurements are performed within a certain time after the end of the separation. Fig. 6 shows the ratio $F = \frac{Rb \text{ activity}}{Kr \text{ activity}}$ as a function of the time t after the end of the separation and with the separation time T as parameter. The curve also shows to what extent the transient equilibrium is reached. In our investigation of the β-spectrum of $Kr^{88} + Rb^{88}$ the separation time T was ~ 2 hr and the measurements began at $t = 1.5$ hr after the end of the separation.

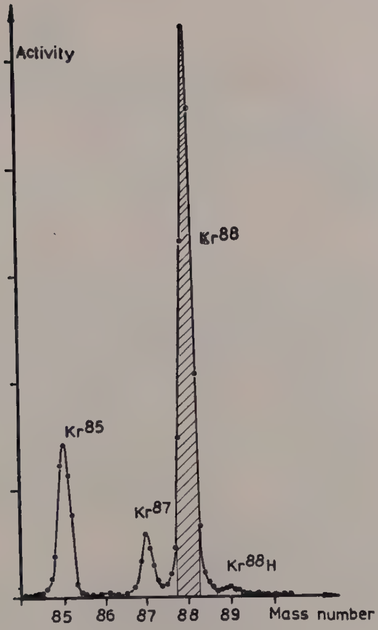

Fig. 7. Activity spectrum for separated Kr, produced by uranium fission.

The relative Rb^{88} activity F at this time was 1.11, as can be seen from Fig. 6. As the ion current at the end of the separations tended to decrease, the activity ratios were closer to the asymptotic value $F = 1.12$ than shown by the curve for 120 min. separation. The change in the intensity ratio during the measurement is therefore estimated to be less than 0.5 %.

f. Possible Kr^{88} impurity in the separated $Kr^{88} + Rb^{88}$ samples

As the 74 min. Kr^{87} emits β-particles of maximum energy 3.2 MeV (10), i.e. a little higher than the weak high energy component of Kr^{88}, it was necessary to estimate the possible contamination of Kr^{87} in our samples. Fig. 7 shows the activity spectrum, obtained when a target foil with the separated Kr mass spectrum was cut into strips 1 mm broad and the activity of each strip measured with a GM-counter. The hump at mass number 89 is due to $Kr^{88}H$ and indicates hydride amounts of about one percent. As Kr^{87} in this case was ~ 10 % of the Kr^{88} activity the $Kr^{87}H$ would be ~ 0.1 % of the activity at mass number 88. The final β-spectrometer sample was obtained after a much longer separation time than that used for Fig. 7 and the measurements began 1.5 hr after the separation. We therefore estimate the amounts of Kr^{87} present in this sample to be less than 0.05 %.

In Fig. 7 the shaded surface shows the part of the activity at mass number 88 used for the β-investigation.

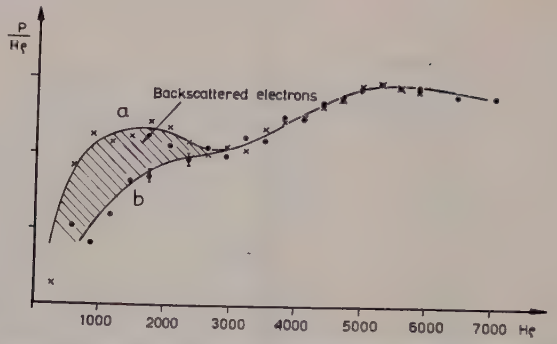

Fig. 8. Low energy region of the Rb^{88} β-spectrum, measured on aluminium backings of different thickness: (a) 2.5 mg/cm², (b) 0,15 mg/cm².

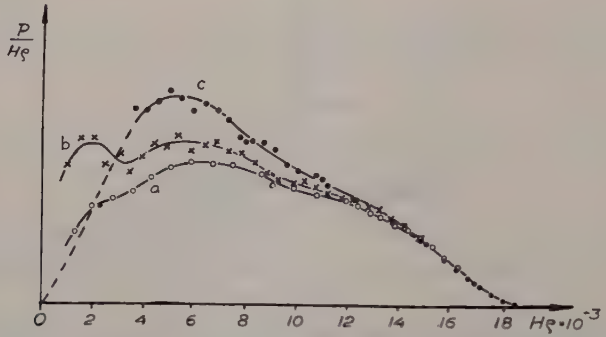

Fig. 9. The β-spectrum of Rb^{88} measured with sources of different thickness. a) weightless sample on 0.15 mg Al/cm², b) stacked sample of thickness 17 mg/cm² (see text), c) the curve of Bunker et al (1) (26 mg Rb_2SO_4/cm²).

β-spectrometer measurements on Rb^{88}

Back-scattering in the aluminium foils

Our preliminary β-spectra of Rb^{88} were measured with samples electrostatically deposited on thick aluminium foils (2.5 mg/cm²), using a primitive locking arrangement. Fig. 8 shows the low energy part of the β-spectrum, measured with samples on different backings: (a) 2.5 mg/cm² and (b) 0.15 mg/cm². As expected the β-spectrum is distorted in the low energy region of curve (a) and it is reasonable to suppose that curve (b) is also distorted to some extent, giving a false low intensity β-component in the Fermi-analysis shown on page 375.

As the samples used by Bunker et al had a thickness of 26–30 mg/cm² and their β-spectrum deviated considerably from the shape obtained by us, a special measurement was carried out to examine the straggling and back scattering effects. A sample corresponding to 17 mg/cm² was made in the following way. Rb^{88} was electrostatically deposited on an aluminium foil of 22 mm diameter and of thickness 2.5 mg/cm². From the activated foil seven small circular pieces, each 6 mm in diameter, were prepared. These were stacked together and fixed on a piece of tape covering the β-sample holder. Fig. 9 shows the β-spectrum of this sample (a) and

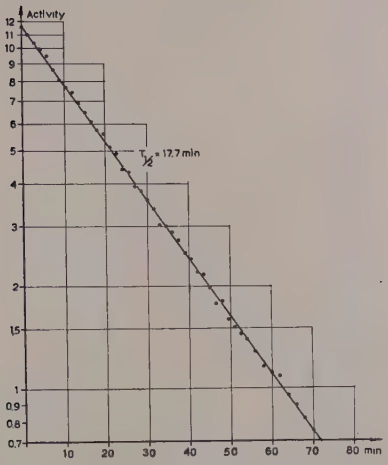

Fig. 10. Half-life of Rb^{88} measured in the β-spectrometer.

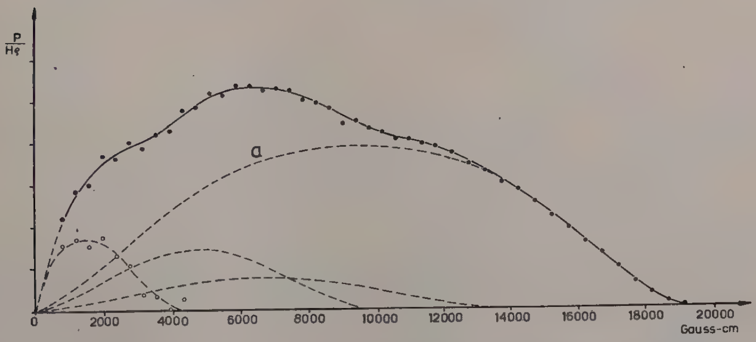

Fig. 11. The β-spectrum of Rb^{88} and the components obtained from a Fermi analysis.

the same spectum measured with a weightless sample on a thin backing (b). Curve (c) is the β-spectrum obtained by Bunker et al with a neutron irradiated Rb_2SO_4 sample of thickness 26 mg/cm^2.

The three curves are normalized at the high energy end. The 17 mg sample shows a pronounced distortion, and it can be concluded, that at least part of the deviation of curve (c) from (a) is due to the sample thickness.

Half-life of Rb^{88} in the β-spectrometer

Due to the short half-life of Rb^{88} the decay corrections for part of the β-spectrum were rather large. These decay corrections assume an accurate knowledge of the half-life. Glasoe and Steigman (7) have reported the value 17.8 ± 0.1 min. As our electrostatically deposited samples were, however, used without any covering material, we had to be sure that the Rb^{88} did not evaporate in the vacuum of the β-spectrometer. Therefore a decay curve was measured at the energy 1.2 MeV (Fig. 10). The decay followed a straight line for 4 half-lives with the half-life 17.7 min., in good agreement with the value of GLASOE and STEIGMAN.

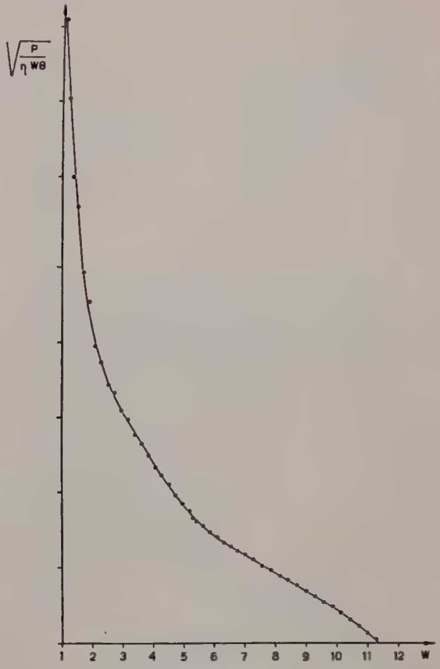

Fig. 12. Conventional Fermi plot of the Rb^{88} spectrum.

β-spectrum of Rb^{88}

The β-spectrum of Rb^{88} was measured in a magnetic lens spectrometer with 7 % resolution. The GM-tube was of the end-window type with a nylon window of cut off ~ 6 KeV. The spectrometer was calibrated by means of the F and X lines of ThB. Fig. 11 shows the β-spectrum of Rb^{88}. It is corrected for the finite resolution of the β-spectrometer, assuming a triangular window curve with half width 7 %. The conventional Fermi plot (Fig. 12) is curved towards the abscissa for the highest W-values. This indicates a first forbidden transition with $\Delta J = 2$ and parity change as reported by BUNKER et al (1).

The high energy part of the Fermi plot is given in enlarged scale in curve (a) of Fig. 13, while curve (b) shows the same part after applying the correction factor $a = W^2 - 1 + (W_0 - W)^2$ (11). The upper limit of this component is 5.30 ± 0.05 MeV.

Assuming that the Fermi plot of the 5.3 meV component, corrected with the a-factor, is a straight line down to $W = 1$, we obtain the β-component (a) of Fig. 11. The complex Fermi plot of the remaining part of the β-spectrum is shown in Fig. 13 (c). After a conventional analysis three more β-components of energies 3.6, 2.5 and 0.7 MeV are obtained. The last one is probably due to back-scattering in the 0.15 mg/cm² aluminium foil (cf Fig. 8 and page 372). The intensities of the 5.30, 3.6 and 2.5 MeV β-components are estimated to be 78, 13 and 9 percent, and the $\log fT_{1/2}$ values appear to be 7.5, 7.5 and 6.9 respectively.

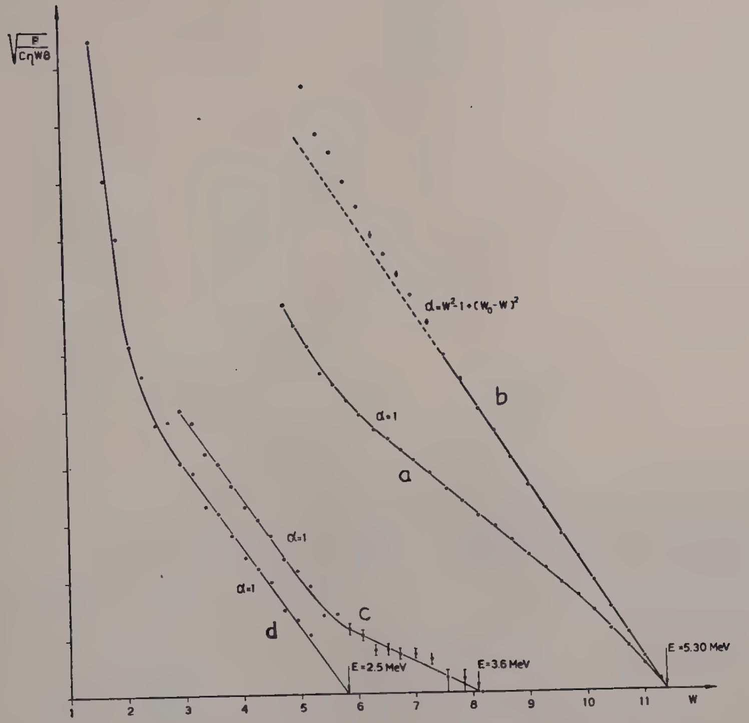

Fig. 13. (a) The upper part of the Fermi plot. (b) The upper part after applying the α-factor. (c) The Fermi plot of the β-spectrum after subtraction of the 5.3 MeV component. (d) The Fermi plot after subtraction of the 5.3 and 3.6 MeV components. The statistical errors of the last 10 points in curves (a) and (b) are equal to or less than the diameter of the points.

Discussion

The present investigation has established at least three β-components in the decay of Rb^{88}, thus confirming the results of Bunker et al (1). The upper limits of the two higher components, however, seem to be somewhat higher in our work, and the intensity values are different from those obtained by Bunker et al with very thick β-samples. Finally the upper limit of the low energy β-component appears to be 2.5 MeV instead of 2.04 ± 0.15 as reported by Bunker et al. In the decay scheme suggested by these authors, two exited levels in Sr^{88} were established by γ-ray measurements on Rb^{88} and Y^{88}. A third level would be required to explain the existence of a 2.04 MeV β-component in Rb^{88}. However, our value 2.5 MeV for the low energy component fits well to a level scheme with only two exited levels, as shown in Fig. 14. This uncertainty in the decay scheme of Bunker et al is thus removed.

The 0.7 MeV component, of the intensity ~ 7 %, which appears in the Fermi analysis, we have assumed to be due to scattering in the backing foil. It is interesting to remark, however, that if this component were real, the corresponding level in Sr^{88} would lie 1.8 MeV above the highest Sr level shown in Fig. 14: such a level would give three more possiblilities for γ-transitions. Two of them would have

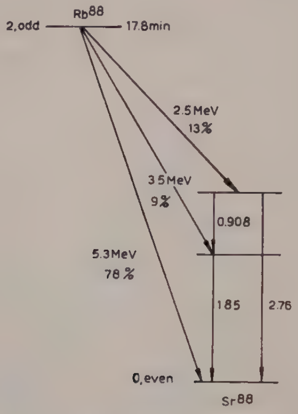

Fig. 14. Decay scheme of Rb^{88}.

energies of ~ 1.8 and ~ 2.8 MeV, and would perhaps be impossible to resolve from the known γ-rays of energies 1.86 and 2.76 MeV.

The high log $fT_{1/2}$ value 7.5 for the 3.6 MeV β-component should be noticed. The value of log $(W_0^2 - 1)\, f T_{1/2}$ is 9.3, which indicates the possibility of a first forbidden shape for this β-component (11). This seems, however, unprobable from spin- and parity considerations. Due to the large errors in the last points of the Fermi plot of the 3.6 MeV β-component (Fig. 13, curve (a)), we cannot from our experiments draw any conclusions regarding the possibility of a forbidden shape.

β-spectrometer measurements on $Kr^{88} + Rb^{88}$

β-spectrum of Kr^{88}

Fig. 15 (a) shows the β-continuum of Kr^{88} + Rb^{88} measured in the same magnetic lens spectrometer as was used in the Rb^{88} investigation. The backing foil was also the same, 0.15 mg/cm^2 aluminium.

In the low energy region two conversion lines appear (Fig. 18), which are certainly due to a 28 KeV γ-ray. This γ-ray will be discussed later.

The curve (b) of Fig. 15 represents the β-spectrum of Rb^{88} normalized to the high energy part of curve (a). The difference spectrum (Fig. 16) corresponds to the decay of Kr^{88} and is seen to be complex. An evaluation of the surfaces under the respective β-spectra gives the value $F = 1.09 \pm 0.05$ for the ratio between the decay rates of Rb^{88} and Kr^{88}. This value agrees within the experimental error with the theoretical value $F \sim 1.11$ (cf Fig. 6).

The Fermi plot of the Kr^{88} difference spectrum appears in Fig.17. A conventional analysis gives three components of energy 2.8, 0.9 and 0.52 MeV and intensities 20, 12 and 68 percent respectively. Fig. 16 shows the difference spectrum and its components. The values of log $fT_{1/2}$ for the 2.8, 0.9 and 0.5 MeV components are 7.7, 5.9 and 4.8 respectively.

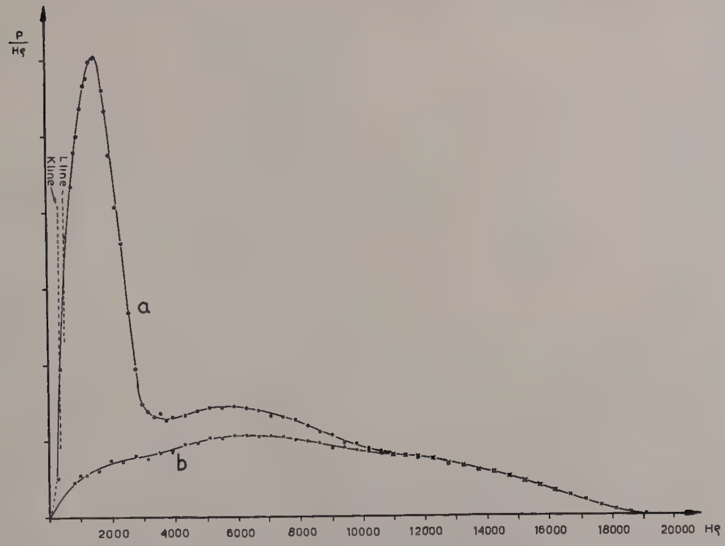

Fig. 15. (a) The β-spectrum of $Kr^{88} + Rb^{88}$. (b) The β-spectrum of Rb^{88} normalized to (a) in the high energy region (12 common points).

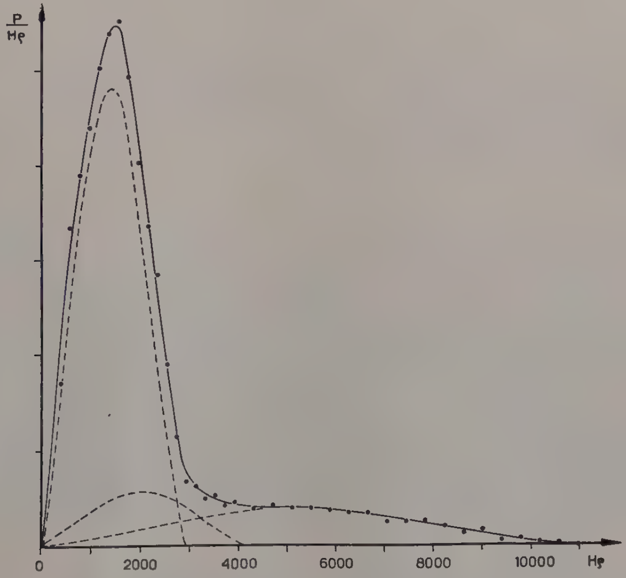

Fig. 16. The Kr^{88} difference spectrum and its components, as obtained from a Fermi analysis.

Conversion lines

Two electron lines at the energies 12.6 and 26.2 KeV have been found (Fig.18.) The energy difference agrees with the K_α energy for Rb within the limits of error. The lines are therefore most probably the K and $L+M$ conversion lines of a γ-ray of

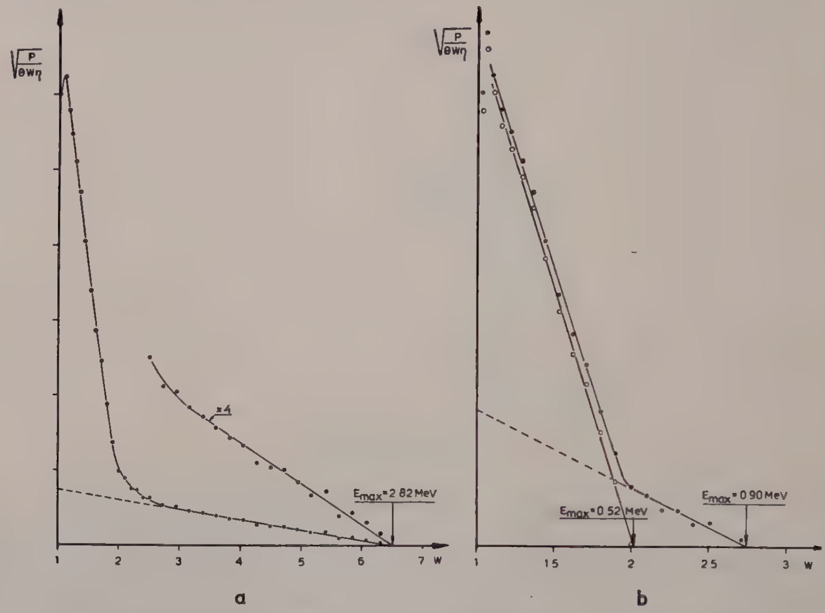

Fig. 17. (a) The Fermi plot of Kr^{88}. (b) The Fermi plot after subtraction of the 2.8 MeV component.

energy 28.0 ± 0.5 KeV. The Auger electrons of Rb have the energies $E_K - 2E_L = 11.4$ KeV and $E_K - E_L - E_M = 13.0$ KeV. The asymmetric shape of the K-line (Fig. 18) indicates the presence of the Auger lines.

In order to calculate the $K/(L+M)$ ratio we have to apply the following corrections:

1. The absorption of the electrons in the GM-window can be roughly calculated from a measurement of the low energy region of a β-continuum, for example that of Co^{60}. The low energy deviation of the Fermi plot is assumed to be due to absorption in the GM-window and back-scattering in the backing. The same method has also been used by I. Bergström in an investigation of the low energy conversion lines of $Kr^{83\,m}$, and is discussed in more detail by him (12). Using this method we found the correction factors 1.3 and 1.0 for the K and $L+M$ lines respectively.
2. The internal conversion coefficient W_K (= 1–fluorescence yield) for the K_a X-rays of Rb is 0.45 (13). In this case W_K is equal to the ratio (Auger line intensity) /(K-line intensity). After correcting for absorption and substracting the intensity of the Auger electrons we obtain:

$$K/(L+M) = 8.$$

The ratio K/L is somewhat higher because of the M electrons. According to the curves of HEBB and NELSON (14) and those of TRALLI and LOWEN (15) the radiation associated with the 28 KeV γ-ray would be of the type E1 or M2. As known, these curves are uncertain. It can, however, be stated, that the radiation is of low multipole order and thus cannot be due to an isomeric transition.

An evaluation of the K-conversion coefficient α_K for the 28 KeV γ-ray presumes a knowledge of the decay scheme. Assuming that the 28 KeV γ-ray is emitted in

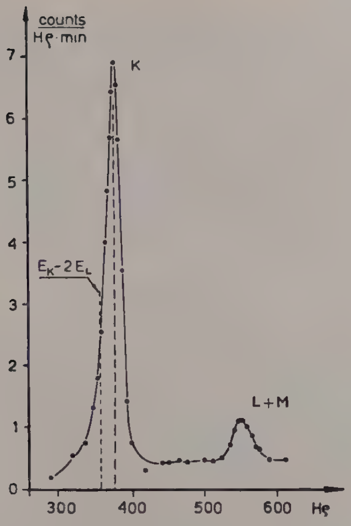

Fig. 18. Conversion lines of Kr^{88}.

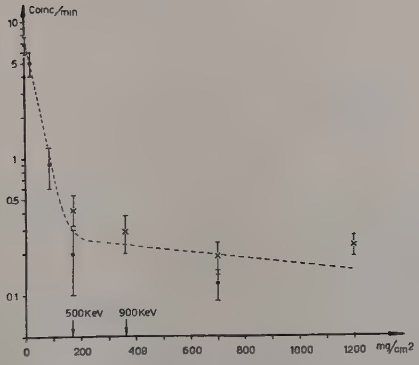

Fig. 19. $e^{-}\beta$-coincidences as a function of β-absorber thickness (β-spectrometer measurements). Crosses and circles refer to different measurements.

cascade after one of the β-components (2.8, 0.9 or 0.5 MeV) the experimental K-conversion coefficient will be 0.64, 2.2 or 0.13 respectively. According to FLÜGGE (16) $\alpha_K \sim 3$ for an El transition. The experimental value would then support the assumption that the 28 KeV γ-ray is in cascade with the 0.9 MeV β-component (cf page 380).

Coincidence measurements

$e^{-}\beta$-coincidences were measured in the β-spectrometer in the following way. The K-line of the 28 KeV γ-ray was focused into the GM-tube of a lens spectrometer. Coincidences were measured between this line and the β-continuum counted in a β-tube (mica window of thickness 3 mg/cm^2) close behind the sample. By means of a vacuum-tight shaft a series of absorbers could be placed between the sample and the β-tube. The coincidence rate for different absorbers is presented in Fig. 19. It is evident that the K-line is in coincidence with a low energy β-component. In spite of the large statistical errors in the measurements it can be concluded that the energy of this β-component is ~ 0.5 MeV.

The background of $\beta\gamma$-coincidences was measured by focusing β-particles of an energy close to the K-line and measuring the coincidence rate. This background has been subtracted in Fig. 19. The coincidence background which appears in Fig. 19 for absorber thickness larger than 200 mg/cm^2 is probably due to $e^-\gamma$-coincidences.

Discussion

From the investigation of the Rb^{88} spectrum, it appears that the ground state of Rb^{88} has the spin 2 and odd parity. As the Kr^{88} nucleus is even-even (spin zero, even parity) a β-component due to a transition from Kr^{88} to the ground state of Rb^{88} should have first forbidden shape ($\Delta J = 2$ yes). As the errors in the last points of the Kr^{88} difference spectrum must necessarily be large, it is not possible to draw any conclusion from our measurements about the shape of the high energy β-component.

A calculation of log $(W_0^2 - 1)\, f T_{1/2}$ for the 2.8 MeV β-component gives the value 9.3. This transition might thus be classified as first forbidden (11). If we apply the factor $a = W^2 - 1 + (6.3 - W)^2$ to the Fermi plot we obtain a straight line which cuts the W-axis at $W = 6.3$. The upper limit of the high energy β-component would then rather be 2.7 MeV.

The upper limit of the high energy β-component of Kr^{88} is of importance for the interpretation of the experiments on the recoil of the Kr^{88} nucleus in β-decay performed by Jacobsen and Kofoed-Hansen (9). These authors determined the maximum recoil energy of the Kr^{88} nucleus by retarding the daughter atoms of Rb^{88} in an electric field. Their experimental value for the maximum recoil energy E_R agrees well with the value calculated for an upper limit of the β-energy of 2.4 MeV. The value 2.7 MeV, obtained by us, causes a discrepancy between the measured E_R value and that calculated from the β-energy.

The 0.9 MeV β-component in the Kr^{88} spectrum should not be considered as unambiguously established. The Kr^{88} spectrum is obtained as a difference of two normalized spectra. These are, indeed, measured under favorable conditions and with small statistical errors (1–2.5 %), but part of the difference spectrum must contain large errors, since it apperars as a small difference between large quantities. The low intensity of the 0.9 MeV β-component (12 %) should be noticed, as well as the fact that its existance is only based on 6 points in the Fermi plot (Fig.17).

The position of the 28 KeV γ-ray in the decay of Kr^{88} is only roughly indicated by the coincidence measurements. The surprisingly low K-conversion coefficient may be explained, if we suppose that the 28 KeV γ-ray is in cascade with another γ, and that a cross-over transition of much higher intensity exists.

From the discussion above it seems probable that the high energy β-component is due to a transition to the ground state of Rb^{88}. The 28 KeV γ-ray would therefore not be in cascade with this component. The coincidence measurements also support such a conclusion.

I wish to thank Professor Kai Siegbahn for suggesting this investigation and for discussions during the course of the work. I also wish to thank Mag. Stig Johansson for valuable advice and help in the β-spectrometer work.

SUMMARY

The decay scheme of the 2.77 hr Kr^{88} is difficult to study because of the active laughter product Rb^{88} (17.8 min.). The author has measured the β-spectra of lectromagnetically separated Kr^{88} + Rb^{88} and of electrostatically deposited Rb^{88}. The Kr^{88} spectrum is obtained as the difference between these two normalized pectra. The investigation includes the following main parts:

Methods of extracting fission gases from n-irradiated uranium samples are described, as well as the technique of preparing weightless β-samples of Rb^{88} on hin backing foils.

The electromagnetic separation of genetic activities is discussed in connection vith the pair Kr^{88} + Rb^{88}.

The β-spectrum of Rb^{88} has been measured. A Fermi analysis gives three comonents of energies 5.30, 3.6 and 2.5 MeV. The later value removes an earlier ncertainty in the decay scheme of Rb^{88}, suggested by BUNKER et al (1).

The β-spectrum of Kr^{88} + Rb^{88} has been measured. An analysis of the Kr^{88} lifference spectrum gives β-components of energies 2.7, 0.9 and 0.52 MeV. Conversion lines of a 28.0 KeV γ-ray were found. $e^{-}\beta$-coincidence measurements in the β-spectrometer show that this γ-ray is in coincidence with a β-component of energy ~ 0.5 MeV.

In a discussion of the results, the possibility that the 2.8 MeV β-component of Kr^{88} may be of first forbidden shape is pointed out. The question of the existence of a 0.9 MeV β-component in Kr^{88} is discussed as well as the low experimental internal conversion coefficient of the 28 KeV γ-ray.

Nobel Institute of Physics, Academy of Sciences, Stockholm.

REFERENCES. 1. **M. E. Bunker, L. M. Langer** and **R. J. D. Moffat,** Phys. Rev. *81* 30 (1951). – **K. Geiger,** Naturforschg *6a* 54 (1951). – 3. **F. A. Heyn, A. H. W. Aten** and **C. J. Bakker,** Nature *143* 516 (1939). — 4. **A. Langsdorf, jr,** Phys. Rev. *56* 205 (1939). — 5. **O. Hahn** and **F. Strassmann,** Naturwiss. *27* 529 (1939). — 6. **W. Seelmann-Eggebert,** Naturwiss. *28* 451 (1940). — 7. **G. N. Glasoe** and **J. Steigman,** Phys. Rev. *58* 1 (1940). — 8. **G. L. Weil,** Phys. Rev. *62* 229 (1942). — 9. **J. C. Jacobsen** and **O. Kofoed-Hansen,** Phys. Rev. *73* 675 (1948). Dan. Mat. Fys. Medd. *23* no 12 1945. — 10. **J. Koch, O. Kofoed-Hansen, P. Kristensen** and **W. Drost-Hansen,** Phys. Rev. *76* 279 (1949). — 11. **F. B. Shull** and **E. Feenberg,** Phys. Rev. *75* 1768 (1949). — **M. G. Mayer, S. A. Moszowski** and **L. W. Nordheim,** ANL-4626 Argonne national laboratory (1951). — 12. **I. Bergström,** Arkiv f. fysik, (in print) (1951). — 13. **H. S. W. Massey** and **E. H. S. Burhop,** Proc. Roy. Soc. A *153* 661 (1935—36). — 14. **M. H. Hebb** and **E. Nelson,** Phys. Rev. *58* 486 (1940). — 15. **N. Tralli** and **S. Lowen,** Phys. Rev. *76* 1541 (1949). — 16. **S. Flügge,** Phys. Zeitschr. *42* 221 (1941). — 17. **I. Bergström, S. Thulin** and **G. Andersson,** Phys. Rev *77* 351 (1950).

Tryckt den 5 februari 1952

Uppsala 1952. Almqvist & Wiksells Boktryckeri AB

ARKIV FÖR FYSIK Band 4 nr 20

Vorgelegt am 12. September 1951

Spaltung und Schalenmodell der Atomkerne

Von LISE MEITNER

In einer vor längerer Zeit veröffentlichten Notiz (1) war auf die Möglichkeit hingewiesen worden, sowohl die symmetrische als die unsymmetrische Spaltung der Atomkerne auf Grund des Schalenmodells (2) verständlich zu machen. Bis vor kurzem war es gerade die unsymmetrische Spaltung bei Bestrahlung mit langsamen Neutronen, die einer befriedigenden Erklärung Schwierigkeiten machte. Trotzdem waren es besonders die experimentellen Befunde bei der symmetrischen Teilung des Bi (3), die mir für einen Einfluss abgeschlossener Neutronenschalen zu sprechen schienen. Die in den letzten Jahren für die Wechselwirkung zwischen energiereichen Partikeln und schweren Kernen entwickelten Vorstellungen (4) unterstreichen die Bedeutung der bei der Wismutspaltung erhaltenen Resultate.

Es ist leicht einzusehen, dass wenn überhaupt die abgeschlossenen Schalen in den Kernen für die Kernspaltung eine Rolle spielen, es wesentlich die Neutronenschalen von 50 und 82 Neutronen sein werden. Der Einfluss der energetisch bevorzugten Neutronengruppierungen kann sich natürlich nur bei kleinen Anregungen des sich spaltenden Kerns geltend machen. Also entweder bei Bestrahlung mit langsamen Neutronen solcher Atomkerne, deren Z^2/A (für den Zwischenkern) nahe dem kritischen Wert liegt (5), wie U 233, U 235, U 238, etz. Oder, wenn man mit energiereichen Partikeln Kerne bombardiert, bei denen, bevor eine nachweisbare Spaltung eintreten kann, so viele Neutronen abdampfen müssen, dass die Spaltung wieder in einem nicht hoch angeregten Kern erfolgt. Das scheint der Fall bei Bi 209 zu sein, wo nach PERLMAN und GOECKERMANN (3) entsprechend ihren experimentellen Ergebnissen 10–12 Neutronen abgedampft sein müssen, ehe der Spaltungsprozess nachweisbar wird.

Atomkerne, deren Z^2/A Wert nahe dem kritischen Wert liegt, sollten bei Bestrahlung mit energiereichen Teilchen jedenfalls symmetrische Teilung zeigen. Denn falls ein Kern in hoch angeregtem Zustand sich spaltet, kann die kleine energetische Bevorzugung geschlossener Schalen keinen Einfluss haben.

Es gibt aber noch eine zweite Möglichkeit, deren Eintreten von der Konkurrenz zwischen Neutronenabdampfung und Kernspaltung in einem hoch angeregten Kern abhängt. Es wäre denkbar, dass die Neutronenabdampfung gegenüber der Spaltung so lange bevorzugt ist, bis die Kernanregung kleiner geworden ist als die Bindungsenergie des am losesten gebundenen Neutrons. Dann würde auch in diesem Fall die Spaltung in einem nicht hochgeregtem Zustand des Kerns erfolgen, wobei der sich spaltende Kern erheblich weinger Neutronen (und vielleicht auch weniger Protonen) besitzen würde als der Ausgangskern.

Nach dem Modell des „durchsichtigen“ Kerns von SERBER (4), und den unter Zugrundelegung dieses Modells von GOLDBERGER (6) durchgefürhten Berechnungen muss man jedenfalls eine sehr breite Energieverteilung der Anregungszustände eines mit sehr energiereichen Partikeln beschossenen schweren Kerns erwarten. Die experimentellen Ergebnisse von O'Connor und Seaborg (7) bei der Bestrahlung von gewöhnlichen Uran mit Alpha-Strahlen von 380 Mev stimmen mit dieser Erwartung überein. Sie sollen später etwas ausführlicher besprochen werden.

Für die Bevorzugung der Neutronenabdampfung, so lange sie energetisch möglich ist, gegenüber der Kernspaltung sprechen verschiedene Versuche über die Verteilung der kinetischen Energie der primären Bruchstücke in Abhängigkeit von der Energie der bombardierenden Teilchen. Z.B. ist die mittlere kinetische Energie bei Bestrahlung von U 235 mit thermischen Neutronen und mit Neutronen von 90 Mev Energie beziehungsweise 78 Mev und 83 ± 1,5 Mev (8). Auch wenn man berücksichtigt, dass nach Goldberger (8) bei Bestrahlung mit 90 Mev Neutronen die mittlere Anregung eines schweren Kerns nur etwa 45 Mev beträgt, zeigen die experimentellen Werte für die kinetischen Energien der Bruchstücke, dass die Kernanregungsenergie in anderer Weise (vermutlich Abspaltung von Neutronen) verbraucht werden muss.

Bei Bestrahlung mit energiereichen Deuteronen von an Pb 204 bzw. Pb 208 angereicherten Bleipräparaten ist für gleiche Energie der Deuteronen die Ausbeute an Mo 99 immer grösser für das Isotop 204, was gleichfalls die Bedeutung der der Spaltung vorangegangenen Neutronenabdampfung unterstreicht und auch von dem Verfasser dahin gedeutet wird, dass so lange Neutronen abgegeben werden, bis der Spaltungsprozess in wirksame Konkurrenz mit der Neutronenemission treten kann und dass das erst der Fall sein wird, wenn die Anregung des Kerns nicht mehr für eine weitere Neutronenverdampfung ausreicht (9).

Wenn die energetische Bevorzugung der Schalen von 50 und 82 Neutronen für die wahrscheinlichste Spaltungsform eine Rolle spielt, so kann natürlich die unsymmetrische Teilung nur eintreten so lange der sich spaltende Kern 132 oder mehr Neutronen besitzt. Das ist immer der Fall bei denjenigen Kernen, deren Z^2/A von vorneherein nahe dem kritischen Wert liegt. Bei dem Prozess U 235 + langsames Neutron sind z.B. rund 140 Neutronen vorhanden, so dass in den Bruchstücken die Neutronenschalen von 50 bzw. 82 Neutronen sich ausbilden können. Dabei scheint es vernünftig, anzunehmen, dass die zugehörige Ladungsverteilung für den wahrscheinlichsten Spaltungsmodus im wesentlichen diejenige sein wird, die in stabilen Kernen mit den betreffenden abgeschlossenen Neutronenschalen auftritt. Unter Berücksichtigung der Tatsache, dass die Summe der Ladungen der primären Bruchstücke gleich der Ladung des sich spaltenden Kerns sein muss, sollten für diese Spaltung eines Urankerns die wahrscheinlichsten leichten primären Bruchstücke Ladungen von 36 bis 38 und die zugehörigen schweren Fragmente Ladungen von 56–54 aufweisen. Das steht in guter Übereinstimmung mit den experimentell festgestellten chemischen Zuordnungen der primären Fragmente in den beiden Maxima bei der unsymmetrischen Teilung des durch langsame Neutronen gebildeten Zwischenkerns U 236 (10).

Werden Atomkerne, deren Z^2/A nahezu den kritischen Wert hat, mit energiereichen Partikeln bombardiert, so wird je nach der Höhe der eingetretenen Anregung der beschossenen Kerne eine kleinere oder grössere Anzahl von Neutronen abdampfen, ehe Spaltung eintritt. Besitzt hernach ein solcher Kern weniger als 132 Neutronen, so kann nur mehr die mit 50 Neutronen energetisch bevorzugte Schale sich ausbilden. Hier kommt die Komplikation hinzu, dass bei Bestrahlung mit sehr energiereichen Partikeln ausser Neutronen auch Protonen abdampfen können, d.h. die Summe der Ladungen der primären Bruchstücke muss nicht identisch sein mit der Atomnummer des beschossenen Kerns. Jedenfalls werden, wie schon früher erwähnt, die entstandenen Zwischenkerne ein breites Gebiet angeregter Zustände umfassen, so dass sowohl Spaltung nach Abdampfen einer geringen Zahl von Neutronen als eine solche nach Abdampfung vieler Neutronen vorliegen kann.

O'Connor und Seaborg (7) haben die Spaltung gewöhnlichen Urans bei Bestrahlung mit Alphastrahlen von 380 Mev Energie untersucht. Sie fanden ein einziges Maximum und eine um dieses Maximum symmetrisch gelegene breite Verteilung der primären Bruchstücke als Funktion der Massenzahl. Die Verff. betonen, dass die Verteilung sicher neidrigere und höhere Massenzahlen umfasst, alls bei der Uranspaltung durch langsame Neutronen gefunden werden (10). Sie deuten ihre Resultate dahin, dass ihre Verteilungskurve eine Überlagerung darstellt von Spaltungsprozessen ohne erhebliche Abdampfung von Neutronen (unsymmetrische Spaltung) bis zu solchen, wo eine grosse Zahl von Neutronen abgedampft war, ehe Spaltung eintrat und schliessen aus der symmetrischen Form ihrer Verteilungskurve, dass der letztere Prozess überwiegen muss. Das ist das Verhalten, das man aus der Theorie von Serber erwarten sollte. Dass die Abdampfung vieler Neutronen und auch einer gewissen Zahl von Protonen in beträchtlichem Mass vorkommt, zeigt die von den Verfassern gefundene relativ grosse Intensität der sogenannten „Spallationprozesse“.

In neuerer Zeit ist von Swiatecki (11) darauf hingewiesen worden, dass die Berücksichtigung der Kompressibilität und Polarisation des Atomkerns (Neutron-Proton-Flüssigkeitströpfchen) die Deformationsenergie in dem Sinn beeinflusst, dass diese Energie für unsymmetrische Teilung kleiner wird. Das kann die unsymmetrische Teilung erklären, wie sie bei Bestrahlung mit relativ langsamen Neutronen im Gebiet von $A = 232$ bis $A = 239$ und $Z = 90$ bis 94 festgestellt ist. Die beobachtete symmetrische Teilung mit energiereichen Neutronen und Deuteronen als bombardierende Partikel soll dann dadurch zustande kommen, dass wegen der hohen Kernanregung (schnelle Spaltung), die primären Bruchstücke sozusagen keine Zeit haben, sich im energetisch günstigsten, unsymmetrischen Massenverhältnis zu teilen. Diese Erklärung der symmetrischen Teilung verlangt, dass für einen hoch angeregten Kern die Wahrscheinlichkeit für Spaltung genügend gross ist gegenüber der Wahrscheinlichkeit für Abdampfung von Neutronen.

Es scheint jedoch kaum möglich diese Erklärung für die symmetrische Spaltung des Bi 209 heranzuziehen. Die Spaltung des Bi ist von Goeckermann und Perlman (3) bei Bestrahlung mit 190 Mev Deuteronen und von Jungerman und Wright (8) bei Bestrahlung mit 90 Mev Neutronen untersucht worden. In beiden Fällen wurde eine symmetrische Spaltung gefunden. Goeckermann und Perlman haben die Verteilungskurve durch chemische Identifizierung der Spaltungsbruchstücke aufgenommen. Die grösste Ausbeute wurde für Mo 99 erhalten und die Verff. geben an, dass der sich spaltende Kern sehr wahrscheinlich Po 198, 199 oder 200 ist. Alle Bruchstücke mit kleinerer Masse als derjenigen, die zur wahrscheinlichsten Teilung gehört, sind Betastrahler. Die schwereren Bruchstücke bis zu Zinn 120 sind entweder Betastrahler oder stabile Isotope. Bruchstücke oberhalb Zinn besitzen, soweit sie nicht stabil sind, einen Unterschuss an Neutronen.

In der Arbeit von Jungerman und Wright wurde die Verteilungskurve der kinetischen Energie der primären Bruchstücke des Bi untersucht und auch nur ein Maximum gefunden. Wenn man berücksichtigt, dass eine erhebliche Anzahl (etwa 10) Neutronen abdampfen müssen, um in die Nähe des kritischen Z^2/A Wertes zu kommen, so kann der sich spaltende Kern kaum genügend hoch angeregt sein, um aus der Anregung die symmetrische Fission zu erklären. Denn in der gleichen Arbeit wird gezeigt, dass U 238 und Th 232 bei Bestrahlung mit etwa 45 Mev Neutronen noch deutlich unsymmetrische Spaltung ergeben, obwohl hier Z^2/A schon ohne erhebliche Neutronenabgabe nahe dem kritischen Wert liegt. Das Minimum beträgt etwa 20 % der Höhe der Maxima. Bei Bi und 45 Mev Neutronenenergie ist der Spaltungsprozess nicht nachweisbar. GOECKERMANN (9) gibt ausdrücklich an, dass sobald die Spaltung bei Bi überhaupt merkbar geworden ist — also oberhalb der experimentell gefundenen Schwelle von 50 Mev — sie schon vorwiegend symmetrisch ist.

Es scheint daher kaum möglich die symmetrische Teilung beim Bi damit zu erklären, dass der sich spaltende Kern in hoch angeregtem Zustand ist und die sich bildenden Bruchstücke keine Zeit haben, sich zu der energetisch günstigeren unsymmetrischen Massenverteilung umzuordnen.

Dagegen scheint das Schalemnodell eine Erklärung bieten zu können.

Der sich spaltende Bi-Kern besitzt nur etwa 115–117 Neutronen, also zu wenige, um eine Schale von 50 und in eine Schale von 82 Neutronen aufgeteilt zu werden, aber genügend, um 2 Schalen von je 50 Neutronen zu bilden. Die wahrscheinlichste Teilung wird daher symmetrisch um ein Isotop mit einer Schale von 50 Neutronen (zusätzlich einiger weiterer Neutronen) erfolgen und die zugehörige Ladung sollte 41–42 sein, wie es das Experiment tatsächlich ergeben hat. Die relativ schmale symmetrische Verteilung der Spaltung um die Schale von 50 Neutronen könnte auch verständlich machen, dass von einer bestimmten Massenzahl ab die schweren Bruchstücke einen Unterschuss an Neutronen aufweisen, der durch die der Kernspaltung notwendig vorausgehende Abdampfung von etwa 10 Neutronen bedingt ist.

Im Zusammenhang mit den hier vorgebrachten Überlegungen wäre es interessant festzustellen, ob es überhaupt eine schnelle Spaltung gibt, d.h. eine direkte Kernspaltung in einem sehr hochangeregten Atomkern. Wenn dies der Fall ist, müssten vermutlich die primären Bruchstücke eine grosse Anregungsenergie besitzen und eine erhebliche Zahl ,,prompter" Neutronen abspalten. Leider ist eine direkte experimentelle Untersuchung dieser Frage wegen der gleichzeitig auftretenden ,,Spallationprozesse" vielleicht nicht möglich.

LITERATUR. 1. **L. Meitner,** Nature *165*, 561, 1950. — 2. **M. Göppert-Mayer,** Phys. Rev. *75*, 990, 1949. — **O. Haxel, J. H. D. Jensen** u. **H. E. Suess,** Naturw. *36*, 153, 155, 1949. — 3. **R. H. Goeckermann** and **I. Perlman,** Phys. Rev. *76*, 628, 1949. — 4. **R. Serber,** Phys. Rev. *72*, 1008, 1114, 1947; *75*, 1352, 1949. — 5. **N. Bohr** and **J. A. Wheeler,** Phys. Rev. *56*, 426, 1939. — 6. **M. L. Goldberger,** Phys. Rev. *74*, 1269, 1948. — 7. **P. R. O'Connor** and **G. T. Seaborg,** Phys. Rev. *79*, 1188, 1948. — 8. **J. Jungerman** and **S. C. Wright,** Phys. Rev. *76*, 1112, 1949. — 9. **R. H. Goeckermann,** AECD-2534, 1949. — 10. Plutonium Project, Journ Amer. Chem. Soc. *68*, 2411, 1946. — 11. **W. J. Swiatecki,** Phys. Rev. *83*, 178, 1951.

Tryckt den 6 februari 1952

Uppsala 1952. Almqvist & Wiksells Boktryckeri AB

ARKIV FÖR FYSIK Band 4 nr 21

Communicated 12 September 1951 by ARNE WESTGREN

A spectrometer for an investigation of angular dependence of the structure in the continuous X-ray spectrum

By PER OHLIN

With 3 figures in the text

In an earlier paper[1] the existence of a structure in the continuous X-ray spectrum was pointed out. The phenomenon was later more closely investigated experimentally [2, 3], but still very little is known about it. Attempts at theoretical explanations have been made [4, 5], but they are not satisfactory. To understand the origin of the structure, more experimental information seems to be necessary. One point which would be of special interest is whether the structure varies with the angle between the electron beam of the X-ray tube and the X-rays.

In order to investigate this a spectrometer with a bent crystal and a Geiger counter was built in which it is possible to change the angle mentioned above without changing any other condition. The principle of the spectrometer arrangement is the same as that earlier described by the present author.[6] Thus the crystal can be moved along two steel rods, which also carries the Geiger counter. Adjustments for different wave-lengths are made by moving the crystal along the rods and turning it around an axis perpendicular to the plane through the rods. The Geiger counter and its slit is adjusted in the same way. The main difficulty in designing the spectrometer consists in the necessity of making the X-ray tube movable in order to vary the angle between cathode-rays and X-rays. Fig. 1 shows the spectrometer from above. *C* is the crystal and its table, and *G* is the counter. They are movable along two steel rods placed on a plane-rectangular steel plate forming the bottom of the spectrometer. As seen from the figure, frame *F* forming the walls of the spectrometer is rectangular. One of its corners, however, is cut by two planes forming an angle of 150°, as indicated in the figure. The *X*-ray tube can be fixed to any one of these planes. The system of the two rods supporting the crystal table and the counter can be turned about an axis through the centre of the crystal. In this way it is prossible to vary the angle between the frame carrying the X-ray tube and the two rods about 15°. By means of these arrangements it is possible to vary the glancing angle from about 45° and down.

---

[1] P. OHLIN, Arkiv för Mat., Astr. o. Fysik, Bd 29 A, N:o 3, 1942.

[2] Å. NILSSON and P. OHLIN, Arkiv för Mat., Astr. o. Fysik, Bd 33 A, N:o 23, 1946.

[3] J. A. BEARDEN and G. SCHWARZ, Phys. Rev., 79, 674, 1950; J. A. BEARDEN, F. T. JOHNSON and H. M. WATTS, Phys. Rev., 81, 70, 1951.

[4] J. LINDHARD, Arkiv för Mat., Astr. o. Fysik, Bd 31 B, N:o 7, 1945.

[5] B. R. A. NIJBOER, Physica, 12, 461, 1946.

[6] P. OHLIN, Diss., Uppsala 1941.

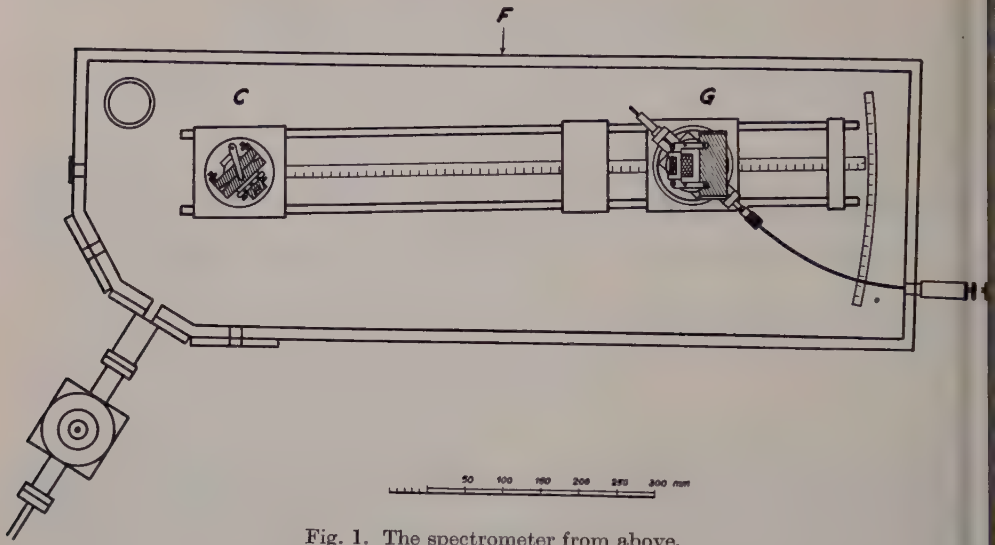

Fig. 1. The spectrometer from above.

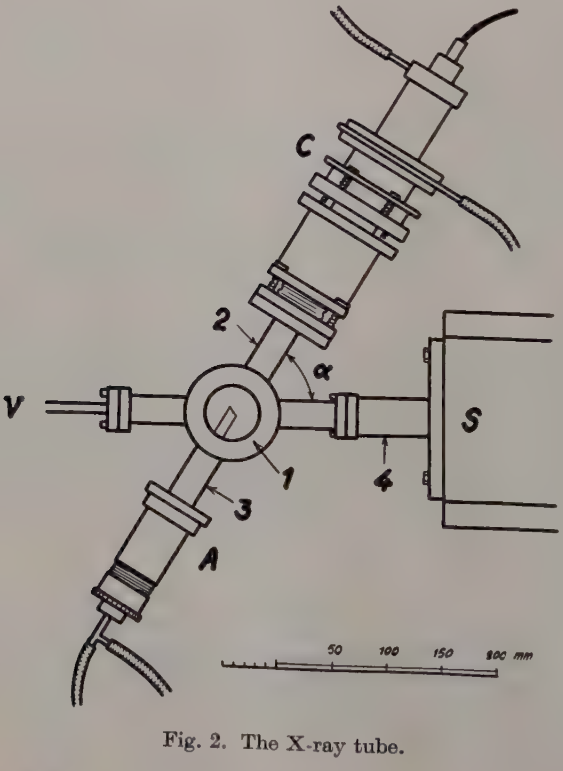

Fig. 2. The X-ray tube.

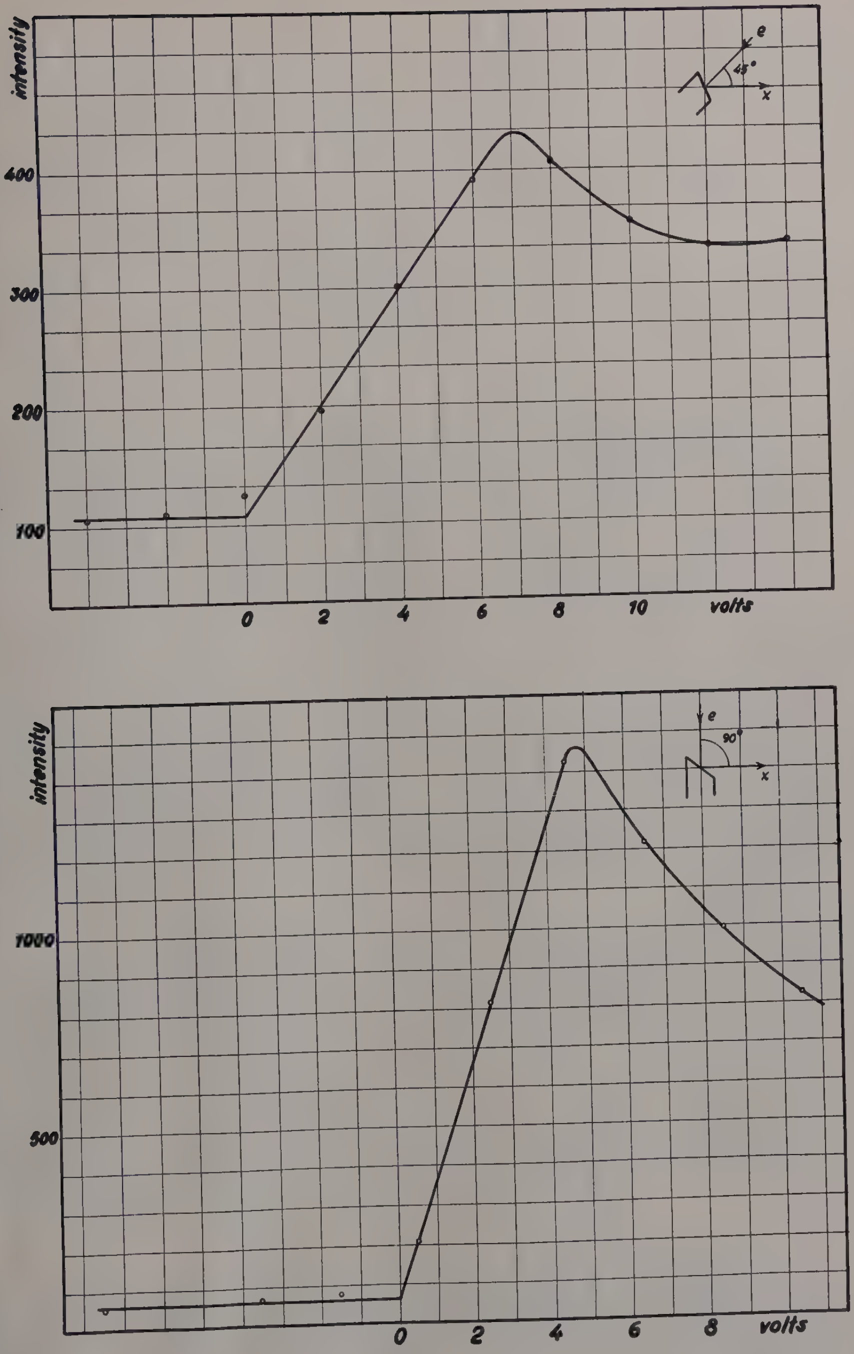

Fig. 3. Isochromats taken at the wave-length 3351 X.U. In the upper corner to the right the angles between electron beam, X-rays and target surface are indicated.

The X-ray tube is shown in Fig. 2. It consists of a brass tube 1 to which two other tubes 2 and 3 are soldered. Tubes 2 and 3, supporting the cathode C and the anticathode A, are placed on opposite sides of tube 1 in such a way that their axes are coincident. By means of another tube 4 the system is attached to the spectrometer frame. A fifth tube connects it to an ionization gauge V. The electrons from the indirectly heated oxide cathode are accelerated by a negative voltage applied to the cathode and by a magnetic lens focused onto the target in the centre of tube 1. By means of the lens it is possible to give the focal spot the correct size, which is very important for the intensity of the X-rays reflected by the crystal. Furthermore, the distance between the focal spot and the crystal is rather great which means that the former is located close to the Rowland circle. As should be expected from theoretical considerations, this is very advantageous with respect to the intensity.

A set of tubes was made for which the angle α of Fig. 2 is different. It is thus possible by steps of 15° to vary α, that is the angle between the electron beam and the X-rays investigated, from 45° to 135°.

The X-ray tube is evacuated by a mercury diffusion-pump which in combination with a liquid air trap keeps the pressure below 10^{-5} mm Hg. The use of a mercury pump eliminates the risk of contaminating the target by organic substances. The spectrometer is separately exhausted by a large molecular pump of the disk type.[1]

As a very preliminary result the two isochromatic curves of Fig. 3 may be given. They are taken at the wave-length of $\mathrm{Ca}_{K\alpha_1}$ (3351.85 X.U.) A quartz crystal ($d = 3336.3$ X.U.) bent to one metre's radius was used, and the slit width corresponded to about 0.9 volts. A tungsten target was used. In the figure are indicated the directions of the electron beam, the X-rays recorded, and the target surface. As may be seen from the curves, the position of the first maximum of the isochromats shows a slight angular dependence. Thus the distance from the threshold voltage to the maximum is in the first case (45°) about 7 volts, and in the second (90°) c. 4.5 volts. It may be observed that in both cases the angle between the electron beam and the target surface was the same, whereas the angle between the X-rays and the target is altered. It seems probable that even this latter angle will influence the shape of the curves.

Physics Laboratory, University of Uppsala, Sept. 10th, 1951.

---

[1] I am indebted to Prof. M. SIEGBAHN for lending me one of his big molecular pumps.

Tryckt den 6 februari 1952

Uppsala 1952. Almqvist & Wiksells Boktryckeri AB

ARKIV FÖR FYSIK Band 4 nr 22

Communicated 12 September 1951 by MANNE SIEGBAHN and ERIK HULTHÉN

An improved recording microphotometer

By LENNART LUNDIN

With 7 figures in the text

The first description of this type of microphotometer was given by M. SIEGBAHN[1] in 1924, when the instrument's special properties were described. A few years afterwards E. BÄCKLIN[2] described a later model of microphotometer, constructed at the Physics Institutions of Upsala University. On the basis of experiments with these instruments and by employing new methods for recording, an improved type of microphotometer has been produced at the Nobel Institute of Physics.

Principles of construction of the microphotometer

The microphotometer was designed with the object of producing automatic recording of a spectral plate, so that the distances between the spectral lines would be reproduced on the recording paper with an accuracy of 1 μ in the spectral plate scale. In order to ensure this exact relation between the distances on the spectral plate and those transferred to the recording paper, it is necessary that the relation between the displacements of the spectral plate and the recording paper during photometering shall be constant. To obtain this, wedge transfer is employed, with which it is only necessary to have the sides of the wedge perfectly straight to attain the desired exactitude in transfer. By making the apex angle of the wedge variable, the ratio between the displacement of the recording paper to the spectral plate (the magnification) can be set to any required value. Previously there was used an adjustable wedge consisting of two accurately ground steel rules, which were fixed to the recording table and as this moved were pressed in between a fixed stud and the measuring table. The principle of transfer is retained in the new design, but one side of the wedge consists in this case of the recording table, the other of a steel rule readjustably mounted on the same. To ensure the above-stated accuracy of 1 μ requires that the edge of the steel rule and the two cylindrical bars on which the recording table runs be straight within 0.5 μ. On the apparatus constructed there has been measured a toral error in transfer of 0.6 μ. The magnification can be set to any value between 3 and 200 ×.

The mechanical arrangement

The mechanical arrangement will be seen from Fig. 4. It consists of a cast-iron base with a vertical and a horizontal frame, in which two pairs of cylindrical bars (A and B in Fig. 4) are fixed. The bars (A) support the recording table (C) which

---

[1] M. SIEGBAHN, Phil. Mag. *48*, 217, 1924.
[2] E. BÄCKLIN, ZS. f. Instr.kunde, *47*, 373, 1927.

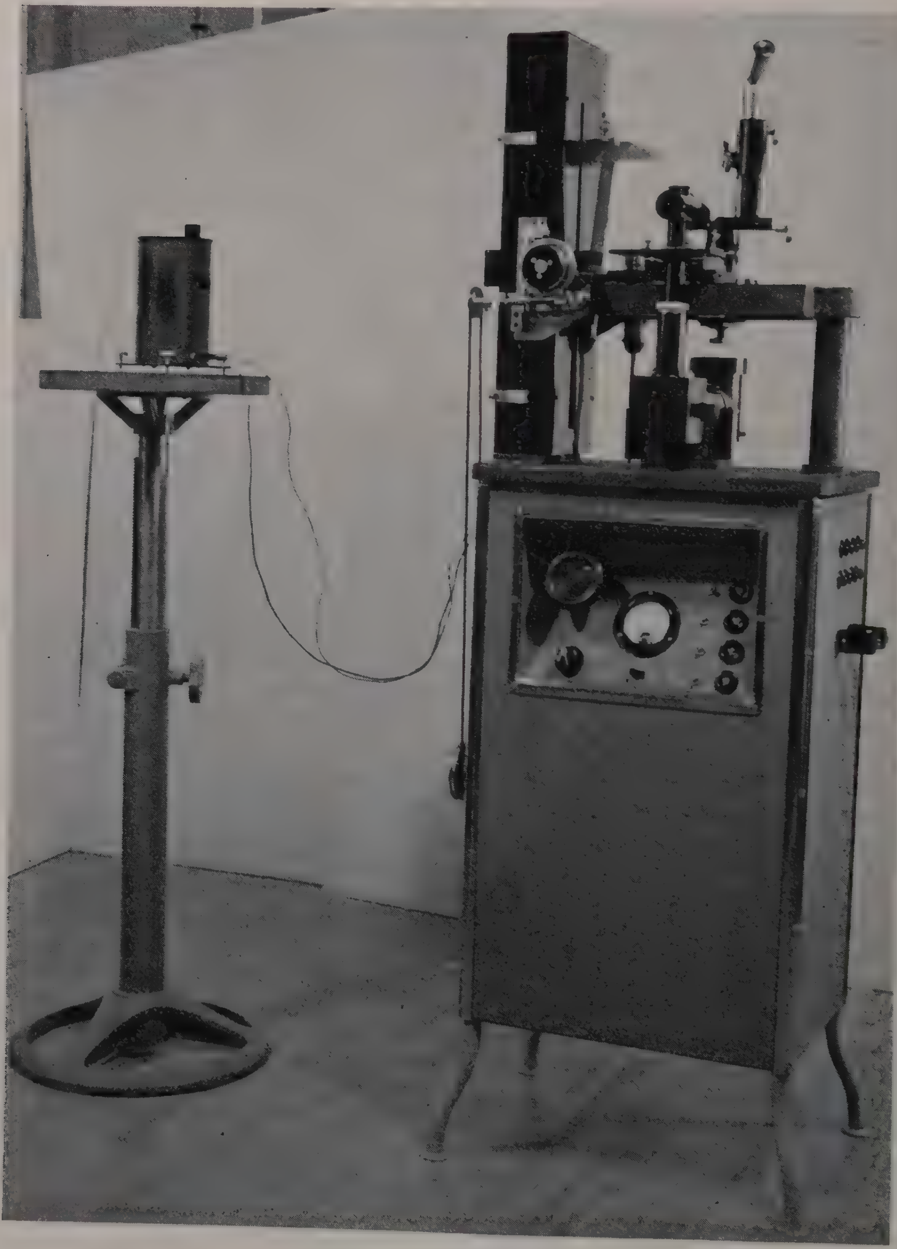

Fig. 1. View of the microphotometer with mirror galvanometer.

can be moved vertically and on which is mounted a frame for holding the recording paper. The recording table is carried on the bars on three studs, two of which are V-shaped and rest against one of the bars, while the third is flat and lies against the

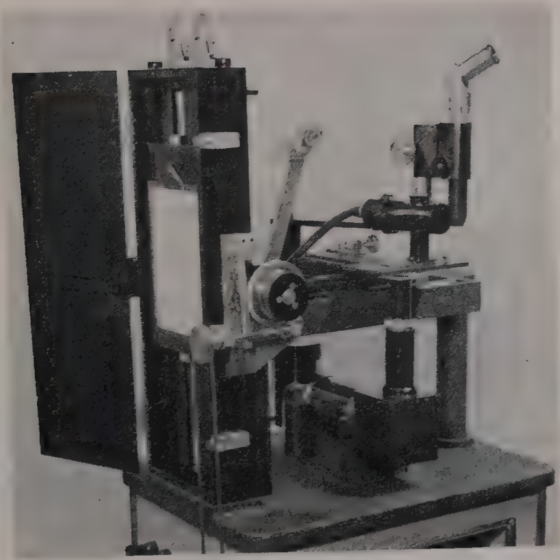

Fig. 2. The recording table may be seen at the left with photographic paper. At the right, the installing microscope and photomultiplier.

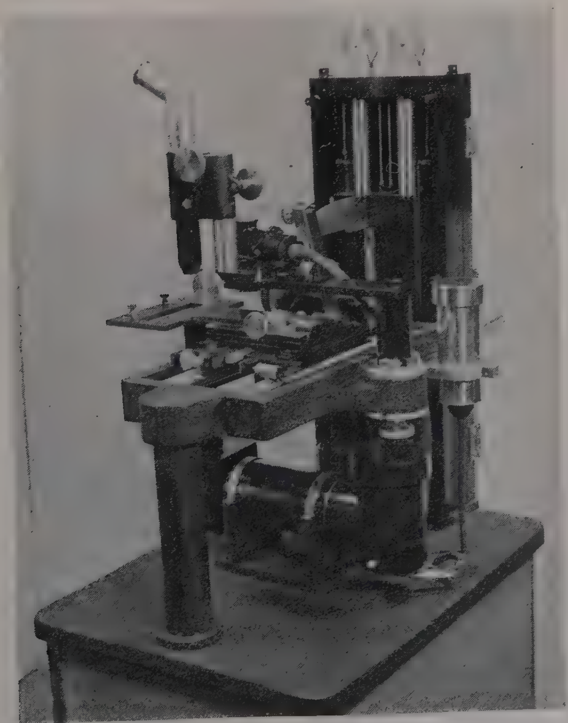

Fig. 3. To the left may be seen the measuring table, in the middle the bars and counterweights for the recording table, and to the right the galvanometer lamp.

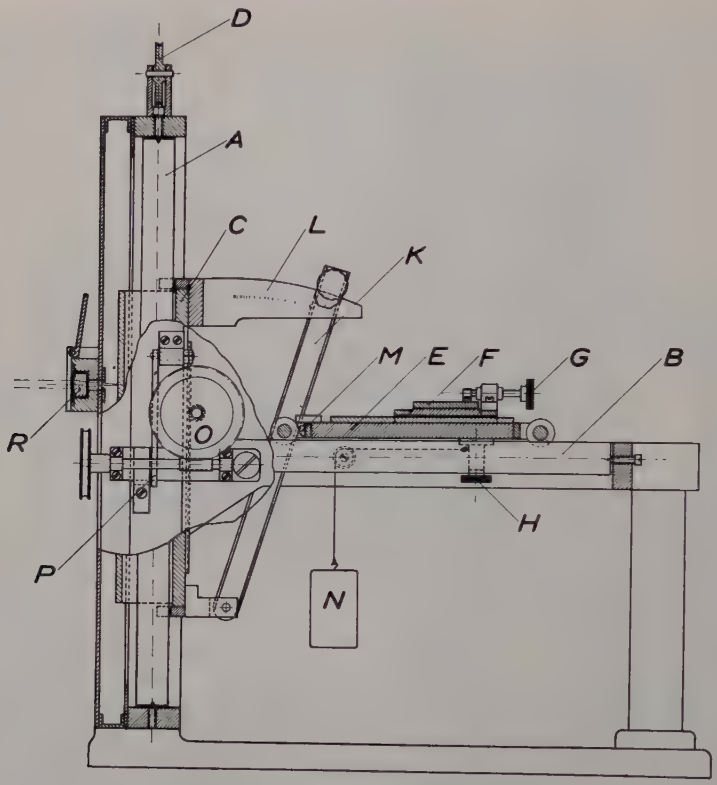

Fig. 4. The mechanical arrangement.

other bar. With this arrangement the table always takes up a fixed position on the bars. Two counter-weights, suspended by wires running over pulleys (D) take up the weight of the recording table. The recording table with its bearing arrangement is enclosed in a light-tight housing.

On the horizontal bars (B) runs a carriage (E) which, like the recording table, is carried on three points. The supports in this case consist of steel rollers, the two running on the front bar having V-shaped tracks. The carriage (E) carries the measuring table (F) on which the spectral plate is placed. To provide adjustment of the desired area on the spectral plate, the measuring table (F) is movable lengthways and crossways on the carriage. Movement of the measuring table is controlled by the knobs (G) and (H).

The steel rule (K), which transfers the movement of the recording table to the carriage, is mounted on the recording table so that it is pivoted round its lower end and adjustable on the scale (L) in its upper end. Movement of the steel rule's upper end on the scale alters the wedge angle and thus the magnification. The scale (L) is graduated for magnifications between 3 and 200 ×. A semi-circular agate plate (M) rests against the front edge of the rule, which is straight and accurately ground. The agate plate is mounted on the carriage, its pressure against the rule being kept constant by the weight (N).

The recording table (C) in photometering is fed downwards and the driving is done by means of a rack fixed to the table, the pinion of which is coupled to the worm gear (O). This in turn is driven by an electric motor over a cord transmission. When the recording table reaches its bottom position, the drive is automatically disconnected by the lever (P), which holds the worm gear tangent screw in mesh with the worm wheel.

Recording device

To record the spectral plate's darkening in the form of a curve on the recording paper, the following method is employed. There is projected on the spectral plate a slit image by means of a slit projector. Above the slit image there is placed a photomultiplier so that the light not absorbed by the spectral plate falls on the cathode of the photomultiplier. A mirror galvanometer connected in the anode circuit of the photomultiplier is illuminated by a single filament galvanometer lamp and the image of the lamp's filament is projected on the recording table by means of a lens located in front of the galvanometer mirror. A cylindrical lens (R in Fig. 4) breaks up the slit-shaped image of the lamp filament to an intensive pointshaped image on the recording table's photographic paper. When, on photometering, the measuring table and the recording table are moved, the lines of the spectral plate will pass before the projected slit image. The light variations thereby caused on the photocathode in the multiplier tube produce a deflection of the galvanometer mirror corresponding to the lighting. Owing to this deflection the light point projected on the recording paper is moved in a horizontal direction. In combination with the recording table's vertical movement, there is then marked on the recording paper a curve corresponding to the darkening of the spectral plate.

The photomultiplier employed is RCA 931 A. The sensitivity to light of the recording device has been increased to a high degree by the high magnification, $\sim 10^6$, of the photomultiplier and it has thus been possible to work with appreciably smaller slit and consequently higher resolving capacity.

The design of the slit projector is shown by Fig. 5. A lamp enclosed in a light-tight chamber illuminates a vertical slit via a condensor. A slide device makes it possible to use one of two fixed slits, 0.1 and 0.01 mm in width. The length of the slit may be varied from 4 to 40 mm. By means of a microscope lens (Nife 3.3) there is projected on the spectral plate an image of the slit reduced in the ratio 1:4. The slit image will then have a width of 25 or 2.5 μ respectively and a maximum length of 10 mm.

The photomultiplier and a microscope tube (Nife BrT 40) are mounted on a swing arm, so that one or the other may be adjusted over the slit image projected on the spectral plate. By means of the microscope the slit projector is so adjusted that the slit image is focussed exactly on the photographic surface of the spectral plate and so that there is parallelity between slit image and the spectral lines.

The stand

The microphotometer is mounted on a stand, with a height suited to comfortable working position. On the front the stand is provided with a control panel for the microphotometer's electric equipment. A stabilised rectifier for dynode and anode voltage of the multiplier tube as also the driving motor for the recording table and

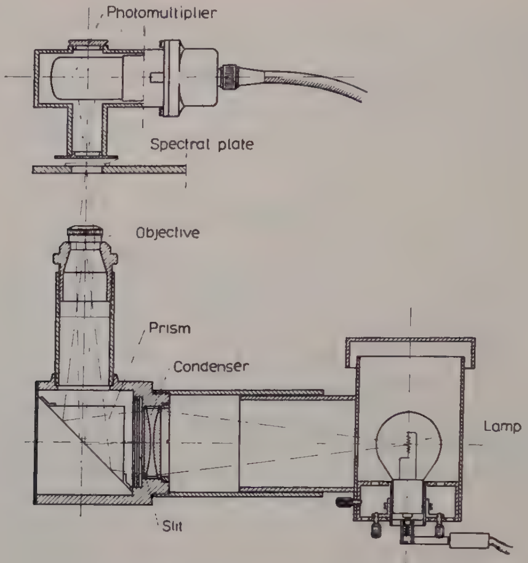

Fig. 5. Slit projector and photomultiplier.

the galvanometer lamp transformer are placed in the stand. The control panel is provided with amperemeter for check of the current to the slit projector lamp and rheostats for rough and fine regulation of same, besides circuit breaker and pilot lamps for motor, rectifier and galvanometer lamp.

Some recordings

To check the exactness of the transfer the steel rule was set parallel with the vertical bars. There should then, if rule and bars are perfectly straight, be obtained no horizontal movement in the measuring table when the recording table moves vertically. The measuring table's movement was measured by means of a microcator and it was found that the maximum deviation between the end points of the rule amounted to 0.6 μ. As a check of the linearity in the reproduction of the curve of darkening there was photometered the scale of a microscope eyepiece. The division of the scale was 0.1 mm and each tenth division line was double length. In the photometering the 0.01 mm slit was used and the slit length was adjusted to agree with the long scale division lines. Fig. 6 a and b show two recordings of the eyepiece scale with magnification set at 20 and 30 × respectively.

It will be seen from the figure that even on the recording paper there is obtained a ratio of 1:2 between the curve peaks corresponding to the respective division lines.

The resolving ability of the microphotometer was checked by photometering a microscope calibration scale with divisions 0.01 mm. In the photometering there were employed magnification 100 × and slit 0.01 mm. Fig. 6 c shows the photometer curve obtained and this shows that the resolving ability of the microphotometer is about 0.01 mm.

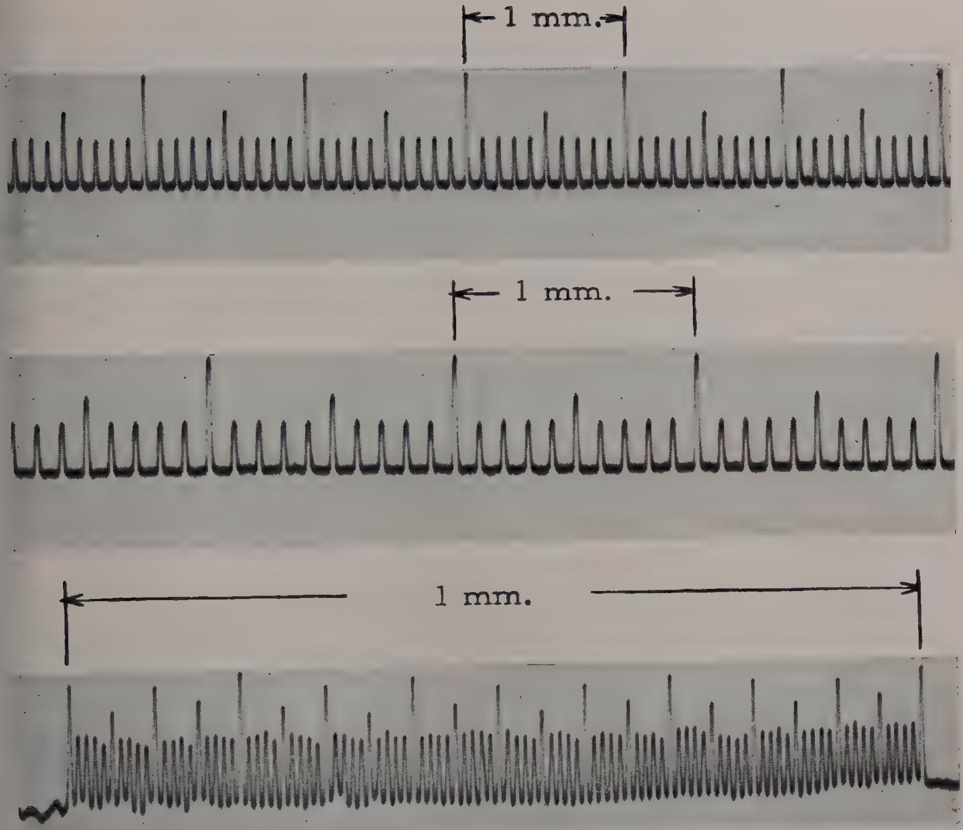

Fig. 6. Microphotogram of a) ocular scale, divisions 0.1 mm. Magnification 20 ×. b) ocular scale, divisions 0.1 mm. Magnification 30 ×. c) calibration scale, divisions 0.01 mm. Magnification 100 ×.

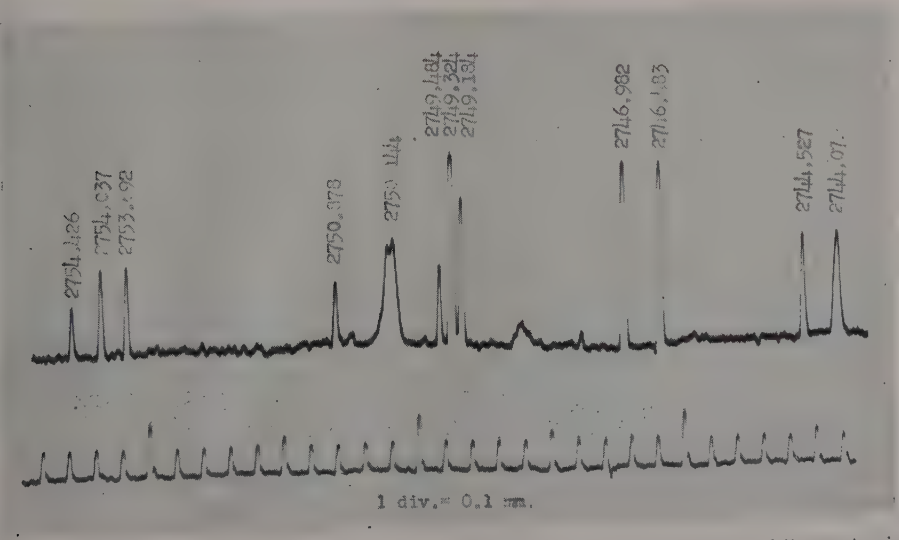

Fig. 7. Microphotogram of the range 2 744—2 754 Å of the Fe spectrum. 0.7 × nat. size.

An example of the microphotometer's employment is shown in Fig. 7, giving the recording of the range 2 744–2 754 Å of the Fe spectrum. The spectral plate photometered was taken with grating spectrograph, the grating used being produced by the ruling machine at the Institute. The grating was set in Rowland mounting and had the following data: Number of lines/mm: 576. Total number of lines: 46 000. Linear dispersion in the first order: 3.645 Å/mm. Radius of curvature: 4.8 metres.

In the triplet at 2 749 Å we have $\Delta \lambda = 0.14$ and 0.16 Å respectively which, with the dispersion 3.645 Å/mm, gives a distance between the lines of 0.039 mm and 0.044 mm respectively on the spectral plate. As is seen, the triplet is well resolved. With unaltered setting of the microphotometer, there was taken on the same photogram a recording of an ocular scale with division 0.1 mm. In this way there was obtained a check of the magnification setting.

Nobel Institute of Physics, Stockholm 50, Sweden.

Tryckt den 2 februari 1952

Uppsala 1952. Almqvist & Wiksells Boktryckeri AB

ARKIV FÖR FYSIK Band 4 nr 23

Read 6 June 1951

Spectroscopic intensity modulation

By Erik Hulthén

With 7 figures in the text

Summary

1. The objects of spectroscopic intensity modulations.
2. Talbot's bands and the Edser-Butler plate.
3. The grating-interferometer.
4. The spectrograph and the grating-interferometer.
5. Performances of the grating-interferometer.
6. Some preliminary results.

1. Investigation of the hyperfine structure of spectral lines and the rotational structure in band- spectra makes great demands on the resolving power of the spectroscope which are not always met even by large diffraction gratings. The hyperfine structure of single atomic lines is successfully investigated by crossing the spectrum of the prism or the grating by the spectrum of an interferometer. The failure in brightness and the complicated evaluation of the diffraction pattern, however, makes this method less attractive for the study of the band-spectra with their overwhelming richness of lines. These difficulties are effectively eliminated with the échelle-grating recently introduced by Harrison. The perfecting of this instrument will probably mean a great advance in spectroscopy. But apart from this the principle of spectroscopic intensity modulation here proposed may be useful in cases where disentanglement or simplification of crowded parts in the spectrum are needed.

The term spectroscopic intensity modulation here used refers to the characteristic periodicity which appears in the spectrum when the spectroscopic beam of rays is divided into interfering parts. With two interfering beams the carrier of the periodicity takes the form of a simple sine-square curve, Fig. 1 a, and with multiple interference a characteristic form indicated in Fig. 1 b.

If we first consider the main object of introducing intensity modulation in a spectrum, we find that the appearance of the lines is governed by their position on the carrier. Thus a strong line which coincides with a minimum on the carrier will be totally quenched, and by increasing the modulation frequency the quenching effect may be used to separate narrow lines from each other. As it is possible to exaggerate this effect by simple methods far beyond the resolving limit of the spectrograph, the individual components in an unresolved group of lines are revealed with very great precision, as the error in a wave-length determination is far smaller than the resolving limit of the spectrograph.

Some typical methods of producing intensity modulation in spectra will now be discussed.

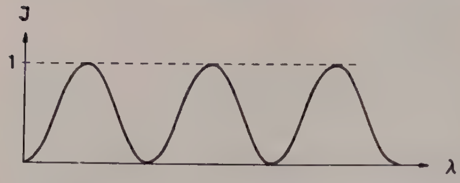

Fig. 1 a.

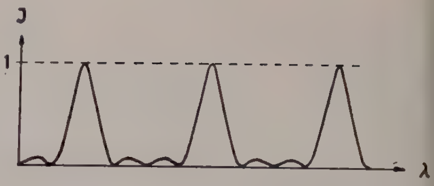

Fig. 1 b.

2. Talbot's bands (1837).

When a thin piece of glass or mica is partly introduced in the beam of rays of a spectroscope, Fig. 2 a, a set of extremely black bands appears, crossing the continuous spectrum parallel to the Fraunhofer lines. The position of these bands obviously obeys the condition:

$$p\lambda = (\mu - 1)\, t, \tag{1}$$

where p stands for half integers, μ for the refraction index of the glass and t for its thickness.

A closely related phenomenon was studied by Fizeau and Foucault in 1850. Here, two semi-transparent and parallel glass plates are introduced in the beam of rays, Fig. 2 b. The interference is now produced between rays passing directly through the plates and rays reflected to and fro between the plates. Thus, the interference here obeys the condition:

$$p\lambda = 2\,\mu\, t, \tag{2}$$

where $\mu \approx 1$ is the refraction index of the air.

Edser and Butler (1898) made use of this method in a simple way to calibrate the prismatic dispersion. The wave-length separation between two neighbouring minima, say p and $p+1$, is given by the relation:

$$F_\lambda = \frac{\lambda^2}{2t} \qquad (\mu = 1). \tag{3}$$

Introducing the wave numbers $\nu = \frac{1}{\lambda}$, we get

$$F_\nu = \frac{1}{2t}\ \mathrm{cm}^{-1}. \tag{3 b}$$

Thus the corresponding wave-number spacing is constant and identical with the not overlapping regions in Michelson's échelon-grating and in Fabry-Perot's étalon-interferometer.

3. From a more detailed analysis of the interference phenomena mentioned above it appears that the intensity minima are due to a shift of the spectrum into neighbouring maxima. Therefore, the spectrum is no longer pure and monotonous.

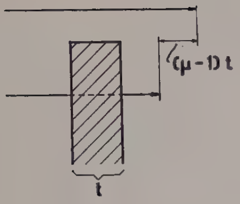

Fig. 2 a.

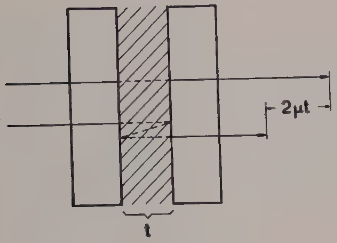

Fig. 2 b.

The author's interest in these phenomena arose from a study of the effects produced when a prism or a diffraction grating is screened by a coarse thread-grating mounted parallel to the prism edge or to the ruling of the grating as the case may be (HULTHÉN and UHLER, 1951).[2] The image of a spectral line was found to split into a diffraction pattern of sharp lines or ghosts symmetrically distributed around its original position. The intensity shift from the spectral line to the accompanying diffraction pattern reaches its optimum when the screened area of the grating equals that of the apertures left open. At the same time the even order images of the diffraction pattern disappear. All these effects are readily deduced from a harmonic analysis of the problem.

In order to make clear the close parallel between these phenomena and the Talbot's bands, the following arrangements were made. In a prism-spectrograph mounted in autocollimation the plane mirror was replaced by a plane-parallel glass plate which reflected the beam of rays in equal amounts from its front and back surfaces. As indicated in Fig. 3, this effect was attained by covering the front surface of the plate with a coarse grating of reflecting strips and apertures while its back surface formed a complete mirror.

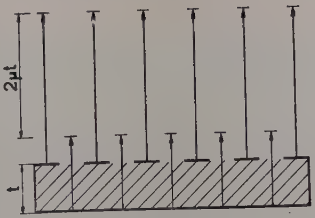

Fig. 3.

The function of this instrument, properly named grating-interferometer, is twofold:

1) to produce perfect interference, according to equations (2) and (3), between the rays reflected from its front and back surfaces;
2) to diffract the reflected beam in different directions, θ, around the normal according to the general grating formula:

$$\sin\theta \approx \theta \approx \pm \frac{\lambda}{\sigma_i} \cdot M. \tag{4}$$

Here σ_i is the grating constant, $\sigma \gg \lambda$, and $M = 0, 1, 3, 5 \ldots$, only the zero and odd orders appearing in the spectrum.

When the beams of rays reflected from the front and back surfaces are in phase, corresponding to integral p-values in (2), the plate acts as a perfect mirror, and the spectral lines will appear unmodified in their position and intensity. At opposite phase, i.e. at half-integral p-values, the zero-order images of the lines are completely absent, their light reappearing symmetrically in the odd orders according to (4). In a coarse grating the intensity rapidly falls off with increasing orders, according to the phase factor $\frac{\sin^2 \theta}{\theta^2}$, thus concentrating the light to the first orders $M = \pm 1$. Simultaneously, however, these images will approach the zero-order image, so that a suitable adaptation of both effects has to be considered.

If we apply the grating-interferometer to the analysis of a narrow group of lines, this will appear much simplified in structure, the quenched components reappearing in symmetrical groups $M = \pm 1$ around the main group $M = 0$. However, if we analyse an extended group of lines, a crowded band-spectrum or the like, this procedure will be inapplicable, owing to the superposition of lines and ghosts in the spectrum. These circumstances, too, point to their close relationship with the Talbot phenomena. The objection to the method is completely removed, however, when the grating-interferometer is rotated 90° in its own plane, so that its spectrum is vertical to the primary spectrum. The application of the method of "crossed spectra" requires a stigmatic primary spectrum. This condition is generally fulfilled by a spectrograph mounted in autocollimation. If we now observe the spectrum thus simplified by modulation of intensity, we find that the totally or partly quenched lines form a complementary spectrum located exactly above and below the primary spectrum.

4. In order to give some preliminary insight into the method of intensity modulation here proposed, the instruments used for these experiments will now be described.

The spectrograph used was composed of a 21-foot concave grating ruled on aluminized pyrex by R. W. WOOD and mounted in autocollimation with a plane mirror, according to a principle earlier described by HULTHÉN and LIND.[3] Like the Wadsworth mounting, the spectrum is stigmatically reproduced around the grating normal, in this case around the slit S, Fig. 4. Although the light is diffracted twice at the grating, this mounting is rather luminous in the blaze direction of the grating, giving double dispersion and resolution as compared with the Wadsworth spectrograph.

In this mounting the grating-interferometer takes the position of the plane mirror M, reflecting the parallel beam of light to the grating for its second diffraction.

Obviously the application of the grating-interferometer is not only restricted to the spectrograph here described. The introduction of additional elements into the optical path of a spectrograph will also deteriorate its resolving power. Great advantages are therefore gained by placing the grating-interferometer outside the spectrograph between the source of light and the slit of entrance. This arrangement requires an external slit in front of the light-source and a good achromatic lens by which the grating-interferometer acts in autocollimation with the external slit and the slit of entrance to the spectrograph. The dispersion of the grating-

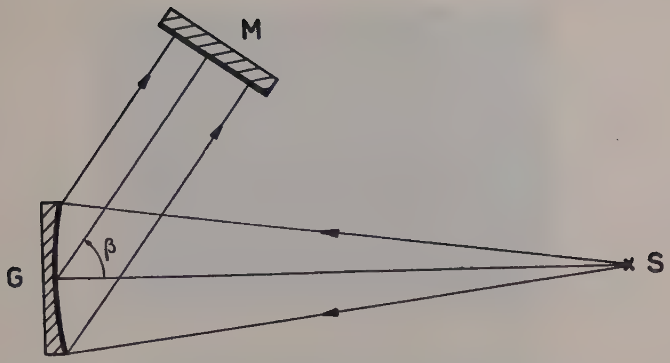

Fig. 4.

interferometer may thus be set parallel or perpendicular to that of the spectrograph. In the first case the image $M = 0$ of the external slit is focussed on the spectrograph slit, the complementary spectrum from $M = \pm 1$ being shut out. In the second case all three orders $M = 0, \pm 1$ are projected on the slit of the spectrograph.

The external mounting of the grating interferometer here proposed will be discussed in greater detail in a coming paper.

5. In our first experiments the intensity modulation was attained with a circular glass plate, Fig. 5, whose front surface was covered with a high reflecting aluminium grating evaporated through a screen-pattern. The reflecting strips and the spaces between them were 2 mm broad ($\sigma = 4$ mm). This glass plate, of 2 cms thickness, was designed to modulate the spectrum in the region of Hg 5461 by a period of ≈ 0.05 Å. Although the dispersion of the spectrograph was sufficient to demonstrate the modulation of a continuous white source of light, the finer details disappeared, probably owing to a slight wedge shape of the plate.

The great demands for plane parallelity in an interferometer of this size (Ø = 11 cm) are most readily met by the airplate formed between two plane glass plates, as in the Fabry-Perot étalon.

In the case of small spacings, 3—5 mms, the glass plates were separated by steel balls and with larger spacings by round ground quartz rods which were held in position by a ring fitting smoothly into the cylindrical housing of the interferometre. The quartz spacers were easily prepared by grinding their ends into 90° cones in the lathe, finally fitting their lengths within 0.001 mms by round-polishing the rod ends.

The front plate of the interferometer was slightly wedge-shaped (36″) in order to deflect disturbing reflections. The étalon also affords the advantage of enabling slow minute displacements of the carrier along the spectrum. In the case of large spacings between the glass plates this is conveniently performed by slight variation of the air-pressure between the plates. For this reason the interferometer was enclosed in an airtight cylinder of aluminium, Fig. 6, mounted on an arm rotatable about the center of the grating. For very large spacings between the glass plates a new housing is at present under construction.

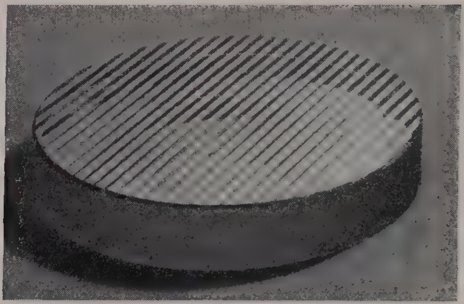

Fig. 5.

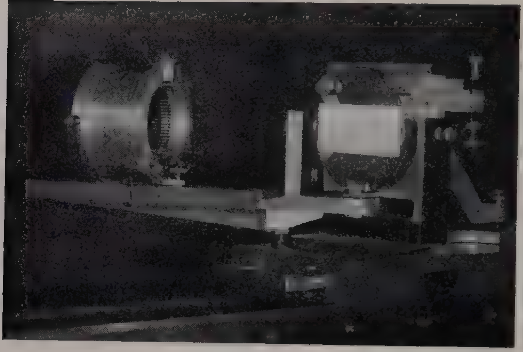

Fig. 6.

At first the spectrograph was set for observations along its focal curve rather distant (~ 100 mms) from the slit S. However, in this region the quenching effects of the spectral lines observed were only partial. With increasing separation ($t > 30$ mm) in the interferometer the quenching completely disappeared. This may be partly ascribed to the lack of parallelity of the monochromatic beam of light passing through the interferometer in these conditions. The primary objection to the operation of the spectrograph in this region, however, refers to the fact that the light rays are not reflected normally from the interferometer surfaces, and therefore by increasing the separation distances between the planes an increasing part of the beam reflected from the back plane will be imprisoned in the instrument.

6. Some preliminary results obtained with this instrument are given in Fig. 7. The green Hg-line λ 5461 was photographed in the first order of a 21′ Wood grating, ruled with 30 000 lines to the inch and mounted according to Fig. 4. This renders a dispersion of 0.86 mm/Å. Higher orders are not available in this mounting as $m\lambda < \sigma_g = 8330$ Å.

In order to illustrate the spectroscopic intensity modulation produced by the grating interferometer, the continuous spectrum from a concentrated arc lamp was photographed in the parallel as well as in the crossed position of the instrument.

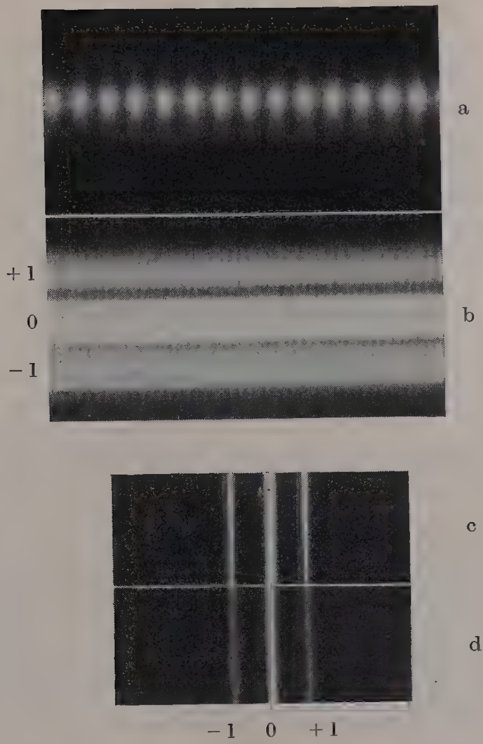

Fig. 7.

- a. The intensity modulation of the continuous spectrum from a concentrated arc lamp in the region of λ 5460, $F\lambda = 0.30$ Å.
- b. The crossed spectra from a concentrated arc lamp, $F\lambda = 0.05$ Å.
- c. The green Hg-line λ 5461. The violet satellite −0.225 Å appears suppressed in $M = 0$ and is correspondingly intensified in $M = \pm 1$. Notice the apparent unsymmetry in the positions of $M = \pm 1$.
- d. The components $M = \pm 1$ noticeably weakened as compared with $M = 0$.

Thus in Fig. 7 b we notice the characteristic alternation of the intensity between the zero-order spectrum, $M = 0$, and its complementary spectra $M = \pm 1$.

A striking effect of quenching appears in the hyperfine structure of Hg 5461 in Fig. 7 c, the first order lines, $M = \pm 1$, exhibiting a noticeable asymmetry in their position around the zero-order line, $M = 0$. The complete quenching of the satellite companion of the 0-line and its reappearance in the ± 1 lines is in agreement herewith.

The spectroscopic intensity modulation here discussed corresponds to the simple sine-square type of Fig. 1 a produced by two interfering beams. Obviously the method of intensity modulation might be appreciably refined by introducing a greater number of interfering beams as illustrated by the four-beams case in Fig. 1 b. Experiments to this end are already under way.

Appendix

From the arguments represented in *5* it was found desirable to restrict the observations to a narrow region within say ± 30 mms from the slit when using the stigmatic plane mirrow mounting there described. This was performed by placing a small 45°-prism in front of the slit of entrance, thus reflecting the spectrum onto a plate-holder mounted horizontally above the slit. With this arrangement the hyperfine structure of Hg λ 5461, not visible in Fig. 7 c and d, was resolved into six components. Individual components of this line appeared more or less quenched when the grating-interferometer was introduced.

It was somewhat surprising to find that the optimal resolution in the spectrum was restricted to such a narrow region around the slit of entrance. It was therefore desirable to secure the coincidence of the slit with the zero direction $m\lambda = 0$ in the spectrum, i.e. to eliminate the error of run of the grating. As a matter of fact this effect may produce a shift amounting to several inches for a good grating between the terminal point of the optical axis and that of the spectroscopic axis. A simple and rapid method for eliminating this error has been devised.

Finally our claims for optimal resolution and quenching assume a certain degree of parallelity between the glass plates of the grating interferometer. It should be emphasized that these claims of parallelity are restricted to the direction *along* the reflecting strips of the grating interferometer, whereas no claims for parallelity perpendicular hereto are necessary. This implies a considerable simplification in the procedure of adjusting the instrument.

A detailed exposition of the points here stressed will be given in a coming paper.

This work was supported by a grant from Statens Naturvetenskapliga Forskningsråd. I wish also to express my thanks to Mr. Aulin, of AGA, for his helpful advice regarding the optical components of the grating-interferometer, and to Mr. H. Neuhaus for his assistance in making the exposures.

Physics Department, The University of Stockholm, June 1951.

REFERENCES. 1. **Harrison, G. R.,** Jour. Opt. Soc. Am. *39*, 522, 1949. — 2. **Hulthén, E.** and **Uhler, U.,** Arkiv f. Fysik, *3*, 393, 1951. — 3. **Hulthén, E.** and **Lind, E.,** Arkiv f. Fysik *2*, 253, 1950.

Tryckt den 2 februari 1952

Uppsala 1952. Almqvist & Wiksells Boktryckeri AB

ARKIV FÖR FYSIK Band 4 nr 24

Read 12 September 1951

)n the Zeeman effect measurements of the sun's general magnetic field

By **Hannes Alfvén**

With 1 figure in the text

The question whether the sun has a general magnetic field and the strength of a possible field is of great importance in astrophysics. It is generally believed that the Zeeman effect measurements give the most direct determination of the solar magnetic field. The method is very difficult from observational point of view because the Zeeman effect displacement in question is only a fraction of a line width. The early measurements by **Hale** and collaborators were reported to give values of the order of 25 gauss. By the new methods introduced by **Thiessen** (1), **von Klüber** (2), and **Kiepenheuer** (3), a much higher accuracy is obtained. Their results indicate that outside sunspot regions there is no Zeeman effect exceeding the observational errors of a few gauss.

From these observations it is usually concluded that the general magnetic field of the sun must be less than a few gauss. Such a low field would lead to difficulties in many parts of astrophysics. It will be shown here that *it is not possible at present to draw any conclusion at all about the value of the general magnetic field from the Zeeman effect measurements.*

The reason for this is that in the photosphere we have turbulence and that the absorption of the Fraunhofer lines depends on temperature.

Suppose that in the photosphere a certain mass dm has the temperature T. The absorption of a spectral line in this element is proportional to a function $\beta(T)$ which mainly depends on the temperature. If we make a Zeeman effect measurement in the direction of a z-axis, we measure *an apparent field* H_z, which is the weighted mean of the magnetic field component in the z-direction.

$$H_z = \frac{\int H \cos\gamma \cdot \beta(T)\, dm}{\int \beta(T)\, dm} \tag{1}$$

H means the real magnetic field in the volume dm and γ the angle between this field and the z-axis.

Because of the granulation the field H is not the same as the sun's general magnetic field H_0. As has been shown earlier (4), the granulation produces a varying magnetic field H_t. The strength of this field can be estimated from the condition that the magnetic energy $H_t^2/8\pi$ should equal the average kinetic energy in the turbulence. It can also be estimated from the temperature fluctuations in the granulation. Both methods indicate that the turbulent field should be of the order of a few hundred gauss. This means that in general we have $H_t \gg H_0$.

As the electric conductivity is so high that the magnetic lines of force are "frozen in", an adiabatic change of the gas density ϱ will be accompanied by a change in the magnetic field. Compressions perpendicular to the magnetic field produce a change in this field proportional to the change in density, whereas the field strength is not changed by a compression parallel to it. The result of this is that in average the change in H is proportional to $\varrho^{2/3}$.

At adiabatic changes also the temperature varies at $\varrho^{2/3}$. Thus, we have a proportionality between H and T, so that we can put

$$T = \alpha H = \alpha\,(H_0^2 + H_t^2 + 2\,H_0 H_t \cos\vartheta)^{1/2} \tag{2}$$

where ϑ is the angle between H_0 and H_t, and α a constant.

As the temperature is coupled to the magnetic field we cannot evaluate (1) unless we know both β and the temperature distribution. This shows that no direct conclusion about the value of the general magnetic field can be drawn from Zeeman effect measurements of H_z.

In order to demonstrate the importance of this systematic error we shall discuss a simple example in which the measured field H_z is not of the same order of magnitude or even of the same sign as the real field H_0. Let us suppose that the turbulent field is isotropic with H_t = constant. This means that if we represent the magnetic field by a vector $\vec{H} = \vec{H}_0 + \vec{H}_t$ this vector is statistically equally distributed over the surface of a sphere with its centre at H_0. See Fig. 1.

As the temperature is coupled to H by (2), the temperature can be represented in the same diagram as a vector from the origin to the surface of the sphere. The mean temperature is given as the average length of this vector which is found to be

$$T_m = \alpha \int_0^{\pi} (H_0^2 + H_t^2 + 2\,H_0 H_t \cos\vartheta)^{1/2}\, \tfrac{1}{2} \sin\vartheta\, d\vartheta \tag{3}$$

which gives

$$T_m = \alpha \left(H_t + \frac{H_0^2}{3\,H_t}\right) \qquad \text{for } H_t > H_0 \tag{4}$$

and

$$T_m = \alpha \left(H_0 + \frac{H_t^2}{3\,H_0}\right) \qquad \text{for } H_t < H_0 \tag{5}$$

Let us suppose that the absorption of a certain Fraunhofer line, the Zeeman effect of which is measured, occurs only at a certain temperature $T = T_a$. This means that we measure the magnetic field only when it has the absolute value $H = \alpha\, T_a$. Hence the Zeeman effect measurements refer to the intersection between the sphere $H = H_0 + H_t$ and the sphere $H = \alpha\, T_a$. If we want to evaluate (1) we must observe that the integral is different from zero only for

$$H = T_a / \alpha. \tag{6}$$

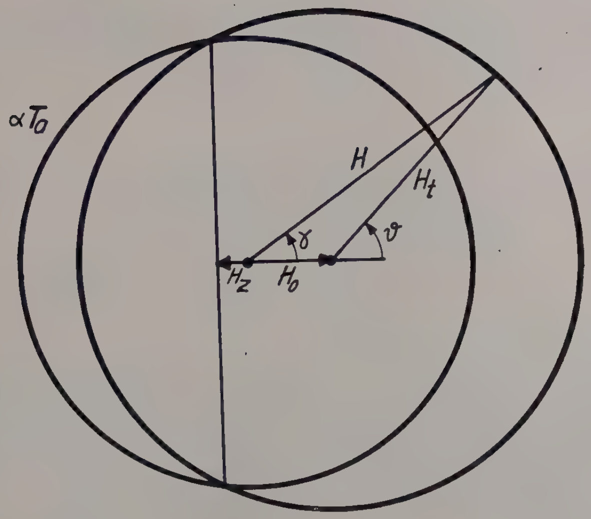

Fig. 1. The magnetic field H is composed of the general field H_0 and a turbulent field H_t. If H_t is constant, the resulting magnetic vector will fall on a sphere. If Fraunhofer absorption occurs only at the temperature T_a, the Zeeman effects measurements refer to the intersection between the sphere α T_a and the other sphere. The figure shows a case when the measured field H_z is opposite to the real field H_0.

Combining (4) and (6) we obtain

$$H = T_a/T_m \left[H_t + \frac{H_0^2}{3 H_t} \right]. \tag{7}$$

Introducing

$$\cos \gamma = (H^2 + H_0^2 - H_t^2)/2 H H_0 \tag{8}$$

we obtain from (1) and (7)

$$H_z = \frac{H^2 + H_0^2 - H_t^2}{2 H_0} = \frac{H_0}{2} \left[1 + \frac{2}{3} \left(\frac{T_a}{T_m} \right)^2 \right] - \frac{H_t^2}{2 H_2} \left[1 - \left(\frac{T_a}{T_m} \right)^2 \right]. \tag{9}$$

For $T_a = 0.9 \; T_m$ and $H_t = 3 H_0$ we have $H_z/H_0 = -0.1$.

Although this is a special case it indicates that we cannot always be sure that Zeeman effect measurements give even the right sign of a weak field. In the figure this corresponds to such a value of the radius of the spheres that the intersection between them is situated to the left of the origin.

It is seen from Fig. 1 that with suitable choice of T_a/T_m we could get any value between $H_0 + H_t$ and $H_0 - H_t$.

In reality the absorption does not take place only at a certain temperature, so we have to introduce into the calculations a statistical distribution of the temperature. A laborious calculation is necessary in order to investigate this case, but it could be expected that in general the measured field should be rather small compared to the real field. It is also possible that lines with different excitations should give different results, as was indeed reported by Hale.

The objections against the Zeeman effect measurements are valid only in the case of a turbulent field which is larger than the real field. If $H_0 > H_t$ we should use (5) instead of (4) which leads to

$$H = \frac{T_a}{T_m}\left(H_0 + \frac{H_t^2}{3\,H_0}\right) \tag{10}$$

instead of (7) and

$$H_z = \frac{H_0}{2}\left[1 + \left(\frac{T_a}{T_m}\right)^2\right] - \frac{H_t^2}{2\,H_0}\left[1 - \frac{2}{3}\left(\frac{T_a}{T_m}\right)^2\right] \tag{11}$$

instead of (9).

Hence the Zeeman effect measurements of the sunspot fields are essentially valid. In this case the turbulence introduces only a small correction.

Neither cosmic ray nor solar noise measurements have given reliable values of the general field. The magneto-hydrodynamic theory of sunspot shows that the rate of progression of the sunspot zone can be accounted for if the general magnetic field is $37 > H > 9$ gauss (5).

There seems at present to be no valid arguments against a dipole field of this order.

Stockholm, September, 1951.

REFERENCES: 1) **G. Thiessen,** Ann. d'Astrophys., *9*, 101, 1946; Zs. Ap., *26*, 16, 1949; Observatory, *69*, 228. 1949. — 2) **H. von Klüber,** Observatory, *71*, 9, 1951. — 3) **K. A. Kiepenheuer,** In the press. — 4) **H. Alfvén,** Monthly Notices of R. Astr. Soc., *107*, 211, 1947. — 5) **H. Alfvén,** Cosmical electrodynamics, Oxford University Press, 1950.

Tryckt den 5 februari 1952

Uppsala 1952. Almqvist & Wiksells Boktryckeri AB

ARKIV FÖR FYSIK Band 4 nr 25

Communicated 12 September 1951 by H. Alfvén

A simple cosmic-ray-meter, plotting hourly values, corrected for pressure

By K. G. Malmfors

With 2 figures in the text

Recordings of C.R. are generally made by automatically photographing one or more mechanical registers once every hour or eventually at shorter time intervals. This procedure involves the disadvantage that the recording diagrams cannot be prepared until the film has been processed and the hourly values calculated and corrected for atmospheric pressure.

For two reasons a direct-reading instrument would be very useful. First it gives a continuous control of the apparatus so that an error is immediately detected. On the other hand irregular variations of C.R. intensity can be studied directly, which means a better coordination with observations in other fields of geophysics (magnetic disturbances, sunspot-groups, ionospheric fade-outs and so on).

An instrument has been constructed and tested for some time at the C.R. laboratory at Frescati near Stockholm. As mentioned in an earlier description of this laboratory[1] the C.R. intensity is measured in 12 separate channels, going to 12 registers which are photographed every hour. Each register operates a switch which is used for giving a short pulse. All such pulses are taken in parallel to a multivibrator which operates a scale-of-32. The total intensity measured at the laboratory is about 100 000 coinc./hour. This rate is reduced by a factor 4 in the amplifiers which gives a mean counting rate of about 800 pulses/hour at the output of the scale-of-32.

The output pulses are led to a relay driving a toothed wheel which operates a contact, A, in such a way that the contact is closed when the toothed wheel has made a constant number of steps. (In this case let us say 750 steps.) This is arranged by means of two cam-wheels. The critical number of pulses is reached after about 57 minutes. The contact A starts a synchronous motor which is running during the remaining part of the hourly interval, moving the writing pencil of a barograph upwards with constant velocity. The deflection of the pencil is thus a measure of the C.R. intensity during the preceding hour. (If the counting rate was high the fixed number of pulses is reached earlier and the motor is running for a longer time than if the counting rate were low.)

During the main part of the hourly interval the barograph performs its normal operation, indicating the atmospheric pressure. As the contact A is closed, a relay in the barograph couples the motor to the writing arm and a (nearly) vertical line is obtained on the paper. If the pressure is low, the line starts from a low level but on the other hand the C.R. intensity is higher than normal, which corresponds to

---

[1] K. G. Malmfors: Recordings of Cosmic Radiation. Tellus *1*, No 2, p. 55.

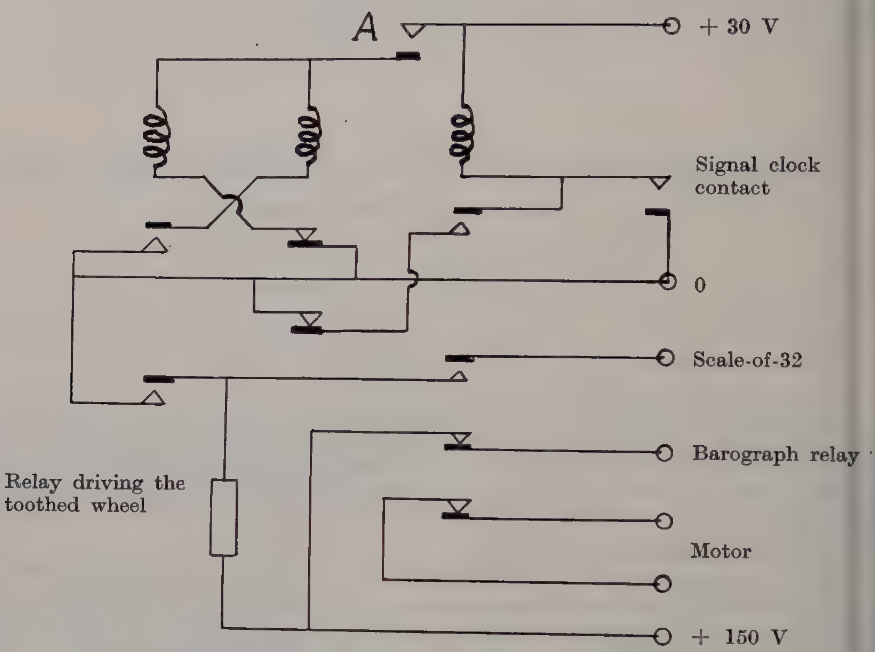

Fig. 1. The relay system.

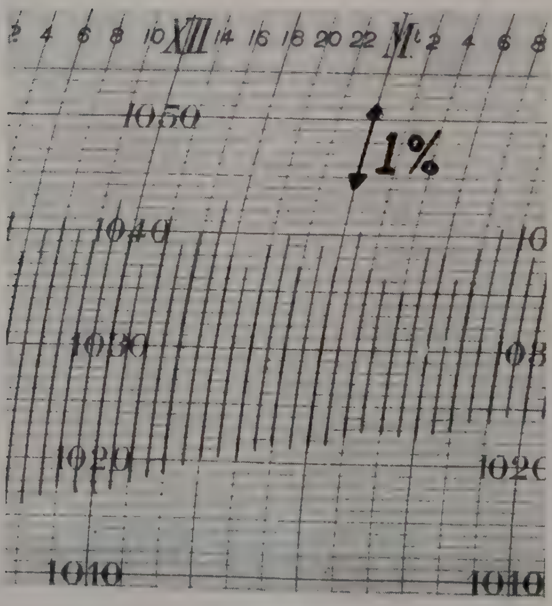

Fig. 2.

long vertical line. By choosing the ratio for the deflection of the writing pencil n accordance with the pressure coefficient these two effects cancel each other so hat the upper end of the vertical lines represent C.R. data *corrected* for the atmosheric pressure.

During the period when the motor is running the counting is interrupted and the oothed wheel is put to zero-position by means of two relays operating as a ringing ell.

Fig. 1 shows the relay system and Fig. 2 gives an example of the recordings.

By this method the counting is reduced to measuring a time interval of some ew minutes' length and the barograph can be placed far from the rest of the apparatus. It seems possible to arrange, in this way, by simple means a remote control of a C.R. station either by using a telephone cable or by wireless transmission.

Nobel Institute of Physics, Stockholm 50, Sweden.

Tryckt den 5 februari 1952

Uppsala 1952. Almqvist & Wiksells Boktryckeri AB

ARKIV FÖR FYSIK Band 4 nr 26

Communicated 23 May 1951 by ERIK HULTHÉN

Tests on dust separators with the Siegbahn-Schönander electron microscope

BY ERNST DE HAAS[1]

With 6 figures in the text

The criterion in evaluating dust separators is usually the efficacy expressed s a function of the size of the particles. It is therefore necessary to know he distribution of the various sizes of particles before testing or else to determine it during the test. Different methods of measurement are employed, depending on the nature of the particles.

Particles with a diameter greater than 42 μ are extracted by screening, while the remainder is examined by sedimentation or by cyclone, the lower limit of diameter being about 7 μ. Smaller particles are examined by microscope.

Notable among dust precipitators is the electrostatic filter because of its ability to extract the very fine dust. The electrostatic filter consists of a cylindrical or rectangular box containing plate and wire electrodes. A DC potential of the order of 50 kV is applied across the electrodes, the wire electrodes being at negative potential. If a gas containing solid particles is passed through the filter, the particles become charged and are attracted to the electrodes, where they give up their charge and cake into a mass, which is shaken off and falls to the bottom of the container.

The electrostatic filter is mainly used for precipitation of dust of submicroscopic size. Development of this type of electrostatic precipitation has, however, been hindered by the lack of a method of grading the particles and has made it impossible properly to evaluate its efficiency as defined above. The advent of the electron microscope, however, has enabled the designer to form some idea of the size and shape of the precipitate.

However, granted the possibility of studying the particles, the problem naturally arises how to segregate representative samples suspended in a gas. The obvious method appears to be to collect samples of the gas before and after passing through the filter, or to sample the precipitated dust, and to blow and sprinkle a suitable quantity of it onto the specimen holder. This procedure is not suitable, however, as the suspended particles have a marked tendency to bind together into larger masses. A sample obtained in this manner will be found to have a distribution of grain sizes that differs from that of the suspended dust.

An improvement on the above method is therefore to expose the specimen holder to the gas and to examine the deposit obtained in this way. One drawback of this method is that no indication is given of the quantity of gas

---

[1] At present with the Hydro-Electric Power Commission of Ontario, Toronto, Canada.

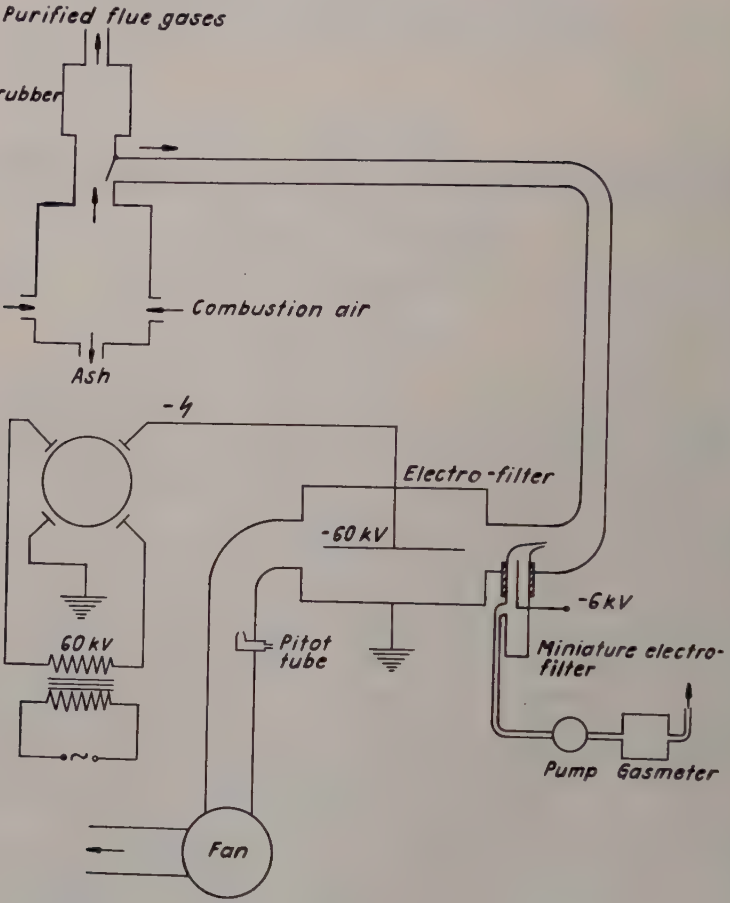

Fig. 1. Electro filter Svenska Fläktfabriken. Field Test Station at Höganäs. Schematically.

from which the deposit has been obtained. Theoretically, the correct method is to extract a definite quantity of gas at the point of sampling and collect all the matter suspended in it without allowing the particles to cake together. Figs. 1 and 3 illustrate a miniature electrofilter, designed in the laboratories of Svenska Fläktfabriken, consisting of a brass cylinder with three slits for the specimen holders. An axial wire passing through the filter is given a potential of 6–8 kV relative to the shell. The filter is connected to a pump, the latter being connected to a gas meter. The filter is inserted in the stream of gas, and the pump then draws a specific quantity of gas through the equipment. The electrostatic forces cause the suspended matter to be deposited on the aluminum-coated specimen holders. The distribution of particle sizes is then determined with an electron microscope, and the number of particles is estimated for a given area on the specimen holder. An estimate can now be

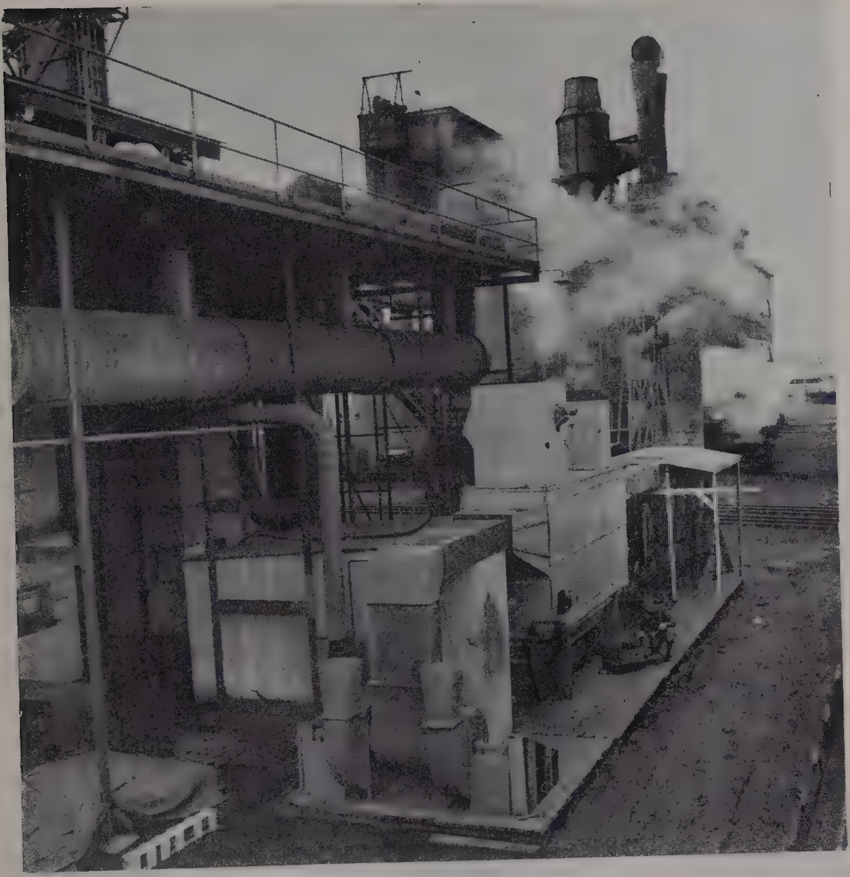

Fig. 2. Electro filter.

made of the total quantity precipitated in the filter and hence its concentration in the gas.

The miniature filter was used for the first time for measurements at the Fan Manufacturers Field Test Station temporarily at Höganäs. Combustion products were taken from a chimney at Höganäs-Billesholms AB. See Fig. 2.

A number of specimen holders were placed in the miniature filter, two of which were selected for the measurements. In order to increase the contrast, they were afterwards shadowed with palladium.

When studied with the electron microscope, the dust was seen to consist of two components, one consisting of round solid particles, which were assumed to be spherical from the length and shape of their shadows. The other component was irregular and sponge-like. See Fig. 4. These are later referred to as »solid» and »loose» particles respectively. The solid particles are probably carbon.

In order to ascertain the total quantity of dust on the slides, the distributions of the two types were assessed separately. The number of particles was then counted for each preparation on a suitable graticule which just filled the fluorescent screen of the microscope (diameter = 79 mm) at a magnification of 5000 times.

Calculation

Specimen 1

The particle size distribution for solid particles is shown in Fig. 5.

The number of particles on 15 slides was 73.

The calculation was carried out as (1) which provides the following formulae

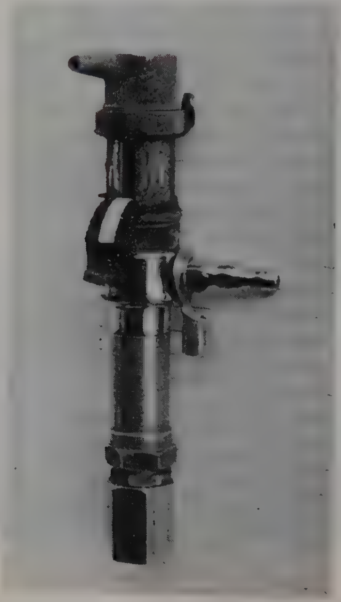

Fig. 3. Miniature electro filter.

$$D_m = D_0 \, e^{3a^2}$$

$$a = \ln \frac{D_0}{D_{84}},$$

where D_0 = mean particle size, 50 % remainder
D_{84} = mean particle size, 84 % remainder
a = range of deviation
D_m = mean particle size in relation to weight.

The graph in Fig. 5 shows that

$$D_0 = 0.49\,\mu, \; D_{84} = 0.23\,\mu.$$

This gives

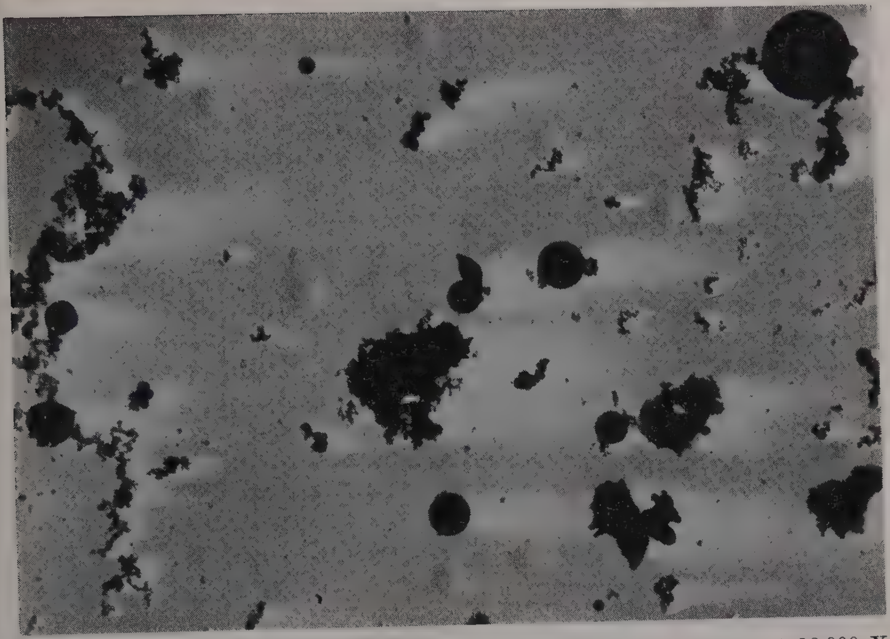

Fig. 4. Dust consisting of two components. (»Solid» and »loose» particles.) 10 000 X.

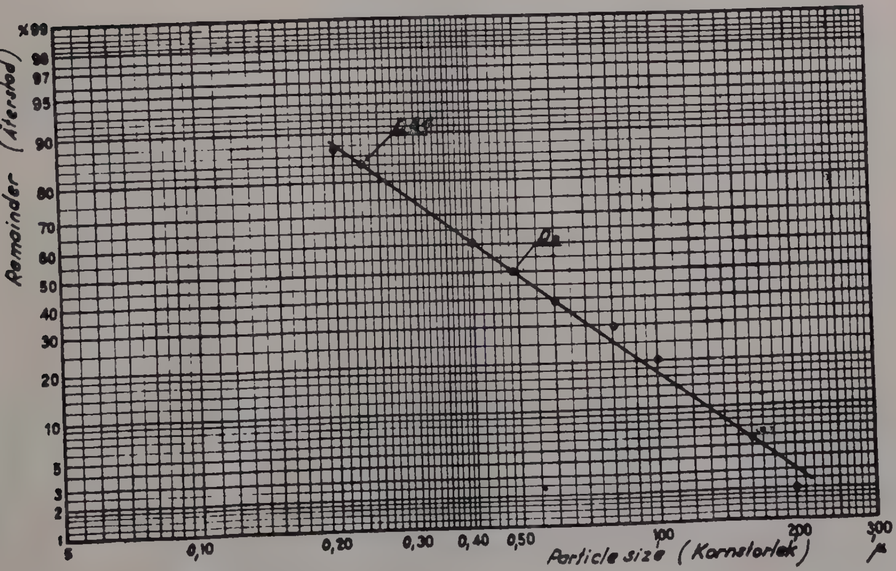

Fig. 5. Size distribution for solid particles.

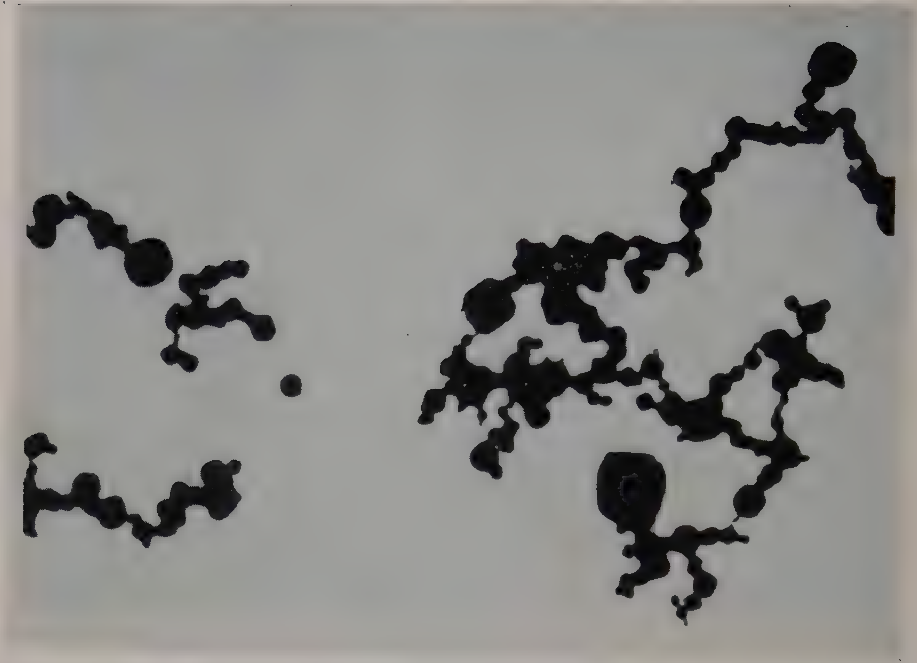

Fig. 6. Dust from Hofors Bruk. The illustration shows that this dust consists of masses of fine particles, which could not be resolved with an ordinary microscope. 20 000 X.

$$a = \ln \frac{0.49}{0.23} = 0.76.$$

So

$$D_m = 0.49 \cdot e^{3a^2} = 2.68\ \mu.$$

The volume of the mean particle is

$$v = \frac{\pi}{6} D_m^3 = 10.1\ \mu^3.$$

The area of the slides are

$$\frac{\pi}{4}(79)^2 = 5\,040\ \text{mm}^2.$$

Each slide at a magnification of the specimen of 5 000 times represents an area of $\frac{5\,040}{5\,000^2}$ mm^2 = 202 μ^2 which gives a total area for 15 slides of 3 030 μ^2. On this there are 73 particles with a total volume of 73 × 10.1 μ^3 = 738 μ^3. On each mm^2 of slide area there is thus $V_a = \frac{738 \times 10^6}{3\,030 \times 10^9} = 2.4 \cdot 10^{-4}$ mm^3 of material.

A similar calculation for specimen 2 gives

$$V_a = 2.1 \times 10^{-4} \text{ mm}^3/\text{mm}.$$

In other words the solid particles form a layer having a mean thickness of .21–0.24 μ.

In the same way the quantity of the loose particles was found to be .3 · 10^{-4} mm³/mm² and 1.0 · 10^{-4} mm³/mm² resp. The total quantity of dust s thus 2.7 · 10^{-4} mm³/mm² and 3.0 · 10^{-4} mm³/mm² resp.

Conclusions

1. The miniature electrofilter is a suitable instrument for tests on finely divided particles. It makes it possible to photograph particles as they actually are in free air without the destructive changes of shape which might occur during sampling.

2. If the assumption is made, that the dust has a natural distribution of particle size the calculation does not involve any great difficulties. The specimen may be quickly prepared for insertion in the microscope.

LITERATURE. 1. **S. Sylvan.** Materiel i styckeform. Fläkten, June 1943 page 78—89.

Allmänna Svenska Elektriska AB, Västerås.

Tryckt den 5 februari 1952

Uppsala 1952. Almqvist & Wiksells Boktryckeri AB

ARKIV FÖR FYSIK Band 4 nr 27

Communicated 6 June 1951 by B. Lindblad and G. Borelius

Phase contrast measurements of the ruling structure of optical gratings. I

By Erik Ingelstam and Erik Djurle

With 17 figures in the text

General remarks on the suitability of the phase contrast method

When for the first time introducing the phase contrast method in 1934, Zernike 1) did so in a field where the quantitative factors are rather complicated, namely n the study of zonal errors and aberrations of mirror and lens systems. In fact, he possibility of acheiving exactly calculable wave-front qualities. from the observed intensities in a phase contrast device, mainly depends upon the structure of the diffraction figure in the plane where the phase plate is inserted. The modifications in the diffraction figures introduced by different aberrations consist of larger or smaller deformations which are only slight compared to a perfect system. In order to analyze them by means of the phase contrast method, the phase turning detail of the spot, ring or slit type must be very accurately dimensioned and the results often be procured by analysis of a complex geometry (2).

In the study of the structure of a wave-front from an optical grating as applied here, the opposite to the study of aberrations is formed, insofar as the structure includes periodic sinuoidal variations due to periodicities in the device for the ruling of the grating. A sinuoidal form of a wave-front corresponds to lines in the diffraction figure situated symmetrically to the main diffraction line and at distances generally far away. Thus, by means of the phase contrast device the light from the object as a whole, i.e. the main spectral line from the grating, can be very easily and quantitatively separated from that due to the sinuoidal structure—the Rowland ghosts adhering to the spectral line. The theory of this application was given in a former publication (3). This paper is a continuation in which quantitative measurements have been made and analyses begun on results received from these measurements. A series of constructions have been performed necessary for the devices to correspond to the minute limits of accuracy following from the principles of the methods. Also some fundamental measurements have been made on phase shift angles and ratios between reflexion intensities etc. in order to settle scales for the wave-front or grating-surface structure.

Optical arrangements

Main features. Fig. 1 shows the main parts of the optical system. It corresponds in main principles to an apparatus for routine analysis of gratings (even when mounted in a spectrographic unit) previously constructed by one of the authors (4).

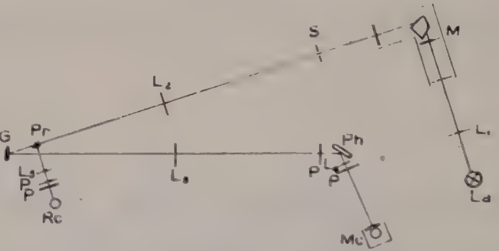

Fig. 1. Optical arrangements. Notations see the text.

In order to correspond to the precise measurements demanded here, it has been built in a rigid system, the optical benches and stands being fixed on an iron fundament.

To exclude from the measurements all possible influence from background light from the lamp *La* (which is a medium pressure mercury lamp specially selected and driven at a current that gives stable conditions), the green line 5461 Å always used has been separated by the prism monochromator *M*. The collimation lens L_2 and the corresponding lens L_3 at the image side are of astronomic type and have a focal length of 500 mms. The quality of these lenses is not of the superior type demanded for phase contrast work, so they have been placed sufficiently far from the sensitive part of the system, and a check of their influence is reported below. The gratings examined have been placed in the *G* position, and the angle between the entrance and exit rays determined so as to correspond to the first order spectral ray (of the intense side, if as usual the grating is "blazed") emerging perpendicularly from the grating. This brings the advantage that the phase contrast image of the grating will be rectangular. When examining a concave grating, the lenses L_2 and L_3 are of course excluded, the grating itself forming the image.

Phase mirrors. The phase turning device is the mirror invented by FRANÇON and NOMARSKI (5), denoted in the figure as *Ph*. It should here be treated with as much detail as necessary as its exact shape and specification enters into the calculations. The mirror is manufactured by evaporation of aluminium to controlled thicknesses as was briefly described in an earlier paper (4). Recently we have extensively used the method of protecting the slit area during the evaporation instead of cutting the metal after the deposition, in order to regenerate the glass surface of this area, as the borders will often be damaged and so reflect the light irregularily. When the slit is rather narrow, of some tens of microns, a stretched molybdenum wire can be used of the same diameter as the slit desired. The interferometric examination then shows that the borders of the slit form a slope not quite perpendicular but not taking up more than a small fraction of the entire slit; provided that the source of the evaporation is far enough from the plate and that its angle sidewards to the slit is sufficiently small. When a broader slit is needed, covering with a metal band is more satisfactory as a round wire will often reflect the metal to the sides, forming an elevation which makes the phase shift amount undefined. The technique for a satisfactory performance of a band is to have it in good contact with the glass surface. We have found the steel bands used for balance-wheel springs in the watchmaker's technique to be very suitable. They can be procured in dimensions from a 100 microns upwards, are very flat, well-defined and can be held close to the surface during the evaporation in vacuo by

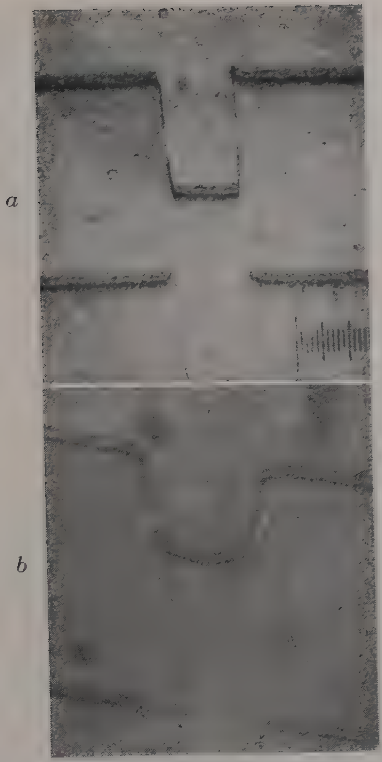

Fig. 2. Examples of interferograms of phase mirror slits: *a* during evaporation covered with a steel band; good edges, right hand edge bordering on a narrow 50 Å high hill on account of deposit reflexion; *b* during evaporation covered with a thick circular wire, slit form not approved.

a strong magnet placed at the back of the glass plate.[1] Interferograms with multiple reflected Fizeau interferences of the Na doublet are shown in Fig. 2. From such interferograms the geometric depth of the step, marked e, is measured very closely, producing an error of only ± 5 Å, according to the perfectness of the glass polish.

The phase mirrors were always used in reflexion under the Brewsterian angle i_B, and surrounded by two polaroids, as marked in Fig. 1. For the sake of the precision, we must accurately know both the phase turning angle ψ and the attenuation factor of the central light in respect to the diffracted light. These two data define the origin O' of the light vectors constituting and are the fundamentals for the evaluation, as later shown in Fig. 7.

The corresponding light paths from a wave-front before the reflexion at the step mirror are as follows

at the glass $\quad l + 2\ e \cos i_B + (\lambda/2)$

at the metal $\quad l + (\lambda/2 + \varepsilon)$

---

[1] The authors are indepted to Prof. Duffieux, à Besançon (France), for sending us samples of bronze bands used by him for a similar purpose.

The last bracketed terms are due to the phase shifts at the reflexions, the phase turning of π at the glass corresponding to an additional path of $\lambda/2$ is exact and reliable. In metallic reflexion it is more complicated as it depends on the angle of reflexion and the state of polarization, even for a layer of non transparent metal as in this case. The phase shifting angles of this reflexion angle in the two cases, when the electric vector is in the plane of incidence (p) and when it is perpendicular to it (s), are calculated from the following formulae derived from the Fresnel formulae with complex quantities. The refractive index n and the extinction coefficient $\varkappa$ also depend on the angle and are calculated before insertion.

$$\operatorname{tg} \delta_p = -\frac{2\frac{\varkappa}{n}\cos i_B\left(1-2\frac{\sin^2 i_B}{n^2}+\varkappa^2\right)}{2\varkappa^2\cos^2 i_B\left(1-2\frac{\sin^2 i_B}{n^2}+\frac{\varkappa^2}{2}\right)+\cos^2 i_B-\frac{1}{n^2}\left(1-\frac{\sin^2 i_B}{n^2}+\varkappa^2\right)}$$

$$\operatorname{tg} \delta_s = -\frac{2\, n\, \varkappa \cos i_B}{n^2 \varkappa^2 + n^2 - 1}$$

The optical data for evaporated aluminium were taken from VALASEK (6), and their validity for our specimens was confirmed by our own measurements at the principal angle. For normal incidence they are, $n_0 = 1.15$ and $\varkappa_0 = 3.5$; and calculated for the angle i_B $n = 1.40$ and $\varkappa = 2.9$. The values for the values according to the formulae are,

$$\delta_p = 133.0^\circ \qquad \delta_s = 165.5^\circ$$

These values or the formulae above are not usually found in publications, as they themselves are of no especial interest when examining metallic reflexion; only their difference, which constitutes the phase difference between the two components together forming an elliptically polarized ray. This angular difference is $|\delta_p - \delta_s| = 32.5^\circ$, which corresponds to an average value measured with low accuracy on these elliptical rays.

An angular phase shift of δ_s, where $O < \delta_s < \pi$, corresponds to a light path amount of more than $\lambda/2$, the quantity above called ε being related to δ_s as $\varepsilon = \frac{\lambda}{2\pi}(\pi - \delta_s)$. Subtracting the light path values from the two different reflexions, we arrive to the real path difference at the phase mirror as

$$\Delta = 2\, e \cos i_B - \varepsilon$$

or the phase turning angle of the mirror as

$$\psi = \frac{4\pi e \cos i_B}{\lambda} - \pi + \delta_s$$

The phase turning angle is often chosen as $\pi/2$, but it is evident that it varies slightly with the direction of polarization of incident light. In this investigation we have had no need of varying the sensitivity, and so have extensively worked with s-polarized light, producing a minimum of sensitivity with this type of mirror. The angles ψ are slightly lower than $\pi/2$ as seen from Table 1.

The second important date for a phase turning mirror is the square root of the atio between the reflected intensities, which gives the ratio between the light vecor lengths. When using one or two polaroids, this ratio can be varied within very ifferent limits, and in the preceding paper (3) it was shown how these variations an be utilized. For a quantitative study, however, it is not sufficient to calculate he ratio values from the projections of light vectors on the oscillation directions f the polaroids, as they are never precise. We always measure the ratio between ntensities, and when the mirror is set in its ordinary place with its adjustment devices, this is most easily and accurately done by means of the photocell used for the main measurements. In the same arrangement as Fig. 1, only with the grating substituted by a plane mirror placed as to reflect the image of the slit onto the phase mirror, the mirror is adjusted either for the slit image to fall on the central glass slit, or for it to be reflected from an adjacent part of a metallic surface. The light flux is registered by the recorder in the ordinary way, so that the ratio of the two intensities is received with greater accuracy than 0.5 per cent. Several measurements at different mirrors have given the same value using s-polarized light of 0.203 for the ratio glass/aluminium reflexion under the Brewsterian angle. The square root of it, 0.450, gives the ratio of the vector lengths. The abnormal value for mirror No. 2 will be explained later. We prefer here, instead of using optical density, to give this ratio q (for the vector) itself, as it enters in this form in all vector calculations.

Table 1 shows the values for the two mirrors, computed as stated above and for $\lambda = 5461$ A. In order to judge the phase contrast resolving power the additional information should be given that the width of the un-screened whole phase mirror is about 30 mms, or in projection 16 mms, thus 75 times the slit width of the first mirror.

Table 1.

Data of the phase turning mirrors.

Mirror No.	Slit width (μ)		Phase turning angle ψ				Vector ratio q
	real	projection	e (A)	$4\pi e \cos i_B/\lambda$	$\pi - \delta_s$	ψ	
1	400	220	1 130	81.0°	14.5°	66.5°	0.450
2	120	65	1 365	98.0°	14.5°	83.5°	0.568

Another direct method of determining the position of O', which has been published by one of the authors (7), is by the aid of standard striae of known phase turning values placed in the phase object space. A provisory check was also made with this method for the mirror No. 1. This gave a ψ of 65° and a vector ratio of 0.43, which, considering the limits of error, is concordant with the previous results.

The greatest errors of the data in Table 1 lie in the δ_s-values, which may be wrong within about 2 degrees an account of the small accuracy with which the optical constants are known. Attempts to measure these δ-values directly by means of properly dimensioned multiple beam interference fringes have hitherto given values of lower precision.

The receiver, optical and mechanical parts. In Fig. 1, the light is seen to continue from the phase mirror through the imaging lens L_4 onto the receiver which consists

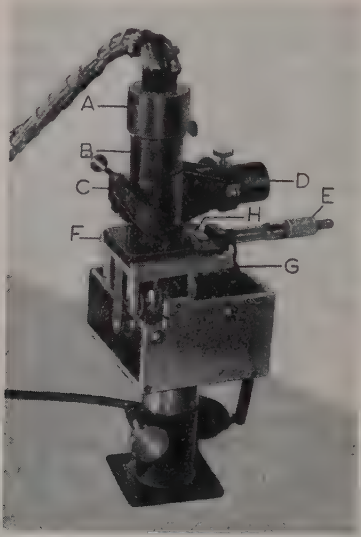

Fig. 3. Photocell receiver unit. Notations see the text.

of a measuring photoelectric cell *Mc*. The construction of the unit carrying the cell is best explained by Fig. 3. The cell is a photomultiplier tube RCA 931-A, its holder *A*, with its screened cables situated on the top of the tube *B* carrying the entrance slit with adjustment devices and screenings, *C*. Before inserting the phototube, the image and the slit system, which need not to be described here, should be carefully adjusted so that the slit and the rulings of the grating image are parallel and in the same plane. This is performed by means of a microscope put into the tube *D* from behind. The micrometer *E* serves to the last mentioned adjustment. During the registration of the intensities of the grating image the tube system should be displaced sideways. Here this movement is maintained in the manner evident from the figure which shows the system built on a carriage *F* carried by three wheels on ball bearings. The carriage is driven by a synchronous motor *G* over an intermediate gear box admitting several speeds. In order to make the arrangement also suitable for cases where the incident light falls obliquely onto the image plane, the system *A*—*D* is turnable around the slit and adjustable by means of the *H* scale.

During the adjustment of the phase plate *Ph*, Fig. 1, a microscope is inserted between L_4 and *Mc*; the phase plate being mounted with easy adjustments as described before (4).

Reference cell. To control the lamp intensity and to correct for possible fluctuations, an additional photomultiplier tube *Rc* is incorporated, taking as is obvious from Fig. 1, part of the lamp flux which is reducible to a proper value by means of polaroids.

Electrical equipment

Fig. 4 gives the block scheme of the electrical parts. The tension to the two multiplier tubes—the measuring cell and the reference cell—is supplied by a rectifier and stabilizer unit. The rectification follows standard practice. The rectified

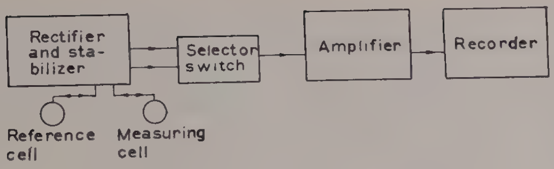

Fig. 4. Electrical block scheme.

igh voltage to the phototubes is fed via a thermionic valve acting as a variable mpedance. This valve is controlled by an amplifier valve with its cathode conected to two reference tubes RCA 5651 and its grid to a potentiometer network cross the output voltage. By selecting different steps of this potentiometer the ollowing dynode voltages are obtained: 50, 70, and 100 volts. The voltage beween the anode and the last dynode (number 9) is stabilized separately and is ontinuously adjustable. The stabilisation ratio is better than 250 for slow changes, which lead to thermal equilibrum of the cathodes, and still better for rapid variations. The ripple voltage at 1 000 volts output is about 10 millivolts.

The two parallel phototubes of the type RCA 931-A are selected to have exactly equal low dark and leakage currents, of about 10^{-9} amperes.

A selector switch permits the connection of either of the photocells to the amplifier. This is a balanced direct current amplifier with an input resistance variable in decades between 5 000 ohms and 50 megohms, and an output directly connected to the recorder.

A Leeds and Northrup Speedomax recorder has been used with the ordinary characteristics except that the time of balance is as low as 1.5 seconds. The input impedance can be a maximum of 10 000 ohms. Full scale deviation of 250 mms corresponds to 10 millivolts intake or $2 \cdot 10^{-9}$ amperes for the most sensitive range of the amplifier and with maximum output resistance. The chart paper speed has been 60 inches per hour, i.e. 0.42 mms per second.

The recorded curves show a fine structure due to reasons of rapid random fluctuations of the mercury lamp and "noise" from the different electrical parts. In order to distinguish between these primary causes which together give maximum fluctuations of 2.5 per cent at the most sensitive range, we have made measurements with the set unchanged, but with the lamp substituted for a tungsten band lamp fed by an accumulator. The fluctuations were then 1.5 per cent, which is

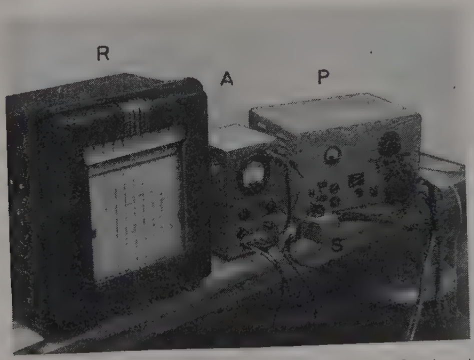

Fig. 5. Electrical parts, *R* recorder, *A* amplifier, *P* power supply (rectifier-stabilizer), *S* switch.

slightly higher than the theoretical estimation for the part due to the phototube, according to DIEKE (8). — These data are for 100 volts dynode voltage. When using a dynode voltage of 50 volts with the same setting on the amplifier the fluctuations are reduced to a tenth.

Fig. 5 is a picture of the electric equipment.

Primary records and their accuracy

A series of small plane gratings numbered G III, G 22, and G 15 (ruled area about 20 × 20 mms) was examined. Further, a test ruling on a concave blank, No. G 73, was registered, its radius being 1 metre and the ruled area 40 × 84 mms.

Examples of the quality of the original records are given in Fig. 6. For a measurement such a curve is repeated twice, once continuously and once with the reference cell switched on at regularly repeated intervals, as shown in Fig. 6 c. The second curve is corrected to constant lamp flux level by means of the reference cell records, and a comparison of the detailed drawing indicates the amount of random fluctuations. These have always proved to be less than 2 per cent, which means that the resultant curve which is drawn as the average of the two original curves, ought to be true within 1 per cent with regard to noise fluctuations.

To this error must be added the possible errors originating from the whole electronic equipment. Namely, the slow individual variations of the two photocells compared to each other, the lack of linearity of the amplifier and the accuracy of the recorder (0.5 per cent), which together may influence the ordinate of the curve. Combined they are well within 1 per cent, i.e. the whole intensity curves are accurate within 2 per cent.

Transfer of intensities to phase differences

The intensities are directly proportional to r^2, the vector length being indicated in Fig. 7 a. The phase differences, represented by the angle φ, oscillates about zero. The relation between r^2 and φ, $a = 1$,

$$r^2 = (\cos \varphi - 1 + q \cos \psi)^2 + (\sin \varphi - q \sin \psi)^2$$

is suitably expressed in graphical form, as shown in an example by Fig. 7 b.

As the structure of the wave-front is required, the phase curves should be so fitted that a plane wave-front corresponds to $\varphi = 0$, i.e. positive and negative phase amounts should equal one another. For a first approximation is chosen a r^2-value for $\varphi = 0$, denoted r_0^2, and a complete transfer of the intensity curve to phase curve is performed. The areas above and below the axis are planimetred, and their difference serves as the origin of the next approximation. Generally two approximations are necessary, and by means of graphical interpolation between these two the final r_0^2-value is obtained within 1 per cent, and the final curve is drawn. According to the geometry in Fig. 7 a, the error of the r_0-value only very slightly affects the distance between maximum and minimum peak values of the curve, and so must not be confused with the maximum amplitude error stated above.

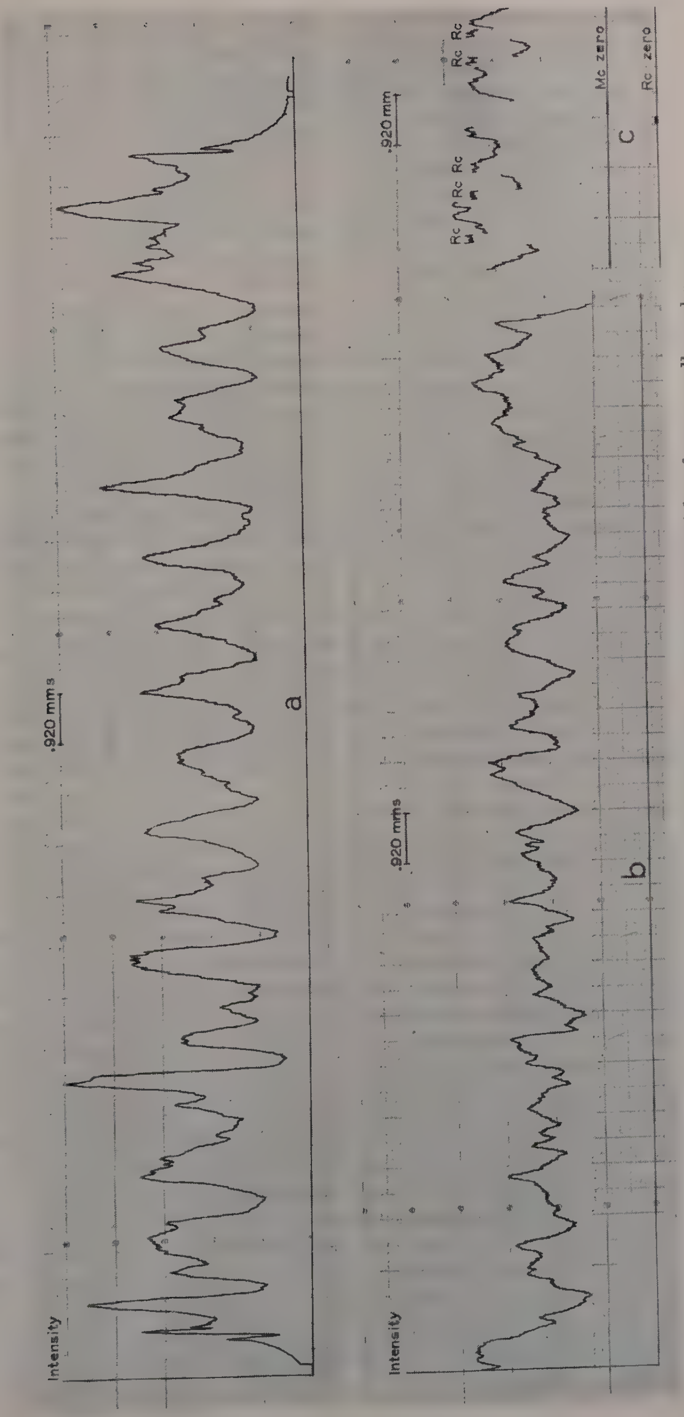

Fig. 6. Original records *a* G III *b* G 22 *c* part of G 22 with reference cell marks.

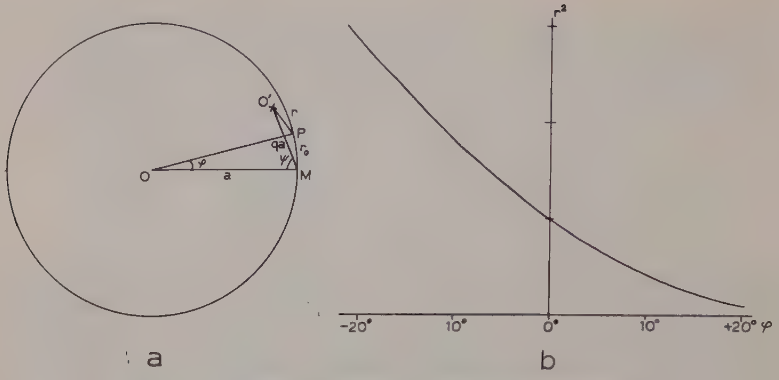

Fig. 7. *a* Vector diagram *b* Evaluation graph.

Figs. 8—12 show the phase curves for all the examined gratings, i.e. the structure of the wave-front, for the first order of diffraction. An even more interesting specification for the grating is the displacements from the ideal equal-spaced positions of the groups of grooves on the grating surface. We have therefore added to these figures a scale giving these displacements, called ε, and calculated as $\varepsilon = d \cdot \varphi / 2\pi$ where d is the spacing.

The total accuracy of these ordinates partly depends on the exactness of the O' position and partly on the procedure just mentioned of registering and calculating the curves. The ψ-value is at present only known within 2 degrees. For an amplitude of $\psi = 5$ degrees this uncertainty introduces an error of 0.5 per cent, whereas the error in q is of quite negligible influence. Thus the total maximum error is 2.5 per cent, which corresponds to an error of the groove position in the ruled surface of 30 A.

Further, we should examine the conditions of precision for the phase contrast method. The projection width of the central slit in the phase mirror being 220 μ, it covers quantitatively the entire diffraction figure of the grating, as its central fringe takes only 28 μ. The slit also well contains the broadening of the figure due to the entrance slit being 30 μ in width. The nearest ghost on either side falls at a distance of 230 μ from the centre, which means that no correction for overlapping should be applied to the values. The resolving power depends on several factors: the limited aperture, the width of the photocell slit, and the speed of the recording system. The aperture is here limited to 16 mms by the phase mirror. Stating that a rectangular phase irregularity at the wave-front is on the point of being resolved when its central diffraction fringe has a width corresponding to this aperture, which is very liberate, we find that its minimum extension should be 34 μ.—As the grating is imaged with a magnification of 0.44 (the corresponding value for the concave grating being 0.24), the real exit slit width of 20 μ (8 μ) should be transferred into 45 μ (34 μ) as counted at the wave-front.—It was found that the Speedomax recorder with its balance time 1.5 seconds for full scale variation, could draw small variations without distorsion in a third of this time. The carriage speed was accordingly chosen as 15 μ/seconds (28 μ/seconds), so that the limit of distorsion, 8 μ (14 μ) was of less influence than the former factors. The sum of these well corresponding limitations of resolving power is safely below 50 μ (50 μ), which is equivalent to 30 grooves of the grating.

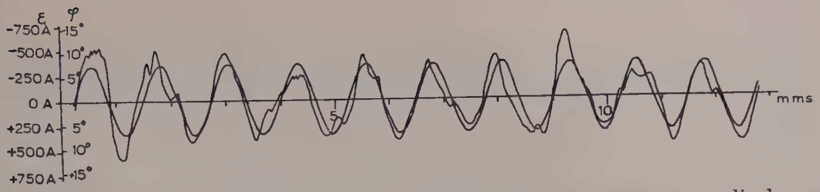

Fig. 8. Phase curve of G III, mirror No. 1 used. The ε-scale gives groove displacements. The sine curve is drawn.

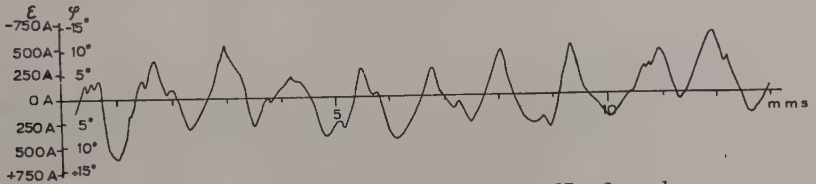

Fig. 9. Phase curve of G III, mirror No. 2 used.

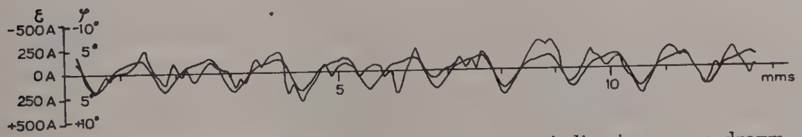

Fig. 10. Phase curve of G 22 with the double-periodic sine curve drawn.

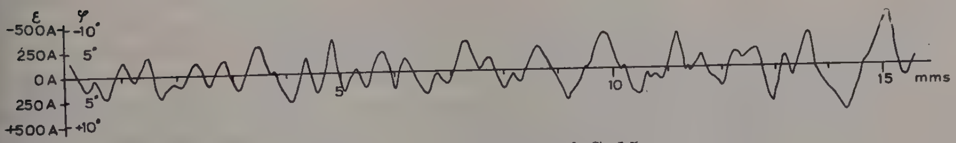

Fig. 11. Phase curve of G 15.

Analysis of the curves

The normal method of investigating curves such as registered here, is to treat them with Fourier's analysis. The length of the fundamental period is obtained according to theory (9, 3) from measurements of the distance between the ghosts and the central line. These measurements indicate the number of turns of the ruling-machine screw that corresponds to the fundamental period. The final measurements, however, were taken from the intercepts of the phase curve at the axis. When the analysis was made by the method of repeated intervals, a result of 35.6 mms at the paper was obtained in two cases; whereas the value calculated from the known pitch of the ruling-machine screw and the magnification of our optics, gave 35.7 mms. The analysis ordinarily contained 10 or 12 periods (each of them 1.25 mms at the grating surface), and was performed by dividing the total curve into its single periods, the average shape being drawn with the greatest care. The maximum random errors introduced by this procedure were estimated to correspond to 0.2 degrees in phase angle. Examples of such curves can be seen in Fig. 16.

The Fourier analysis is performed with a calculation scheme giving the first six periods (10), and has the same degree of accuracy as mentioned above. With

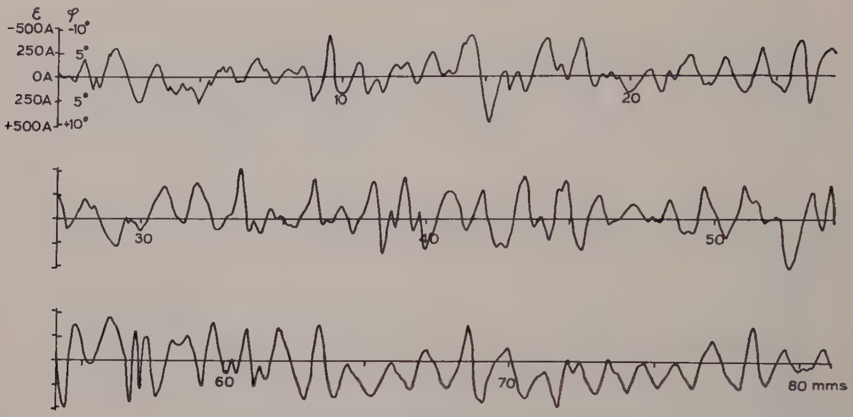

Fig. 12. Phase curve of G 73.

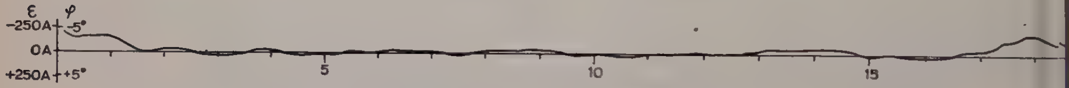

Fig. 13. Phase curve with plane mirror inserted showing lens irregularities.

regard to the accuracy of the entire method the amplitudes are only safe within 0.6 degrees, i.e. 30 A counted at the grating surface. Therefore an amplitude of this value or lower, cannot claim upon any real significance.

Before commenting on the analyses of the different gratings we must investigate the possible distorsion introduced in the curves on account of the imperfect lenses L_2 and L_3. Fig. 13 shows a phase curve derived from a record made solely to check the amount of irregularities from this reason. A very plane stellite mirror (plane within 20 A in depth profile and less than 100 A deviation from the planeity over the area used), was put into the same position as the grating, but with its normal bissecting the incident and the exit ray so that the entrance slit image falls onto the phase mirror. As obvious from the curve, rather slow phase changes of about 1 degree are present in the central part, and larger ones up to 4 degrees at the ends due to spherical aberration, though its influence was decreased thanks to the choice of a broad phase mirror slit.

Grating No. G III. As this test grating has a single periodicity of relatively large amplitude, it was estimated suitable for making a rather important investigation concerning the method. Following directly from the diffraction theory of the phase contrast method, one must carefully choose the width of the central slit of the phase turning plate or mirror. When its angular width is $2\,\lambda/b$, it corresponds exactly to the central fringe of diffraction of a rectangular phase irregularity with a width of b. The phase contrast image then contains those details truely imaged, whose extensions are less than b. If the phase mirror slit is increased, one obviously loses some details of intermediate size. In our case, we judged it convenient, as previously reported, to have a rather wide phase mirror slit as the periodic errors give ghost lines widely separated from the centre, but the different resolution on account of various widths of the slit is of importance for the non-

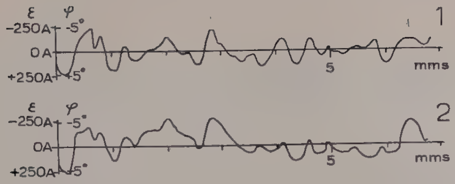

Fig. 14. Random structure of G III, taken with mirrors Nos. 1 and 2.

periodic part of the structure. Another reason for having a rather large slit width was to incorporate a comparatively long spectral line, which is curved on account of the grating interference conditions. However, with the present technique of manufacturing phase mirrors it is easily possible to curve the slit accordingly, though such mirrors were not used for this investigation.

As the main investigation was performed with the broad-slit phase mirror No. 1, this grating was also recorded with the phase mirror No. 2 (Table 1) which has a slit below a third of the former. In fact, the slit was slightly too small to allow the entire long line to fall inside its area. The q-value was determined by the principle mentioned before, but with the grating in the first order position acting as a mirror. The consistency of the resulting higher q-value of this mirror with the normal one of mirror No. 1, follows from the amplitude values given by the Fourier analysis. For mirror No. 1, the fundamental period was found to have 345 A, and for mirror No. 2, 315 A, thus within the limits of error covering each other. All the higher periodicities are found to be less than 25 A and therefore immeasurable.

The comparison between the two curves is interesting and important also for the interpretation of wave-front structure as stray light. The difference is most sensitively shown in those curves where the sinuoidal periods have been subtracted. The central part of the two curves Fig. 8 and Fig. 9 are shown in this way as Fig. 14, curve 1 and 2 respectively. Concerning curve 2, it must be recognized that the structure is significient, but not the ordinates for larger regions, as they have been distorted on account of the lack of quantitative phase contrast mentioned. On comparison one sees that the structure repeats itself very closely, so that no important error has been introduced in the investigation even with regard to random fine structure.

Summarizing the result for this grating, the first period has an amplitude of 345 A, and no further periods exist. It corresponds to a 0.39 per cent ratio of first ghost/parent line, whereas previously this ratio was measured photoelectrically to be 0.5 per cent. The random structure shows maximum peak values of about 250 A. In order to characterize its total importance, one can consider the square mean value, which is 100 A. Besides this, a discontinuity is present outside the measured region (see Fig. 6 a).

Grating No. G 22. This grating is of a superior quality, as the fundamental period has an amplitude of 145 A corresponding to a ghost ratio of 0.07 per cent. Also a double period is present with an amplitude of 50 A, i.e. a ghost ratio of 0.01 per cent. These ghosts are only visible with this dispersion in a microscope if the parent line intensity is considerably reduced. Under these conditions the random structure (see Fig. 15) is of the same order of magnitude, the peak maximum being about 250 A and the square mean value being 90 A, which thus renders greater relative uncertainty to the Fourier analysis.

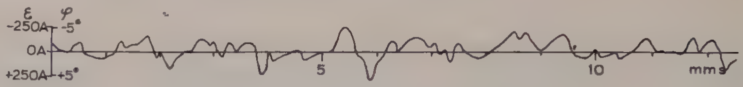

Fig. 15. Random structure of G 22.

Grating No. G 15. The main interest in the analysis of this grating is due to its complex structure. Contrary to the preceding ones, whose periodicities were 1.25 mms = 1 turn, this specimen has its fundamental period equal to 2.50 mms = 2 turns. As seen in Fig. 11, the structure is irregular, so that the Fourier analysis was performed for the entire grating (6 periods), as well as for 4 periods and 2 periods. The last were selected to be rather regular. The results are given in Fig. 16, partly as averages of the curves for a period and partly as Fourier spectra. The irregular character of the ruling is confirmed by the difference of these results, as for instance, the third and fifth periods have been greatly reduced in the first spectrum by two anomalies. The second periodicity (= 1 turn) corresponds to the ghost ratio of 0.07 per cent. Viewing the spectral line, the second and the fifth ghosts are visible, the latter very faintly.

Discussion of the method and its possibilities

Periodic structure. With regard to analysing and measuring periodic errors, the present method is the most sensitive of existing ones. With a maximum error of 30 A for a displacement of a group of grooves at the grating surface, consisting of about 30 grooves at an ordinary grating, the precision in measuring the average displacement for this small part of the grating is only 1/500 of the spacing. This precision when measuring an amplitude of the periodicity in groove displacement, corresponds to a change in intensity of a 0.1 per cent ghost produced by it in the first order spectrum which is 0.03 per cent. The absolute value of a measurable ghost intensity is only 0.003 per cent. It is evident that such small errors of the periodic type ought to be almost impossible to correct for by mechanical means, and for spectroscopic purposes ghosts of such low amounts are very difficult to detect and of no importance.

Nevertheless there appear to be several possibilities for utilizing this method to improve or to analyze the grating qualifications when the periodic errors are of real importance. It is known that in some gratings, there exist discontinuities in the ruling. Their phase difference quantities can be measured, and their possible influence on the resolving power estimated. Such portions which show extremely large discontinuities or periodic displacements of the wave surface can be screened off most effectively by analysing the phase contrast curve.

In the diffraction figure produced by the grating it is very easy to screen off those portions which are due to one or several special periodicities. To do so, an opaque double slit, consisting of two thin metal rods, is placed near the front of the phase contrast mirror and adjusted to cover the corresponding ghost on each side. This may be a method which also can be employed for separation of objects with different extensions (and consequently different widths of their diffraction patterns) in their phase contrast examination. This is of value for example in the analysis of the irregularities in the polish of optical surfaces.

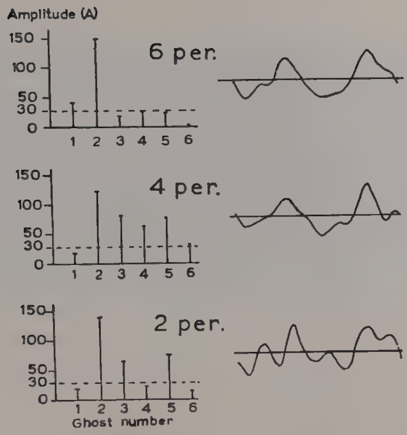

Fig. 16. G 15, Fourier spectra and average period curves.

Random structure. This method has revealed the detailed shape and amount of the groove displacements which remain after subtracting the periodic variations from the phase curve. It is not surprising that such a random structure exists. We realise that the accuracy of the determination is 1/500 of the grating spacing, and a peak value of the amount shown in Fig. 14 is less than 1/100 of it. From photographs of ruled surfaces taken in recent years by electron microscopes (11) the detailed shape of the grooves is in some cases known, and the conditions were examined for a good "blaze" in a grating. The shape has also been measured roughly by means of microphotogrammetry. When studying the profile curves resulting from such investigations, it is well understood that a sideways displacement of the reflecting groove portion of the order of 1/100 of the spacing is very small. A further study of the curves originating either from different shapes of the diamonds or from different blank surface material may possibly reveal some differences.

The main practical disadvantage from these small errors in the wave-front is that they give stray light. The total amount of stray light and its angular distribution can, in principle, be calculated by integration from the wave-front curve. The types of irregularities shown in the gratings examined mainly give rise to stray light in rather large angles from the main spectral lines. When more facts are obtained, it could be interesting to compare the values of the stray light received from this structure in the wave-front; the additional values from the bi-maxima due to regular interference from the entire grating, and possibly those from other sources, with the values of the stray light obtained experimentally (12).

For prism instruments, this type of stray light from the random irregularities in the grooves, has its corresponding causes in two factors, firstly, the presence of local inhomogeneities in the glass, and secondly the deviation from planeity of the glass surface due to the shape caused by the polish. Even when the glass is very carefully selected and everything is done to avoid inhomogeneities, striae may be present; but generally they are of negligible importance when they are below the order of magnitude of 100 A in optical path difference. Therefore irregular wave-front from a spectral line produced by a prism can be expected when examined by the same phase contrast method. We have not as yet made an extensive

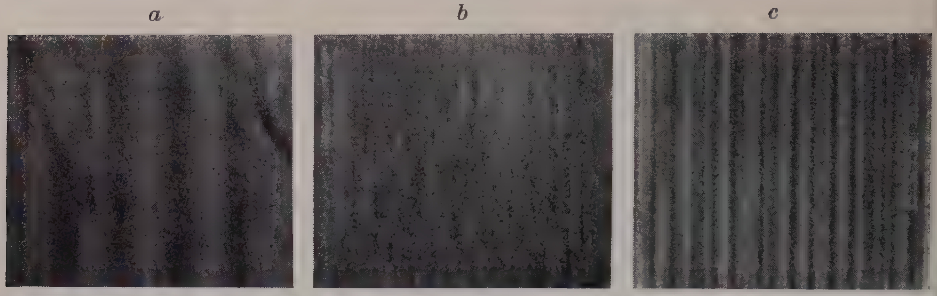

Fig. 17. Comparative phase contrast photographs showing the wave-front structure for the spectral line 5461 A, *a* quartz prism, ray in axis direction, calculated resolving power 2,800. (the periodic structure due to Young interferences between the two rays) *b* flint glass prism, calc. resolving power 5,000 *c* grating G 22, calc. resolving power 11,500.

comparison between prisms and gratings or between different prisms, but Fig. 17 contains two phase contrast pictures taken with prisms, and one picture showing one of the gratings examined here. All the pictures were taken with the same apparatus, film, setting of sensitivity and slit widths. As estimated from density differences, the path differences contained in the random striae of the quartz prism (see the legends) are about 500 A, and those of the glass prism some 100 A, in maximum. It should be remarked that these phase contrast pictures have according to the conditions in spectroscopy been taken with a slit arrangement, and are thus selective for the variations perpendicular to the slit. To the stray light produced by the fine wave-front structure in a prism instrument one should add the amount introduced by unwanted reflexions from the surfaces.

Optics Laboratory, Royal Institute of Technology, Stockholm 26, June 1951.

REFERENCES. 1. **F. Zernike,** M.N.R.A.S. *94*, 377, 1934, and Physica *1*, 689, 1934. — 2. See e.g. **M. Françon,** Le contraste de phase en optique et en microscopie. Paris 1950. — 3. **A. M. Camus, M. Françon, E. Ingelstam** and **A. Maréchal,** Revue d'Optique *30*, 121, 1951. — 4. **E. Ingelstam,** Arkiv för fysik, *3*, Nr 2, 1951. — 5. **M. Françon** and **G. Nomarski,** C.R. (Paris) *230*, 1392, 1950. — 6. **J. Valasek,** Introduction to Theoretical and Experimental Optics. New York 1949. — 7. **E. Ingelstam,** Communication No. I, Colloque international sur le contraste de phase et le contraste par interférence, en mai 1951. Un. Int. d'Opt., 3 Boul. Pasteur, Paris (in print). — 8. **C. H. Dieke,** Photoelectric Intensity Measurements in Spectra. Transact. Instrum. and Measurem. Conf., Stockholm 1947. — 9. **C. Runge,** Ann. der Physik *71*, 178, 1923. — 10. **H. A. Lorentz, G. Joos** and **Th. Kaluza,** Höhere Mathematik für den Praktiker, p. 286. Leipzig 1938. — 11. **R. D. Heidenreich,** J. O. S. A. *35*, 139, 1945. — 12. **E. Ingelstam** and **E. Djurle,** Arkiv för fysik *3*, Nr 6, 1951.

*

The senior of the authors would like to take this opportunity of expressing his sincere thanks to Prof. MANNE SIEGBAHN for true personal friendship since the first of the years he was my teacher. A special thanks on this occasion is based upon his great activity in improving the conditions of optics science. In the Swedish Council for Technical Research he proposed a committee work on the subject and undertook the great work of being its president. Whilst awaiting the Government's decision to creat an institute for optics in Stockholm, as was proposed, Prof. SIEGBAHN

many respects promoted the provisory research centre where the present authors e now working.

It is therefore a great pleasure for myself, on behalf also of the other workers, dedicate to him a paper dealing with the phase contrast methods developed ere. We do hope that the future work to some extent will conform to his own eas of persuing this branch of Swedish physics and technics.

Tryckt den 31 januari 1952

Uppsala 1952. Almqvist & Wiksells Boktryckeri AB

ARKIV FÖR FYSIK Band 4 nr 28

Read 14 November 1951

Observations on the He I isoelectronic sequence

By Bengt Edlén

With 4 figures in the text

Introduction. The two-electron systems of the helium-like atoms have a higher ionization energy and, consequently, resonance lines with shorter wave-lengths than any other atoms at the same stage of ionization. The elucidation of these spectra has, therefore, been intimately connected with the development of the technique of vacuum spectroscopy. Since Lyman's pioneering work on the helium spectrum the resonance lines of helium-like atoms have been marking the progress toward shorter wave-lengths. Thus, λ 100 of Be III (Edlén & Ericson, 1929), and λ 40 of C V (Edlén, 1931), have been in turn the shortest wave-length observed in optical spectra. This series was followed to F VIII by Tyrén (1940), and to Al XII by Flemberg (1942), pushing the limit of the observable range down below 7 A. These investigations, since 1929, were all carried out at the Physics Laboratory of the University of Uppsala, initiated and furthered by Manne Siegbahn and entirely depending on the spectrographs designed by him.

In this article some previously unpublished observations obtained at Uppsala years ago are presented, followed by a discussion of some special features of the helium-like spectra and a survey of the present knowledge of their term systems.

Experimental data. The new data are given in Table 1. The lines have been observed in a vacuum spark by means of a Hilger E1 quartz spectrograph and, in the vacuum region, with a grazing incidence spectrograph of Siegbahn's design (Edlén, 1936). Other experimental data discussed below are drawn from the following sources: Atomic Energy Levels (1949) for He I; Werner (1927) and Schüler (1927) for Li II; Edlén (1934) for Li II, Be III, B IV, C V; Robinson (1937) for Li II, Be III, B IV, C V; Tyrén (1940) for B IV, C V, N VI, O VII, F VIII; Flemberg (1942) for Mg XI, Al XII.

Structure of $1s\,2p\,^3$P. The discussion of the fine structure of $1s\,2p\,^3\mathrm{P}_{2,1,0}$, which has previously been confined to He I and Li II, can now be extended to C V. The observed intervals, $^3\mathrm{P}_1 - {}^3\mathrm{P}_2$ and $^3\mathrm{P}_0 - {}^3\mathrm{P}_2$, obtained from observations[1] of the transition $1s\,2s\,^3\mathrm{S} - 1s\,2p\,^3\mathrm{P}$, are collected in Table 2, col. 4–5. Although the intervals approach those of a normal triplet when the nuclear charge Z increases, they are far from normal even in C V. As is well known, the explanation of the anomalous

---

[1] For He I from Meggers & Humphreys (1934); for Li II from Schüler (1927), components n:o 14, 7, 11 of λ 5 485; for Be III, B IV, and C V from Edlén (1934) and Table 1.

Table 1.

Observed lines in spectra of the He I isoelectronic sequence, not previously published.

λ, A(air)	ν, cm^{-1}	Identification
6 141.2	16 279	Be III $1s2s\ {}^1S_0 - 1s2p\ {}^1P_1$
2 824.57	35 393.2	B IV $1s2s\ {}^3S_1 - 1s2p\ {}^3P_0$
2 277.92 (2*d*)	43 886.1	C V $1s2s\ {}^3S_1 - 1s2p\ {}^3P_1$
2 277.25 (1*d*)	43 899.0	${}^3S_1 - {}^3P_0$
2 270.91 (3*d*)	44 021.6	${}^3S_1 - {}^3P_2$
λ, A(vac.)	**ν, μ^{-1}**	
128.500 (0)	77.821	O VII $1s2p\ {}^3P_2 - 1s3d\ {}^3D_3$
128.412 (00)	77.874	${}^3P_{1,0} - {}^3D_{2,1}$
120.331 (00*d*)	83.104	$1s2s\ {}^3S_1 - 1s3p\ {}^3P_{2,1,0}$
98.799 (0)	101.216	F VIII $1s2p\ {}^3P_2 - 1s3d\ {}^3D_3$
98.707 (0*b*)	101.310	${}^3P_{1,0} - {}^3D_{2,1}$

Table 2.

Intervals of $1s2p\ {}^3P_{2,1,0}$.

	Z	Observed intervals			Formula (9)		a	$\frac{{}^3P_2 - {}^3P_c}{a}$	$\frac{{}^3P_1 - {}^3P_c}{a}$	$\frac{{}^3P_0 - {}^3P_c}{a}$
		${}^3P_2$	${}^3P_1$	${}^3P_0$	${}^3P_1$	${}^3P_0$				
He I	2	0	− 0.078	− 1.074	− 0.081	− 1.073	0.2073	+0.70	+0.32	−4.48
Li II	3	0	+ 2.10	− 3.05	+ 2.13	− 2.87	1.321	−0.27	+1.32	−2.58
Be III	4	0	+ 14.8	—	+ 14.9	+ 3.4	4.116	−1.29	+2.31	—
B IV	5	0	+ 52.3	+ 36.3	+ 52.6	+ 35.8	9.368	−2.29	+3.29	+1.58
C V	6	0	+135.5	+122.6	+135.8	+ 121.8	17.85	−3.29	+4.30	+3.57
N VI	7				+292	+ 298	30.34			
O VII	8				+553	+ 611	47.61			
F VIII	9				+959	+1115	70.43			

structure of $1s2p\,{}^3P$ was given by HEISENBERG (1926), who derived the following expression for the combined effect of the various factors that cause the triplet splitting:

$$\Delta E({}^3P_{2,1,0}) = a\,[(Z-3)\,(1,\,-1,\,-2) + 1/4\,(1,\,-5,\,10)], \tag{1}$$

where, as a rough approximation, a was taken as

$$a = \frac{R\alpha^2\,hc\,(Z-1)^3}{2n^3\,l(l+\frac{1}{2})(l+1)}, \quad (R\alpha^2 = 5.843\ \text{cm}^{-1},\ n=2,\ l=1) \tag{2}$$

From (1) the *relative* positions of the levels referred to ${}^3P_2$ are obtained:

$$E\,(^3\mathrm{P}_{2,1,0}) = a\,[(Z-3)\,(0,\,-2,\,-3) + 3/4\,(0,\,-2,\,3)] \tag{3}$$

This formula has been shown to reproduce with good approximation the interval ratios as observed in He I and Li II, although the absolute intervals come out too small. Subsequent theoretical work by BREIT and others (cf. INGLIS, 1942) has shown that the effect of an incorrect step in Heisenberg's derivation and the effect of deliberate approximations nearly cancel each other with the result that, except for the factor a, Heisenberg's formula still holds good when compared with higher approximations. In any case, theory predicts

$$E\,(^3\mathrm{P}_{2,1,0}) = C\,(0,\,-2,\,-3) + D\,(0,\,-2,\,3), \tag{4}$$

C and D being functions of Z, which, however, do not seem to have been given explicitly for higher approximations. In order to derive an empirical extrapolation formula we put in accordance with (4) and changing sign according to $\Delta T = -\Delta E/hc$

$$^3\mathrm{P}_{2,1,0} = A\,[B\,(0,\,2,\,3) + (0,\,2,\,-3)] \tag{5}$$

where the functions $A(Z)$ and $B(Z)$ are to be determined from the observations. From (5) follows

$$\left.\begin{aligned} ^3\mathrm{P}_1 &= 2A\,(B+1) \\ ^3\mathrm{P}_0 &= 3A\,(B-1) \end{aligned}\right\} \quad \left.\begin{aligned} A &= (3\,^3\mathrm{P}_1 - 2\,^3\mathrm{P}_0)/12 \\ B &= (3\,^3\mathrm{P}_1 + 2\,^3\mathrm{P}_0)/(3\,^3\mathrm{P}_1 - 2\,^3\mathrm{P}_0) \end{aligned}\right\} \tag{6}$$

If A and B are computed by means of (6) from the observed intervals one finds, in accordance with Heisenberg's formula, that $\sqrt[3]{A}$ and B plotted against Z are straight lines within the experimental uncertainty.

The linearity accepted, the parameters are determined by first making a least square solution for B using the four values obtained by means of (6) for $Z = 2$, 3, 5, and 6. The weights assumed in this calculation correspond roughly to an estimated error of 5 units in the last decimal place of the interval as given in Table 2. Using the derived expression for B, the values for A are then obtained from the total observed splitting according to the following expressions for different Z's:

$$\left.\begin{aligned} Z &= 2 & {}^3\mathrm{P}_0 - {}^3\mathrm{P}_2 &= 3A\,(B-1) \\ Z &= 3 & {}^3\mathrm{P}_0 - {}^3\mathrm{P}_1 &= A\,(B-5) \\ Z &= 4,\,5,\,6 & {}^3\mathrm{P}_1 - {}^3\mathrm{P}_2 &= 2A\,(B+1) \end{aligned}\right\} \tag{7}$$

In this way the incomplete observation in Be III can be utilized and the influence of the relatively large uncertainty in the measurements of $^3\mathrm{P}_0$ in B IV and C V is avoided.

From the expressions for A and B the following formula is finally obtained:

$$\left.\begin{aligned} ^3\mathrm{P}_{2,1,0} &= a\,[(Z-2.960)\,(0,\,2,\,3) + 0.765\,(0,\,2,\,-3)] \\ a &= 0.1291\,(Z-0.829)^3 \end{aligned}\right\} \tag{8}$$

Formula (8) gives

$$\left.\begin{aligned} ^3\mathrm{P}_1 &= 2a\,(Z-2.195) \\ ^3\mathrm{P}_0 &= 3a\,(Z-3.725) \end{aligned}\right\} \tag{9}$$

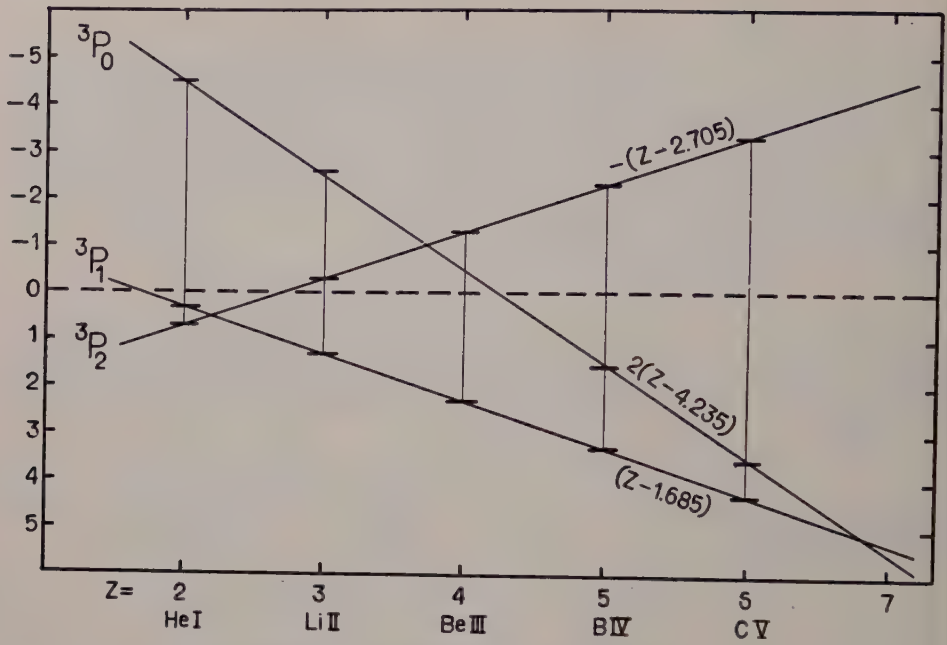

Fig. 1. Observed structure of $1s\,2p\,^3P$.

As shown in Table 2 these expressions reproduce the observed intervals very closely except for $^3P_0$ in Li II, where the discrepancy possibly surpasses the observational uncertainty.

For the purpose of comparison with Heisenberg's expression

$$\frac{R\alpha^2}{48}(Z-1)^3\,[(Z-3)\,(\ldots)+3/4\,(\ldots)] \tag{10}$$

we transform the empirical expression (8) to

$$1.061\,\frac{R\alpha^2}{48}(Z-0.829)^3\,[(Z-2.960)\,(\ldots)+0.765\,(\ldots)] \tag{11}$$

Except for the factor $(Z-\sigma)^3$ the agreement is remarkable. As mentioned above, however, the accuracy of the theoretical formula is somewhat fortuitous.

According to formula (1) the centre of gravity of the levels, weighted as $2J+1$, is equal to zero. The experimental formula (8) transformed to the same zero point ^3P_c is

$$^3P_{2,1,0}=a\left[(Z-2.96)\,(-1,\ 1,\ 2)+\frac{0.765}{3}\,(-1,\ 5,\ -10)\right] \tag{12}$$

giving

$$\left.\begin{aligned} {}^3\mathrm{P}_2 &= -\ \ a(Z-2.705) \\ {}^3\mathrm{P}_1 &= +\ \ a(Z-1.685) \\ {}^3\mathrm{P}_0 &= +2a(Z-4.235) \end{aligned}\right\} \tag{13}$$

The observed values of ${}^3\mathrm{P}_J - {}^3\mathrm{P}_c$ divided by a are found in the last columns of Table 2. They are also plotted in Fig. 1, together with the straight lines ${}^3\mathrm{P}/a$ from (13), to visualize how the term structure changes with Z.

Intensity of $1s^2\ {}^1\mathrm{S}_0 - 1s2p\,{}^3\mathrm{P}_1$. According to the selection rules the ground term $1s^2\,{}^1\mathrm{S}_0$ combines only with the terms $1s\,np\,{}^1\mathrm{P}_1$, giving rise to the resonance series. In addition to this expected series a number of relatively faint "non-diagram" lines are observed, which have been interpreted as due to doubly excited states (Edlén and Tyrén, 1939). They will not be further discussed here. One of these extra lines, however, which is observed throughout the whole series of atoms, from B IV onward, with increasing strength, was identified with the intercombination $1s^2\,{}^1\mathrm{S}_0 - 1s2p\,{}^3\mathrm{P}_1$ on account of a perfect coincidence with the predicted position. The transition $1s\,2p\,{}^3\mathrm{P} - 1s\,3d\,{}^3\mathrm{D}$ being observed for C V, O VII, and F VIII and the term $1s\,3d\,{}^3\mathrm{D}$ being very nearly hydrogen-like, the prediction is fairly precise and the tolerance for a coincidence only a few thousandths of an Ångström, which renders the evidence for the identification very strong. However, in a theoretical paper on the interpretation of the "non-diagram" lines mentioned above, Ta-You Wu (1940) calculated the ratio of the transition probabilities for $1s^2\,{}^1\mathrm{S} - 1s2p\,{}^1\mathrm{P}_1$ and $1s^2\,{}^1\mathrm{S} - 1s2p\,{}^3\mathrm{P}_1$. Finding a value about 10^5 he concluded that the intercombination line would be too faint to be observed and rejected the identification, tacitly identifying the intensity ratio with the transition probability ratio. These two ratios, however, may have quite different values as the following analysis will show.

The intensity (I) of an emission line is obviously proportional to the number of atoms (ΔN) arriving in the initial level per second, and to the probability for the transition concerned divided by the *total* probability (D) for a de-excitation of the initial level, i.e.

$$I \sim h\nu \Delta N \cdot A/D \tag{14 a}$$

The two levels $1s2p\,{}^1\mathrm{P}_1$ and $1s2p\,{}^3\mathrm{P}_1$, having the same statistical weight and nearly the same position, cannot have very different N. Consequently, the intensity ratio of the transitions from these levels into $1s^2\,{}^1\mathrm{S}$ will be determined by (for the notation see Fig. 2)

$$\frac{I}{I'} = \frac{A_1}{D} \cdot \frac{D'}{A_1'} \tag{14}$$

The total de-excitation probability (D) is the sum of the radiation probabilities A_1 and A_2 and the probability for collisional de-excitation (C), which may be assumed the same for $1s2p\,{}^1\mathrm{P}_1$ and $1s2p\,{}^3\mathrm{P}_1$. Thus,

$$\frac{I}{I'} = \frac{A_1}{A_1 + A_2 + C} \cdot \frac{A_1' + A_2' + C}{A_1'} \tag{15}$$

The relative magnitude of the A's can be roughly estimated by considering that $A \sim \nu^2 f$. Assuming the osc. strength f to be roughly of the order of unity for a

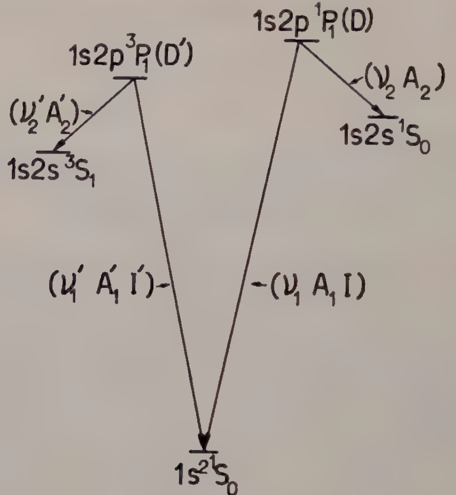

Fig. 2.

Table 3.

Observed intensity ratio I/I' for the transitions $1s^2\,{}^1S_0 - 1s2p\,{}^1P_1$ and $1s^2\,{}^1S_0 - 1s2p\,{}^3P_1$.

	I/I'	ν_1'	ν_2'	$(\nu_1'/\nu_2')^2$
C V	20	246 μ^{-1}	4.39 μ^{-1}	0.3×10^4
N VI	10	344 »	5.24 »	0.4 »
O VII	5	459 »	6.10 »	0.6 »
F VIII	3	590 »	6.98 »	0.7 »
Mg XI	2	1 083 »	9.7 »	1.2 »

"permitted" transition (cf. CONDON & SHORTLEY, 1935), and observing that $(\nu_1/\nu_2)^2$ is of the order of 10^4, one finds that A_2 is vanishingly small compared to A_1. Furthermore, as according to WU's calculation $A_1/A_1' = 10^5$, A_1' will be approximately of the same order of magnitude as A_2. Then, considering separately the two possible cases, we obtain

$$\left.\begin{array}{lll} \text{a)}\ C \gg A_1 & I/I' = A_1/A_1' = 10^5 \\ \text{b)}\ C \ll A_1 & I/I' = 1 + A_2'/A_1' + C/A_1' \end{array}\right\} \qquad (16)$$

Evidently, the intercombination could be observed only in case *b*. Conversely, accepting its appearance as an observed fact, we may conclude that condition *b* was fulfilled in the experiment.

Because of both the ν^2-factor and the increasing departure from LS coupling, which makes the intercombination less "forbidden", the probability A_1' will increase rapidly with Z, while A_2' and C change much more slowly. Consequently, in case *b* the ratio I/I' will decrease rapidly towards the limiting value 1. This is in complete

Table 4.

Derivation of an extrapolation formula for $1s2s\,^3S_1 - 1s2p\,^3P_1$.

	Z	ν, cm^{-1}	Δ'	Δ''	$1745/Z$	$2569/Z^2$	$0.205 \times (Z-1)^4$	ν calc.
H	1				1 745	2 569	0	− 1 912
He I	2	9 230.9	8994.4		872.5	642.2	0.2	9 230.9
Li II	3	18 225.3	8627.3	−367.1	581.7	285.4	3.3	18 225.3
Be III	4	26 852.6	8524.6	−102.7	436.2	160.6	16.6	26 852.6
B IV	5	35 377.2	8508.9	− 15.7	349.0	102.8	52.5	35 377.2
C V	6	43 886.1			290.8	71.4	128.1	43 886.2
N VI	7				249.3	52.4	265.7	52 428
O VII	8				218.1	40.1	492.2	61 042
F VIII	9				193.9	31.7	839.7	69 765

accordance with the observations. The observed ratio I/I' can be estimated for C V, N VI, O VII, F VIII, and Mg XI from the spectrum reproductions given by TYRÉN (1940) and FLEMBERG (1942). The result is shown in Table 3. Although the figures are uncertain, perhaps by a factor 2, the qualitative picture is clear. After first appearing very faintly in boron ($Z=5$) the relative intensity of the intercombination line increases rapidly with Z so as to become in magnesium ($Z=12$) only slightly less than that of the main line. The figures indicate roughly a relationship $(I/I'-1) \sim (Z-1)^{-4}$ as one might have reason to expect for the expression $(A'_2 + C)/A'_1$.

This discussion shows that there is no reason not to accept the identification of $1s^2\,^1S_0 - 1s\,2p\,^3P_1$, which then can be used to connect the singlet and triplet term systems in these spectra.

Formula for $1s2s\,^3S_1 - 1s\,2p\,^3P_1$. Observations of the transition $1s\,2s\,^3S - 1s\,2p\,^3P$ are now available for the first 5 members of the isoelectronic series. This transition, occurring between states with equal n, has an exceptional position as remaining at relatively long wave-lengths, while the rest of the spectrum is displaced toward very short wave-lengths with increasing Z. In C V, for instance, $2s-2p$ falls at λ 2300, whereas the resonance transition $1s^2 - 1s\,2p$ falls at λ 40. This makes the wave-number accuracy of $2s-2p$ several orders of magnitude better than that otherwise obtained in the same spectrum. For instance, an error of ±0.01 Å at λ 2300 causes a wave-number error which is only about 1/300 of that corresponding to ± 0.001 Å at λ 40. As, moreover, the wave-number of $2s-2p$ shows a very regular variation with Z the conditions for a useful extrapolation are very good.

We propose to derive an extrapolation formula for $2s\,^3S - 2p\,^3P$ and choose specifically the component $2s\,^3S_1 - 2p\,^3P_1$ of which the observed wave-numbers (ν) are collected in Table 4. The differences show that ν is essentially a linear function of Z, but that non-linear terms, preferably inverse powers of Z, must be included to account for the deviation which is noticeable especially for small Z. In order to take care of spin and relativity effects the formula should also contain a term of the form $a(Z-1)^4$. Having 5 observations we may include 5 adjustable parameters in the formula and obtain finally for $1s\,2s\,^3S_1 - 1s\,2p\,^3P_1$

$$\nu(\mathrm{cm}^{-1}) = 8343.7\,(Z-1) + 2401.7 - 1745\,Z^{-1} - 2569\,Z^{-2} + 0.205\,(Z-1)^4 \qquad (17)$$

The non-linear terms are tabulated to show their relative importance for different Z. Table 4 also gives the extrapolated wave-numbers for $Z=1$, 7, 8, and 9.

The terms in Z^{-1} and Z^{-2} may of course be replaced by one of the form $C(Z-\sigma)^{-1}$, in which case the formula becomes

$$\nu = 8328.1(Z-1) + 2566.8 - 2513(Z-0.49)^{-1} + 0.216(Z-1)^4 \tag{17 a}$$

giving for $Z=1$, 7, 8, 9 the values -2361, 52429, 61047, and 69781 respectively. The difference between the values extrapolated by means of (17) and (17 a) may give a hint as to the reliability of an extrapolation of this kind.

Formula for $1s\,2p\,^3P_1$. Of triplet transitions in Be III only $1s2p\,^3S - 1s\,2p\,^3P$ has been observed, and as intercombination lines are also missing the absolute values of the triplet terms can be found only by some kind of interpolation. A formula for an absolute[1] term value as a function of Z would also furnish a welcome check on the series limit determination in the individual spectra. For this purpose we will choose $1s2p\,^3P_1$ for which the spin and relativity term is already known from the discussion of the fine structure.

From the well-known Moseley approximation $T = R(Z-\sigma)^2/n^2$ it follows that $T - RZ^2/n^2$ will be nearly linear in Z. The spin and relativity contribution is obtained from (13) as $\Delta T = +0.1291\,(Z-0.829)^3\,(Z-1.685)$, which for the sake of simplicity may be approximated to $0.125(Z-1)^4$. The departure from linearity which remains after subtraction of these second and fourth order terms is similar to that for $2s - 2p$, discussed above. We adopt therefore the following general expression for $1s\,2p\,^3P_1$

$$T = R\,(Z-1)^2/4 + A\,(Z-1) + B + CZ^{-1} + DZ^{-2} + 0.125\,(Z-1)^4 \tag{18}$$

The data are collected in Table 5. Here $T' = T - R(Z-1)^2/4 - 0.125(Z-1)^4$ and $R = 109737$. The stated experimental uncertainties ΔT are merely rough estimates. Only their relative magnitudes, which determine the weight factors $p \sim \Delta T^{-1}$, are of importance in this connection. The term value for helium has a much higher accuracy than the rest and will be taken as exact. By subtracting the helium value one obtains 6 equations of the form

$$p(T' - T'_{\mathrm{He}}) = p(Z-2)A + p(Z^{-1} - 1/2)C + p(Z^{-2} - 1/4)D \tag{19}$$

The least square solution gives A, C, and D. Then, B is obtained from T'_{He}. The result is

$$T'_{\mathrm{calc}} = 5\,715\,(Z-1) - 9\,603 + 15\,520\,Z^{-1} - 8\,327\,Z^{-2} \tag{20}$$

As shown in the last column of Table 5 formula (20) reproduces the observed values well within the assumed experimental uncertainty. The formula gives for Be III $1s2p\,^3P_1 = 257\,820$ cm^{-1}, which is accepted as basis for the Be III triplets in Table 6[2].

Attempts to find a formula with fewer adjustable parameters showed that if $D=0$ then B becomes nearly equal to $-C$ which suggested a further simplification resulting finally in the two-parameter formula:

---

[1] I.e. a term value referred to the ionization limit.

[2] A formula derived for $1s2p\,^3P_1 - 1s2p\,^1P_1$, $\nu = 7\,469\,(Z-1) - 10\,993 + 10\,105\,Z^{-1} + 2\,079\,Z^{-2} + 0.1\,(Z-1)^4$, gives, in fair agreement, 257 837 for Be III $1s2p\,^3P_1$.

Table 5.

Derivation of an interpolation formula for $1s2p\,{}^3P_1$.

	Z	T, cm^{-1}	$R(Z-1)^2/4$	$0.125 \times (Z-1)^4$	T'(obs) $\pm \Delta T$	p	T'(calc)	calc-obs
H^-	1	—	0	0	—	—	− 2 410	—
He I	2	29 224	27 434	0	1 790 ± 0	∞	1 790	0
Li II	3	115 812	109 737	2	6 073 ± 5	80	6 075	+2
Be III	4	—	246 908	10	—	—	10 902	—
B IV	5	454 980	438 948	32	16 000 ± 40	10	16 028	+28
C V	6	707 320	685 856	78	21 386 ± 60	7	21 327	−59
N VI	7	1 014 480	987 633	162	26 685 ± 150	3	26 734	+49
O VII	8	1 376 690	1 344 278	300	32 112 ± 200	2	32 212	+100
F VIII	9	1 794 000	1 755 792	512	37 696 ± 400	1	37 739	+43
Mg XI	12	3 375 300	3 319 544	1 830	53 926 ± 1 000	0	54 497	+571
Al XII	13	4 014 800	3 950 532	2 592	61 676 ± 2 000	0	60 122	−1 554

Table 6.

Term values (in μ^{-1}) of He I-like spectra.

	Be III	B IV	C V	N VI	O VII	F VIII	Mg XI	Al XII
$1s^2\ {}^1S_0$	124.1225	209.196	316.245	445.280	596.300	769.34	1420.92	1682.50
$1s2s\ {}^1S_0$	26.0038							
$1s2p\ {}^1P_1$	24.3759	43.394	67.921	97.901	133.380	174.35	330.19	393.31
$1s3p\ {}^1P_1$	10.8902	19.378	30.310	43.641	59.445	77.68	147.08	175.23
$1s4p\ {}^1P_1$	6.1395	10.921	17.077	24.599	33.490		82.81	98.64
$1s5p\ {}^1P_1$	3.9331	6.996	10.939		21.455		52.86	
$1s6p\ {}^1P_1$	2.7294	4.860	7.603		14.905			
$1s7p\ {}^1P_1$	2.0090							
$1s2s\ {}^3S_1$	28.4686	49.0357	75.1206	[106.691]	143.773	[186.376]		
$1s2p\ {}^3P_2$	25.7805	45.4928	70.7184	[101.419]	137.614	179.304		
${}^3P_1$	25.7820	45.4980	70.7320	101.448	137.669	179.400	337.53	401.48
${}^3P_0$	25.7808	45.4964	70.7307	[101.449]	137.675	179.415		
$1s3p\,{}^3P_{210}$					60.670			
$1s3d\,{}^3D_3$			30.5164		59.793	78.088		

$$T' = (Z-1)\,(5520 - 7462\,Z^{-1}) \tag{21}$$

which still gives an acceptable fit to the observations.

Term Tables. The foregoing discussions furnish the complement to observed data required for the derivation of coherent sets of triplet terms connected with the singlets. Table 6 gives the complete collection of terms derived for helium-like spectra from Be III to Al XII. The absolute values are based on determinations of the series limit ($1s^2\,{}^1S$) of the resonance series. No reason has been found to change the value for this limit as derived by ROBINSON (1937) for Be III, B IV, C V; by TYRÉN (1940) for N VI, O VII, F VIII; and by FLEMBERG (1942) for Mg XI, Al XII. The values for $1snp\,{}^1P$ are also taken without change from the authors mentioned,

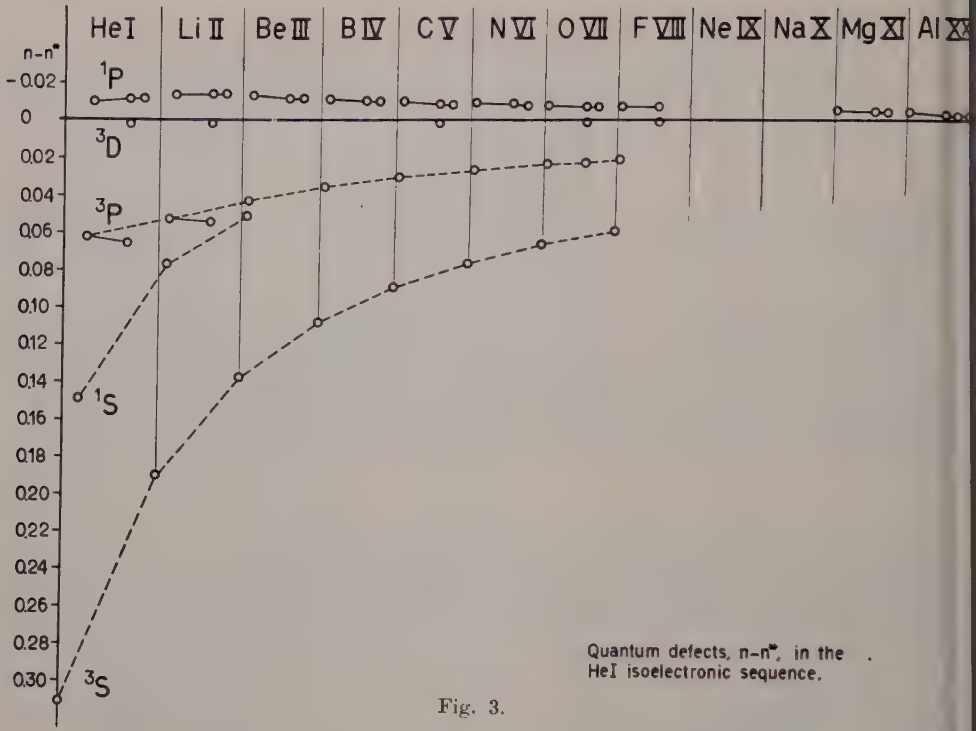

Quantum defects, n–n*, in the He I isoelectronic sequence.

Fig. 3.

for B IV and C V as amended by TYRÉN. The singlets have been included in Table 6 for the sake of completeness and convenience. – The triplet values are slightly different from those in "Atomic Energy Levels", which were furnished as unpublished results by the author in 1947. The small differences arise from utilizing in the present calculation the observed values for the intercombination $1s^2\,{}^1S - 1s\,2p\,{}^3P_1$ of which the identification may now be considered as definitely established. — Brackets designate terms that are not involved in any observed combinations.

The plot in Figure 3 of the "quantum defects" $n^* - n$, n^* being defined by $T = R\,(Z-1)^2/(n^*)^2$, has been included to give a useful bird's-eye view of the term systems and of the term values as compared with the corresponding hydrogen-like values.

"Lamb shift" in $1s^2\,{}^1S$. The terms of the helium spectrum have been subject to extensive theoretical calculations and for the ground term exists, as is well known, a theoretical formula explicit in Z which is considered as very accurate. In connection with the publication of experimental values of $1s^2\,{}^1S$ for various elements comparisons with the theoretical values have been made by ROBINSON (1937), TYRÉN (1940), and FLEMBERG (1942). These comparisons reveal a small but systematic difference between the calculated and the observed values. ERIKSSON (1948) pointed out the possibility to interpret this difference as a counterpart to the deviation from the Dirac formula observed in hydrogen-like spectra and known as the "Lamb shift". Attempts to apply to $1s^2\,{}^1S$ the theory for this shift as developed

Table 7.

Experimental evidence for a "Lamb shift" in $1s^2\,{}^1S$.

	Z	T(obs), μ^{-1}	T(calc), μ^{-1}	ΔT, cm^{-1}	$\Delta\lambda$, $A \pm d\lambda$	$\Delta T/Z^4$	$\Delta' T$, cm^{-1}
He I	2	19.8312	19.8319	7	-0.018 ± 0.010	0.44 ± 0.25	+3
Li II	3	61.0079	61.0092	13	$-0.003_5 \pm 0.003$	0.16 ± 0.14	−7
Be III	4	124.1225	124.1309	84	$-0.005_5 \pm 0.002$	0.33 ± 0.12	+20
B IV	5	209.196	209.215	190	$-0.004_3 \pm 0.001_5$	0.31 ± 0.10	+30
C V	6	316.245	316.276	310	$-0.003_1 \pm 0.001$	0.24 ± 0.08	−10
N VI	7	445.280	445.333	530	$-0.002_7 \pm 0.001$	0.22 ± 0.08	−70
O VII	8	596.300	596.407	1 070	$-0.003_0 \pm 0.001$	0.26 ± 0.09	+50
F VIII	9	769.340	769.523	1 830	$-0.003_1 \pm 0.002$	0.28 ± 0.18	+190
Mg IX	12	1 420.92	1 421.40	4 800	$-0.002_4 \pm 0.001$	0.23 ± 0.10	−400
Al XII	13	1 682.50	1 682.99	4 900	$-0.001_7 \pm 0.001_5$	0.17 ± 0.15	−2 200

for hydrogen have since been made by GÜNTHER (1949) for He I, and by HÅKANSSON (1950) for arbitrary Z.

The experimental evidence for this shift in $1s^2\,{}^1S$ will be briefly reviewed here. The values for T(obs) and T(calc) in Table 7 are taken from FLEMBERG with a slight change of T(calc) due to a change of the fine structure constant to the more recent value $\alpha = 137.041^{-1}$. T(obs) for He I has been replaced by a value derived from the wave-lengths 584.331 and 537.024 for the first two lines of the resonance series given in the "Wave-length Identification Lists" by BOYCE and ROBINSON (1936) from unpublished measurements by BOYCE. It should also be mentioned that HOPFIELD (1930) obtained from his measurements $T_{\mathrm{He}} = 198314 \pm 5$.

The difference $\Delta T = T_{\mathrm{calc}} - T_{\mathrm{obs}}$ is without exception positive. In order to judge its accuracy more easily ΔT has been converted to the corresponding wave-length difference in the series limit

$$\Delta\lambda_A = \Delta T_{\mathrm{cm}^{-1}} / (T_{\mu^{-1}})^2 \tag{22}$$

which is tabulated in column 6 together with an estimate of the experimental uncertainty $\pm d\lambda$. The present estimate is somewhat narrower than previous ones (cf. FLEMBERG's table).

Figure 4 shows that $\sqrt[4]{\Delta T}$, plotted against Z, is well represented by a straight line which as the best choice passes through the origin. We are therefore entitled to put $\Delta T = aZ^4$ and get the values for a with their limits of error $\pm d\lambda T^2/Z^4$, as given in column 7. The weighted mean is $a = 0.25 \pm 0.03_5$. The residuals $\Delta' T = T(\mathrm{calc}) - 0.25\,Z^4 - T(\mathrm{obs})$ are shown in the last column of Table 7. The fact that the relatively large discrepancy for Al XII comes out rather similar to that in Table 5 indicates that the experimental determination of the series limit may not be so good in that case. It is further noteworthy that the residuals on the whole are considerably smaller than the assumed errors.

If the quantity aZ^4 is interpreted as the experimentally determined Lamb shift in $1s^2\,{}^1S$ we may put $aZ^4 = R\alpha^2 Z^4 \Lambda$ and get

$$\Lambda = a/R\alpha^2 = 0.043 \pm 0.006, \tag{23}$$

which may be compared with $\Lambda = 0.048$ and 0.040 found for $1s\,{}^2S$ in H I and He II respectively.

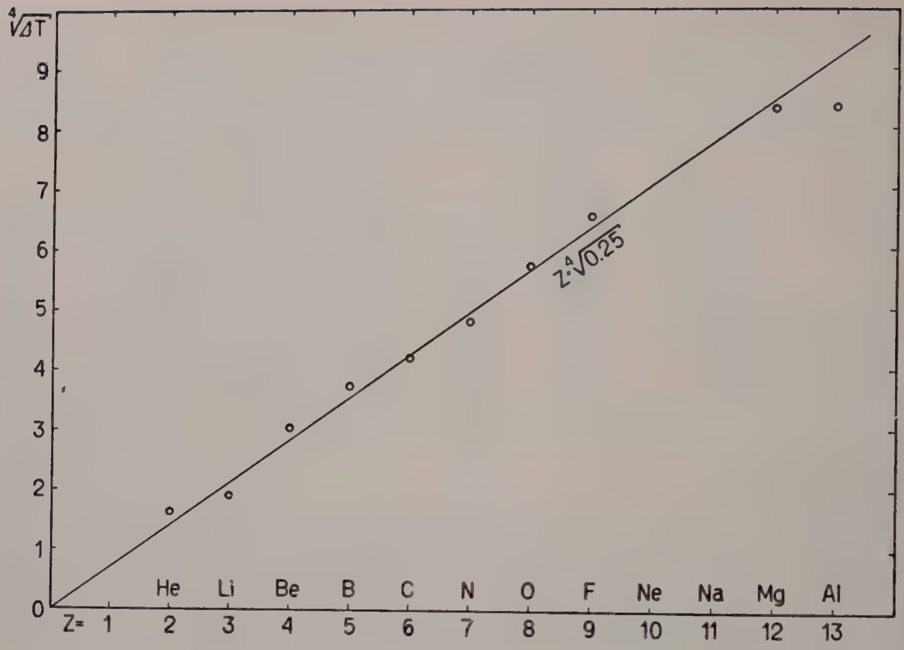

Fig. 4. $\Delta T = 1s^2\,{}^1S$ (calc) — $1s^2\,{}^1S$ (obs).

The shift thus derived for $1s^2\,{}^1S$ is at least twice as large as theoretically expected (cf. HÅKANSSON, 1950). One systematic error affecting the observed values is due to the Lamb shift in hydrogen-like spectra because the measurements, especially for the elements from boron to fluorine, were largely based on reference wave-lengths in Be IV, B V, C VI, N VII, and O VIII, calculated with the uncorrected Dirac formula. A correction for this error would, however, *increase* the observed Lamb shift in $1s^2\,{}^1S$. A definite disagreement, therefore, seems to exist at the moment between theory and observation.

SUMMARY. Some new wave-length data for Be III, B IV, C V, O VII, and F VIII are presented. An empirical formula for the structure of $1s\,2p\,{}^3P_{2,1,0}$ is derived from observations in the five elements from helium to carbon and compared with theory. The factors determining the intensity of the transition $1s^2\,{}^1S - 1s\,2p\,{}^3P_1$ are discussed with the conclusion that its identification, which had been subject to some doubts, is confirmed for the elements from boron to aluminium. Interpolation formulae for the wave-numbers of certain transitions and terms are derived and utilized in the calculation of the triplet term systems. Complete term tables are compiled for Be III, B IV, C V, N VI, O VII, F VIII, Mg XI, and Al XII. Finally, a discussion of the evidence for a "Lamb shift" in $1s^2\,{}^1S$ leads to an "observed" shift of $(0.043 \pm 0.006)R\alpha^2 Z^4$.

Department of Physics, University of Lund, October 1951.

REFERENCES. Atomic Energy Levels Vol. I, Circular 467 Nat. Bur. Stand., Washington (1949). — **J. C. Boyce** and **H. A. Robinson,** J. O. S. A. *26,* 133 (1936). — **E. U. Condon** and **G. H. Shortley,** The Theory of Atomic Spectra, Cambridge (1935). — **B. Edlén,** Nova Acta Reg. Soc. Sci. Ups. 9, No 6 (1934). — ——, ZS f. Phys. *100,* 621 (1936). — **B. Edlén** and **F. Tyrén,** Nature *143,* 940 (1939). — **H. A. S. Eriksson,** Nature *161,* 393 (1948). — **H. Flemberg,** Ark. Mat. Astr. o. Fys. *28 A,* No 18 (1942). — **M. Günther,** Physica *15,* 675 (1949). — **W. Heisenberg,** ZS f. Phys. *39,* 499 (1926). — **J. J. Hopfield,** Astrophys. J. *72,* 133 (1930). — **H. E. V. Håkansson,** Arkiv f. Fysik *1,* 555 (1950). — **D. R. Inglis,** Phys. Rev. *61,* 297 (1942). — **W. F. Meggers** and **C. J. Humphreys,** B. S. J. R. *13,* 293 (1934). — **H. A. Robinson,** Phys. Rev. *51,* 14 (1937). — **H. Schüler,** ZS f. Phys. *42,* 487 (1927); *66,* 431 (1930). — **F. Tyrén,** Nova Acta Reg. Soc. Sci. Ups. *12,* No 1 (1940). — **S. Werner,** Studier over Spektroskopiske Lyskilder, Diss. Copenhagen (1927). — **Ta-You Wu,** Phys. Rev. *58,* 1114 (1940).

Tryckt den 31 januari 1952

Uppsala 1952. Almqvist & Wiksells Boktryckeri AB

ARKIV FÖR FYSIK Band 4 nr 29

Communicated 12 September 1951 by G. Borelius and R. Sievert

Hyperfine structure and nuclear moments of Xe^{129} and Xe^{131}

By Aage Bohr, Jørgen Koch, and Ebbe Rasmussen

With 5 figures in the text

1. Introduction

The hyperfine structure of the arc spectrum of xenon was first investigated by Kopfermann and Rindal (1) and by Jones (2). In spite of the complicated line patterns for the natural mixture of the isotopes, the spins for the two odd isotopes Xe^{129} and Xe^{131} could be determined and were found to be 1/2 and 3/2, respectively. In the case of Xe^{129}, the hfs splittings are rather large ($\sim 0.1\ \text{cm}^{-1}$) and were measured by Jones for a number of lines in the infrared. Kopfermann and Rindal were able to construct term diagrams for both isotopes which, in addition to the spins, gave the value —1.1 for the ratio μ_{129}/μ_{131}, the lighter isotope having the negative magnetic moment. From these measurements Bethe and Bacher (3) later estimated the magnetic moment of Xe^{129} to be —0.9 nuclear magnetons (μ_N). Recently, the more accurate value $\mu_{129} = -0.777\ \mu_N$ was obtained by Proctor and Yu (4) by means of the nuclear induction method. For Xe^{131}, the smaller nuclear g-factor prevented the use of this method. In the search for a quadrupole effect of Xe^{131}, Korsching (5) obtained indication of a deviation from the interval rule in one of the lines of XeI, but was able only to give the estimate $|Q| \leq 0.1 \times 10^{-24}\ \text{cm}^2$.

The infrared spectrum of XeI has recently been investigated with samples of pure Xe isotopes with the purpose of studying isotope shifts as well as nuclear moments. Preliminary results (6) confirmed the spin values for the odd isotopes and gave definite evidence for a negative quadrupole moment for Xe^{131}. The isotopic samples were prepared electromagnetically by means of a new technique for the collection of ions of gaseous elements (7, 8). The present report contains a more detailed analysis of the hfs for the odd Xe-isotopes, which leads to improved values for the moments of Xe^{131}. Moreover, a description is given of the electromagnetic isotope separation of inert gases and the preparation of samples for spectroscopic investigations.

2. Electromagnetic isotope separation

The isotope separator at the Institute for Theoretical Physics in Copenhagen has previously been described in some detail (9). The ions, produced in a low voltage arc, were accelerated by a voltage of 60–80 kV and focused by a system of electrostatic lenses. For magnetic analysis, the parallel ion beam was deflected by 90 degrees in a wedge-shaped magnetic field having a mean radius of

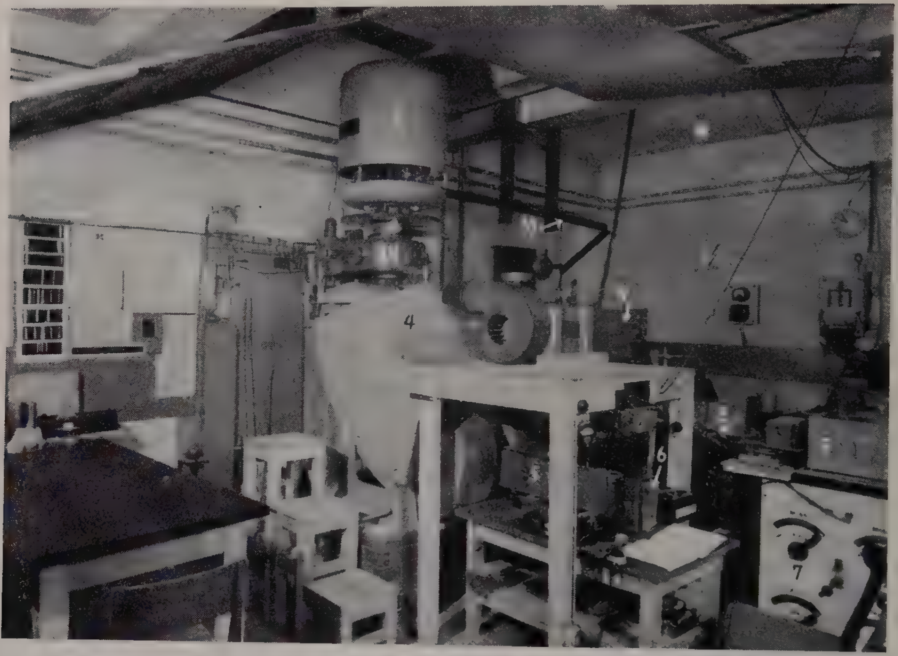

Fig. 1. General view of the isotope separator at the Institute for Theoretical Physics, Copenhagen. 1) Corona screen with ion source, gas containers etc. This part of the apparatus is mounted on a large glass insulator. 2) Electrostatic lens system. 3) Chamber carrying diffusion pumps. 4) Magnet. 5) Analyzing chamber. 6) Fluorescent screen and collector arrangement. 7) Regulation of magnetic field. 8) Regulation of acceleration voltage. 9) Compensator. 10) Power supply for ion source. Power stack and high voltage plant are placed in the adjacent room.

curvature of 80 cm. A fluorescent screen for visual observation of the beam, and equipment for the collection of isotopes, were mounted at a distance of 80 cm from the edge of the pole pieces, where maximum resolving power is obtained.

A general view of the isotope separator at its present stage of development is shown in Fig. 1. In the course of time several improvements have been made, especially with the purpose of ensuring stable operating conditions at a high accelerating voltage, necessary for the maintenance of the resolving power, in the case of large ion currents. The ion source was therefore enclosed in a large corona screen and the lens system was reconstructed without change in its ion optical properties. In order to stabilize the beam at the place of collection, fluctuations in the acceleration voltage were compensated for by means of an electronic device (10) based on a special principle of focusing (11).

The mass spectrum of xenon in Fig. 2 shows the isotopic beams clearly resolved. By opening a shutter, the ions of the isotope to be investigated were allowed to pass through a metal slit and were collected in the surface layer of a 0.5 mm aluminium plate, 25 by 40 mm in size. This collector was previously degassed in a special tube by high-frequency induction heating. By moving the collector behind the slit, its surface was exposed, a portion at a time, to irradiation of the isotopic beam (10–20 μA) until saturation with xenon atoms

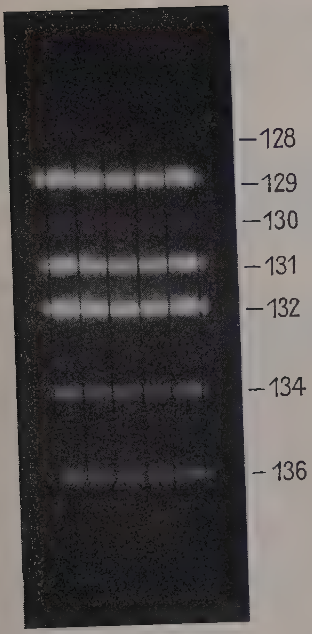

Fig. 2.

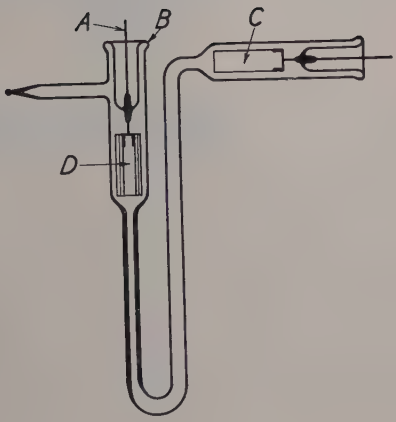

Fig. 3.

Fig. 2. Mass spectrum of xenon photographed to scale. Visible isotopes: ^{128}Xe (1.9 %), ^{129}Xe (26.2 %), ^{130}Xe (4.1 %), ^{131}Xe (21.2 %), ^{132}Xe (27.0 %), ^{134}Xe (10.5 %), and ^{136}Xe (8.9 %). The picture is a photograph of the fluorescent screen (ZnS on glass), taken through a glass window at the end of the deflection chamber. The vertical black stripes originate from molybdenum wires, stretched across the glass surface, in order to prevent accumulation of electric charges, which would give rise to disturbing flickering effects. — Fig. 3. Discharge tube. Scale 1/3.

in the entire surface was obtained (7). The collector then contained a high concentration of rare gas in a surface layer some hundred atomic diameters thick. During the time of separation of about two hours, an amount of a few tenths of a milligram of xenon gas was collected. The isotopic purity was estimated from the spectroscopic observations to be higher than 99 per cent. In the preparation of samples of the isotopes ^{129}Xe and ^{131}Xe the formation of $(XeH)^+$ ions, which cannot be entirely avoided, does not limit the purity, since the isotopes ^{128}Xe and ^{130}Xe are rather rare.

It has been found that aluminium collectors containing xenon isotopes could be stored for several months at room temperature without losing a noticeable fraction of their content of rare gas.

3. Spectroscopic technique

The pyrex discharge tube of Fig. 3 was found most suitable for the experiments and was prepared in the following way: With very clean tools, the irradiated collector was rolled around a steel cylinder (diameter 5 mm) in order to give it a shape appropriate for installation as an electrode in a discharge tube. This electrode D was mounted on a 1 mm tungsten wire A and the tube was

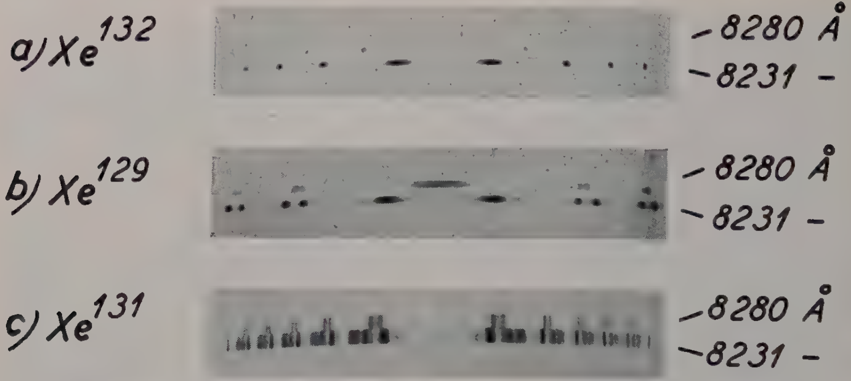

Fig. 4. Interferometer exposures of the lines 8231 Å ($1s_5-2p_6$) and 8280 Å ($1s_4-2p_5$). Scale 4/1. Fig. 4 a. Xe^{132}, 15 mm spacer; Fig. 4 b. Xe^{129}, 15 mm spacer; Fig. 4 c. Xe^{131}, 25 mm spacer. The lines for Xe^{132} are single. For Xe^{129} the lines 8280 and 8231 have two and four components, respectively. For Xe^{131} the line 8280 has three components of which the two outermost are not resolved due to the quadrupole effect which has almost compensated the magnetic splitting between the term components $F = 3/2$ and $F = 1/2$. The line 8231 shows at least 6 components. Compare the term diagram in Fig. 5.

fused together at *B*. During evacuation the tube was degassed by heating the electrode *C* with high-frequency induction and the glass wall with a flame. Helium was admitted to the tube at a pressure of 5–10 mm Hg in order to obtain favourable conditions for the excitation of the small amounts of xenon. After the tube had been sealed off, a pure helium spectrum was emitted from the discharge. The content of xenon gas was finally released by keeping the electrode *D* on dull red glow for a few minutes by means of induction heating. In addition to xenon, some impurities, such as H_2O and CO_2, were given off. After the discharge had run for a short time, these impurities partly disappeared again, presumably by occlusion in the electrodes. The tube was inserted in liquid air in order to obtain a pure spectrum and to reduce the Doppler broadening. In spite of the low vapour pressure at this temperature, the intensity of the xenon spectrum was hereby only slightly reduced. The spectral tube was operated with a transformer at a current of 5–10 mA. Due to the low sputtering of the aluminium electrodes, the clean-up of the xenon took place rather slowly. After having been used for a number of exposures, the tube could be regenerated by induction heating of the electrodes.

The spectrum was investigated with a Fabry-Perot interferometer with invar spacers of 10, 15, 25, and 35 mm, placed in the parallel beam of light of a Steinheil 3 prism glass spectrograph. Optical contact between the polished facets of the invar spacers and the surfaces of the interferometer plates, required for mechanical stability of the etalon, was tested by means of Newtons rings (12). For long exposures, the interferometer was placed in an air-tight box to ensure a constant index of refraction of the air (12). Exposures were made of the $1s-2p$ combinations of XeI, lying in the infrared. The lines were photographed on Kodak I.R.E.R. and Eastman Type I.N. emulsions, with times of exposure varying from a few seconds to several hours, depending on the intensity of the lines. As an example, exposures of two of the strongest XeI lines are reproduced in Fig. 4, which clearly shows the hyperfine structure for different isotopes.

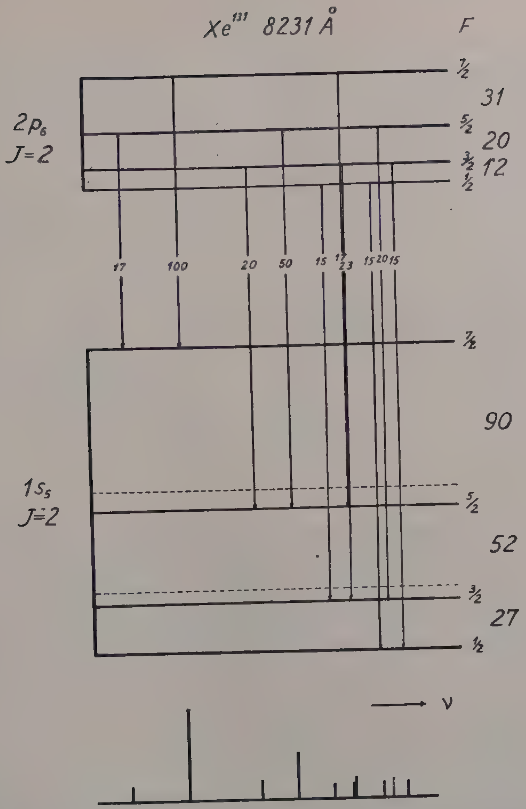

Fig. 5. Term diagram for the line 8231 in Xe^{131}. The arrows show the possible combinations and their relative intensities. The line pattern drawn below shows that the first four components of longest wavelengths are clearly separated. They yield the first interval of $1s_5$ and the two first intervals of $2p_6$. The dotted levels in $1s_5$ indicate the positions of the terms calculated from the total term splitting by means of the Landé interval rule. The observed deviations from this interval rule show the influence of the nuclear quadrupole moment.

4. Measurements of hfs intervals

The plates were measured with a Zeiss Abbe comparator and the line separations were evaluated by the usual method of quadratic interpolation (12 a). All the stronger $1s - 2p$ combinations in the region 7600–9200 Å were investigated and each line was measured on several plates taken with different spacers and with two different spectral tubes for each isotope. In cases where the lines were clearly separated, the individual measurements showed good agreement, and the average values obtained are believed to be accurate to $0.5 - 1.0 \times 10^{-3}$ cm^{-1}.

For each of the measured lines, term diagrams were drawn similar to that shown in Fig. 5 for 8231. Especially in the case of Xe^{131}, such diagrams were indispensable in order to decide which of the term intervals for the line in question are free from disturbances from nearlying components and can therefore be directly measured.

Table I

Term	*jj*-notation	J	Xe^{129}	Xe^{131}	Lines involved
$1s_2$	(1/2, 1/2)	1	−289.7	144.4, 82.9	7887, 8346
$1s_3$	(1/2, 1/2)	0	0	0	8206
$1s_4$	(3/2, 1/2)	1	− 48.1	(27) (7)	8280, 8952, 9162
$1s_5$	(3/2, 1/2)	2	−198.4	89.7, (52.9), (27.3)	8231, 8409 8819, 9045
$2p_1$	(1/2, 1/2)	0	0	0	7887
$2p_2$	(1/2, 3/2)	1	+ 99.0	− 48.5, −28.1	7642
$2p_3$	(1/2, 3/2)	2	−241.6	(98.4), 71.7, 44.7	8346
$2p_4$	(1/2, 1/2)	1	−223.6	110.7, 63.8	8206
$2p_5$	(3/2, 3/2)	0	0	0	8280
$2p_6$	(3/2, 3/2)	2	− 73.3	31.0, 20.5, (11.9)	8231, 8952
$2p_7$	(3/2, 3/2)	1	− 64.0	33.3, (15.4)	8409, 9162
$2p_8$	(3/2, 3/2)	3	−101.4	43.8, 27.5, (16.0)	8819
$2p_9$	(3/2, 1/2)	2	−112.0	54, (27), (12)	9045
$2p_{10}$	(3/2, 1/2)	1	(−69)*	(34), (20)	—

* Measured by Jones (2).

The term splittings determined from the line intervals are listed in Table I. The first column gives the Paschen notation for the terms investigated. The second column shows the notation for *jj* coupling; the first number in the brackets gives the *j*-value of the ion, which is a p^5-configuration and may be in a $P_{3/2}$ or $P_{1/2}$ state; the second number refers to the *j*-value of the outer electron, which in the case of the "*s*"-terms is a 6*s*-electron and, for the "*p*"-terms, a 6*p*-electron. The total *J*-value is shown in the third column.

In the case of Xe^{129}, with $I = 1/2$, all terms, except those with $J = 0$, are double, and the splitting is given in the fourth column. All these term separations could be directly measured and the numbers are given in units of 10^{-3} cm^{-1}. The separations are given as positive when the upper hfs-term has the largest *F*-value. For Xe^{131}, with $I = 3/2$, the term intervals are given in column 5 in the order of decreasing *F*-values. The numbers in brackets refer to intervals which could not be accurately measured because of overlapping of components. These intervals the separations were estimated by making use of theoretical considerations (see Sections 5 and 7).

The term separations for Xe^{129} agree rather well with those given by KOPFERMANN and RINDAL (1), and by JONES (2). Only in a few cases, e.g. for $1s_4$, there are significant discrepancies which may be due to the fact that the present measurements are based exclusively upon infrared lines for which the resolving power is higher than for the visible spectrum. KOPFERMANN and RINDAL have also given separations for some of the terms of Xe^{131}, which, in spite of the complicated line patterns for natural xenon gas, are in fair agreement with the data given here.

5. Determination of interval factors

For the interpretation of the measured data we assume that the hfs of a spectrum level can be expressed (13) by the formula

$$E = E_0 + a\frac{C}{2} + b\left[\frac{\frac{3}{4}C(C+1) - I(I+1)J(J+1)}{2I(2I-1)J(2J-1)}\right], \qquad (1)$$

here

$$C = F(F+1) - I(I+1) - J(J+1). \tag{2}$$

he position of the level, in the absence of nuclear moments, is denoted by E_0. The second and third terms in (1) give the displacements due to a nuclear nagnetic moment and an electric quadrupole moment, respectively. The constants and b are referred to as the interval factors. In the case of Xe^{129}, the last erm vanishes and a can be directly determined from the level splittings. In Xe^{131} the determination of a and b requires the measurement of at least two evel separations.

The spectral terms for which a can be determined in this way for both isoopes are given in Table II. The ratio of the interval factors a_{129} and a_{131} was found to be a constant within the accuracy of the measurements. This is n agreement with the formula

$$\frac{a_{129}}{a_{131}} = \frac{I_{131}\,\mu_{129}}{I_{129}\,\mu_{131}} \tag{3}$$

which should hold very accurately, since there are no perturbing terms which can influence the ratio significantly, and since the effect of the finite size of the nuclei (14) is expected to be too small to be detected. Among the terms in Table II, the latter effect should be largest for $1\,s_2$ due to the influence of the s-electron. However, for this term the s-electron contributes only by about 30 per cent to the magnetic splitting, and the effect is therefore estimated to be but a small fraction of one per cent.

Table II

Term	J	a_{129}	a_{131}	μ_{129}/μ_{131}
$1\,s_2$	1	-193.1	57.1_4	-1.127 ± 0.005
$2\,p_2$	1	66.0	-19.2_3	-1.144 ± 0.015
$2\,p_3$	2	-96.6	27.8_4	-1.16 ± 0.04
$2\,p_4$	1	-149.1	43.8_4	-1.134 ± 0.01
$2\,p_6$	2	-29.3_2	8.5_3	-1.14 ± 0.03
$2\,p_8$	3	-28.9_7	8.5_6	-1.13 ± 0.02

The values for the magnetic moment ratio obtained from (3) together with their estimated accuracies are listed in the last column of Table II. As a mean value one may take

$$\frac{\mu_{129}}{\mu_{131}} = -1.131 \pm 0.005. \tag{4}$$

From the ratio (4) one can now compute a_{131} by means of the accurately measured values of a_{129} and the relation (3). The results are given in Table III. This procedure yields an improved value for the terms in Table II and in addition gives the values of a_{131} for the remaining terms, for which this quantity could not be directly determined.

By means of the a_{131}-values thus obtained, the quadrupole interval factor b can be evaluated for each measured term interval in Xe^{131}. The results are shown in the last column of Table III. For terms with two measured intervals,

Table III

Term	a_{129}	a_{131}	b_{131}
$1s_2$	−193.1	56.91	1.3 ±0.4
$1s_4$ *	− 32.1	9.46	(3)
$1s_5$	− 79.36	23.39	8.9 ±0.9
$2p_2$	66.0	−19.45	−0.3 ±0.3
$2p_3$	− 96.64	28.48	−1.5 ±1.0
$2p_4$	−149.1	43.94	0.8 ±0.3
$2p_6$	− 29.32	8.64	1.2 ±0.6
$2p_7$	− 42.67	12.57	1.5 ±0.6
$2p_8$	− 28.97	8.54	7.1 ±0.8
$2p_9$	− 44.8	13.20	9 ±2
$2p_{10}$	− 46	13.6	(0)

* The effect of the finite size of the nuclei, referred to on p. 461, may become significant for the term $1s_4$, where the s-electron contributes to the hfs by about −140 per cent. An approximate estimate indicates that the value of a_{131} for this term will be about one per cent larger than the value calculated from the moment ratio and given in Table III.

the b-values were found to agree within the accuracy of measurement and the weighted mean values have been listed. The values for the terms $1s_4$ and $2p_{10}$ are theoretical estimates derived in Section 7. From the values of a and b the term intervals which could not be directly measured can be calculated from (1). They are given in brackets in the second-to-last column of Table I.

6. Nuclear moments

The value of μ_{129} has been measured with great precision by means of the nuclear induction method (4), which gave $\mu_{129} = -(0.7726 \pm 0.0001)\,\mu_N$, disregarding the diamagnetic correction. From this value one obtains

$$\mu_{131} = (0.683 \pm 0.003)\,\mu_N \tag{5}$$

from the ratio (4). For a diamagnetic correction of 0.56 percent (15), the moments become $-0.777\,\mu_N$ and $0.687\,\mu_N$ for Xe^{129} and Xe^{131}, respectively.

The quadrupole moment Q of Xe^{131} can be calculated (13) from the value of b by means of the expression

$$b = -Qe^2\,\overline{\left(\frac{3\cos^2\theta - 1}{r^3}\right)}_{M=J}, \tag{6}$$

where the mean value is to be taken for the electronic density distribution in the magnetic level $M = J$. If we measure Q in units of 10^{-24} cm² we may write

$$b = qQ, \tag{7}$$

where

$$q = -\overline{(3\cos^2\theta - 1)\,\frac{a_0^3}{r^3}}\,7.89 \times 10^{-3}\,\text{cm}^{-1}, \tag{8}$$

a_0 being the radius of the hydrogen atom.

From Table III it is seen that the terms $1\,s_5$ and $2\,p_8$ give the greatest relative accuracy in b, and therefore are best suited for the determination of Q. Moreover, for these two terms which have maximum J, the estimate of q is particularly simple, since the coupling between the ion and the outer electron is unique. For the other terms, deviations from jj coupling have to be taken into account.

For $1\,s_5$, only the ion contributes to q. Since the ion forms a $P_{3/2}$-state, which can be represented by a closed shell minus a $p_{3/2}$-electron, the value of $\overline{(3\cos^2\theta - 1)}$ equals $+\,2/5$. The mean value of $\overline{(a_0/r)^3}$ may be estimated from the fine structure separation Δ of the ion by means of the relation

$$\overline{\left(\frac{a_0}{r}\right)^3} = 0.114\,\Delta\,\frac{R'}{H\cdot Z_i}, \tag{9}$$

where Δ is measured in cm^{-1}. The effective nuclear charge Z_i may be taken to be about $Z - 4 = 50$. The quantities R' and H are relativistic correction factors tabulated by CASIMIR (13); for $Z_i = 50$, one finds $R' = 1.12$ and $H = 1.07$. An estimate of Δ may be obtained from the multiplet separations of the $1\,s$ terms (13; p. 41 ff.) which give $\Delta = 9372\ \text{cm}^{-1}$. One thus obtains $\overline{(a_0/r)^3} = 22.4$ and $q = -\,70.6 \times 10^{-3}\ \text{cm}^{-1}$, from (8). The b-value in Table III together with (7) finally give $Q = (-\,0.12 \pm 0.01) \times 10^{-24}\ \text{cm}^2$.

In $2\,p_8$ the outer $p_{3/2}$-electron, as well as the $P_{3/2}$-ion, contributes to q. The effect of the ion is the same as for $1\,s_5$ while the contribution of the outer electron has the opposite sign. According to (9) we have

$$q\,(2\,p_8) = q\,(1\,s_5)\left(1 - \frac{\delta}{\Delta}\right), \tag{10}$$

where δ is the doublet separation for the p-electron, which is estimated at about 5–10 per cent of Δ (cf. CONDON and SHORTLEY (17; p. 306 ff.)). From the value of b for $2\,p_8$ one thus obtains $Q = (-\,0.11 \pm 0.01) \times 10^{-24}\ \text{cm}^2$.

While the uncertainty in the determination of Q, which lies in the measurement of b, is estimated to about 10 per cent, further sources of error are entailed in the calculation of q. In order to test formula (9), an alternative estimate of $\overline{(a_0/r)^3}$ for the ion may be derived from the measured values of the magnetic interval factor a. For the term $2\,p_8$ we have

$$a\,(2\,p_8) = \tfrac{1}{2}\,a\,(P_{3/2}) + \tfrac{1}{2}\,a\,(p_{3/2}), \tag{11}$$

where $a\,(P_{3/2})$ and $a\,(p_{3/2})$ are the interval factors for the ion and the outer $p_{3/2}$-electron, respectively. In analogy to (10) we have

$$a\,(p_{3/2}) = \frac{\delta}{\Delta}\,a\,(P_{3/2}). \tag{12}$$

Moreover

$$a\,(P_{3/2}) = \frac{\mu}{\mu_N\,I}\,\overline{\left(\frac{a_0}{r}\right)^3}\,\frac{F'}{R'}\,1.69 \times 10^{-3}\ \text{cm}^{-1}, \tag{13}$$

where $F' = 1.06$ (for $Z_i = 50$), is a further relativistic correction factor (13). From (11), (12), (13) and the measured value of $a(2p_8)$ one finds $\overline{(a_0/r)^3} = 21.6$, which agrees with the value 22.4 derived from the doublet separation.

The estimate of q needs a certain correction due to the quadrupole moment induced by the nucleus in the electron shells. According to the calculations by STERNHEIMER (18) the effect is, however, expected to be rather small for a low-lying $P_{3/2}$ state, for which the quadrupole interaction with the nucleus takes place primarily at small distances from the center of the atom. In the present case the effect is expected to decrease q by an amount not exceeding 5 per cent.

As a final estimate of Q we give the value

$$Q = -0.12 \times 10^{-24}\ \mathrm{cm}^2 \tag{14}$$

which is believed to be reliable to within about 15 per cent in so far as the theory of quadrupole interactions is applicable.

The spin and magnetic moment of ${}^{77}_{54}Xe^{131}$ may to a first approximation be ascribed to an unpaired $d_{3/2}$-neutron. The negative Q-value moreover indicates (19, 20) that the nucleus contains a single $d_{3/2}$ neutron rather than three $d_{3/2}$-neutrons. This indication is supported by the fact that none of the odd neutron nuclei with neutron number in the region below 77 has spin 3/2, while this spin value occurs again for the Ba-isotopes with neutron numbers 79 and 81. In addition, for odd proton nuclei, spin 3/2 has been found in this region only for $Z = 77$ and $Z = 79$.

7. hfs and term analysis

The hfs of $1s_5$ and $2p_8$, considered in the preceding section, can further be used to calculate the interval factors for the remaining $1s$ and $2p$ terms, assuming simple coupling schemes. The comparison of the calculated values with the measured hfs for these terms not only gives additional tests of the internal consistency of the hfs data, but also yields information regarding the properties of the $1s$ and $2p$ terms. It is of interest to compare the results of such an analysis with the information derived from the Zeeman effect and the multiplet structure.

As a first step we calculate a_{129} and b_{131} for all $1s$ and $2p$ terms, assuming jj coupling. The results are listed in columns 4 and 6 of Table IV; all interval factors are given in units of $10^{-3}\ \mathrm{cm}^{-1}$. The a and b factors for the ion and the outer electron were estimated in the following manner.

From (11) and (12) and by means of the measured value for Xe^{129} of $a(2p_8)$, one finds $a(P_{3/2}) = -53.8$ and $a(p_{3/2}) = -4.0$. From these values, $a(P_{1/2})$ and $a(p_{1/2})$ may be obtained, by means of the relation (13)

$$\frac{a(P_{1/2})}{a(P_{3/2})} = \frac{a(p_{1/2})}{a(p_{3/2})} = 5\frac{F''}{F'}, \tag{15}$$

where F'' and F' are relativistic correction factors, which for $Z_i = 50$ are equal to 1.32 and 1.06, respectively. From (15) one obtains $a(P_{1/2}) = -334.8$ and $a(p_{1/2}) = -25.1$.

The interval factor for the s-electron may be found from the observed $a(1s_5)$, which gives the value $a(s) = -156.0$, by means of the expression in Table IV.

An estimate of $a(s)$ may also be obtained from the semi-empirical Fermi-Segré formula

$$a(s) = \frac{\mu}{\mu_N I} Z F \frac{1}{(n^*)^3} \frac{dn^*}{dn} 8.48 \times 10^{-3} \text{ cm}^{-1}, \tag{16}$$

where F is a relativistic correction factor equal to 1.39 for $Z = 54$. The effective quantum number n^* can be deduced from the term value and for $1s_5$ one finds $n^* = 1.89$. The derivative of n^* with respect to the principal quantum number n cannot be determined empirically with accuracy since the term series does not obey a Ritz formula. It is estimated that the value of dn^*/dn exceeds unity by some per cent. To a certain extent the factor dn^*/dn may be compensated by the correction to (16) due to the finite size of the nucleus, which modifies the s-electron wave function in the central part of the atom (21). This last correction decreases the numerical value of $a(s)$ for Xe by about 3 per cent. By neglecting dn^*/dn in (16) we find $a(s) = -146$, which is in rather good agreement with the value deduced from ($1s_5$), considering the approximations involved.

The interval factors $b(P_{3/2})$ and $b(p_{3/2})$ were estimated in the preceding section. As a mean of the values obtained from $1s_5$ and $2p_8$ we may take $b(P_{3/2}) = 8.3$ and $b(p_{3/2}) = -0.6$.

The two last columns in Table IV show the atomic g-factors, the calculated values for jj coupling as well as the values measured by Zeeman effect (22).

In the discussion of the data collected in Table IV we first consider the $1s$-terms. For $1s_5$ the measured g-factor confirms that the term is accurately represented as (3/2, 1/2). In the case of $1s_2$ and $1s_4$ the observed a- and b-factors, as well as the g-factors and the multiplet structure of the $1s$ terms (17) (p. 304), indicate deviations from jj coupling.

If we attempt to write the wave functions for $1s_2$ and $1s_4$ in the form

$$\psi = c_1 \varphi\left(\tfrac{3}{2}, \tfrac{1}{2}\right) + c_2 \varphi\left(\tfrac{1}{2}, \tfrac{1}{2}\right) \tag{17}$$

the constants c_1 and c_2 can be determined from the multiplet separations. One finds $c_1 = 0.994$, $c_2 = 0.111$ for $1s_4$ and $c_1 = 0.111$, $c_2 = -0.994$ for $1s_2$. For these values of c_1, c_2, the a-factors are not significantly different from those given in column 4 for pure jj coupling. The b-factors may be calculated from the expression (13)

$$b = \tfrac{1}{2} b(P_{3/2}) (c_1^2 - 3.02\, c_1 c_2) \tag{18}$$

which gives $b(1s_2) = 1.4$ and $b(1s_4) = 2.7$. The g-factors corresponding to wave-functions (17) equal 1.220 and 1.280 for $1s_2$ and $1s_4$, respectively.

The measured g-factors as well as the a-values show that (17) does not account adequately for the two states, although it may represent a certain improvement over the pure jj coupling scheme. Presumably the states are perturbed by the near-lying ($3d$) and ($2s$) levels. Due to these perturbations the above estimate of $b(1s_4)$ is somewhat uncertain. For $b(1s_4) = 3$, the term splittings in $1s_4$ of Xe^{131} are given in Table I. The calculated values are consistent with the fact that the two lower hfs terms could not be resolved (cf. Fig. 4).

Table IV

Term	jj-not.	J	$(-a_{129})$calc.	$(-a_{129})$obs.	(b_{131})calc.	(b_{131})obs.	$g$calc.	$g$obs.
$1s_2$	(1/2, 1/2)	1	$1/2\,a\,(P_{1/2}) + 1/2\,a\,(s) = 245.4$	193.1	0	1.3 ± 0.4	1.333	1.321
$1s_4$	(3/2, 1/2)	1	$5/4\,a\,(P_{3/2}) - 1/4\,a\,(s) = 28.3$	32.1	$1/2\,b\,(P_{3/2}) = 4.2$	(3)	1.167	1.204
$1s_5$	(3/2, 1/2)	2	$3/4\,a\,(P_{3/2}) + 1/4\,a\,(s) = 79.4$	79.36	$b\,(P_{3/2}) = 8.3$	8.9 ± 0.9	1.500	1.500
$2p_2$	(1/2, 3/2)	1	$-1/4\,a\,(P_{1/2}) + 5/4\,a\,(p_{3/2}) = -78.7$	-66.0	$1/2\,b\,(p_{3/2}) = -0.3$	-0.3 ± 0.3	1.500	1.552
$2p_3$	(1/2, 3/2)	2	$1/4\,a\,(P_{1/2}) + 3/4\,a\,(p_{3/2}) = 86.7$	96.64	$b\,(p_{3/2}) = -0.6$	-1.5 ± 1.0	1.167	1.195
$2p_4$	(1/2, 1/2)	1	$1/2\,a\,(P_{1/2}) + 1/2\,a\,(p_{1/2}) = 180.0$	149.1	0	0.8 ± 0.3	0.667	0.790
$2p_6$	(3/2, 3/2)	2	$1/2\,a\,(P_{3/2}) + 1/2\,a\,(p_{3/2}) = 28.9$	29.32	0	1.2 ± 0.6	1.333	1.379
$2p_7$	(3/2, 3/2)	1	$1/2\,a\,(P_{3/2}) + 1/2\,a\,(p_{3/2}) = 28.9$	42.67	$-2/5\,[b\,(P_{3/2}) + b\,(p_{3/2})] = -3.1$	1.5 ± 0.6	1.333	1.022
$2p_8$	(3/2, 3/2)	3	$1/2\,a\,(P_{3/2}) + 1/2\,a\,(p_{3/2}) = 28.9$	28.97	$b\,(P_{3/2}) + b\,(p_{3/2}) = 7.7$	7.1 ± 0.8	1.333	1.336
$2p_9$	(3/2, 1/2)	2	$3/4\,a\,(P_{3/2}) + 1/4\,a\,(p_{1/2}) = 46.7$	44.8	$b\,(P_{3/2}) = 8.3$	9 ± 2	1.167	1.106
$2p_{10}$	(3/2, 1/2)	1	$5/4\,a\,(P_{3/2}) - 1/4\,a\,(p_{1/2}) = 61.0$	46	$1/2\,b\,(P_{3/2}) = 4.2$	(0)	1.500	1.852

As regards the $2p$ terms, we first note that $2p_8$ on which, together with s_5, the analysis of the preceding section was based, appears from the Zeeman ata to be free of perturbations. In discussing the remaining $2p$ terms we shall ssume that the j of the ion may be considered a good quantum number. The oupling is then intermediate between the jj and the so-called jl scheme (23).

For the lower group of $2p$ terms, the ion has $j = 3/2$. In the case of $2p_6$ nd $2p_9$, with $J = 2$, the agreement between the measured and the calculated a- nd g-factors shows that we are close to pure jj coupling. Also the measured -factors confirm this conclusion, although $b(2p_6)$ gives some indication of a minor deviation from the simple coupling scheme. This deviation arises from a partial decoupling of the l and s of the outer electron, and, in addition, from the interaction with the $2p_3$ term, as is indicated by the fact that the sum rule for the g-factors is more accurately obeyed if all three p-terms with $J = 2$ are considered together.

In the case of $2p_7$ and $2p_{10}$, a major deviation from jj coupling is indicated by the measured a- and b-factors as well as by the g-factors. Considerably improved agreement is obtained, however, by representing the terms in jl coupling. For $2p_7$ one finds $a = -46.4$ $b = 1.1$, $g = 1.055$ and for $2p_{10}$ one obtains $a = -43.5$, $b = 0$, $g = 1.778$.

As regards the higher group of p terms, $2p_3$ should have pure jj coupling if the ion is in a $j = 1/2$ state. The agreement between the calculated and the measured values of a, b and g is fair. The deviations may be due partly to the interaction with p_6 and p_9 terms, referred to above.

For $2p_2$ and $2p_4$, greater deviations from the jj coupling scheme is indicated by the a-factors as well as by the g-factors. Since the sum rule is not obeyed, this discrepancy cannot be removed by considering combinations of the (1/2, 3/2) and (1/2, 1/2) configurations. The presence of rather strong perturbations is also indicated by the multiplet separations (17; p. 312). The perturbations must be ascribed primarily to the influence of the nearlying $3p_7$ and $3p_{10}$ terms, as follows from the anomalous g-factors (22), a-factors (2), and effective quantum numbers (16) found for these terms.

It may be concluded that the analysis of $1s$ and $2p$ terms, on the basis of the hfs, is in good accordance with the results obtained from the analysis of the Zeeman effect and of the general structure of the spectrum.

SUMMARY

By means of an electromagnetic isotope separator, targets have been prepared containing the odd xenon isotopes Xe^{129} and Xe^{131} in great purity. With these targets as electrodes in a Geissler tube, the infrared spectrum of XeI has been investigated with a Fabry-Perot interferometer. The hfs of a number of lines has been measured and the splittings of $1s$ and $2p$ terms have been determined. The data yield directly the ratio $\mu_{129}/\mu_{131} = -1.131 \pm 0.005$. From the deviations from the Landé interval rule, the quadrupole moment of Xe^{131} was estimated to be -0.12×10^{-24} cm^2. In this estimate, use was made of the magnetic moment ratio to find term splittings which could not be directly measured. A theoretical analysis of the $1s$ and $2p$ terms of XeI is made on the basis of the hfs data. The results are compared with the information obtained from Zeeman effect and multiplet structure.

The authors wish to thank Professor NIELS BOHR for his continual interest in this work. One of us (E.R.) is very much indebted to Professor BOHR for the permission to use the spectroscopic equipment of the Institute for Theoretical Physics for researches at the Royal Veterinary and Agricultural College.

June 1951. Institute for Theoretical Physics, University of Copenhagen, and Physical Laboratory, The Royal Veterinary and Agricultural College, Copenhagen.

REFERENCES: (1) **H. Kopfermann** and **E. Rindal.** Zs. f. Phys. *87*, 460, 1934. — (2) **E. Gwynne Jones.** Proc. Roy. Soc. *144*, 587, 1934, Proc. Phys. Soc. *46*, 634, 1934. — (3) **H. Bethe** and **R. F. Bacher.** Rev. Mod. Physics. *8*, 82, 1936. — (4) **W. G. Proctor** and **F. C. Yu.** Phys. Rev. *81*, 20, 1951. — (5) **H. Korsching.** Zs. f. Phys. *109*, 349, 1938, Zs. f. Phys. 111, 165, 1938. — (6) **J. Koch** and **E. Rasmussen.** Phys. Rev. *77*, 722, 1950. — (7) **K. J. Broström, T. Huus** and **J. Koch.** Nature *160*, 498, 1947. — (8) **J. Koch.** Nature *161*, 566, 1948. — (9) **J. Koch** and **B. Bendt-Nielsen.** Dan. Mat. Fys. Medd. *21*, No 8, 1944. — (10) **J. Koch.** Phys. Rev. *69*, 238, 1946. — (11) **J. Koch.** Dan. Mat. Fys. Medd. *24*, No 7, 1948. — (12) **K. W. Meissner.** Journ. Opt. Soc. *31*, 405, 1941. — (12 a) **S. Tolansky.** Journ. Sci. Inst. *8*, 223 (1931). — (13) **H. B. G. Casimir:** On the Interaction between Atomic Nuclei and Electrons, Teylers Tweede Genootschap, Haarlem 1936. Cf. also **H. Kopfermann:** Kernmomente Leipzig, 1940. — (14) **A. Bohr** and **V. Weisskopf.** Phys. Rev. *77*, 94, 1950. **A. Bohr.** Phys. Rev. *81*, 331, 1951. — (15) **W. E. Lamb Jr.** Phys. Rev. *60*, 817, 1941. — (16) **C. J. Humphreys** and **W. F. Meggers.** Bur. Stand. J. Research 10, 139, 1933. — (17) **E. U. Condon** and **G. H. Shortley:** The Theory of Atomic Spectra, Cambridge 1935. — (18) **R. Sternheimer.** Phys. Rev. *80*, 102 (1950). — (19) **C. Townes, H. Foley** and **W. Low.** Phys. Rev. *76*, 1415, 1949. — (20) **J. Rainwater.** Phys. Rev. *79*, 432, 1950. — (21) **M. F. Crawford** and **A. Schawlow.** Phys. Rev. *76*, 1310, 1949. — (22) **J. B. Green, E. H. Hurlburt** and **D. W. Bowman.** Phys. Rev. *59*, 72 (1941). — (23) **G. Racah.** Phys. Rev. *61*, 537 (1942).

Tryckt den 5 februari 1952

Uppsala 1952. Almqvist & Wiksells Boktryckeri AB

ARKIV FÖR FYSIK Band 4 nr 30

Communicated 12 September 1951 by MANNE SIEGBAHN

Energy determination of the Se^{77m} γ-ray

By JONAS ORRING

With 1 figure in the text

Se^{77} (1) has a metastable state with half-life 17.5 sec (2, 3), which decays to the ground state by emission of a strongly converted γ-ray. The energy of this γ-ray has been found to be 150 KeV (2, 3), by measurement of the absorbtion in aluminium of the conversion electrons.

This isotope has now been studied by means of a β-spectrometer. The sample consisted of a layer of fine selenium powder of 9 mg/cm^2 thickness. This sample was irradiated for 50 seconds before each measurement with fast neutrons from the Li (d, n) reaction, using 6 MeV cyclotron deuterons. Special care was taken to hold the irradiation constant.

Because of the short half-life the sample could not be introduced into the spectrometer, which was therefore fitted with a mica window (4.6 mg/cm^2) against which the sample could be mounted quickly. The time between the end of each irradiation and the beginning of the corresponding measurement was about 20 seconds.

For each point of the spectrogram the counting rate was measured over consecutive 10-second intervals. In this way a complete decay curve was taken, the half-life checked, and the counting rate at the end of the irradiation time found by extrapolation. Each point was corrected for the intensity of the irradiation.

During the irradiation other activities were produced, with longer half-lives. In the energy region of this measurement these gave a very low counting rate, which was negligible compared to the background (10 counts/min.).

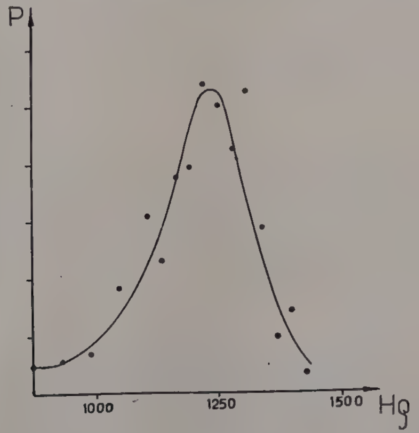

Fig. 1. Internal conversion line of Se^{77m}.

The internal conversion line measured in this way is shown in Fig. 1. Because of the spread due to the mica window and the thick source the K and L lines are not resolved.

For this measurement it was necessary to make a special calibration. The F line of ThB was used for this purpose. In order to reproduce the conditions under which the selenium was measured the thorium source was mounted in the same way against the mica window, and covered with an aluminium foil equivalent to the half-thickness of the selenium source. Since the thorium F-line and the Se^{77m} γ-line have very similar energies, the line broadening and the displacement towards lower energy should be about the same in each case. The value found for the γ-ray energy was 165 KeV.

CANADA, CUFFEY, LESSOR and MITCHELL (4) have recently found the Se^{77m} conversion line in the particle spectrum of Br^{77}. They find 159.9 ± 1.0 KeV for the energy of the γ-ray.

I am greatly indebted to Professor MANNE SIEGBAHN for allowing me to proceed with my work at the Nobel Institute for Physics, and to Professor KAI SIEGBAHN, who suggested this investigation.

REFERENCES. 1. **M. Goldhaber, C. O. Muehlhause,** Phys. Rev. *74*, 1248 (1948). — 2. **D. N. Gideon, W. C. Miller, B. Waldman,** Phys. Rev. *75*, 329 (1949). — 3. **J. R. Arnold, N. Sugarman,** J. Chem. Phys. *15*, 703 (1947). — 4. **R. Canada, W. H. Cuffey, A. E. Lessor, A. C. G. Mitchell,** Phys. Rev. *82*, 750 (1951).

Tryckt den 5 februari 1952

Uppsala 1952. Almqvist & Wiksells Boktryckeri AB

ARKIV FÖR FYSIK Band 4 nr 31

Communicated 9 May 1951 by Manne Siegbahn and Erik Hulthén

Application of the ultrathin freezing-sectioning technique to the study of cell structures with the electron microscope

By H. Fernández-Morán

With 8 plates

I. Introduction

In most methods currently used for ultra-thin sectioning of tissue (4, 14, 15, 19, 21), the required consistency is imparted to the fixed object by a process which involves dehydration with alcohol-ether and embedding in collodion-paraffin or methacrylate resins. While fixation artifacts are generally recognized as one of the principal factors limiting the structure resolution which is possible in such thin sections with the electron microscope, other processes in the initial treatment must also be considered. Dehydration with alcohol-ether, for example, often amounts to varying degrees of extraction, depending upon the type of fixation used, specially in the case of nerve tissue with its high lipoid content. The effects of permeation with an embedding medium on tissue ultrastructure have not been studied yet, and the presence of the embedding matrix not only reduces contrast but intereferes also with any chemical investigations or other experiments requiring untreated material. That these factors must play a role in addition to fixation is apparent from a comparison of embedded and sectioned material like collagen, with corresponding fragmentation preparations fixed under identical conditions. The other alternative method of solidifying the tissue by freezing can generally dispense with preliminary treatments and thus approach the natural condition of the tissue more closely, but difficulties in obtaining frozen sections thinner than a few microns had retarded its application in electron microscopy.

It was shown recently (9, 10) that well preserved ultrathin frozen sections of unembedded fixed or fresh material can be cut from small tissue blocks in a modified microtome based on the thermal expansion technique of Newman, Borysko and Swerdlow (19, 20). Further improvements in preparing and mounting serial frozen sections combined with a freezing-drying procedure carried out directly on the ultrathin sections, now make it possible to examine fresh biological tissue with the electron microscope in which three dimensional structure is preserved. These fresh frozen sections, only fractions of a micron thick (0.5–0.1 micron), are admirably suited for correlation studies with the polarized light and phase contrast microscopes. Since they can be subjected to enzymatic digestion, cytochemical reactions, or micro-incineration experiments and the results followed with the electron microscope, the range of applications of this instrument is considerably extended. Moreover, the simplicity of the method cuts down the usual specimen preparation time of one or more days to a few hours.

The method has been tested on a variety of tissues and microorganisms, proving conclusively that satisfactory ultrasectioning of frozen tissues and not mere cleavage along arbitrary potential submicroscopic boundaries is possible. The purpose of this report is to point out the unique advantages and the present limitations of the technique, which make it a valuable and in many ways indispensable complementary procedure among the generally adopted sectioning methods for electron microscopy.

II. Description of the equipment and methods for preparing ultrathin frozen sections

A. Equipment

A standard unmodified Spencer rotary microtome model No. 820 mounted on a thick slab of marble was used, but any stable rotary microtome is suitable. An electric motor drive was provided to deliver 50–100 microtome wheel revolutions per minute. The small 1/12 or 1/24 hp electric motor is attached to a heavy lead block and shock mounted on sponge rubber. A rubber transmission band connects the motor pulley with the microtome drive wheel. A conventional freezing microtome brass stage was modified (Fig. 1) by fixing a Plexiglass disc (18 mm in diameter and 1 mm thick) to its center with 4 screws. The plastic disc has a rilled surface for holding the frozen specimen and serves as a thermal isolator. Stages of nickel-steel alloys with lower thermal expansion rates were also used. The stage is firmly clamped between plastic blocks in the specimen holder of the microtome (Fig. 2) and connected through a carefully balanced pressure hose with the carbon dioxide container. A special nozzle for deep freezing of the knife holder and the stage are provided with needle valves, which can be firmly closed to avoid vibrations caused by the escaping gas. Two types of knives were used routinely: thick razor blades (Schick: 38 × 8 mm, or Eskilstuna) fastened in a specially constructed knife holder; or glass knives obtained by thermal fracture of 6–8 mm thick panes of glass mounted in the special holder described by Hartmann and Latta (13). Liquid reservoirs for collecting the sections are made from thin aluminum strips bent to form a trough which is fastened close to the knife edge. The trough is filled with distilled water, Ringer solution or glycerine. Frozen sections of fresh material are collected on detachable polished metal strips or on collodion covered metal screens touching the knife edge, which can be transferred directly to the deep cooled copper blocks in a vacuum chamber. Prompt freezing is facilitated by inverting a metal cup over the stage when opening the valve. The sectioning process is continuously observed through a binocular microscope (25 × magnification), using a large fluorescent light placed 1 meter above the instrument to illuminate the field. Sectioning is carried out at room temperature or in a cold room. Routine preparations include careful lubrication and running the microtome for 15 minutes before sectioning.

B. Sectioning

A piece of tissue not exceeding 8–10 mm^3 in volume is drained of excess fluid, and suitably oriented on a disc of moist filter paper which is placed directly on the plastic disc of the freezing stage. The small tissue block is immediately frozen by apidly cooling down the stage to a temperature of —35° C approximately, inverting he metal cup over the specimen as the compressed carbon dioxide is bled into the hamber. The proper degree of freezing for each specimen is easily determined after everal trials under microscopic control. (Exact determination of the suitable temperature range by using a thermocouple would be necessary for more critical work.)

The well frozen specimen *which must be free at all times from ice formation* is advanced until it comes in contact with the knife edge, and a series of 1 micron sections cut with the dry knife. These first sections are discarded, and the reservoir is then filled adjusting the liquid level until a plane or slightly convex surface is obtained ust below the knife edge.

Adjustment of the liquid level is one of the critical factors in this technique, since a slight excess will inevitably result in ice formation around the specimen which ruins the knife edge and completely thwarts the cutting of sections. Specimens on which ice formation has occurred should preferably be discarded, or salvaged in exceptional cases by cutting away the ice and trimming the block with a sharp razor. Knife tilt is different for each specimen and critical, since it can determine a clean slice or various degrees of specimen fragmentation. Good 1 micron sections can already be recognized by their unmarred, transparent and fully extended serial appearance; they are best obtained by quick chopping strokes. Manual operation is recommended in the beginning until more practice is acquired in the use of the motor drive. Once a uniform ribbon of serial 1 micron sections is obtained, the microtome's advance mechanism can be disengaged by setting the pointer at zero. The continuous thermal expansion of the cold stage then advances the specimen at a variable rate of tenths of a micron or less, depending upon the temperature rise. Since the temperatures necessary for freezing the specimen are much lower than those employed by Newman, Borysko and Swerdlow (19, 20), the time interval between each cutting stroke must be made correspondingly shorter in order to obtain ultrathin sections. In practice, continuous refreezing of the specimen at intervals of 1–3 minutes and the use of a motor drive delivering a certain fixed number of revolutions per minute produced serial sections of 0.2—0.05 micron thickness, which can be maintained constant or varied at will. Satisfactory ultrathin sections flatten out immediately, are nearly invisible and adhere edgewise to form a thin uniform ribbon which advances steadily with each cutting stroke. Compression and accordion like folding (15) occur frequently at high cutting velocities, and are either due to dulling of the knife edge or to inadequate freezing of the specimen. Other types of tissue distortion are readily detected by continuous observation of the cutting process at high magnifications, and can be avoided as experience accumulates.

The main sources of trouble are in approximate order of importance: (a) proper degree of tissue freezing, (b) adjustment of the liquid meniscus, (c) correct sharpness and tilt of the blade, (d) cutting rate, (e) smooth operation of the collecting mechanism, and (f) mechanical performance of the microtome. Despite these numerous factors the method has been found to work remarkably well in routine sectioning, giving constant, reproducible results. It requires of course more vigilance and practice than ordinary methods, but the time invested is more than amply compensated by the rapid results obtained once the method is operating satisfactorily.

C. Cutting, mounting and freeze-drying ultrathin frozen sections of fresh tissues

Small blocks of fresh tissue removed from the animal under narcosis and preferably not exceeding 1–4 mm^3 in volume are oriented and frozen on to the stage of the freezing microtome. Contact with saline or other liquids must be avoided in order to prevent ice formation around the specimen, which is specially detrimental in the case of fresh tissues. The tissue block must be frozen down as quickly as possible, and after having reached the proper degree of freezing, which can only be determined by repeated microscopic control of the sections, the required temperature is maintained throughout the cutting process. Cooling of the knife is also necessary, the temperature depending upon the type of liquid contained in the collecting trough. Even when using physiological saline solutions it is best to operate close to the freezing point of the liquid, in order to prevent drastic thawing of the thin sections. Correct adjustment of the liquid level relative to the knife edge is very important, since too high a level will inevitably result in ice formation around the specimen, ruining both the tissue block and the knife edge. Manual operation is only suitable for cutting sections thicker than 0.5 microns, because the movement of the specimen past the knife edge is often not rapid enough to prevent contamination with the liquid and disturbing ice formation. The motor drive (operating at 50–80 revolutions of the microtome wheel per minute) is therefore used mainly. The usual cutting procedure is followed: after the tissue block has come in contact with the dry knife edge, a few 1 micron sections are cut and discarded. The collecting trough is then filled with cold liquid until the correct level just below the knife edge is reached, and a series of ultrathin sections obtained by turning on the motor drive. The process is interrupted at periodic intervals of 1–2 minutes to refreeze the specimen or to change the liquid in the trough. Good serial sections form extremely tenuous and uniform ribbons, and any departure from this appearance indicates the presence of inadequate specimen freezing, defects of the cutting edge, insufficient height of the liquid level, disturbances in the mechanical performance of the microtome or any of the other sources of trouble already mentioned. In an attempt to control the formation of ice crystals in the process of freezing and nevertheless attain a suitable consistency for sectioning, the blocks of tissue were immersed in glycerine or glycol-physiological saline solutions of different concentrations prior to freezing. Although these experiments are still in a preliminary stage, a definite protective action of the glycerine treatment (22) could be detected in fresh and fixed material at a concentration which was compatible with adequate freezing. There are 3 ways of collecting the fresh frozen sections: (a) on cold Ringer or physiological saline; (b) on undercooled (—20° to —30° C) glycerine or glycol solutions; (c) on dry frozen surfaces like polished stainless steel strips attached to the knife edge, or directly on the frozen electron microscope grids covered with collodion.

Examination of the thin frozen sections with the phase contrast or polarized light microscopes does not require special manipulations other than transfer of the sections to a cold observation chamber. For electron microscopy, the sections floating on the liquid of the collecting reservoir are picked up by lowering a collodion covered electron microscope screen parallel to the water surface until the sections touch the dry film to which they firmly adhere. If properly carried out, this operation transfers the intact sections to the plane collodion film, providing a convenient support to the wet tissue slice over its entire surface. Best results are obtained, however, with frozen sections picked up without thawing on dry frozen surfaces or on undercooled glycerine.

Drying of the frozen sections produces distortions due to surface forces and other artifacts which can only be avoided if the sections are frozen-dried (1, 24) or subjected to the ingenious critical point drying method described by ANDERSON (2). The latter method requires dehydration of the specimen in alcohol and is therefore unsuitable for this purpose, unless glycerine or some similar dehydrating agent can be substituted for the alcohol.

In this work, the modified freezing-drying procedure described by WYCKOFF (24) for electron microscope preparations, has made it possible to eliminate many of the drying artifacts in ultrathin frozen sections, while at the same time preserving important details of their three dimensional structure.

The frozen sections which have been prevented from thawing by mounting on the cooled grids, are placed immediately on a block of brass cooled with dry ice, and the block is quickly transferred to an insulated base in a vacuum chamber which is then promptly evacuated. The frozen water in the sections sublimes directly in the high vacuum under *optimal conditions*, since the sections are only fractions of a micron in thickness and present a large exposed surface. Therefore, the solid-vapor boundary moving through the specimen during sublimation of the frozen matrix has less possibilities of disrupting the structures than in any of the commonly used freezing-drying methods where the frozen tissues are at least one hundred times thicker. Once a high vacuum is reached and manitained for 1–2 hours to insure complete dehydration, the sections are shadowed by oblique evaporation of platinum/palladium at a 10°–30° angle, followed by vertical deposition of a reinforcing aluminum or silicon monoxide film 50–100 Å thick, without breaking the vacuum. Since we are dealing with sections of only a few hundred millimicrons thickness already mounted on collodion films, deposition of an additional film of these dimensions on its other surface provides ideal support to the section when it is removed from the vacuum. The coated sections are now ready for examination with the electron microscope or for further treatment according to the complementary procedures listed below.

The frozen sections floating on undercooled glycerine can also be transferred to the vacuum chamber on a cold metal block, where metal films can be evaporated directly on to the glycerine and the sections because of its low vapor pressure (12).

D. Cutting and mounting frozen sections of fixed tissues

The tissues examined in these experiments were fixed mainly in buffered solutions (pH 7–7.2) of 1 % osmium tetroxide or 10 % formalin for periods ranging between 6 to 48 hours. Special mixtures of formalin with potassium bichromate were also used for fixing bacteria and other microorganisms. Osmium tetroxide is by far the most suitable fixative for ultrathin freezing-sectioning, because it not only preserves and stabilizes the fine structure of biological specimens very well, but also imparts a desirable firm consistency and rigidity to the tissue. This is particularly apparent in thin frozen sections of nerve tissue, which due to their high lipoid content display a marked tendency to disintegrate and spread out to form monolayers if not properly fixed. Formalin fixation is unsatisfactory as a rule for tissues with a large lipid component, since it does not prevent the lipoids from migrating and contaminating other structures of the thin, unsupported frozen section in the process of mounting. The small blocks of the fixed and well rinsed tissue are oriented and frozen on the stage of the freezing microtome as described previously. Osmium fixed sections can be collected on cold distilled water in the trough attached to the knife edge, while formalin fixed sections are preferably picked up in glycerine-water mixtures cooled several degrees below zero or on dry, deep frozen metal strips to avoid disruption by thawing. The sections floating on the liquid are picked up directly on the collodion covered grids and allowed to dry in air or subjected to the modified freezing-drying procedure. Air drying of the fixed frozen sections produces the same type of artifacts like collapsing of cell membranes or flattening of delicate structures as those commonly seen in dried cellular suspensions. Since one of the planes of the tissue section is firmly anchored to the collodion supporting film, gross distortions of the fine structure are prevented. Metallic shadow casting of the dried frozen sections can be performed without having to dissolve the embedding matrix and running the risk of introducing large scale distortions in the process of extraction. Fixed tissue can also be embedded in 10 % or 20 % gelatine solutions and ultrathin frozen sections prepared of this embedded material. Gelatine embedding is used mainly to preserve the continuity in sections of tissues with large hollow spaces and as a valuable control method.

Ultrathin frozen sections can be prepared of cell suspensions and of bacteria by amassing them through centrifugation and sectioning the sediment. Special centrifugation tubes with a detachable bottom are used for this purpose, so that the sediment pellet of fixed or fresh cells can be transferred to the freezing stage without disruption. The pellets are firm enough for sectioning and require no embedding. Furthermore, since the sedimented micro-organisms show a certain degree of orientation, serial frozen sections of groups of bacteria or of isolated cells can be obtained. The frozen bacteria sections spread out on the collecting fluid to form practically invisible films which are often difficult to locate and pick up. The whole process takes only a few hours in contrast to the prolonged treatment necessary for embedding, and unembedded frozen sections of bacteria are generally more suitable for electron microscopy than embedded specimens.

E. Complementary preparation procedures for frozen sections

Thin frozen sections of fresh tissues can be further subjected to a number of complementary preparation procedures which may eventually make it possible to correlate the morphology of the specimen with its chemical composition. The most important procedures which can only be carried out on fresh frozen sections are:

1. Enzymatic digestion. The fresh frozen sections floating on cold Ringer or saline solutions are picked up on collodion covered stainless steel grids or on glass coverslips covered with a thin collodion film, and transferred to the buffered solutions of trypsin, pepsin, ribonuclease or any other enzyme under investigation. The process of digestion is followed under light microscope control in special chambers designed to maintain constant temperature. *Since thin frozen sections are ideal for phase contrast microscopy,* structural modifications induced by digestion can be detected at an early stage and the process stopped at suitable intervals for observation with the electron microscope. Structural relationships are generally well preserved in the section, even at advanced stages of digestion, partly due to the supporting action of the collodion film. The method is therefore indicated for sequential studies on the effects of enzymatic digestion with the electron microscope.

2. Microincineration. *Ultrathin frozen sections which have been subjected to the modified freezing-drying procedure are specially suitable for studies on the localization of inorganic tissue constituents by means of microincineration.* The sections mounted on silicon monoxide films can be easily incinerated by the electron-induced micro-incineration technique described by DRAPER and HODGE (7), or with conventional methods in an electric oven. Migration of the mineral residue and loss of many of the volatile substances in the specimen can be prevented by depositing a silicon monoxide or aluminum supporting film on top of the specimen before incineration. This "Replica-incineration" procedure (8) preserves a cast of the original specimen before incineration in addition to the mineral residue which is enclosed between the two films and can thus be more accurately localized. If the electron microscope is provided with a device for obtaining electron diffraction patterns of restricted areas of the specimen in the normal object position (3, 11), an analysis of the mineral residue may be carried out by electron diffraction.

3. Electron diffraction studies. There are numerous components in frozen sections of fresh or fixed tissues which can be profitably studied by means of electron diffraction. Here again sections without an embedding matrix like frozen sections are more suitable for this type of investigation. This also holds true for studies involving fractional extraction of certain components of the tissue or treatment with specific cytochemical reagents.

4. Ultracentrifugation studies. If fresh tissues are subjected to ultracentrifugation, a characteristic separation of its submicroscopic elements and rearrangement of the structural relationships within the tissue are produced. These induced structural modifications are reproducible and can best be studied in thin frozen sections with the electron microscope's higher resolving power. The method has been found particularly valuable in studying the behaviour of the different components of medullated nerve fibres in an ultracentrifugal field. Its application depends however on the possibility of being able to "fix" the stratification produced by ultracentrifugation through immediate freezing and freeze drying.

In addition to these procedures, two supplementary preparation techniques will be mentioned which have been used extensively in connection with freezing-sectioning:

a) *Replica-adhesion sections.* Extremely thin coherent sections (below 0.05 microns) can be prepared from frozen sections of fresh tissues mounted and frozen dried on glass slides by means of the replica-adhesion technique. The frozen sections are covered with a 1 % collodion solution in amylacetate or with a 5 % gelatine solution, and the resulting thick collodion or gelatin film is then stripped off, carrying with it a very thin layer of the section. The bulk of the frozen section sticks firmly to the glass slide and is left behind, allowing the procedure to be repeated many times. The thin tissue section embedded in the collodion or gelatin film can be shadowed with platinum-palladium and examined after dissolving the film.

b) *Dissociation of frozen sections.* Thin frozen sections of osmium fixed tissues display a marked tendency to dissociate into their submicroscopic components upon being subjected to gentle fragmentation procedures. Sonic fragmentation or simple dissociation by light tapping on sections enclosed between glass slide and plastic cover slips under microscopic control were most effective. This is a valuable preparation technique since it often yields large, well preserved pieces of delicate membranes or lamellar structures which are impossible to obtain by any other methods. There is also the possibility of rapidly producing an extreme degree of fragmentation by changing the angle of the knife in the freezing sectioning procedure, so that the knife edge scrapes off thin layers of the frozen specimen instead of slicing it into sections.

An RCA Model EMU electron microscope with a self-biased electron gun and an accelerating potential of 40 kV was used in this study. By installing a removable intermediate lens and a fine condenser aperture (200 microns diameter) of the type described by BOADWAY (3), electron diffraction patterns may be taken from small areas of a preparation in the normal object position without breaking the vacuum or removing the object and projector pole pieces (11).

III. Results obtained with the freezing-sectioning technique

The examples presented in the accompanying micrographs were chosen to illustrate the degree of preservation and resolution of structure achieved routinely with the freezing-sectioning techniques, and to demonstrate the obvious limitations which frozen sections still share with comparable sections of embedded material. However, since most of these sections were obtained from fixed material, picked up on liquids and simply dried in air, they are not intended to show the higher degree of structure resolution which can be attained with unfixed material and by careful application of the modified freezing-drying technique.

The method was primarily developed for the study of nerve fibre ultrastructure which is extremely sensitive to the action of chemical and physical agents and thus affords a suitable test object for investigating preparation artifacts. Labile components like the myelin sheath are well preserved in thin longitudinal or transverse frozen sections of nerve fibres (Fig. 3), judging from their appearance under the polarized light and phase contrast microscopes. Delicate structures like the incisures in the internode portion or the structures of the node also show up in such thin frozen sections with a greater clarity of detail than is ordinarily discernible in whole single fibres. It is becoming increasingly apparent that the examination of such thin frozen sections with the phase microscope reveals structural details and interrelationships which have been hitherto inaccessible to direct observation in fresh tissues. Examination of ultrathin frozen sections of osmium fixed nerve fibres with the electron microscope (9, 10) has revealed a concentric laminated fine structure of the order of 80 Å in the myelin sheath, which is difficult to demonstrate in sections prepared by the ordinary embedding methods. Instead, in many of these formalin fixed sections of embedded material (23) the myelin sheath presents the aspect of a coarse lamellar net which is clearly due to the effects of lipid extraction and represents a gross preparation artifact. Other instances of better preservation of nerve fine structure in frozen sections than in embedded sections could be cited (10), but as a rule, a combination of both preparation techniques has given best results in the study of nerve tissue with the electron microscope. A further advantage offered by fresh frozen sections is the possibility of carrying out microincineration experiments to determine the specific localizations of inorganic constituents in the nerve fibre.

The preparation and mounting of ultrathin frozen sections of bacteria and other microorganisms proved to be surprisingly easy by these methods. A detailed account of these experiments, which are being carried out in collaboration with Dr. G. HEDÉN, will be published later. Only a few specimens of sectioned normal and bacteriophage infected E. coli bacteria will be shown here to demonstrate the type of structures observed. The bacteria were fixed with formalin/potassium bichromate mixtures and sedimented by short centrifugation. The sediment pellet was then frozen and the sections collected on cold distilled water, air-dried and shadowed with platinum-palladium. Section thickness varied between 0.2 and 0.05 microns and was generally determined by evaluating the length of the shadows cast by the section edge in relation to the shadows of Dow Latex spherical particles of known diameter (2 600 Å) (Fig. 6). Although no embedding medium was present and despite their extreme tenuity, longitudinal and transverse sections of normal and infected bacteria reveal a remarkable integrity and preservation of structure. In sections of normal E. coli (Figs. 5, 6) details of the protoplasmic membrane and of the cell wall are clearly visible. The fixed bacterial protoplasm seems to consist of fine granules 50–100 Å in diameter which form dense conglomerates in certain areas, resulting in a pattern of light and dark areas probably corresponding to similar patterns described in unsectioned whole bacteria (18).

Sections of E. coli infected with T2 bacteriophage in advanced stages of development (Figs. 7, 8, 9) show numerous elongated or spherical elements the size of phage particles to which structures resembling tails are often attached, within the bacterial protoplasm. In addition to the large phage particles which frequently show a characteristic morphology in thin sections, numerous smaller spherical particles of all dimensions down to a diameter of 50 Å or below are clearly discernible. This wealth of fine structural detail visible in frozen sections contrasts with pictures of embedded sections of the same object (26) in which all but the largest particles are obscured by the embedding mass. The freezing sectioning technique should therefore be of particular value in studying the early stages of bacteriophage multiplication within bacterial cells.

Fixed human spermatozoa have also been sectioned by the same methods applied to sedimented material. The sperm heads are exceptionally dense and provide a convenient test object to determine the thickness and quality of the frozen sections. In such ultrathin longitudinal and transverse frozen sections of osmium fixed spermatozoa heads (Figs. 11, 12) the membrane systems and particularly the innermost membrane are clearly visible. The internal structure of the head is seen to consist of an extraordinarily compact mass of minute particles of different sizes, the finest of which are close to the resolving power of the electron microscope. Considerable detail was also visible in the neck and middle piece structures. Longitudinal sections through the tail (Fig. 13) show numerous fibrils surrounded by a helical structure. Application of the freezing sectioning technique discloses a variety of new structural details in spermatozoa which require special investigation.

Satisfactory frozen sections have also been obtained from connective tissue, cartilage, muscle, liver cells, anterior lobe cells of the hypophysis (Fig. 10) and mature pollen grains. All of these sections compare favourably with corresponding sections of embedded material, but it is evident that best results are obtained with structures in the size range of a few microns, like microorganisms. Embedded sections preserve structural relations involving larger areas of tissue better than frozen sections, which in view of this limitation should always be supplemented with the study of embedded material.

Finally, as an example of the application of electron diffraction studies in connection with frozen sections, electron diffraction patterns obtained from osmium fixed piles of lamellae are presented (Figs. 14 a, 14 b). It has been shown that lamellar structures closely resembling myelin lamellae isolated from osmium fixed nerve fibres give typical cross-grating electron diffraction patterns (11). Utmost caution must be exercised however in the interpretation of these results, since there is always the possibility of contamination with extraneous crystalline material or with osmium-lipid compounds resembling myelin lamellae. In this case, the use of frozen sections was particularly valuable in identifying the myelin lamellae which were still attached to the myelin sheath in suitable preparations, and thus avoid confusing them with crystalline impurities.

IV. Discussion

The remarkable preservation of structural integrity in the ultrathin frozen sections devoid of an embedding matrix can be partly attributed to the favourable conditions offered by the small tissue block for freezing and sectioning. Collecting of the sections on a liquid surface and direct transfer to the supporting collodion film also eliminates many of the distortions attending the mounting of frozen sections in conventional techniques. A detailed discussion of the numerous other factors involved in the freezing and sectioning of tissue and on which little information is at present available, is beyond the scope of this report.

However, a series of observations carried out on fresh frozen sections of nerve fibres collected on undercooled glycerine and examined before thawing had occurred, suggest a tentative explanation for the good sectioning qualities of frozen tissue. In these sections ice formation appeared only in the form of longitudinal columns lodged in the interstices between the fibre bundles, while the fibres themselves were mostly free of ice and evidently in an undercooled state. The pictures resembled the conditions described by CHAMBERS and HALE (6) for subcooled muscle fibres.

In frozen tissues we are therefore probably dealing with a combined undercooling of small masses of "bound water" (16, 17) in the macromolecular protein complexes of protoplasm, in addition to a more extensive ice formation of the "interstitial water" (17). This three dimensional submicroscopic framework of congealed "interstitial water," formed along natural crevices and cleavage boundaries, permeates the entire tissue and imparts the rigidity necessary for freezing-sectioning. The process of cutting would actually represent a "splitting" along natural cleavage boundaries facilitated by this interstitial ice framework. Moreover, it is conceivable that the undercooled "bound water" exerts a protective action on the associated protoplasm complexes, which would remain essentially unaltered throughout the entire procedure.

Regardless of the postulated freezing sectioning process, it is clear that the complex problem of freezing of protoplasm can now be studied directly on frozen sections aided by the electron microscope's higher resolving power. Likewise, a more direct approach to the problem of fixation effects is now possible by using frozen sections of fresh tissues. The wide range of applications of the freezing-sectioning technique together with its numerous advantages and comparative simplicity make it worthwhile developing further as an important research tool in electron microscopy.

SUMMARY

1. An improved method is described for preparing ultrathin (0.2—0.05 micron) serial frozen sections of fresh or fixed, unembedded tissues. The method is particularly suitable for the examination of fresh biological tissues with the electron

microscope, in combination with a modified freezing-drying procedure carried out directly on the ultrathin sections. The fresh tissue sections can also be subjected to enzymatic digestion, microincineration and different cytochemical reactions, and the effects followed with the electron microscope.

. The factors involved in the freezing and sectioning of tissues are discussed briefly, and a comparison is made with the current methods for preparing ultrathin sections of embedded, dehydrated material.

. By means of ultracentrifugation of fresh tissues a characteristic stratified separation of its submicroscopic elements is produced which can be studied in thin frozen sections with the electron microscope.

. A series of electron micrographs of ultrathin frozen sections of medullated nerve fibres, normal and bacteriophage infected E. coli bacteria and of spermatozoa is shown to illustrate the applications of the method. Examples are also presented of the application of electron diffraction techniques to the study of isolated components in frozen sections.

Acknowledgements

Several of the ideas upon which this study is based stem from the period of apprenticeship in electron microscopy which the author spent at the Nobel Institute for Physics. I wish to express my sincere gratitude to Professor MANNE SIEGBAHN for his generous hospitality and kind support at all times. The work described here was carried out at the Institute for Cell Research, Karolinska Institutet, and I am deeply indebted to the director of this Institute, Professor TORBJÖRN CASPERSSON for his kind help and for placing all the facilities of his institute at my disposal. Sincere thanks are also due to Mr. H. WALÉN, C. BLOMQVIST and specially to Ing. H. KABE for the excellent photographic reproductions. The author wishes to thank Professor ARNE WESTGREN for many helpful discussions and suggestions in the course of the electron diffraction studies. Part of the expenses for this investigation were defrayed from research grants by the Wallenberg Foundation and by the Venezuelan Government.

REFERENCES. 1. **Anderson, T. F.**, Trans. New York Acad. Sc., *13*, 130 (1951). — 2.
——, J. Appl. Phys., *27*, 724 (1950). — 3. **Boadway, J. D.**, J. Appl. Phys., *22*, 104
(1951). — 4. **Bretschneider, L. H.**, Mikroskopie, *5* (1950). — 5. ——, Proc. Kon. Ned. Akad.
v. Wetensch., *LIII*, 531 (1950). — 6. **Chambers, R.**, and **Hale, H. P.**, Proc. Roy. Soc. London,
Ser. B., *110*, 336 (1932). — 7. **Draper, M. H.**, and **Hodge, A. J.**, Austral. J. Exp. Biol. and Med.
Sc., *XXVIII*, 549 (1950). — 8. **Fernández-Morán, H.**, Arkiv. Zool. K. Sv. Vet. 40 A, 6 (1948).
— 9. ——, Exper. Cell Res., *1*, 141 (1950). — 10. ——, Exper. Cell Res., *1*, 309 (1950). — 11.
——, Exper. Cell Res., *2*, 673–679 (1951). — 12. **Hast, N.**, Kosmos, *27*, 161 (1949). — 13. **Hart-**
mann, J. F., and **Latta, H.**, Proc. Soc. Exp. Biol. and Med., *74*, 436 (1950). — 14. **Hillier, J.**, and
Gettner, M., Science, *112*, 520 (1950). — 15. ——, Appl. Phys., *21*, 889 (1950). — 16. **Kistler,**
S. S., J. Phys. Chem., *36*, 52 (1932). — 17. **Moran, T.**, Proc. Roy. Soc. London, *A 112*, 30
(1926). — 18. **Mudd, S.**, **Hillier, J.**, and **Smith, A. G.**, J. Bact., *57*, 319 (1949). — 19.
Newman, S. B., **Borysko, E.**, and **Swerdlow, M.**, J. Res. Nat. Bur. Stand., *43*, 183 (1949).
— 20. ——, Science, *110*, 66 (1949). — 21. **Pease, D. C.**, and **Baker, R. F.**, Proc. Soc. exp.
Biol. Med., *67*, 470 (1948). — 22. **Polge, C.**, **Smith, A.**, and **Parkes, A.**, Nature, *164*, 666
(1949). — 23. **Rozsa, G.**, **Morgan, C.**, **Szent-Gyorgyi**, A., and **Wyckoff, R. W. G.**, Biochimica
et Biophysica Acta, *6*, 13 (1950). — 24. **Wyckoff, R. W. G.**, Science, *104*, 36 (1946). — 25.
——, Biochimica et Biophysica Acta, *2*, 27 (1948). — 26. ——, Presse Méd., *82*, 1439 (1950).

Stockholm, September 12th, 1951.

Department of Cell Research, Karolinska Institutet, Stockholm, and Department of Biophysics, University of Caracas, Venezuela.

Texts to the plates

Plate I

Fig. 1. Modified freezing microtome with electric motor drive for ultrathin sectioning. The freezing stage is clamped in the specimen holder of a standard Spencer rotary microtome, and is connected with the carbon dioxide container through a suspended pressure hose. The special knife holder with attached collecting trough, and the freezing cup are also shown.

Fig. 2. Glass knife in the special holder described by Hartmann and Latta, used for cutting ultrathin frozen sections. Notice the plastic disc carrying the frozen specimen and the collecting trough filled with liquid on which sections are floating.

Plate II

Fig. 3. Transverse frozen section of fresh medullated nerve fibres picked up on Ringer solution. (Thickness: 1 micron.) Phase contrast micrograph. Magnification: 1200 ×.

Fig. 4. Bundle of collagen fibrils from the outer layers of a longitudinal nerve fibre section. Frozen section of fresh nerve subjected to the modified freezing-drying procedure and shadowed with platinum/palladium. Electron micrograph. Mag.: 24 000 ×.

Plate III

Fig. 5. Longitudinal frozen section of a normal E. coli bacteria fixed with formalin-potassium bichromate mixture. (Air dried section, unshadowed. Thickness: 0.2 micron.) Details of the internal structure and of the bacterial cell wall are visible. Magnification: 20 000 ×.

Fig. 6. Longitudinal frozen sections of normal E. coli bacteria with Dow Latex calibration particles. (Formalin-potassium bichromate fixation. Air dried section shadowed with platinum-palladium. Thickness: 0.2 micron.) The fine granular structure of the fixed bacterial protoplasm is seen. Magnification: 24 000 ×.

Plate IV

Fig. 7. Longitudinal frozen section of E. coli bacteria infected with T2 bacteriophage. (Formalin-potassium bichromate fixation. Air dried section shadowed with platinum-palladium. Thickness: 0.2 micron.) Structures resembling tails are attached to some of the phage particles (arrow) within the infected bacteria. Magnification: 24 000 ×.

Plate V

Fig. 8. Longitudinal frozen section of E. coli bacteria infected with T2 bacteriophage. (Formalin-potassium bichromate fixation. Air dried section shadowed with platinum-palladium. Thickness: 0.2 micron.) In addition to phage particles with tails (arrow) numerous smaller spherical particles and minute granules are seen. Magnification: 24 000 ×.

Plate VI

Fig. 9. Transverse and longitudinal frozen sections of E. coli infected with T2 bacteriophage. (Formalin-potassium bichromate fixation. Air dried section shadowed with platinum-palladium. Thickness: 0.2 micron.) This micrograph illustrates the type of serial sections of bacteria obtained by this technique. Magnification: 12 000 ×.

Fig. 10. Frozen section of nucleus from a cell of an eosinophilic pituitary adenoma. (Osmium tetroxide fixation. Air dried section shadowed with platinum-palladium. Thickness: 0.1 micron.) Details of the internal structure of the nucleus, of the nucleolus and nuclear membrane are visible. Magnification: 12 000 ×.

Plate VII

Fig. 11. Longitudinal frozen sections of human spermatozoa heads. (Osmium tetroxide fixation. Air dried section, unshadowed. Thickness: 0.1 micron.) Details of the head membrane, of the head's internal structure and of the middle piece can be seen. Fenestrated appearance of the head is probably a drying artifact. Magnification: 16 000 ×.

Fig. 12. Transverse frozen section through the head of a human spermatozoa. (Osmium tetroxide fixation. Air dried section shadowed with platinum-palladium. Thickness: 0.1 micron.) The extremely compact internal structure of the head consisting of very fine granules is shown. The head membrane is also discernible. Mag.: 40 000 × .

Fig. 13. Longitudinal frozen section through the tail of a human spermatozoa. (Osmium tetroxide fixation. Air dried section shadowed with platinum/palladium. Thickness: 0.2 micron.) Several fibrils of the tail are seen, surrounded by a helical structure which is partly cut away. Magnification: 40 000 × .

Plate VIII

Fig. 14 a. Pile of lamellae isolated from a frozen section of osmium fixed rat sciatic nerve fibres on collodion supporting film. This pile of lamellae produced the electron diffraction pattern shown in Fig. 14 b. Magnification: 16 000 × .

Fig. 14 b. Electron diffraction cross-grating pattern obtained from the pile of lamellae of Fig. 14 a, using the specimen in the object position of an RCA EMU electron microscope with a condenser aperture of 200 microns and an intermediate lens.

Tryckt den 5 februari 1952

Uppsala 1952. Almqvist & Wiksells Boktryckeri AB

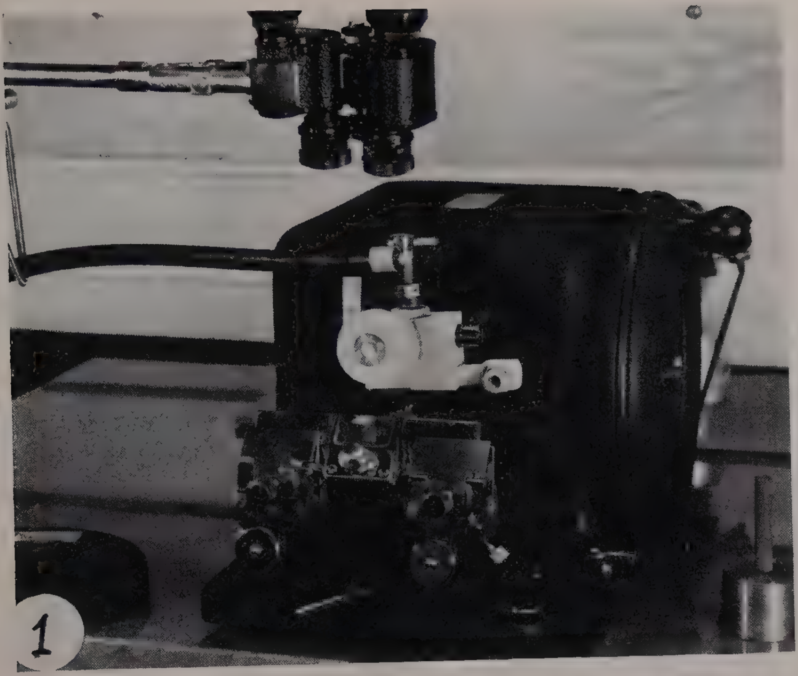
1

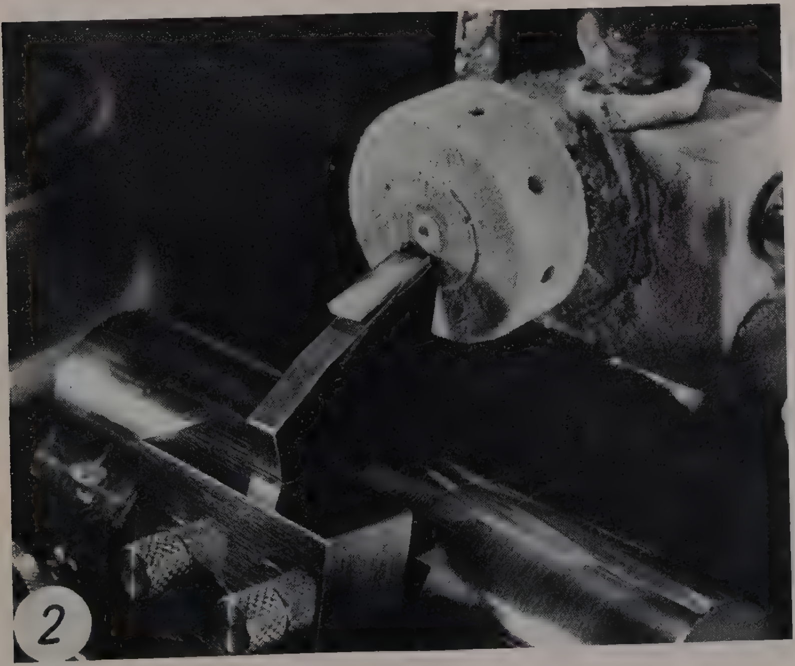
2

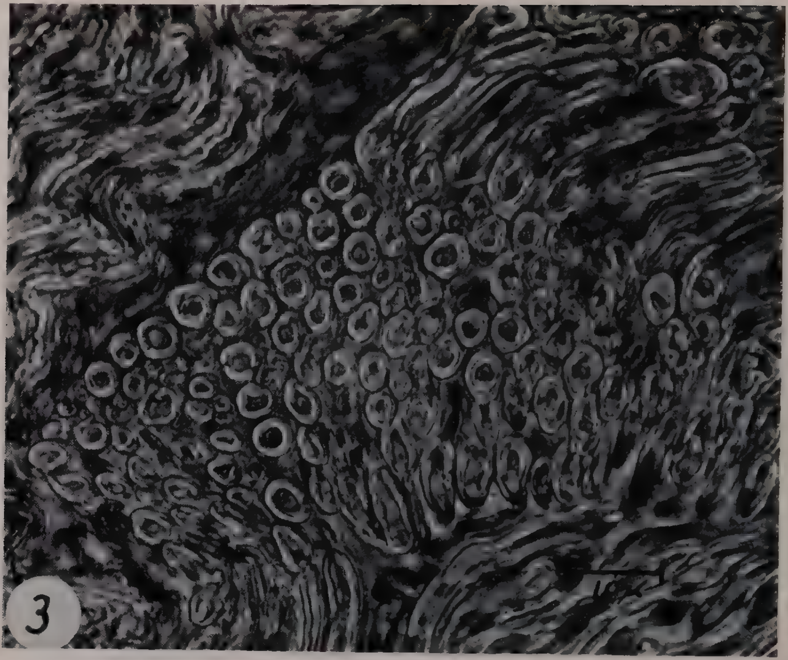

3

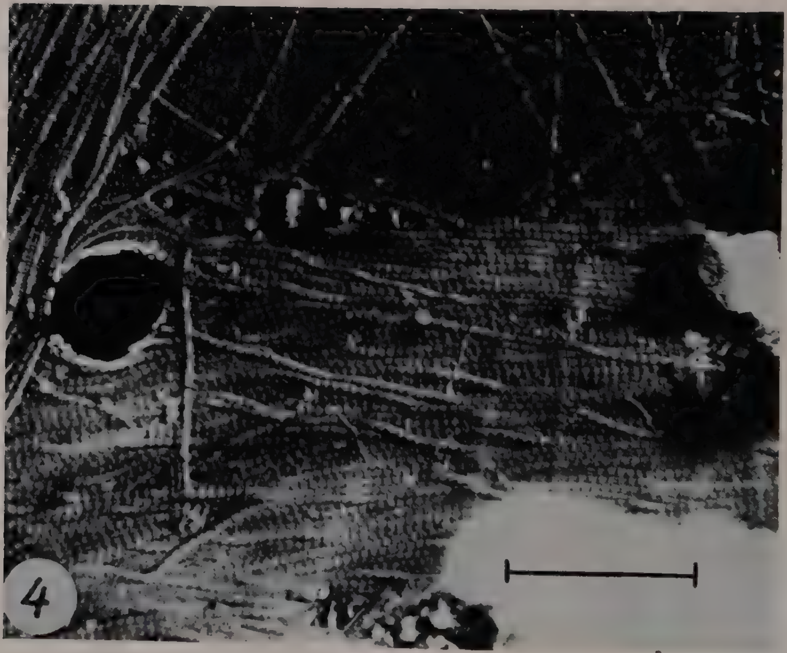

4

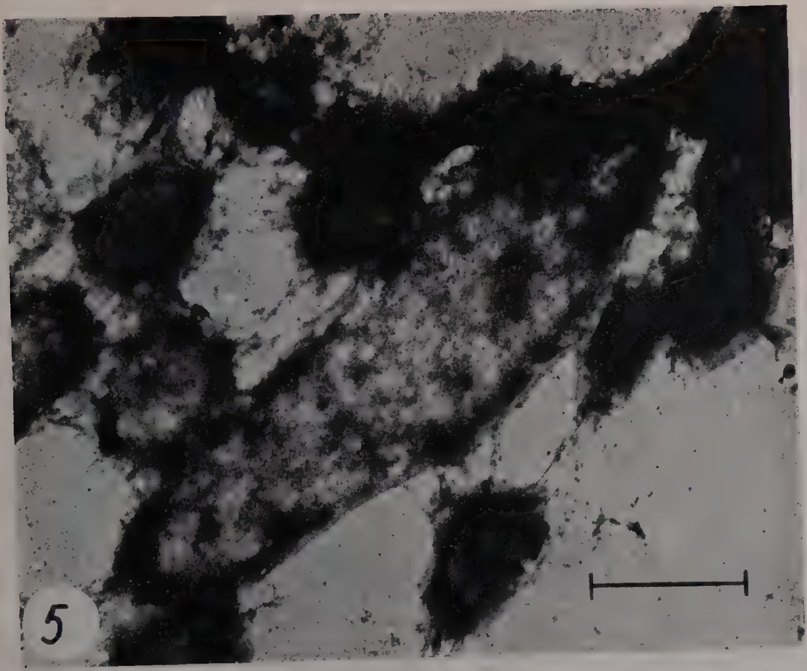

5

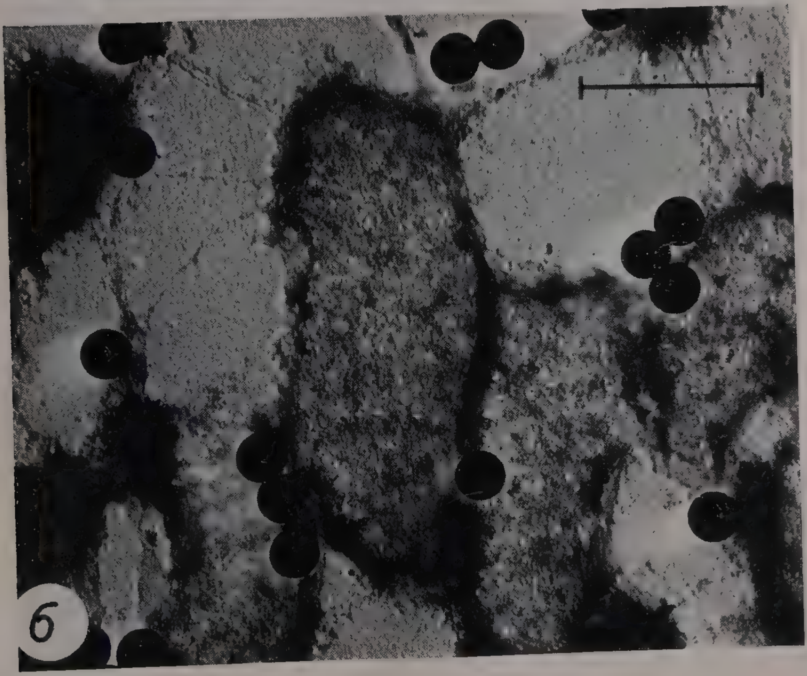

6

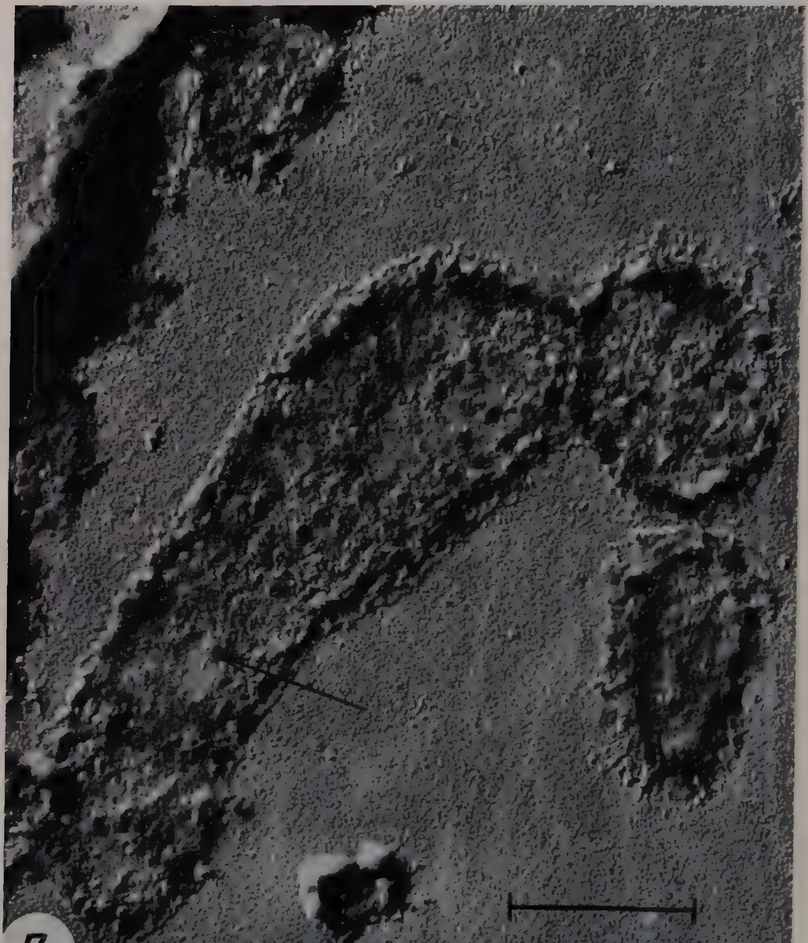

7

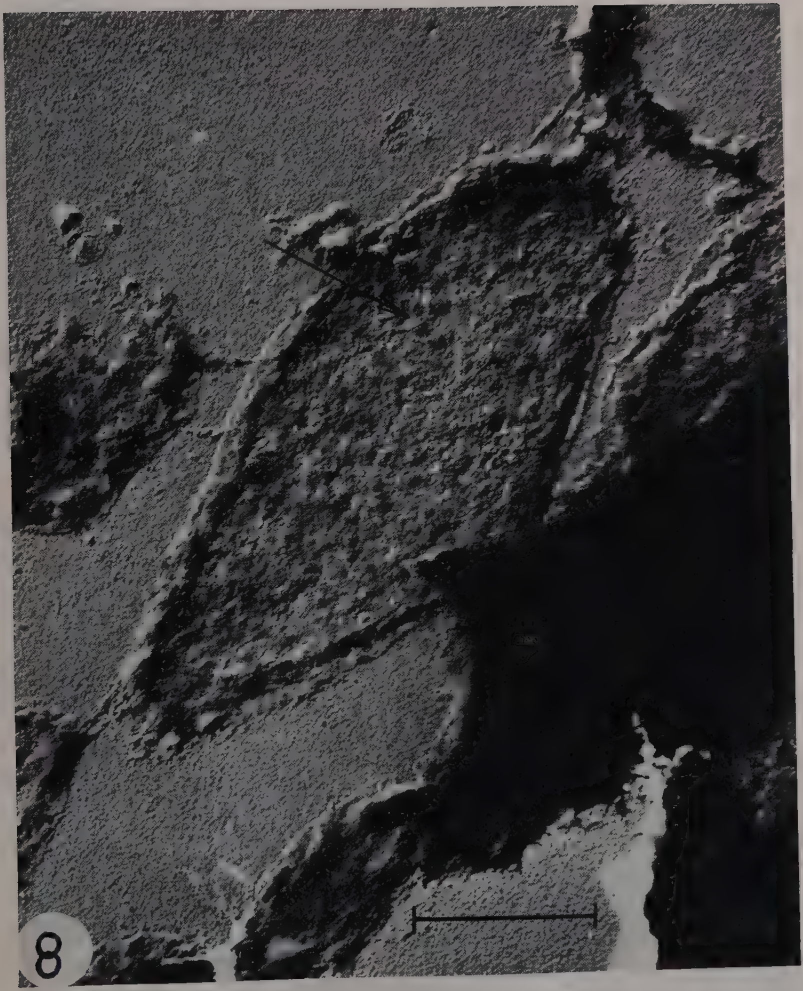
8

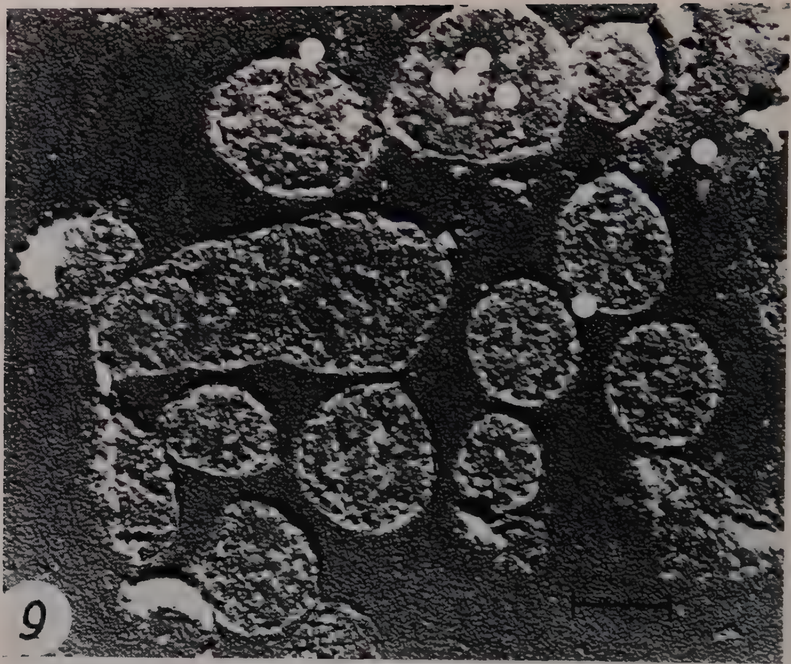

9

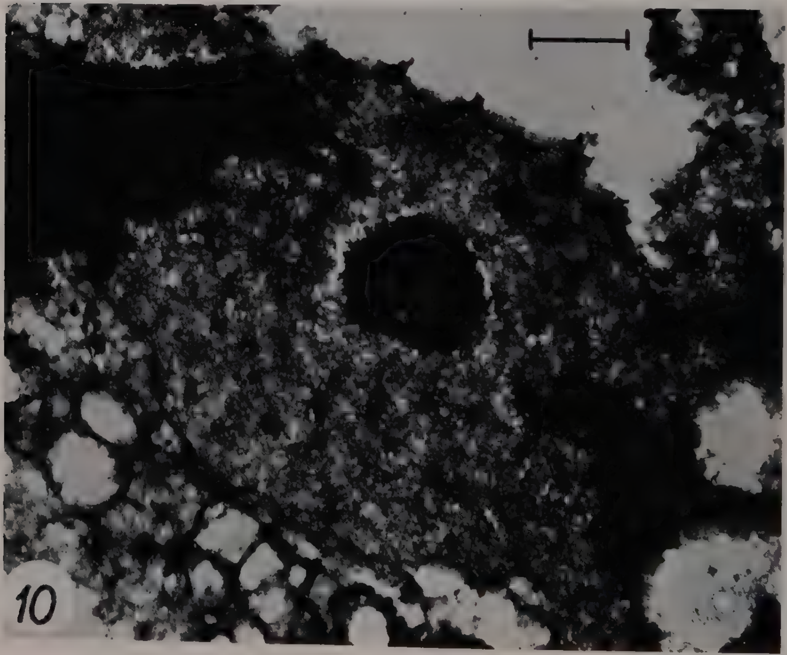

10

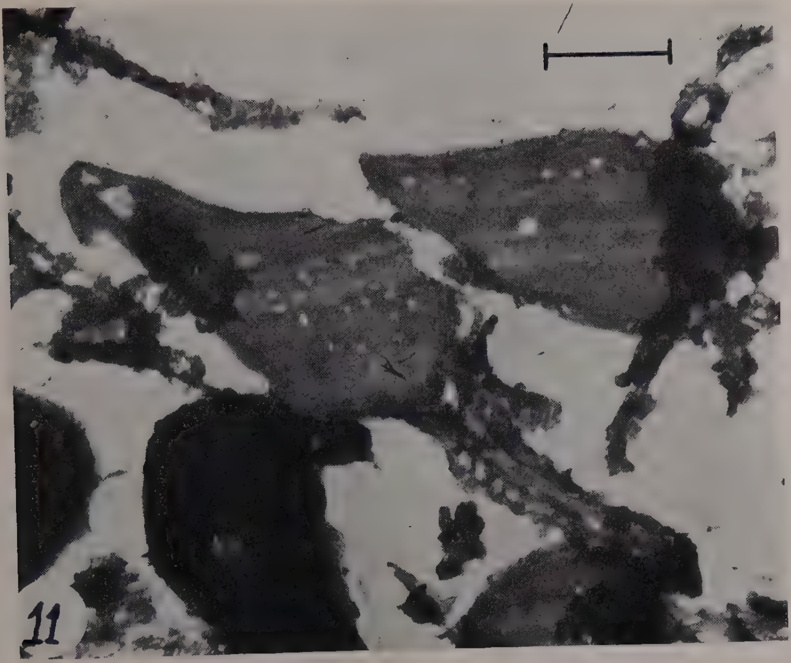
11

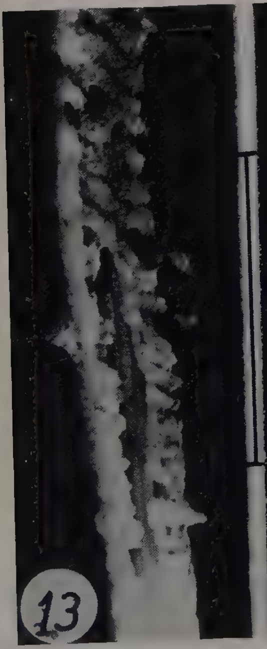
13

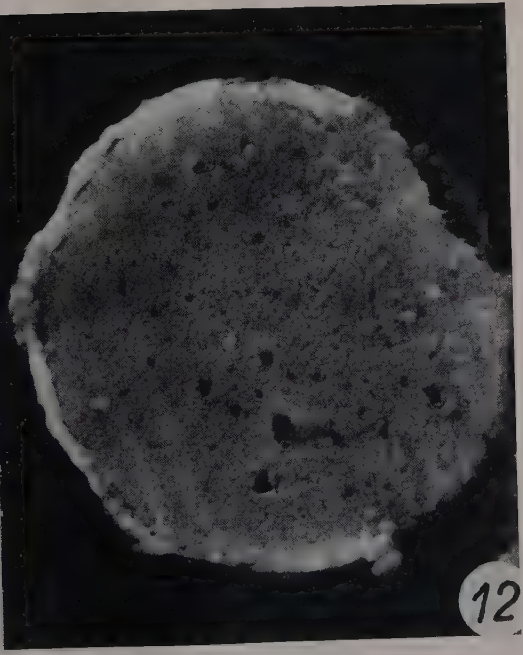
12

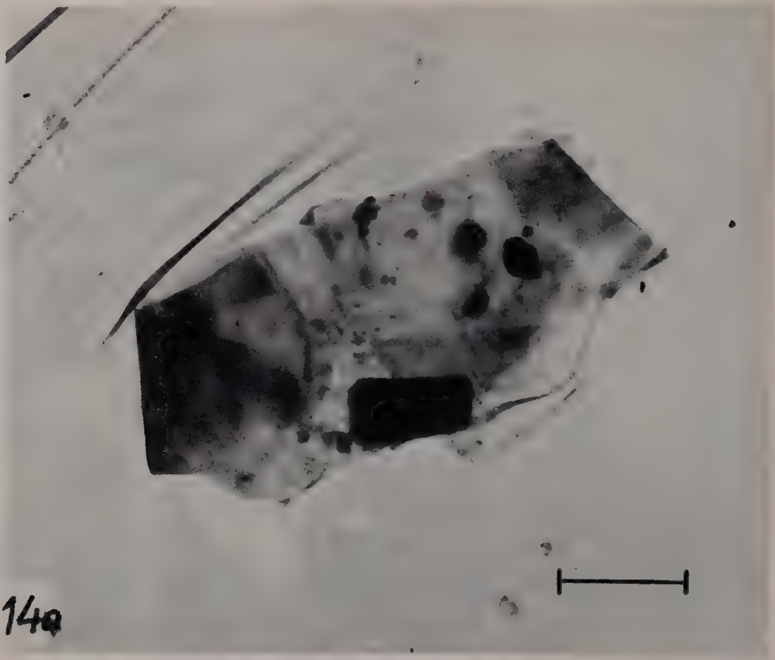

14a

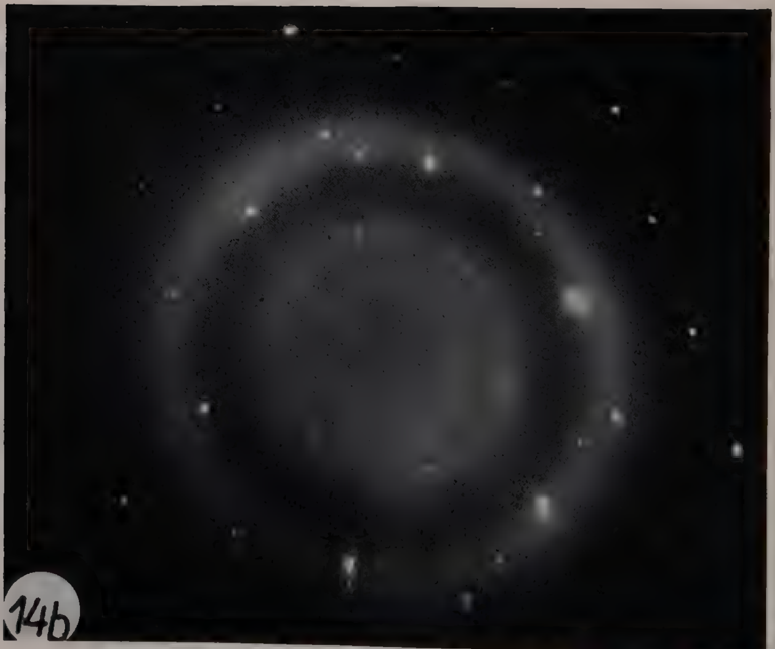

14b

ARKIV FÖR FYSIK Band 4 nr 32

Communicated 12 September 1951 by MANNE SIEGBAHN and ERIK HULTHÉN

Determination of multipole orders from internal pair formation

By HILDING SLÄTIS and KAI SIEGBAHN

With 7 figures in the text

General Introduction. In order to provide some ground for the discussion of present theories of nuclear shell structure considerable experimental efforts have recently been made to determine the spins and parities of excited nuclear levels. The most convenient and precise way of doing this is no doubt to measure the internal conversion coefficients associated with the γ-transitions. In particular, the conversion coefficients for electric and magnetic multipole radiations have been accurately calculated by ROSE et al (1), in order to enable multipole assignments to be made and there exist also theoretical calculations of the K/L conversion ratios made for the same purpose (2). In several cases where two γ-rays are emitted in cascade transitions, $\gamma\gamma$-angular correlation and polarization studies of the emitted γ-rays may determine the spins and parities of the three levels involved (3). Other types of angular correlations may also give similar information, e.g. between β and γ, e^- and e^-, etc. Except for isomeric states, direct measurements of the usually very short life times of the states have only rarely been made (4) to determine the type of radiation.

It should also be mentioned that the interpretation of γ-radiation probabilities in terms of multipole orders is rather uncertain because of the estimates which must be made of the unknown nuclear matrix elements, which do not enter into the other methods.

By using β-selection rules and experimentally determined ft-values in β-decay, spin and parity assignments may often be made.

There still remains one more possible method of measuring multipole orders, namely by using the internal pair formation effect. To date however, this has been tried only fragmentarily, the main reasons being the high threshold of the effect ($2\,m_e c^2$) and the small magnitude of the cross section. γ-rays of more than 1 MeV do not occur too frequently in the radiation of radioactive atoms, in the disintegration of which light particles are often emitted, thus making it very hard to detect the additional very faint continuous electron spectra due to internal pair formation.

Only in the case of a transition taking place between two states both of zero angular momenta may the pair emission be appreciable. In this case γ-ray emission is strictly forbidden (all terms in the multipole expansion vanish) and the nucleus is deexcited only by pair emission. Depending on whether the parity changes or not, the pair creation takes place either inside the nucleus or at a distance of th order of the Compton wave length from it. An example of this has been found an studied in detail in the reaction F^{19} $(p\,\alpha)$ O^{16}, where in the transition from the 5 MeV excited level in oxygen to the ground state, pairs are emitted which turn ou to be of "nuclear" origin (5).

In all other cases when γ-emission is not strictly forbidden the "internal pa conversion coefficient" (in the following denoted by I) is quite small, being of th order of 10^{-4}–10^{-3} for γ-rays of 1–3 MeV. It resembles the ordinary K etc. conve sion in that the conversion coefficient is a function of energy, multipole type, an Z-value, but the general trend is completely opposite in the two cases. Thus, th pair conversion increases with decreasing multipole order and with increasing γ energy. The Z dependence is not very pronounced, the conversion being slightl higher for low than for high Z. These facts taken together (6) may under certain con ditions result in a pair conversion which is comparable to or even higher than th ordinary K conversion. For instance in light elements at high γ-energies the ordinar K conversion is known to be extremely small (in the case of the 2.76 MeV γ-ray o Na^{24} the K conversion coefficient (7) is only $\sim 10^{-6}$) and in such cases it may b much more favourable to use the pair conversion for a multipole order determination

Until now this method has been used only on heavy elements (in a few cases see below) whereas in the case of light elements, when it should be much more useful it has been tried only in one single case, namely Na^{24}. The experimental result which were obtained in that case indicated, however, a rather serious discrepancy with other existing data concerning the multipole order of the particular transition and it was therefore considered necessary to repeat this investigation in our work Furthermore we have, in addition to the hard γ-rays from ThC″, selected for study in the present paper the internal pair conversion occurring in some light nuclei i.e. Mn^{56} and Co^{60}.

Earlier experiments. The *external* conversion of a γ-ray into a positron-electron pair in heavy elements was first observed in 1933 almost simultaneously by CURIE and JOLIOT (8), ANDERSON and NEDDERMEYER (9) and MEITNER and PHILIPP (10). The pairs were created in lead foils by the hard γ-rays from the Be^{9} $(\alpha\, n)$ C^{12} reaction (8), or from ThC″ (9, 10). Early in 1934 CHADWICK, BLACKETT and OCCHIALINI (11) observed *internally* created positrons, i.e. positrons originating in the radioactive atoms themselves (ThC″). All the quoted investigations were performed by means of Wilson chambers in magnetic fields. ALICHANOV and KOSODAEV (12) studied pair formation using a semicircular spectrometer and counted the positrons from radon by means of two Geiger counters in coincidence. This coincidence arrangement was necessary in order to eliminate the large background of penetrating γ-radiation in the instrument, which was small. The same arrangement was used in 1936 by ALICHANOV, ALICHANIAN and KOSODAEV (13) for the study of the positrons from ThC + C″ and from RaC. Besides the possibility of the creation of positrons (pairs) by conversion of γ-rays, it was also possible that pair formation might occur at the moment of the emission of a β-particle from the nucleus (in this case one positron and two electrons should be emitted simultaneously). The number of positrons released by the 2.62 MeV ThC″ γ-ray was $2-4\times10^{4}$ per β-particle from ThC + C″ (internal pair formation). The number of positrons from a thick lead foil (external pair formation) covering the ThB + C + C″ sample was about 4 times larger than the number of positrons from the uncovered sample. The measurenents confirmed the predicted shape of the positron spectrum. For heavy elements he number of positrons emitted increases with increasing positron energy and de- reases abruptly at the upper limit, the energy of which is $E_\gamma - 2\, m_e\, c^2$, m_e being he electron rest mass. However, for lower energies there was a surplus of positrons. These were thought to be created by the conversion of the energy of the β-particles. f these extra positrons were not considered, the number of emitted positrons was n agreement with the theory of Jaeger and Hulme (14). Later Alichanov (15) ound the absolute value of the conversion coefficient for the ThC″γ-ray of 2.62 MeV to be $4-5 \times 10^{-4}$, in good agreement with the value 4.6×10^{-4} computed rom the theory of Jaeger and Hulme.

In an investigation on pair formation in ThC″, Bradt, Halter, Heine and Scherrer (16) showed that the extra positrons found by Alichanov et al were created by the 1.80 MeV γ-line belonging to the transition ThC–ThC′. Bradt et al found the internal pair fomation coefficient to be 2.3×10^{-4} pairs per ThB disintegration, in good agreement with the value 2.4×10^{-4} computed from the theory of Jaeger and Hulme. As 33.7 % of the ThC nuclei give rise to ThC″, the value found by Bradt et al corresponds to 6.8×10^{-4} pairs per ThC″ disintegration. According to Jaeger and Hulme the 1.80 MeV γ-line gives rise to 10 % of the total positron emission. Hence the experimental value for the pair formation coefficient found by Bradt et al corresponds to an upper limit equal to 6.1×10^{-4} pairs per ThC″ 2.62 MeV γ-quantum.

Latyshev (17), using the semicircular spectrometer of Alichanov et al, measured the intensities of γ-lines from RaC and ThC + C″ with energies exceeding $2\, m_e\, c^2$, using recoil eletron spectra. These intensities were compared with the intensities obtained from the corresponding spectra of the positrons created by pair fomation. As mentioned before each γ-line in the positron spectrum appears as an abrupt break at $E = h\nu - 2\, mc^2$. By measuring the heights of the breaks in the experimental curve and utilizing the theory of Jaeger and Hulme it was possible to plot the positron spectrum for each γ-line, and by addition of these spectra to obtain the total theoretical spectrum of the positrons formed by all the γ-rays. The multipolarity of several γ-lines from RaC and ThC + C″ was determined. As an example the 2.62 MeV γ-line from ThC″ was found to be of electric quadruple origin.

So far internal pair formation coefficients had been investigated only for γ-rays from heavy elements. Rae (18) tried to determine the multipolarity of the 2.76 MeV γ-line, which is emitted in cascade with the 1.38 MeV γ-line after the β-decay of Na^{24}. The experiment was carried out with a spectrometer similar to that used by Alichanov et al. The Na^{24} source consisted of 100 mg of active sodium carbonate deposited on a piece of 0.002″ aluminium foil measuring 3.5 cm by 8 mm, and had an initial strength of 10 mC. The technique[1] was to record the positron spectrum while the source was strong, and then to compare the area under this curve with the area under the curve obtained by recording the β-ray spectrum, the latter measurement being made after the source had aged for a few days. Rae found an internal pair formation coefficient equal to $(1.16 \pm 0.10) \times 10^{-3}$ and concluded that the 2.76 MeV γline in the Na^{24} decay is of electric dipole type.

This result is in contradiction to for instance that found by Deutsch et al (3), who measured the angular correlation between the two γ:s. Their results favoured a spin assignment of 4, 2, 0 to the three levels involved.

---

[1] See also preliminary note by K. Siegbahn and S. du Toit ref. 7

Considering these contradictory results it seemed to be worth while renewi the investigation on the γ-rays from Na^{24}.

The experimental arrangement. The positron and electron spectra were inves gated in an intermediate image β-spectrometer of high transmission (19). By the use this spectrometer no coincidence counters were necessary to distinguish the positro from the background. The positrons were separated from the electrons by mea of a baffle, consisting of eight radial "wings" twisted in the same direction as t positron paths. The paths of the particles in space were accurately known fro previous experiments (19). Using this arrangement, only a few per cent of the pos trons were cut off, while the electrons were completely stopped. By changing t directions of the current in the coils the shutter transmitted the electrons a stopped the positrons.

When the half-life of the isotope in question was short, of the order of some hour the positron spectrum was recorded while the activity was strong. Without changi the position of the sample or the shutters the electron spectrum was then take when the activity had decayed by a factor of about a thousand. For Co^{60}, howeve the half-life of which is 5.3 years, two samples of the same thickness, but differi in activity by a factor of about a thousand, were made. These samples were ob tained by electrolysis.

Estimate of the efficiency of external pair formation

Pair formation is of both internal and external origin. The internal part of th pair creation is found from the total measured value by subtracting the externa calculated, component. The magnitude of the external part may be calculate from the absorption coefficient due to pair absorption, and the geometry of th source. All the γ-quanta absorbed will not give rise to detectable positrons, becaus part of the positrons are annihilated in the sample itself. When the sample i thin enough, this part may be neglected. The pair formation absorption coefficien $\varkappa$ per cm may be computed form the value $\varkappa_{Pb}$ for lead by means of the formula (20

$$\varkappa = \varkappa_{Pb}\,(\varrho/11.3)\,(207.2/W)\,(Z/82)^2, \tag{1}$$

where ϱ is the density, W the atomic weight, and Z the atomic number of the atom in the sample.

For a circular disk of thickness a and radius $n\,a$, consisting of a γ-emitting substance one may easily derive the following approximate formula for the fraction p of γ quanta absorbed:

$$p = \frac{a\,\mu}{2\,\varrho}\,[1 + \log n], \tag{2}$$

where μ/ϱ is the absorption coefficient in cm²/gr.

Measurements

ThC″

The sample consisted of ~ 0.1 mC Th B + C″, deposited on an aluminium foil of 2 mm diameter and 2.5 mg/cm² thickness. Fig. 1 shows the number of positrons

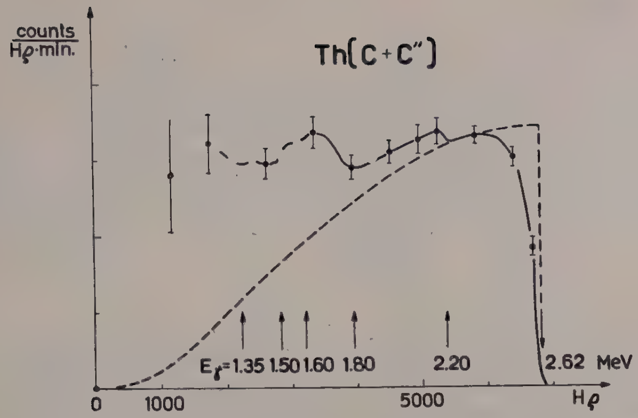

Fig. 1. Positron spectrum of ThC + C″ as a function of the momentum of the positrons. The dotted line represents the theoretical shape of the positrons released from the 2.62 MeV γ-line, according to the theory of Jaeger and Hulme. Compare also Latyshev.

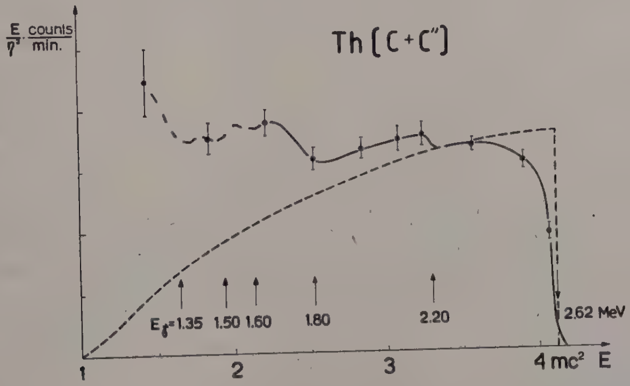

Fig. 2. Positron spectrum of ThC + C″ as a function of the energy of the positrons. The dotted line represents the theoretical shape of the positrons released from the 2.62 MeV γ-line, according to the theory of Jaeger and Hulme. Compare also Latyshev.

emitted per unit time (divided form) as a function of the momentum of the positrons. Fig. 2 shows the positrons as a function of the energy of the positrons. The dotted line is the theoretical distribution for positrons formed by the 2.62 MeV γ-line of ThC″. This dotted curve together with the different γ-energies are taken from the previously quoted work of Latyshev ref. (17). The electron spectrum was taken about 77 hours later. This consisted of the β-spectra of Th B + C + C″. The area of the Th C + C″ electron spectrum was computed. 33.7 per cent of these decays belong to Th C″ (21). The area under the positron spectrum corresponded to 168.8 positrons per minute and the Th C + C″ spectrum was equivalent to 11 400 β-particles. The strength of the sample when the β-spectrum was taken was 0.0098 of the strength when the positrons were observed. From these data we obtain the pair formation coefficient I for the 2.62 MeV Th C″ γ-line:

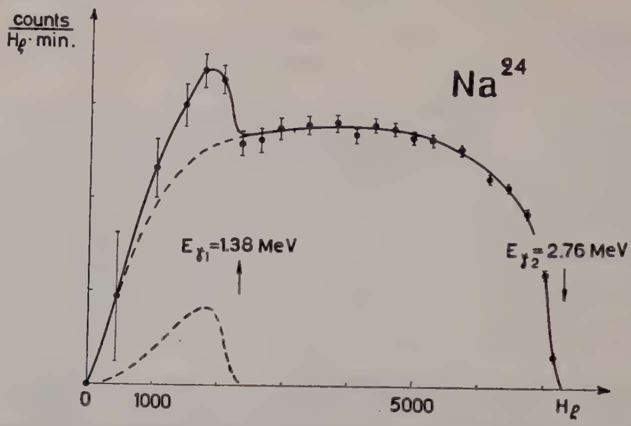

Fig. 3. Positron spectrum of Na^{24} as a function of the momentum of the positrons.

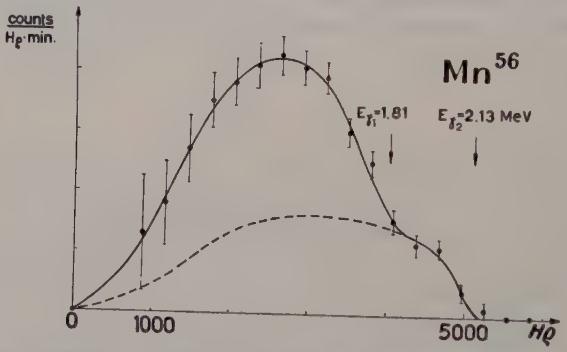

Fig. 4. Positron spectrum of Mn^{56} as a function of the momentum of the positrons.

$$I = 4.30 \cdot 10^{-4}$$

The formulae (1) and (2) give, for the external pair formation coefficient for the thin aluminium foil on which the thorium sample was deposited, the value $4 \cdot 10^{-6}$. Thus, the value $I = 4.30 \cdot 10^{-4}$ for the pair formation coefficient represents the internal pair formation.

Fig. 7 shows the internal pair formation coefficient as a function of the γ-ray energy as computed by JAEGER and HULME[1] (D = electric dipole, Q = electric quadrupole radiation, Z = atomic number) and by WANG (22) (M = magnetic dipole radiation). Our value for I is plotted in this figure. The position in which it falls agrees closely with the theoretical one for quadrupole radiation and is almost identical with that found by ALICHANOV et al. The value marked "Bradt et al." represents an upper limit, which we have computed from the data given by BRADT et al (see p. 155).

---

[1] The theoretical curves in Fig. 7 are based entirely on the corresponding diagram drawn in their work. In the neighbourhood of the threshold, however, no exact calculations have yet been performed, and there may therefore be deviations from the true theoretical curves in this region. Civiling. S. BRIMBERG is performing such calculations and will publish his results in the near future.

Na^{24}

The sample consisted of ~ 0.14 mC sodium carbonate deposited on rubber hydro-hloride film of 0.5 mg/cm² thickness. The thickness of the sodium carbonate spot was ~ 0.9 mg/cm², the diameter of the spot ~ 7 mm. Fig. 3 shows the positron pectrum obtained. The electron spectrum was taken 117 hours later. We got the ollowing values for the internal pair formation coefficients (the number of external pairs was computed to be less than 0.3 per cent of the total pairs created):

$$I_{2.76\,\mathrm{MeV}} = 8.0 \cdot 10^{-4}$$

$$I_{1.38\,\mathrm{MeV}} = 4.4 \cdot 10^{-5}\,^{1}$$

The corresponding points plotted in Fig. 7 show that both radiations correspond to electric quadrupole transitions.

Mn^{56}

The activity was obatined in the ordinary manner by irradiation of an aqueous solution of potassium permanganate by slow neutrons and collecting the slight Mn O_2 precipitate).[2] The strength of the sample was 180 μC, the diameter 6 mm and the thickness 27 mg/cm². The activity was deposited on a rubber hydrochloride film of 1 mg/cm² thickness.

Fig. 4 shows the positron spectrum recorded. The electron spectrum was taken 17 hours after the positron spectrum. According to the accepted scheme the 1.81 MeV and 2.13 MeV γ-lines follow the emission of the β-components with upper limits 1.04 MeV and 0.75 MeV, respectively. The number of these γ-quanta emitted is equal to the number of electrons in the corresponding continuous β-components. Since the difference between the upper limits happens to be small, it is only possible to measure the sum of the β-particles considered. The number of particles in each group is easily found, if we know the ratio of intensities of the two γ-lines. This ratio was not known with certainty. We have therefore investigated the K-photoelectrons released from a thin lead converter irradiated with the manganese γ-lines. The photo lines were taken by means of the double-focusing spectrometer (23). Fig. 5 shows the result. From the measured areas and the known photo absorption coefficients (20), 0.084 and 0.068 cm^{-1} respectively, for the two γ-rays, we got 1.00 for the ratio between the intensities of the two γ-lines. In this way the number of β-particles and hence γ-quanta emitted was known. The corresponding pair conversion coefficients are then $5.8 \cdot 10^{-4}$ and $4.9 \cdot 10^{-4}$, respectively. When these figures are corrected for the external pair effect ($0.2 \cdot 10^{-4}$ and $0.3 \cdot 10^{-4}$ respectively), we get the internal pair formation coefficients

$$I_{1.81\,\mathrm{MeV}} = 5.6 \cdot 10^{-4}$$

$$I_{2.13\,\mathrm{MeV}} = 4.6 \cdot 10^{-4}$$

These values are included in Fig. 7, which indicates that the multipolarities of the γ-lines may be electric dipole for the 1.81 MeV γ-line, and electric quadru-

---

[1] *Note added in proof:* A new run with better statistics has yelded the somewhat lower value $I_{1.38\,\mathrm{MeV}} = 3.0 \cdot 10^{-5}$.

[2] The chemical preparation was kindly performed by Dr LARS MELANDER.

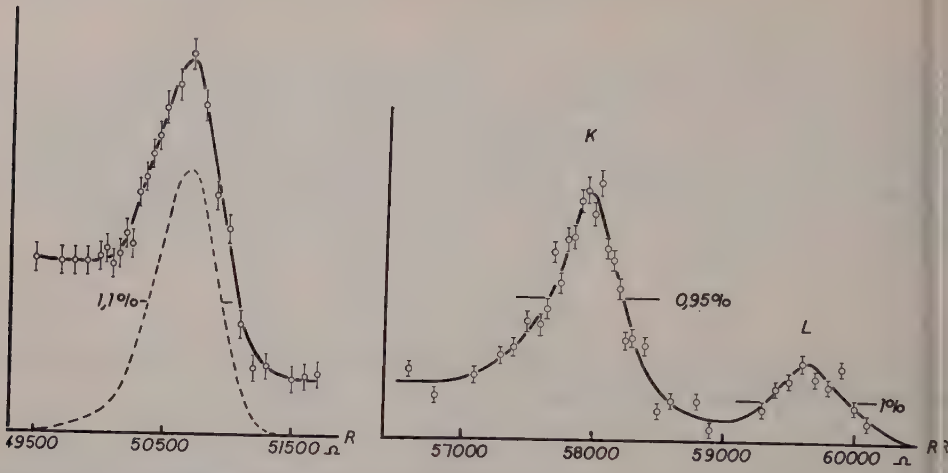

Fig. 5. The K-photo lines released in a thin lead converter by the 1.81 MeV and 2.13 MeV γ-radiations from Mn^{56}. The lines were taken with the double focusing β-spectrometer. From these lines it was found that the ratio of the intensities of the γ-lines was 1:1.

pole for the 2.13 MeV γ-line. The difficulty in resolving the rather closely spaced components in this case may, however, give rise to some uncertainty about the certainty of the multipole assignment here.

Co^{60}

Only one preliminary investigation has yet been made by us on Co^{60}. This isotope is known to disintegrate with the emission of two equally intense γ-rays of 1.17 and 1.33 MeV energy. Thus, they are both very near the threshold of the pair formation process.

The cobalt samples were prepared by electrolytic precipitation of cobalt from a solution of $CoCl_3$, containing 1.8 mg Co per ml, and having an activity of 1 mC per ml. This high specific Co activity solution was purchased from Oak Ridge.

The electrolytic solution was prepared in the following manner. Concentrated sulphuric acid was added to the $CoCl_3$-solution. The solution was evaporated, the HCl removed by heating, and after the solution had cooled down an excess of concentrated ammonia was added.[1]

The cobalt was electrodeposited on thin copper foils (2.7 mg/cm^2), made by evaporating copper onto aluminium foils. These copper foils were pressed against the lower end of a glass tube, the inner diameter of which was 6 mm. The electrolysis was performed in the container formed in this way, with the copper foil as cathode and a platinum wire at the upper end of the glass tube as anode. The current was about 1 mA flowing for 20–30 hours, and the yield of the activity 70–95 per cent.

Though our results in this case as yet are too preliminary to enable us to give any values of the pair cross sections here, Fig. 6 definitely shows that the internal positron spectrum of Co^{60} consists of *two* components with the

---

[1] This method was recommended to us by Dr. David A. Lind, Calif. Institute of Technology, Pasadena.

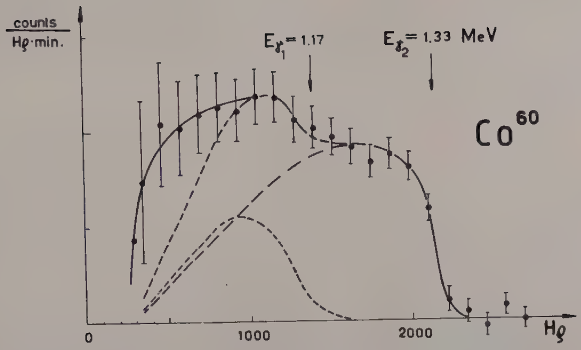

Fig. 6 Positron spectrum of Co^{60} as a function of the momentum of the positrons.

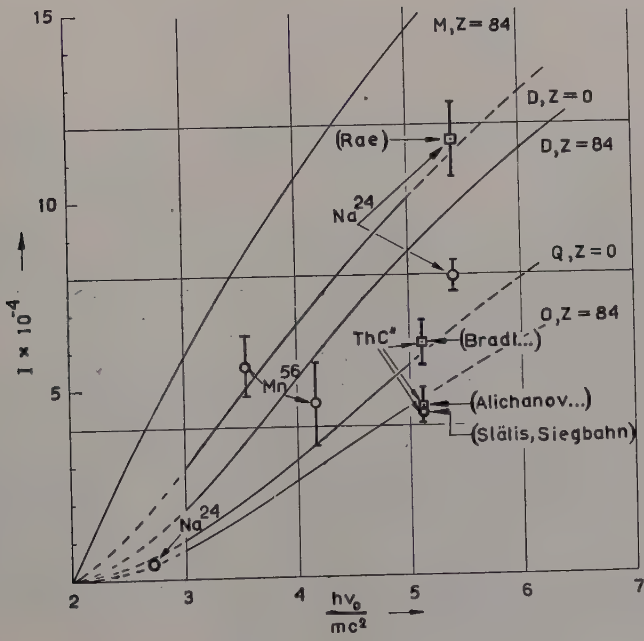

Fig. 7. The measured internal pair formation coefficients compared with the theoretical curves calculated by Jaeger and Hulme (D = electric dipole, Q = electric quadrupole radiation) and by Wang (M = magnetic dipole). Z = atomic number. The results found by Alichanov and by Rae are also marked. The value marked Bradt et al. represents an upper limit, computed by us from the data given by them.

appropriate upper energy limits, expected from the energies of the correspondin γ-rays of 1.17 and 1.33 MeV energy. It is, however, obvious that there is a unexpected surplus of low energy positrons. The true nature and origin o these low energy positrons is at the moment subject for further investigations Before this question has been solved we will not try to make any estimate o the necessary corrections in this case.

SUMMARY

1. A survey is given of the different ways in which the multipole orders o transitions may be determined.

2. Earlier measurements of positrons originating in pair creation are described

3. By the use of a β-spectrometer with high transmission (the intermediate image β-spectrometer) the internal pair formation for the γ-rays emitted in the decay of ThC″, Na^{24}, Mn^{56} and Co^{60} were investigated. The coefficients were compared with the theoretical ones of JAEGER and HULME, and the multipole orders are given (Fig. 7).

4. Some general conclusions about the metod are drawn.

Nobel Institute of Physics, Stockholm 50, Sweden.

REFERENCES. 1. **M. E. Rose, G. H. Goerzel** and **C. L. Perry,** K-Shell internal conversion coefficients. Oak Ridge National Laboratory, 1951. — 2. An excellent discussion on present internal conversion data has been given by **P. Axel** and **R. Goodrich,** Office of Naval Research, Contract N 6 ori-7 b. — 3. **F. Metzger** and **M. Deutsch,** Phys. Rev. *78*, 551, 1950. **E. Brady** and **M. Deutsch,** Phys. Rev. *78*, 558, 1950. — 4. See e.g. **L. Elliott** and **R. Bell,** Phys. Rev. *74*, 1869, 1948. — 5. **S. Devons** and **G. Lindsey,** Nature *164*, 539, 1949. **V. Rasmussen, W. Hornyak, C. Lauritsen** and **T. Lauritsen,** Phys. Rev. *77*, 617, 1949. **G. C. Phillips** and **N. P. Heydenburg,** Phys. Rev. *83*, 184, 1951. — 6. **M. E. Rose,** Phys. Rev. *76*, 678, 1949. — 7. **K. Siegbahn** and **S. du Toit,** Ark. f. Fysik *2*, 211, 1949. — 8. **I. Curie** and **F. Joliot,** Comptes Rendus *196*, 1581, 1933. — 9. **C. D. Anderson** and **S. H. Neddermeyer,** Phys. Rev. *43*, 1034, 1933. — 10. **L. Meitner** and **K. Philipp,** Naturw. *21*, 468, 1933. — 11. **J. Chadwick, P. M. S. Blackett,** and **G. P. S. Occhialini,** Proc. Roy. Soc. *144*, 235, 1934. — 12. **A. I. Alichanov** and **M. S. Kosodaev,** Z. Physik, *90*, 249, 1934.—13. **A. I. Alichanov, A. I. Alichanian** and **M. S. Kosodaev,** J. de Phys. *7*, 163, 1936. — 14. **J. C. Jaeger** and **H. R. Hulme,** Proc. Roy. Soc. *148*, 708, 1935. — 15. **A. I. Alichanov,** Bulletin de l'Academie des Sciences de l'.U.R.S.S. N 1–2, 33, 1938. — 16. **H. Bradt, J. Halter, H. G. Heine** and **P. Scherrer,** Helv. Phys. Acta, *19*, 431, 1946. — 17. **G. D. Latyshev,** Rev. Mod. Phys. *19*, 132, 1947. — 18. **E. R. Rae,** Phil. Mag. *40*, 1155, 1949. — 19. **H. Slätis** and **K. Siegbahn,** Phys. Rev. *75*, 1955, 1949. Ark. för Fysik *1*, 339, 1949. — 20. **R. D. Evans** and **R. O. Evans,** Rev. Mod. Physics, *20*, 305, 1948. — 21. Compare for instance "Nuclear Data", National Bureau of Standards, Circular 499. — 22. **M. H. Wang,** Nature *162*, 264, 1948. — 23. **A. Hedgran, K. Siegbahn** and **N. Svartholm,** Proc. Phys. Soc. *63*, 960, 1950. — 24. Compare for instance **L. E. Glendenin,** Nucleonics, *2*, 12, 1948. — 25. **K. Siegbahn** and **M. Deutsch,** Ark. f. Fysik *2*, 9, 1950. — 26. **M. A. Waggoner, M. L. Moon** and **A. Roberts,** Phys. Rev. *80*, 420, 1950.

Tryckt den 4 februari 1952

Uppsala 1952. Almqvist & Wiksells Boktryckeri AB

ARKIV FÖR FYSIK Band 4 nr 33

Communicated 6 June 1951 by Axel E. Lindh and Harald Norinder

Scintillation counters for X-rays

By Gösta Brogren and Carl-Gösta Rylander

With 3 figures in the text

Hitherto accurrate measurements of the intensity of X-rays are made mostly by means of Geiger-Müller counters and ionisation chambers. The Geiger-Müller counter has a high sensitivity in the soft X-ray region, and works as a quantum counter. If it is constructed in a suitable way, it is possible to make absolute measurements of the number of X-ray quants falling in. The instrument is, however, most fitted for rather soft X-rays. Argon-filled counters with a high efficiency can be used down to about 1 000 X.U., and those krypton-filled down to about 550 X.U. Counters for harder X-rays must be very long, and filled with gas of a rather high pressure. Their sensitivity falls rapidly with decreasing wave-length of the incident radiation. This disadvantage appears also in the above argon- and krypton counters.

However, the scintillation counters seem to offer a new possibility of constructing good detectors for X-rays. During the last year we made some preliminary experiments with such a detector by using different crystals and uncooled E.M.I. photo-multiplier tubes, type 5311. The X-rays were monochromized by a double crystal spectrometer. The Cu Kα_1, Mo Kα_1, Ag Kα_1, and Ag Kβ_1-lines were recorded both with the different scintillation counters and with a Geiger counter. The latter had a sensitive length of 100 mm, and was filled with a mixture of argon (pressure 300 mm) and alcohol vapour. The efficiencies with respect to the different lines were 50, 10, 5, and 3 per cent respectively. Naphtalene, silveractivated zinc sulphide, cadmium tungstate, and thalliumactivated sodium iodine crystals were tested. The crystals were stuck to the window of the photo-multiplier tube and covered with a thin aluminum reflector.

The naphtalene crystal was very insensitive to X-rays. No increase in the number of counts registered could be observed when it was irradiated with monochromatic Cu Kα or Mo Kα-radiation, but a slight one was recorded when the detector was placed in the direct beam from the X-ray tube. The yield was very little. Hence, naphthalene crystals are too intensitive to be suitable for this purpose.

Screens of silveractivated ZnS from different sources were prepared from small crystals and zapon, and fixed on the photomultiplier tube. The best results were obtained when using a commercial fluorescence screen (Siemens Super Astral-screen), where the thickness of the ZnS-layer was 80 mg/cm^2. The sensitivity to the Ag Kα_1- and Kβ_1-lines is rather good (see Fig. 1). ZnS, however, has some disadvantages. Big single crystals are not available, it is fluo-

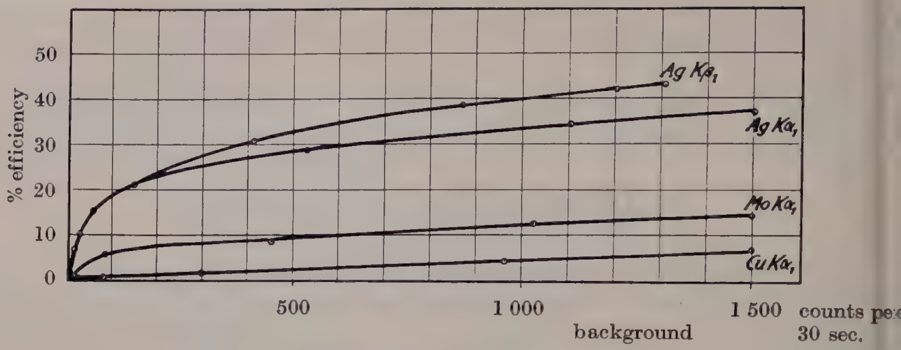

Fig. 1. The efficiency of the ZnS-counter.

rescent and is transparent to its own fluorescent radiation only if the ZnS- layer is less than 80 mg/cm^2 [1]. As appears from Table 1, 80 mg/cm^2 ZnS will absorb 96 % at 700 X.U., 70 % at 500 X.U., 45 % at 400, and 10 % at 200 X.U. Hence, it is not possible to attain a sensitive ZnS-counter for hard X-rays. When large single crystals can be obtained, it will perhaps be possible to construct more sensitive ZnS-counters.

The results with cadmium tungstate crystals are rather promising. Synthetic single crystals are available from Linde Air Products Company, Tonowanda, New York, from where we got ours. The time constant of the phosphor decay is about 0.5 microseconds, there is a peak in the emission curve at 5 300 A (under X-ray stimulation) and the crystal is nearly transparent to its own fluorescent radiation [2]. The absorption of both X-rays and gamma-rays is great because the density is high and because the crystal contains 51 per cent tungsten and 31 per cent cadmium. (See Table 2.) A disadvantage is the high refractive index ($n_D = 2.2 - 2.3$) which prevents a great part of the fluorescent radiation from leaving the crystal. A ray of light can leave the crystal only if it hits the surface under an angle of incidence that is less than the critical angle φ. For this we have $\varphi = \sin^{-1}\frac{n}{n_c}$, where n_c is the refractive index of the crystal, and n that of the surrounding medium. If we have a crystal in the form of a cube and consider light coming from a point in the crystal, only the light within a straight cone of half-angle φ can pass out through a cube-side. The solid angle subtended by a cone of half-angle φ is

Table 1.
The absorption of X-rays in ZnS.

Wave-length in X.U	72	98	130	178	200	260	417	492	613	710	1 000	1 280	1 540
μ cm^{-1}	0.9	1.2	2.0	3.7	5.3	10.6	36	61	123	172	428	172 857	284
% absorption in 80 mg/cm^2 ...	1.8	2.4	3.9	7.2	10.3	19.5	52.5	70	92	97	100	97 100	100

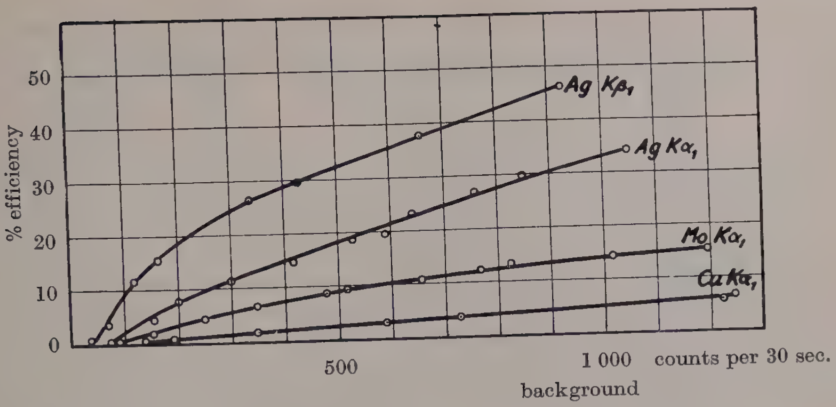

Fig. 2. The efficiency of the Cd WO_4-counter.

$2\pi(1-\cos\varphi)$. If we assume that the crystal is completely transparent, and free from scattering materials, isotropic, and has its faces optically polished, the maximum part of the fluorescent light that can escape the crystal through a cube-surface is

$$\frac{2\pi(1-\cos\varphi)}{4\pi}=\frac{1-\cos\varphi}{2}.$$

Considering a $CdWO_4$-crystal we find that, if a RCA photo multiplier type 931 A is used, where the light must pass through vacuum before it reaches the photo-cathode, only 5 per cent of the radiation can escape through the side and reach the cathode. When a photo-multiplier is used where the photo-cathode is applied direct onto the inner side of the glass wall, the crystal is cemented to the tube so that the light never passes through air or vacuum. If the refractive index of the envelope is assumed to be 1.5, 12 per cent of the fluorescent, radiation can pass to the photo-cathode. This amount can be increased by using suitable mirror arrangements.

In our case we made a rectangular parallellepiped (dimensions 5 × 5 × 12 mm) having optically polished surfaces, cemented on to the window of the photo-multiplier. In order to concentrate as much fluorescent light as possible to the

Table 2.

The absorption of X-rays in $CdWO_4$.

Wave-length in X.U.	50	64	98	130	178	200	260	417	497	631
μ cm^{-1}	3.8	6.7	13.8	26.1	53 19	28	56	193	175	351
% absorption in 3 mm	68	87	99	100	100	100	100	100	100	100
% absorption in 6 mm	90	100	100	100	100	100	100	100	100	100

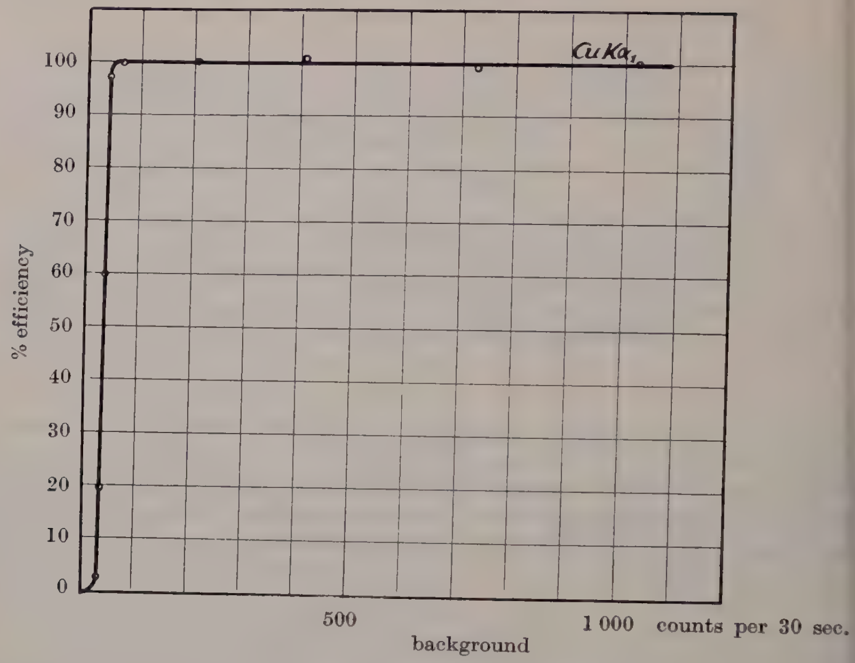

Fig. 3. The efficiency of the NaI (Tl)-counter.

photo-cathode, the crystal was covered with a hemispherical aluminum mirror, in which there was a small opening 2 × 2 mm through which the X-rays entered. The opening was covered with a thin aluminum foil, 0.01 mm thick. The sensitivity was determined as a function of the background. The results appear from Fig. 2. The efficiency is low for Cu Kα_1 even when the background is high, so it seems to be difficult to construct a good detector for that wave-length region with a $CdWO_4$-crystal. As to the other lines used, the conditions are more promising. The efficiency increases rapidly with increasing energy of the X-radiation.

It seems to be possible to construct a sensitive detector for hard X-rays by means of this crystal. The background can be reduced by cooling the photo-multiplier, but it is presumably better to work with two photo-multipliers in coincidence on the same crystal. As the time constant of the phosphor decay

Table 3.

The absorption of X-rays in NaI.

Wave-length in X.U. ...	64	98	130	178	200	374	417	497
μ cm^{-1}	3.67	4.22	8.2	16.0	45	111 20.3	29	49
% absorption in 3 mm ...	64.5	73	90	99	100	100	100	100
% absorption in 6 mm ...	87	93	99	100	100	100	100	100

s 0.5 microseconds, it is possible to have a noise level of 1 000 counts/second n each tube before the background of the coincidence circuit reaches the alue of one count a second. As appears from the figure, the sensitivity is great t such a high noise level.

In the present investigation we used a parallelepipedic crystal and an external emispherical reflector. A higher part of the fluorescent can be directed to the hoto-cathode, if aluminum is vapourised on all sides of the crystal, but for he one cemented to the tube. If the crystal is given a more convinient form, much higher percentage of the fluorescent radiation can be directed to the hoto-cathode. In this way it may be possible to obtain a high sensitivity at low background even at room temperature and without a coincidence circuit.

The last experiment was to determine the efficiency of a NaI (Tl) counter. A crystal was cleaved under oil by means of a shave-blade so that a parallelepiped, 7 × 7 × 3 mm, was obtained. A “box” with one of the sides open was made of an aluminum foil, 0.02 mm thick. Its dimensions were somewhat larger than those of the crystal. The latter was placed in the box, which was filled with oil and fixed on the top of the photo-multiplier. The box functioned as a reflector, and the oil prevented the crystal from being destroyed by the humidity in the air. The disadvantage of this arrangement was that the X-rays had to pass a thin layer of oil before they entered the crystal. The thickness of this layer was estimated to some ten microns, so its influence could be neglected.

The efficiency was 100 per cent even at normal background for all wavelengths, so we give only a diagram for the recordings with the longest wavelength used, the Cu $K\alpha_1$-line. As appears from Table 3, the absorption in a crystal, 6 mm thick, is 95 % at the K-absorption limit of uranium and 100 % from about 140 X.U. and upwards. Hence it is possible to use a NaI (Tl)-scintillation counter as an X-ray detector with a high sensitivity in the whole hard X-ray region.

We wish to express our gratitude to Professor A. E. Lindh for his kindness of placing the necessary equipment at our disposal, and to Professor P. Ohlin for valuable discussions. We are also indepted to Mr B. Åström for the loan of the NaI (Tl)-crystals.

Department of Physics, University of Uppsala, May 1951.

REFERENCES: 1. **W. H. Jordan** and **P. R. Bell,** Nucleonics *5,* N:o 4, 30, 1949. — 2. **R. H. Gilette,** Rev. Sci. Instr. *21,* 294, 1950.

Tryckt den 4 februari 1952

Uppsala 1952. Almqvist & Wiksells Boktryckeri AB

ARKIV FÖR FYSIK Band 4 nr 34

Communicated 6 June 1951 by HILDING FAXÉN

On the stress-tensor of viscous isotropic fluids

By BENGT ANDERSSON

When deducing the Navier-Stokes equations for viscous fluids, isotropic with espect to the inner friction, one assumes that the stresses are linear functions of the rate of deformation [1]. This is a hypothesis of NEWTON [2] and for a great number of fluids the equations are verified experimentally for the cases of Couette- and Poiseuille-flow (steady laminar flow between two concentric rotating cylinders and steady laminar flow through a circular pipe). In this work the author investigates, whether or not the general linearity strictly follows from the linearity in these special cases.

Let P and Q be two adjacent points in the fluid following it in the direction of flow, and $\bar\varrho = \overline{PQ}$. If $\bar u$ is the velocity vector and t is time then

$$\frac{\partial \bar\varrho}{\partial t} = \bar u(Q, t) - \bar u(P, t) \tag{1}$$

We introduce suitable coordinates x^i $(i = 1, 2, 3)$ for description of the fluid-filled part of the space. If the left and right members of eq. (1) are projected on the base-vectors at P, we get the following equality between the contravariant components:

$$\left(\frac{\partial \bar\varrho}{\partial t}\right)^i = \nabla_k u^i \varrho^k + o(\varrho) \tag{2}$$
$$= d^i_k \varrho^k + \lambda^i_k \varrho^k + o(\varrho),$$

where

$$d^i_k = \tfrac{1}{2}(\nabla_k u^i + \nabla^i u_k), \quad \lambda^i_k = \tfrac{1}{2}(\nabla_k u^i - \nabla^i u_k),$$

and all tensor components are calculated at P. When studying the immediate neighbourhood of P we may neglect the $o(\varrho)$-term in eq. (2). The term $\lambda^i_k \varrho_k$ denotes a pure rotation and the term $d^i_k \varrho^k$ can be interpreted as a superposition of extensions in three orthogonal directions, the principal directions at (P, t). The tensor d^i_k is called "the rate of deformation". If we use a cartesian coordinate-system with the axis-directions coinciding with the principal directions (here called normal coordinates at (P, t)), we get

$$d^i_k = \begin{cases} 0 & \text{if} \quad i \neq k \\ \underset{i}{d} & \text{if} \quad i = k, \ i = 1, 2, 3. \end{cases}$$

where $\underset{i}{d}$ are the roots of the equation

$$(3)\qquad \begin{gathered} d^3 - \underset{1}{D}\, d^2 + \left(\tfrac{1}{2}\underset{1}{D}^2 - \underset{2}{D}\right) d - \left(\tfrac{1}{6}\underset{1}{D}^3 - \underset{1}{D}\,\underset{2}{D} + \underset{3}{D}\right) = 0 \\ \underset{1}{D} = d^i_i = \operatorname{div} \bar{u},\ \ \underset{2}{D} = \tfrac{1}{2} d^i_j d^j_i,\ \ \underset{3}{D} = \tfrac{1}{3} d^i_j d^j_l d^l_i \end{gathered}$$

The $\underset{\nu}{D}$'s are invariant at transformations of the coordinates.

In contravariant form the equations of motion are

$$\varrho\left(\frac{\partial u^i}{\partial t} + u^j \nabla_j u^i\right) = \nabla^j p^i_j + X^i \quad (i = 1, 2, 3)$$

where ϱ is the density, p^i_k the stress-tensor, and X^i the components of the external force. Let p be the pressure that corresponds to the actual density ϱ and temperature θ and put

$$p^i_k = -p\,\delta^i_k + \gamma^i_k, \qquad \delta^i_k = \begin{cases} 0, & i \neq k \\ 1, & i = k \end{cases}$$

If the inner friction is neglected, then $\gamma^i_k \equiv 0$. A pure energy discussion gives the following expression for the dissipation function Φ:

$$\Phi = \gamma^i_j d^j_i$$

From the second law of thermodynamics follows the condition that $\Phi \geq 0$. There are three hypotheses that form the foundation of the classical theory.

A. *γ^i_k is a function of ϱ, θ and $\{d^n_m\}$ only.*

Then Φ is a function of the same variables, and after choosing normal coordinates we can write

$$\Phi = \Phi\left(\underset{1}{d}, \underset{2}{d}, \underset{3}{d}, \varrho, \theta\right)$$

and because of the isotropy Φ is a symmetric function of the d's. If all γ^i_k, and therefore Φ, are polynomials of $\{d^m_n\}$, the Φ is a polynomial of the coefficients in eq. (3) and hence a polynomial of $\underset{\nu}{D}$. From this result it readily follows that we must have

$$(4)\qquad \gamma^i_k = \psi_1\left(\underset{\nu}{D}, \varrho, \theta\right) d^i_k + \psi_2\left(\underset{\nu}{D}, \varrho, \theta\right) d^i_j d^j_k + \delta^i_k\, \psi_3\left(\underset{\nu}{D}, \varrho, \theta\right)$$

where ψ_μ are polynomials[1] of $\underset{\nu}{D}$.

---

[1] We observe that any tensor $t^i_k = d^i_{j_1} d^{j_1}_{j_2}, \ldots d^{j_{n-1}}_k$ can be written in the form

$$t^i_k = \varphi_1\left(\underset{\nu}{D}\right) d^i_k + \varphi_2\left(\underset{\nu}{D}\right) d^i_j d^j_k + \delta^i_k\, \varphi_3\left(\underset{\nu}{D}\right)$$

where φ_μ are polynomials.

From the Weierstrass approximation theorem it follows that if all γ^i_k are continuous functions of $\{d^n_m\}$, then these functions must be of the form (4) with continuous functions ψ_μ.

For the case in which γ^i_k can be developed in a power series of $\{d^n_m\}$ Truesdell [4] has stated a formula very like (4).

B. *The theory shall agree with the experimental results for Couette- and Poiseuille-flow.*

In both cases we introduce cylindrical coordinates, $x^1 = r$, $x^2 = \varphi$, $x^3 = z$ so that the z-axis coincides with the axis of the cylinders or pipes. Then it is found by experiment that

$$d^i_k = 0 \text{ if } (i, k) \neq (1, 2),\ (2, 1),\ \text{Couette-flow},$$
$$d^i_k = 0 \text{ if } (i, k) \neq (1, 3),\ (3, 1),\ \text{Poiseuille-flow},$$

and

$$\gamma^i_k = 2\,\mu\,(\varrho, \theta)\, d^i_k,$$

where μ is the "coefficient of viscosity". Here we have $\underset{1}{D} = \underset{3}{D} = 0$.

C. γ^i_k *is a linear function of the rate of deformation.*

Then eq. (4) has the form

$$\gamma^i_k = 2\,\mu\,(\varrho, \theta)\,[d^i_k + \lambda\,(\varrho, \theta)\,\delta^i_k\,\underset{1}{D}] \tag{5}$$

Putting this formula in the equations of motion we get the Navier-Stokes equations. That C does not follow immediately from A and B can be shown by examples, for instance

$$\begin{cases} \gamma^i_k = 2\,\mu\,[1 + \alpha\,|\underset{1}{D}| + \beta\,|\underset{3}{D}|]\,(d^i_k + \lambda\,\delta^i_k\,\underset{1}{D}) \\ \alpha > 0,\ \beta > 0 \end{cases}$$

which satisfies A and B, but not C and gives $\Phi \geq 0$. It seems to the author that the final step from B to C requires more knowledge of the interaction between the molecules in the fluid and it is impossible at the present time to proceed by pure macroscopic methods.

REFERENCES: [1] **Lamb.** Hydrodynamics. — [2] **Newton.** Principia II. Section IX. — [3] **Truesdell.** A new Definition of a Fluid. 7th Int. Congr. f. Appl. Mech. London 1948. Vol. 2. Part II. — [4] **L. Brillouin.** Les Tenseurs en Mécanique et en Élasticité. Masson et Cie 1938. Paris. — [5] **Levi-Civita.** Der absolute Differentialkalkül. Springer 1928, Berlin.

Tryckt den 4 februari 1952

Uppsala 1952. Almqvist & Wiksells Boktryckeri AB

ARKIV FÖR FYSIK Band 4 nr 35

Communicated 14 March 1951 by Manne Siegbahn and Bengt Edlén

Photo-electric determination of the density of tracks in nuclear emulsions

By Sten von Friesen and Krister Kristiansson

With 8 figures in the text

In the investigation of nuclear events by means of the nuclear research emulsions the determination of the number of developed grains along the tracks of ionizing particles plays an important rôle. When the ionizing power of the particles is low, the grains can be counted separately under the microscope. The grain-counting technique is by now highly developed and has been discussed by several authors[1]. The desirability of registering tracks of particles at minimum-ionization has induced Messrs Ilford and Eastman-Kodak to produce new extremely sensitive emulsions capable of satisfying this condition to the full. The high sensitivity of their emulsions causes the more heavily ionizing particles to give tracks which are so dense that the individual grains overlap, thereby making grain-counts unreliable, and in many cases impossible, in the fully developed emulsion.

One has, in certain cases, resorted to a partial development in order to facilitate the distinguishing of separate grains in the tracks of more heavily ionizing particles. This may imply, however, that low-ionization tracks are lost, making a comparative study of fast and slow particles impossible in the same emulsion.

There is also reason to believe that in the dense, fully developed tracks of the electron-sensitive emulsions, a certain variation of the density exists along the track and that there are differences between tracks from particles of different velocity and charge. Such a variation should allow us to get a relation between velocity, mass and residual range of a kind similar to the one found by means of grain counts. A photoelectric instrument has been devised and built in our laboratory for measuring track densities and has been in use for some time[2]. The aim of the present paper is to give a description of the experimental arrangements and to report on the results of measurements on plates exposed to cosmic radiation at an altitude of about 20 kms.

Experimental arrangement and method of measurement

The body tube and the eyepiece of a Leitz model BST 48 microscope have been removed and new parts have been substituted. Their construction is shown in Fig. 1. The field lens (1) of the Huyghenian eyepiece is situated immediately above a bearing (2) permitting the eyepiece to be turned around the axis of the body tube. A glass scale (3) divided at .1 mm intervals has been placed in the image plane of the field lens making possible a displacement by an accurately known amount of

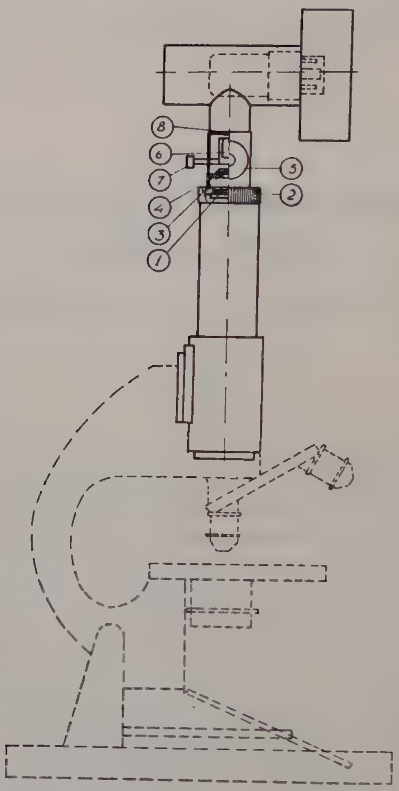

Fig. 1. Arrangement for measuring the density of tracks in nuclear emulsions.

the track under investigation. Immediately above the scale there is a removable slit (4) which, to a very good approximation has also been placed in the image plane of the field lens. A rectangular opening in the side of the tube of the eyepiece allows one to move or to replace the slit. When a track is to be measured the image is made to fall on the slit, which is then made parallel to the track by turning the eyepiece as a whole. For these adjustments the track can be viewed through the eye lens (5) in the side of the tube, by means of the mirror (6). When the image of the track has been brought to the desired position, the mirror can be removed from the beam of light by means of the pin (7). The light then passes through a diaphragm (8) on to the cathode of a photo-multiplier tube. The slit acts as a luminous object with a light density which is everywhere constant over the surface of the slit except in the region where silver grains in the emulsion give an image in the slit; in this region it is zero. The divergent light from the slit hits the cathode surface and gives an output current from the photo-multiplier tube, which decreases in proportion to the area of the slit screened by the track. When the output current has been read, the track is moved at right angles to its own direction until it is just outside the slit. A reading is now taken of the light corresponding to this region of the photographic emulsion. It is advisable to repeat this measurement

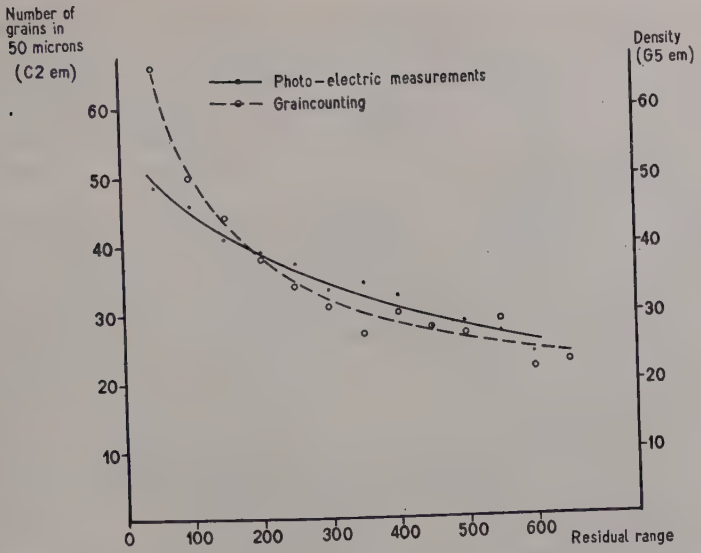

Fig. 2. Comparison between grain counting and density measurements.

with the track on the opposite side of the slit. The difference between the reading with the track in position and the mean of the background readings gives a measure of the projected area of the track, and thus a function of the grain density caused by the charged particle. The method eliminates to a great extent both background and differences in the transparency of the emulsion.

Slits of different widths have been used. The slit width was chosen with regard to the width of the track. It was found that a width corresponding to 3–4 times the width of the track is an optimum value. A more narrow slit makes the adjustments rather critical, a broader slit means a lower relative sensitivity. Measurements on tracks of mesons, protons, and heavier particles in the G5 emulsion have been made with slits .15 to .20 mms wide, which correspond to 1.5 to 2.0 microns in the object plane. The mean width of a track of a proton, near the end of its range, is about .5 microns. The most favourable length of the slit is governed by several factors. A long slit diminishes the influence of statistical variations in the grain density, and decreases the number of readings necessary to measure the whole of a track. On the other hand, a short slit must be used if the track is bent or if it dips steeply in the emulsion. In our case the slit lengths have varied between 4 and 2 mms corresponding to 40 to 20 microns of the track itself.

The light passing through the slit has been measured by means of a photo-multiplier tube RCA 1P21 at a carefully stabilized total voltage of 800 volts. The voltage fluctuations have been less than 1 volt. The dynode voltages were obtained by means of a voltage divider, consisting of ten 50 000 ohm resistors. The photo current was read on a galvanometer with a sensitivity of about 10^{-8} amps per division. A storage battery was used for the microscope lamp to avoid the fluctuations of the mains voltage.

As a first test of the performance of the new instrument about fifty tracks of different kinds of particles have been measured. The width of the slit has been

.198 mm throughout these measurements. The density has been determined a every 50 microns, and the tracks have been measured from the end of their rang to a point 1 200 microns from the end, if the track did not leave the emulsion before then. All tracks belong to four plates which were exposed together in a balloon flight that reached an altitude of about 20 kms. The plates were Ilford G5 with 200 microns emulsion. They were devloped simultaneously by means of a temperature development method.

The density of a π-meson track measured on the instrument just described has been plotted against the residual range i Fig. 2. A second curve in the same diagram shows the relation between grain density from grain counts and residua range for tracks of π-mesons in the Ilford C2 emulsion. The latter values are mean values for the π-mesons of the first determination of the ratio between the masses of π- and μ-mesons by *Lattes*, *Occhialini* and *Powell*[1]. The curves have the same general appearance, which makes us confident that determinations of the density in the manner attempted by us, can be used as a substitute for grain counts in the cases where the latter method fails. Our curve rises less steeply towards the end of the range. This may be explained by the circumstance that the denser tracks in the G5 emulsion have a higher probability for individual grains to get superimposed upon each other.

Because of small irregularities in the emulsion and statistical variations the relative deviation of the number of grains in an interval from the mean gets larger the smaller the number of grains, that is, the shorter the interval. The conditions are the same when we measure the density of a track. The shorter the interval, the more will the density vary about the mean value. In all cases we have used a slit corresponding to 30 micron intervals of the track. Intervals of that small size give variations which are relatively great, because of irregularities of the emulsion. To compensate for this as far as possible we have calculated the density in each point as the mean of the values in two or three intervals. The larger interval has been chosen in such a way as to place the point where we want to know the density as near as possible to the middle of the interval. A determination of the mean in this way gives a certain systematic error because of the curvature of the density curve. This error is very small compared to other errors because of the large radius of curvature.

Results of measurements on tracks caused by different kinds of ionizing particles

The results of measurements according to the method described in this paper on tracks of protons and mesons are given in Tables 1, 2 and 3 and in diagrams Figs. 3 and 4. The tables show the variation of the density along the individual proton and meson tracks for the last 400 microns from the ens of the track.

The total density of the last column has been used for the histogram Fig. 3. One sees from the histogram that it is possible fo distinguish with certainty between π-mesons and μ-mesons, already at 400 microns. It is not possible in this diagram to separate completely protons, deuterons and tritons. The π- and μ-mesons have been identified by means of the reactions caused in the emulsion. The two tracks in the histogram which have been marked α-particle and Li, have not been identified with complete certainty. They are too short to permit an identification by means of δ-rays. It has been found, however, that the δ-ray density was twice as high for the "Li"-track as for the "α"-track. Furthermore, the density near

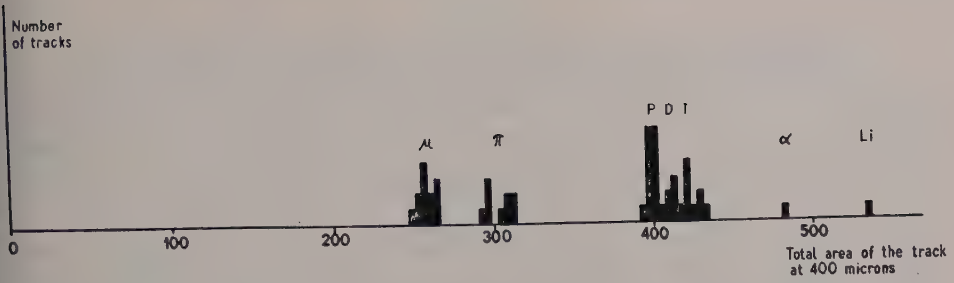

Fig. 3. Histogram of number of tracks v. total area at 400 microns. G5 emulsion.

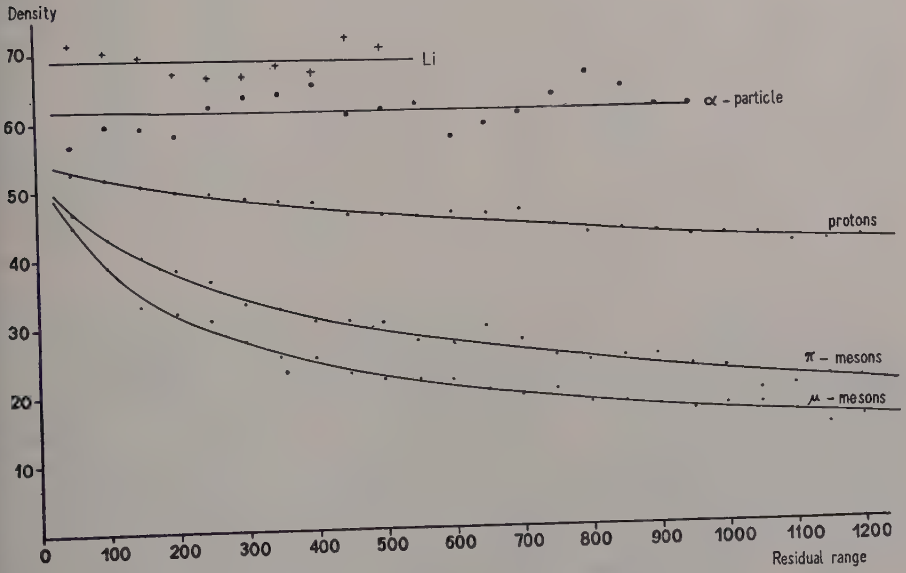

Fig. 4. Density v. residual range in G5 emulsion.

the end of the "α"-track is the same as that of several short tracks from stars, commonly believed to be caused by α-particles. These circumstances support our conjecture as to the identity of the particles in question.

Diagram 4 gives the relation between density and residual range for the groups of particles of diagram 3. The numerical values of the density give the average width of the track in hundredths of a micron.

The measured density values are to a small extent dependent upon the size of the diaphragms in the microscope, as a result of their influence upon the stray light. The diaphragms should therefore always retain the same size if comparable values are to be attained. The π- and μ-meson curves in Fig. 4 are based upon means of all the mesons that have been measured. The curve labelled "protons" has been constructed from values out of the group containing protons, deuterons

Table 1.

The variation of the density with the residual range for protons.

Particle No	Density								Total Density
	R = 50	R = 100	R = 150	R = 200	R = 250	R = 300	R = 350	R = 400	
1	56.2	51.7	50.5	47.8	47.8	45.9	46.5	46.7	393
2	52.1	51.7	51.0	52.5	47.8	44.6	46.6	49.3	396
3	50.7	51.2	48.6	48.5	50.3	51.2	49.3	46.2	396
4	48.9	49.3	49.7	49.7	50.5	50.5	49.3	49.5	397
5	50.5	52.5	51.2	50.3	49.9	50.7	47.2	44.9	397
6	51.5	51.3	46.5	48.7	50.7	49.2	49.9	49.9	398
7	52.6	54.2	54.6	51.2	47.3	46.7	46.3	45.5	398
8	52.0	52.6	53.6	51.3	48.8	46.3	47.1	47.1	399
9	55.3	51.9	50.1	48.7	48.9	49.5	46.6	47.9	399
10	56.0	52.8	51.6	50.5	48.5	46.5	45.7	47.9	400
11	51.7	50.5	49.5	50.2	51.1	49.5	49.8	48.0	400
12	50.1	52.7	51.1	51.5	51.8	48.2	46.7	49.3	401
13	52.3	49.7	50.3	45.5	50.1	52.0	52.4	48.5	401
14	51.1	52.6	49.7	48.7	46.5	50.8	53.0	53.6	406
15	53.8	54.6	53.2	52.7	51.9	48.1	46.7	47.3	408
M.V.	52.3	52.0	50.7	49.9	49.5	48.6	48.2	48.1	399

Table 2.

The variation of the density with the residual range for π-mesons.

Particle No	Density								Total Density
	R = 50	R = 100	R = 150	R = 200	R = 250	R = 300	R = 350	R = 400	
1	43.4	42.4	35.0	38.8	40.6	33.6	30.5	29.2	294
2	46.5	41.0	41.9	36.2	35.8	30.9	31.7	30.9	295
3	44.5	40.3	37.5	39.3	37.7	34.9	31.3	30.9	296
4	43.7	37.6	38.6	42.6	38.2	33.4	34.4	28.3	297
5	50.3	48.3	44.1	35.0	34.6	30.1	29.5	31.2	303
6	50.3	45.5	41.9	41.6	38.0	31.2	31.8	29.1	309
7	46.0	43.9	44.2	38.4	35.0	35.8	35.2	31.8	310
8	50.2	42.9	39.6	39.1	37.4	37.0	33.4	32.6	312
9	48.4	46.0	41.1	38.7	37.7	33.4	34.8	33.0	313
M.V.	47.0	43.1	40.4	38.9	37.2	33.4	32.5	30.8	303

and tritons. The values which have been used belong to the first maximum of this group in Fig. 3. This is the same group of values which has been used for Table 1. For the α- and the Li-curve the individual values had to be used. The deviations from the mean of the individual proton and meson tracks are of the same order of magnitude as the spread of the values around the α- and Li-curves. This can be seen from tables I, II, and III.

Table 3.

The variation of the density with the residual range for μ-mesons.

Particle No	Density								Total Density
	R = 50	R = 100	R = 150	R = 200	R = 250	R = 300	R = 350	R = 400	
1	49.7	41.0	28.1	25.0	27.5	30.0	25.3	22.9	250
2	43.8	39.4	34.2	31.9	30.7	26.4	23.0	24.0	253
3	(34.4)[1]	37.4	33.3	33.3	31.2	25.9	27.5	(31.3)[2]	254
4	44.7	36.4	31.8	32.0	31.1	27.5	25.9	25.5	255
5	47.6	39.0	34.1	32.1	28.4	26.6	23.4	23.8	255
6	42.4	40.4	35.0	31.5	30.9	27.7	25.2	23.8	257
7	45.3	38.0	32.4	33.2	29.3	29.7	27.5	23.0	258
8	44.6	39.0	30.9	34.8	36.8	26.9	24.2	22.4	259
9	44.5	41.6	30.1	31.7	27.7	26.3	28.1	29.7	260
10	46.2	35.0	32.2	32.2	31.6	32.4	31.0	24.3	265
11	45.5	44.9	38.6	30.1	36.8	27.7	18.4	22.8	265
12	40.8	36.8	37.8	37.4	29.1	26.3	28.1	29.9	266
M.V.	45.0	39.1	33.2	32.1	30.9	27.8	25.6	24.7	258

[1] Close to the glass

[2] Close to the surface

On the reliability of the method and the instrument

The same portion of a track has been measured repeatedly as test of the reliability of the measurements, without any signs of a lack of reproducibility.

An investigation has shown that there is direct proportionality between the galvanometer readings and the amount of light that hits the cathode of the photomultiplier cell. To illustrate this determinations were made in two different ways of the areas of the slits which we have used. One way has been to measure the linear dimensions of the slits, the other has been to compare the amounts of light passing the slits when they are placed in turn in their usual position in the microscope. The light flux should be proportional to the area of the slit if the light density of the light source is uniform. Table IV gives results of measurements of this kind. For both methods the area of one slit has been given the arbitrary value of 1.000 and the other areas expressed in fractions of this unit area.

The satisfactory agreement between the results shows the proportionality between the amount of light falling on the cathode and the galvanometer reading.

In measurements of the kind described in this paper it is very important, that the emulsion should have been evenly developed. A test can be made by means

Table 4.

Slit nr	Geometrically measured area	Photo-electrically measured area
1	1.000	1.000
2	1.096	1.094
3	0.583	0.583
4	0.275	0.269

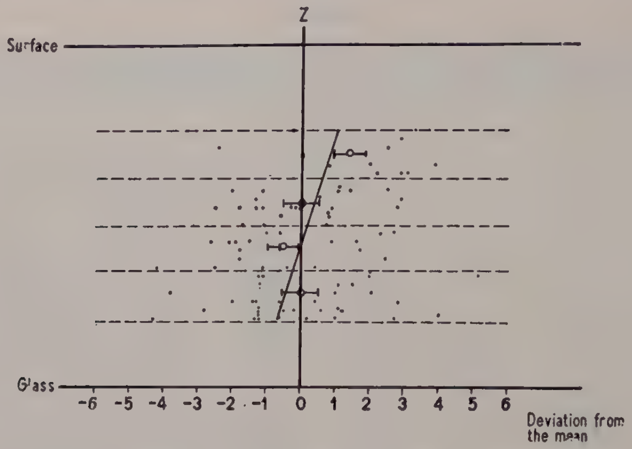

Fig. 5. Influence on track density of depth in the emulsion.

of measurements of a number of proton tracks distributed at random in the emulsion. We have taken the last 400 microns of our proton tracks and have subtracted from the density at every 50 microns in each one of the tracks the mean value for the corresponding points in all the tracks. The figures obtained in this way have been plotted in diagram 5 against the depth in the emulsion. We have used emulsions 200 microns thick, and have rejected all tracks but the ones which fall between 40 microns and 150 microns from the glass in the undeveloped emulsion. This region has been divided into four layers of equal thickness. For each one of the layers the mean value of the differences has been calculated and marked in the diagram. The variation of the density amounts to 3 % of the total density.

In diagram 6 the number of tracks has been plotted against the total projected area of the first 400 microns from the end of the track. The measured area has been corrected for the variation with the distance from the glass, which we have just mentioned. The recalculation has been made to a position of the track in the

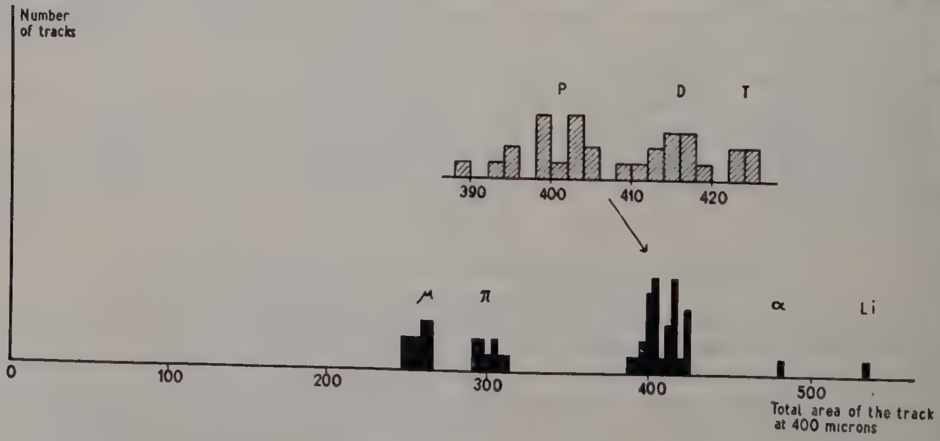

Fig. 6. Histogram fig. 3 corrected for depth in the emulsion.

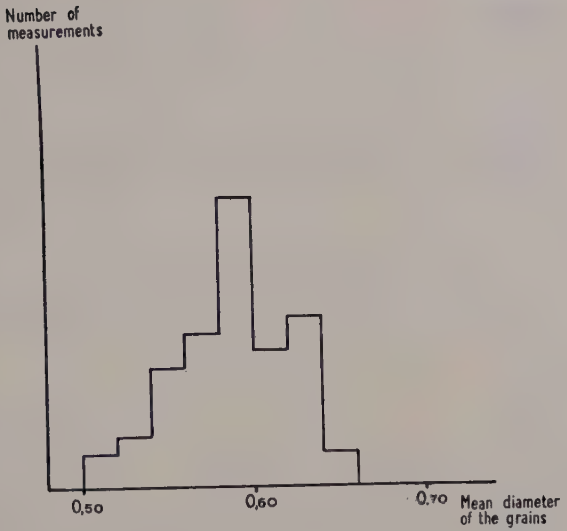

Fig. 7. Measured mean diameter of the developed grains in G5 emulsion.

middle of the emulsion. It can be seen that a tendency to a division of the proton-deuteron-triton group into subgroups which could be traced already in diagram 3, has become more marked. In diagram 6 there is an insert of the region in question at higher resolution, which shows a full separation of the tracks into three groups. We find it probable that the three groups contain on the whole, only protons, deuterons and tritons respectively. This would mean that it should be possible to tell with a fair degree of probability if a track has been caused by a proton, a deuteron or a triton, even if the track is relatively short. A prerequisite is, however, that the emulsion should have been carefully developed and that variations in density with depth should have been corrected.

Comparison between the photo-electric and the grain counting methods

If the grain density of a track in the Ilford G5 emulsion is less than about four times the density at minimum ionization we find ordinary grain counting superior to the photoelectric method, since one can count the grains in a shorter time than it takes to make a measurement. The risk of false counts then becomes rather small since the grains are far apart.

To enable us to use a relation between the grain density as expressed in grains per unit length and the density measured on the photometer we have determined the conversion factor by measuring corresponding portions of a track according to both methods. We have used the same slit for this comparison as for the measurements on meson and proton tracks. The length of the slit is 30 microns and the width 1.98 microns as measured in the object plane of the microscope. The measurements give the density in square microns, since we know the area of the slit and have found how large a portion of that area is covered by the track. A division by the number of grains has given the mean projected area of an individual

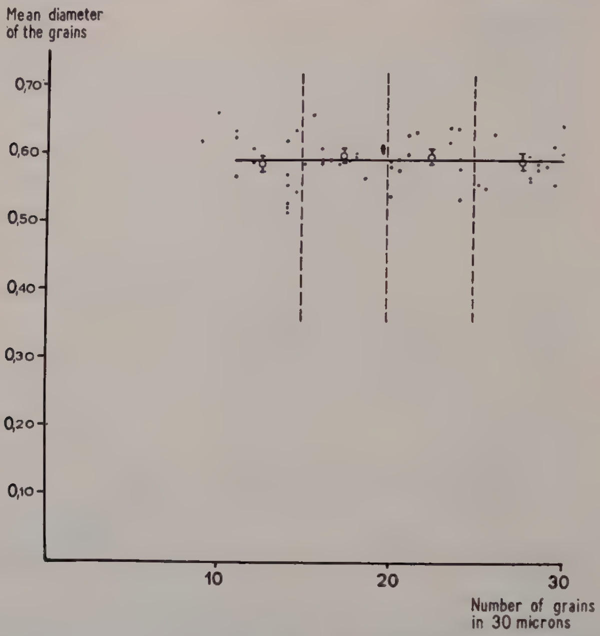

Fig. 8. Relation between diameter of the grains and grain density.

grain. When this area is known, the mean diameter of the grains may be calculated on the assumption that the cross-section of the grains is circular, which, of course, is not exactly true. The histogram Fig. 7 shows the distribution of a number of mean diameters calculated in this way. The mean diameter from all the measurements is 0.59 microns. There is a slight uncertainty about this value, as a result of the influence of the size of the apertures, which has been mentioned previously. The grain diameters given should therefore be seen only in relation to the measurements of the mean width of the tracks.

In all the density measurements reported above the results have been given as mean widths of the tracks, if their area were looked upon as evenly distributed along the total length of the slit. As the unit of track width we have chosen one hundreth of a micron. A single grain drawn out in this way to 30 microns, which is the length of the slit, corresponds to 0.910 units. We obtained this figure by dividing the mean area of the grains 0.273 square microns by the length of the slit 30 microns and multiplying by 100. When the conversion factor is known any number of grains can be converted to units of track density. We have performed the conversion for tracks of a particle causing minimum ionization. Such tracks give in our case 20 grains per 100 microns of track length. This represents a density of $\frac{20}{100} \cdot 30 \cdot 0.910 \simeq 5.5$ units.

In order to find out whether the size of the developed grains depends upon the grain density a comparison has been made between grains from tracks of different grain density. In Fig. 8 the measured mean diameter of the grains has been plotted against the total number of grains in the opening of the slit. 58 measurements of this kind ave been made and the results were divided into four groups according to the rain density. The groups have been shown in the diagram by means of dotted ines. For each group the mean diameter has been found. The four groups give ractically the same mean value. It can thus be said that in this region the grain ensity does not influence the size of the grains. Once a grain of silver bromide as been made developable by some ionizing process a complete development will ake place of the whole grain, independent of the amount of a possible surplus onization.

REFERENCES. 1. **Lattes, Occhialini** and **Powell,** Proc. Phys. Soc. *61,* 173, 1948. — 2. **v. Friesen** and **Kristiansson,** Nature *166,* 686, 1950.

Tryckt den 4 februari 1952

Uppsala 1952. Almqvist & Wiksells Boktryckeri AB

ARKIV FÖR FYSIK Band 4 nr 36

Communicated 12 September 1951 by ARNE WESTGREN and AXEL E. LINDH.

A large bent crystal vacuum spectrograph

By ARNE ELD SANDSTRÖM

With 13 figures in the text

Introduction

The decade 1930—40 saw the development of two new types of X-ray spectrographs, the double crystal instrument introduced in 1927 by EHRENBERG and MARK[1], and the bent crystal spectrograph first described in 1931 by JOHANN[2]. In 1932 CAUCHOIS[3] adapted the second type for short wave-length X-rays by using the crystal as a sort of cylindrical transmission grating. As early as 1933 instruments of the Johann as well as of the Cauchois type were designed and built in Siegbahn's laboratory at Uppsala.[4] During the following years the bent crystal spectrographs were developed in several European laboratories while the double crystal spectrometers became almost an American monopoly. In Uppsala spectrographs of the Johann type were designed by SANDSTRÖM[5], HAGLUND[6], OHLIN[7], SANNER[8], and FLEMBERG[9]. In 1933 JOHANSSON[10] published a very interesting instrument utilizing a crystal, first ground to a certain radius and then bent to half that radius. Unknown to Johansson the geometry of such an instrument had already been indicated by DU MOND[11].

The early bent crystal spectrographs were adapted for photographic recording on film, the curvatures of the instruments being small. Sandström used an arrangement (never published), where glass plates were placed tangentially to the "Rowland" circle. In this case plate-holder and crystal were adjusted for the right Bragg angle by means of circular scales while the distance between plate and crystal was varied by sliding the plate-holder along a pair of guides. Similar arrangements were employed by HAGLUND[6] and OHLIN[7]. The latter recorded his spectrograms by means of a slit and counter, which could be displaced along a tangent to the "Rowland" circle.

The solving of many present day problems in X-ray spectroscopy demands instruments with a high resolving power readily adapted to record small intensities. As in this respect the bent crystal spectrographs answer the purpose, a new large instrument of that kind was built, making use of all the experience gathered from the early types. As at present the long wave-length region is the most interesting, especially as regards solid state physics, the spectrograph was designed for use in a high vacuum.

The geometry and the main features of the spectrograph

When recording a spectrum by means of a counter a finit wave-length region enters the counter through a slit parallel to the spectral lines. Evidently, there are certain advantages to a system, where the scanning of the spectrum can be done along a straight line without sacrificing the focussing as will happen, when the slit is being moved along a tangent to the "Rowland" circle. In the latter case only very narrow wave-length regions can be covered without resetting and re-adjusting crystal and counter. The problem can be solved in the following way:

The distance from the slit to the middle of the crystal constitutes a chord in the "Rowland" circle. The length of this chord will vary but its direction can be fixed if the crystal is mounted in such a way that it can be rotated around an axis perpendicular to the plane of the "Rowland" circle. Naturally, this axis has to intersect the "Rowland" circle in its point of tangency with the reflecting surface of the crystal. For convenience the rotation ought to be automatically coupled to the displacement of slit and counter. This can be attained by employing a lever system like that, which for a long time has been used when mounting concave gratings.[12] The geometry of the arrangement follows from Fig. 1.

Let R be the radius of the bent crystal, d_n the lattice constant in the n:th order, φ the Bragg angle, and λ the wave-length. According to Bragg's law and Fig. 1, we have

$$n \cdot \lambda = 2\, d_n \sin \varphi \tag{1}$$

$$x = R - R \sin \varphi \tag{2}$$

x is the difference between the diameter R of the "Rowland" circle and the chord AB. It is also the displacement of the point B, when the chord AB is shortened by the rectilinear shifting of B in the direction of A. Eliminating φ we have:

$$\lambda = \frac{2\, d_n}{n} - \frac{2\, d_n}{n \cdot R} \cdot x \tag{3}$$

According to this equation the wave-length is a linear function of the displacement x, the dispersion being

$$\frac{2\, d_n}{n \cdot R} \tag{4}$$

This is very convenient as good reference-lines are scarce in the X-ray region and the instrument necessarily has to be adapted for relative measurements.

The main features of the instrument follow from Fig. 1. A represents the axis of rotation of the crystal, B an axis coincident with the slit in front of the counter. AC and BC are two levers of equal length, R/2, and turning on a common axis in C. The lever AC has to be perpendicular to the reflecting surface of the crystal and rigidly fixed to its axis of rotation. The levers are, in all positions, radii of the "Rowland" circle. When the slit is displaced along the chord AB, the lever combination turns the crystal in such a direction as to allow eqs (1) and (2) to be satisfied for every position of the system. As an additional condition of focussing a wave-length on the slit the beam from the X-ray tube has to strike the crystal surface under the corresponding Bragg angle. For this purpose it will be most con-

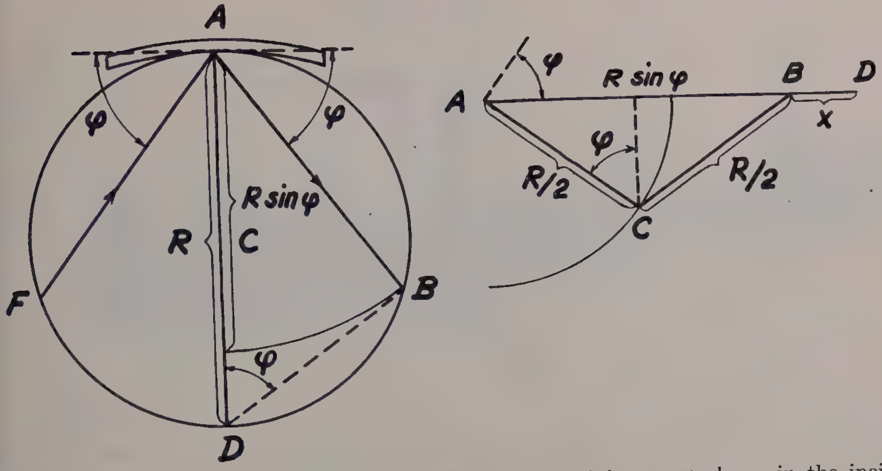

Fig. 1. The geometrical principles of the spectrograph. FA is a central ray in the incident X-ray beam. B is the focus point of a wave-lengt λ, D the focus point when $\varphi = 90°$. C is the center of the "Rowland" circle.

venient to mount the X-ray tube coaxially with the crystal, although this makes the instrument more complicated.

For accurate measurements the point B (representing the slit in front of the counter) has to be moved by means of a precision screw. However, it is inconvenient to make a precision screw long enough to cover the whole angular region. This difficulty can be circumvented by making the support of the axis A mobile, which is done by introducing another screw covering the whole region. The pitch of this slave-screw can be fairly high as, in this case, precision is unessential. Naturally, A will be kept in a fixed position while a spectrum is being recorded.

The spectrograph

In the following description of the spectrograph the photographs should be compared with the drawn figures. The same number always indicates the same detail regardless of the figure, in which it appears.

The two axes A and B (Fig. 1) have to be as rigidly supported as possible. Likewise, the lever system must not be subjected to distorting forces. From both these reasons the levers ought to move in a vertical plane. Accordingly, the beam of steel *1* (Fig. 3), forming the base of the spectrograph, was given a cross section like that in Fig. 2. Two [-beams were welded together at both ends leaving an open slit, *2*, allowing the levers a free passage. The base is strengthened by cross-pieces, which are indicated in Fig. 2 and can be easily recognized in the side view of the instrument (Fig. 3). They are unevenly distributed to prevent, as far as possible, resonant vibrations. Fig. 2 gives some of the dimensions of the base. It is 240 cm in length. At one end it rests on a conical foot *4* and at the other end on a cross beam *3* with two adjusting screws for a proper levelling of its upper plane. Along its whole length this plane has been cut off on one side to allow more space to the X-ray tube and other equipment.

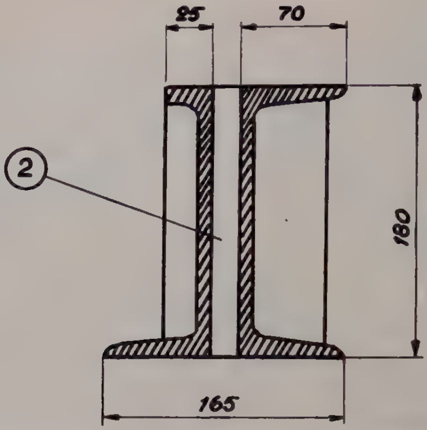

Fig. 2. Cross-section of the spectrograph base. The dimensions are in millimeters. The width of the opening *2* is 25 mm.

The two axes *A* and *B* (Fig. 1) of the lever system rest on slide bearings in the supports *5* and *8* respectively (Fig. 3 and 4). These supports are mounted on sliding-tables (*40* in Fig. 5), which can be displaced along parallel pairs of steel guides. The guides carrying the support *5* are precision ground and form the lower part of a contraption *6* consisting of two brass end plates kept together by four steel rods. This contraption is adjustably mounted on the base *1*.

The table carrying the other support *8* can slide along another pair of steel bars which are fixed to the base *1*. The tables of both supports, *5* and *8*, are worked by screws, *5* by a precision screw with a pitch of 1 mm, *8* by a square-thread slave-screw with a pitch of 6 mm. Both screws are supported by bearings mounted directly on the base. One of the pivots of the precision screw extends through a hole in the end-plate *15* and overreaches also the end of the base. It carries the wheel *12* of a worm-gear. *13* indicates the tangent screw of this gear. On the front of the wheel is a scale allowing the position of the support *5* to be read to 10^{-3} mm. *11* is a small bulb illuminating the scale with its vernier. A displacement of more than one millimeter is read on a scale fixed to the table *40*. This scale is also illuminated by a small bulb and its image projected on to a semi-transparent screen with an index. In Fig. 3 the wiring of all scale bulbs appears as an irregular white line. The two levers are indicated by *9*. They are coupled through a sort of elbow-joint *10*, corresponding to the point *C* in the right part of Fig. 1. As both levers have to be of the same length, this elbow-joint is adjustably connected to the rods. A detailed description seems unneccessary as this part is comparatively simple. The details are illustrated by the upper half of Fig. 8. A skew side view of the contraption *6* is displayed in the upper half of Fig. 4. The lower half offers a bird's-eye view of the support *5* with the slit-holder *22*, and a small bracket *25* on which the counter is to be mounted.

To allow a free movement of the lever *9*, when in a nearly horisontal position, the end-plate *15* has an opening exactly fitting the slit *2* of the base *1*. Part of the lever (here indicated by *16*) is visible. It is in a position showing that another slit had to be cut in the sliding-table *40* to ensure the use of the instrument down to Bragg angles of 35°. *17* is one of the precision ground steel rods. To prevent these

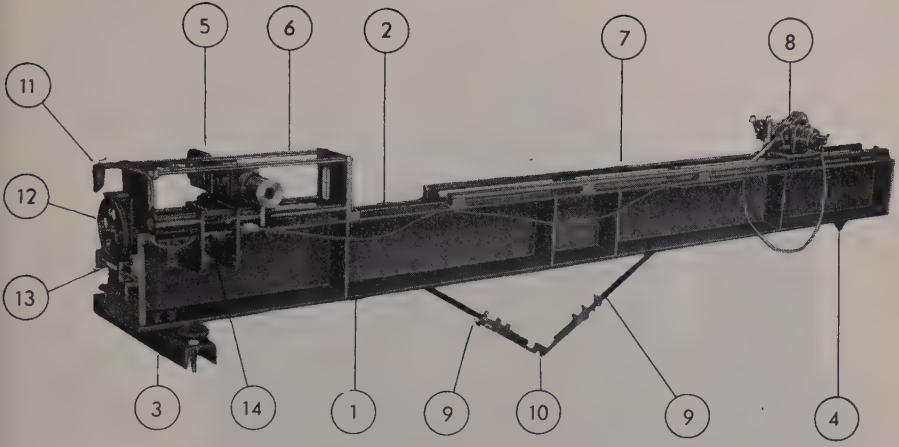

Fig. 3. The spectrograph removed from its place inside the vacuum tank.

rods from bending under the wheight of all the appliances most of the pressure is unloaded by a couple of small bogies *18*, running directly on the base. Small roller bearings are employed as wheels. Each bogie supports the table through four springs.

The supports *5* and *8* are mounted on their sliding-tables in such a way as to enable the axes *A* and *B* (Fig. 1) to be adjusted in parallel and perpendicular to the plane on the lever system. They can be turned a small angle around the screw *48* (Fig. 5) by means of two short adjusting screws acting upon the other end of the support. One of these screws is indicated by *45* in Fig. 6. When finally adjusted the support will be clamped into position by means of the screw *48* and, in the other end of the support, by two other screws, one on each side of the axis.

The axis *19*, corresponding to *B* in Fig. 1, rests in two close-fitting slide bearings. It is fixed in its longitudinal direction by a thrust bearing *50* in the cylindrical part *20* of the support. Ordinarily this axis is only a part of the lever system and does not carry any other movable parts. Nevertheless, it is an exact twin of the axis carrying the crystal holder. Thus, one end of it is formed into a female cone enabling us to mount adjusting appliances on cones and, if need be, to clamp them to the axis. In the same way a plate holder can be affixed to the axis, should photographic recording become necessary. For evacuation purposes a couple of holes *51* have been drilled in each axis to serve in cases when their axial borings are closed at both ends. *52* indicates the slit-ring attaching the lever *9* to its axis *19*.

21 is a cross-table carrying the slit-holder *22*. It is rigidly mounted on one end of the support as shown in Fig. 5. The brass cylinder *49* serves as a link allowing free space for the motion of the end of axis *19*. A couple of brackets (*58* in Fig. 5) attach the slit-holder at right angles to the cross-table. The two halfs of this table can be displaced by means of screws having a pitch of 0.5 mm. This affords us the possibility to bring the slit to coincide with the axis of rotation of the lever *16*. The slit-holder has a sliding part *53* (compare Fig. 5) making it possible to displace the slit parallel to the lever axis (*B* in Fig. 1). This is done by means of another screw *23*, also with a pitch of 0.5 mm. For the complete adjustment of the

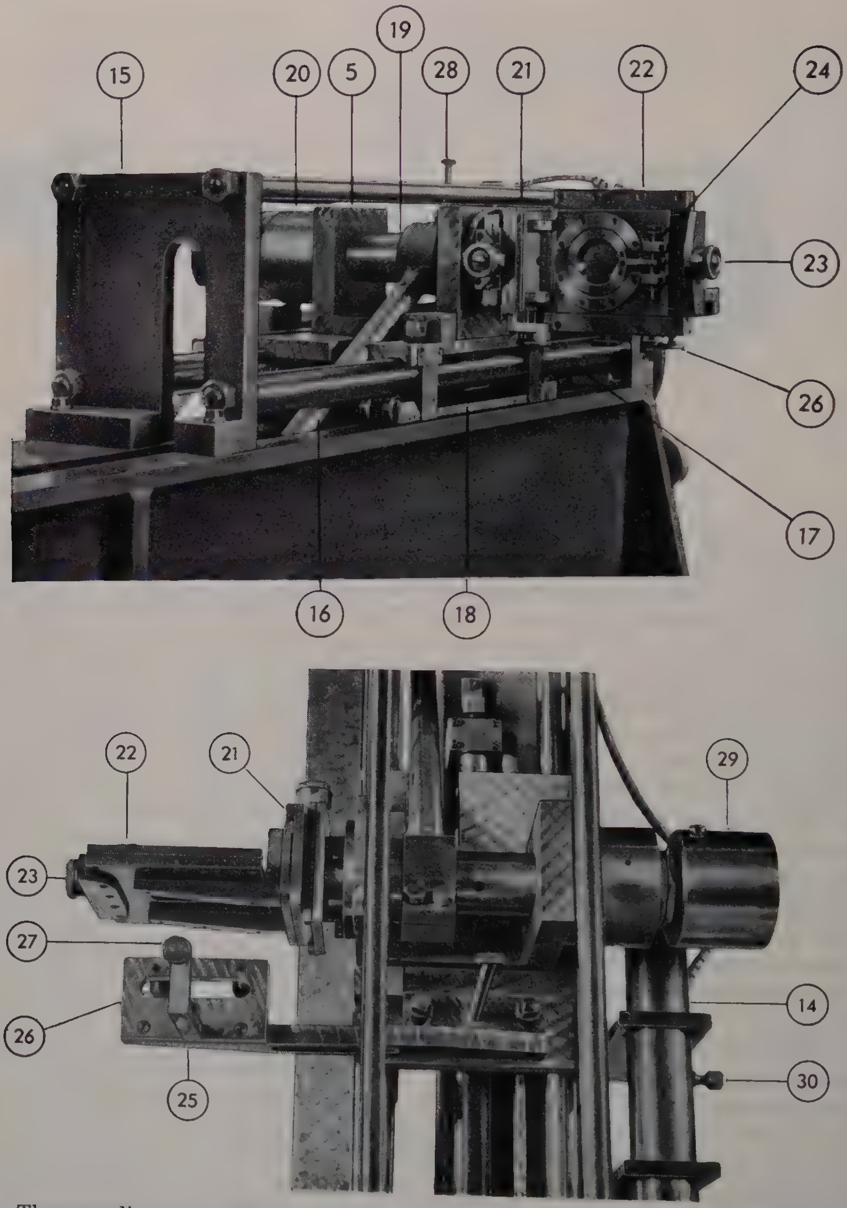

Fig. 4. The recording part of the spectrograph. Above is a side view displaying most of the details; below is a birds-eye wiew of the central part with the lever on its axle, the slit-holder, and the bracket on which the counter is to be mounted.

slit parallel to all the three lever axis we have to be able to rotate the slit around an axis perpendicular to its plane. Therefore the slit *56* is mounted in a frame *54*, fitting a circular aperture in the slide *53*. This frame can be rotated a small

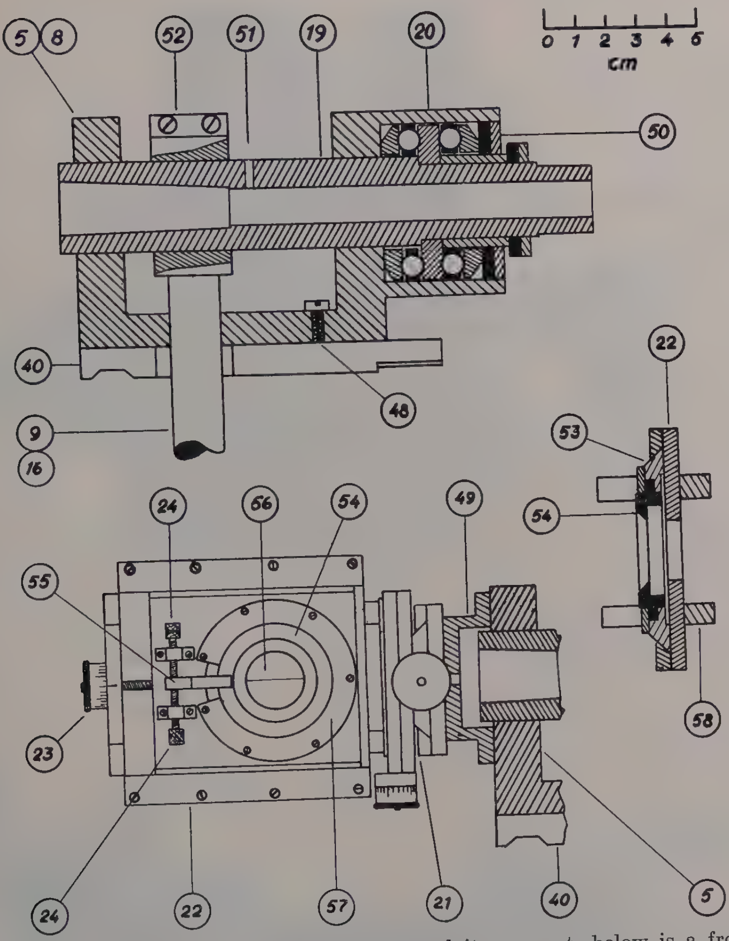

Fig. 5. Above is a cross-section of a lever axle and its support; below is a frontal view of the slit-holder with the slit and a cross-section of its union with the lever support. To the right is a cross-section through the central part of the slit-holder.

angle by means of a short lever *55*, and two screws *24*. The slit itself is of a kind which for a long time has been used in X-ray technique.[13] When changing the slit width or if otherwise needed the frame with the slit can be removed as a whole by the unscrewing of the ring *57*.

Behind the slit-holder is the bracket *25* for the counter. By means of three screws, one of them indicated by *26*, the counter is adjusted to the right height as regards the slit, whereafter it will be locked in position through a fourth screw *27*.

Some other details are to be noted in the lower part of Fig. 4. *29* is a leaden weight in a brass casing balancing the load of counter and slit-holder. Below this weight we have the mirror-lens appliance *14* for the projection of the scale, mentioned above. *30* indicates a screw with which the lens can be focussed and clamped. Part of the precision screw appears underneath the sliding-table. In the up-

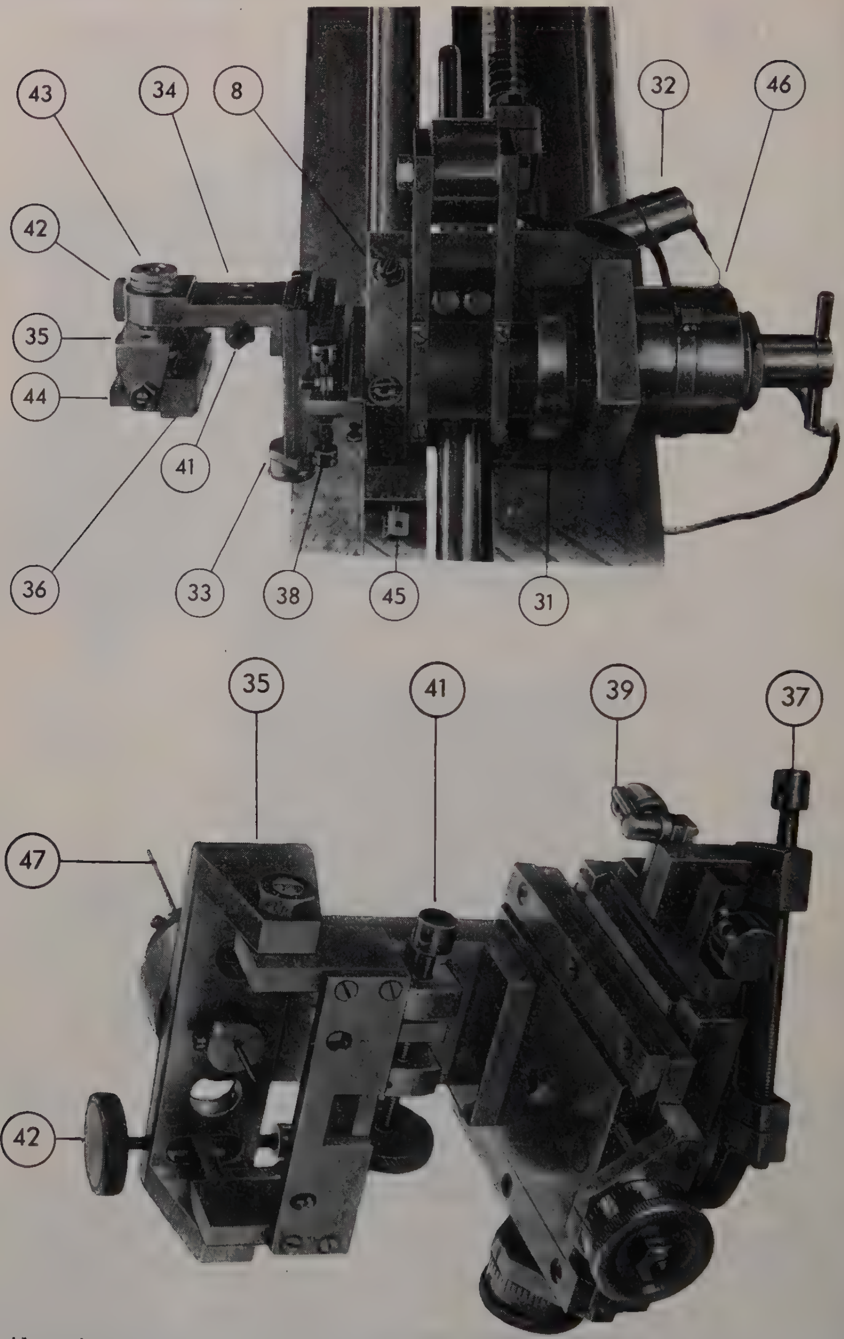

Fig. 6. Above is a birds-eye view of the support carrying the lever axle of the crystal-holder. Below is a close-up displaying more details as regards the appliances for mounting and adjusting the crystal.

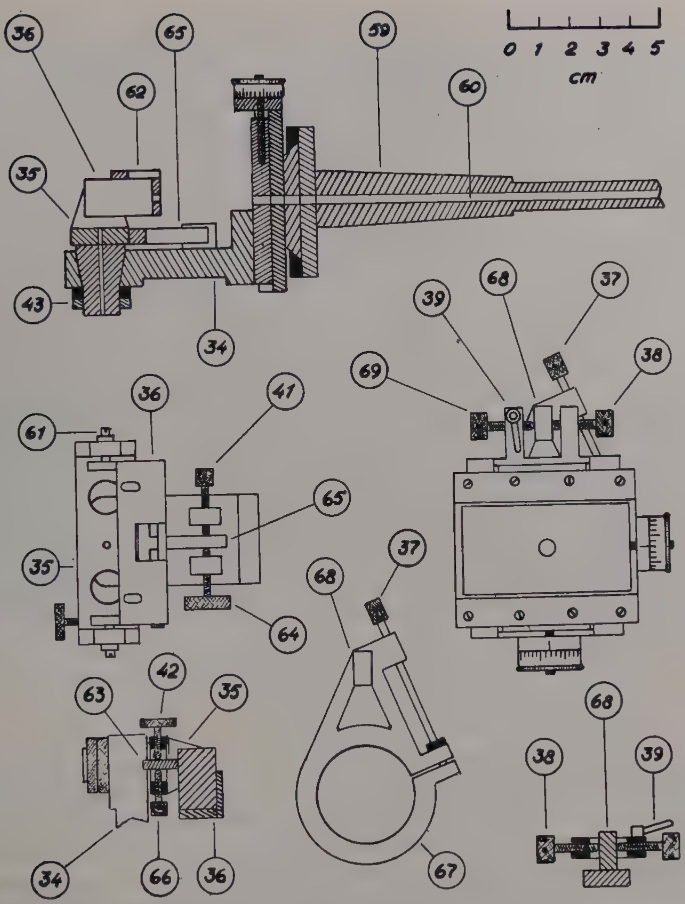

Fig. 7. Details of the appliances for mounting and adjusting the crystal-holder. The cross-section in the lower left corner is supposed to be through one end of the cradle *34*.

per edge of the figure one of the bearings is barely visible below the cross head keeping the screw in its right longitudinal position.

The coaxial cable to the counter is supported by a small rod indicated by *28* in the upper photograph but also clearly visible in the bird's-eye view below.

The two photographs in Fig. 6 show some details of the support *8* which carries the axle with the crystal holder. Still more details may be gathered from Fig. 7. The construction of this support with its sliding-table, axle, and bearings is in every detail like that of the first one. The displacement of the table along the steel guides *7* is read on a small circular scale *31*. The scale can be illuminated by a small bulb *32* in a holder clamped to the cylindrical box *46* of the thrust bearing.

The cross-table *33* carrying the crystal holder is mounted on a cone *59* which fits the female cone in the end of the tubular axes. A long rod extends from the male cone and projects at the other end of the axis where it carries a wing-nut. The cone is securely clamped to the axle by means of this nut.

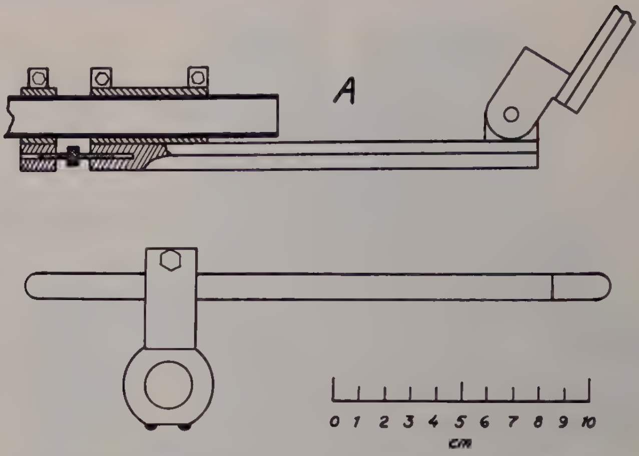

Fig. 8. *A* is the adjustable joint between one of the lever rods and the precision pivot uniting the two levers. *B* is the nut and rod driving the trolley with the X-ray tube. The nut travels along the plane of the spectrograph base on four small balls. Two of these balls are indicated in the figure.

The upper slide of the cross-table carries a column *34* with rectangular cross section. The column has a conical hole in which a cone fits carrying the yoke *35*. The cone is kept in position by a spring lock with two nuts *43*. The construction of the yoke is easily understood from Figs. 6 and 7. In the yoke hangs a cradle *36*, mounted between two pivots *61*, allowing it to be rotated a small angle around an imaginary axis approximately tangential to the crystal surface. The small contraption *44* in which the crystal is placed and bent, is placed in the cradle and clamped to its frontal plate *62* by means of two screws. The upper half of the frontal plate has been cut off to allow the X-rays a free passage. The position of the cradle is controlled by means of a short lever *63*, passing through a slit in the yoke. The lever is held in position between two screws *42* and *66*. By loosening one of them the other one can be used for adjusting the generatrices of the crystal surface parallel with a plane through the axis *A* (Fig. 1).

To adjust the generatrices parallel to the axle of rotation we have to be able to rotate the yoke around the perpendicle to the crystal surface in its center. Accordingly there is a lever *65* attached to the yoke also. This lever runs down between two screws *41* and *64* on the column *34*. One of them, *64*, is employed for the actual setting while the other one, *41*, will be used only for the secure clamping of the lever, the adjusting of screw *64* being counteracted by a spring.

From Fig. 1 follows that it is essential that the crystal is adjusted with the perpendicle to its center parallel to the lever controlling its position. This is attained by turning the cone of the cross-table *33 in situ*. For this purpose a circular frame *67* is placed on the end of the axle. This frame can be locked in position by means of a screw *37* which extends beyond the cross-table. The frame carries an arm with a perpendicular cross piece *68* which enters between the two branches of a yoke fixed to the cross-table. Each branch has an adjusting screw *38* and *69*, making it possible to rotate the crystal holder a small angle in both directions. As soon as the crystal is finally adjusted one of these screws *69* will be clamped by means of another small screw *39* which acts upon the nut of *69*. This arrangement enables

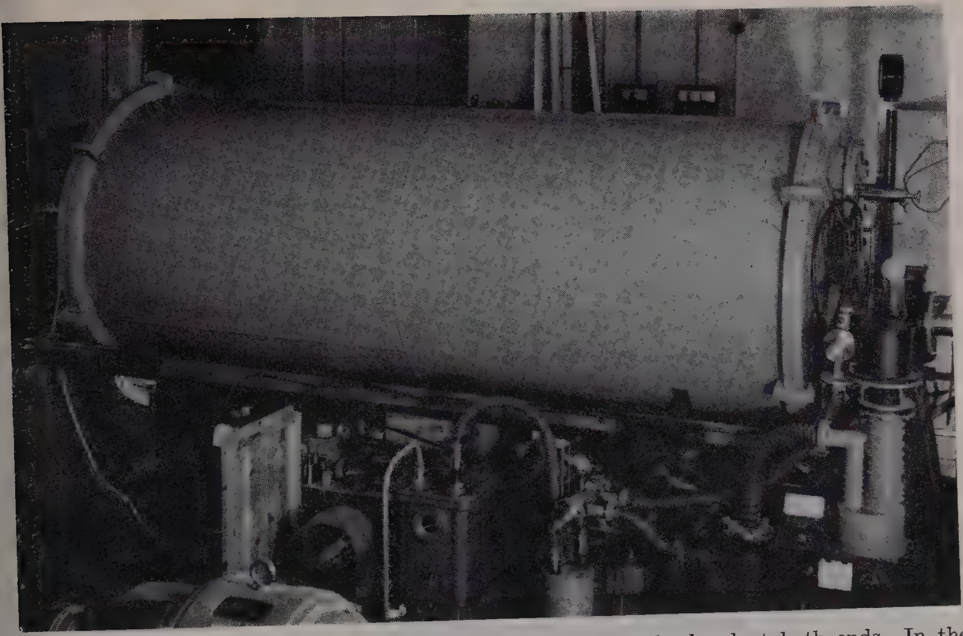

Fig. 9. The spectrograph as it appears with the vacuum tank closed at both ends. In the foreground is the evacuation system, consisting of a backing pump, a booster pump, and a high vacuum pump VMF 260.

us to remove the cone with cross-table and crystal holder, and bring it back again into its original position without seriously damaging the adjustment. All the adjusting screws have a pitch of 0.5 mm.

The crystal holder proper, which constitutes the small apparatus *44* for the bending of the crystal, is of a type designed by JOHANSSON.[10] A complete description will be found in his paper and, accordingly, only a few details are given here. The steel block is, in the present case, 45 × 30 mm with a thickness in the center of 9 mm. It is precision ground to a radius of 2000 mm, the ground surface being 45 × 24 mm. The small window giving the X-ray beam access to the reflecting surface of the crystal is 20 mm long and has a height of 2 mm. The window widens to the front allowing Bragg angles down to 30°.

The vacuum tank

Fig. 9 illustrates the exterior of the vacuum tank. It is cylindrical with an internal length of 250 cm and a diameter of 100 cm. It is closed at both ends by plane steel plates strengthened with radially arranged braces (Fig. 10). The cylinder rests on a rigid structure consisting of two steel plates 30 cm from each end and straightened by steel rods. This support is also being used for the mounting of such auxiliary equipment as the vacuum pumps.

Small lugs are welded on to the wall at each end of the cylinder. These lugs carry two horisontal steel beams which support the spectrograph. The position of

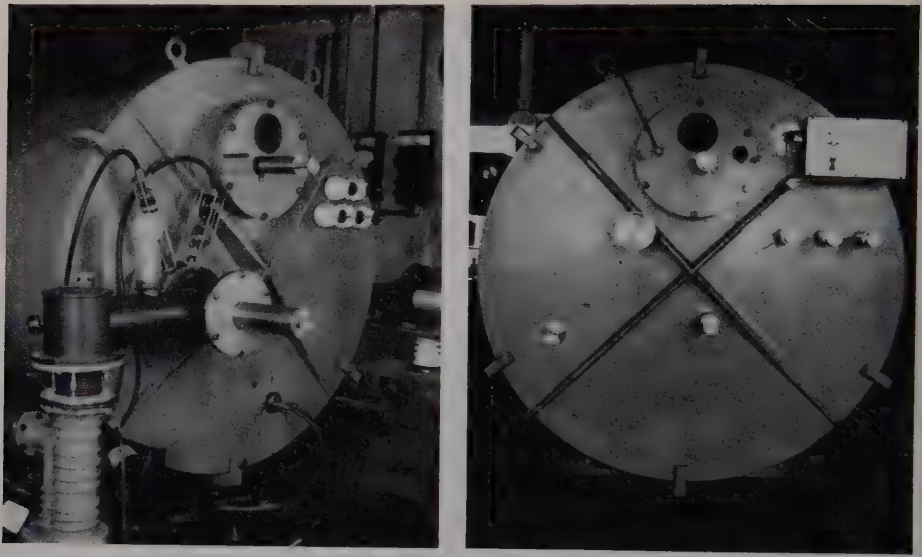

Fig. 10. The two end-plates of the spectrograph tank. In the *rear* end (to the left) a big valve connects the tank with the evacuation system. At the bottom of the figure are two flexible pipes for the water cooling of the X-ray tube. Five insulated conductors and a manipulator for the slave-screw are also mounted on this end-plate. The *fore* end (to the right) mounts six manipulators for the movable parts of the spectrograph as well as three insulated conductors.

the beams can be changed to some extent, thus making the mounting of the spectrograph more flexible. Although the weight of the large instrument keeps it fairly well in position it is necessary, from reasons of adjustment, to have some means of fixing its position. Therefore a small rod runs through a small hole in the cross beam *3* (Fig. 3) and, also, through another hole in the cross beam of the vacuum tank.

The tank cylinder is intact, the end plates (Fig. 10) carrying all the equipment for manipulating the instrument. In the top quadrant both end-plates have collars with covers having glass-windows. All the spectrograph scales can be read through these windows. Each cover has also a manipulator for the screws, the slave screw being turned from the rear (to the left in Fig. 10) and the precision screw from the front (to the right in Fig. 10). The rear end-plate also has a collar for the union of the tank with the evacuation system.

The fore end has five more manipulators. The one in the bottom quadrant releases the tangent from the worm wheel of the precision screw. One of the three manipulators to the right acts upon the tangent screw. The other two are employed for a shutter and for the shifting of diaphragms. To the left is a manipulator with a large drum. It is driving a sliding axle inside the tank making it possible to turn the X-ray tube from the outside. Inside the tank the manipulators are connected with the movable parts of the spectrograph either by means of universal knots or by flexible axles.

The square box contains a Neher-Pickering circuit for the counter. In the opposite direction is an insulated rod for carrying large currents when an evaporation

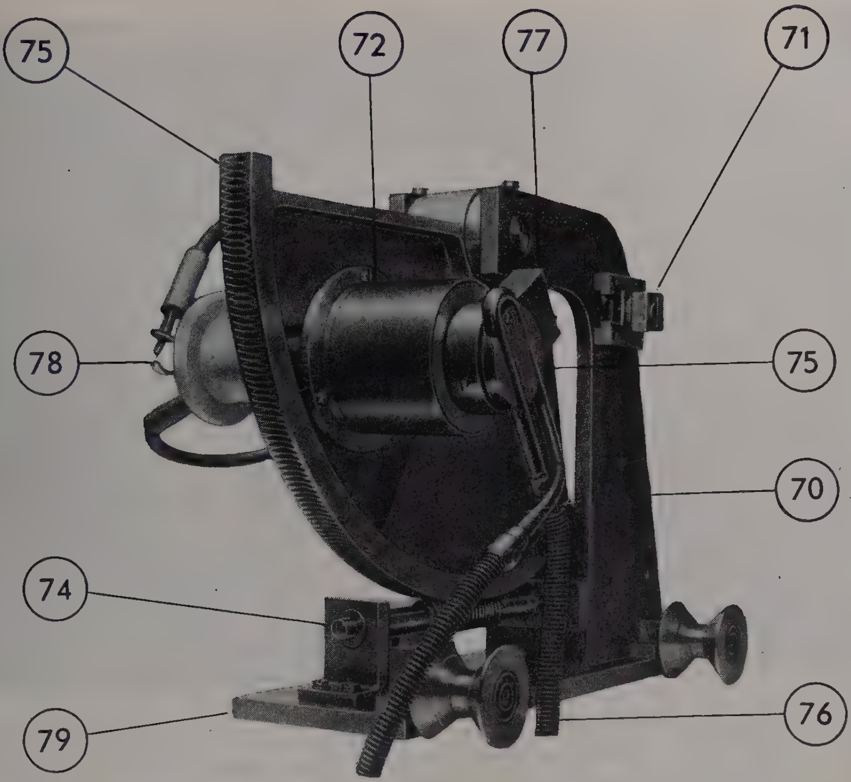

Fig. 11. The X-ray tube mounted on a trolley with a davit.

furnace is employed inside the tank. The power for the scale bulbs is carried by a small insulated conductor through the cover on the collar of the fore end-plate.

The X-ray tube

The diametrically mounted beams in the tank also serve the purpose to carry two parallel stainless steel tubes forming a track for a trolley with the X-ray tube. In Fig. 12 the track can be seen alongside the spectrograph.

As has been pointed out already, the X-ray tube has to move coaxially with the crystal. Accordingly, when the crystal is displaced along the base of the spectrograph, the trolley with the X-ray tube has to be shifted the same distance. This is engineered by an extra nut on the slave-screw placed behind the sliding-table. This nut carries a long rod with a flattened end fitting into a kind of fork *71* on the davit *70* (Fig. 11). The functioning of this arrangement will be clear from Fig. 12 compared with Fig. 8 where the nut is illustrated with its rod. Using a separate nut for its displacement prevents the comparatively heavy trolley, *79*, from interfering with the proper setting of the crystal holder.

The X-ray tube *72* is mounted as shown by Fig. 11. *73* is a sector of a worm

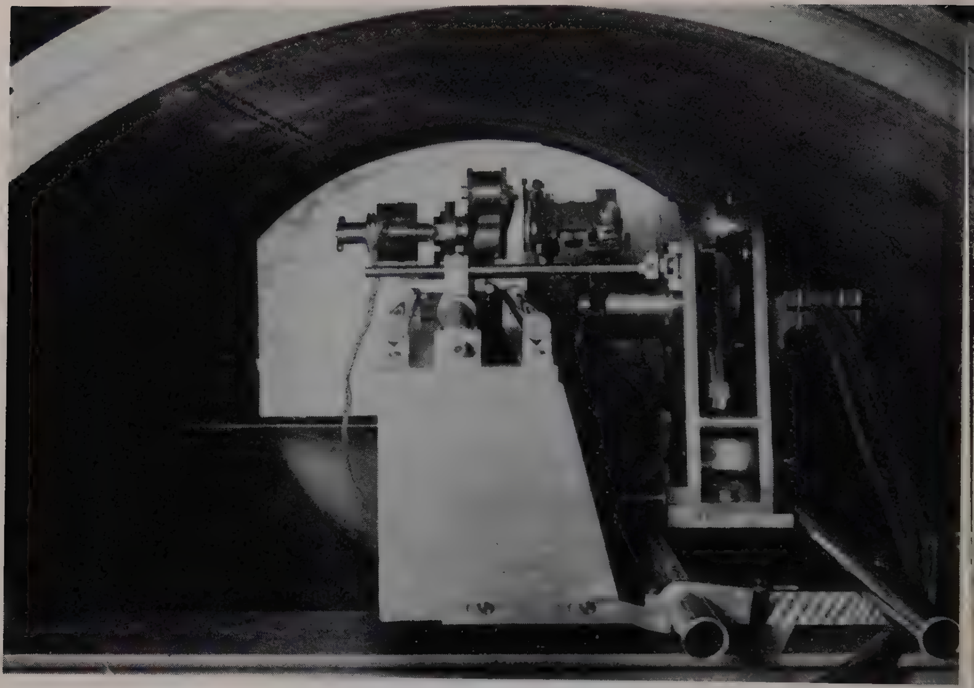

Fig. 12. The interior of the spectrograph tank as seen from the rear end with the spectrograph *in situ*. The figure shows distinctly how the trolley of the X-ray tube davit is brought along when the crystal is moved forward by means of the slave-screw. The high voltage cables are temporarily brought aside. Usually they hang loose from the bracket on the davit.

gear wheel worked by the screw *74*. This arrangement enables us to put the tube to the right angle in relation to the crystal. As this has to be done from outside the tank a sliding axle connects the screw with one of the manipulators in the fore gable. This axle can be seen dimly in Fig. 12.

As the spectrograph is designed for a very wide wave-length region it becomes necessary to work with several slightly different X-ray tubes. These tubes will be described separately in papers dealing with the various spectral regions. A brief outline will be given here as to those of their properties which arise from the special arrangement with the tube as a whole inside the vacuum tank.

All the tubes will have the cylindrical body in common. The anticathode *75* has to be earthed to ensure an effective cooling. The water flows through two rigid pipes passing through the rear gable and connected with the anticathode through a couple of flexible tubings *76*. The anticathode is clamped to a part of the X-ray tube having a smaller diameter than the rest of its body. This is to ensure a free passage of the reflected X-rays when the spectrograph is being set for large angles of incidens. The narrow part of the tube carries a small box *77*, in which diaphragms can be mounted to limit the height of the X-ray beam.

The cathode *78* has to be on the high voltage side. It has to be air-cooled as it was found to be very difficult to employ an electrically insulating cooling-system nside the vacuum tank. High loads at a low accelerating voltage usually demand pecial arrangements to guarantee a good focussing of the cathode rays. Accordingly t becomes necessary to equip the instrument with a sufficient number of insuated high voltage conductors. As can be seen from Fig. 10 five such conductors ead through the rear end-plate, two of them also carrying the filament current, he other three being intended for auxiliary voltages.

During the early stages of the experiments a singularly complicated contraption vas used for connecting the insulated conductors in the end-plate with the X-ray ube. It consisted of a system of rods and sliding contacts offering too many starting points for discharges no matter how good the vacuum. It was found, however, hat highly insulated cables could be used without interfering with the evacuation process. To prevent any mechanical stress on the cathode these cables are fixed to the davit by means of a perspex bracket.

The track of the trolley has to be parallel with the guides of the spectrograph. As soon as they have been adjusted a small bracket is fixed on the spectrograph base with its edge in contact with one of the rods of the track (compare Fig. 12). Thus both ends of the spectrograph base are fixed relative the track of the X-ray tube (compare above).

The adjustments

The two pairs of guides have to be parallel. This was adjusted once for all with gauge blocks and a very accurate rule, two meters in length.

The two axles in the supports *5* and *8* are to be parallel and at right angles to their direction of translation. A small mirror was mounted on a cone placed in the female of one of the axles. In the usual way it was made parallel to the axis of rotation. A thin beam of light, parallel to the guides, was then thrown on the mirror. The support was turned by means of its adjusting screws (one of them indicated by *45* in Fig. 6) until the reflected and incident beams coincided.

The axle also has to be parallel to a plane through the guides. Before clamping the support this was adjusted by putting a sufficiently thick pad of aluminium foils under that end of the support which was too low. The right height was determined simply by measuring the distance from axle to guide at both ends of the support. This second adjustment need not to be quite as accurate as the first one.

One of the axles adjusted, a small tube was directed with its optical axis perpendicular to the mirror. The cone with the mirror was then moved to the other axle where once again the mirror was made parallel to the axis of rotation. The support was turned until in this position, also, the optical axis of the tube became perpendicular to the mirror.

To bring the slit in position the cylinder *49* with the slit-holder was first removed from the support *5*, and a cone brought into the female of the axle. This cone supports a small ivory pin, movable in all directions (Fig. 13). Such pins have been widely used as an aid in adjusting plane crystal spectrographs.[13] The point of this pin was brought to coincide as nearly as possible with the axis of rotation. A small steel bar with a blunt point was affixed to one of the upper rods of the contraption *6*. The support was pushed slowly in the direction of this bar until its point just touched that of the ivory pin. Then the cone with the latter was removed and the slit-holder on its cylinder *49* was brought back in its original position. By means of one of its cross-table slides the slit-holder was moved forward until the blunt

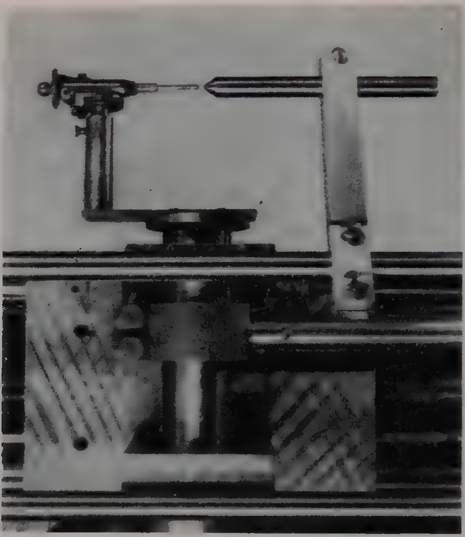

Fig. 13. The ivory-pointed pin and the pointed steel rod while adjusting the axis of rotation to fall in the plane of the slit.

point of the steel bar was observed to meet its image in the polished surface formed by the two halfs of the slit.

The next stage of the procedure was to mount a mirror on the axle of the crystal holder and adjust it as before. Light was sent through the slit and reflected by the mirror. A lens, between slit and mirror, was adjusted until an image of the slit was projected in the immediate vicinity of the slit itself. By means of the lever *55* the frame *54* was rotated until image and slit appeared to be parallel. This was also controlled photographically.

As regards adjusting the slit in the vertical plane, measurements with a cathetometer were regarded as quite satisfactory.

The lengths of the levers were adjusted with the system set for a Bragg angle of 90° and with the levers supported to form a straight line. Center points were mounted on all the axles and the distances set with an accuracy better than 0.05 per cent.

All these adjustments are of a more or less permanent character. This is not the case as regards those related to the crystal. Certain difficulties accompany these adjustments, especially when the surface of the crystal has been etched and, accordingly, it does not reflect optically.

With all springs and screws removed the steel block of the crystal-holder was brought into position in the cradle *36*. A needle was introduced through the narrow hole in the cone carrying the yoke *35*. This needle was fixed in a position where its point was in contact with the cylindrical surface of the block. After removing the block the slides of the cross-table were adjusted until the point of the needle coincided with the axis of rotation.

The crystal holder proper was then placed in its cradle but with a small mirror instead of the crystal. Intense light was thrown through the slit and reflected by the mirror. By means of a lens an image of the slit was projected once again on

e slit itself. The slit and its image were made parallel by adjusting the cradle
two perpendicular planes. This was done by means of the two screw combina-
ons *41—66* and *42—64*. As the slit image will be very short because of the small
eight of the crystal these adjustment were only approximate. The crystal was
t finally by taking photographs of X-ray lines. Protected by black paper a small
rcular film was placed in front of the slit in the aperture of the frame *54*. A Kα-
oublet was then photographed with the slit between its lines. The film had no
aper on its back and, thus, an image of the slit could be obtained by a short ex-
osure to visible light[7]. The parallelism of the lines and the slit image was con-
olled by measurements.

Then, the crystal lever being parallel to the perpendicle in the center of the crystal,
he levers were brought into position for a Bragg angle of 90°. By means of the
rrangement for rotating the cone of the cross-table (*67—68* in Fig. 7) the crystal
as turned in such a direction as to bring the slit image to coincide with the slit.

Conclusion

When not otherwise stated the material is brass for the spectrograph with ac-
essories. Where convenient most surfaces are nickel plated.

All joints of the vacuum tank and the evacuation system are sealed with rubber
ackings. Between the tank and the high vacuum diffusion pump there is a valve
Fig. 10) making it possible to shut the tank from the pumps. A bypass with an-
ther valve enables us to evacuate the system from a full pressure down to 0.1—
.5 mm mercury with the backing pump alone. The pirani- and ionization gauges
re connected to the collar uniting the tank with the main valve. With the spectro-
raph in the tank the lowest pressure, as yet attained, is 3×10^{-5} mm. The pres-
ure does not rise more than 3×10^{-3} mm in 12 hours. This has to be regarded as
good considering the large internal surface and all cavities necessarily existing
on an apparatus, with so many mechanical parts. No leakage through the welding
seams was ever observed.

To prevent direct radiation from the X-ray tube to reach the counter the upper half of the tank is partitioned by a shield having a small aperture for the reflected X-ray beam. This shield was made from a 6 mm thick aluminium sheet. It can be seen in the background of Fig. 12. When the primary radiation is not too hard aluminium is better for shielding purposes than heavier materials as it will not give any appreciable secondary radiation. It was soon found, however, that secondary and tertiary radiation entered the space behind the aluminium sheet. Thus, it became necessary to surround the precision part of the spectrograph with a whole system of shields. The edge of one of these appears to the left of the spectrograph base in Fig. 12. In this way most of the disturbing radiation was repressed.

The spectrograph covers an angular range from 35° to 80° approximately. With the crystals commonly used in X-ray spectroscopy it is possible to cover a wavelength region from 3500 X U (calcite) to 19600 X U (mica). Unfortunately there is a region of approximately 400 X U (between quarz and gypsum) which cannot conveniently be traversed unless the crystal radius is made short enough to allow Bragg angles down to 30°.

The X-ray spectrograph described above was planned several years ago. Two grants from Statens Naturvetenskapliga Forskningsråd rendered the construction possible. Further grants from the same source enabled the author to engage a assistent, Mr Bertil Nordfors, who has taken an active part in assembling an trimming the spectrograph. The author seize the opportunity to express his gratitude for the possibilities which hereby have been opened as regards his futur researches.

Department of Physics, University of Uppsala, June 1951.

REFERENCES. 1. **W. Ehrenberg** and **H. Mark,** ZS. f. Physik *42,* 807 (1927). — 2. **H Johann,** ZS. f. Physik *69,* 185, 1931. — 3. **Y. Cauchois,** Journ. de phys., et le Radium (7) 320 (1932); *4,* 61, (1933); Ann. de Physique (11) *1,* 215 (1934). — 4. **H. Karlsson** and **M. Siegbahn,** ZS. f. Physik *88,* 76 (1934). — **A. Sandström** and **E. Carlsson(-Ingelstam),** ZS. Physik *80,* 597 (1933). — **A. Sandström,** ZS. f. Phys. *84,* 541 (1933). — 5. **A. Sandström** Nova Acta Reg. Soc. Ups. (1935). — 6. **Ph. Haglund,** Ark. f. Mat., Astr. o. Fys. *28 A,* n:r (1941). — 7. **P. Ohlin,** Uppsala Univ. Årsskrift, Uppsala 1941. — 8. **V. H. Sanner,** Uppsal Univ. Årsskrift, Uppsala 1941. — 9. **H. Flemberg,** Ark. f. Mat., Astr. o. Fys. *33 A,* n:r 2 (1945). — 10. **T. Johansson,** ZS. f. Phys. *82,* 507 (1933). — 11. **J. W. Du Mond** and **P. Kirkpatrick,** Rev. Sci. Insts. *1,* 88 (1930). — 12. **M. Siegbahn,** Spectroskopie der Röntgenstrahlen, 2 ed. 76, Berlin 1931. — 13. Ibid. 117.

Tryckt den 5 februari 1952

Uppsala 1952. Almqvist & Wiksells Boktryckeri AB

ARKIV FÖR FYSIK Band 4 nr 37

Communicated 12 September 1951 by MANNE SIEGBAHN and ERIK HULTHÉN

Observations regarding resistant surface films of crystals

By NILS HAST

During 1948 at the Nobel Institute of Physics, the writer carried out electron-microscopic investigations of certain crystallization effects, inter alia with sodium chloride. These proved, surprisingly enough, that a regular, cubic sodium chloride crystal formed by evaporation of the water of a saturated salt solution does not completely redissolve when the crystal is immersed in pure water. A veil-like membrane or film is left which, when not deformed, reproduces the original contour of the crystal. These crystal surface films could not be observed except in an electron microscope, thereby necessitating placing the specimens in vacuum. The capillary forces normally occurring in the drying deform and break the residual surface films.

When continued investigations of the crystal surface films were resumed during the current year, the first step was to develop a method of drying the preparation after redissolving the salt, so that the deformation of the free surface films would be as small as possible. By means of stereophotography of the salt crystals, before as well as after the redissolution, and collocation of a left picture taken before with a right picture taken after, or vice versa, a clear picture is obtained of how closely the resistant surface films fit the original boundary surfaces of the crystal and to what degree the deformative effect of the capillary forces has been successfully prevented. It is well known that the capillary forces in the drying of porous material with low strength could give rise to deformations which quite change the microscopic structural picture of the material in question, in light as well as electron-microscopic examinations. In such instances, the methods of preparation described hereafter may be used to advantage.

Methods of decreasing the deformative effect of capillary forces in the drying of porous materials

Method I

A preparation of crystals formed by evaporation of the water of NaCl solution, for example, is immersed in distilled water. After several hours' redissolution and washing, the water in which the preparation is immersed is successively replaced with acetone, which mixes with water, until the liquid is practically pure acetone. The acetone is similarly replaced with ether, which mixes with acetone. When the specimen is subsequently dried, the material is exposed to approximately one fifth as great capillary forces as in drying directly from the water-soaked condition. At ordinary room temperature, the capillary constant of water is approximately

74, whereas that of ether is only about 15. The deformative damage occurrin with the evaporation of ether is so inconsiderable that the crystal surface film which resist the redissolution are not notably deformed, if the dimensions of th crystals are not too large.

Method II

Another method which also permits photography of the porous material in vacuum in undeformed condition is as follows. An inconsiderable quantity of glycero (boiling point, 290° C) is added to the washing water. The glycerol will concentrat in the porous structure and prevent its collapse when the vacuum-dry state is reached. Because of the defraction of the electrons in the glycerol, the electron-microscopic pictures lose a little of their sharpness with this method of stabilizing the porous structures. It is necessary, therefore, to see that the quantity of glycerol added is not unnecessarily great. Naturally, glycerol may only be used with substances with which it does not react chemically.

The pictures shown are taken with the described first method.

The appearance and properties of the crystal surface films observed

As mentioned in the introduction, the dissolution-resistant surface films of crystals are extremely thin. They contain such small quantities of material that an electron beam perpendicular to the film in question ordinarily is not sufficiently diffracted within the film to permit its being photographed. On the other hand, surface films that are traversed in a slope direction by the electron beam become more visible as the angle decreases. Folds in the film can be seen in consequence.

Accordingly, in ordinary electron-microscopic pictures, it is possible to observe more or less clearly these resistant products from redissolved crystals as residues on the specimen film. A clear conception of the crystal surface films can not be formed, on the other hand, unless photographs of the electron-microscopic pictures are made and studied steroscopically. Fig. 1–5 are also presented in this way with the use of the anaglyphic procedure. In these pictures the stereoscopic effect appears when the picture is viewed through "glasses" with one blue and one red glass or film.

The minute structure of the surface films is built by threads, woven together like a porous mat. The redissolved material diffuses through this mat. A slow

---

Fig. 1. (Upper picture.) NaCl crystals formed from a salt solution (by evaporation) and redissolved in distilled water. There are resistant crystal surface films, one with an almost cubic shape and one coming from a twin crystal (the stereophotos are not rectified). The latter is not quite regular and is partially deformed. The resistant film on the top of the twin is visible only where the film is folded. Surface films perpendicular to the top film show a thread structure. At those points inside the crystal, where the twin starts, the resistant surface film is folded 180° and is doubled. The pictures 1–5 have to be viewed with blue glass etc. before the right eye and red glass before the left (these glasses are enclosed). × 18 000

Fig. 2. (Lower picture.) NaCl crystals formed within a saturated solution (slow evaporation of the water) and subsequently redissolved in distilled water without drying. The preparation holder has been immersed in the saturated salt solution (temperature 40° C) for 10 hours. During this period the metal of the holder has been chemically attacked by the salt forming indissoluble particles which are lying directly on the bearing Al-membrane. The resistant crystal surface films are veil-like and visible where they are located perpendicular to the membrane. × 21 000

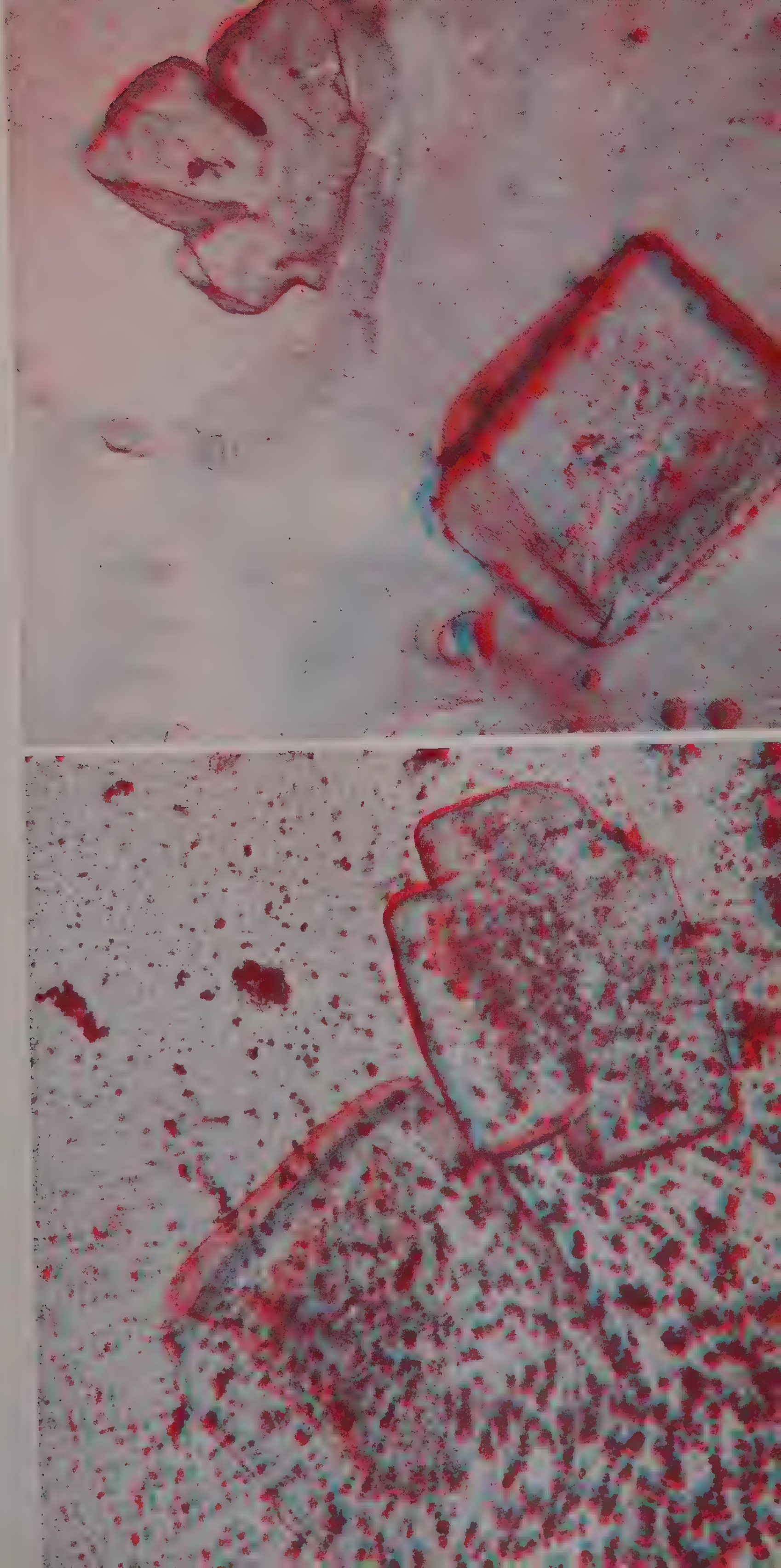

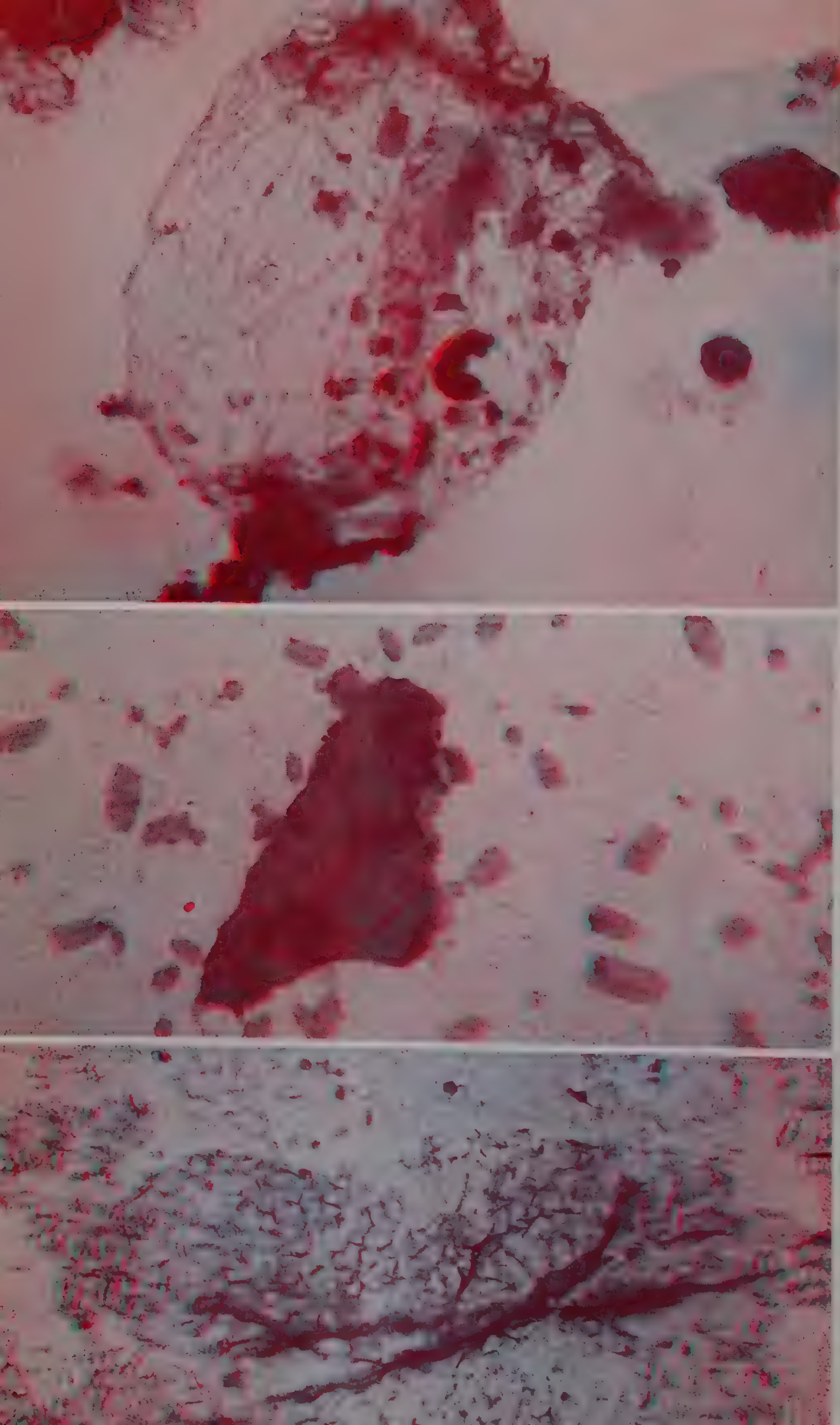

crystal growth seems to make the surface films very thin and almost structureless, while a rapid crystal growth results in surface films more marked with fibrous structure. Sometimes a change takes place with time, consisting of the fibres' becoming more pronounced.

Resistant surface films remaining after the redissolution of crystals formed from a salt solution. Evaporation freely in the air

On a specimen holder with the supporting membrane of a thin aluminium film[1] (thickness of solid material approximately 20 Å) a drop of NaCl solution is allowed to dry freely in the air. By heating, the course of the crystallization may be accelerated. The preparate is immersed immediately thereafter in distilled water, wherewith the salt crystals are redissolved, except for the aforementioned crystal surface films. The acetate-ether produre described earlier is used in the drying.

Fig. 1 shows residues of crystals of NaCl. The simplest explanation of these crystal surface films appears to be that a layer of impurities such as oxygen or nitrogen molecules, or dust particles from the air is adsorbed at the free outer surface of the crystals.

Resistant surface films remaining after the redissolution of crystals formed within a saturated salt solution when cooled. Contact between crystal and air prevented

It may be seen from this experiment that the resistant films in this case can not consist of impurities adsorbed from the air such as gas molecules, dust particles, etc.

A specimen holder is immersed in a saturated solution of a salt which has greater solubility at higher temperature than at lower, or vice versa. As an example, KCl solution at +50° C may be selected. When it is cooled to +30° C, crystals are formed, inter alia, on the supporting membrane of the specimen holder. The tem-

Fig. 3. (Upper picture.) Minute grains of powdered marble are placed on a preparation holder with a thin Al-membrane and immersed in 6 % water-solution of HNO_3 for half an hour, then washed and dried according to the acetone-ether method. The resistant surface films of large crystals are deformed but those of small crystals are undeformed. The small crystals may be those units which together form the grains (see also fig. 4). × 20 500

Fig. 4. (Middle picture.) A quantity of fine powdered marble is mixed with 20 % water-solution of HCl. After 6 hours the mixture is dialysed during 24 hours, first in running water and then in distilled water to wash away the soluble salts. A drop of the dialysed fluid with marble crystal residues is placed on a preparation holder and photographed in the electron microscope. Fig. 4 is such a photo. It shows that a great number of small units are obtained with this method of preparation. These are probably the surface films of the marble crystallites. There is a large resistant surface film also. It may be observed that the small units are not quite clear inside. × 15 000

Fig. 5. (Lower picture.) Small grains of crushed rock salt are placed on a preparation holder (with a thin Al-membrane) and immersed in distilled water. The acetone-ether method is used for the drying. Many interior crystallite surface films, resistant to the attack of water, are visible and it is also possible to see the contours of the whole grain. × 42 000 perature is subsequently raised again to +50° C or, in certain experiments, the solution is diluted with distilled water. The crystals formed are then redissolved. The specimen holder is transferred to pure water which is successively replaced by acetone and that later by ether. The preparation may thereafter be dried without damage to the minute structures of the crystal surface films by the capillary forces. Surface films with the appearance earlier described remain with this procedure. Consequently, the resistant films can not always be comprised of impurities coming from the air.

---

[1] Preparation of thin specimen films. Nature Vol. 159, page 370 March 15, 1947. Extremt tunna metallhinnor. Kosmos, band 27. 1949.

Crystal surface films which remain after dissolving powdered marble and pure calcite in an acid

A bit of crystalline marble was very finely powdered. A gold-plated specimen holder with a thin aluminium film was dipped into the powder, wherewith fine grains adhered to the film. The preparation was immersed in a six percent water solution of HNO_3. After approximately half an hour, the holder was transferred to distilled water for washing. Drying of the preparation was carried out in the manner described, using the acetone-ether procedure, in order to reduce the effect of the capillary forces significantly.

As is apparent from pictures 3 and 4, there are abundant crystal surface films which are resistant to the attack of the acid. The surface films from the small grains remain undeformed, while those from larger grains have been deformed by the capillary forces. These stereophotographs show further that, in addition to the larger resistant films, there are numerous "secondary" films bounding smaller units which are located within the former. It may be that these units are the crystallites, which together form the larger grains. Investigations have also been carried out on crushed material from pure calcite crystals instead of marble, with the same result.

Crystal surface films which remain after dissolving crushed rock salt in water

A rock salt crystal (volume approximately 1 cm^3) is dried at +100° C and crushed at the same temperature to a fine powder. A specimen holder with a thin Al-membrane is dipped into the powder and immersed for a period of three hours in distilled water. Washing and drying of the preparation is carried out in the same manner as in the experiment with the powdered marble.

Fig. 5 shows steroscopically the conture of dissolved large grains. The space they enclose is divided into smaller cells by a number of inner "secondary" films with the same veil-like structure.

Summary and conclusions

The investigations made show the existence of veil-like surface films of crystals. These films have a porous structure of threads, through which the material of the crystal diffuses during the dissolving process. The rate of the growth of the crystals and the rapidity of the change from the growing process to a dissolving one has some influence, giving rise to more or less marked thread structures.

The genesis of the surface films mentioned may depend on or be influenced by the existence of impurities in the solutions. The amount of material in such films is so extremely small, that even in the most purified liquid or other material there is ordinarily enough impurities to form these films.

It has been proved that the resistant surface films or crystals do not come from the air through an adsorption of gas molecules or dust particles etc. Large crystals often consist of smaller units, crystallites, having secondary surface films. Crushed crystals of ice from distilled water leave surface films, resistant to melting as well as to dissolution in water. Even the condensation of water vapour as drops on a cold preparation holder, with subsequent freezing and then heating, gives resistant crystal surface films; extremely thin ones in this case, however.

The investigations on the crystal surface films are currently going on. The possibility that impurities from the salt solutions form the resistant crystal surface films may be accepted as a working hypothesis. It seems probable that the foreign ions will concentrate — form an atmosphere of such ions — in the immediate vicinity of the crystals' surfaces, all during the growth. There are, however, as a rule no traces of residues in the interior of the original crystals after dissolution. The foreign ions then seem to coagulate, forming the resistant porous film in the very moment, when the crystallization process is changed to a dissolving one (see the experiment described).

However, from observations made it also seems to be possible to accept another working-hypothesis, the theory that the crystal surface films form an integrating part of the normal growth process of crystals. Such a hypothesis is contradictory to the theories of crystallization now accepted. According to these the ions just crystallizing on a surface are the most easily dissolved and not indissoluble as has been found here. With the material used in the present investigation and until more definite results in agreement with the latter theory have been brought forward it must be considered most probable that the crystal surface films are caused by impurities from the crystallizing solution.

The pictures shown have been taken with a Siegbahn-Schönander electron microscope. Ing. Arne Rosenqvist has assisted me in carrying out the investigation.

Tryckt den 5 februari 1952

Uppsala 1952. Almqvist & Wiksells Boktryckeri AB

ARKIV FÖR FYSIK Band 4 nr 38

Communicated 6 June 1951 by G. BORELIUS and LISE MEITNER

An investigation of the validity of the Wiedemann-Franz-Lorenz law

By J. O. LINDE

With 8 figures in the text

Introduction

The classical Wiedemann-Franz-Lorenz law, which connects the thermal conductivity (λ) and the electrical conductivity (σ) or resistivity (ϱ) of metallic conductors at different temperatures can be written

$$\frac{\lambda \varrho}{T} = L \tag{1}$$

where T is the absolute temperature and L the Lorenz constant (1). According to modern theories, based on the Fermi-Dirac statistics, the theoretical value of L is

$$L = \frac{\pi^2}{3} \left(\frac{k}{e}\right)^2$$

where k is Boltzmann's constant and e the elementary electronic charge. This expression was first obtained by SOMMERFELD (2). If ϱ is expressed in ohm × m, λ in watt/m × degree, k in joule/degree, and e in coulombs (MKS-units) the value of L becomes

$$L = 2.445 \cdot 10^{-8} \text{ (Volt/degree)}^2. \tag{2}$$

Evidently these figures for L are still valid, if λ is instead expressed in watt/cm × degree and ϱ in ohm × cm. W-F-L's law concerns only the part of the thermal conductivity that is caused by the free electrons of the metal. In checking eq. (1) the observed value λ' of the thermal conductivity is therefore to be corrected for the conductivity λ_i due to the lattice of the metal.

One difficulty in checking W-F-L's law is due to the fact that the lattice conductivity cannot be measured directly. In the following I shall give a critical investigation of the consistency of the law according to measurements of the conductivities given in the literature. Due attention will be paid to the lattice conductivity of the metals. In this paper the investigation will be restricted to the normal (non-transition) metals and alloys with such an element as basic metal.

1. Thermal conductivity of pure metals as a function of temperature

A survey of the values of the conductivities of pure metals at normal temperatures given in the literature shows that for very good conductors such as Cu, Ag and Au deviations from the W-F-L law appear; the experimental values are found to be lower than the theoretical at given values of the electrical resistivity. Consequently a correction of the experimental λ'-values owing to the conductivity (λ_i) due to the lattice will make the deviations from the law still greater. As an illustration of the deviation from W-F-L's law some data are given in Tab. 1 (experimental data from (3)). For Pb there is a fairly good agreement between the theoretical and the experimental values but the application of a reasonable correction, $-\lambda_i$, to λ' would give a deviation from W-F-L's law also for this metal of the same kind as observed for Cu, Ag, Au and Al. The same conclusion can be made regarding the conductivity of other normal metals.

Table 1

Observed values (λ') and values according to W-F-L's law (λ_{calc}) of the heat conductivity of some pure metals at 20° C (λ in watt/cm × degree)

Metal	λ'	λ_{calc}
Cu	3.94	4.20
Ag	4.18	4.50
Au	2.95	3.24
Al	2.25	2.62
Pb	0.34	0.34

In order to examine the validity of the W-F-L law for pure metals within a given temperature range, the theoretical values have been calculated for λ at different temperatures between 90° and about 1000° K, using eq. (1) and the known values of ϱ as a function of the temperature for Cu, Ag, Au and Al. Results of these calculations are given in Figs. 1–4. In the diagrams the experimental λ'-values corresponding to samples of very high purity (3) have also been plotted. Moreover a curve showing the ϱ, T relation of the metals concerned has been inserted in the diagrams.

At the rather high temperatures here concerned, the theoretical curves are valid within the accuracy of the drawing of the lines for ideal pure substances and samples of high purity as well.

As to the lattice conductivity of metallic conductors it may be reasonable to assume this to be of the same order of magnitude as the thermal conductivity of ion crystals at the corresponding temperatures (possibly corrected for differences in the characteristic temperature). For pure substances such as rock-salt and sylvin the temperature dependence of the conductivity is found to be inversely proportional to the absolute temperature T (Fig. 5). In the following it is assumed that this law is valid (more or less exactly) also for the lattice conductivity of metallic conductors. From an investigation referred to in the following (SMITH and PALMER) the value 0.08 watt/cm × degree is

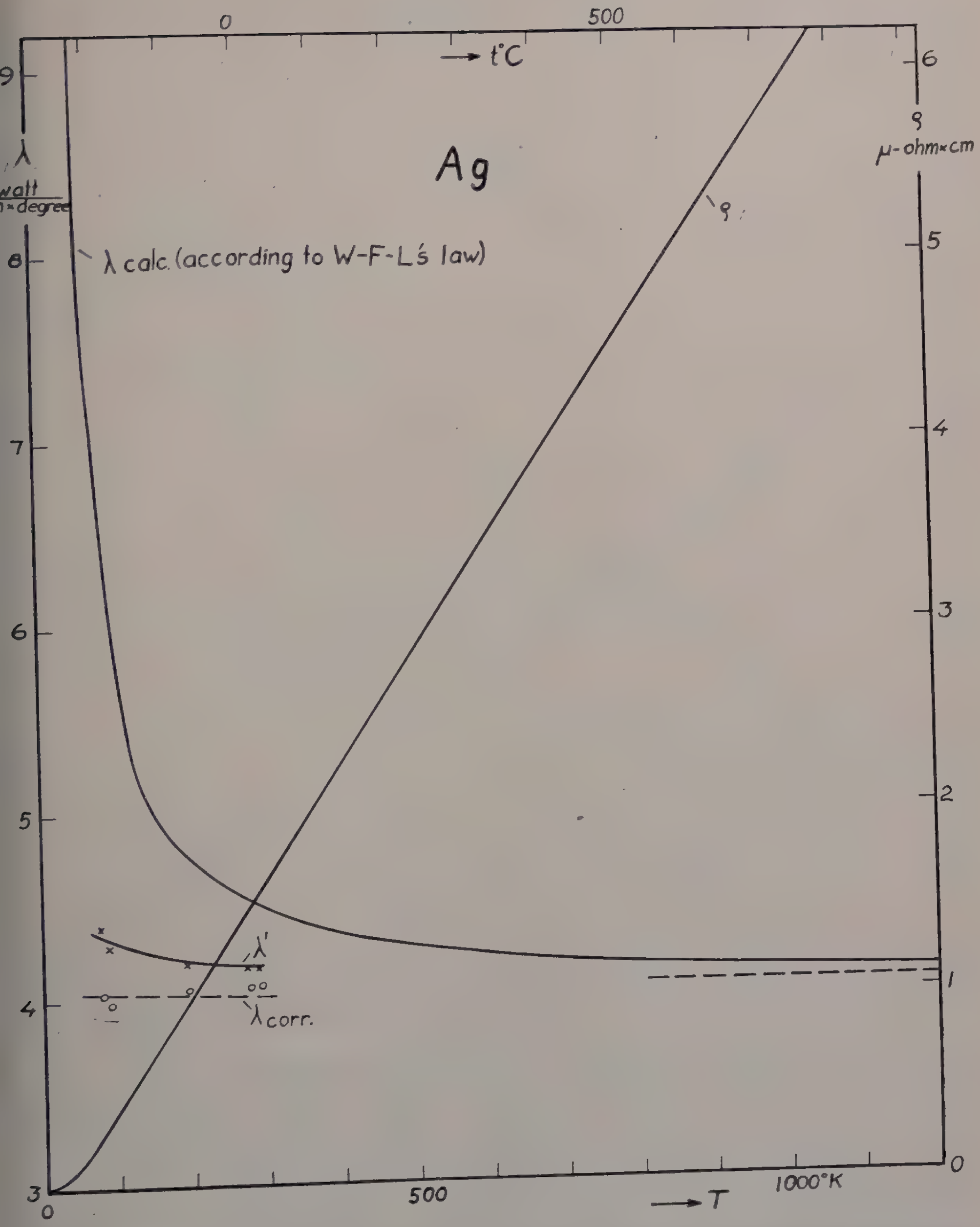

Fig. 1. Thermal conductivity of Ag according to measurements (λ') and calculated from the W-F-L law (λ_{calc}) as a function of temperature. (Data from (3)).

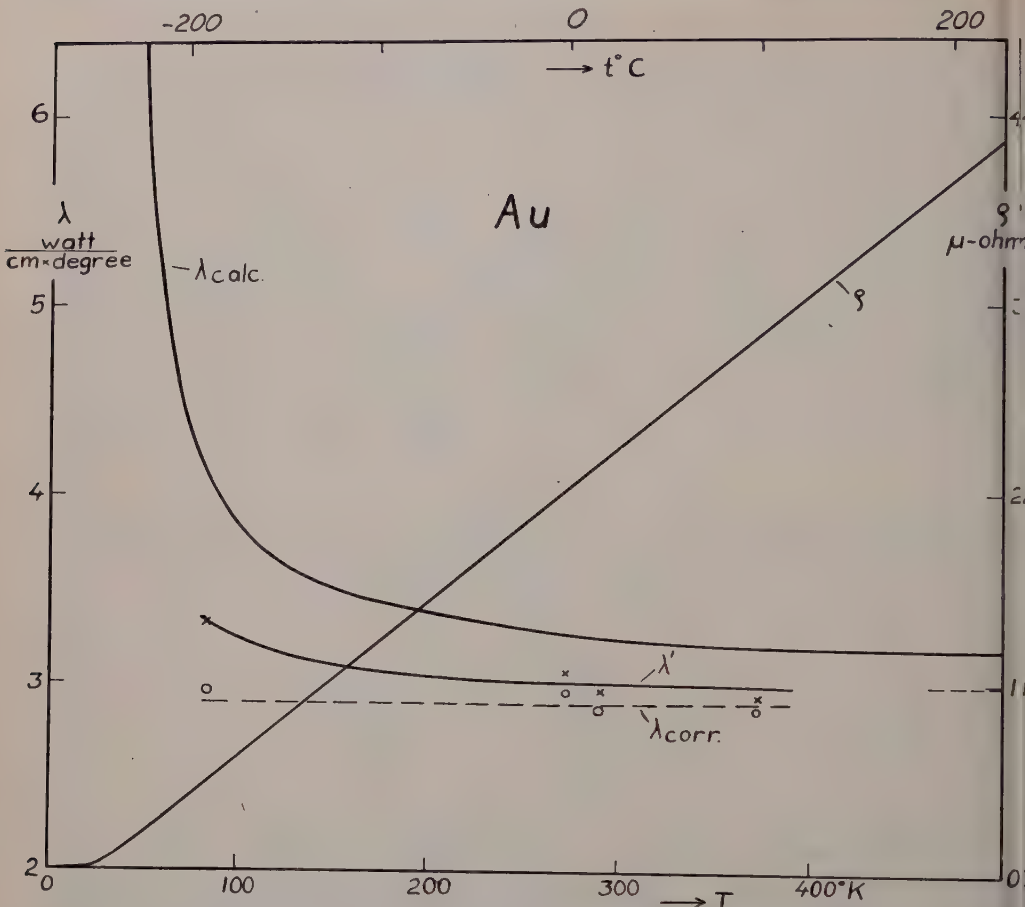

Fig. 2. Thermal conductivity of Au according to measurements (λ') and calculated from the W-F-L law (λ_{calc}) as a function of temperature. (Data from (3)).

deduced for copper and copper alloys at 293° K. Starting from this value for copper and a rounded off value of 0.1 watt/cm × degree for other metals and using the $1/T$ law for λ_i the experimental λ'-values have been corrected and $\lambda_{\text{corr.}}$ has been plotted in the diagrams of Figs. 1–4.

It can be seen from the graphs that deviations from the W-F-L law are present in the whole temperature range investigated, the deviations becoming smaller when the temperature is increased. Evidently the general character of the curves (increasing λ with decreasing temperature), does not change if L is given another value than the theoretical. It is therefore of interest to note that if, for instance, L is given the value 2.2×10^{-8} (Volt/degree)^2 (which value sometimes is postulated in the literature (6) on empirical grounds) agreement between experimental and calculated values would certainly be achieved for a certain temperature but not in a larger temperature range, the deviation from W-F-L's law changing sign at the temperature where agreement is obtained.

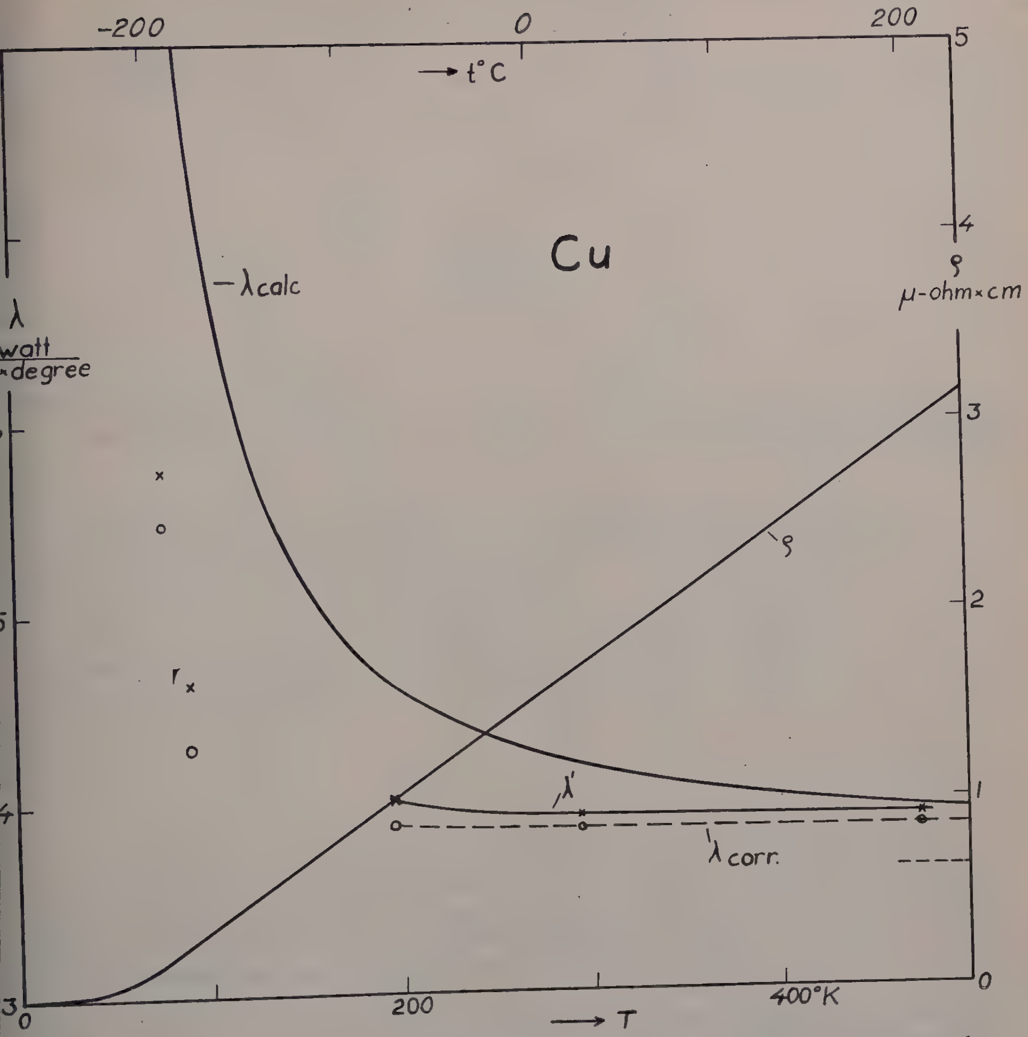

Fig. 3. Thermal conductivity of Cu according to measurements (λ') and calculated from the W-F-L law (λcalc) as a function of temperature. (Data from (3) and (5)).

Thus the picture obtained of the conductivity properties of metals when using an "empirical" L value is more complicated than found when the theoretical L is used.

As a very noteworthy result of this investigation it is evident from Figs. 1–4 that the experimentally determined λ'-values are much less dependent on temperature than the W-F-L law predicts. This fact is still more marked in the case of the corrected λ-values. In addition the theoretical values are as already stated at all temperatures higher than the experimental ones. As a matter of fact the regularities found here for pure metals seem to be best expressed by the statement that in the range of temperature investigated *the*

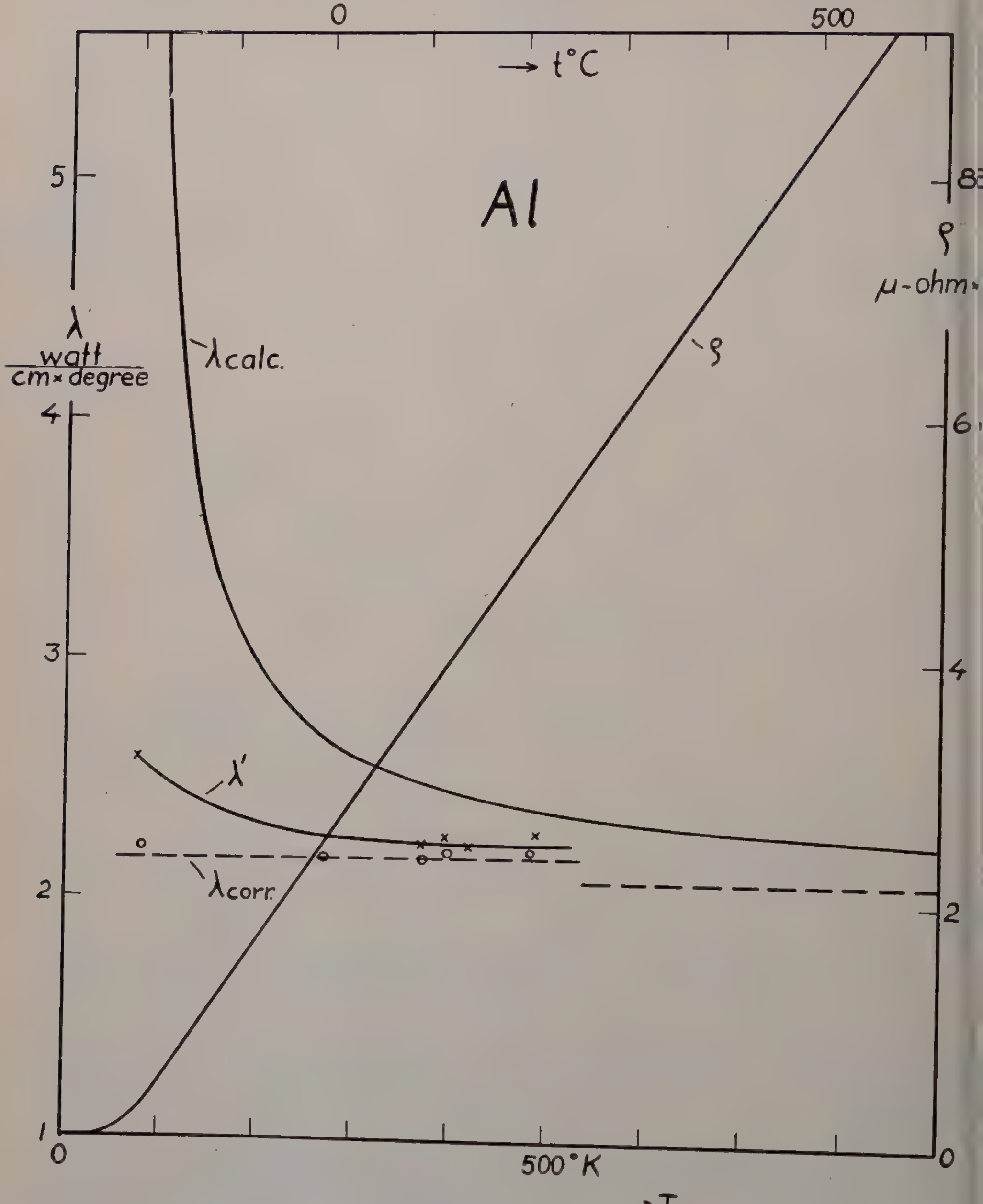

Fig. 4. Thermal conductivity of Al according to measurements (λ′) and calculated from the W-F-L law (λcalc) as a function of temperature. (Data from (3)).

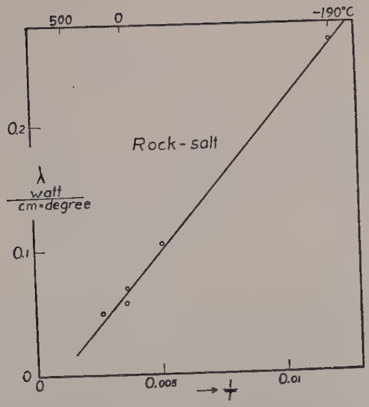

Fig. 5. Thermal conductivity (λ) of rock-salt as a function of $1/T$. (Data from (3)).

electronic part of the heat conductivity is for pure metals independent of the temperature (this contrary to W-F-L's law). The uncertainty in the assumptions made regarding the lattice conductivity cannot essentially change this deduction.

From the course of the curves of Figs. 1–4 it could be assumed that the theoretical λ-values tend to coincide with the experimental ones at very high temperatures. Assuming a linear relationship between ϱ and T to be valid to the highest temperatures, the limiting value of λ for $T=\infty$ can, as is easily found, be calculated from

$$\lambda_{T=\infty}=\frac{1}{\alpha\varrho_0}$$

α being the resistivity temperature-coefficient of the metal and ϱ_0 the electrical resistivity at 0° C. These extrapolated values are marked in Figs. 1–4 for the different metals by a dashed line to the right of the diagrams. As is seen from the graphs, the limiting values are in some cases somewhat above, in others somewhat below, the experimental, corrected values.

The empirically found regularity (λ being independent of temperature) is assumed to be valid in the temperature range where the electrical resistivity of the metal is a linear function of temperature, the deduction being made on the basis of experimental data from this temperature range. It is certainly not valid in cases where the relation between electrical resistivity and temperature is not linear. Thus deviations are likely to occur for normal metals at very low temperatures and for ferromagnetic metals at high and low temperatures. The deviation from the regularity that the values for Cu in the temperature range of liquid oxygen in Fig. 3 show cannot, however, be correlated with a deviation of the electrical resistivity curve from a straight line in the temperature range concerned. It could be assumed that the lattice conductivity of the single-crystal specimen used in one case (value at 80° K) is higher than the λ_i-value used in correcting λ'.

2. The thermal conductivity of alloys

In the examination of W-F-L's law for alloys either or both of the following methods is generally employed.

1) Using the notations inserted above, eq. (1) can be written

$$\lambda' - \lambda_i = L\frac{T}{\varrho}.$$

Provided that λ_i is independent of the composition of the alloys a graph of the directly measured λ' as a function of T/ϱ should give a straight line for a given temperature, if W-F-L's law holds, the slope of the line determining L, while the ordinate for $T/\varrho = 0$ gives λ_i.

2) Another way of proceeding, which has often been used by certain German scientists (4), consists in plotting $1/\lambda'$ as a function of ϱ at a fixed temperature. Thereby straight lines are often obtained ("isoterme Geraden"). I shall return later to questions regarding this method.

The following discussion of the thermal conductivity of alloys is made in connection with the results of measurements existing in the literature of different alloy series, especially the comprehensive measurements on certain copper alloys by SMITH and PALMER (5).

In their work SMITH and PALMER have used a graphical construction corresponding to method 1) above. Referring to Fig. 6 the general character of the curves obtained can be described as follows: In the range of low λ'-values a straight line is obtained, the slope of which gives $L = 2.39 \times 10^{-8}$ (Volt/degree)^2 as mean value from the measurements on six alloy series at two temperatures (293° and 473° K). This value is in fairly good agreement with Sommerfelds theoretical value, $L = 2.45 \times 10^{-8}$ (Volt/degree)^2. On the other hand the λ'-values of the most dilute alloys and the pure basic metal fall decidedly below the straight line of the diagrams. This implies that W-F-L's law is not obeyed for the alloy series as a whole especially not for the pure basic metal, which result could also be anticipated in the light of the results in section 1. The λ_i-values obtained from curves of the type in Fig. 6 are of the order of magnitude 0.1 watt/cm × degree at 20° C. Mean values evaluated for the different alloy series at the two temperatures are

T °K	λ_i watt/cm × degree
293	0.08
473	0.06

Within experimental errors these values obey the $1/T$ law valid for ion crystals, but the accuracy of the values is not high.

Because of the deductions of section 1 with regard to the temperature dependency of the heat conductivity of pure metals, it seems appropriate to try another graphic representation of the results of Smith and Palmer. The method here used is the following.

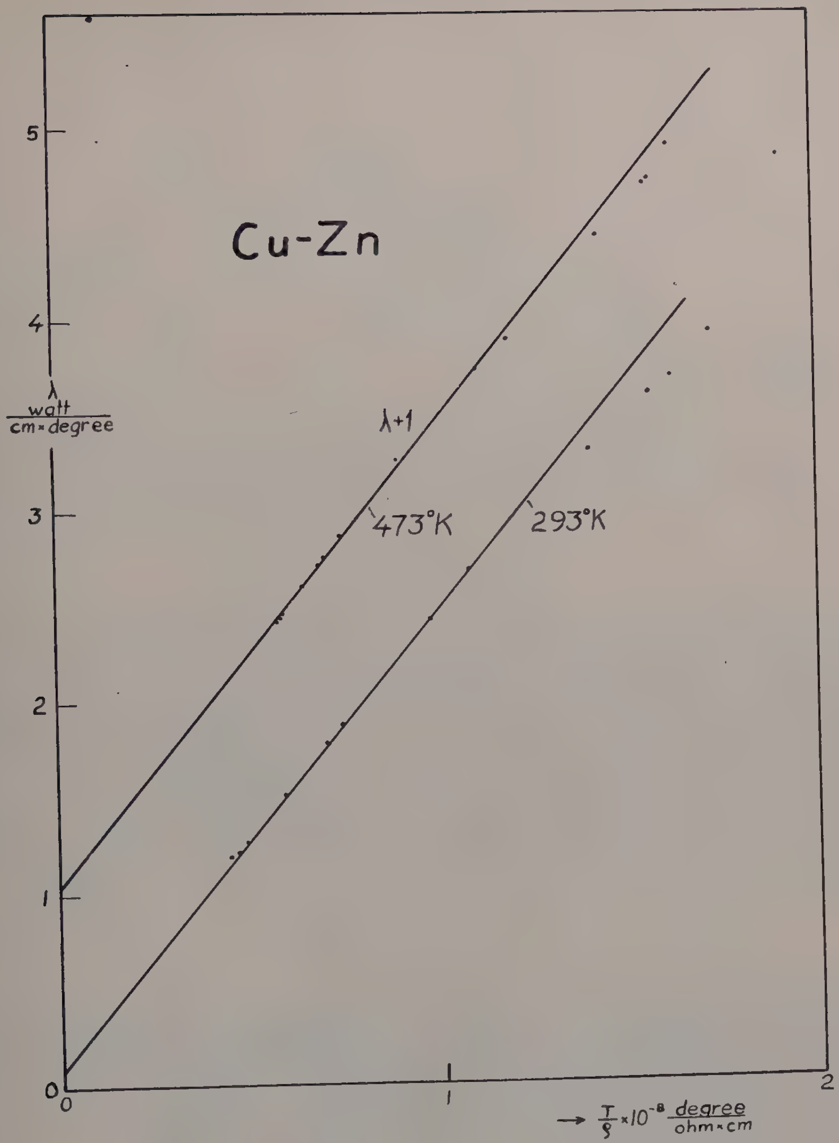

Fig. 6. Thermal conductivity (λ) as a function of T/ϱ for Cu-Zn alloys. Measurements by SMITH and PALMER (5).

Without postulating a constant value for L, the following transformations of eq. (1) are made

$$\lambda' - \lambda_i = \frac{T\,L}{\varrho_t + \Delta\varrho}$$

and

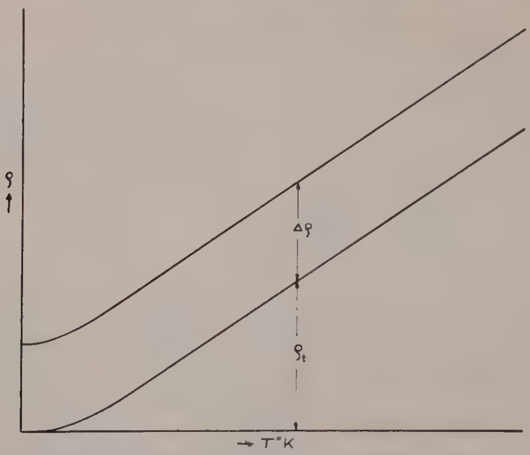

Fig. 7. Resistivity-temperature curves for a pure metal and a solid solution of this metal as basic metal according to Matthiessen's law.

$$\frac{1}{\lambda' - \lambda_i} = \frac{\varrho_t}{LT} + \frac{\Delta\varrho}{LT}. \tag{3}$$

In these expressions ϱ_t is the electrical resistivity caused by the atomic vibrations and $\Delta\varrho$ is the additional resistivity caused by the solute atoms of the alloy (Fig. 7). In eq. (3) the different terms represent the *thermal resistivity* of the alloy. The members on the right side of the equation give a separation of the thermal resistivity into two parts, one representing the resistivity caused by the atomic vibrations and the other caused by the solute atoms of the alloy.

On account of the results of section 1 it is reasonable to assume that the first term on the right of eq. (3) is constant for alloys of the same basic metal as long as ϱ is a linear function of T. The equation may therefore be written

$$\frac{1}{\lambda' - \lambda_i} = \frac{1}{\lambda_0} + \frac{\Delta\varrho}{LT} \tag{3 a}$$

where λ_0 is the constant (i.e. independent of temperature) conductivity of the basic metal. In checking eq. (3 a) the measured λ'-values should be corrected for the lattice conductivity λ_i and the corrected $1/\lambda$-values are to be plotted as a function of $\frac{\Delta\varrho}{T}$. It may be remarked that a representation of the uncorrected $1/\lambda'$-values in such a diagram would not make an evaluation of the constants of eq. (3 a) possible, and would therefore be of no physical interest. In reproducing Smith and Palmer's values for copper alloys in a diagram according to eq. (3 a) the values $\lambda_i = 0.08$ and 0.05 watt/cm × degree at 293° and 473° K have been used. Of course it is an approximation to use these values not only for alloys with low λ'-values for which they are deduced but also for the dilute alloys and the pure basic metal. However considering the smallness of λ_i relative to λ' of the last mentioned good conductors this approximation may be legitimate.

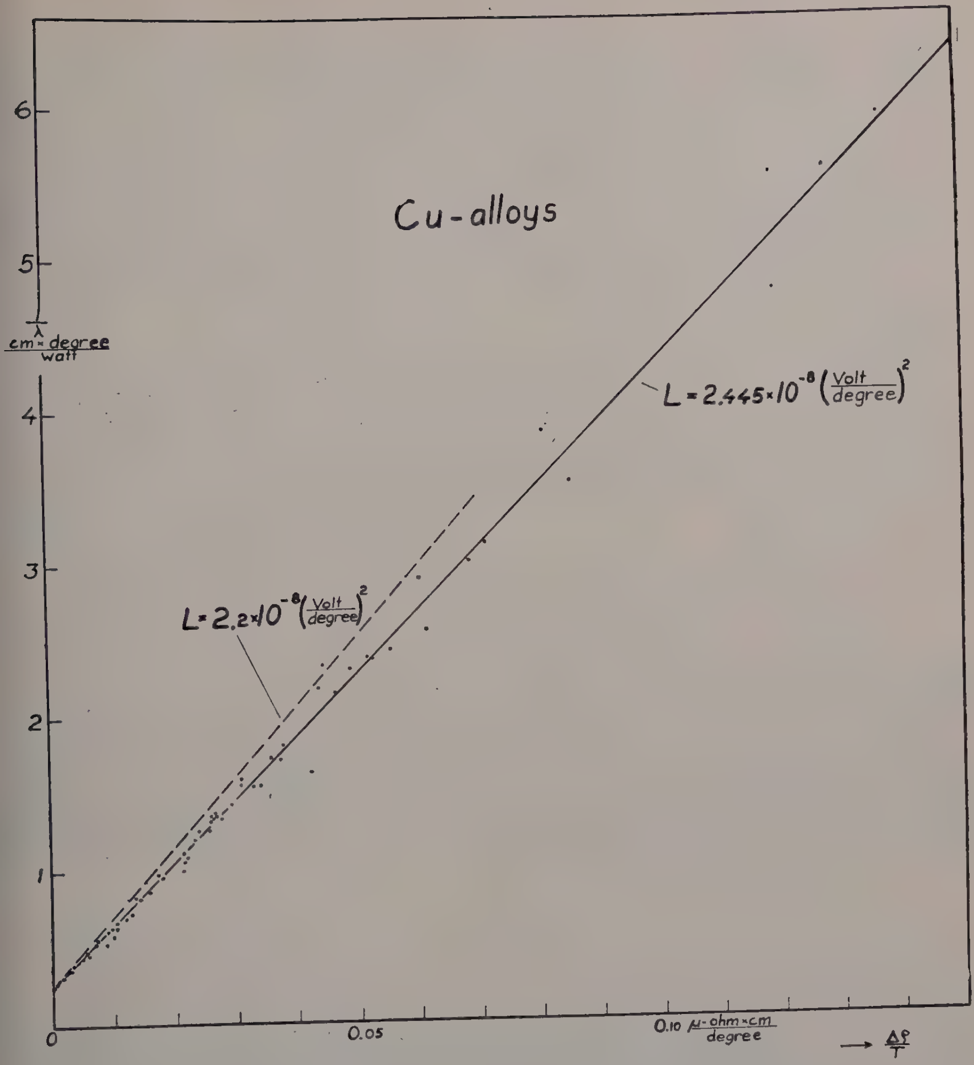

Fig. 8. Thermal resistivity $(1/\lambda)$ of a number of copper alloys as a function of $\Delta\varrho/T$. Measurements by Smith and Palmer at 293° and 473° K (5).

The results obtained are given in Fig. 8.

The fully drawn line in the diagram is given a slope corresponding to the theoretical value $L = 2.445 \times 10^{-8}$ (Volt/degree)^2 of the Lorenz constant. The scattering of the measured values from this line seems to be random. Thus the deviations from the line are not substantially caused by the uncertainty of the λ_i-values used.

The experimental fact that a better conformity to W-F-L's law usually is obtained for the additional resistivity than for the total resistivity of metallic samples has originally been established by Grüneisen et al. (4) from measurements on different alloys series and cold worked samples of pure metals. It is also in accordance with the theoretical results of Wilson and Makinson (7). In discussions in the literature one sometimes finds the opinion represented that the true value of L should not be the theoretical value 2.445×10^{-8}, but about 2.2×10^{-8} (units as above) which value should have been deduced from measurements. However, no support has been found in this investigation for such an assumption. This is evident from Fig. 8, where a line corresponding to $L = 2.2 \times 10^{-8}$ has also been drawn. The deviations that the measured values show from this line are, as can be seen, largely of a systematic character. Furthermore the value $L = 2.2 \cdot 10^{-8}$ finds no support in the results given in section 1.

With the aid of eq. (3 a) a method can be found to determine λ_i for metallic conductors especially for those with rather low conductivity. In fact, assuming that the equation represents an exact law in the temperature range concerned it may be possible to evaluate λ_i when λ_0, λ' and $\Delta\varrho$ are given. Assuming the uncertainty in the measured λ' to be of a lesser order of magnitude than the absolute value of λ_i the lattice conductivity could be evaluated with good accuracy.

The conformities to law which, according to eq. (3 a) are valid for the heat resistance in metallic conductors, have direct correspondence in the behavior of the electrical resistivity of metallic conductors, i.e. the regularities which are expressed by Matthiessen's law. On one side Matthiessen's law states that the electrical resistivity of an alloy is composed of one part dependent on temperature, which is caused by the atomic vibrations, and one part independent of temperature, caused by the solute atoms. On the other hand eq. (3 a) states that the thermal resistivity is composed of one part independent of temperature, caused by the atomic vibrations, and one part dependent on temperature, caused by the solute atoms. The correspondences found are thus of a reciprocal nature.

3. Special problems concerning the lattice conductivity of metallic conductors

According to measurements by Eucken et al. (8) the lattice conductivity of metals is much more dependent on the crystalline grain structure than is the case with the electron conductivity. The influence of the grain size is especially marked at low temperatures when very fine grained structures as well as normal structures are considered. Even at the temperature of liquid oxygen the conductivity of fine grained samples has been found to be much lower than for a sample of the same metal with ordinary crystal size. On the other hand single crystals show perceptibly higher heat conductivity than samples with ordinary crystal size. The validity of the conclusions made in this investigation are, as can be assumed, not substantially influenced by differences in crystal structure. (Only the result for copper at 80° K refers to measurements on a single crystal and very fine grained structures seem to be excluded). The effect found by Eucken emphasizes, however, the complicated nature of the conductivity problem of metallic conductors.

As a result of theoretical investigations SOMMERFELD and BETHE (9) conclude that the lattice conductivity of a given metal can never be greater than about four percent of the total conductivity. However, this low relative theoretical value of λ_i seems to be inconsistent with certain experimental facts. Thus results of measurements at low temperatures on Au-Pd and Cu-Pd alloys by GRÜNEISEN et al. (4) require λ_i-values of more than 30 percent of the total conductivity if the measurements are to give the theoretical value $L = 2.45 \times 10^{-8}$ (Volt/degree)^2 for the Lorenz constant. Also EUCKEN's method of evaluating λ_i for pure metals (8) gives higher values of this quantity than the upper limit of the value according to the calculation of SOMMERFELD and BETHE.

On the other hand, the absolute value of λ_i deduced from GRÜNEISEN's measurements (4) for the Cu-Pd and Au-Pd alloys (which are all poor conductors at the temperatures concerned) is rather low, and it seems therefore as if the value of the lattice conductivity for metallic conductors decreases under the value calculated with the aid of the $1/T$ law, when the electron conductivity is very low, which result is in qualitative accordance with the statement of SOMMERFELD and BETHE, and also with the theoretical results of PEIERLS (10) and MAKINSON (7).

SUMMARY

A critical investigation of data concerning the thermal conductivity of normal metals and alloys given in the literature has made the following conclusions possible.

The heat conductivity by electrons of pure metals is always lower than would follow from the validity of the Wiedemann-Frans-Lorenz (W-F-L) law, and is at all temperatures less dependent on temperature than is required by this law. A reasonable correction of the measured conductivity of different metals for the conductivity by the lattice gives as result that the electron conductivity of pure metals is at not too low temperatures practically independent of temperature.

In the case of alloys, W-F-L's law is found to be obeyed as regards the part of the electrical resistivity which is independent of temperature (the "additional resistivity") but not for the part caused by atomic vibrations.

A formula is presented for the relation between thermal and electrical resistivity which takes into account the different behaviour of the two parts of the thermal resistivity of an alloy as regards their temperature dependence. This formula is closely analogous to Matthiessen's law for the electrical resistivity of alloys.

Experimental data for a great number of copper alloys according to measurements by SMITH and PALMER give with the formula presented values of the Lorenz constant L which, within experimental errors, are in good accordance with the theoretical value ($L = 2.45 \times 10^{-8}$ (Volt/degree)^2).

The conductivity properties of transition metals are not included in this investigation.

REFERENCES. (1) **Wiedemann, G.** and **Franz, R.,** Pogg Ann. *89* (1853) 497. **Lorenz, L.,** Wied. Ann. *13* (1881) 422. — (2) **Sommerfeld, A.,** ZS. f. Phys. *47* (1928) 1. — (3) **Landolt-Börnstein,** Physikalisch-Chemische Tabellen, Berlin 1923—1936. — (4) **Grüneisen, E.** and **Goens, E.,** ZS. f. Phys. *44* (1927) 615. **Grüneisen, E.** and **Reddemann, H.,** Ann. d. Phys. *20* (1934) 843. **Reddemann, H.,** Ann. d. Phys. *20* (1934) 615. — (5) **Smith, C. S.,** Trans. AJME. Inst. Met. Div. *89* (1930) 84 and *93* (1931) 176. **Smith, C. S.** and **Palmer, E. W.,** Metals Technology *2* 1935, AIME. Met. Div. Technical publ. nr. 648. — (6) **Justi, E.,** Leitfähigkeit und Leitungsmechanismus fester Stoffe, Göttingen 1948. — (7) **Wilson, A. H.,** The theory of metals, Cambridge 1936; Proc. Cambr. Phil. Soc. *33* (1937) 371; **Makinson, R. E. B.,** Proc. Cambr. Phil. Soc. *34* (1938) 474. — (8) **Eucken, A.,** ZS. f. techn. Phys. *6* (1925) 689. ZS. f. phys. Chem. *134* (1928) 220. Phys. ZS. *29* (1928) 563. — (9) **Sommerfeld, A.** and **Bethe, H.,** Handbuch der Physik *24*: 2, Berlin 1933. — (10) **Peierls, R.,** Ann. d. Phys. *4* (1930) 121.

Department of Physics, Royal Institute of Technology, Stockholm, June 1951.

Tryckt den 2 februari 1952

Uppsala 1952. Almqvist & Wiksells Boktryckeri AB

ARKIV FÖR FYSIK Band 4 nr 39

Communicated 12 September 1951 by S. NAUCKHOFF and W. WEIBULL

Experimental determination of the speed of propagation of cracks in glass as a function of the stress

By N. LUNDBORG[1] and C. H. JOHANSSON[1]

With 4 figures in the text

According to investigations by SCHARDIN and STRUTH (1) (2), SMEKAL (3) and others, the speed of propagation of cracks in glass is a constant with a value of 1500 to 1600 m/sec. EDGERTON and BARSTOW (4) observed as well lower values.

The present investigation shows that the speed of propagation depends on the magnitude of the stress. The above mentioned constant represents an upper limiting value to which the speed of propagation tends as the static stress increases.

Measuring method

The glass plate was loaded as shown in Fig. 1 with a constant bending moment between *a* and *b*. In order to make the crack propagate in the required direction a scratch of some millimeters' length had been made with a diamond on the underside of the plate at the edge *A* in Fig. 1. The plate broke at the following values of the maximum stress:

Initial state	$\mathrm{kp/mm^2}$
Without diamond scratch	7.5 ± 0.8
With » »	2.3 ± 0.1

For $\sigma > 2.3$ kp/mm² the glass plate was supported in *A* when it was loaded, and cracking started when the support was removed. At smaller loads the crack was started by tapping gently on the glass plate at *A*.

To determine the crack velocity, plates of mirror glass were used, 2 mm thick, with an electrically conducting coating on the under side. By means of slits the coating was divided into strips perpendicular to the direction of the crack, and the strips were connected to the source of voltage and the cathode ray oscillograph as shown in Fig. 2.

Results

In Fig. 3 are given some oscillograms and the corresponding distance-time diagrams. Fig. 4 gives a survey of the obtained results with the speed of frac-

---

[1] Physical Research Departement, Nitroglycerin AB. Stockholm.

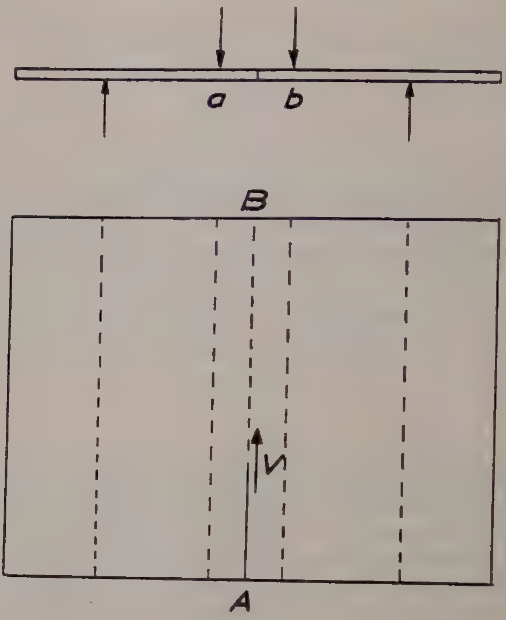

Fig. 1.

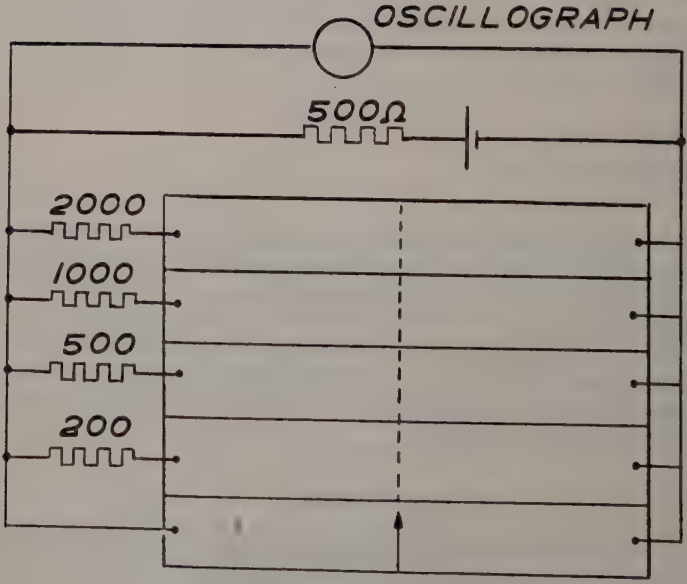

Fig. 2.

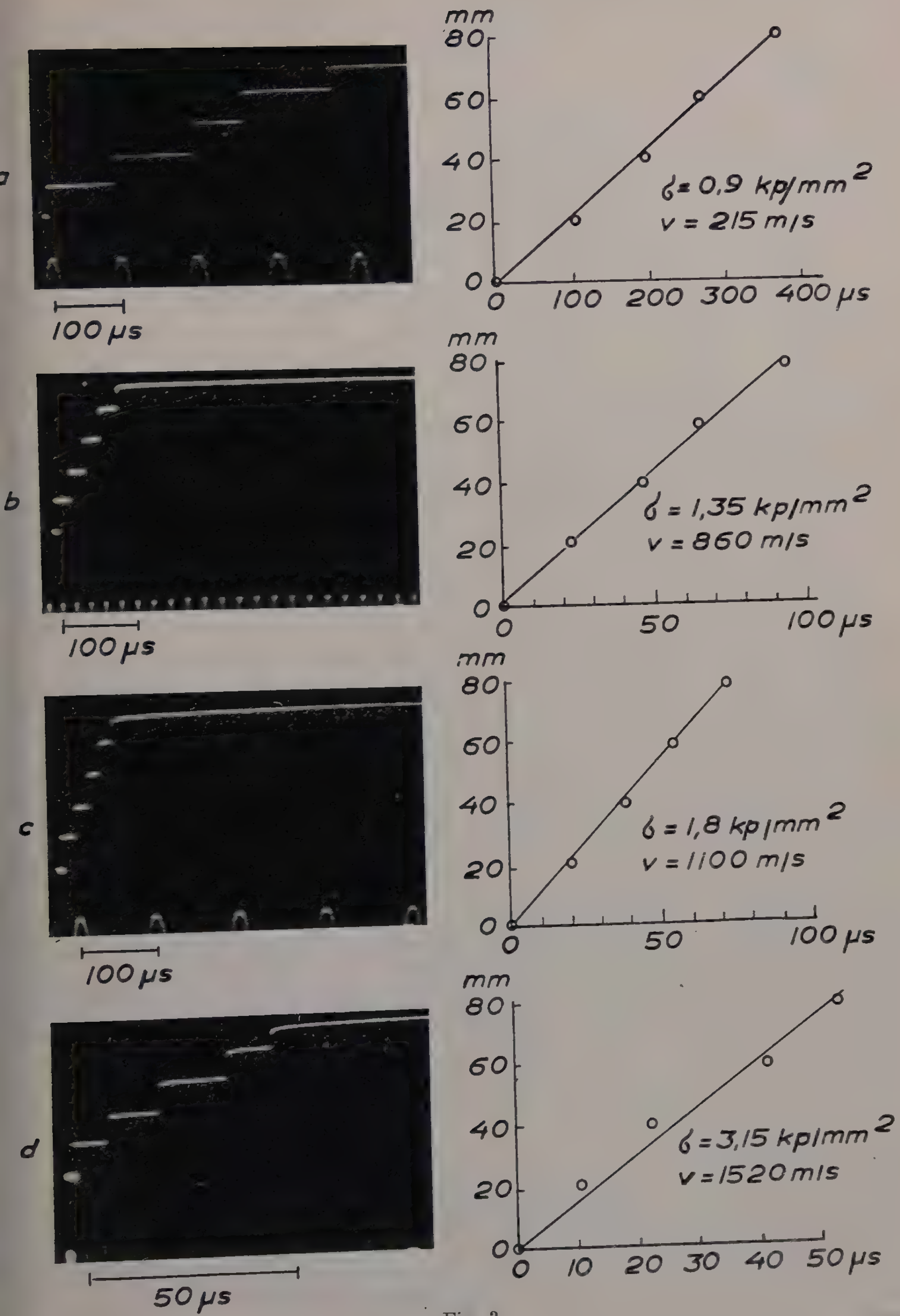
a
100 μs
mm
80
60
40
20
0
0
100
200
300
400 μs
$\sigma = 0{,}9$ kp/mm^2
$v = 215$ m/s
b
100 μs
mm
80
60
40
20
0
0
50
100 μs
$\sigma = 1{,}35$ kp/mm^2
$v = 860$ m/s
c
100 μs
mm
80
60
40
20
0
0
50
100 μs
$\sigma = 1{,}8$ kp/mm^2
$v = 1100$ m/s
d
50 μs
mm
80
60
40
20
0
0
10
20
30
40
50 μs
$\sigma = 3{,}15$ kp/mm^2
$v = 1520$ m/s

Fig. 3.

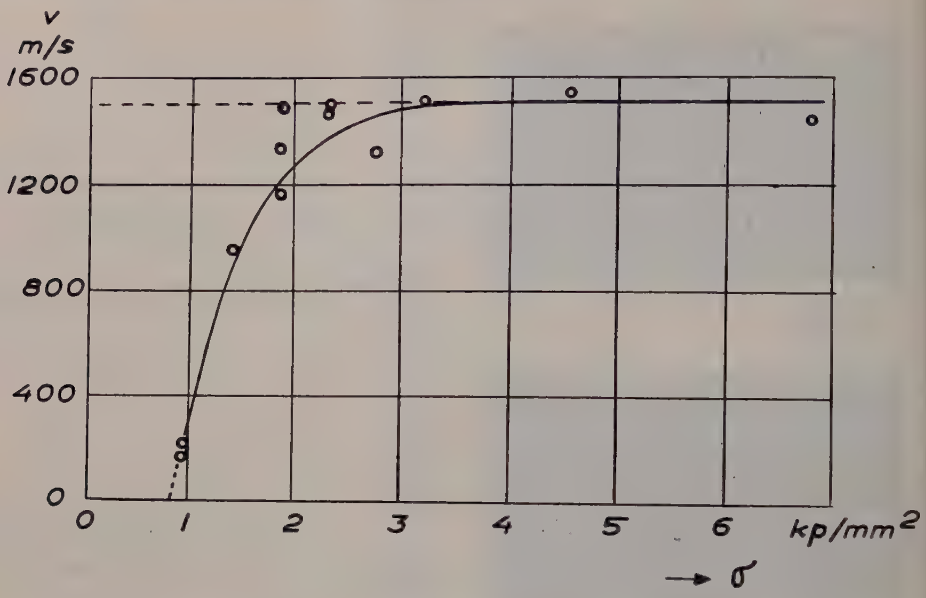

Fig. 4.

ture (v) as function of the maximum tensile stress with a bending load according to Fig. 1. The diagram shows that v is approximately independent of the load when σ is larger than about 3 kp/mm^2, but that at lower σ-values the v-σ-curve bends towards the abscissa and goes towards zero at $\sigma = 0.8$ to 0.9 kp/mm^2. The fact that the speed of fracture at low stresses retains its low value unchanged along the entire length of the crack is due to the low natural frequency of the system for a bending oscillation which is so low, that σ does not change noticeably in the unbroken section as the crack propagates through the plate.

LITERATURE. 1. **H. Schardin** und **W. Struth,** Hochfrequenzkinematographische Untersuchung der Bruchvergange im Glas. Glastechn. Ber. *16* (1938), S. 219—227. — 2. **H. Schardin,** Ergebnisse der kinematographischen Untersuchung des Glasbruchvorganges. Glastechn. Ber. *23* (1950), S. 1—10, 67—79, 325—336. — 3. **A. Smekal,** Über den Anfangsverlauf der Bruchgeschwindigkeit im Zerreissversuch. Glastechn. Ber. *23* (1950), S. 186. — 4. **H. E. Edgerton** and **F. E. Barstow,** Journ. Amer. Ceram. Soc. *24* (1941), p. 131—137.

Tryckt den 5 februari 1952

Uppsala 1952. Almqvist & Wiksells Boktryckeri AB

ARKIV FÖR FYSIK Band 4 nr 40

Communicated 12 September 1951 by MANNE SIEGBAHN and ERIK HULTHÉN

Notes on the 225-cm cyclotron at the Nobel Institute for Physics, Stockholm

By HUGO ATTERLING and GUNNAR LINDSTRÖM

With 2 figures in the text

The present paper will briefly report the initial performance of the 225-cm cyclotron at the Nobel Institute for Physics in Stockholm. This cyclotron is of the conventional type, i.e., operating with a constant frequency. It has been designed to produce deuterons of energy 25 MeV. For the acceleration of deuterons to this energy in a conventional cyclotron, very high dee potentials (at least 200 kV across the dees) are necessary. In the initial stage of performance the machine described here is able to produce 21 MeV deuterons but attempts are at present being made to attain the design energy.

The design of the equipment was started in the spring of 1946. Some of the work performed on this project has been reported in two previous papers.[1,2] A detailed description of the complete cyclotron will be published later in Ark. f. Fysik by the present authors.

A schematic diagram of the cyclotron including the grounded grid oscillator circuit is shown in Fig. 1. The photograph of Fig. 2 shows the present appearance of the cyclotron, as seen from the dee line side.

The poles of the magnet[3] are 225 cm in diameter at the faces. The smallest diameter of the conical pole tips, which are incorporated in the acceleration chamber, is 210 cm. Maximum radius for the acceleration is 90 cm. Without the shims which are used for correcting the magnetic field, the total gap between the pole faces is 350 mm, the distance between the pole tips being 330 mm. The latter distance is somewhat reduced at the central part of the chamber due to the shims now installed. A maximum field of about 18 000 oersteds can be obtained with a power input of 240 kW. The field necessary for producing 25 MeV deuterons is about 11 500 oersteds, the power input in this case being roughly 60 kW. The first tests of the magnet after it had been erected in the Institute were performed in June, 1948.

The oscillator tube (Standard Telephones and Cables, Ltd, London, type 4067 A) permits a maximum plate dissipation of 160 kW. The high voltage rectifier for supplying power to the oscillator has a maximum output of 400 kW.

---

[1] GUNNAR LINDSTRÖM, Ark. f. Mat., Astr. o. Fysik *35* A, N:o 15, 1948 ("Some high-frequency measurements on a cyclotron model").

[2] HUGO ATTERLING, Ark. f. Fysik *2*, 559, 1951 ("Design of acceleration chamber and dees for the 225-cm cyclotron at the Nobel Institute for Physics, Stockholm". This paper also describes the magnetic shims so far used.)

[3] The basic design of the magnet was made by Dr. L. DREYFUS of the ASEA Co. The construction was performed by this company.

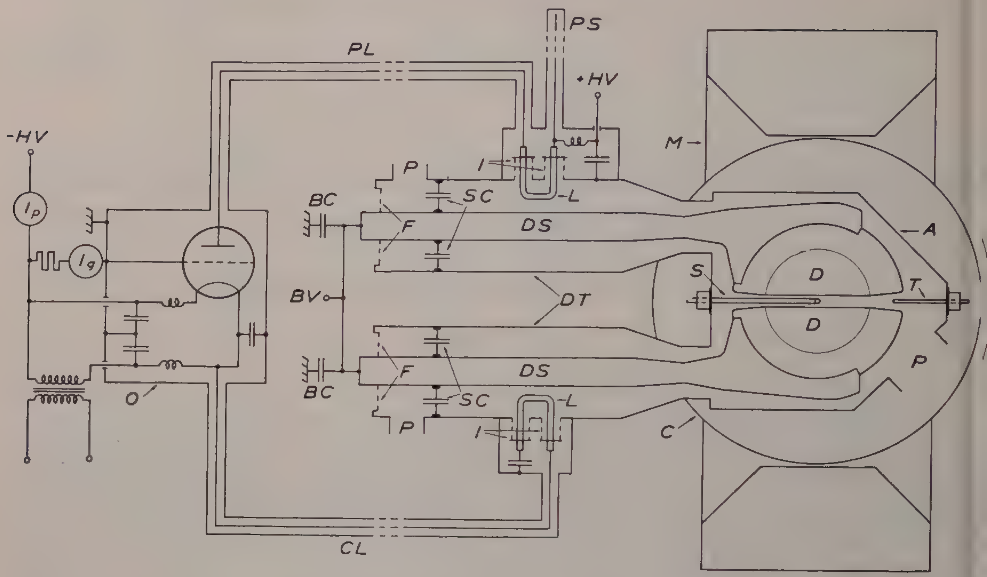

Fig. 1. Schematic diagram of the cyclotron. M — magnet. C — magnet coil. A — acceleration chamber. P — pump connections. S — ion source. T — target. D — dees. DT — dee line tanks (outside conductors). DS — dee stems (inside conductors). SC — short-circuiting condensers. I — insulators. F — flexible and insulating seals. BC — blocking condensers. L — coupling loops. PL — plate line. PS — plate stub line. CL — cathode line. O — oscillator. The d.c. plate voltage and the d.c. cathode voltage are connected at +HV and —HV respectively. The bias voltage is applied to BV. In the actual design the pump connections at the ends of the dee line tanks are placed below these tanks and the coupling loops above. The arrangements for supporting and adjusting the dee stems, at the ends of the dee line tanks, are not shown in the figure.

For evacuating the acceleration chamber and the dee line tanks, three oil-diffusion pumps are used, each with an unbaffled speed of 4 000 litres per second at 10^{-5} mm Hg. The total volume to be evacuated is about 7 000 litres.

A low-voltage arc ion source is used for producing the deuterons. The probe-target between the dees is adjustable for intercepting the ion beam at any desired radius.

In conventional cyclotrons with concentric dee lines, the dee stems are grounded at their ends. Originally the cyclotron described here had dee lines of this design. This has been changed, however, as seen from Fig. 1. The dee stems are now insulated from ground and the ordinary shorting spiders which determine the length of the dee lines have been replaced by short-circuiting condensers. With this arrangement it is possible to apply a d.c. bias to the dees in order to prevent discharges in the acceleration chamber.

When the first tests of the radio-frequency system with the chamber and dee line tanks under vacuum were performed, the dee stems were grounded at the ends in accordance with the original design. Difficulties were then experienced as a result of discharges in the space above and below the dees. These discharges prevented the build-up of the radio-frequency voltage on the dees. The discharges occurred even under good vacuum conditions (a pressure less than 10^{-5} mm Hg) and they

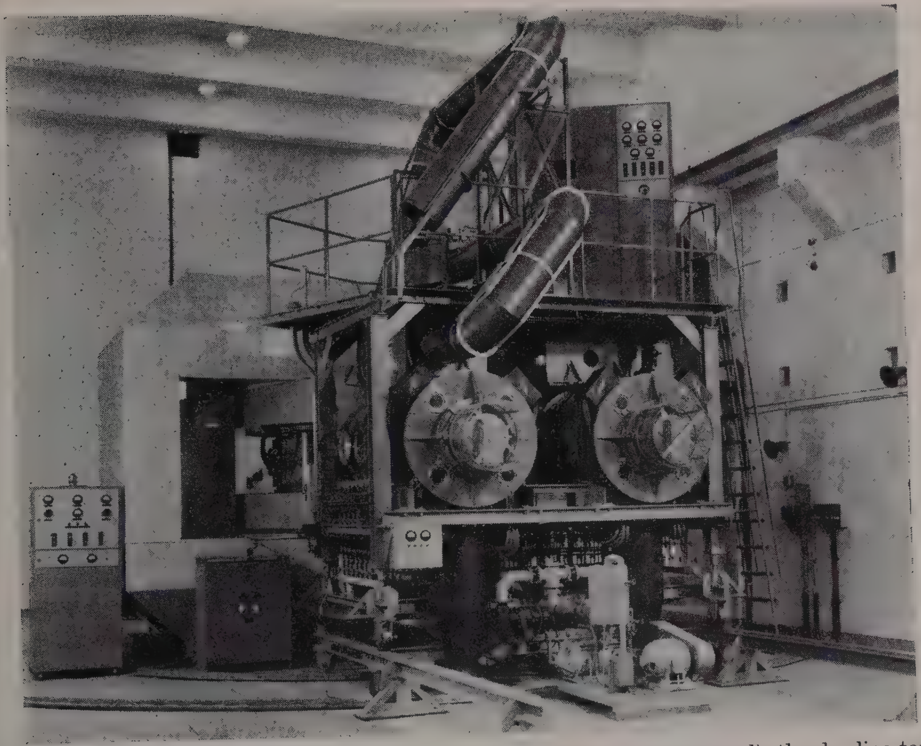

Fig. 2. Photograph of the cyclotron showing the magnet (in the background), the dee line tanks with their vacuum pumps and the oscillator (on the balcony).

seemed to be caused by oscillating electrons as discussed by MacKenzie et al.[1] Attempts were made to overcome the difficulties by using a small booster oscillator coupled to the cathode loop (see Fig. 1). This booster oscillator had been built to be incorporated in the system from the very beginning, as it was felt necessary on the basis of recommendations by the 60-inch cyclotron group in Berkeley[2] to have such an arrangement available. The experiments made with this system gave some weak indications that the booster oscillator might be able to push the system in the correct mode of oscillation, thus producing enough dee voltage to prevent electrons from executing resonant oscillations. The operation of this radio-frequency system, however, was very unstable, possibly due to the booster oscillator.

Thus, as the booster oscillator used seemed to be inadequate for the purpose in question it was decided to change the system in such a way that a d.c. bias voltage could be applied to the dees. The purpose of this bias voltage was to provide a sweeping field to remove the electrons giving rise to the discharge.[1, 3] As these changes could be performed in a rather short time (about two months) they were preferred to the building of and experimenting with a new booster oscillator. Moreover, the use of a booster oscillator always introduces a complication. The successful use of a bias voltage for avoiding discharges in the frequency-modulated cyclotrons also suggested trying this method in a conventional type, notwithstanding that the necessary use of condensers instead of the ordinary short-circuiting spiders introduced a new problem. This problem was, obviously, how to design high capacity condensers which would be able to withstand in vacuum the very high radio-frequency currents (several thousand amperes) flowing at the voltage nodes of the dee lines.

---

[1] K. R. MacKenzie, F. H. Schmidt, J. R. Woodyard, and L. F. Wouters, Rev. Sci. Instr. *20*, 132, 1949.

[2] Their experience was placed at our disposal at the end of 1945 by courtesy of Prof. E. O. Lawrence. Information concerning these problems was kindly given us by Dr. J. G. Hamilton and several members of the cyclotron group.

[3] W. M. Brobeck, E. O. Lawrence, K. R. MacKenzie, E. M. McMillan, R. Serber, D. C. Sewell, K. M. Simpson, and R. L. Thornton, Phys. Rev. *71*, 449, 1947.

An alternative using grids[1] above and below the dees for eliminating the discharges was discussed and rejected, as the grids were believed to cause sparking and to need rather high potentials if they were to be effective in sweeping electrons.

The dee stems were now insulated from ground by changing the arrangements for supporting and adjusting the stems (these arrangements are not seen in Fig. 1; they are situated at the ends of the surrounding vacuum tanks). Furthermore, the short-circuiting spiders in the old design were replaced by water-cooled mica condensers (giving a capacity of 40 000 micro-microfarads between dee stem and ground). These changes were finished at the beginning of June, 1950. With a negative bias of about 500 volts applied to the dees, radio-frequency power could now be fed into the system without the occurrence of disturbing discharges above and below the electrodes. In July, 1950, deuteron resonance was attained for the first time with a target inserted at a radius of 48 cm (corresponding to a deuteron energy of about 6 MeV). The dee voltage used during these experiments was rather low (less than 100 kV across the dees). Shortly after this first beam was obtained, troubles occurred with the mica condensers which broke down at a fairly low radio-frequency voltage in vacuum despite testing with 4 kV in air. It was not possible to ascertain whether this was due to local heating caused by the high radio-frequency currents or to some other effect, for example gassing from the mica sheets. After a few additional experiments with the mica condensers without success, an attempt was made to use commercial Mycalex condensers in vacuum, but this attempt failed too.

The next step was to try vacuum condensers, and the arrangement now in use was designed. This arrangement consists of six water-cooled plate condensers around each dee stem, giving about 40 000 micro-microfarads from stem to ground. The condensers were constructed at the Institute in the course of a few months and thereafter thoroughly tested in vacuum at 14 kV d.c.

The installation of these condensers in the dee line tanks was completed at the end of May, 1951. The tests immediately performed proved the possibility of obtaining voltages across the dees of 100–150 kV without any condenser trouble. So far this voltage range has not been exceeded. A negative bias of about 500 volts was sufficient to avoid discharges above and below the dees.

Using a fairly low dee voltage of about 100 kV, we made attempts to find a deuteron beam at full radius (90 cm). From geometric considerations the corresponding energy should be 21 MeV (the frequency used being 7.95 megacycles per second). In the beginning of July, 1951, a beam current of a few μA of 21 MeV deuterons was observed, the current intensity being determined by measuring the heating of the cooling water in the target. At the fairly low dee voltage used, higher intensities could hardly be expected.

---

[1] See for example the construction report on the 130-inch cyclotron at the University of Rochester, U. S. A., 1949 (S. W. Barnes et al.).

As already mentioned, the work under way at the time of writing has in view the realization of a 25 MeV deuteron beam. For this purpose the dee voltage must be increased to at least 200 kV.

In conclusion, we wish to express our gratitude to the Director of the Institute, Professor MANNE SIEGBAHN, for the confidence he has shown in us by assigning us to the work on the project described herein, and for the constant interest he has displayed in this work.

We are indebted to our colleague, Mr. BJÖRN ÅSTRÖM, Civilingenjör, for his helpful cooperation during the first phases of the work. Our further thanks are due to several members of the technical staff of the Institute for their valuable assistance.

We also wish to acknowledge the assistance of many people not connected with the Institute, of several industrial firms and of members of foreign laboratories, in particular in U.S.A. The contributions of different kinds given by these people and firms will be mentioned in more detail in the paper soon to be published.

Nobel Institute for Physics, Stockholm 50.

Tryckt den 5 februari 1952

Uppsala 1952. Almqvist & Wiksells Boktryckeri AB

ARKIV FÖR FYSIK Band 4 nr 41

Communicated 12 September 1951 by Arne Westgren and Rolf Sievert

The translucent zone of reaction in the dentin. A radioautographic study

By Helge Berggren and Ivar Cederberg

With 6 figures in the text

Introduction

The familiar occurrence of the translucent zone in the dentin, which has long been recognized as being due to a reaction of the pulp to the invasion of the dentin by caries, or to irritation caused by severe attrition, is seen only in teeth with vital pulps. It is limited by the dentin tubules leading towards the pulp from the outer margins of the affected area.

The translucent zone in the dentin was first observed by Tomes (10) who described it as "a barrier erected by nature, more or less perfect, to save the pulp from irritation."

The conception that the translucent zone is due to, and derives its character from two degenerative processes, a lime degeneration and a fat degeneration, in the dentin tubules has hitherto been generally accepted. It is thought that the plug of calcified material deposited in the peripheral ends of the tubules prevents fluid communication between the lesion and the vital contents of the tubules. The region seems to permit no penetration of stains.

Berggren (4), in his permeability experiments *in vivo* on man, found that the translucent zone is not stained by methylene blue, thus verifying earlier experimental results (Figs. 1, 2).

However, in similar experiments by the same investigator (4), but using neutral red quite another picture was obtained (Fig. 3). Only the translucent zone was stained red, the adjacent parts of the dentin taking on a yellowish hue, the major part of the tissue remaining unstained. In experiments on children 12–14 years of age no staining of the dentin of intact permanent teeth with neutral red could be observed. The results were somewhat confusing, especially as the grain size of neutral red is larger than that of methylene blue. The phenomenon can be explained only by the fact that neutral red exhibits this red shade in vital tissues only if the pH is below 6.8 (7).

The experiments with neutral red have thus shown the translucent zone to be permeable, and the pH of the tissue of the zone to be at an acid level. This fact provides the explanation of the absence of staining in the methylene blue experiments; this dye cannot be seen in a vital tissue having so low a pH, even if it has permeated the tissue.

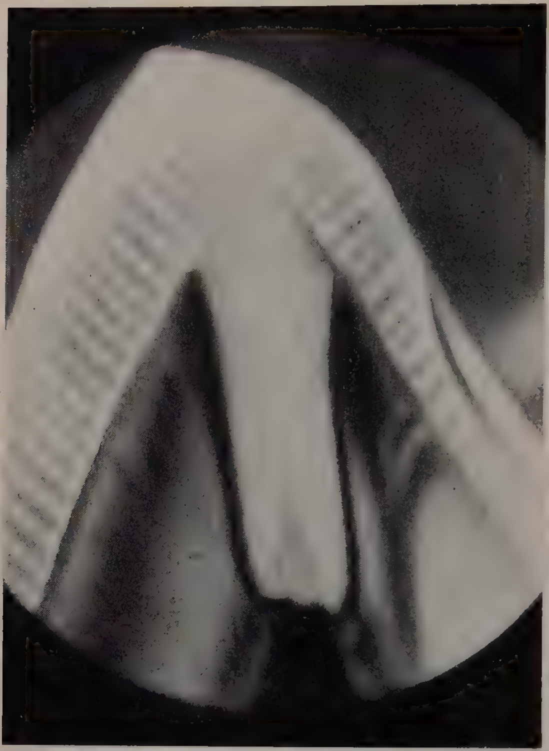

Fig. 1. Human canine. Translucent zone in the dentin beneath worn enamel, unstained by methylene blue. Reflected light. Leitz' Ultropak.

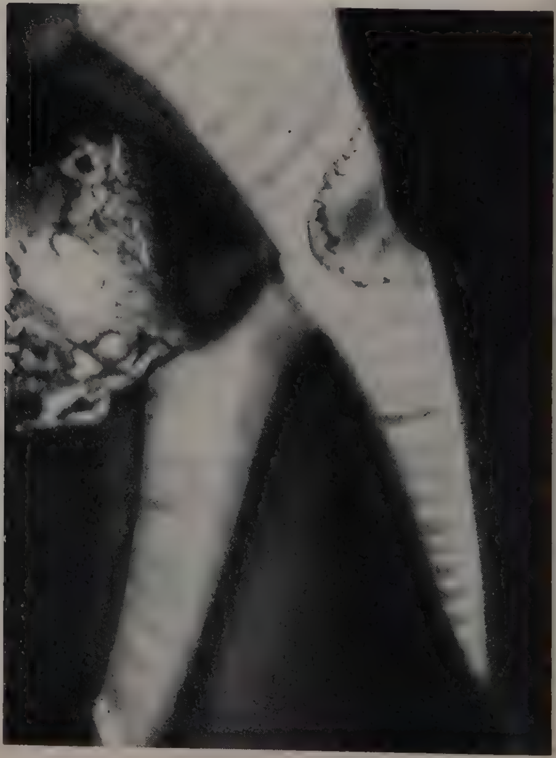

Fig. 2. Human bicuspid. Translucent zone in the dentin corresponding to carious lesion of enamel, unstained by methylene blue. Reflected light. Leitz' Ultropak.

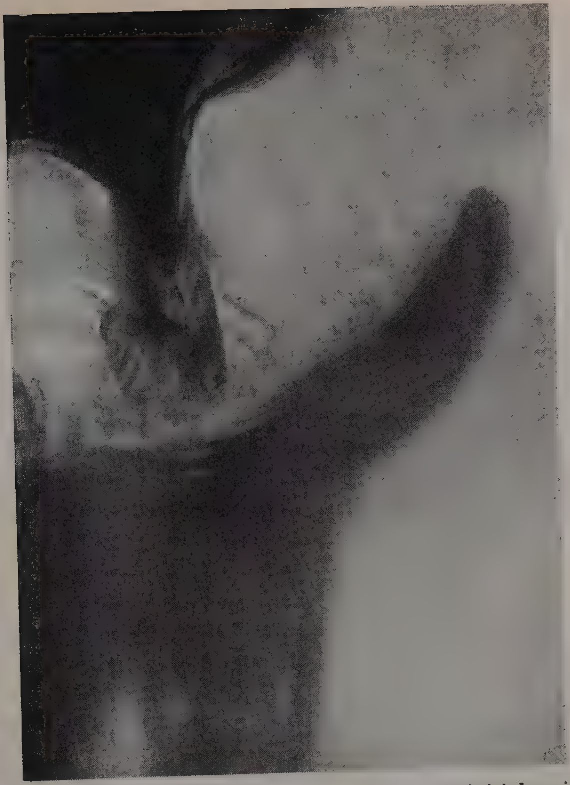

Fig. 3. Human molar. Translucent zone in the dentin beneath initial cariou lesion in a fissure, stained red by neutral red. Adjacent parts of the tissue are of a yellowish hue. Reflected light. Leitz' Ultropak.

Bartelstone (1) has recently reported the results of interesting radioautographic studies on the permeability of the dental hard tissues in man. After injection of 100 mC J^{131}, survey radioautographs of ground sections of the teeth showed an increase in uptake of dentin beneath pathological disturbances at the surface such as caries, decalcification, abrasion, erosion, and periodontoclasia. These results thus verify Berggren's findings in the permeability experiments with neutral red. Evidence of the permeability of the translucent zone would appear conclusive.

Experimental

In order to perform detail radioautographic studies of the permeability of the translucent zone, experiments were carried out on Syrian hamsters and abino rats.

Materials and methods

Twelve Syrian hamsters from different litters were put on a caries producing diet (8) for a period of six weeks, and seven albino rats on a Hoppert, Webber and Canniff diet (6) for 12 weeks. The animals were divided in three groups corresponding to subcutaneous injections of each animal with 0.5 ml of a solution of Na_2HPO_4, containing 0.11, 0.25 and 0.5 mC P^{32}.

After a lapse of 2–4 days the animals were sacrificed, and 100 micra ground sections of the jaws and teeth were prepared. With the aid of a biobjective microscope the sections were cut through carious areas and worn cusps, where translucent zones were to be found (Figs. 4–6). The sections were mounted on slides with a trace of Canada balsam. No cover glasses were used.

Three different techniques of radioautography are in use. The first consists of placing the specimen in absolute contact with the emulsion and observing the radioautograph and section separately (1, 4). In the second technique (2, 3) which is more difficult, the emulsion is run directly on to the section. Recently an emulsion has been developed which may be stripped away from its supporting base and applied directly to the section. The film is used in a stripping film technique (5, 9) which may prove to be very useful. In the two last techniques the emulsion remains on the section throughout the procedure which includes developing and, perhaps, tissue staining. Thus we have here automatically and permanently superimposed radioautographs and sections.

The first technique was applied to the first series, where Eastman Kodak Nuclear Track Plates (N. T. 1 A.), Ilford Line Film and Gevaert Dental X-ray Film were used. The time of exposure was 14 days.

In the second series the emulsion was detached from the base of Eastman Kodak Matrix Film and dissolved in water at 38°C. The emulsion was then run on to the sections and dried in hot air. The time of exposure was 8 days.

The stripping film technique was applied to the third series, where Eastman Kodak Sheet Film (N. T. B.) and Eastman Kodak Autoradiography Plates where used. The thin emulsion film was carefully loosed from the base and placed upon the water surface in a basin. The slide with the mounted sections was placed under and brought up to the film which was thus stretched over the sections; it was then dried. The exposure time was 10 days.

Results

The first method, where the specimen was placed in absolute contact with the emulsion, proved to be less convenient for this purpose. It was difficult, to say the least, to achieve suitable orientation of the sections and developed emulsion. Detail studies were therefore impossible to perform.

Belanger & Leblond's (2, 3) method and the stripping film technique indicated by Pelc (9) and Boyd & Williams (5) proved to be more suitable in our experiments where the uptake of radiophosphorus by the dental hard tissues is relatively low. However, to produce radioautographs of practical value it was necessary to use longer exposure times in the stripping film method.

The results are given in Figs. 4, 5 and 6 where it will be clearly seen that the translucent zones in the dentin corresponding to affected areas of the enamel have taken up the injected radiophosphorus to a far greater degree than the adjacent parts of the tissue.

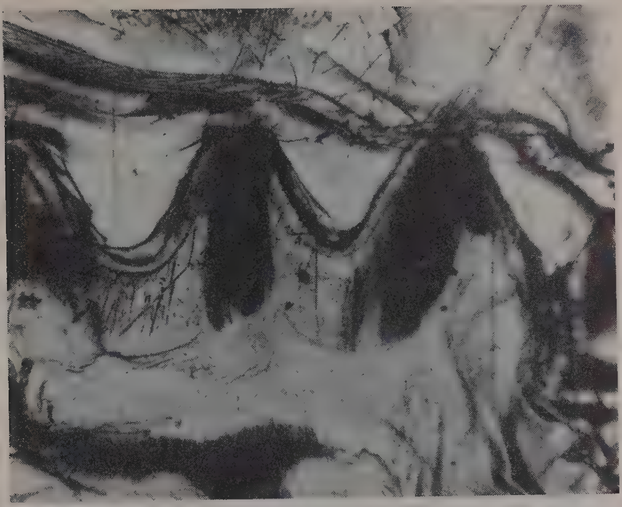

Fig. 4. Rat teeth. Uptake of P^{32} in translucent zone in the dentin beneath worn cusps. Transmitted light. 3.5 × 6.

Discussion

The classical conception in which the translucent zone in the dentin is seen as an impermeable barrier between lesions on the tooth surface and the vital contents of the dentinal tubules has already been proved erroneous (4). Experience has shown radiophosphorus to be an important research tool in the study of the mineral metabolism of the dental hard tissues, and its further application in the experimental inquiry into the development of the translucent zone will be awaited with interest. It is, above all, important to study this development in carious teeth, where the translucent zone always precedes the carious attack. This is one of the most interesting of the innumerable problems occupying the attention of dental research workers, and it is here that the use of radioactive isotopes will, in all probability, prove of the greatest value.

The isotopes have been put at our disposal by the Nobel Institute of Physics and the Isotope Committee of the Research Councils.
The photomicrographs have been prepared by GUNNAR BERGMAN, Assistant Professor of histopathology at the Royal School of Dentistry, Stockholm.

Dept of Operative Dentistry, Royal School of Dentistry, Stockholm.

REFERENCES: 1. **Bartelstone, H. J.,** Survey Use of Radioactive Isotopes in Dentistry. New York J. Dent. *20*: 280–350, 1950. — 2. **Belanger, L. F.,** and **Leblond, C. P.,** A Method for Locating Radioactive Elements in Tissues by Covering Histological Sections with a Photographic Emulsion. Endocrinology *39*: 8, 1946. — 3. **Belanger, L. F.,** A Method for Routine Detection of Radiophosphates and other Radioactive Compounds in Tissues. Anat. Rec. *107*: 149, 1950. — 4. **Berggren, H.,** Permeability of Enamel and Dentine. Sv. Tandl.-Tidskr. *40*: 1 B, 1947. — 5. **Boyd, G. A.,** and **Williams, A. I.,** Stripping Film Tech-

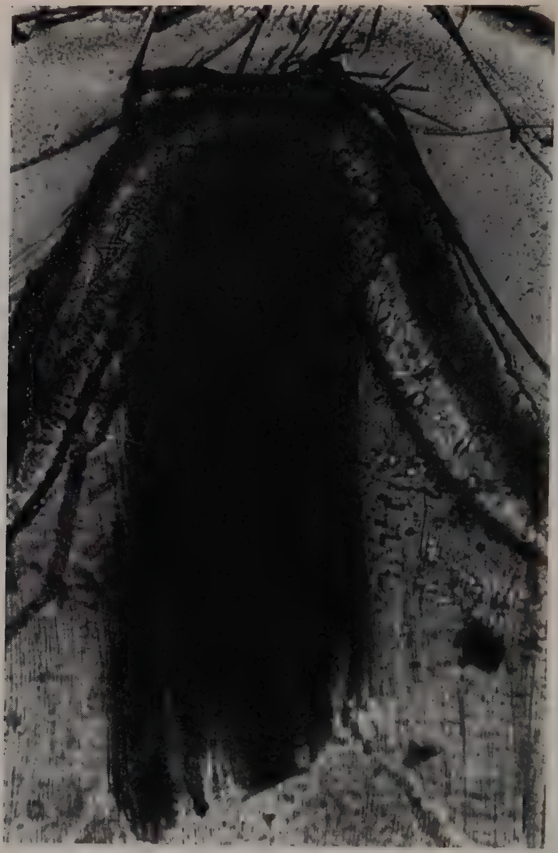

Fig. 5. Rat tooth. Uptake of P^{32} in translucent zone in the dentin beneath worn cusp. Transmitted light. 12 × 6. Cf. Fig. 1.

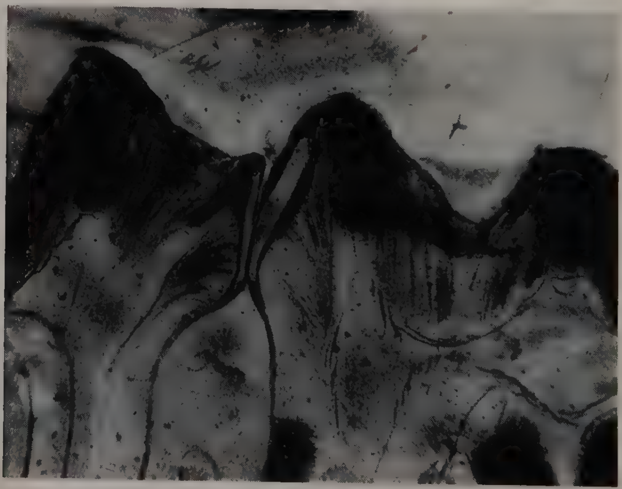

Fig. 6. Rat teeth. Uptake of P^{32} in translucent zone in the dentin beneath worn cusps. Transmitted light. 3.5 × 6.

niques for Histological Autoradiographs. Proc. Soc. Exptl. Biol. Med. *69*: 225, 1948. — 6. **Hoppert, C. A., Webber, P. A.,** and **Canniff, T. L.,** The Production of Dental Caries in Rats Fed on Adequate Diet. J. D. Res. *12*: 161, 1932. — 7. **Karrer, P.,** Organic Chemistry. New York 1947. — 8. **Keyes, P. H.,** Dental Caries in the Syrian Hamster. J. D. Res. *25*: 341, 1946. — 9. **Pelc, S. R.,** Autoradiographic Technique. Nature *160*: 749, 1947. — 10. **Tomes, J.,** Dental Physiology and Surgery. London 1948.

Tryckt den 6 februari 1952

Uppsala 1952. Almqvist & Wiksells Boktryckeri AB

ARKIV FÖR FYSIK Band 4 nr 42

Communicated 12 September 1951 by OSKAR KLEIN

On the determination of eigenvalues and eigenphase for the Yukawa potential

By KARL-GUSTAV FOGEL

The treatment of the connection between eigenphase and potential presented by JOST [1] and BARGMANN [2] makes it possible to determine the eigenvalues as well as the eigenphases for a given potential by analogous procedures. In this paper the method is applied to the Yukawa potential. The Schroedinger equation for $l=0$ is solved by an expansion in terms of the binding constant. The eigenvalues appear as zeros of a real transcendental function of the energy parameter and the binding constant; the eigenphase, on the otherhand, as the argument of a complex function of these variables. The first eigenvalue corresponding to zero energy is calculated to the fifth approximation. A computation is made of the second approximation of the eigenphase. The results are compared with those of KÄLLÉN and HULTHÉN.

General

In a two-particle problem ψ/x is the radial part of the wave function for $l=0$. The differential equation for ψ is then

$$\psi'' + (a + b\,v(x))\,\psi = 0 \tag{1}$$

where $v(x)$ is the interaction potential, b the binding constant and a the energy parameter.

Furthermore we assume that

(2 a) $v(x)$ is continous and bounded when $x \geqq \delta > 0$,

(2 b) $\int\limits_0^\infty x\,|v(x)|\,dx$ is finite.

Putting [3], [4][1]

$$\psi = \sum_{\nu=0}^{\infty} \psi_\nu \tag{3}$$

equation (1) can be replaced by the following recurrent system

---

[1] HELLUND [5] uses a similar expansion, but his solution is not convergent (cf. [3]).

$$\begin{aligned} &\psi_0'' + a\,\psi_0 = 0 \\ &\psi_\nu'' + a\,\psi_\nu = -\,b\,v(x)\,\psi_{\nu-1} \qquad (\nu = 1, 2, \ldots). \end{aligned} \tag{4}$$

If the series (3) is convergent it is a solution of equation (1).

We shall now proceed to consider the physical solutions.

A. Discrete spectrum

In this case $a < 0$, and we may therefore put $a = -\,k^2$. The boundary conditions

$$\psi(0) = \psi(\infty) = 0 \tag{5}$$

together with conditions (2) determine, apart from an arbitrary constant factor, the following asymptotic solution of equation (1)

$$\psi_{as} = e^{-kx}. \tag{6}$$

In order to find the solution of (4) with the asymptotic form (6) we choose (cf. [2], [3], [6, p. 292])

$$\psi_0 = e^{-kx} \tag{7}$$

$$\psi_\nu = -\,b\,e^{-kx} \int_x^\infty e^{2kx_1}\,d\,x_1 \int_{x_1}^\infty e^{-kx_2}\,v(x_2)\,\psi_{\nu-1}(x_2)\,d\,x_2 \qquad (\nu = 1, 2, \ldots) \tag{7'}$$

i.e.

$$\begin{aligned} \psi_\nu = (-1)^\nu\,b^\nu\,e^{-kx} \int_x^\infty e^{2kx_1}\,d\,x_1 \int_{x_1}^\infty e^{-2kx_2}\,v(x_2)\,d\,x_2 \cdots \\ \cdots \int_{x_{2\nu-2}}^\infty e^{2kx_{2\nu-1}}\,d\,x_{2\nu-1} \int_{x_{2\nu-1}}^\infty e^{-2kx_{2\nu}}\,v(x_{2\nu})\,d\,x_{2\nu}. \end{aligned} \tag{7''}$$

When ψ_ν is determined from (7) and (7″) ψ has the asymptotic behaviour (6) and constitutes a continuous and bounded solution to equation (1) [2, Appendix (a)]. Defining $\psi(0) = f(b, 2\,k)$, we have

$$\begin{aligned} f(b, 2\,k) = 1 + \sum_{\nu=1}^\infty (-1)^\nu\,b^\nu \int_0^\infty e^{2kx_1}\,d\,x_1 \int_{x_1}^\infty e^{-2kx_2}\,v(x_2)\,d\,x_2 \cdots \int_{x_{2\nu-2}}^\infty e^{2kx_{2\nu-1}}\,d\,x_{2\nu-1} \cdot \\ \cdot \int_{x_{2\nu-1}}^\infty e^{-2kx_{2\nu}}\,v(x_{2\nu})\,d\,x_{2\nu}. \end{aligned} \tag{8}$$

The condition

$$f(b, 2\,k) = 0$$

then determines the eigenvalues.

If we now consider the Yukawa potential

$$v(x) = e^{-x}/x$$

we get from (7″)

$$(9)\quad \psi_\nu = (-1)^\nu b^\nu e^{-kx} \int\limits_x^\infty e^{2kx_1}\,dx_1 \int\limits_{x_1}^\infty \frac{e^{-(2k+1)x_2}}{x_2}\,dx_2 \cdots \int\limits_{x_{2\nu-2}}^\infty e^{2kx_{2\nu-1}}\,dx_{2\nu-1} \int\limits_{x_{2\nu-1}}^\infty \frac{e^{-(2k+1)x_{2\nu}}}{x_{2\nu}}\,dx_{2\nu}.$$

In order to simplify the above integrals we shall consider the integral

$$(10)\qquad I = \int\limits_y^\infty e^{2ky_1}\,dy_1 \int\limits_{y_1}^\infty \frac{e^{-(2k+r)y_2}}{y_2}\,dy_2.$$

After differentiating it with respect to r, the y_1 and y_2 integrations can be carried out and we obtain

$$(10')\qquad I = \int\limits_r^\infty \frac{e^{-sy}}{s(s+2k)}\,ds.$$

Using this transformation we get

$$(11)\qquad \psi_\nu = (-1)^\nu b^\nu e^{-kx} \int\limits_1^\infty \frac{ds_1}{s_1(s_1+2k)} \int\limits_{s_1}^\infty \frac{ds_2}{(s_2+1)(s_2+1+2k)} \cdots \int\limits_{s_{\nu-2}}^\infty \frac{ds_{\nu-1}}{(s_{\nu-1}+\nu-2)(s_{\nu-1}+\nu-2+2k)} \int\limits_{s_{\nu-1}}^\infty \frac{e^{-(s_\nu+\nu-1)x}}{(s_\nu+\nu-1)(s_\nu+\nu-1+2k)}\,ds_\nu$$

which gives

$$(12)\qquad f(b, 2k) = 1 + \sum_{\nu=1}^\infty (-1)^\nu b^\nu \int\limits_1^\infty \frac{ds_1}{s_1(s_1+2k)} \int\limits_{s_1}^\infty \frac{ds_2}{(s_2+1)(s_2+1+2k)} \cdots \int\limits_{s_{\nu-2}}^\infty \frac{ds_{\nu-1}}{(s_{\nu-1}+\nu-2)(s_{\nu-1}+\nu-2+2k)} \int\limits_{s_{\nu-1}}^\infty \frac{ds_\nu}{(s_\nu+\nu-1)(s_\nu+\nu-1+2k)}.$$

The integral coefficients are quite complicated for arbitrary values of k. But when $k = 0$ the first five integrals permit a not too difficult computation. Denoting the result $f(b, 0; 5)$ we obtain

$$f(b, 0; 5) = 1 - b + (1 - \log 2) b^2 - (1 + \log 2 - \tfrac{3}{2} \log 3) b^3 + \tag{13}$$

$$+ \{1 - 4 \log 2 + \tfrac{3}{2} \log 3 - \tfrac{1}{2} \log^2 2 + \tfrac{1}{2} \log^2 3 - \frac{\pi^2}{12} + 2 \Phi(\tfrac{1}{2}) - \Phi(\tfrac{1}{3})\} b^4 -$$

$$- \{1 + 4 \log 2 - \tfrac{5}{2} \log 5 + 2 \log^2 2 - \tfrac{1}{2} \log 2 \cdot \log 3 - 2 \Phi(\tfrac{2}{3}) + \Phi(\tfrac{1}{2}) + 2 \Phi(\tfrac{1}{3}) -$$

$$- \Phi(\tfrac{1}{4})\} b^5$$

where

$$\Phi(z) = \int_0^z \frac{\log(1 + t)}{t} \, dt. \tag{14}$$

The smallest root of $f(b, 0; \nu) = 0$ for the first five successive values of ν is given in Table I.

Table I.

ν	1	3	4	5
b	1	1.600784	1.689830	1.679147

Using a variational method HULTHÉN and LAURIKAINEN [7] found for the lowest eigenvalue

$$b = 1.679820.$$

A comparison between this value for b and the values in Table I gives us some information as to the convergence when $f(b, 2k)$ is approximated by $f(b, 2k; \nu)$.

B. Continuous spectrum

Now $a > 0$, and we may put $a = k^2$. The boundary condition is

$$\psi(0) = 0. \tag{15}$$

In this case the solution satisfying (15) has the asymptotic form

$$\psi_{as} = \sin(kx + \delta) \tag{16}$$

where δ is the eigenphase. In order to determine it we shall look for two solutions of equation (1) with an asymptotic form [1]

$$\psi_{as}^{\mathrm{I}} = e^{-ikx} \tag{17 a}$$

$$\psi_{as}^{\mathrm{II}} = e^{ikx}. \tag{17 b}$$

As in the previous case we obtain

$$\text{(18 a)} \qquad \psi^{\mathrm{I}} = e^{-ikx}\left(1 + \sum_{\nu=1}^{\infty}(-1)^{\nu} b^{\nu} \int_{x}^{\infty} e^{2ikx_1}\, dx_1 \cdot \right.$$

$$\left. \cdot \int_{x_1}^{\infty} e^{-2ikx_2}\, v(x_2)\, dx_2 \cdots \int_{x_{2\nu-2}}^{\infty} e^{2ikx_{2\nu-1}}\, dx_{2\nu-1} \int_{x_{2\nu-1}}^{\infty} e^{-2ikx_{2\nu}}\, v(x_{2\nu})\, dx_{2\nu}\right) \cdot$$

$$\text{(18 b)} \qquad \psi^{\mathrm{II}} = \overline{\psi^{\mathrm{I}}}.$$

In order to satisfy condition (15) we choose two complex constants α and β, such that

$$\text{(19)} \qquad \alpha\, \psi^{\mathrm{I}}(0) + \beta\, \psi^{\mathrm{II}}(0) = 0.$$

Then

$$\text{(20)} \qquad \psi = \alpha\, \psi^{\mathrm{I}} + \beta\, \psi^{\mathrm{II}}$$

is a solution of equation (1) satisfying condition (15). As before we put

$$\text{(21)} \qquad \psi^{\mathrm{I}}(0) = f(b,\, 2ik)$$

and obtain (apart from an arbitrary real factor $\neq 0$) when taking into consideration (18) and (19)

$$\text{(22)} \qquad \alpha = \overline{\beta} = \tfrac{1}{2}\, e^{i\left(\frac{\pi}{2} - \delta\right)}$$

where

$$\text{(23)} \qquad \operatorname{tg} \delta = \frac{Im\,\{f(b,\, 2ik)\}}{Re\,\{f(b,\, 2ik)\}}.$$ [1]

The equations (20), (22) and (17) give

$$\text{(24)} \qquad \psi_{as} = \sin(kx + \delta)$$

and thus δ, defined in equation (23), is the asymptotic phase. The Yukawa potential yields (cf. equation (12))

$$\text{(25)} \qquad f(b,\, 2ik) = 1 + \sum_{\nu=1}^{\infty}(-1)^{\nu} b^{\nu} \int_{1}^{\infty} \frac{d s_1}{s_1(s_1 + 2ik)} \int_{s_1}^{\infty} \frac{d s_2}{(s_2 + 1)(s_2 + 1 + 2ik)} \cdots$$

$$\cdots \int_{s_{\nu-2}}^{\infty} \frac{d s_{\nu-1}}{(s_{\nu-1} + \nu - 2)(s_{\nu-1} + \nu - 2 + 2ik)} \int_{s_{\nu-1}}^{\infty} \frac{d s_{\nu}}{(s_{\nu} + \nu - 1)(s_{\nu} + \nu - 1 + 2ik)}.$$

---

[1] After the manuscript had been finished, Prof. L. HULTHÉN informed me, that similar results have been obtained by JOST and PAIS (Phys. Rev. 82, 840 (1951)).

The second approximation is

$$(26)\qquad f(b, 2ik; 2) = 1 + i\frac{b}{2k}\log(1+2ik) - $$

$$-\frac{b^2}{4k^2}\left\{\tfrac{1}{2}\log^2(1+2ik) + \frac{\pi^2}{12} + \Phi\left(\frac{1-2ik}{1+2ik}\right) - 2\Phi\left(\frac{1}{1+2ik}\right)\right\}.$$

It is of interest to note that formula (14) after a change of variable becomes

$$(27)\qquad \Phi(z) = \int\limits_0^{\log(1+z)} \frac{t\,e^t}{e^t-1}\,dt$$

which for $|\log(1+z)| < 2\pi$, gives

$$(27')\qquad \Phi(z) = \log(1+z) + \tfrac{1}{4}\log^2(1+z) - \sum_{\nu=1}^{\infty}(-1)^\nu \frac{B_\nu \log^{2\nu+1}(1+z)}{(2\nu+1)!}$$

where B_ν are Bernoullis numbers (cf. [8] p. 127). The expansion (27) converges rapidly for small values of $|\log(1+z)|$ (≤ 1.5).

The numerical values of tg δ calculated from (23) and (26) are given in Table II for certain values of k and b. For the sake of comparison the corresponding values of the second approximation obtained by Källén [4] and the values derived from Hulthén's variational formula [4], [9] are included.

Table II.

$k \diagdown b$		0.25	0.50	0.75	1.00	1.25	1.50	1.75	2.00
2.0	tg δ	0.0901	0.184	0.282	0.386	0.496	0.617	0.752	0.908
	tg δ_K	0.0900	0.183	0.279	0.38	0.48	0.59	0.69	0.80
	tg δ_H	0.0908	0.186	0.287	0.39	0.50	0.62	0.75	0.88
1.5	tg δ	0.0986	0.203	0.313	0.431	0.558	0.695	0.865	1.015
	tg δ_K	0.098	0.20	0.31	0.42	0.54	0.67	0.80	0.93
	tg δ_H	0.098	0.22	0.35	0.50	0.65	0.80	0.94	1.08
1.0	tg δ	0.1052	0.220	0.345	0.480	0.622	0.766	0.897	0.984
	tg δ_K	0.105	0.219	0.342	0.47	0.62	0.77	0.92	1.09
	tg δ_H	0.104	0.218	0.345	0.49	0.68	0.92	1.27	1.85
0.5	tg δ	0.0943	0.205	0.333	0.473	0.607	0.687	0.639	0.376
	tg δ_K	0.0934	0.202	0.32	0.46	0.61	0.78	0.96	1.16
	tg δ_H	0.0944	0.209	0.35	0.55	0.84	1.33	2.40	7.14

We notice that the second approximation obtained above gives on the whole the same results as Källén's approximation.

The author expresses his gratitude to Prof. Lamek Hulthén, Dr. G. af Hällström and Dr. G. Källén for valuable criticism.

Åbo Akademi, Åbo, Finland.

REFERENCES. 1. **Jost, R.,** Helv. Phys. Acta 20, 256 (1947). — 2. **Bargmann, V.,** Rev. Mod. Phys. 21, 488 (1949). — 3. **Fröberg, C.-E.,** Ark. Mat. Astr. o. Fysik Bd. 34 A, N:o 28 (1948). — 4. **Källén, G.,** Arkiv f. Fysik 2, N:o 6 (1950). — 5. **Hellund, E. J.,** Phys. Rev. 59, 398 (1941). — 6. **Courant-Hilbert,** Methoden d. math. Physik I. Berlin (1931). — 7. **Hulthén, L.** and **Laurikainen, K. V.,** Rev. of Mod. Physics, 23, 1–9 (1951). — 8. **Whittaker-Watson,** Modern Analysis 4th ed. Cambridge (1950). — 9. **Hulthén, L.,** Ark. Mat. Astr. o. Fysik Bd. 35 A, N:o 25 (1948).

Tryckt den 26 februari 1952

Uppsala 1952. Almqvist & Wiksells Boktryckeri AB